

**Prediction of sub-seismic faulting and fracturing in Mesozoic
carbonate rocks, Southern Gulf of Mexico**

Ulises de Jesus Rodriguez del Angel

Submitted in accordance with the requirements for the degree of
Doctor of Philosophy

The University of Leeds

School of Earth and Environment

January, 2021

The candidate confirms that the work submitted is his/her own and that appropriate credit has been given where reference has been made to the work of others.

This copy has been supplied on the understanding that it is copyright material and that no quotation from the thesis may be published without proper acknowledgement.

The right of Ulises de Jesus Rodriguez del Angel to be identified as Author of this work has been asserted by him in accordance with the Copyright, Designs and Patents Act 1988.

© 2021 The University of Leeds and Ulises de Jesus Rodriguez del Angel

Acknowledgements

This work is dedicated to:

My beloved sons Ulises and José Manuel....

Walk on through the wind, walk on through the rain though your dreams be tossed and blown. Walk on with hope in your heart and you'll never walk alone

My best friend, wife and life partner Myriam.....

My parents Carlos and Alba Guadalupe.....

My brothers Carlos and Ariel.....

“Music was my first love, and it will be my last.

Music of the future and music of the past”

“To live without my music would be impossible to do,
In this world of troubles, my music pulls me through”

John Miles, 1976

I want to thank my supervisors Douglas Paton and Estelle Mortimer for their guidance, advisory, support, patience and the friendly and respectful treatment during all this time.

Thanks to my examiners, Dr Piroska Lorinczi, Prof. Agust Gudmundsson and Dr. Richard Collier for their support, time, feedback and making the Viva an unforgettable experience.

Thanks to my PEMEX supervisor, MSc Rolando Peterson, for his friendship, time and support.

Thanks to PEMEX E&P for giving me the opportunity to carry out this research and provide all the required information.

This work has been funded by CONACYT and could not have occurred without their generous contribution.

Thanks to Aurelio, Rosi, Karmina, Jesus, Arely y Raul for their love and support.

No words are enough to express my gratitude to Sergio Gámez for his priceless support, great friendship and all the good times we shared together during our time in Leeds.

Mi gratitud eterna a mi tía Gris Gómez por su gran cariño, infinitas atenciones y hospitalidad durante mi estancia en la Ciudad de México.

Thanks to Erika Carmona for her great support and patience during the entire MSc and PhD processes.

Thanks to my dear friends Martin Lima and Christian Aragon for their friendship and disinterested support during all this time.

This work would not have been possible without the disinterested support, advise and contribution of many people, so I take this opportunity to thank and mention them in no particular order: Juan Rogelio Ramos, Guillermo Mora, Alberto Abarca, Alberto Santana, Juanita Salas, Jesus Camacho, David Corral, Mario Aranda, Irasema Olvera, Mark G. Rowan, Pete Bretan, Ricardo Trejo, Mauricio Galindo, Elsa Zavala, Pedro Peña, Laura Sanchez, Amista Antonio Cervantes, Luis Lauro Villanueva, Bernardo Matias, Luis Vega Muñoz, Saleh Al-Qatani, Nick Shaw, Simon Oldfield, Ben Craven, James Norcliffe, Hector Lopez Cespedes, Jose Alfredo "Chepe" Guerrero, Victor Garduza Rueda, Ricardo "Mezcalino" Dominguez.

Finally, I would also like to thank my dear Cuervos friends for all those great and unforgettable evenings together watching and playing football, sharing a drink, and having a really good time. My best wishes to you all.

Abstract

Currently, a large proportion of conventional oil reserves are contained within hydrocarbon systems primarily composed of naturally fractured carbonate reservoirs. Natural fractures result from the complex interaction between multiple geological factors and may enhance reservoir permeability by facilitating oil and gas flow. The Southern Gulf of Mexico is an area with important naturally fractured Mesozoic carbonate reservoirs as well as new prospective areas that need to be assessed in order to maximize hydrocarbon exploration. A key limitation is how to predict more accurately fracture orientation and density in undrilled areas.

This study proposes a multidisciplinary methodology intended to predict natural fracturing in carbonate reservoirs that can be applied at early stages of the hydrocarbon exploration process. This methodology combines geological and geophysical tools and techniques such as seismic interpretation, 2D structural restoration, geometrical seismic attribute analysis, well data analysis and numerical modelling (fracture modelling).

Orientations of modelled fractures show a good correlation with orientations of lineaments observed in mapped surfaces and depth slices where ant-tracking attribute was applied as well as with orientations measured in FMI and core samples. Regarding to fracture intensity, a good degree of correlation is observed between Maximum Coulomb Shear Stress (MCSS) and modelled strain distribution, which are two parameters used as a proxy for fracture intensity. Likewise, there is a moderate to good degree of correlation between MCSS and fracture intensity obtained from borehole data.

These results indicate that a combination of fracture modelling, structural seismic attributes and geomechanical modelling has a good potential to estimate location, orientation and intensity of medium-scale fracture sets in areas where borehole data is scarce or null. Reliability of these estimations depends mainly on the amount and quality of borehole data, quality of seismic data as well as complexity of structural geology; in the case of fracture orientation, the estimation is of quantitative nature whereas for fracture intensity, the estimation is rather qualitative.

Table of Contents

Acknowledgements.....	iii
Abstract.....	v
Table of Contents.....	vi
List of Tables.....	xii
List of Figures	xiii
Abbreviations.....	xxvi

Chapter 1 Introduction 1

1.1 Rationale.....	1
1.2 Aim and objectives	2
1.3 Location of the study area	3
1.4 Layout of thesis	4

Chapter 2 Fundamentals of Rock Fractures..... 6

2.1 Natural rock fractures	6
2.2 Stress and deformation definitions	7
2.2.1 Principal stresses.....	9
2.3 Rock failure	10
2.3.1 Fracture initiation and propagation.....	10
2.3.2 Fracture termination.....	11
2.4 Classification of fractures	12
2.5 Geological controls in fractured carbonates	14
2.5.1 Lithology.....	15
2.5.2 Texture.....	16
2.5.3 Porosity	18
2.5.4 Pore pressure	19
2.5.5 Bed thickness.....	20
2.5.6 Effects of structural position	22
2.5.7 Deformation mechanism	23
2.6 Fractured reservoirs	24
2.6.1 Mechanical and fracture Stratigraphy	25
2.6.2 Fracture occurrence.....	25
2.6.2.1 Fault-related fractures	25
2.6.2.2 Fold-related fractures	27
2.7 Salt tectonics and fracture development	28
2.8 Fracture detection in subsurface	30
2.9 Fracture prediction	31

2.10 Summary	32
Chapter 3 Geological Setting of Southern Gulf of Mexico	34
3.1 Overview	34
3.2 Stratigraphy	37
3.3 Tectonic Evolution of South-eastern Mexico	40
3.3.1 Gulf of Mexico Opening Phase (210-137 Ma).	42
3.3.2 Cretaceous Post-Sea floor spreading (137 – 84 Ma).	43
3.3.3 Late Cretaceous - Middle Eocene (84 to 41 Ma).....	45
3.3.4 Oligocene – Late Miocene (33 to 5.3 Ma)	46
3.3.5 Late Miocene - Present day (5.3 to 0 Ma)	49
3.4 Deformational events in Southern Gulf of Mexico	50
3.4.1 D1 (Late Jurassic- Late Cretaceous):.....	50
3.4.2 D2 (Late Eocene-Oligocene):.....	52
3.4.3 D3 (Middle-Late Miocene):	53
3.4.4 D4 (Late Miocene-Present day):	54
3.5 Summary	55
Chapter 4 Structural evolution of salt-related traps in Southern Gulf of Mexico	56
4.1 Introduction.....	56
4.1.1 Salt-related hydrocarbon traps	59
4.1.2 Regional Structural Setting	61
4.2 Dataset and Methods	68
4.2.1 Seismic Data	68
4.2.2 Well Data	73
4.2.3 Methodology.....	76
4.2.3.1 Seismic Interpretation.....	77
4.2.3.2 2D Kinematic Modelling.....	85
4.2.3.3 Integration and Analysis of Results	86
4.3 Results	87
4.3.1 Seismic interpretation.....	87
4.3.1.1 Structure maps	87
4.3.1.2 Thickness maps.....	92
4.3.1.3 Structural Restoration of 2D Seismic Cross-Sections..	100
Section A-A'	102
Section B-B'	107

Section C-C'	111
4.3.1.4 Characterization of structural traps	115
4.4 Discussion	120
4.4.1 Structural style of traps	120
4.4.2 Structural evolution	122
4.4.2.1 Anticline A	122
4.4.2.2 Anticline B	125
4.5 Conclusions	127
Chapter 5 Analysis of well data for fracture interpretation	128
5.2. Introduction	128
5.3 Dataset and Methods	129
Well logs	129
Lithological descriptions	129
Biostratigraphic analysis	129
5.3.1 Methods	130
5.3.1.1 Cutting/core samples analysis	130
5.3.1.2 Well log data	131
5.3.2 Image well logs	131
5.4 Stratigraphy	133
5.4.1 Late Cretaceous (93-66 Ma)	135
5.4.2 Middle Cretaceous (113-93 Ma)	135
5.4.3 Early Cretaceous (145-113 Ma)	136
5.4.4 Late Jurassic Tithonian (152-145 Ma)	137
5.4.5 Late Jurassic Kimmeridgian-Oxfordian? (163?-152 Ma)	138
5.5 Fracture analysis in core samples	140
5.6 Image log analysis	150
5.6.1 W-1	150
5.6.2 W-2	156
5.7 Discussion	162
5.7.1 Fracture intensity vs lithology	162
5.7.2 Fracture intensity vs Texture	163
5.7.3 Fracture intensity vs Bed thickness	164
5.7.4 Fracture intensity vs faulting	167
5.8 Integration of core and well log data	168
5.9 Conclusions	169

Chapter 6 Analysis of structural seismic attributes and geomechanical modelling for fracture interpretation	170
6.1 Introduction.....	170
6.2 Background	172
6.2.1 Seismic Data.....	172
6.2.2 Reverse Time Migration (RTM).....	172
6.2.3 Structural Seismic Attributes	173
Curvature.....	174
Variance	176
Ant-tracking.....	179
6.3 Methods.....	180
6.3.1 Seismic attributes.....	180
6.3.2 Geomechanical Modelling.....	185
6.4 Results	187
6.4.1 Curvature/Variance analysis	187
6.4.2 Ant-tracking analysis	193
6.4.3 Cross-Section Analysis	196
W-1	197
W-2	197
W-3	198
6.4.4 Depth slices analysis.....	202
6.4.5 Geomechanical Modelling (GM).....	202
Anticline A.....	204
Anticline C	205
Anticline B.....	206
6.4.6 Fault Response Modelling (FRM).....	208
6.5 Integration of strain and attribute maps	211
6.6 Discussion	215
6.6.1 Role of structural position.....	216
6.6.2 Role of mechanism of deformation.....	216
6.6.2.1 Anticline A.....	217
6.6.2.2 Anticline B.....	218
6.6.3 Fracture intensity.....	220
6.6.4 Fracture orientation	221
6.7 Conclusions.....	224

Chapter 7 Modelling of sub-seismic fractures in Southern Gulf Of Mexico.....	225
7.1 Introduction	225
7.1.1 Elastic Dislocation Background.....	226
7.2 Methods	228
7.2.1 Elastic dislocation (ED) modelling.....	228
7.2.2 Seismic interpretation.....	231
7.3 Results	232
7.3.1 Anticline B.....	236
7.3.1.1 Fracture orientation	237
Top Kimmeridgian	237
Top Tithonian.....	239
Top Cretaceous	240
7.3.1.2 Fracture Intensity.....	242
Top Kimmeridgian	242
Top Cretaceous	244
7.3.2 Anticline A.....	248
7.3.2.1 Fracture orientation	249
Top Kimmeridgian	249
Top Tithonian.....	250
Top Cretaceous	250
7.3.2.2 Fracture intensity	251
Top Kimmeridgian	251
Top Tithonian.....	252
Top Cretaceous	252
7.4 Discussion.....	255
7.4.1 Comparison between modelled, seismic attributes and well data.....	255
7.4.1.1 Fracture orientation	255
7.4.1.2 Fracture density.....	256
7.5 Conclusions.....	259
 Chapter 8 Integration and testing of a multidisciplinary methodology for fracture prediction.....	 260
8.1 Introduction	260
8.2 Background	261
8.2.1 Integration of techniques.....	261

8.2.1.1	Seismic Interpretation.....	261
8.2.1.2	2D Restoration.....	263
8.2.1.3	Analysis of borehole data	264
8.2.1.4	Structural seismic attributes.....	265
8.2.1.5	Geomechanical Modelling	266
8.2.1.6	Elastic Dislocation (ED) Modelling.....	267
8.2.2	Methodology for assessment of reservoir rock.....	269
8.2.3	Estimation of probability of geological success (PoS)	269
8.3	Methodology Test.....	274
	Anticline C.....	274
8.3.1	Assessment of reservoir rock.....	276
8.3.1.1	Presence of reservoir rock.....	276
8.3.1.2	Quality of reservoir rock.....	279
8.3.2	Comparison with borehole data.....	288
8.4	Discussion	291
8.5	Conclusions.....	295
Chapter 9	Conclusions and Further Work	296
9.1	Conclusions.....	296
	1. <i>What is the influence of structural evolution on natural fracturing of carbonate rocks?</i>	296
	1. <i>What are the geological factors that control natural fracturing within the study area?</i>	296
	2. <i>How can geological and geophysical data be integrated for fracture prediction?</i>	297
	3. <i>Assessment of reservoir rock during prospect evaluation.</i>	297
9.2	Recommendations for future work.....	298
	1. <i>Influence of diagenesis on natural fracturing.</i>	298
	2. <i>Definition of mechanical and fracture stratigraphy from borehole data.</i>	298
	Bibliography	299

List of Tables

Table 1.1. Thesis layout.....	5
Table 2.1: Main factors controlling fracturing (modified from Hunt et al., 2009).....	6
Table 2.2: Causes for overpressure (Kopf, 2002).....	20
Table 3.1. Summary of the elements of Petroleum systems present in South Eastern Basins (Adapted from CNH, 2014).....	37
Table 5.1. Summary of well logs from the boreholes within the study area.	129
Table 5.2. Summary of descriptions from the core samples available for this study.	130
Table 5.3. Paragenetic chart from Core-1, W-1.	142
Table 5.4. Paragenetic chart from Core-1C, W-2.	144
Table 5.5. Paragenetic chart from Core-3, W-2.	145
Table 5.6. Paragenetic chart from Core-4, W-2.	146
Table 5.7. Paragenetic chart from Core-3, W-3.	148
Table 5.8. Paragenetic chart from Core-4, W-3.	149
Table 5.9. Comparison between lithology from cores, fracture intensity and Young's modulus for the study area.	162
Table 6.1. Parameters used for seismic attribute calculations.....	181
Table 6.2. Parameters used for strain calculation in Geomechanical Modelling.	204
Table 7.1. Geomechanical parameters used for ED modelling.	230
Table 7.2. Comparison of the degree of correlation between predicted fracture orientation and intensity and results obtained from borehole data, ant-tracking attribute and geomechanical modelling for anticlines A and B.....	258
Table 8.1. Example of a CEROE format used to calculate the probability of geological success of an exploratory well proposal.....	272
Table 8.2. Proposed format for assessment of reservoir rock, where the main elements, Presence and Quality, are subdivided into different categories and sub-elements. Numerical values are assigned according to the amount, type, quality and level of confidence of data (top right).	273
Table 8.3. Geomechanical parameters used for fracture modelling of borehole W-4.	276
Table 8.4. Assessment of the presence and quality of reservoir rock in the proposed borehole W-4 for Late Cretaceous and Late Kimmeridgian targets. Calculated values of 0.7 indicate a moderate/regular probability of finding a potential reservoir rock, which in turn, is more likely to be of a regular quality.	277
Table 8.5. Summary of the different parameters used for fracture prediction and comparison between their relationships in the boreholes within the study area.	293

List of Figures

Figure 1.1. Tectonic map of Southern Gulf of Mexico showing the location of the study area in the south-western portion of the Akal-Reforma Block (in blue). Modified from PEMEX (2008) and CNH (2014).	4
Figure 2.1: Components of stress acting on a plane.	7
Figure 2.2: Geometric representation of a state of stress at a point (Gudmundsson, 2011).	7
Figure 2.3: The three components of deformation: Rigid body rotation and translation and strain (Van Der Pluijm, 2004).	8
Figure 2.4: Orientation of principal stresses in the stress ellipsoid (Fossen, 2004).	9
Figure 2.5: Relationship between principal stresses and faulting (After Anderson, 1951).	9
Figure 2.6: Combined rock-failure criterion as a function of normal stress (Gudmundsson, 2011).	10
Figure 2.7: Fracture propagation from a Griffith crack in a compressive stress field (Hoek and Martin, 2014).	11
Figure 2.8: Mechanisms for fracture termination (Modified from Gudmundsson, 2012).	12
Figure 2.9: Relationship between principal stresses and types of fractures (Fossen, 2004).	13
Figure 2.10: Modes of fractures (Fossen, 2004).	14
Figure 2.11: Fracture intensity as a function of lithology and grain size (Nelson, 2001).	16
Figure 2.12: Fracture intensity is controlled mainly by lithology (b) rather than bed thickness (a) (Ortega et al., 2010).	16
Figure 2.13: Fracture intensity as a function of rock texture and bed thickness. (Wennberg, 2006).	17
Figure 2.14: Fracture intensity as a function of crystal size in dolomites. (Giorgioni et al., 2016).	18
Figure 2.15: Fracture intensity as a function of porosity for limestone and dolomite facies. (Barbier et al., 2012).	19
Figure 2.16: Effect of pore-fluid pressure in rock failure (Gudmundsson, 2011).	20
Figure 2.17: Effect of layer thickness in fracture spacing (Giorgioni et al., 2016).	21
Figure 2.18: Fracture intensity is controlled by bed thickness rather than lithology (Awdal et al., 2015).	22
Figure 2.19: Fracture intensity is higher in the forelimb of the anticlinal than in the backlimb (Watkins et al., 2015).	23

Figure 2.20: Effect of structural position on fracturing in fault-related folds (Xiubin et al., 2010).....	23
Figure 2.21: Classification of fractured reservoirs (Nelson, 2001).	24
Figure 2.22: Extension fractures (EF) and shear fractures (ShF) in the Husavik-Flatey Fault zone (Modified from Gudmundsson et al., 2002).	26
Figure 2.23: Internal structure of a fault zone (Modified from Gudmundsson, 2011).....	26
Figure 2.24: Sets of fold-related fractures and inferred principal stresses. a) Tensile fractures, b) and c) Conjugate shear fractures (Liu et al., 2016).....	28
Figure 2.25: a) Pattern of radial faults in plan view around a salt diapir in Southern Gulf of Mexico (Rodriguez del Angel, 2012). Faulted roof above an active salt diapir (Alsop et al., 2016).	29
Figure 2.26: Kinematic model of diapir-flank folding (Rowan et al., 2003).....	29
Figure 2.27: Folding and faulting in minibasins around passive diapirs (Alsop et al., 2016).....	30
Figure 3.1. Outline of the Gulf of Mexico. Modified from Salvador (1991).	35
Figure 3.2: Tectonic map of Southern Gulf of Mexico. (Modified from PEMEX, 2008 and CNH, 2014).....	35
Figure 3.3. Stratigraphy of Southern GOM, where SW portion corresponds to the study area Modified from PEMEX, 2014.....	39
Figure 3.4. Early Triassic reconstruction of western equatorial Pangea (Martini et al., 2016).....	41
Figure 3.5. Early Triassic reconstruction of western equatorial Pangea (Stern and Dickinson, 2010).....	42
Figure 3.6. Sequential restoration of GOM opening (Hudec et. al, 2013).	44
Figure 3.7. (a) Uninterpreted and (b) interpreted tilt derivative of the residual gravity from Sadwell et al. (2014).	45
Figure 3.8. Plate Tectonic reconstruction at Eocene times (46 Ma). Modified from Pindell and Kennan, (2009).	46
Figure 3.9. Map of Southeastern Mexico showing the Chiapas foldbelt and other tectonic elements (Mandujano and Keppie, 2009).	47
Figure 3.10.: Plate tectonic reconstruction at Miocene times (10 Ma). Modified from Pindell and Kennan, (2009).	47
Figure 3.11.: Reconstruction at 13-0 Ma showing the proposed migration westward of the Tehuantepec Transform/ Middle America Trench intersection, (Mandujano and Keppie, 2009).	48
Figure 3.12. Schematic section showing the tectonic conditions during development of Chiapas fold-and-thrust belt c.13-10 Ma. (Mandujano and Keppie, 2009).	48

Figure 3.13: Map showing major tectonic elements in Southern Gulf of Mexico (above). Cross-section illustrating the Akal Block and its bounding basins (below). CNH, 2014.	49
Figure 3.14: Tectonostratigraphic chart of Southern GOM (Modified from PEMEX, 2013).	51
Figure 3.15: Normal listric faults and salt diapirs developed during D1 event. (CNH, 2014).	52
Figure 3.16: Salt canopies emplaced along with folding during D2 event. (CNH, 2014).	53
Figure 3.17: Cantarell anticline is a representative structure from D3 event. (Mitra et al., 2005)	53
Figure 3.18: Depocenter originated by gravitational extension during D4 event. (CNH, 2014).	54
Figure 4.1. Diagram showing the great variety of salt structures associated to line sources (a) and point sources (b). Hudec and Jackson (2007).	56
Figure 4.2. Different fracture sets identified within folded structures. (Liu et al., 2016).	58
Figure 4.3. Diapir-related hydrocarbon traps (Selley, 1998).	59
Figure 4.4. Hydrocarbon traps associated to contractional domains (Mount et al., 2007).	60
Figure 4.5. Trap styles associated to early post-salt carbonate section. East Texas Salt Basin (Montgomery et al., 1999).	60
Figure 4.6. Map showing three regional sections crossing the study area.	61
Figure 4.7. Regional cross-section A-A'. (Modified from Sanchez-Rivera et al., 2011).	63
Figure 4.8. Regional cross-section B-B'. (PEMEX, 2013).	65
Figure 4.9. Regional cross-section C-C'. (modified from CNH, 2014).	67
Figure 4.10. Location map of the 3D seismic survey and the study area.	69
Figure 4.11. Schematic illustration of differences in subsurface velocities in Vertical, Tilted and Horizontal Transverse Isotropy models respect to bedding orientation. (Hall, 2015).	69
Figure 4.12. Random cross-section showing the distribution of velocities used for depth migration.	70
Figure 4.13. Visual comparison between (a) PSTM and (b) PSDM seismic datasets in the study area.	72
Figure 4.14. Methodology workflow.	76
Figure 4.15. Confidence map on seismic interpretation for Mesozoic section.	77
Figure 4.16. Seismic cross-section showing the differences in quality image in the Mesozoic section.	78

Figure 4.17. Synthetic seismogram from W-1 and correlation along a seismic line crossing the borehole.....	80
Figure 4.18. Synthetic seismogram from W-2 and correlation along a seismic line crossing the borehole.....	80
Figure 4.19. Synthetic seismogram from W-3 and correlation along a seismic line crossing the borehole.....	81
Figure 4.20. Random sections crossing the three boreholes in the study area.	83
Figure 4.21. Stratigraphic column of the study area and corresponding seismic response from every borehole.	84
Figure 4.22. Major interpreted faults affecting Mesozoic section. Top Tithonian structure map.....	84
Figure 4.23. Thickness maps for the two stratigraphic packages that constitute the main economic targets in the study area.	85
Figure 4.24. Structure maps showing the distribution of autochthonous salt.....	88
Figure 4.25. Structure maps illustrating the contouring similarity between Mesozoic and Paleogene horizons as a result of salt distribution	88
Figure 4.26. Structure maps of allochthonous salt.....	89
Figure 4.27. Uninterpreted and interpreted cross-section from Figure 4.26.	89
Figure 4.28. Slice of the amplitude volume at 2500 m extending outside the limits of the study area	91
Figure 4.29. Structure maps showing the effects of D4 event in the study area.....	91
Figure 4.30. Structure maps of Top Kimmeridgian and Top Pliocene	92
Figure 4.31. Thickness maps for Mesozoic and Palaeogene packages.....	94
Figure 4.32. Seismic cross-section flattened at Top Early Miocene.	95
Figure 4.33. Cross section between two salt diapirs.....	95
Figure 4.34. Different scenarios for emplacement of allochthonous salt (Hudec and Jackson, 2006).	96
Figure 4.35. Top: Interpreted section showing the allochthonous salt sheet in the study area. Bottom: Conceptual model illustrating the concept of diapir rejuvenation by contraction (Hudec and Jackson, 2007).	98
Figure 4.36. Thickness maps for Neogene packages.....	99
Figure 4.37. contour configurations between structure map (left) and thickness map (right).	100
Figure 4.38. Structure map of Top Cretaceous showing the orientations of the three cross-sections that were restored.....	102
Figure 4.39. Sequential restoration of cross-section A-A', across Anticline A.	104
Figure 4.40. Sequential restoration of cross-section B-B', across Anticline A	108
Figure 4.41. Sequential restoration of cross-section C-C', across Anticline A.....	112

Figure 4.42. Top Cretaceous structure map showing the different cross-sections analysed to characterize the structural traps.	115
Figure 4.43. Cross section A-A' from Figure 4.42	116
Figure 4.44. Interpreted seismic Inline (B-B') and Cross-line (A-A').....	117
Figure 4.45. Parallel interpreted seismic cross-sections showing the variability in geometry along strike of Anticline A. Structure map of Top Kimmeridgian.	117
Figure 4.46. Interpreted seismic Inline (above) and Cross-line (left below) showing the geometry of Anticline B and the effects of the different deformational events. Structure map of Top Kimmeridgian (right below).	118
Figure 4.47. Interpreted seismic cross-section showing the geometry of Anticline B. Structure map of Top Kimmeridgian (right below).....	119
Figure 4.48. Parallel interpreted seismic cross-sections showing the variability in geometry along strike of Anticline B. Structure map of Top Kimmeridgian.	119
Figure 4.49. Cross section F-F' from Figure 4.42.....	120
Figure 4.50. 3D, time migrated seismic cross-sections illustrating the lateral variation in geometry of a counterregional fault associated to salt-cored structure in the Espirito Santo Basin, Brazil.	121
Figure 4.51. a) Depth slice from the amplitude volume at 8300 m illustrating the present-day distribution of autochthonous salt, which corresponds to the purple-coloured area (Study area delimited by red rectangle); b) Experimental model showing minibasin and salt distribution (Rowan and Vendeville, 2006).	123
Figure 4.52. Conceptual model of Anticline A's structural evolution.....	124
Figure 4.53. Models of salt tectonics showing effects of regional shortening (Hudec and Jackson, 2007).	125
Figure 4.54. Development of wedge (left) and tapered (right) halokinetic sequences during salt diapirism (Giles and Rowan, 2011).	126
Figure 4.55. Conceptual model of Anticline B's structural evolution.....	126
Figure 5.1. Imaging tool for FMI-HD log. (Brown et al., 2015).....	132
Figure 5.2. FMI log image. Standard color code assigns dark colors to high conductivities and light colours to high resistivities (Brown et al., 2015).....	132
Figure 5.3. Illustration of detection and plotting of bedding planes and fractures in the FMI log (Brown et al., 2015).	133
Figure 5.4. Correlation between the stratigraphic columns from the boreholes in the study area.....	134
Figure 5.5. Foraminifera wackestone. W-1, Late Cretaceous, C-1,	135
Figure 5.6. Foraminifera mudstone-wackestone. W-1, Middle Cretaceous,.....	136

Figure 5.7. Left: Hand sample from W-3, C-3. Top right: Foraminifera Mudstone-wackestone. W-1. Bottom right: Stylolite and sealed fractures in Mudstone, W-3, C-3. 2.5X. Polarized light.....	137
Figure 5.8. Left: Fragments from W-2, C-2. Right: shaly foraminifera mudstone-wackestone with microfractures. W-2, C-2. 2.5X, Natural light.....	138
Figure 5.9. Late Jurassic Kimmeridgian thin sections. A) Dolomitized mudstone, W-1; B) shaly mudstone, W-2, C-3.	139
Figure 5.10. Left: Fragment from W-3, C-4. Top right: dolomitized oolitic grainstone, W-3, C-4. Bottom right: dissolution cavity in dolomitized grainstone, W-3, C-4.....	139
Figure 5.11. Left: Fragment from W-3, C-5. Right: Micro-mesocrystalline dolomite, W-3, C-5.....	140
Figure 5.12. A) fragment from C-1; B) cross-cut relationship between f1 and f2 fractures (2.5x); C) close-up from f2 fracture in B showing calcite cementation (10x). W-1, C-1.....	141
Figure 5.13. Centre: three fragments from base, middle and top of W-2, C-1. Right: close-up from fragment 1 showing lateral offset of f1 fracture caused by cross-cutting of a later f3 fracture, W-2, C-1. LC= Late Cretaceous, MC= Middle Cretaceous, EC= Early Cretaceous.	143
Figure 5.14. Centre: Shaly mudstone-wackestone with vertical stylolites, Fragment 3, C-3. Right: thin sections showing cross-cutting relationships between f2 and f3 fractures (top) and f1 and f2 fractures (bottom), W-2, C-3 (Top).	144
Figure 5.15. Centre: Fragment 31, C-4. Top right: Dolomite partially cementing fractures with remnant porosity. Bottom right: cross-cutting fractures from different families. Thin sections from fragment 31, C-4.	146
Figure 5.16. Centre: Fragment 3 from C-3. Right: cross-cutting relationships between fractures from f1, f4 families and stylolites. W-3, C-3.....	147
Figure 5.17. Centre: fragments from bottom, middle and top C-4. Top right: dissolution cavities and fractures. Bottom right: stylolite with some dissolution.....	149
Figure 5.18. Composite log. W-1, Late Cretaceous.....	151
Figure 5.19. Composite log. W-1, Middle and Early Cretaceous.	153
Figure 5.20. Composite log from W-1, Late Jurassic Tithonian.	154
Figure 5.21. Image logs for W-1, Late Jurassic Kimmeridgian.	155
Figure 5.22. Composite log from W-2, Late Jurassic Tithonian.	157
- Figure 5.23. Composite log. W-2, Late Jurassic Kimmeridgian.....	158
Figure 5.24. Composite log. W-3, Cretaceous.....	160
Figure 5.25. Composite log from W-3, Late Jurassic Tithonian.	161

Figure 5.26. CFI plot showing the presence of mechanical layers in Tithonian sediments from borehole W-2.	164
Figure 5.27. Comparison of fracture patterns (orange dots) in Cretaceous rocks between boreholes W-1 (top) and W-3 (bottom).	165
Figure 5.28. Relationship between FI and bed thickness from Kimmeridgian sequences in boreholes W-2 (top) and W-1 (bottom)..	166
Figure 5.29. CFI plot showing the presence of intervals where bed thickness seems to control FI.....	167
Figure 5.30. CFI plot from borehole W-3.	168
Figure 5.31. Rose diagrams showing a comparison between fracture orientations obtained from image logs and core samples.	169
Figure 6.1. Top Kimmeridgian structure map showing the locations of the three analysed anticlines (A, B and C) and locations of boreholes used for this study.....	171
Figure 6.2. Comparison between different migration algorithms. NEXt Training course notes (2011).	173
Figure 6.3. Definition of 2D curvature (Chopra and Marfurt, 2007.)	174
Figure 6.4. Curvature shape classification (Roberts, 2001).	174
Figure 6.5. Application of curvature attribute in fault interpretation. (Roberts, 2001).....	175
Figure 6.6. Relationship between stress and curvature. (Roberts, 2001).	175
Figure 6.7. Different curvature attributes. From left to right: Most Positive curvature, Most Negative Curvature and Most Extreme Curvature.	176
Figure 6.8. Semblance estimation of coherence. (Chopra and Marfurt, 2007).....	177
Figure 6.9. Variance slice at a depth of 4000 m.	178
Figure 6.10. Attribute sensitivity to faults, folds and flexures (Chopra and Marfurt, 2007).....	178
Figure 6.11. Standard Workflow used to generate an ant-tracking attribute volume.....	179
Figure 6.12. Depth slice at 2500 m.	180
Figure 6.13. Depth slices at 6100 m of most positive curvature attribute calculated with different values of input parameters (V.R= vertical radius, IL/XL R=IL/XL Range).....	182
Figure 6.14. Depth slices at 6100 m of variance attribute calculated with different values of input parameters (V.S= vertical smooth, IL/XL R=IL/XL Radius).....	183
Figure 6.15. Depth slices at 6100 m of Ant-tracking attribute calculated from different edge detection attributes.....	184
Figure 6.16. Comparison in the response of different seismic attributes calculated at different depths.	185

Figure 6.17. Top Cretaceous surface with different seismic attributes applied.....	188
Figure 6.18. Top Tithonian surface with different seismic attributes applied.	189
Figure 6.19. Top Kimmeridgian surface with different seismic attributes applied.....	190
Figure 6.20. Interpreted faults in Mesozoic surfaces with variance attribute (left) and their character in seismic cross-section (right).	192
Figure 6.21. Top: Cross-section in amplitude volume. Bottom left: Ant-tracking from variance volume. Bottom right: Ant-tracking from Most Positive Curvature.....	194
Figure 6.22. Ant-tracking/structure surfaces from Top Cretaceous (left), Top Tithonian (center) and top Kimmeridgian (right).	195
Figure 6.23. Close-ups from Fig. 6.22 showing a comparison between the ant- tracking lineaments adjacent to the boreholes with similar orientations (inside black dashed ovals) to fracture orientations measured in FMI logs (red lines)..	196
Figure 6.24. (a) Cross-section with ant-tracking attribute shown. (b) Close-up in the Well-1 showing the location of production tests (dashed rectangles) and faults interpreted in FMI logs (F).	198
Figure 6.25. (a) Cross-section with ant-tracking attribute shown and, (b) close- up in Well-2 showing the Production tests and fault interpreted in FMI logs (F).....	198
Figure 6.26. (a) Cross-section with ant-tracking attribute shown and, (b) close- up in Well-3 showing the Production tests and zones associated to presence of fractures in Kimmeridgian section.....	200
Figure 6.27. Thin sections from the Production test I interval, showing the different oil-prone carbonate facies. Late Kimmeridgian, Well-3.	201
Figure 6.28. Thin sections from the interval 5640-5950 mbsl.	201
Figure 6.29. Depth slices showing the comparison between the orientations of lineaments interpreted in ant-tracking attribute and orientations measured in FMI logs and core samples.....	203
Figure 6.30. Fe1 strain (maximum finite strain) distribution calculated from GM Module displayed on the Anticline A deformed state.....	205
Figure 6.31. Sensitivity analysis of Fe1 strain (maximum finite strain) distribution calculated from Geomechanical Modelling Module displayed on Anticline C deformed state.....	206
Figure 6.32. Fe1 strain (maximum finite strain) distribution calculated from GM Module displayed on the Anticline B deformed state.....	207
Figure 6.33. E1 Strain (maximum stretching) distribution calculated from FRM Module displayed on the Anticline A deformed state.....	209

Figure 6.34. E1 Strain (maximum stretching) distribution calculated from FRM Module displayed on the Poo-Up Anticline deformed state.	210
Figure 6.35. E1 Strain distribution calculated from FRM Module displayed on the Anticline B deformed state.	211
Figure 6.36. Comparison between strain calculated with Geomechanical Modelling and structural position for Anticline A using ant-tracking attribute superimposed on structure map.....	213
Figure 6.37. Comparison between strain calculated with Geomechanical Modelling and structural position for Anticline C using ant-tracking attribute superimposed on structure map.....	214
Figure 6.38. Comparison between strain calculated with Geomechanical Modelling and structural position for Anticline B using ant-tracking attribute superimposed on structure map.....	215
Figure 6.39. Schematic evolution of fracture development in Anticline A.....	218
Figure 6.40. Rose diagram from Anticline A showing different fracture sets measured in W-3.....	218
Figure 6.41. Schematic evolution of fracture development in Anticline B.....	219
Figure 6.42. Rose diagram from Anticline B showing different fracture sets measured in W-2 and possible σ_1 stress orientations of D2/D3 events.	219
Figure 6.43. Fold-related fracture sets observed in the study area and their associated orientations of maximum and minimum stresses (Modified from Liu et al., 2016).	222
Figure 6.44. Combination of structure with ant-tracking attribute for Top Cretaceous surface.	223
Figure 6.45. Combination of structure with ant-tracking attribute for Top Kimmeridgian surface..	223
Figure 7.1. The basic input for the ED solution is a rectangular fault panel with a constant slip and a position defined by xyz coordinates (Dee et al., 2007).....	227
Figure 7.2. Mohr-Coulomb diagram illustrating definitions of failure criterion. (Dee et al., 2007).	227
Figure 7.3. Data subsets used to model the three anticlines within the study area. Top Late Cretaceous structure map.	228
Figure 7.4. Interpreted cross-section from Figure 7.3 showing the structural style of the Mesozoic structural traps.	229
Figure 7.5. Orientation of shear and tensile fractures respect to the orientation of applied stresses (Hunt et al., 2009).	231
Figure 7.6. Interpreted cross-section showing the modelled Mesozoic horizons: Top Cretaceous, Top Tithonian and Top Kimmeridgian.	232

Figure 7.7. Distribution of MCSS at each of the three Mesozoic mapped surfaces in anticline B.....	234
Figure 7.8. Distribution of MCSS at each of the three Mesozoic mapped surfaces in anticline A.....	235
Figure 7.9. Interpreted cross-section showing the geometry of anticline B.....	236
Figure 7.10. a) Predicted orientations of fractures around borehole W-1 superimposed on MCSS distribution (RF3 is the input reverse fault for fracture modelling); b) rose diagram comparing the predicted orientations (blue) with FMI orientations measured in FMI log (black), red line corresponds to the anticline axis; c) Depth slice and, d) Top Kimmeridgian surface with ant-tracking attribute showing the lineaments around W-1.....	238
Figure 7.11. a) Predicted orientations of fractures around borehole W-2 superimposed on MCSS distribution (NF4 is the input normal fault for fracture modelling); b) rose diagram comparing the predicted orientations (blue) with orientations measured in Core-3; c) Depth slice and Top Kimmeridgian surface with ant-tracking attribute showing the lineaments around W-2; d) rose diagram comparing the predicted orientations (blue) with FMI orientations measured in FMI log (black), red line corresponds to the anticline axis.....	238
Figure 7.12. a) Predicted orientations of fractures around borehole W-1 superimposed on MCSS distribution; b) rose diagram comparing the predicted orientations (blue) with FMI orientations measured in FMI log (black), red line corresponds to the anticline axis; c) Depth slice and, d) Top Tithonian surface with ant-tracking attribute showing the lineaments around W-1.....	239
Figure 7.13. a) Predicted orientations of fractures around borehole W-2 superimposed on MCSS distribution; b) rose diagram comparing the predicted orientations (blue) with FMI orientations measured in FMI log (black), red line corresponds to the anticline axis; c) Depth slice and, d) Top Tithonian surface (right) with ant-tracking attribute showing the lineaments around W-2.....	240
Figure 7.14. a) Predicted orientations of fractures around borehole W-1 superimposed on MCSS distribution; b) rose diagram comparing the predicted orientations (orange) with FMI orientations measured in FMI log (blue), red line corresponds to the anticline axis; c) Depth slice and, d) Top Cretaceous surface with ant-tracking attribute showing the lineaments around W-1.....	241
Figure 7.15. a) Predicted orientations of fractures around borehole W-2 superimposed on MCSS distribution; b) rose diagram comparing the	

<p>predicted orientations (blue) with FMI orientations measured in FMI log (black), red line corresponds to the anticline axis; c) Depth slice and, d) Top Cretaceous surface with ant-tracking attribute showing the lineaments around W-2.</p>	241
<p>Figure 7.16. Comparison between the distribution of MCSS and ant-tracking for Mesozoic surfaces in anticline B.</p>	243
<p>Figure 7.17. Comparison between the distribution of MCSS and ant-tracking for Mesozoic surfaces in Anticline A.</p>	244
<p>Figure 7.18. a) distributions of MCSS and strain in Top Kimmeridgian show some similarities around reverse fault RF3 and a low strain zone to the north of normal fault NF4; b) Cumulative Fracture Intensity (CFI) plot show high fracture density in the Kimmeridgian uppermost sequence for borehole W-1, confirmed by a production test that resulted water invaded thus indicating good permeability; c) Similarly to borehole W-1, CFI plot shows relatively high fracture density in the Kimmeridgian uppermost sequence for borehole W-2. Another water invaded production test confirmed good permeability, probably assisted by interconnected fracture sets.</p>	245
<p>Figure 7.19. a) MCSS and strain in Top Tithonian show similar distributions of high strain zones around fault planes and the anticline's hinge; b) CFI plot showing a moderate fracture intensity in the Tithonian uppermost sequence; c) CFI plot showing low fracture density but with the presence of an interval with high fracture density in the Tithonian uppermost sequence for borehole W-2.</p>	246
<p>Figure 7.20. a) distribution of MCSS and strain in Top Cretaceous follow similar patterns with high strain zones around the fault planes and the fold hinge and relatively low strain values in the borehole locations; b) CFI plot shows intervals of low and relatively high fracture density in the Late Cretaceous uppermost sequence for borehole W-1; c) CFI plot showing absence of fractures in the Late Cretaceous uppermost sequence for borehole W-2.</p>	247
<p>Figure 7.21. Series of interpreted cross-sections illustrating the along-strike variability of anticline A's geometry associated to the variations in the thickness of autochthonous salt.</p>	248
<p>Figure 7.22. a) Predicted fractures around borehole W-3, anticline A; b) rose diagram comparing the predicted orientations (blue) with orientations measured in Core-4, red line corresponds to the anticline axis; c) Depth slice and, d) Top Kimmeridgian surface with ant-tracking attribute showing the lineaments around W-3.</p>	249

Figure 7.23. a) Predicted fractures around borehole W-3, anticline A; b) rose diagram comparing the predicted orientations (blue) with orientations measured in FMI logs (black), red line corresponds to the anticline axis; c) Depth slice and, d) Top Tithonian surface with ant-tracking attribute showing the lineaments around W-3.	250
Figure 7.24. a) Predicted fractures around borehole W-3, anticline A; b) rose diagram comparing the predicted orientations (blue) with orientations measured in Core-3, red line corresponds to the anticline axis; c) Depth slice, d) Top Cretaceous surface with ant-tracking attribute showing the lineaments around W-3; e) rose diagram comparing the predicted orientations (blue) with orientations measured in FMI logs (black).....	251
Figure 7.25. Distribution of MCSS (left) and strain (right) in Top Kimmeridgian show similar patterns for anticline A.	252
Figure 7.26. Left: Comparison between distribution of MCSS and strain in Top Tithonian, anticline A; Right: Cumulative Fracture Intensity (CFI) plot.	253
Figure 7.27. Left: Comparison between distribution of MCSS and strain in Top Cretaceous, anticline A; Right: Cumulative Fracture Intensity (CFI) plot.....	254
Figure 8.1. Flow diagram illustrating the developed methodology for fracture prediction.	262
Figure 8.2: Comparison between strain distribution and ant-tracking lineaments applied to mapped surfaces..	268
Figure 8.3. Location of borehole W-4 within the study area. Top Kimmeridgian structure map.....	274
Figure 8.4. Uninterpreted and interpreted cross-section A-A'	275
Figure 8.5. Regional maps illustrating the distribution of lithofacies for Late Kimmeridgian (top) and Late Cretaceous (bottom). Modified from PEMEX (2015).....	278
Figure 8.6. Seismic cross-section across the proposed W-4 well illustrating its folding style. Top Kimmeridgian structure map.....	279
Figure 8.7. Depth slice at 5400 m showing the distribution of lineaments around borehole W-4 for Late Cretaceous target.	281
Figure 8.8. Depth slice at 6100 m showing the distribution of lineaments around borehole W-4 for Late Kimmeridgian target.....	281
Figure 8.9. Top Cretaceous surface with different attributes applied. A) Most negative curvature, b) variance and, c) Ant-tracking from Most Positive Curvature.	282
Figure 8.10. Top Kimmeridgian surface with different attributes applied. A) Most negative curvature, b) variance and, c) Ant-tracking from Most Positive Curvature..	282

Figure 8.11. Cross-sections showing the distribution of lineaments around borehole W-4 in the Mesozoic section..	283
Figure 8.12. Distribution of strain around the proposed borehole W-4.	284
Figure 8.13. Distribution of MCSS in Top Cretaceous surface calculated with geomechanical parameters from W-1 (left) and W-3 (right).	285
Figure 8.14. Distribution of MCSS in Top Kimmeridgian surface calculated with geomechanical parameters from W-1 (left) and W-3 (right).	285
Figure 8.15. a) Predicted fractures around proposed borehole W-4; b) rose diagram showing the predicted orientations of fractures inside the square window around W-4; bottom: c) Depth slice and, d) Top Cretaceous surface with ant-tracking attribute showing the lineaments around W-4.	286
Figure 8.16. a) Predicted fractures around proposed borehole W-4; b) rose diagram showing the predicted orientations of fractures inside the square window around W-4; c) Depth slice and, d) Top Kimmeridgian surface with ant-tracking attribute showing the lineaments around W-4.	287
Figure 8.17. Top Cretaceous map showing the location of boreholes W-4 and W-5 in anticline C.	289
Figure 8.18. Cross section A-A' from Fig. 7.15 showing the trajectories of boreholes W-4 and W-5.	289
Figure 8.19. Well log correlation between wells W-3 and W-5.	290
Figure 8.20. Depth slices at 5850 md showing the distribution of ant-tracking lineaments in the vicinity of boreholes W-4 and W-5.	290

Abbreviations

2D=Two dimensional

3D= Three dimensional

AVAZ= Amplitude versus azimuthal angle

CEROE= Format for Registration and Assessment of Exploratory Opportunities

CFI= Cumulative Fracture Intensity

CFM= Continuous fracture modelling

CNH= Hydrocarbons National Committee

fe1= Finite strain

FI= Fracture intensity

FMI= Fullbore Formation MicroImager

FRM= Fault response modelling

f/m= fractures per meter

GM= Geomechanical modelling

GOM= Gulf of Mexico

GPa= Gigapascals

IL= Inline

IMP= Instituto Mexicano del Petroleo

km= kilometres

m=meters

Ma= Million years (Mega-annum) for time before present

mbsl= meters below sea level

MCSS= Maximum Coulomb shear stress

mD= milidarcys

MEC= Most Extreme Curvature

MNC=Most negative curvature

MPa= Megapascals

MPC= Most positive curvature

PEMEX= Petroleos Mexicanos

PoS= Probability of geological success

ν = Poisson's ratio

PSDM= Pre-stack depth migration

PSTM= Pre-stack time migration

RTM= Reverse time migration

SEB= South-eastern Basins

SEG= Society of Exploration Geophysicists

TTI= Tilted Transverse Isotropy

UCS= Uniaxial compressive strength

VTI= Transverse Isotropy

XL= Cross-line

E = Young's modulus

σ = Normal stress

μ = Coefficient of internal friction

C = Cohesive (shear strength)

Chapter 1

Introduction

1.1 Rationale

Significant volumes of hydrocarbon production in the world come from carbonate reservoirs (Nelson, 2001; Akbar et al., 2001). Since most carbonate host rocks have low to very low matrix permeabilities (<0.1 mD, Rashid et al., 2001; Nelson, 2001), the majority of the hydrocarbon volume is contained within fracture sets (Bourbiaux, 2010; Ahr, 2008); therefore, characterization of fracture sets (location, orientation, density and, most importantly, apertures) is critical to reservoir evaluation and production. Traditionally, rock mechanical properties and fracture prediction have been focused on reservoir characterization stages, where abundant information from well logs and core sampling exist (Jenkins et al., 2009; Ameen et al., 2009; Sagi et al., 2013). However, this results in significant uncertainty at early stages of the exploration process where such information is absent or is sparse. Estimation of reservoir rock's quality at this phase remains a challenging task and is the focus of this study.

Fractures are discontinuities in rock formed as a combination of both a brittle response to applied stress and diagenetic processes during burial history that exert a significant effect on fluid flow by enhancing reservoir's permeability and thus representing prospective targets in hydrocarbon exploration (Nelson, 2001; Ahr, 2008). Estimation of intensity and orientation of fracturing in carbonate rocks at subsurface in exploratory areas represents a highly complex problem due to the fact that most fractures and faults that increase fluid flow or compartmentalize a reservoir are below seismic resolution (Lohr et al., 2008; Endres et al., 2008), whereas core samples and well logs provide punctual information at a much smaller scale than that provided by seismic information (Ameen et al., 2009; Sagi et al., 2013). Moreover, carbonate fracturing is controlled by the interplay of multiple factors (lithology, texture, porosity, bed thickness) that usually show strong vertical and lateral variability (Wennberg et al., 2016; Nelson, 2001; Hunt et al., 2009) and therefore makes difficult to estimate fracturing in inter-well areas where little or no well data are available (Lohr et al., 2008; Endres et al., 2008; Jenkins et al., 2009).

As a consequence of the uncertainty outlined above, it is necessary to develop a multidisciplinary approach by combining geological and geophysical tools and techniques such as seismic interpretation, 2D/3D structural restoration, seismic attribute analysis, well data analysis and fracture modelling in order to investigate the relationship between large-scale features observed in seismic data (major faults and folds), medium-scale features (seismically resolvable attributes) and sub-seismic observations (well logs and core data). This project proposes a methodology for fracture prediction based on this approach, with direct applicability at the early stages of hydrocarbon exploration by defining location, orientation and relative intensity of sub-seismic scale fractures, which are fundamental parameters in both reservoir rock quality assessment and adequate drilling program for oil wells.

1.2 Aim and objectives

The overall aims of the project are to develop a multidisciplinary methodology for prediction of natural fractures in carbonate reservoirs that can be applied at early stages of the hydrocarbon exploration process and to propose an improved methodology for a more detailed assessment of the reservoir rock during the estimation of the probability of geological success (PoS) of exploratory prospects. To achieve these aims, specific objectives are posed, which are framed by the following research questions:

1. What is the influence of structural evolution on natural fracturing of carbonate rocks?

Deformational events play an important role in fracture development by applying tectonic stresses to subsurface rocks. At the same time, structural position within a geological structure influences intensity and distribution of natural fractures; moreover, fracture sets show predictable symmetric orientations with respect to the fold geometry if strata are not fractured prior to folding. Analysis of the tectonic evolution of individual structural traps indicates how likely is to find natural fracturing, its relative intensity according to the structural position as well as probable orientations of fractures.

2. What are the geological factors that control natural fracturing within the study area?

Existing knowledge of the individual effects of different geological factors, such as lithology, texture, porosity, structural position and bed thickness on natural fracturing has been provided by extensive fieldwork and laboratory experiments, from which some general assumptions have been made. For this work, these effects are defined through

the analysis of well data (core samples and FMI logs) although the results may be limited by restrictions inherent to subsurface sampling.

3. *How can geological and geophysical data be integrated for fracture prediction?*

Natural fracturing is the result of a complex interaction between multiple geological factors through time, which may also have strong spatial variations. Moreover, fracturing occurs at different scales of observation, from micro-fractures not visible to naked eye to major faults recognizable on seismic data, which may or not show geometric relationships. Due to this, prediction of location, orientation and intensity of natural fracturing at subsurface can be achieved by integrating different analysis that encompass different scales of observation. Borehole data provides information from small-scale (thin sections and hand samples) and medium-scale (FMI logs) fractures, whereas seismic derived analyses (mapping of amplitude volume and structural seismic attributes) provide information from large-scale faults and fractured zones. Finally, geomechanical and fracture modelling provide proxies for relative fracture intensity (strain and maximum Coulomb shear stress, respectively), as well as orientation of predicted fracture sets.

1.3 Location of the study area

The study area is located in the south-western portion of the Akal-Reforma Block which, in turn, is one of the major tectonic elements that comprise the South-eastern Basins (SEB) oil province (Figure 1.1). This province is the most prolific and important hydrocarbon province in Mexico, with most of the production coming from Mesozoic carbonate reservoirs, and extensive hydrocarbon exploration in the Southern Gulf of Mexico has taken place through the analysis of several 2D/3D seismic surveys and information from hundreds of boreholes. Structural traps are predominant and their geometries may vary from simple to very complex as a result of a complex tectonic evolution with multiple deformational events where salt tectonics has had a great influence and implication on the different elements of the existing petroleum systems.

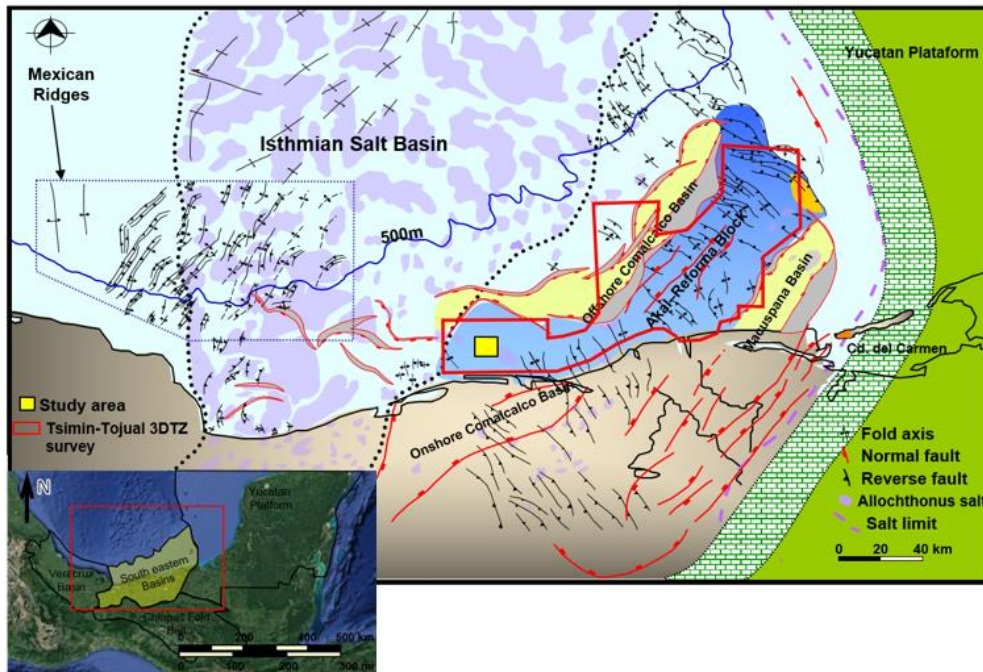


Figure 1.1. Tectonic map of Southern Gulf of Mexico showing the location of the study area in the south-western portion of the Akal-Reforma Block (in blue). Modified from PEMEX (2008) and CNH (2014).

1.4 Layout of thesis

This thesis comprises nine chapters (Table 1.1). Chapter 1 provides a general overview of the project by mentioning the rationale, aims and objectives; Chapter 2 includes a review of relevant literature about previous studies on geological controls on natural fracturing and detection of subsurface fractures; Chapter 3 presents a review of literature about the tectonic evolution of Southern Gulf of Mexico and its implications in the formation of hydrocarbon traps in the study area; Chapter 4 describes the evolution of the salt-cored structural traps within the study area defined by 2D restoration and the implications for natural fracture development; Chapter 5 describes the relationship between lithology, texture, bed thickness and faulting with fracture intensity obtained from the analysis of borehole data; Chapter 6 investigates the influence of structural position on the development of natural fracture systems in the study area by integrating structural seismic attributes and geomechanical modelling; Chapter 7 describes the integration of Fracture Modelling, seismic attributes and strain maps for fracture prediction and compare their different results with borehole data in order to assess their potential as a predictive tool; Chapter 8 presents a study case where the proposed methodology for fracture prediction is applied in the study area along with an improved assessment of the presence and quality of reservoir rock for a proposed exploratory prospect. Finally, Chapter 9 summarizes the main conclusions obtained from this research and suggests further research options in order to complement this work.

Chapter	Content
Chapter 1	Introduction; overview and aims of the study.
Chapter 2	Literature review from previous studies on geological controls of natural fracturing and fracture prediction.
Chapter 3	Geological Setting of Southern Gulf of Mexico and its implications on the formation of structural traps.
Chapter 4	Seismic interpretation and the evolution of salt-related structural traps.
Chapter 5	Influence of geological controls on natural fracturing from analysis of borehole data.
Chapter 6	Integration of strain maps and structural seismic attributes with borehole data for fracture interpretation.
Chapter 7	Comparison between modelled fractures, seismic attributes and borehole data.
Chapter 8	Testing the proposed methodology for fracture prediction
Chapter 9	Conclusions and further work

Table 1.1. Thesis layout.

Chapter 2

Fundamentals of Rock Fractures

2.1 Natural rock fractures

A natural fracture is defined by Nelson (2001) as “a naturally macroscopic planar discontinuity in rock due to deformation or physical diagenesis”. Fossen (2004) defines fractures as sub-planar discontinuity surfaces that have formed within a rock as a result of external and/or internal stresses applied. More specifically, a fracture forms when applied stress reaches a certain limit, named rock strength, involving loss of cohesion of the rock body across the fracture plane (Gudmundsson, 2011). The study of rock fractures is crucial in several fields within earth sciences such as structural geology, tectonics, hydrogeology, and seismology, among others. Practical applications of rock fractures studies in industry include civil engineering, and natural resources exploration (hydrocarbon, geothermal, underground water).

Several factors that are important in exerting a control on the orientation and density of fracturing within a rock mass in the subsurface are shown in Table 2.1. These factors include applied stresses, pore pressure, rock properties (lithology, texture, porosity, Young’s modulus and Poisson’s ratio), bed thickness and structural position (Nelson, 2001). An analysis of the way each one of these factors influence rock fracturing is fundamental to the analysis and understanding of natural fracturing at subsurface (Gillam, 2004).

Type	Parameter		Direction of correlation
Material Property	Rock brittleness	Young’s modulus	Positive
		Poisson’s ratio	
	Rock strength	Grain size	Negative
		Porosity	Negative
	Bed Thickness		Negative
In-Situ	Depth		Variable Effect
	Pore Pressure		May hold fractures open
Strain	Structural Position		Positive with strain

Table 2.1: Main factors controlling fracturing (modified from Hunt et al., 2009).

2.2 Stress and deformation definitions

Stress is a vectorial (has magnitude and direction) quantity defined as force (F) per unit area (A). The unit of measure of stress is Pascals, where $1 \text{ Pa} = 1 \text{ N} / \text{m}^2$. Stresses in the crust are sufficiently high that they are preferably expressed in MegaPascals (10^6 Pa) or GigaPascals (10^9 Pa). When acting on a plane, stress can be subdivided into two components (Figure 2.1: Components of stress acting on a plane.): 1) Normal stress perpendicular to the plane (σ_n); and 2) Shear stress parallel to the plane, (τ). Since any given point in the subsurface experiences stresses from all directions, a stress field or state of stress can be represented mathematically as a stress tensor and geometrically as shown in Figure 2.2: Geometric representation of a state of stress at a point (Gudmundsson, 2011).

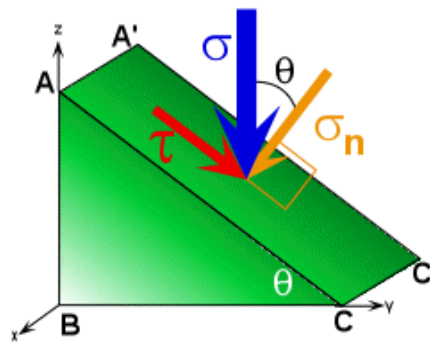


Figure 1

Figure 2.1: Components of stress acting on a plane.

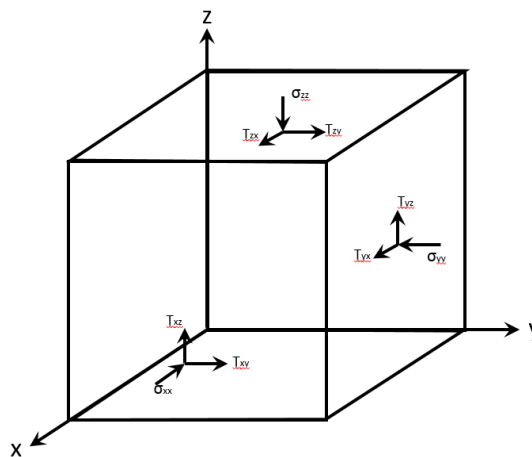


Figure 2.2: Geometric representation of a state of stress at a point (Gudmundsson, 2011).

In this case, all stresses acting on the cube are equal and, therefore, the cube is in equilibrium, so it is not moving or rotating (remains undeformed). However, as is clearly observed in both outcrop and subsurface examples, rocks can be deformed (fractured,

folded or both) in a brittle and/or ductile manner, which implies that stresses have different magnitudes acting in different directions at a given point (differential stress).

Deformation is defined by Van Der Pluijm (2004) as “changes in shape, position, or orientation of a body resulting from the application of a differential stress (i.e., a state in which the magnitude of stress is not the same in all directions)”, and has three components (Figure 2.3): 1) rigid body rotation, which is the pivoting of a body around a fixed axis; 2) rigid body translation, which is a change in the position of a body, and; 3) strain, which is a distortion or change in shape of a body related to the displacement of inner particles from their original position to a new position (Gudmundsson, 2011). Deformation can be brittle or ductile according to the way solid materials change permanently after a state of stress has been applied, which depends on the elastic properties of the rock defined by Young’s modulus and Poisson’s ratio. Brittle deformation occurs due to the growth of fractures and only occurs when stresses exceed a critical value after a rock has already undergone some elastic and/or plastic behaviour (Van der Pluijm, 2004). In the other hand, ductile deformation occurs when there is a substantial change of shape in a rock without gross fracturing (Gudmundsson, 2011) and involves processes such as cataclastic flow, diffusional flow and crystal plasticity. The main differences between brittle and ductile deformation are: 1) ductile strain is uniformly distributed within the rock, whereas brittle strain is mostly localized around and inside fractures (Gudmundsson, 2011), and; 2) Ductile deformation is strongly temperature and time dependant, while brittle deformation depends mostly on applied stress (Suppe, 1985).

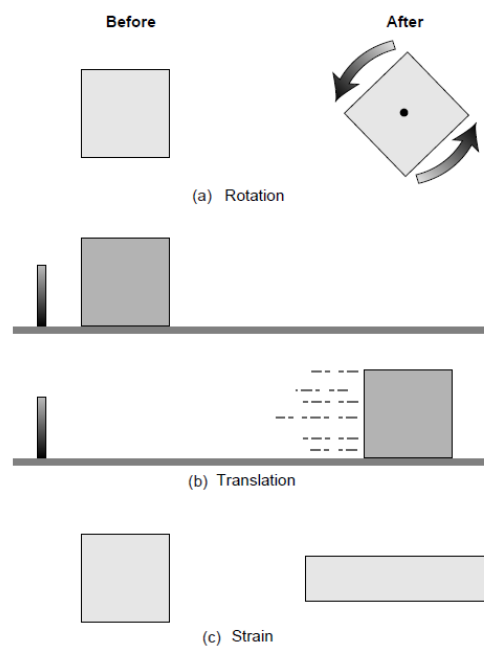


Figure 2.3:The three components of deformation: Rigid body rotation and translation and strain (Van Der Pluijm, 2004).

2.2.1 Principal stresses

The normal stresses acting on the three mutually perpendicular principal planes of stresses at any point are known as principal stresses (Gudmundsson, 2011). Principal stresses are denoted by σ_1 , σ_2 and σ_3 and are arranged so they correspond to the maximum, intermediate and minimum principal compressive stresses, respectively. Any state of stress at a point in a rock body can be represented by the stress ellipsoid (Figure 2.4).

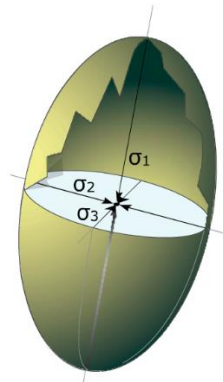


Figure 2.4: Orientation of principal stresses in the stress ellipsoid (Fossen, 2004).

According to Anderson (1951), the configuration of the principal stresses is directly related to the type of faults originated as shown in Figure 2.5. This model assumes that all principal stresses are compressive and that $\sigma_1 > \sigma_2 > \sigma_3$. Moreover, it allows us to infer (or predict) the orientations of the principal stresses based upon geological features observed in field and subsurface data. Conversely, if the relative magnitude and orientation of the principal stresses are known; the orientation and type of faults and folds can be inferred or even predicted.

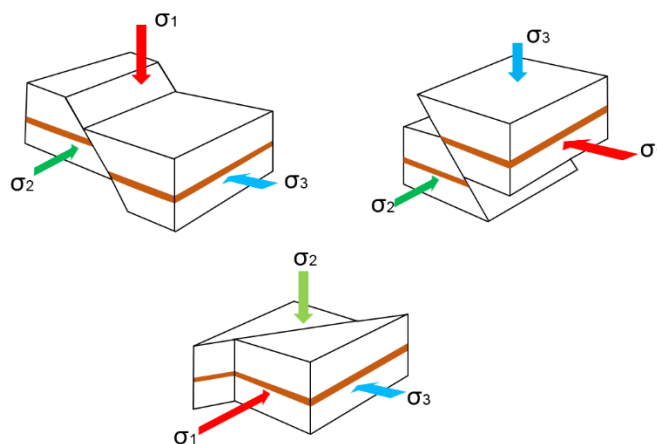


Figure 2.5: Relationship between principal stresses and faulting (After Anderson, 1951).

2.3 Rock failure

Gudmundsson (2011) defines failure as “the stress condition at which a solid starts to flow or break”, and it is related to the maximum stress or stress difference that the solid can sustain. A failure criterion is a mathematical model that explains and predicts rock failure and describes the stress conditions of permanent deformation in brittle, quasi-brittle and ductile solids. For the brittle field, the Griffith criterion is used primarily for the tensile regime, while the Mohr-Coulomb and Hoek-Brown criteria are used mainly for the compressive regime. Von Mises and Tresca criteria are used to describe plastic deformation. Figure 2.6 represents a combined rock-failure criterion to explain the differences in rock failure as a function of normal stress or depth.

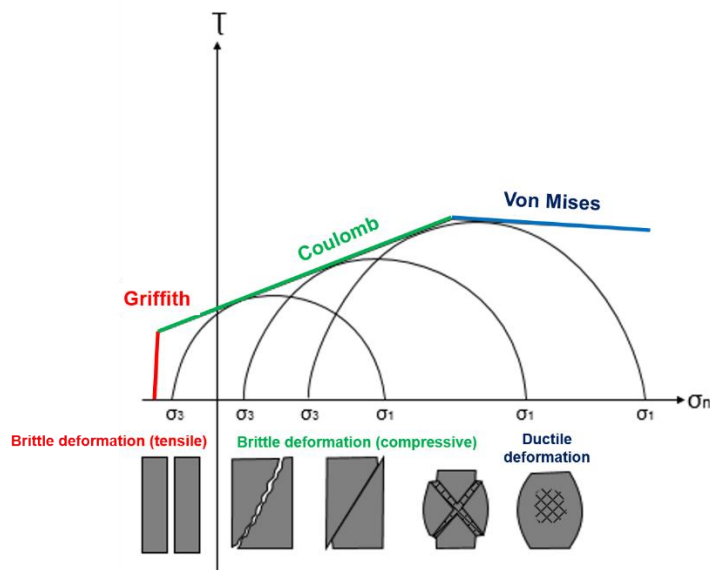


Figure 2.6: Combined rock-failure criterion as a function of normal stress (Gudmundsson, 2011). As differential stress ($\sigma_1 - \sigma_3$) increases, deformation changes from brittle to ductile, so different failure criterion is needed to describe the stress conditions at each case.

2.3.1 Fracture initiation and propagation

Griffith (1920, 1924) suggested that fracture initiation in a brittle material occurs from points of high tensile stress concentrations around the tips of suitably oriented flaws (Griffith cracks). In sedimentary rocks, these flaws can be fossils or vugs, and within brittle units, the largest flaws often occur at bedding planes (Pollard and Aydin, 1988). Griffith's theory deals only with the initiation of tensile failure and it cannot be extended to deal with failure propagation and eventual shear failure in compression. However, under certain conditions when tensile stresses exceed the tensile strength, tensile failure initiation can lead to crack propagation. In these cases the tensile cracks propagate along the major principal stress (σ_1) trajectory as shown in Figure 2.7. Moreover, the

location of fracture initiation depends not only on the distribution of the largest flaws (Gross, 1993; Renshaw et al., 2003) but also on the tensile strength of the rock. For practical purposes, the model of isolated Griffith cracks is inadequate because it does not match the grain boundary network in which tensile failure originates and propagates in intact rock; therefore, the tensile crack path would follow a path dictated by grain boundaries with only isolated cracks running across intact grains (Hoek and Martin, 2014).

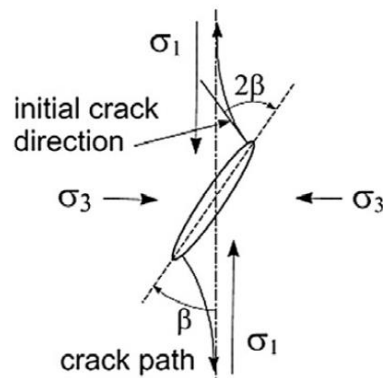


Figure 2.7: Fracture propagation from a Griffith crack in a compressive stress field (Hoek and Martin, 2014).

2.3.2 Fracture termination

When a propagating fracture meets an interface or discontinuity (a contact, an existing fracture), one of the following will occur: 1) it will become arrested (stops propagating); 2) penetrate the contact; or, 3) deflect in one or two directions along the contact (Gudmundsson, 2011). A layer or rock unit where local stress does not allow a fracture to propagate is known as a stress barrier. Figure 2.8 illustrates the most common mechanisms of fracture termination, which control the development of fracture networks and, therefore, the fluid flow paths through the rock mass. These potential barriers comprise:

- 1) Compressive stresses generated by earlier fractures (Figure 2.8a)
- 2) Rotation of the principal stresses at the contact from favourable to unfavourable propagation (Figure 2.8b).
- 3) Opening of a weak contact (discontinuity) in front of a propagating fracture (Figure 2.8c).
- 4) Material toughness mechanism, namely differences in material toughness at the contacts in adjacent layers, can control fracture arrest, penetration or single/double deflection (Figure 2.8d).

The predominance of one or another of these mechanisms is dictated by the sedimentology of the rock succession. In an interbedded sequence of brittle and ductile strata, such as chalk and marl, fractures develop within the brittle layer, and may terminate at the bounding ductile layer (e.g. Friedman et al., 1994; Rijken and Cooke, 2001). In more homogeneous strata, such as thick carbonate deposits without marl layers, fracture termination can occur at weak bedding planes in the stratigraphic sequence (e.g., Underwood et al., 2003).

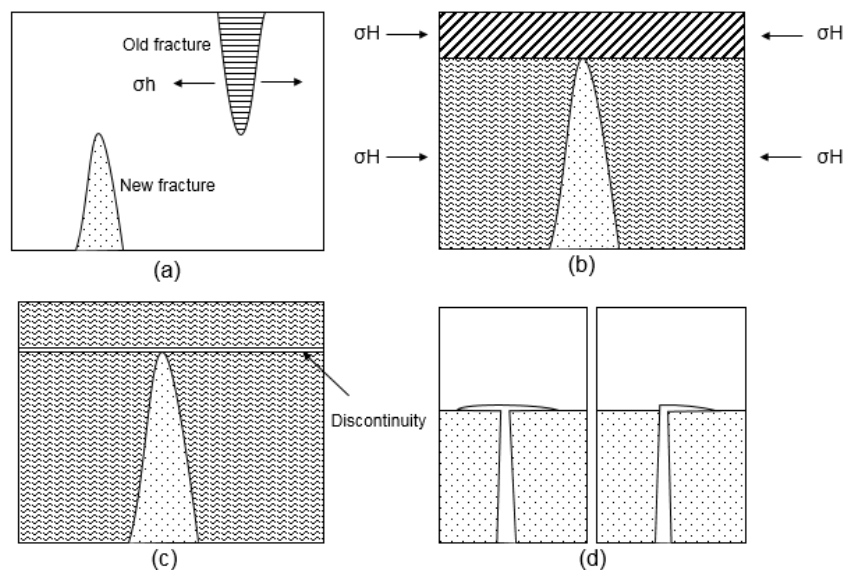


Figure 2.8: Mechanisms for fracture termination (Modified from Gudmundsson, 2012).

2.4 Classification of fractures

Fractures, being geologic features, can be described in terms of their shape, form and distribution and, therefore, different classification schemes can be used to organize their description (Van der Pluijm, 2004). As a result, many different fracture classifications may exist in scientific literature depending on the author's interest to describe a specific characteristic of fracture, thus leading to a wide terminology. However, a general consensus exists regarding to descriptive and genetic classification criteria.

- **Generic classification:** It is based on the relative displacement across the fracture plane (Nelson, 2001; Gudmundsson, 2011), so every fracture in rock can be either an *extension fracture* (the sense of displacement is perpendicular to, and away from, the fracture plane) or a *shear fracture* (the sense of displacement is parallel to the fracture plane) (Figure 2.9). Extension fractures include joints, veins, dykes, sills and artificial

hydraulic fractures, whereas the most common shear fractures are the principal types of fault (normal, reverse and strike-slip).

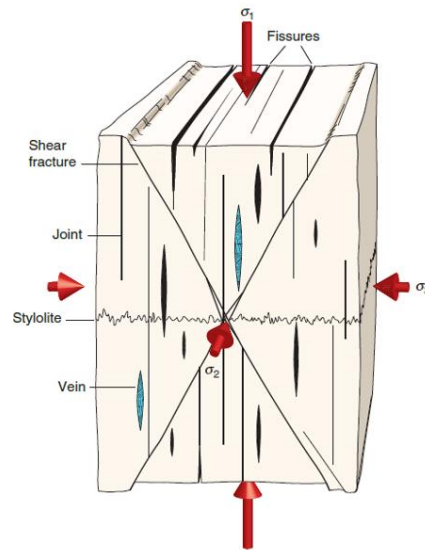


Figure 2.9: Relationship between principal stresses and types of fractures (Fossen, 2004).

- **Genetic classification:** It is based on the origin of loads that cause fracturing in rocks. Nelson (2001), identifies the following types of fractures according to their origin:
 - **Tectonic fractures:** associated with tectonic events and form in networks with specific spatial relationships to faults and folds. Tectonic fractures are important in hydrocarbon industry due to the fact that they contribute to permeability in low-porosity matrix naturally fractured reservoirs.
 - **Regional fractures:** developed over large areas of the earth's crust with little change in orientation, show no evidence of offset across the fracture plane, and are perpendicular to bedding plane. Their origin is suggested to be associated with large-scale vertical movements in earth's crust.
 - **Contractional fractures:** associated with a bulk volume reduction of the rock and are the result of processes such as dessication, syneresis, pressure-solution, thermal gradients and mineral phase changes. Under very specific depositional and diagenetic circumstances, these fractures can be important in hydrocarbon production.
 - **Surface-related fractures:** are created by unloading, release of stored stress and strain and weathering. They are related to hydrocarbon production only in the case of karstification.

Fractures can also be classified according to their displacement mode into three ideal types (Gudmundsson, 2011): Mode I (pure extension) where the wall cracks move apart; Mode II, where fracture walls slide over one another in a direction perpendicular to the leading tip of the crack, and: Mode III, where fracture walls move relative to one another in a direction parallel to the leading tip of the crack. A fourth type, Mode IV, is considered (Fossen, 2004), in which fracture walls tend to close one against the other as is the case of stylolites (Figure 2.10).

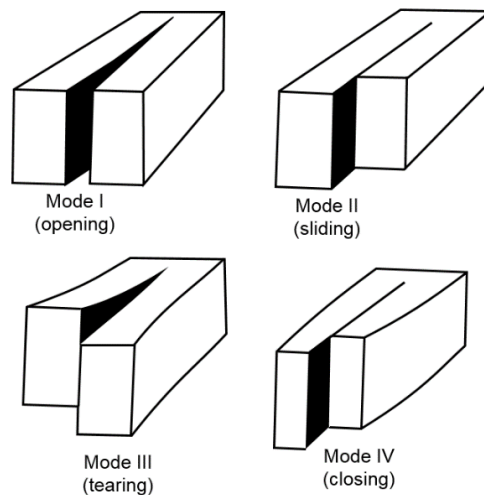


Figure 2.10: Modes of fractures (Fossen, 2004).

Nelson (2001) classified fractures according to the morphology of fracture planes in four basic types: 1) Open fractures (with no filling material between the walls); 2) Deformed fractures (physically altered by later tectonic shear motions); 3) Mineral-filled fractures (filled by secondary or diagenetic mineralization) and; 4) Vuggy fractures (result from the matrix alteration surrounding the fracture).

Fractures can also be classified according to their timing of formation relative to a specific geological event into: Pre, syn, and post-formational fractures, thus establishing a chronology of the fractures and their relationship to major tectonic episodes (Casini et al, 2011).

2.5 Geological controls in fractured carbonates

Fractures are present in virtually every rock as macroscopic scale features (visible at naked eye), microscopic scale features (visible only at microscope) or both. Fracture intensity within a subsurface rock unit is directly associated to rock strength (amount of load a material can bear before it deforms) and Young's modulus, which is a measure of stiffness (inverse to flexibility) and is also related to brittleness (material rupture without any deformation), which in turn is controlled by the occurrence and interaction of different

geological factors, such as lithology, grain size (texture), porosity, bed thickness and structural position (Hugman and Friedman, 1979; Nelson, 2001). Diagenetic processes (compaction, dolomitization,) play an important role since they directly affect lithology, texture and porosity thus modifying the rocks' mechanical properties and, therefore, fracture intensity. Finally, the number and intensity of deformational events during a basin's geological history, associated either directly to plate tectonics (rifting, orogenic-related folding and thrusting, and strike-slip) or to gravitational-related tectonics in passive margins, plays a role in subsurface rock fracturing. Extensive fieldwork and laboratory experiments have provided most of the knowledge about the relationships between the geological factors mentioned above and development of fractures. This study aims to identify these relationships at subsurface through the integration of different analysis of seismic and borehole information.

2.5.1 Lithology

In general, and assuming all other geological controls to be equal, rocks with a high percentage of brittle particles (quartz, feldspar, dolomite) will have a higher fracture density (Nelson, 2001, Figure 2.11). In carbonate rocks, Schmoker et al. (1985) suggest that dolomitic reservoirs are characterized by more effective fracture networks, supported by laboratory experiments and field observations that show that, under similar conditions, dolomite is more pervasively fractured than limestone (Stearns and Friedman, 1972; Hugman and Friedman, 1979; Sinclair, 1980). Ortega et al. (2010), demonstrated that dolomite content, rather than bed thickness, is the dominant control on fracture intensity in outcrops of Cupido and Tamaulipas Formations (Mexico, Figure 2.12), thus highlighting the potential importance of diagenetic and mechanical-property history in governing fracture patterns (Laubach et al., 2009). Offshore well data from the south-eastern Gulf of Mexico has also shown that dolomites exhibit higher fracture densities than limestones. Conversely, Wennberg et al. (2006) suggest that the degree of dolomitization in platform carbonate rocks from Asmari Formation in Iran does not have a significant effect on fracture density. These contradictory results may indicate that other parameters (rock texture, bed thickness and structural position), also exert a role in porosity/permeability and fracture development (Giorgioni et al., 2016). Therefore, the potential impact of dolomitization should not be simplified to general rules.

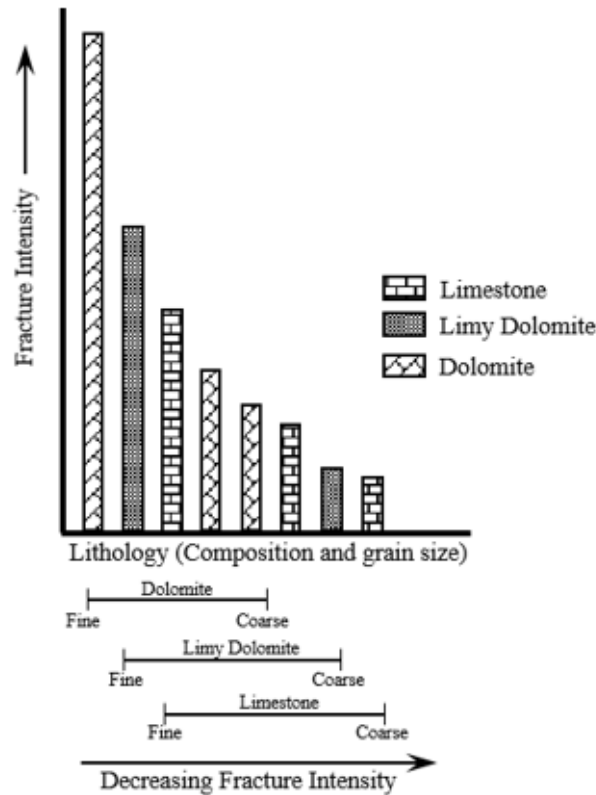


Figure 2.11: Fracture intensity as a function of lithology and grain size (Nelson, 2001).

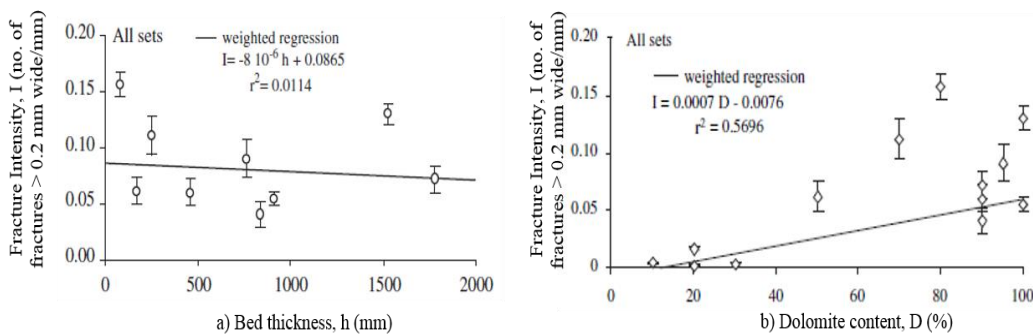


Figure 2.12: Fracture intensity is controlled mainly by lithology (b) rather than bed thickness (a) (Ortega et al., 2010).

2.5.2 Texture

Texture can be defined as the size, shape, and arrangement (packing and orientation) of the discrete grains or particles within a rock. For sedimentary rocks, these grains are subdivided into clastic (or fragmental) and non-clastic (essentially crystalline). Grain size is related to rock strength in a linear relationship, where a rock with lower size grain has a higher strength (Hughman and Friedman, 1979) or brittleness. As a result, rocks that are more brittle tend to have higher fracture intensities (Nelson, 2001). As facies

distribution, including texture, is controlled by the depositional environment, this too may be considered to strongly influence the likely fracture density. Wennberg et al. (2006) found that Mud-supported textures (mudstone-wackestone), according to the Dunham (1962) classification, have a higher fracture intensity than grain-supported textures (packstone-grainstone; Figure 2.13). Nelson and Ward (1993) observed a slight increase in fracture intensity with decreasing in grain size. Di Naccio et al. (2005) observed a systematic decrease in fracture density moving from subtidal (mud-supported textures) to intertidal to inter-supratidal and tepee facies (grain-supported textures), suggesting that mud content may influence fracture intensity, although in the same study it was also observed that extent and degree of early diagenesis had major influence on fracture development. However, fracture density within intertidal or subtidal intervals also depends on the degree and extent of early diagenesis across the sedimentary cycle. Giorgioni et al. (2016) found that intensity of top-bounded fractures (fractures smaller than bed thickness) is distinctly lower in coarse-crystalline dolomites than in fine-crystalline dolomites and limestones, both at the macro- and the micro-scale (Figure 2.14). The same relationship has been found for similar dolomitized carbonates in borehole cores of the deeply buried reservoir of the Basilicata oilfield, this indicating that rock texture (crystal/grain size) is more important than lithology (dolomite vs. limestone) in regulating the fracture pattern.

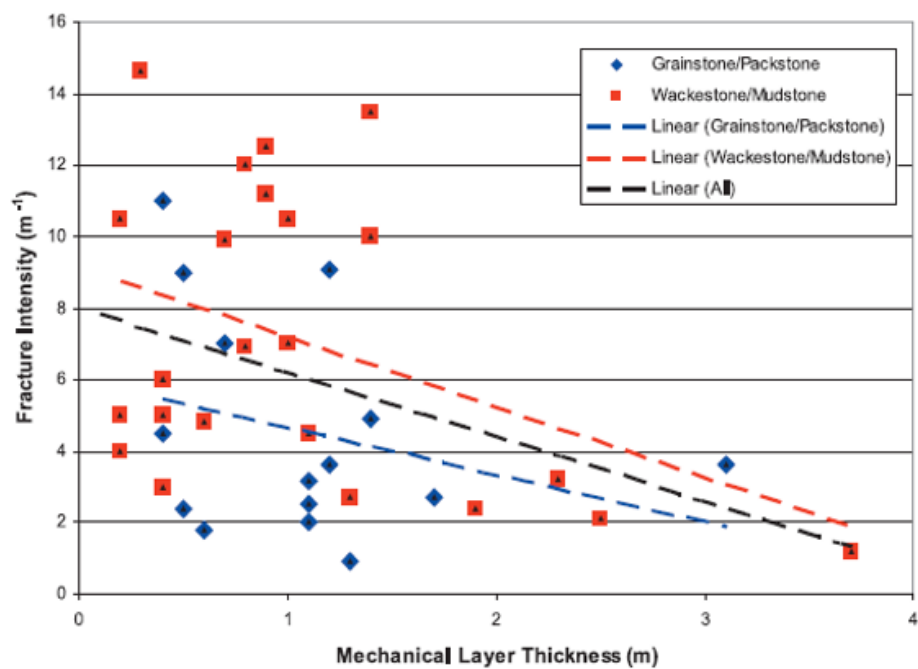


Figure 2.13: Fracture intensity as a function of rock texture and bed thickness. (Wennberg, 2006).

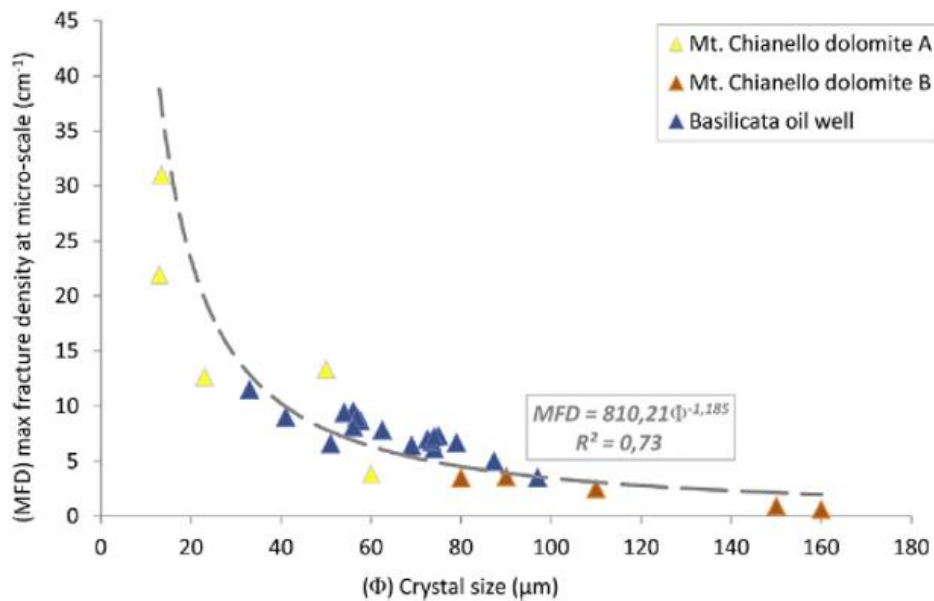


Figure 2.14: Fracture intensity as a function of crystal size in dolomites. (Giorgioni et al., 2016).

2.5.3 Porosity

The porosity of a rock is the proportion of its volume filled with a gas or liquid (Nichols, 2009). According to Sinclair (1980) and Nelson (2001), fracture intensity is generally related to the rock strength and brittleness, both of which decrease with increasing porosity for rocks of similar composition and fabric. Nelson and Ward (1993) observed that fracture density increases with decreasing porosity in Lower Palaeozoic dolomites from the Sawtooth Mountains, Montana, USA. Porosity within a rock mass varies with time due to diagenetic processes, which either reduce pore size by cementation and compaction, or increase it by dissolution, recrystallization or replacement (Ahr, 2008). Moreover, the proportion of cementation can change the mechanical properties of rocks such as the tensile strength, elasticity and brittleness (Rijken, 2005). Indeed, the early cementation of grainstones and packstones produces a greater competency and a different response to fracturing than the sucrosic dolomite (Barbier et al., 2011), where dolomite crystals are just in contact without too much cohesion. Amthor et al. (1994) concluded that dolostones undergo less porosity loss with depth than limestones as they are more resistant to chemical and mechanical compaction. Barbier et al. (2012) found that fracture intensities are higher in porous dolostones than in the well-cemented limestones and observe a positive correlation between porosity and fracture intensity in these two lithologies (Figure 2.15). These apparently contradictory findings are the result of diagenesis acting as a primary factor controlling fracturing rather than porosity.

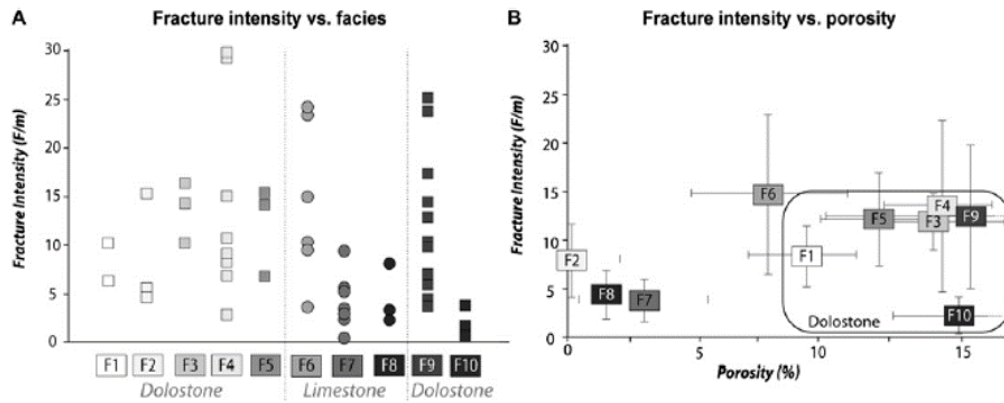


Figure 2.15: Fracture intensity as a function of porosity for limestone and dolomite facies. (Barbier et al., 2012).

2.5.4 Pore pressure

Fluid pressures in a deep basin are generated by several mechanisms related to burial (sedimentary loading, compaction), tectonic (tectonic loading) and thermogenic (hydrocarbon generation, hydrothermal fluids, etc.) origins (Kopf, 2002), and are summarized in Table 2.2: Causes for overpressure (Kopf, 2002). During sedimentation, seawater is commonly trapped into the pore space, which is a function of grain size and sedimentation rate. Overpressure occurs when rapid sedimentation rates overcomes pore fluid dissipation and, therefore, pore pressure exceeds hydrostatic pressure (Maltman, 1994).

Fluid pressure in the pores of a rock can have a large effect on the failure conditions (Gudmundsson, 2011). Sedimentary rocks contain a significant fluid component that will affect their mechanical behaviour under stress (Van der Pluijm, 2014). Pore pressure (P_f) operates equally in all directions and reduces the effective normal stress (confining pressure, P_c) in the rocks, resulting in an effective pressure $P_e = P_c - P_f$. As a result, there is a decrease in rock's strength and ductility, and the Mohr's circles are shifted to the left (Figure 2.16). In other words, rocks are weaker when the pore-fluid pressure is high. Under a very low differential stress (σ_1 almost equal to σ_3) regime, increasing pore pressure may shift the Mohr's circle to the tensile part of the diagram, resulting in the formation of extension fractures (hydrofractures) when $-\sigma_3 = T_0$, the tensile strength of the rock (Gudmundsson, 2011).

Origin	Mechanism	Environment	Significance	Selected References
Burial	sedimentary loading, compaction/settling	any sedimentary setting (i.e., deltas and active and passive margins)	major in such settings	<i>Braunstein and O'Brien</i> [1968] <i>Morgan et al.</i> [1968] <i>Moon and Hurst</i> [1984]
	slumping, sliding	marine slopes of active and passive margins	major on slopes	<i>Hovland and Judd</i> [1988]
Tectonic	tectonic loading	any compressional margin, thrust zones, and wedges	major in such settings	<i>Shipley et al.</i> [1990] <i>Westbrook and Smith</i> [1993]
	deep level ducting	accretionary complexes	major in such settings	<i>Moore</i> [1989]
Thermogenic	smectite dehydration	accretionary complexes	can be major	<i>Fitts and Brown</i> [1999]
	opal/quartz reactions	any setting with biosilica	usually minor	<i>Kastner</i> [1981]
	smectite dehydration	any setting with abundant clay deposition	can be major	<i>Schoonmaker</i> [1987] <i>Colten-Bradley</i> [1987]
	other diagenesis	deeper subduction zone	minor?	<i>Moore and Saffer</i> [2001]
Biogenic	metamorphism	deep subduction zones and other collision zones	usually minor, but locally important	<i>Bebout et al.</i> [1999]
	methanogenesis/hydrocarbon generation	any setting and reservoirs	can be locally important	<i>Ridd</i> [1970] <i>Hedberg</i> [1974]
	thermal expansion; hydrothermal pressuring	magmatic arcs and ridges	can be locally important	<i>Barker and Horsfield</i> [1982]
Other	osmosis	shallow marine settings and accretionary prisms	can be very important	<i>Rüger et al.</i> [1987] <i>Suess et al.</i> [1999]
		clay-bearing sedimentary environments	very minor	<i>Fertl</i> [1976]

Table 2.2: Causes for overpressure (Kopf, 2002).

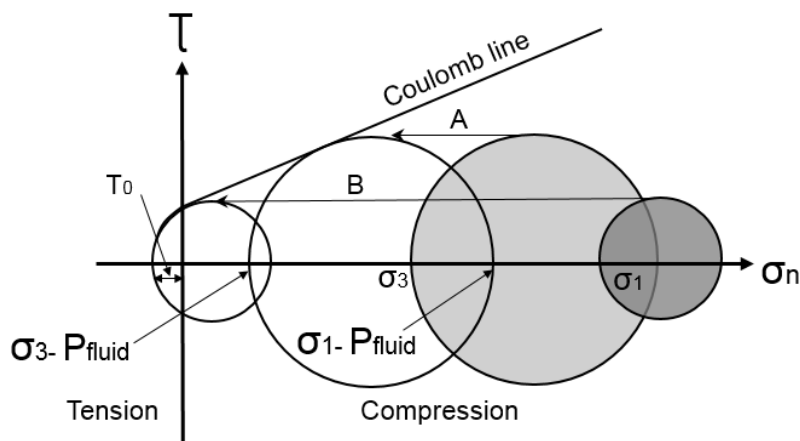


Figure 2.16: Effect of pore-fluid pressure in rock failure (Gudmundsson, 2011). Circles A (gray coloured) and B are shifted to the left due to the presence of pore pressure, which reduces rock's strength. Consequently, they will touch the enveloping Coulomb line, and rock will fail in a brittle way, producing shear fractures (great circle B) or tensile fractures (small circle B).

2.5.5 Bed thickness

Thinner beds will have a higher fracture density than thicker beds, if all other parameters and loading conditions are equal (Nelson, 2001). This relationship has been widely recognized by several authors. Ding et al. (2012) showed that fractures are more developed in thin beds (>10-20 cm) than in thicker beds. Giorgioni et al. (2016) concluded that spacing (density) of perfect bed-bounded fractures is mainly controlled by fracture bed thickness, with no significant effect of lithology and dolomite texture (Figure 2.17: Effect of layer thickness in fracture spacing (Giorgioni et al., 2016).). Awdal

et al. (2016) similarly propose that bed thickness, rather than lithology, exerts a primary control on fracture intensity, being three times higher in thin bedded limestones than in massive bedded dolostones (Figure 2.18). Cooke et al. (2006) also found in their study that the mechanical unit thickness, or spacing of mechanical interfaces, controls fracture height length and spacing. One explanation for this observed field relationship relies on the concept of a stress shadow; a stress shadow is a zone of decreased stress adjacent to an open fracture that inhibits new fracture growth (Pollard and Segall, 1987). The size of the stress shadow, and therefore the spacing of fractures, is directly proportional to the height of the fracture (Pollard and Segall, 1987; Gross, 1993). Thus, thicker mechanical units (i.e., those with more widely spaced mechanical interfaces) will have longer and more widely spaced fractures than thinner units. In the other hand, Di Naccio et al. (2005) explained that the lack of correlation between facies thickness within each sedimentary cycle (subtidal to intertidal to inter- supratidal and tepee facies) and fracture density is probably due to the fact that the interface between each interval is not as sharp as the diagenetic discontinuity delimiting cycles (bedding). The lack of such a sharp discontinuity might impede the mechanical decoupling between petrofacies-controlled layers during stress transfer.

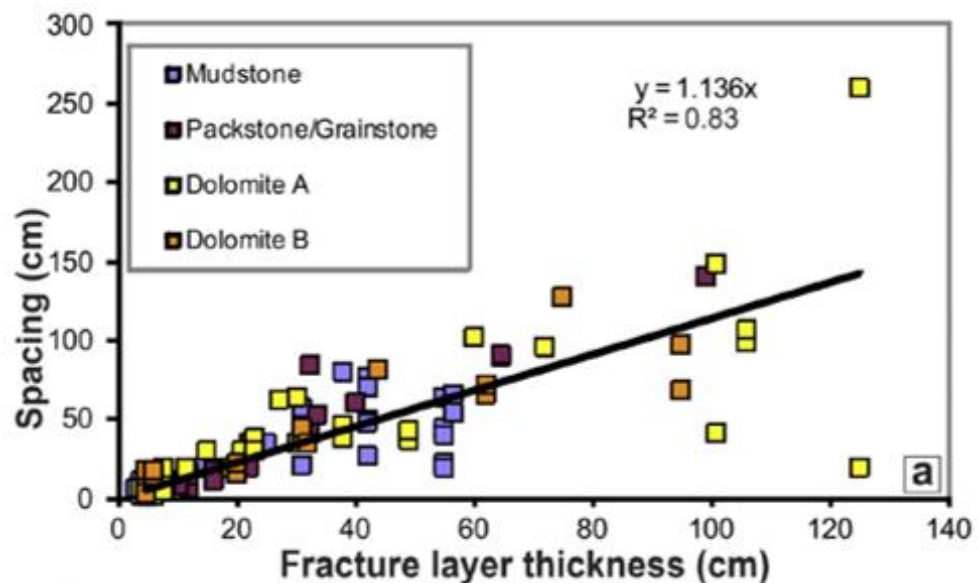


Figure 2.17: Effect of layer thickness in fracture spacing (Giorgioni et al., 2016).

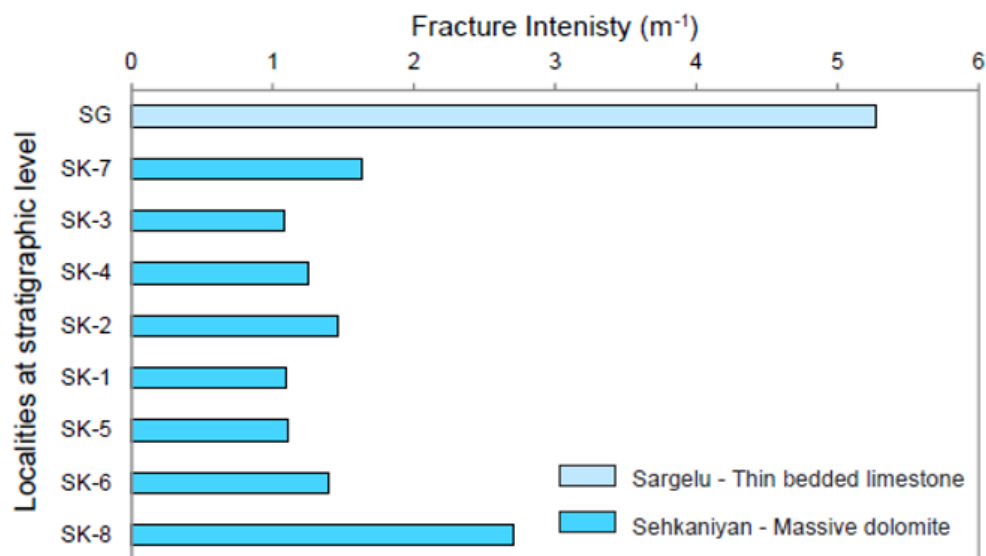


Figure 2.18: Fracture intensity is controlled by bed thickness rather than lithology (Awdal et al., 2015).

2.5.6 Effects of structural position

Rocks with a brittle behaviour have higher fracture density with increasing strain (Price, 1966; Nelson, 2001). This approach is useful to predict fracture intensity related to structural position, since it assumes that flexure-related fracturing will have maximum density where the rate of change of dip (curvature) is also maximum (Murray, 1968; McCaleb and Wayhan, 1969; Watkins et al., 2015). Ghosh and Mitra (2009) found that structural positions control fracture density and length and these are higher on the multiple hinges than on the limbs. Watkins et al. (2015) and Hanks et al. (1997) suggest that in deformed regions such as folds, lithology may still influence fracture intensity but that the structural position becomes increasingly important as strain increases (Figure 2.19: Fracture intensity is higher in the forelimb of the anticlinal than in the backlimb (Watkins et al., 2015)). Moreover, regional and local structural position may influence the development of fractures. For example, Lisburne Group carbonates in Alaska, USA deformed into tight, upright detachment folds in regional synclinoria are more likely to have dissolution fabrics related to folding instead of extension fractures, despite having greater degrees of curvature than detachment folds developed above the crests of anticlinoria (Hanks et al., 1997). As a result, fracture density can vary abruptly even across an individual structure such that rock types less prone to fracturing in the less deformed sections, may experience a higher relative increase in fracture intensity as deformation increases.

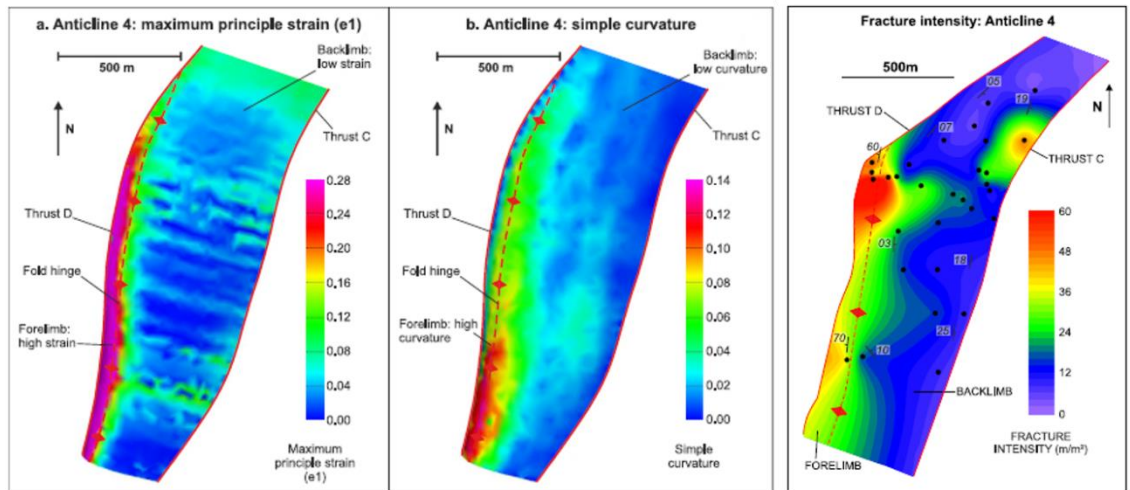


Figure 2.19: Fracture intensity is higher in the forelimb of the anticlinal than in the backlimb (Watkins et al., 2015).

2.5.7 Deformation mechanism

The mechanism of folding is also a critical controlling factor for fracture development. Xiubin et al. (2010) proposed conceptual models of fracturing related to fault-related folding (fault-bend folds, propagation folds and break-forward imbricates) where higher fracture densities can be localized either in the crest, backlimbs or forelimbs depending on the folding mechanism and the step-up angle of the fault (Figure 2.20). However, these models do not take into account other factors such as lithology or contrasts in mechanical properties of rocks. Eckert et al. (2014) proposed that fracture development in buckle folding depends on the mechanical properties of rocks and a fold's strain history. Also, fracture sets develop due to pure bending in subsiding minibasins around salt diapirs during passive diapirism and in a diapir's roof due to upward pushing during active salt diapirism (Alsop et al., 2016).

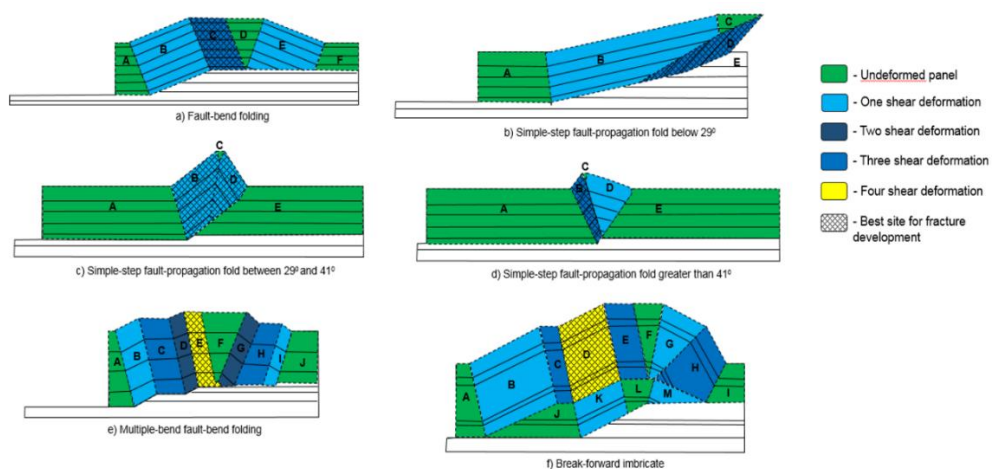


Figure 2.20: Effect of structural position on fracturing in fault-related folds (Xiubin et al., 2010).

2.6 Fractured reservoirs

Currently, approximately 60% of hydrocarbon reservoirs in the world correspond to carbonate of which around 85% are naturally fractured reservoirs (Lamarche et al., 2012). Nelson (2001) defines fractured reservoirs as “reservoirs in which natural fractures have, or are predicted to have, flow either in the form of increased reservoir permeability and/or reserves or increased anisotropy”. According to this definition, reservoir permeability and/or anisotropy depend on fracture attributes such as length, size, aperture, spacing and orientation and their distribution within the rock unit. In particular, fractured carbonate reservoirs are extremely complex because they are strongly heterogeneous at all scales from micro-scale to full field in terms of origin, nature, evolution and geometry (Wennberg et al., 2006; Lamarche et al., 2012). Moreover, reservoir and mechanical properties highly depend on the gain or loss of porosity during diagenesis and deformation. Fractures control the permeability and sometimes the porosity, thus enhancing or impeding the oil recovery; additionally, they may drain the fluids (injected or not) or may constitute barriers and therefore perturb the fluid flow (Larsen et al., 2010), thus varying dramatically well performance even between nearby wells (Wennberg et al., 2006).

Fractured reservoirs can be classified according to the positive effects on reservoir quality the fracture system exerts, which is determined during the reservoir development stages, when flow interaction between rock matrix and fractures is investigated (Nelson, 2001). Thus, reservoirs can be classified in four types (Figure 2.21):

- I: Fractures provide essential reservoir porosity and permeability
- II: Fractures provide essential reservoir permeability
- III: Fractures assist permeability in an already producible reservoir
- IV: Fractures create significant reservoir anisotropy (flow barriers).

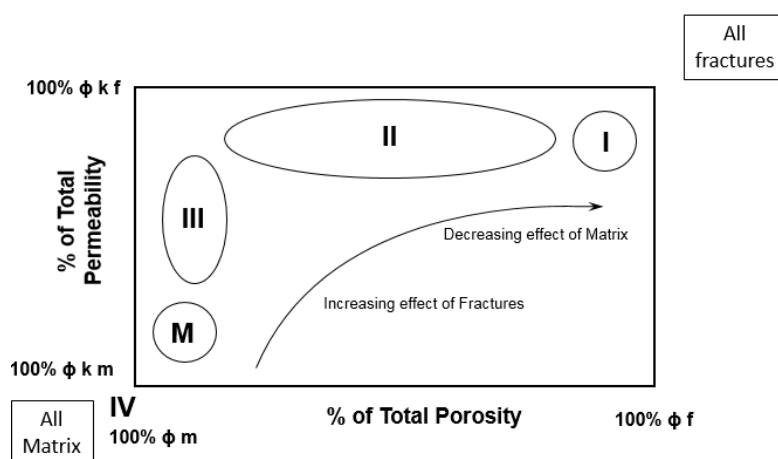


Figure 2.21: Classification of fractured reservoirs (Nelson, 2001).

2.6.1 Mechanical and fracture Stratigraphy

The limits of a fractured carbonate reservoir are determined primarily by lateral and vertical variations of the rock mechanical properties, which in turn, are controlled by geological factors such as lithology, porosity and texture that also control fracture spacing (Wennberg et al., 2006). Lateral limits can be defined by either sealing faults acting as flow barriers or lateral facies changes, whereas vertical limits are defined by mechanical stratigraphy and/or fracture stratigraphy associated to gradational changes in sedimentation with time, unconformities, overlapping of rock units by thrusting, etc.

Mechanical stratigraphy refers to the mechanical properties of the different rock layers within a sequence, where a mechanical layer represents one or more stratigraphic units that fracture independently of other units (Underwood et al., 2003), meanwhile fracture stratigraphy refers to the mechanical response of the different rock layers to an applied force (Laubach et al., 2009). Commonly, these two terms coincide; however, a mismatch between fracture stratigraphy and mechanical stratigraphy indicates that complex and progressive diagenesis may alter the rock such that mechanical properties no longer match those that governed the growth of earlier fracture patterns (Marin et al., 1993; Shackleton et al., 2005; Lavenu et al., 2013), which formed in a different rock diagenetic state than more recent ones, and present-day properties may only explain the attributes of recently formed fractures.

2.6.2 Fracture occurrence

Tectonic fractures tend to form in networks with specific, and predictable, orientations with respect to faults and folds (Nelson, 2001), which makes it possible to determine the direction of principal stresses at the time of their formation.

2.6.2.1 Fault-related fractures

Faults (conceptualized as macro-scale features) and their associated fractures (meso and micro-scale features) result from the same stress field and, therefore, there is a spatial relationship between them on all scales (Nelson, 2001). A careful analysis of fault-related fractures makes possible to determine the orientation of principal paleo-stresses as well as the sense of fault movement. Fractures developed close to a fault are not only shear fractures (which are orientated parallel and conjugate to the fault) but also extension fractures may occur bisecting the acute angle between the shear fractures (Figure 2.22). Gudmundsson et al. (2002) observed that 80% of fractures in a damage zone of a fault in North Iceland correspond to extension fractures and the 20% remaining being shear fractures.

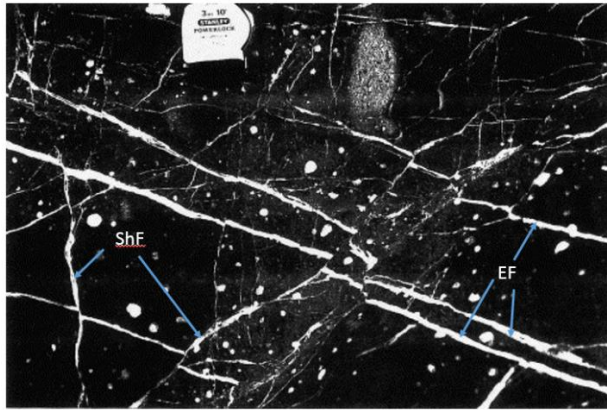


Figure 2.22: Extension fractures (EF) and shear fractures (ShF) in the Husavik-Flatey Fault zone (Modified from Gudmundsson et al., 2002).

According to Caine et al. (1996), natural fault zones comprise three structural units (Figure 2.23): 1) *Fault core*, where most of the displacement is accommodated and consists mostly of breccia and gouge; 2) *Damage zone*, where rocks are also brecciated but fractures are the predominant features, whose intensity increases irregularly towards the fault core (Gudmundsson, 2009). Reyer et al. (2012) reported that fracture orientation within the damage zone is predominantly sub-parallel to major faults. These authors also found that damage zone widths in carbonate rocks are usually higher than in clastic rocks, and that significantly thicker in the hanging-walls compared with the footwalls; 3) *Protolith*, or host rock, which surrounds the core and damage zones, where the effects of fault-related deformation are minor or absent. Fault zones are of great economic interest because of their ability to increase permeability and, therefore, allow fluids flow. For example, fractures in the damage zone control fluid flow during a period of quiescence on a fault, while, it is the contact between core and damage zones where permeability may increase by many orders of magnitude during fault activity (Gudmundsson, 2011).

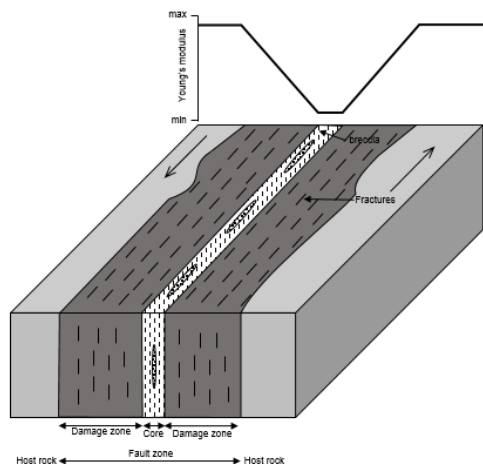


Figure 2.23: Internal structure of a fault zone (Modified from Gudmundsson, 2011).

2.6.2.2 Fold-related fractures

The relationship between natural fracture development and folding has been extensively studied, and conceptual models have been proposed (Figure 2.24) by several authors (Price, 1966; Stearns, 1968; Price and Cosgrove, 1990; Bergbauer and Pollard, 2004; Liu et al., 2016), where fracture sets show predictable symmetric orientations with respect to the fold geometry. These models, however, assume that strata are not fractured prior to folding. During fold evolution, fracture development depends on parameters such as layer thickness, lithology, rheology, elastic property contrasts, state of stress (Stearns, 1968), interlayer slip, the deformation mechanism (Xiubin et al., 2010; Eckert et al., 2014) and position in the fold. Since folds of sedimentary strata are common traps for hydrocarbons, and fractures can play an important role in hydrocarbon migration and production by increasing the quality of reservoir rock, it becomes critical to predict the location, type, extent, and orientation of these fold-related fractures. However, this may present a complex task, since a distinction has to be made between pre, syn and post-folding fractures due to the fact that pre-folding fractures alter the stress field in their vicinity such that nearby fractures would form in a perturbed stress field (Bergbauer and Pollard, 2004). Specifically, pre-folding fractures might not be symmetrically oriented with respect to the geometry of the evolving fold (Price and Cosgrove, 1990) and might change the stress field in which later syn-folding fractures form. Liu et al. (2016) proposed that the different fracture sets observed in various types of folds can be categorized into three main groups (Figure 2.24):

- **Group I:** Fractures directly related to stress conditions during buckling and likely initiated during folding (Sets 1, 4, 5, 6 and 11).
- **Group II:** fractures that are thought to represent pre-folding features and, therefore, unlikely to be initiated during folding (Sets 3, 7, 8 and 9).
- **Group III:** Fractures that are unlikely to be initiated during folding and thought to be caused by erosional unloading processes (Sets 2 and 10).

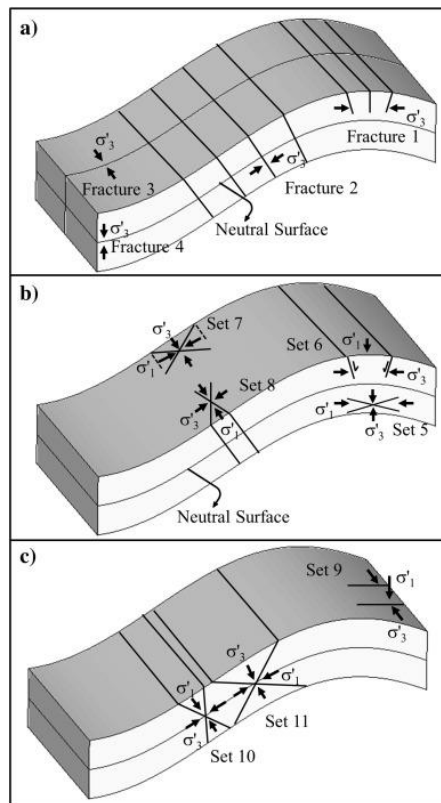


Figure 2.24: Sets of fold-related fractures and inferred principal stresses. a) Tensile fractures, b) and c) Conjugate shear fractures (Liu et al., 2016).

2.7 Salt tectonics and fracture development

The presence of evaporitic sediments strongly influences the style of deformation in a basin. Moreover, salt movement in the subsurface may control the distribution of fractured zones (Tuncay et al., 2003). Diapirism commonly involves near-salt deformation where adjacent, underlying strata and the overburden are folded and faulted in most cases (Rowan et al., 2003). Active diapirism can fold and generate several interconnected sets of mostly extensional faults and fractures in the overburden and, to a lesser extent, around the diapir due to salt's upward pushing forces. These fractures maintain high angles ($>70^\circ$) with respect to the bedding (Davison et al., 2000; Alsop et al., 2016) and are typically arranged in radial patterns in plan view (Figure 2.25).

During passive diapirism, near-diapir flank folding is caused by draping of beds as bathymetric relief increases due to two main factors: 1) changing rates of salt inflation/deflation, and 2) high-frequency variations in sedimentation rate as illustrated in Figure 2.26 (Rowan et al., 2003). As a result, radial faulting in plan view can develop adjacent to the diapir. Moreover, these authors also found that the amount of faulting, which is small-scaled and related to passive diapirism, is proportional to the amount of bed rotation and the plan-view geometry of the salt body, so faulting is more intense with a higher degree of upturn of beds and can extend farther from the diapir. However, it has

been observed that near-diapir deformation can vary from severe overturn and thinning of beds to undeformed, constant-thickness strata. Also, fracture sets may develop due to pure bending (Figure 2.27) in subsiding minibasins around salt diapirs during passive diapirism (Alsop et al., 2016).

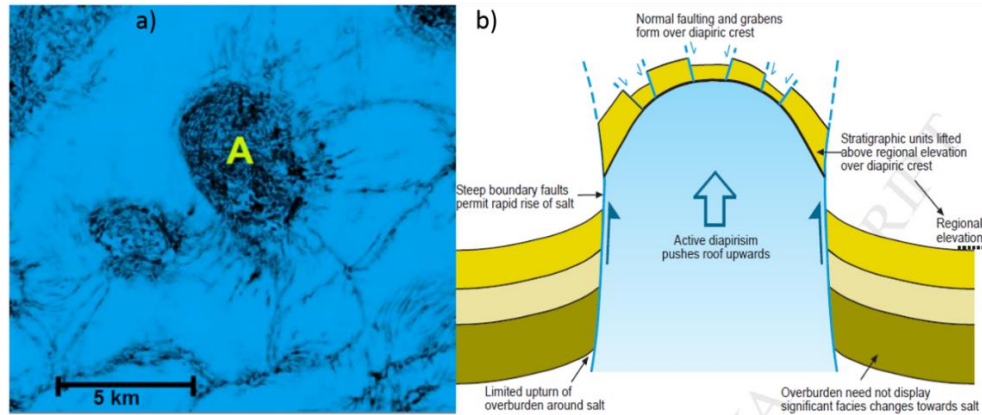


Figure 2.25: a) Pattern of radial faults in plan view around a salt diapir in Southern Gulf of Mexico (Rodriguez del Angel, 2012). Faulted roof above an active salt diapir (Alsop et al., 2016).

Fractures can also form adjacent to vertical welds, which result from squeezing of a salt wall due to compressional stresses. Rowan et al. (2012) relate fracture density variations along-strike to factors such as the presence of evaporitic residues, original width and shape of the salt wall, intensity of shortening and its orientation respect to the weld, and post-welding weld-parallel slip due to oblique shortening.

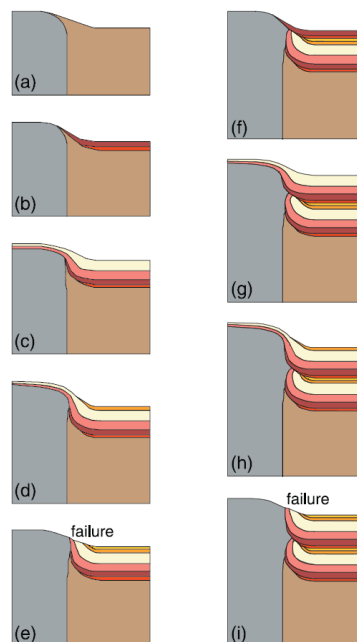


Figure 2.26: Kinematic model of diapir-flank folding (Rowan et al., 2003).

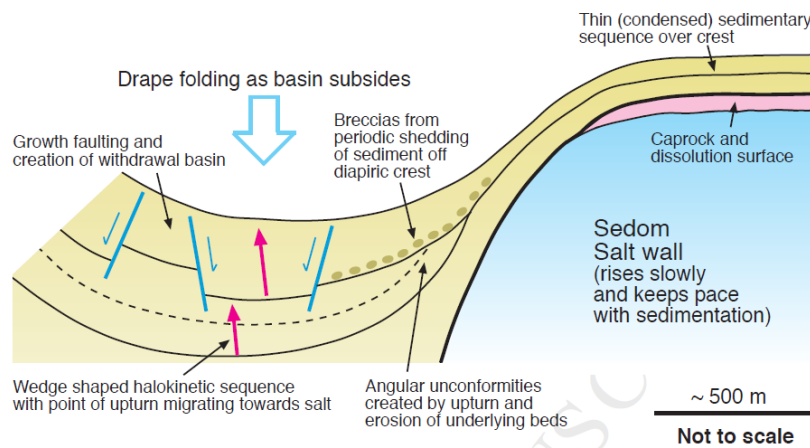


Figure 2.27: Folding and faulting in minibasins around passive diapirs (Alsop et al., 2016).

2.8 Fracture detection in subsurface

Fractures are geological features that may allow fluid-flow in the subsurface and, therefore, are closely related to important economic resources (Ortega-Marrett, 2000). In the hydrocarbon industry, the presence of open fractures is especially important as: 1) open fracture networks increase the quality of reservoir rocks by enhancing original low-matrix permeability allowing hydrocarbon accumulation and effective reservoir performance; 2) fractures can also act as a barrier for fluids, thus acting as a seal and promoting reservoir compartmentalization; 3) fractures can affect integrity of traps by breaching seal rocks, thus promoting hydrocarbon migration and leaking reservoirs.

The presence of fractures in the subsurface can be detected by direct and indirect methods. Among the former, core and cutting samples from wellbores provide direct evidence of subsurface fractures. Core material in particular provides information not only about fracture characteristics such as dip, density, aperture and even orientation but also data on rock-strength, lithology, porosity and permeability (Nelson, 2001). However, the volume of rock obtained in core sampling is too small to confidently identify and characterize large fractures, which commonly are greater and with a wider spacing than the core's diameter (Laubach, 1988). As a result, well data provide details of small-scale fracture density and orientation, but carry very little information about the extent of the fractures and their connectivity (Casini et al., 2011). While drilling a borehole, the mud and drilling logs may also indicate the presence of natural fractures (Norbeck, 2011) by measuring parameters such as variations of mud volumes, sudden changes in penetration rates and gas peaks. Poor core recovery may also indicate the presence of fractures. Other indirect methods used at boreholes include flow test evaluations and analysis of reservoir rock data (Nelson, 2001).

Indirect methods for natural fracture detection comprise seismic data and well logs. Well logs are mainly used to detect highly fractured zones rather than determine fracture spacing due to sampling limitations (Nelson, 2001). A combination of the response of several tools are commonly used to detect fractures, the most important being: Sonic logs, caliper log, imaging logs, resistivity logs. Fracture parameters such as density, aperture, size, length and fluid content may produce anomalous response in well logs that may be considered as fractured zones. Well log analysis must be complemented with data from core analysis, seismic information and geological knowledge (Gartner and Suau, 1980).

Seismic methods have been successfully employed to detect natural fractures, and have been used extensively for reservoir development purposes by characterizing spatial variability of fracture density. Methods based on post-stack attributes such as coherence, ant tracking, and curvature have been used to predict fracture properties from narrow- and wide-azimuth seismic data; however, such methods are unable to distinguish between open and closed fractures (Narhari et al., 2015). Curvature analysis is based on the general assumption that fracture density may be directly related to the degree of curvature of the fold (Lisle, 1992). However, fracture density may be relatively high in flat areas due to stress differences related to material heterogeneities or changing pore pressure (Smart et al., 2009). Analysis of shear-wave data, vertical seismic profiling, compressional and shear wave anisotropy and waveform scattering studies may be used to locate subtle structural features that control fracture distribution within a reservoir (Arre et al., 2012). State of the art techniques used to detect subtle faults and fractures that cannot be interpreted in a standard amplitude volume include AVAZ (amplitude versus incident and azimuthal angle), which uses amplitude variations that varies with azimuth and dip in the long shot/receiver offsets of P-wave seismic data to determine the intensity and orientation of fractures (Gray et al., 2003; Narhari et al., 2015). However, this technique assumes only a single set of parallel and nearly vertical fractures and the background rock mass is isotropic, which represents a limited approach given the observed heterogeneity and anisotropy in rocks.

2.9 Fracture prediction

There are few studies that have integrated geological and geophysical data in order to predict subsurface fracturing in inter-well areas. Lohr (2008) integrated 3D seismic data, 3D retro-deformation, coherency analysis, geostatistics and well data in order to predict the relative density of small-scale fractures in areas without well data; however, this methodology is limited by not considering heterogeneous sedimentology, variable

diagenetic processes and multiple deformational events. Endres et al., (2008) quantified subsurface fracturing by combining coherency attributes, borehole images and geostatistical analysis, showing a good correlation between different scales of fracturing. Ding et al. (2012) predicted fracturing in carbonates by simulating the effects of faults on fracture formation with 3D FEM analysis of paleotectonic stress based on geological, geomechanical and numerical models. They suggest a positive correlation between intensity of tensile stress and fracture density. However, even when their results from simulation match with FMI data, they considered that fractures in the interval studied were formed at a single deformational event only and ignore the effects of additional events.

Jenkins et al. (2009) describe the Continuous Fracture Modelling (CFM) technique, based on the neural network methodology described by Ouenes, H. (2000), which establishes a relationship between fracture drivers (lithology, log data, structural curvature, proximity to faults, different seismic attributes, impedance from seismic inversions, among others) and fracture indicators (fracture count from image logs and cores, drilling losses, well-test permeabilities) in order to predict location fractures in the reservoir. To achieve this, the first step is to rank each fracture driver according to its effect on the final output (Fracture Intensity). Then, stochastic models are created to quantify the relationship between fracture drivers and fracture intensity. Finally, an uncertainty analysis is carried out by examining the results from the stochastic models, and a map of probability is created for a study area. Since predictive capability of CFM relies strongly on the amount and quality of available data, the absence or use of little and/or poor-quality seismic attributes, poor-quality seismic data, and well data will result in the generation of inaccurate fracture indicators and, consequently, will reduce the reliability of fracture prediction.

2.10 Summary

Natural rock fractures are geological features that can enhance fluid flow in the subsurface, and have a great impact when those fluids are of economic importance (groundwater, hydrocarbons). Fracture intensity is controlled by a complex interaction of several factors such as lithology, porosity, texture, structural position, bed thickness, deformation mechanism and pore pressure through time. Extensive laboratory and fieldwork-based research about the particular relationship of each factor to fracture intensity has been undertaken by many authors, which has led to the establishment of a suite of generally accepted assumptions; however, contradictory results from these

studies also indicate that it can be difficult to estimate the contribution of individual factors, or their relative importance to fracture density.

Fracture prediction in the subsurface presents a challenging, complex task requiring a multidisciplinary approach: combining geological and geophysical disciplines such as seismic interpretation, structural geology, petrophysics and petrography. Several attempts have been undertaken and one of the key take-home messages has been that the reliability of the results fundamentally depends on the amount and quality of data available, which usually consists of indirect but spatially extended information (seismic data) or direct but very spatially restricted, fragmentary information (cutting and core samples, well data).

This project aims to estimate the fracture orientation and intensity in areas where there is little or no well data available to support analysis derived from seismic data. Information available consists of a Pre-Stack Depth Migrated (PSDM) seismic survey and information from three vertical boreholes (reports, well data and lithological samples). The approach will be to combine standard seismic interpretation with 2D restoration, structural seismic attributes (curvature and coherence), image logs, core samples into a single model intended to estimate fracture intensity in Mesozoic carbonate rocks, which are targets for hydrocarbon exploration. The results from this work will complement existing studies on fracture density, and can be used to improve our understanding of some of the geologic controls of natural fracturing (mainly tectonic history, structural position and lithologic facies); how relative fracture intensity can be estimated from different independent analysis; and, most importantly, what are the implications for hydrocarbon exploration.

Chapter 3

Geological Setting of Southern Gulf of Mexico

3.1 Overview

The Gulf of Mexico (GOM) basin is located at the south-eastern continental margin of the North American Plate, it covers an area of approximately 1,600,000 km² (Stern and Wilkinson, 2010) and its limits correspond mostly to structural features (Figure 3.1). To the north, from west to east, it is bounded by the flanks of the Marathon uplift, Ouachita orogenic belt and mountains, Central Mississippi belt and southern Appalachian Mountains; the western limit corresponds to the Coahuila platform, the Sierra Madre Oriental and the Chiapas Massif; the southern and eastern limits correspond to the Yucatan and Florida carbonate platforms respectively (Salvador, 1991a). The GOM encompasses several smaller sub-basins and is filled with up to 18 km of sedimentary strata ranging in age from Late Triassic to Recent in its northern portion (Peel et. al, 1995), with water depths of up to 4,350 m on the Sigsbee abyssal plain.

South-eastern Basins (SEB) oil province is located within the GOM South Coastal Plain and South Eastern GOM Continental Shelf physiographic provinces, and comprises both onshore and offshore portions. It is limited to the north by the 500 m isobath; to the south by the Chiapas Fold Belt; to the west by the Veracruz Basin and to the East by the Yucatan Platform (inset Figure 3.2). From NW to SE, it comprises the following major tectonic elements: 1) Isthmian Salt Basin; 2) Comalcalco Basin; 3) Reforma-Akal Block (where the study area is located); 4) Macuspana Basin (Figure 3.2).

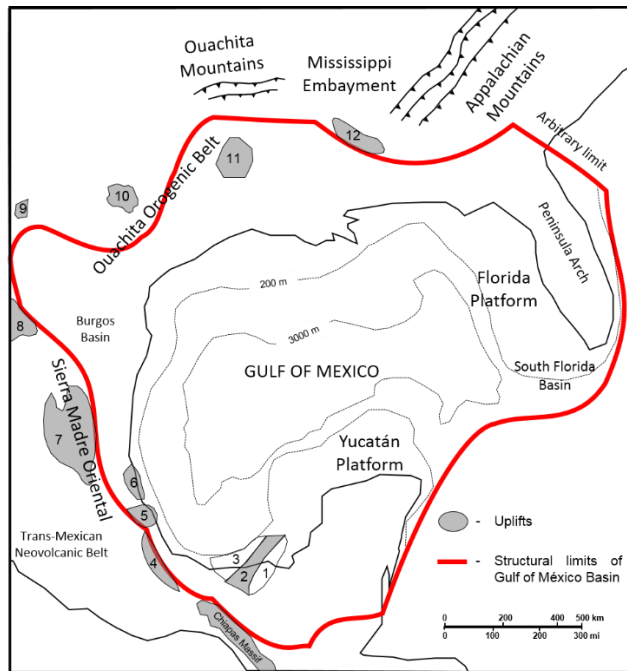


Figure 3.1. Outline of the Gulf of Mexico. Second-order structural features within the basin: 1) Macuspana Basin, 2) Akal-Reforma Block, 3) Comalcalco Basin, 4) Cordoba Platform, 5) Santa Ana Massif, 6) Tuxpan Platform, 7) Valles-San Luis Platform, 8) Coahuila Platform, 9) Marathon Uplift, 10) Llano Uplift, 11) Sabine Uplift, 12) Central Mississippi Deformed Belt. Modified from Salvador (1991).

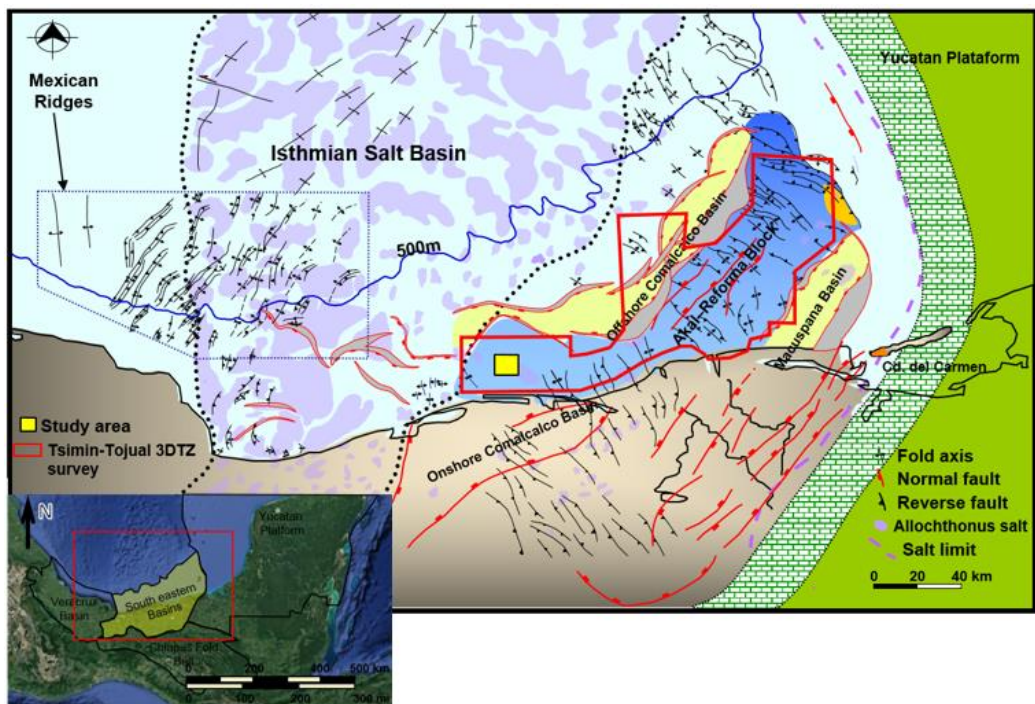


Figure 3.2: Tectonic map of Southern Gulf of Mexico. The study area is located in the south-western portion of the Akal-Reforma Block (in blue), which is a mega-raft block formed during Late Miocene-Pleistocene times and bounded by Comalcalco and Macuspana Basins (in yellow) (Modified from PEMEX, 2008 and CNH, 2014).

The SEB is the most prolific and important hydrocarbon province in Mexico, with most of the production coming from Mesozoic carbonate reservoirs and, to a lesser extent, from Tertiary siliciclastic reservoirs. The first offshore discovery occurred in 1976 with the Chac-1 well as a result of several geophysical studies carried out since 1972. Since then, several important oilfields have been discovered (Cantarell, Ku, Maloob, Zaap, Ek-Balaam, etc.) and have contributed an elevated percentage of Mexico's daily production. Extensive hydrocarbon exploration in the Southern GOM since the 1970's has made possible a better understanding of basin's structural evolution through the analysis of several 3D seismic surveys and data information from hundreds of wells drilled since then. Despite this, relatively little information about its tectono-stratigraphic evolution has been published due mainly to confidential policies from PEMEX E&P. Comprehensive overviews about regional geological framework have been published by Angeles-Aquino et al. (1994), Angeles-Aquino and Cantu-Chapa (2001), Angeles-Aquino (2006), and Padilla y Sanchez (2007). Peterson et al. (2013) proposed a model of the structural evolution in the southwestern offshore portion of the SEB. Additionally, Petroleum Geological Synthesis from both offshore shallow and deep water areas was released online by Mexico's Hydrocarbons National Committee (CNH) in 2014.

Structural traps are predominant and their geometries may vary from simple to very complex. Mitra et al. (2005, 2006, 2007) proposed models of the structural evolution of the Cantarell, Ku, Zaap, Maloob and Ek-Balam oilfields, which are located in the northeastern portion of the SEB. These models propose three main episodes of deformation: Early Mesozoic extension, Miocene contraction and Pliocene-Holocene extension. The presence of evaporitic sediments (mainly halite) has greatly influenced the style of deformation and added complexity to the analysis of the structural evolution and the associated fracture development of prospective hydrocarbon traps (Sanchez Rivera et al., 2011; Cruz-Mercado et al., 2011). Furthermore, evaporites also have implications as a seal rock, as well as in the distribution of reservoir facies and thermal maturity of the source rock. Table 3.1 summarizes the characteristics of the petroleum systems present in the SEB. A review of geochemical interpretation of source rocks in SEB is available on Valdes et al. (2009), Santamaria Orozco (2008) and Guzman et al. (2001).

Element	Age	Lithology	Trap Type	Trap Sub-Type
Source Rock	Oxfordian	Shales, calcareous shales (Type II)	-	-
	Tithonian	Shales, Shaly limestones (Type II)		
	Early Cretaceous	Shaly limestones (Type II)		
	Early Miocene	Calcareous shales (Type IV/III)		
Reservoir Rock	Oxfordian	Sandstone	-	-
	Kimmeridgian	Packstone/Grainstone of ooids; dolomite.		
	Early Cretaceous	Mudstone-Wackestone		
	Upper Cretaceous	Mudstone-Wackestone; calcareous breccia		
	Eocene	Packstone of intraclasts		
	Miocene, Pliocene	Sandstone		
Seal Rock	Oxfordian	Shale	Salt can also act as lateral seal or vertical seal when diapirism is involved	
	Kimmeridgian	Shale		
	Tithonian	Shale, limestone		
	Cretaceous	Shale, limestone		
	Palaeogene	Shale		
	Miocene, Pliocene	Shale		
Trap	Late Jurassic-Cretaceous (D1)	-	Structural	Fault-related folds Salt-related Extensional
	Eocene-Early Miocene (D2)			
	Middle-Late Miocene (D3)		Stratigraphic	Pinch-outs Lateral facies changes Salt-related
	Late Miocene-Present (D4)		Mixed	Extensional Salt-related
HC Generation	Middle Miocene - Late Pliocene			
HC Expulsion	Middle Miocene - Pleistocene			
HC Accumulation	Late Miocene-Present			

Table 3.1. Summary of the elements of Petroleum systems present in South Eastern Basins (Adapted from CNH, 2014).

3.2 Stratigraphy

Due to the fact that the study area corresponds to an offshore oilfield, knowledge of local stratigraphy comes from well's cores and cutting samples. Ages were determined, when possible, by foraminifera faunal associations combined with lithologic changes, and/or by electric logs correlation with nearby wells. The stratigraphic description below follows the depositional order and is illustrated in Figure 3.3.

- **Pre-Callovian:** These sediments have not been drilled in Southern GOM and therefore remain unknown to date, although correlations with continental red beds outcropping in Chiapas have been made (CNH, 2014).

Callovian: Evaporites (salt/anhydrite) are the oldest sediments drilled and correlate with Louann salt of Northern GOM and, therefore, are considered Callovian in age

(Salvador, 1991). Although these sediments have not been drilled in the study area, their presence can be deduced from seismic interpretation.

- **Oxfordian:** In early Late Jurassic, shallow marine conditions (inner ramp) were established in what is now the Southern GOM. From base to top, it consists of a gradational succession of shallow marine sandstones, sabkha evaporites, dolomites and supratidal siltstones and organic matter-rich carbonates, which are transitional with the base of Kimmeridgian-age sediments. Factors such as dolomitization, scarce index microfossils and lack of correlation with nearby wells, makes very difficult to define the top of this interval; however, presence of Oxfordian algae without any other accompanying Kimmeridgian algae at the base of the column, could date these sediments as Oxfordian in age.
- **Kimmeridgian:** Outer platform conditions prevailed during this time, and relief associated to salt diapirism controlled the location of oolitic banks. Sedimentation is carbonate and the base of the sequence consists of supratidal shaley mudstone-wackestone that gradates upwards into packstone-grainstone of ooids deposited locally under intertidal conditions in an inner platform setting.
- **Tithonian:** Thermal subsidence caused a deepening of the basin. As a result, during this time, deposition took place under deep marine conditions and consists of alternating shaley limestone and calcareous, bituminous, organic matter-rich shales.
- **Cretaceous:** Tectonic stability, climatic conditions and lack of terrigenous supply allowed the development of an extended carbonate platform during Late Jurassic and Cretaceous times in the Southern GOM. As a result, thick sequences of mudstone-wackestone were deposited from Early to lower Late Cretaceous (Turonian). During the Campanian-Maastrichtian, sedimentation graded from carbonate to terrigenous as a response to increasing terrigenous supply, resulting in the deposition of an alternating sequence of marls, shales and mudstone.
- **Cenozoic:** The change of sedimentary regime from carbonate to siliciclastic, as a response of regional tectonic events, led to the deposition of up to 6 km of terrigenous sediments in some areas of SEB during the Cenozoic. The depositional environment varied from bathyal (Paleocene-Miocene) to neritic (Pliocene-Pleistocene).

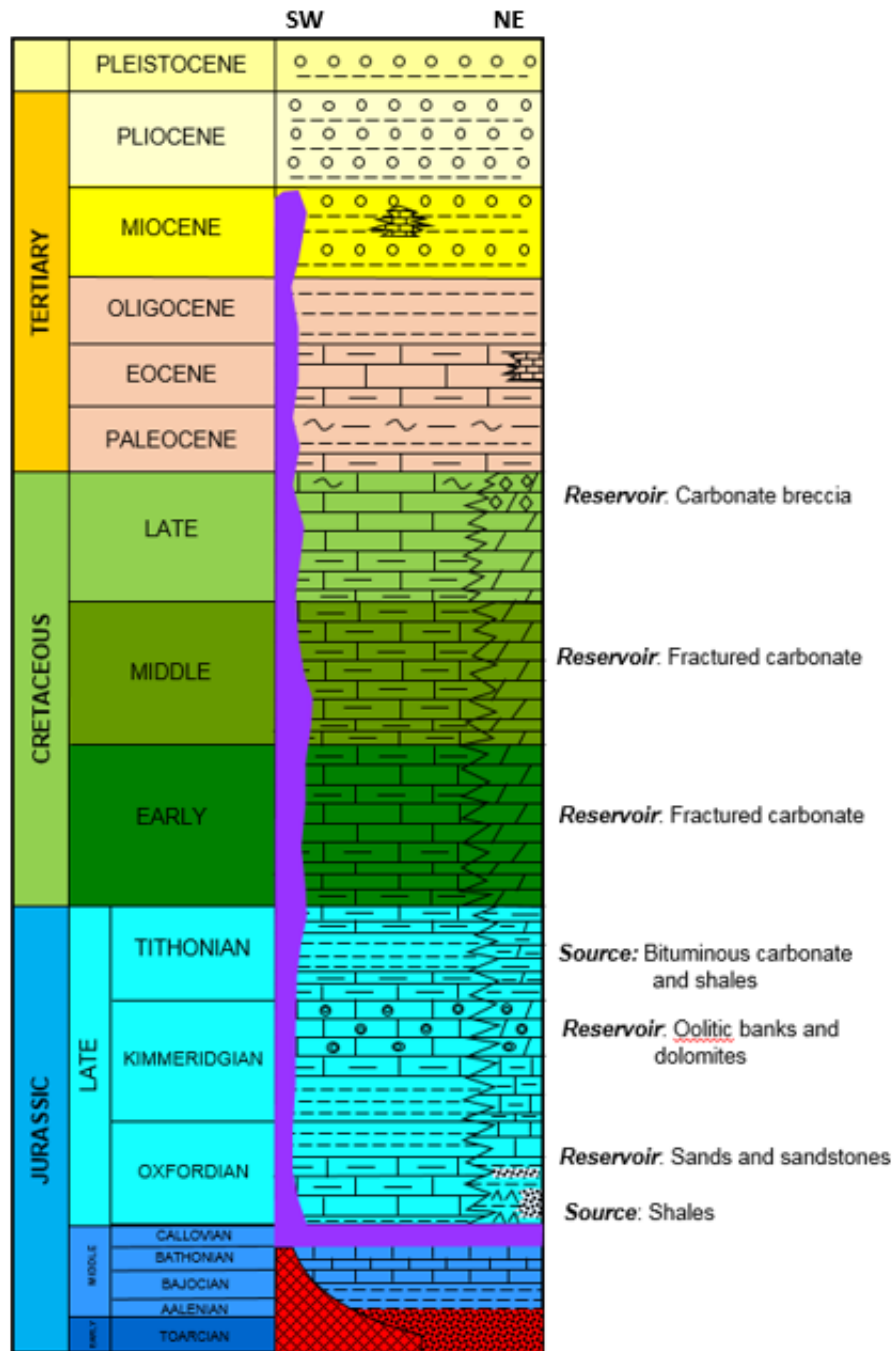


Figure 3.3. Stratigraphy of Southern GOM, where SW portion corresponds to the study area Modified from PEMEX, 2014.

3.3 Tectonic Evolution of South-eastern Mexico

Extensive literature regarding the tectono-stratigraphic evolution of the GOM has been published (Salvador, 1987, 1991; Winker and Buffler, 1988; Marton and Buffler, 1994; Pindell and Kennan, 2001, 2006, 2009; Bird, et al., 2005; Hudec et al., 2013, etc.) and it is based mainly on data from its Northern portion consisting of thousands of wells, a large amount of 2D and 3D seismic surveys and potential methods. In spite of this, some aspects of its geological evolution are still speculative and open to debate, due mainly to poor seismic imaging caused by the presence of salt sediments (Hudec et al., 2013) and lack of lithological information of the pre-salt stratigraphy from wellbores. However, recent improvements in seismic imaging and availability of information from the Southern GOM have made possible more constrained interpretations. This section aims to summarize the knowledge about GOM's evolution within plate tectonics context.

Geological events prior to Upper Triassic rocks in the GOM are very difficult to determine due to the very limited information available, which consists mainly of few Paleozoic rocks outcrops surrounding the basin, with a reduced exposed area and separated from each other by great distances (Salvador, 1991b). In contrast, geological events from Late Triassic that led to the formation of GOM can be reconstructed based on much more abundant and reliable information. Several authors (Dickinson and Lawton, 2001; Bird et al., 2005; Pindell and Kennan, 2009) agree on plate reconstructions where most of the Paleozoic and Precambrian rocks that presently constitute the backbone of Mexico were located along the North America-South America nascent plate boundary during the earliest Mesozoic (Figure 3.4). In a general way, the GOM evolution can be subdivided into three major tectono-stratigraphic stages:

- 3 Rift basin during GOM opening in Late Triassic to Upper Jurassic as a part of Pangea's breakup.
- 4 A passive margin stage with the development of an extended platform with carbonate sedimentation during sea-floor spreading (Late Jurassic to Early Cretaceous).
- 5 A foreland basin with mainly siliciclastic sedimentation since Late Cretaceous/Early Palaeocene to Present day associated with plate tectonics compression/transpression activity.

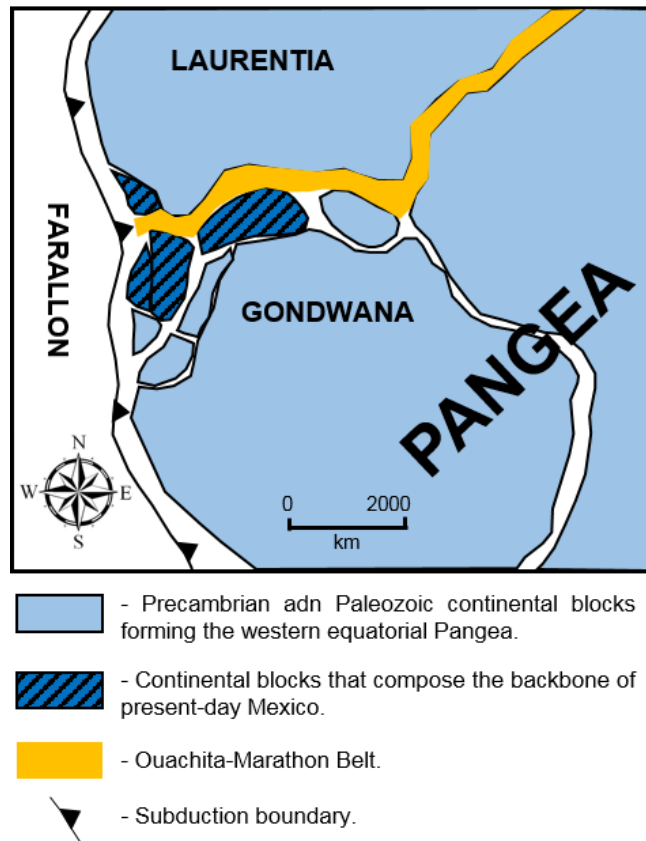


Figure 3.4. Early Triassic reconstruction of western equatorial Pangea (Martini et al., 2016).

Two main hypothesis have been proposed to explain the origin of Gulf of Mexico Basin: 1) it developed as an intracontinental rift basin (Salvador 1991; Pindell and Kennan, 2009) associated with the breakup of the supercontinent Pangea and the opening of Central Atlantic, and; 2) it developed as a back-arc basin located behind the Jurassic Nazas arc, which was associated with an east-dipping subduction zone of oceanic crust beneath westernmost Pangea (and its fragments) in the region now occupied by Mexico, (Stern and Dickinson, 2010; Figure 3.5). Moreover, this second hypothesis also considers the possibility that GOM opening occurred partially as a response from Pangea's breakup, which is in agreement with Martini et al. (2016) who suggest that the North America-South America plate boundary was developed, at least in an initial phase, under the combined influence of the Atlantic and Pacific processes until Late Jurassic.

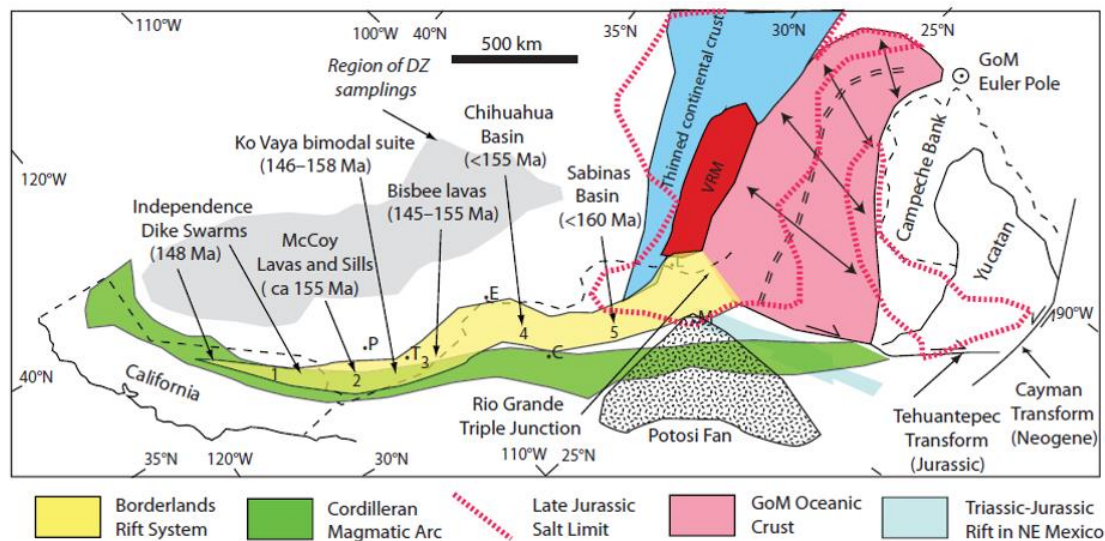


Figure 3.5. Early Triassic reconstruction of western equatorial Pangea (Stern and Dickinson, 2010).

3.3.1 Gulf of Mexico Opening Phase (210-137 Ma).

A general consensus exists regarding the plate kinematic history and the main stages of the tectonic evolution of the GOM (Salvador, 1987, 1991; Winker and Buffler, 1988; Marton and Buffler, 1994; Pindell and Kennan, 2002, 2009; Bird, et al., 2005; Hudec et al., 2013); however, some discrepancies regarding the exact kinematics and timing of Mesozoic rifting, as well as the formation and crustal structure of GOM result from the difficulty in imaging the deeper structures beneath its thick sedimentary cover and the presence of evaporites. As more and better quality information is available, more constrained interpretations will improve the knowledge of the GOM basin (Eddy et al., 2014; Sandwell et al., 2014; Nguyen and Mann, 2016). Hudec et al. (2013) propose the following main stages of the opening of Gulf of Mexico (Figure 3.6):

- 1) **Rift Stage (210-163 Ma):** The Gulf of Mexico began to open as a rift basin during the Late Triassic as part of the breakup of the supercontinent Pangea whereas the Yucatan microplate began to move south-eastward away from North America with a total counter-clockwise rotation of 10-15° (Pindell et al., 2006, Figure 3.6A-B). This rotation occurred along two transform systems. The western consists of a linear, north-south trending, right-lateral transform fault zone, the Tamaulipas-Golden Lane-Chiapas fault zone (Pindell, 1985) or Western Main Transform fault (Marton and Buffler, 1994), which also represents a crustal boundary between oceanic crust in western GOM and continental crust of Eastern Mexico (Figure 3.7).

- 2) Salt Deposition (163-161 Ma): Timing of salt deposition in GOM is poorly constrained and age is based on correlations with evaporites in the upper Bathonian or lower Callovian Huehuetepic Formation and calcarenites in the Callovian Tepexic Formation of Central Mexico (Salvador 1991b). It is also consistent with the volcanic xenoliths in Louisiana salt diapirs, dated at 158 to 160 Ma (Stern et al., 2011). However, anhydrite outcrops in Galeana, Mexico, along with gypsum from Minas Viejas Sierras and salt in the La Popa Basin have all been dated as Oxfordian in age based on its stratigraphic position (Padilla y Sánchez, 1986; Díaz et al., 1959; Lawton et al., 2001), suggesting that salt deposition was diachronous, with the youngest sediments deposited towards the edge of the basin. Analysis of better-dated salt basins suggest that an estimated thickness of 3 to 4 km of depositional salt in the thickest parts of the central Louann salt basin, which could have been deposited in a conservative time period ranging from less than 1 Myr. up to 2 Myr. (Hudec et al., 2013).

- 3) Post-salt Crustal Stretching (161 to 154–149 Ma): Continental rifting continued for 7 to 12 Myr. after salt deposition (Hudec et al., 2013). During this stage, most of the salt basin widened from 100 to 250 km, and extension tapered to zero at the edges of the basin (Figure 3.6C-F). The Yucatan Block continued its rotation along the Tamaulipas-Golden Lane-Chiapas fault zone.

- 4) Sea-Floor Spreading (154–149 to 137 Ma): Sea-floor spreading is considered to have begun prior to the end of the Jurassic, since the oldest sediments deposited on oceanic crust are identified as Tithonian in age; therefore, significantly after salt deposition. Assymetry of the limits of oceanic crust on the northern and southern sides of GOM suggest that this continental separation must have been diachronous, beginning in the Kimmeridgian in the eastern and western GOM, but not until the early Tithonian in the central GOM. The counter-clockwise rotational phase of seafloor spreading, including the Yucatan Block, continued in the Gulf of Mexico until the early Cretaceous (Neocomian), when it fixed to its current position, thus giving the present tectonic configuration of GOM. Rotation during this stage was around 30-35° (Pindell et al., 2006).

3.3.2 Cretaceous Post-Sea floor spreading (137 – 84 Ma).

Tectonic stability in GOM prevailed during the Early and most of Late Cretaceous after sea-floor spreading ceased (Salvador, 1991) and a passive margin regime was established in both northern and southern portions of the basin. Subsidence continued throughout the basin, which caused continuous thin-skinned deformation of sedimentary cover detaching on Jurassic autochthonous salt. This salt-related deformation developed as a gravitational linked system with updip extension and downdip contraction (Sanchez

Rivera et al., 2011; Cruz Mercado et al., 2011). However, during Late Cretaceous (Intra-Cenomanian), a regional unconformity, recognized in most of the GOM periphery, developed as a consequence of major sea-level fall in the region and other factors such as local igneous intrusions and volcanism (Salvador, 1991).

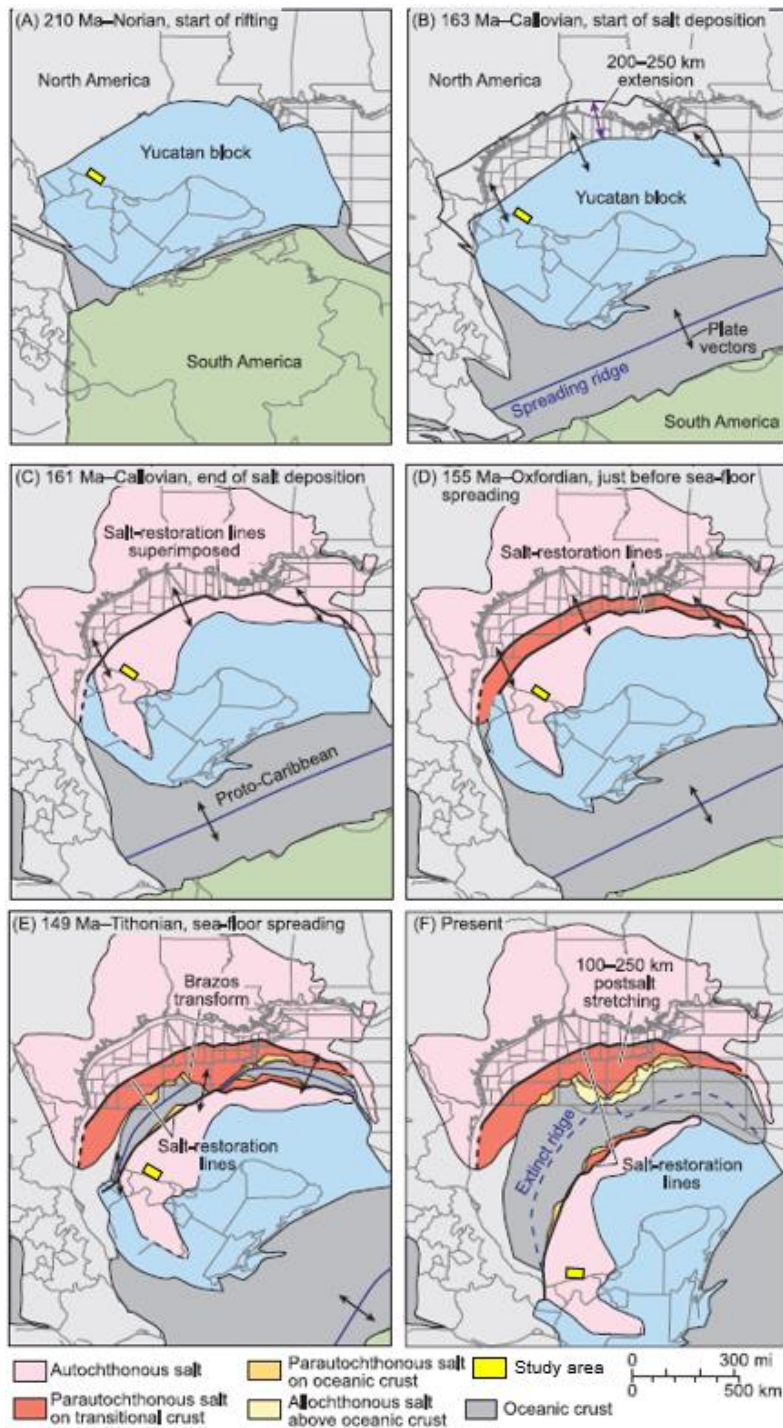


Figure 3.6. Sequential restoration of GOM opening (Hudec et. al, 2013).

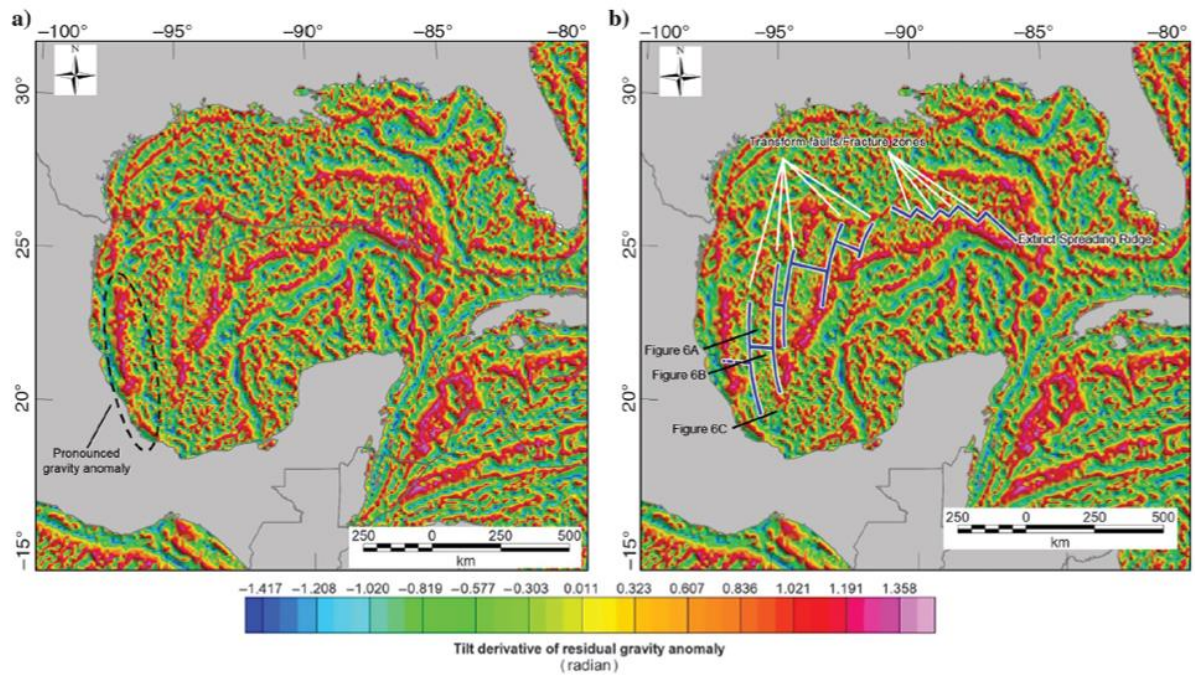


Figure 3.7. (a) Uninterpreted and (b) interpreted tilt derivative of the residual gravity from Sadwell et al. (2014) showing a close correspondence between the pattern of gravity high and lows to ridges and fracture zones (Nguyen and Mann, 2016).

3.3.3 Late Cretaceous - Middle Eocene (84 to 41 Ma)

From Late Cretaceous to Middle Eocene, the Laramide Orogeny progressively affected the Gulf of Mexico Basin from west to east drastically modifying the paleogeography, by uplifting of the Sierra Madre Oriental and switching sedimentation from carbonate to terrigenous due to drowning of the pre-existent carbonate platforms (Salvador, 1991; Moran-Zenteno et al., 2007). This event is the result of subduction of Farallon Plate under North American Plate at a low angle (Figure 3.8) due to the increase in the rate of convergence between the two plates (Moran-Zenteno, 2007 and references therein) which caused long-distance deformation from the trench zone and uplift of the meridional portion of North American Plate (Padilla y Sanchez, 2007). A peak of deformation during Eocene has been recognized for the orogenic front of the Sierra Madre Oriental by Eguluz de Antunano et al. (2000). Subsidence continued through this period, as a result of loading of the crust by thick wedges of Cenozoic sediments in the foreland regions adjacent to uplifted fold and thrust belts (Salvador, 1991; Padilla, 2007) during Paleogene times.

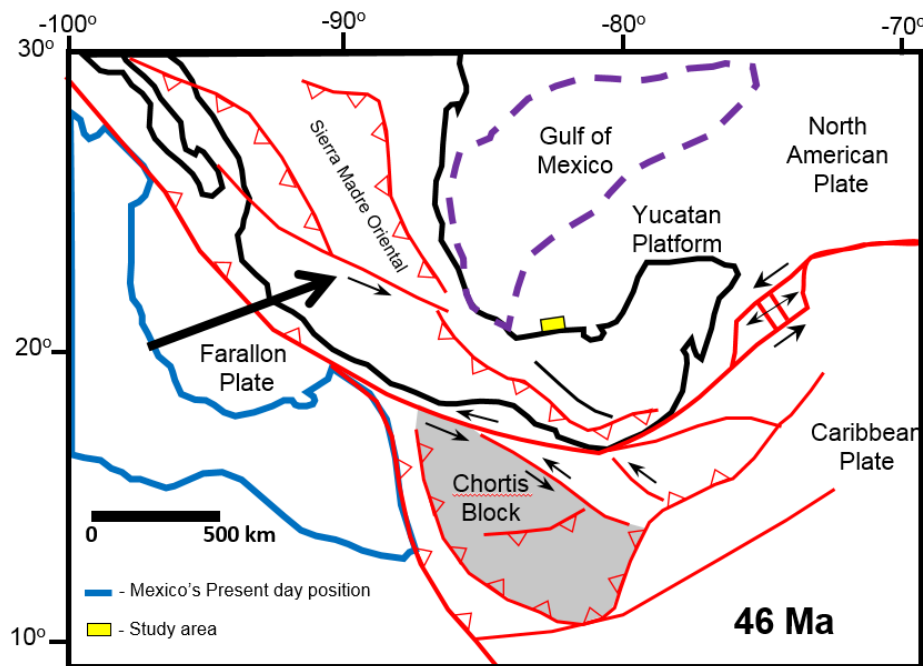


Figure 3.8. Plate Tectonic reconstruction at Eocene times (46 Ma). Modified from Pindell and Kennan, (2009).

3.3.4 Oligocene – Late Miocene (33 to 5.3 Ma)

During Middle to Late Miocene, a transpressional regime, the Chiapaneco Event (Sánchez Montes de Oca, 1980), formed the Chiapas-Tabasco-Campeche fold-thrust belt in South Mexico during a restricted time interval (c. 2.5 Myr) and a restricted size (Mandujano and Keppie, 2009). Figure 3.9 illustrates this fold belt extending towards the NE into the Campeche marine zone constituting the Reforma-Akal structural high. Traditionally, the Chiapas Belt origin is associated to the left-lateral eastward movement of the Chortis Block along the Motagua-Polochic fault zone (Pindell et al., 1988) since Eocene times (Figure 3.10). However, the duration of both events (2.5 Myr of Chiapaneco Event vs 45 Myr for Chortis Block movement) is incompatible with this model. Alternatively, Keppie and Moran-Zenteno (2005) proposed another model where the fold-thrust belt resulted from the collision of the Tehuantepec Ridge with the Middle America Trench, whose intersection migrated westwards along the Chortis Block and Chiapas margins from 15–12 Ma to 12–0 Ma (Figure 3.11), respectively. Moreover, these authors suggest that topography of the subducting plate played an important role for the short-lived formation of the fold belt in the overriding plate (Mandujano and Keppie, 2009; Figure 3.12).

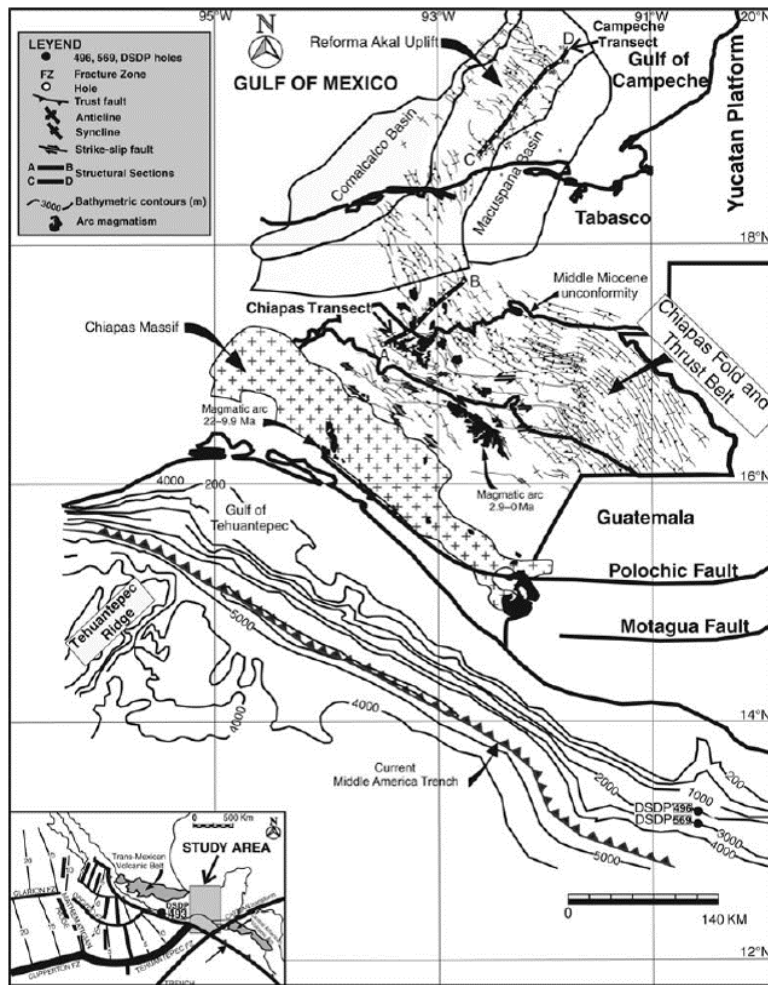


Figure 3.9. Map of Southeastern Mexico showing the Chiapas foldbelt and other tectonic elements (Mandujano and Keppie, 2009).

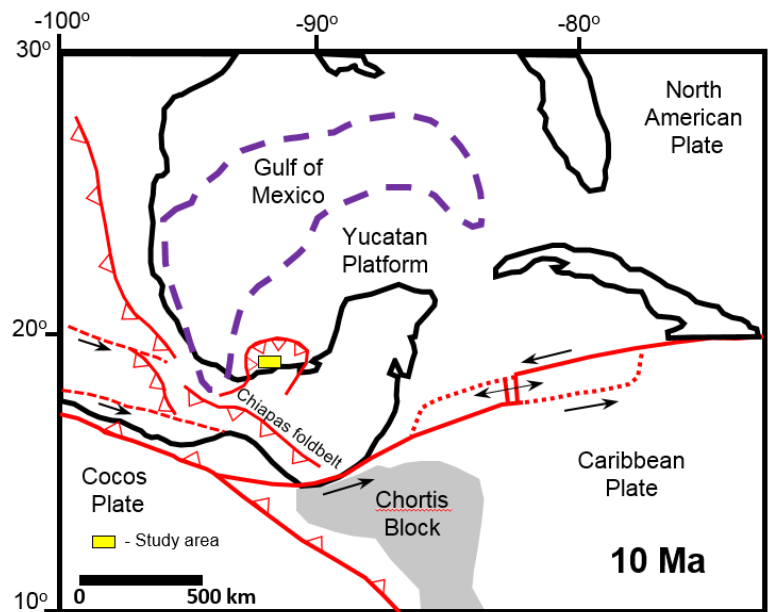


Figure 3.10.: Plate tectonic reconstruction at Miocene times (10 Ma). Modified from Pindell and Kennan, (2009).

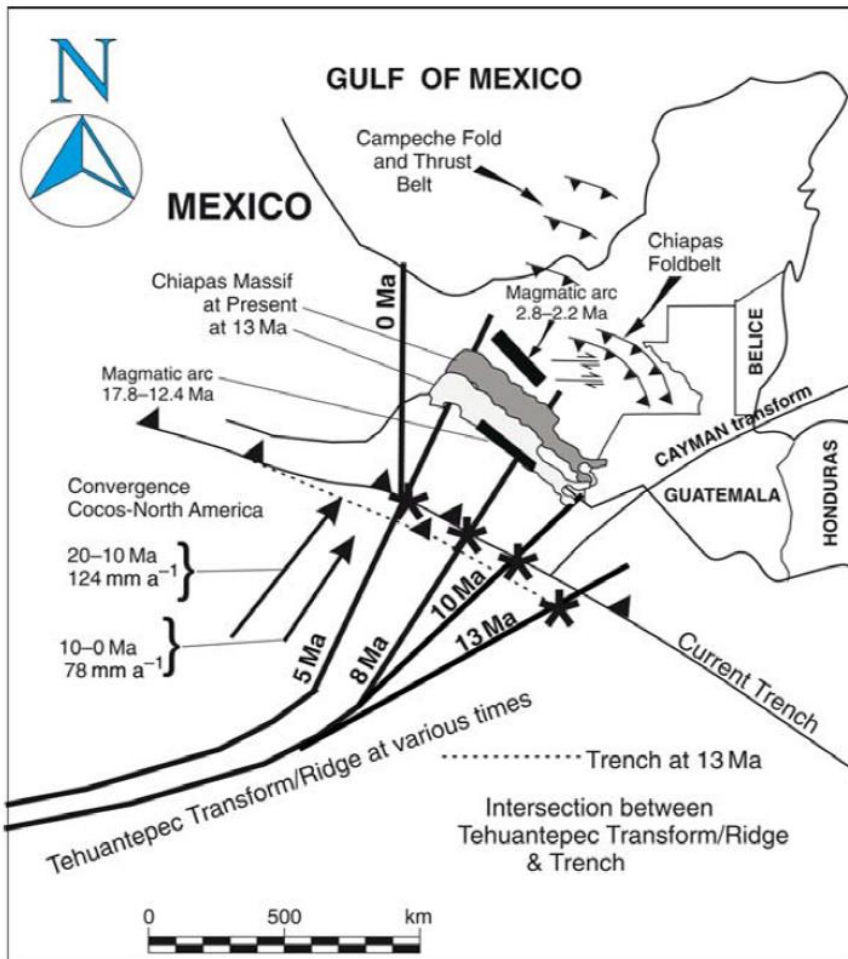


Figure 3.11.: Reconstruction at 13-0 Ma showing the proposed migration westward of the Tehuantepec Transform/ Middle America Trench intersection, (Mandujano and Keppie, 2009).

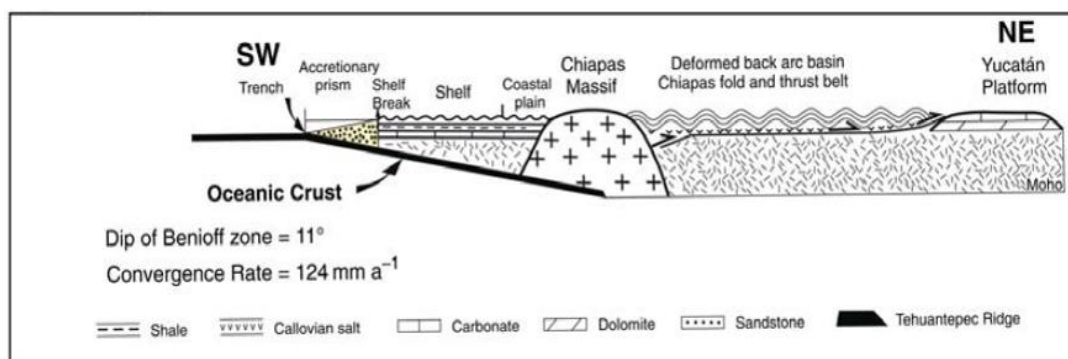


Figure 3.12. Schematic section showing the tectonic conditions during development of Chiapas fold-and-thrust belt c.13-10 Ma. (Mandujano and Keppie, 2009).

3.3.5 Late Miocene - Present day (5.3 to 0 Ma)

By Late Miocene, after the Chiapaneco Event ceased, the Chiapas fold belt tilted towards the NNW as a response to withdrawal of Callovian autochthonous salt (Padilla y Sanchez, 2007) and subsidence caused by deposition of several kilometres of syntectonic terrigenous sediments. Consequently, a gravitational linked system of updip extension–downdip contraction detaching on autochthonous salt developed and controlled deformation. High rates of prograding sedimentation and extension detaching on the salt layer resulted in the formation of a mega-raft block, the Reforma-Akal Block, which is limited to the southeast and northwest by two large extensional basins of Late Miocene–Pliocene (Macuspana) and Pliocene-Pleistocene (Comalcalco) age, which in turn are bounded by large regional and counter-regional normal faults (Sanchez Rivera et al., 2011) and oriented perpendicular to the axis of the fold belt (Figure 3.13).

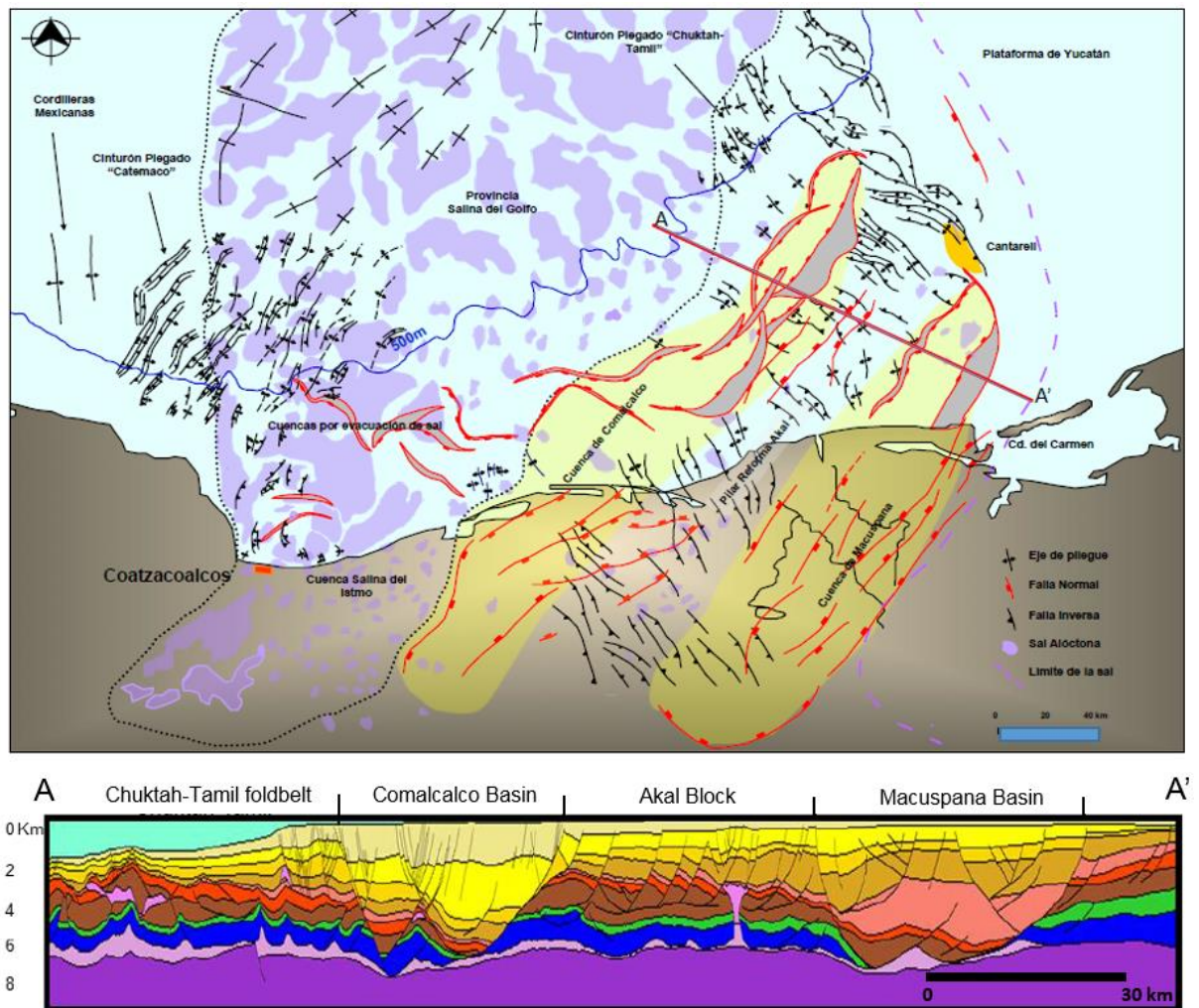


Figure 3.13: Map showing major tectonic elements in Southern Gulf of Mexico (above). Cross-section illustrating the Akal Block and its bounding basins (below). CNH, 2014.

3.4 Deformational events in Southern Gulf of Mexico

The complex tectonic evolution of Southern Gulf of Mexico has had a major influence on the economic importance of the South-Eastern Basins by having an impact on the different elements of existing Petroleum systems such as hydrocarbon generation and migration, as well as formation and re-deformation of structural and stratigraphic traps.

Significant hydrocarbon accumulations in Southern Gulf of Mexico have led to an extensive exploration since the 1970's with extensive coverage of 2D and 3D seismic surveys. The analysis of this massive amount of information has led to a continuously evolving understanding of the basins to correctly assess the economic potential of exploratory areas located onshore and offshore (Angeles-Aquino et al., 1994; Padilla y Sanchez, 2007; Sanchez Rivera et al., 2011; Cruz-Mercado et al., 2011; Peterson Rodriguez et al., 2013). As a result, four deformational events have been recognised and summarised with their respective nomenclature (PEMEX internal reports, 2009; 2013, 2017) by PEMEX's geoscientists (Figure 3.14). Such events are described below within the regional context of Southern Gulf of Mexico evolution explained above, as well as their implications in hydrocarbon trap formation:

3.4.1 D1 (Late Jurassic- Late Cretaceous):

This event is related to the Gulf of Mexico opening, where thermal subsidence originated a gravitational linked system with up-dip (South) extension and down-dip (North) contraction detaching on salt. As a result, a wide range of structures developed and their geometries varied depending on their particular positions across the basin. Extension on the periphery of the Yucatan Platform generated normal faulting and half graben structures and salt rollers developed. On the other hand, in response to extension, the transitional and contractional counterparts of the system is represented by salt pillows/anticlines, folded structures, and passive and reactive diapirs located toward the centre and northern parts of the basin. These structures are frequently associated with structural traps for hydrocarbons (Figure 3.15).

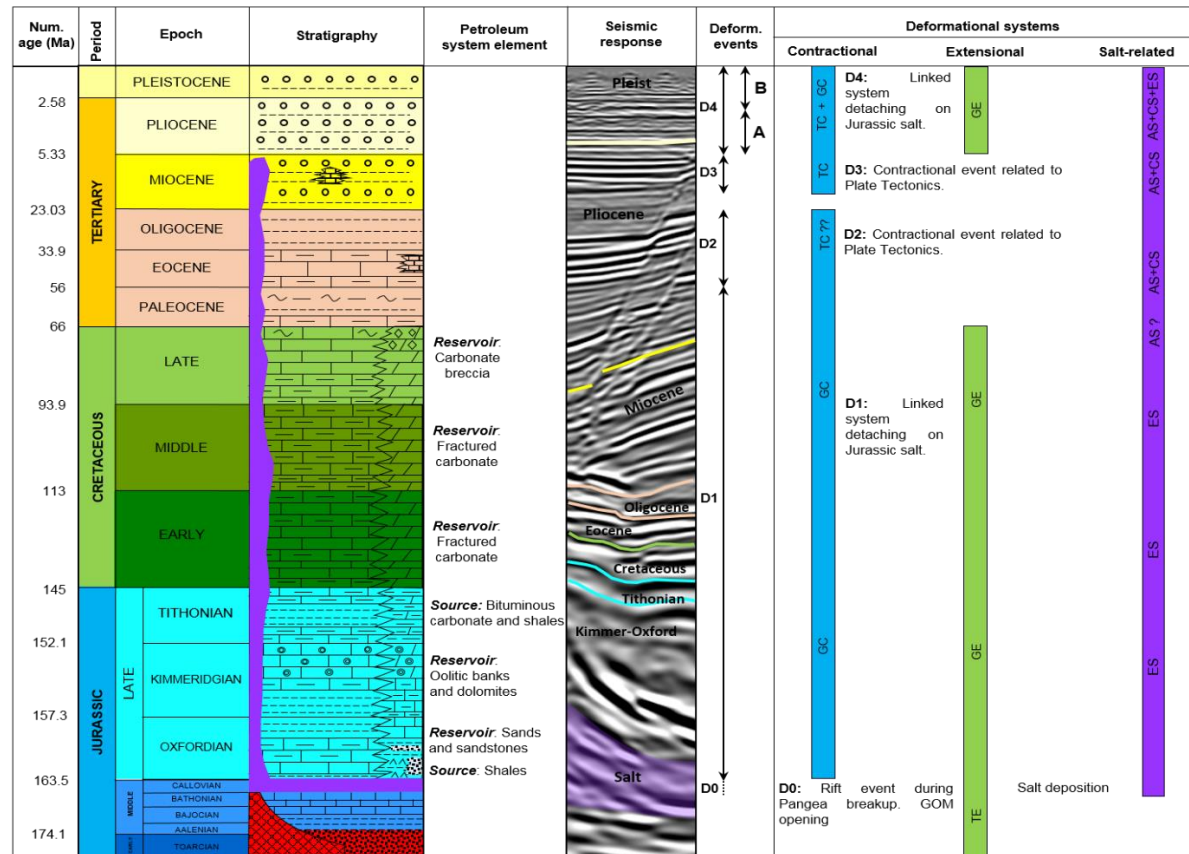


Figure 3.14: Tectonostratigraphic chart of Southern GOM (Modified from PEMEX, 2013) showing Mesozoic Petroleum Plays. TE: Tectonic Extension; GE: Gravitational Extension; GC: Gravitational Contraction; TC: Tectonic Contraction; ES: Extensional System; AS: Allocthonous System; CS: Contractional System.

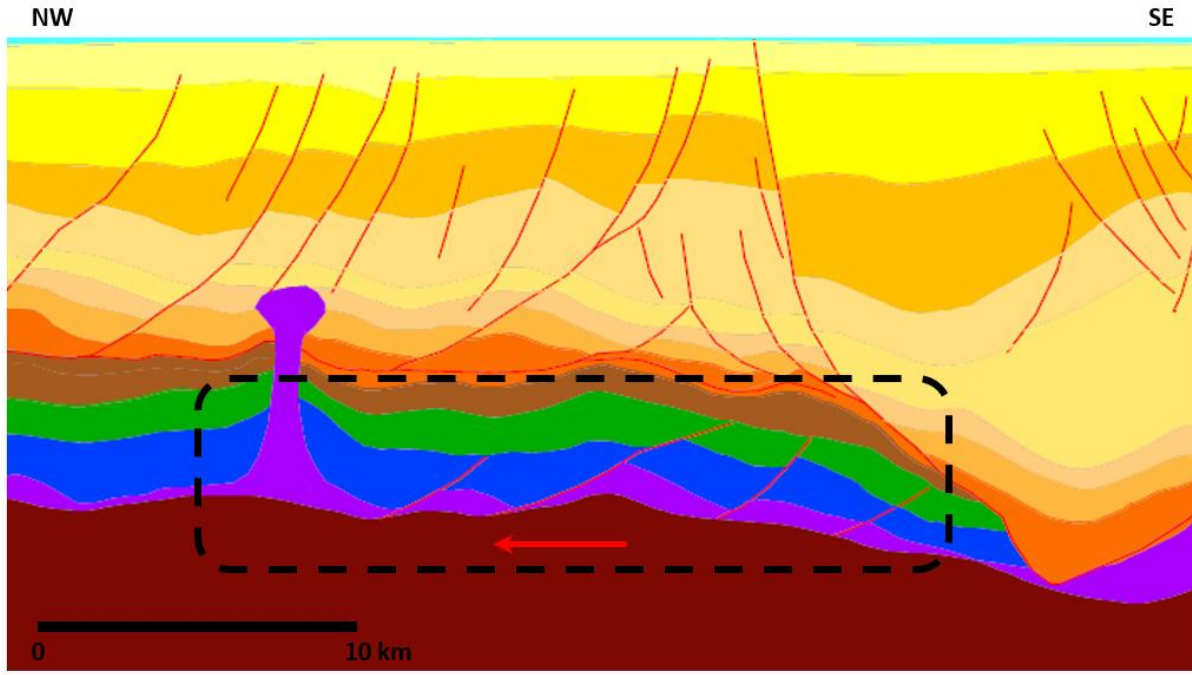


Figure 3.15: Normal listric faults and salt diapirs developed during D1 event. (CNH, 2014). Red arrow indicates direction of down-dip salt flow.

3.4.2 D2 (Late Eocene-Oligocene):

This compressional event is believed to be associated to the the Laramide orogeny according to its age and deformation style (Moran-Zenteno et al., 2007). Although the age of D2 event is constrained to Late Eocene-Oligocene in the offshore portion of the basin, reported evidence further from the south suggest that this event could have an earlier onset at Palaeocene times (personal communication from PEMEX personnel, 2014). Sediment loading during this time also contributed to subsidence, so sedimentation switched gradually from platform carbonates to deep marine (bathyal) environments. This event is difficult to recognize in the seismic data because it is masked and superimposed by the further D3 event, which has a contractional origin as well and generated similar structures to those formed by the D2 event (Figure 3.16). However, interpreted syn-kinematic sequences suggest that the intensity of deformation was relatively low (Peterson et al., 2017). D2 event represents the first episode of reformation of preexistent structures generated during D1.

At the same time, salt mobilization and withdrawal continued due to high rates of sediment loading, which originated salt welds and salt emplacement at allochthonous levels forming canopies. Also, some diapirs developed during D1 continued their growth as passive diapirs whereas other diapirs may switched from passive to active mechanism in response to compressional tectonic forces.

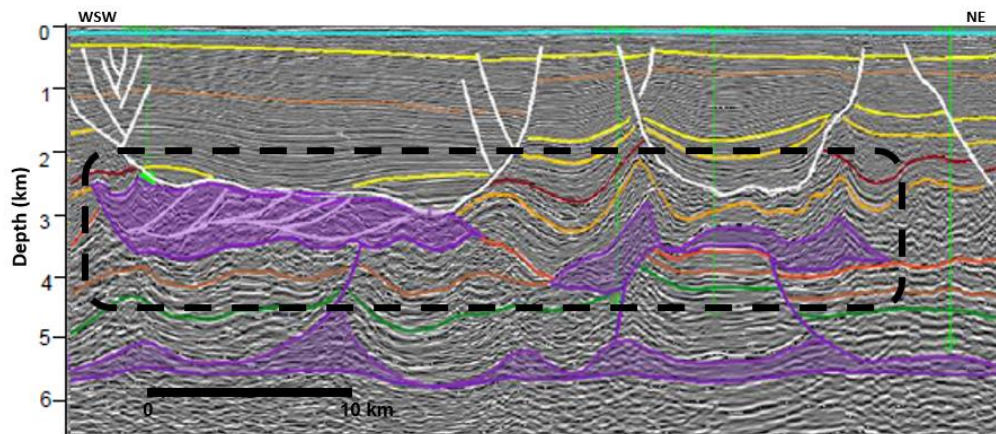


Figure 3.16: Salt canopies emplaced along with folding during D2 event. (CNH, 2014).

3.4.3 D3 (Middle-Late Miocene):

This event is associated to the Chiapaneco Event (Sánchez Montes de Oca, 1980), which originated the Sierra de Chiapas fold belt that extends into the Campeche marine zone constituting the Reforma-Akal structural high (PEMEX, 2005). Furthermore, extensive folding and thrusting of both new and pre-existent structures originated many of the structural hydrocarbon traps from the main oilfields in Southern GOM basins. These traps are associated to different types of folds, fault-related folds and folded salt bodies. Analysis of syn-kinematic sequences show that the strongest deformation pulse has an age of Middle Miocene in the west, whereas in the East the same pulse has been dated as Middle to Late Miocene, suggesting a diachronic migration (Peterson et al., 2017). Giant oilfield Cantarell is an example of a structural trap formed during this event (Figure 3.17).

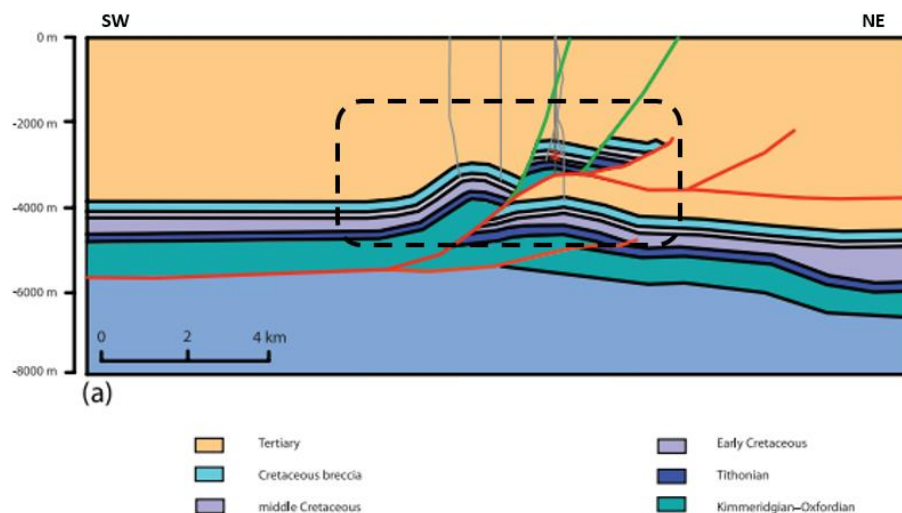


Figure 3.17: Cantarell anticline is a representative structure from D3 event. (Mitra et al., 2005)

Siliciclastic sedimentation remained constant and was deposited in depocenters generated by salt withdrawal (PEMEX, 2009). By Late Miocene, the uplifting generated by compression originated huge amounts of sediments that were distributed into the basin as submarine fans and as a result, the basin is tilted to the north and salt is withdrawn towards the same direction.

3.4.4 D4 (Late Miocene-Present day):

This event is associated to the deformation process that formed the Reforma-Akal Block. Up-dip extension was accommodated by intense normal faulting over a detachment level of Tertiary age (Oligocene) which, depending on the location in the basin, lithologically consists of either shale or allochthonous salt. These faults, which may or not have a strike-slip component, often act as lateral boundaries for hydrocarbon stratigraphic traps in Neogene plays. Down-dip contractional domain associated to this linked system is located towards the deeper north-western portion of the basin and deformational features include folds, fault-related folds, allochthonous salt bodies and contracted pre-existent diapirs (Figure 3.18).

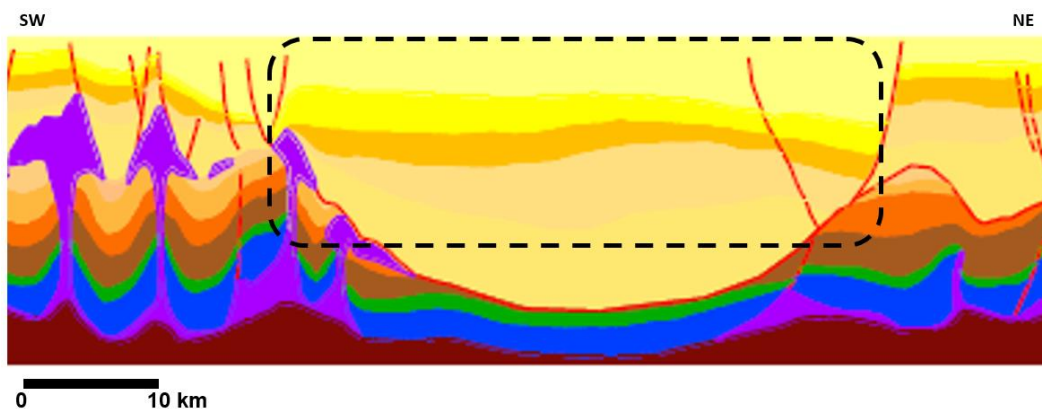


Figure 3.18: Depocenter originated by gravitational extension during D4 event. (CNH, 2014).

3.5 Summary

South Eastern Basins is the most prolific and important hydrocarbon province in Southern Gulf of Mexico, with most of the production coming from Mesozoic carbonate reservoirs, and to a lesser extent, from Tertiary siliciclastic reservoirs. The economic importance of this province has led to extensive exploration since the 1970's, resulting in a continuously increasing understanding of its complex structural evolution within the context of the evolution of the Gulf of Mexico and its implications for hydrocarbon exploration. This evolution which can be divided into three major tectono-stratigraphic stages:

- 1) Rift basin during Gulf of Mexico opening in Late Triassic to Late Jurassic as a part of Pangea's breakup;
- 2) A passive margin stage with the development of an extended platform with carbonate sedimentation during sea-floor spreading (Late Jurassic to Late Cretaceous); and,
- 3) A foreland basin with mainly siliciclastic sedimentation since Late Cretaceous/Early Palaeocene to Present day associated with plate tectonics compression/transpression activity.

Chapter 4

Structural evolution of salt-related traps in Southern Gulf of Mexico

4.1 Introduction

South-Eastern Basins contain prolific hydrocarbon reservoirs in Mesozoic carbonate reservoirs and, therefore, they are recognized as highly prospective targets for hydrocarbon exploration due to the strong influence of salt in the different elements of Petroleum Systems. Salt-related deformation is present in different tectonic settings (extensional, compressional and strike-slip) and typically results in a great variety of salt structures (Figure 4.1) which, in turn, are directly associated to many different styles of structural, stratigraphic and combined traps (Montgomery et al., 1999; Mount et al., 2007). These traps can develop in either allochthonous or autochthonous salt bodies.

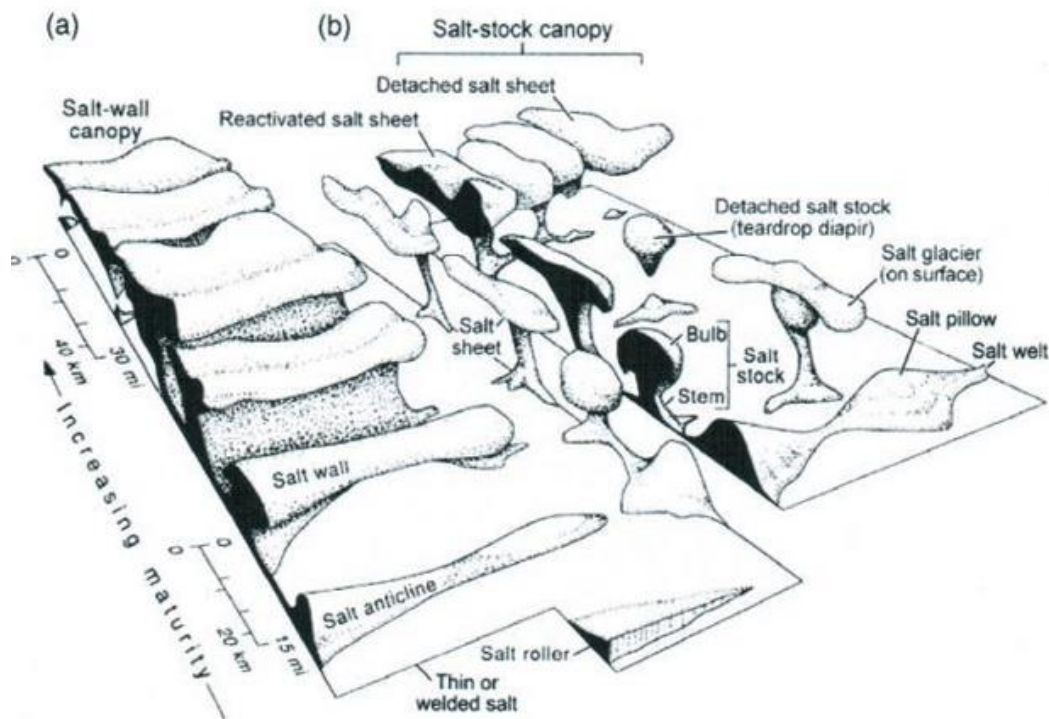


Figure 4.1. Diagram showing the great variety of salt structures associated to line sources (a) and point sources (b). Hudec and Jackson (2007).

Brittle deformation of Mesozoic age carbonate rocks during deformational events resulted in the formation of naturally fractured reservoirs, whose quality is directly related to parameters such as porosity, permeability and anisotropy which depend, in turn, on the orientation and intensity of open fracture sets. The relationship between fracture orientation and intensity with structural position in a fold has been widely recognized by several authors (Price, 1966; Stearns, 1968; Nelson, 2001; Ghosh and Mitra, 2009), where syn-folding fracture sets show predictable symmetric orientations with respect to the fold geometry (Figure 4.2). However, pre-folding fractures might change the stress field in which later syn-folding fractures form (Price and Cosgrove, 1990), and therefore, their orientations may deviate from traditional conceptual models. Moreover, the complex interplay of another factors such as lithology, texture, porosity, bed thickness and pore pressure can also influence the occurrence of fractures (Nelson, 2001; Giorgioni et al., 2016; Barbier et al., 2012; Awdal et al., 2016; Gudmundsson, 2011) thus complicating a more accurate fracture prediction. In spite of this, traditional conceptual models are useful as a preliminary estimation of possible fracture orientations in prospective structural traps, where little or no borehole information is available. These orientations need to be compared with information obtained from structural seismic attributes and integrated to borehole information, if available, in order to produce a more robust estimation of fracture orientations.

Extensive hydrocarbon exploration in Southern Gulf of Mexico since the 1970's has made possible a better understanding of basin's structural evolution through the analysis of several 3D seismic surveys and data information from hundreds of wells drilled since then; however, relatively little information about its tectono-stratigraphic evolution has been published due mainly to confidential policies from PEMEX E&P. Comprehensive overviews about regional geological framework have been published by Angeles-Aquino et al. (1994), Angeles-Aquino and Cantu-Chapa (2001), Angeles-Aquino (2006), and Padilla y Sanchez (2007). Peterson et al. (2013) proposed a model of structural evolution in the southwestern offshore portion of the SEB.

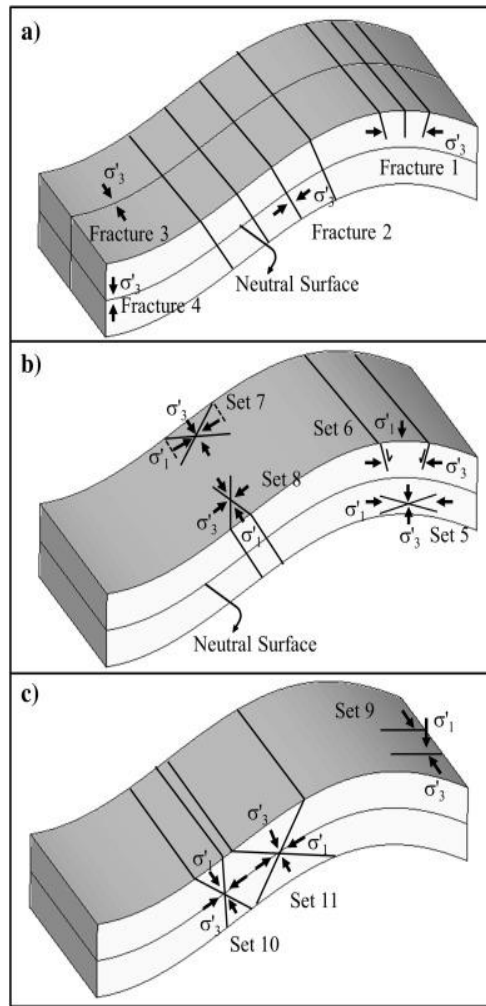


Figure 4.2. Different fracture sets identified within folded structures. a) Tensile, b) and c) Shear fractures associated to buckle folds (Liu et al., 2016).

The aim of this chapter is to propose a model for the formation and evolution of salt-cored structures in a passive margin setting and their implications as prospective hydrocarbon traps as well as their influence for fracture development in Mesozoic low-matrix porosity carbonate rocks located at different Mesozoic stratigraphic levels. Detailed seismic interpretation of the available 3D volume was undertaken from which structural and isopach maps were generated. These maps, in turn, were used as the basis of 2D restoration in order to define the structural evolution. Moreover, these results were used as inputs for further Strain analysis and Fracture Modelling Analysis, which represent a valuable guide to assess the presence and quality of reservoir rock in exploratory prospects and will be discussed in subsequent chapters.

4.1.1 Salt-related hydrocarbon traps

Presence of salt in sedimentary basins impacts on every element of Petroleum systems. Salt can act as a seal and its thermal conductivity may retard or accelerate hydrocarbon maturation. Diapirs can create topographic relief, which can control sediment distribution (reservoir facies). Also, salt-related deformation is associated with most of hydrocarbon traps in salt basins.

Since early 20th century, hydrocarbon production from cap rocks associated to salt domes triggered the interest for salt tectonics and the relationship between salt bodies and hydrocarbon occurrence (Jackson, 1995). An ongoing increase in the quantity of acquisition of seismic data as well as the improvement in processing techniques have provided the main source of information for the study of salt bodies in the subsurface. As a result, it has been recognized the influence of salt on the formation of hydrocarbon traps (structural, stratigraphic and combined), encompassing several deformation styles in different tectonic settings.

Traditionally, hydrocarbon accumulations are associated to salt diapirs (Halbouty 1979; Selley, 1998), which are related in turn with several trap styles (Figure 4.3). However, another salt bodies also influence the formation of traps such as salt rollers, which develop in extensional domains and are related to distinctive geological structures and their corresponding trap geometries (Krezsek et al., 2007). Contractional domains can generate structures such as salt anticline/pillows, squeezed diapirs and allochthonous salt bodies, all of which can be associated to three-way and/or four-way closure hydrocarbon traps (Pilcher et al., 2011; Mount et al., 2007, (Figure 4.4). In the case where carbonate sediments comprise the immediate suprasalt stratigraphy (Montgomery et al., 1999), as in the study area, traps may be associated to salt rollers and pillows of different amplitudes (Figure 4.5).

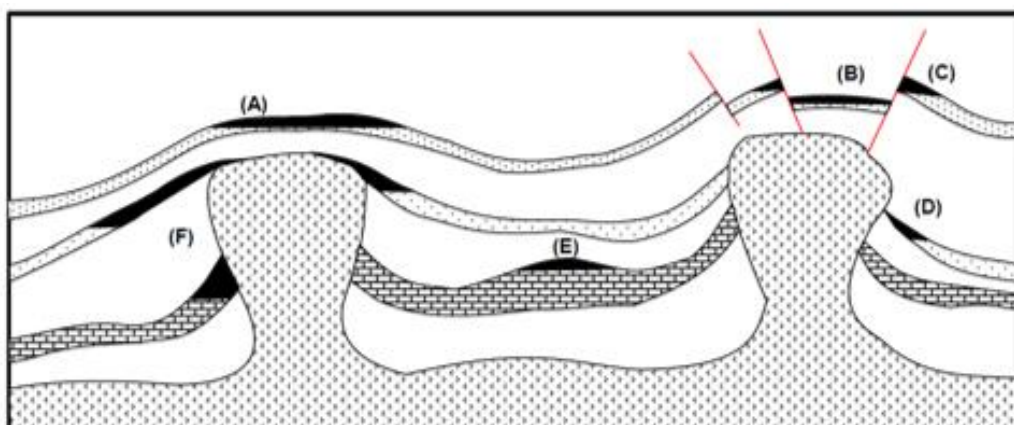


Figure 4.3. Diapir-related hydrocarbon traps. (A) domal trap, (B-C) fault traps, (D) pinch-out trap, (E) turtle-back or sedimentary anticline trap, and (F) truncation trap (Selley, 1998).

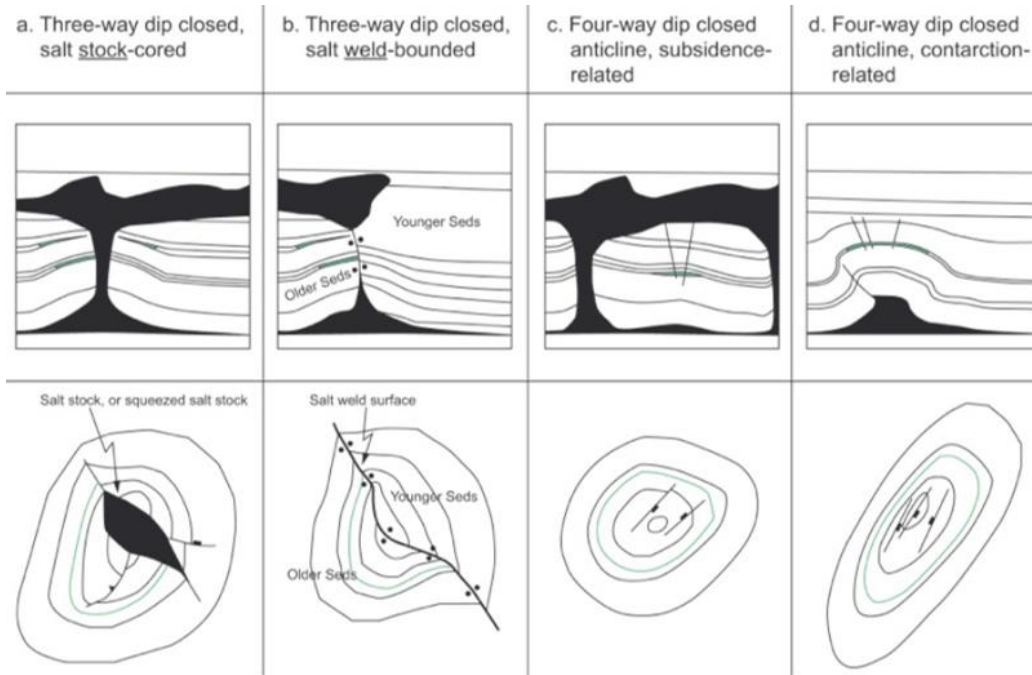


Figure 4.4. Hydrocarbon traps associated to contractional domains (Mount et al., 2007).

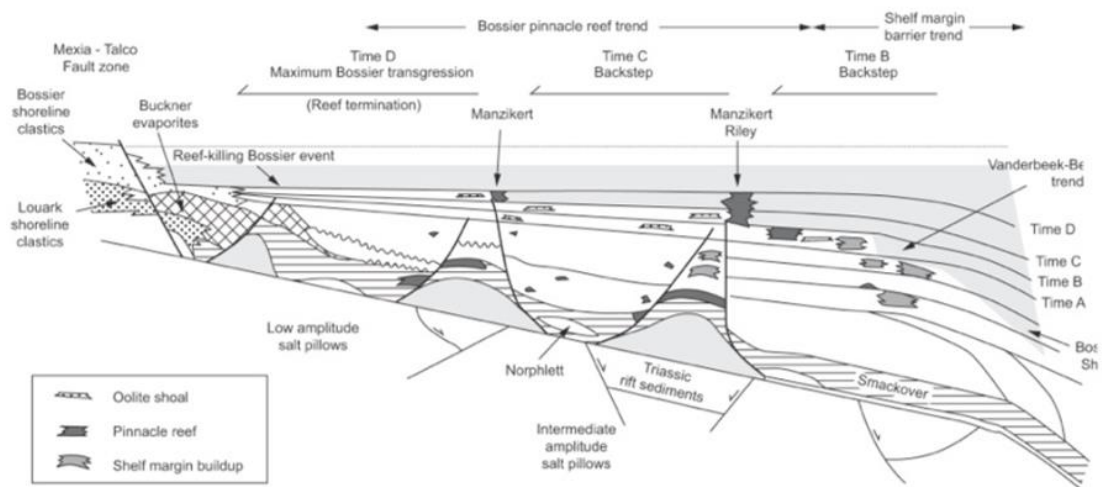


Figure 4.5. Trap styles associated to early post-salt carbonate section. East Texas Salt Basin (Montgomery et al., 1999).

4.1.2 Regional Structural Setting

The analysis of the massive amount of seismic and borehole information acquired in the last decades in Southern Gulf of Mexico has led to a continuous process of understanding the basin's tectonic evolution in order to correctly assess the economic potential of exploratory areas located onshore and offshore (Angeles-Aquino et al., 1994; Padilla y Sanchez, 2007; Sanchez Rivera et al., 2011; Cruz-Mercado et al., 2011; Peterson Rodriguez et al., 2013). As a result, deformational events D1-D4 (previously described in more detail on Chapter B) have been recognised by PEMEX's geoscientists (PEMEX internal reports, 2009; 2013, 2017).

In order to get a better understanding of the tectonic setting of the study area and conceptualize its structural style, three regional seismic cross-sections crossing through the study area were selected from available literature and analysed. Deformational events D1 to D4 can be identified by analysing growth strata and the relationships between structural elements. Figure 4.6 shows the location of the three lines, which are described below:

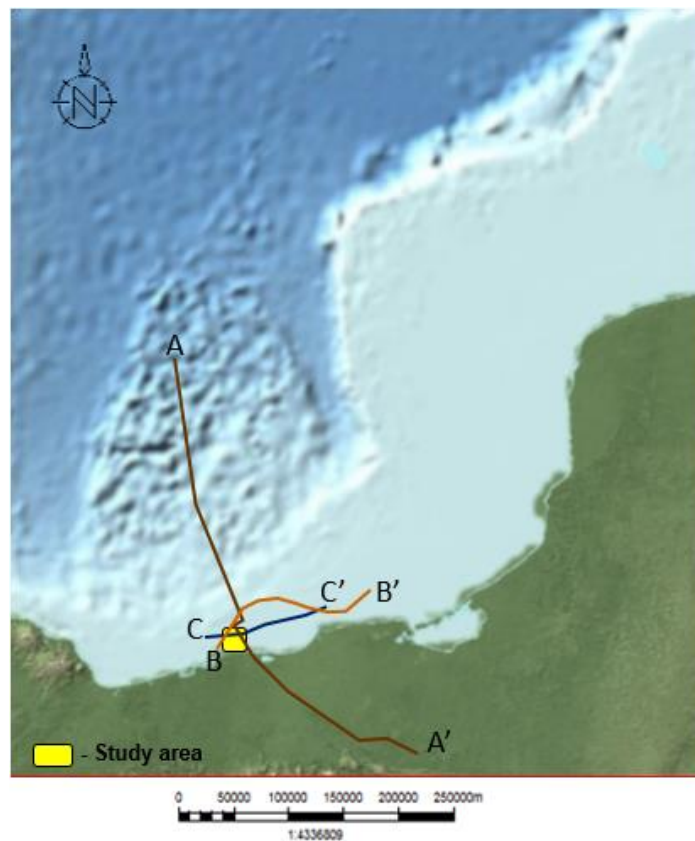


Figure 4.6. Map showing three regional sections crossing the study area.

Line A-A': This line has a length of approximately 370 kms, it is oriented NW-SE and illustrates the development of a linked system with up-dip extension in the SE and down-dip contraction to the NW detaching on Callovian-age autochthonous salt in Southern Gulf of Mexico (Figure 4.7). From SE to NW, different tectonic elements and their particular styles of deformation, are recognizable. These are: Yucatan Platform, Macuspana Basin, Akal-Reforma Block, Comalcalco Basin and Isthmian Salt Basin.

The project's study area is located in the southern portion of the Akal-Reforma Block (center of the section), which is a mega-raft block developed during Late Miocene-Pleistocene as a result of a gravitational-related extensional event detaching on autochthonous salt (Sanchez-Rivera et al., 2011). Deformation within the Akal-Reforma Block is mostly salt-related, and it is associated to both pre-raft deformational events (early salt movement, tectonic contraction, allochthonous salt emplacement) and syn-raft events (trans-tension). Analysis of the extensive coverage of 2D and 3D seismic during hydrocarbon exploration in Southern Gulf of Mexico suggests that salt-related deformation is considered thin-skinned, since there is no strong evidence of basement controlling the location and distribution of salt structures (diapirs, anticlines, pillows, etc). Moreover, most deformation is related to gravitational processes, which is typical in passive margin settings (Marton et al., 2000; Fort et al., 2004) by a combination of gravity gliding and gravity spreading (Rowan et al., 2004).

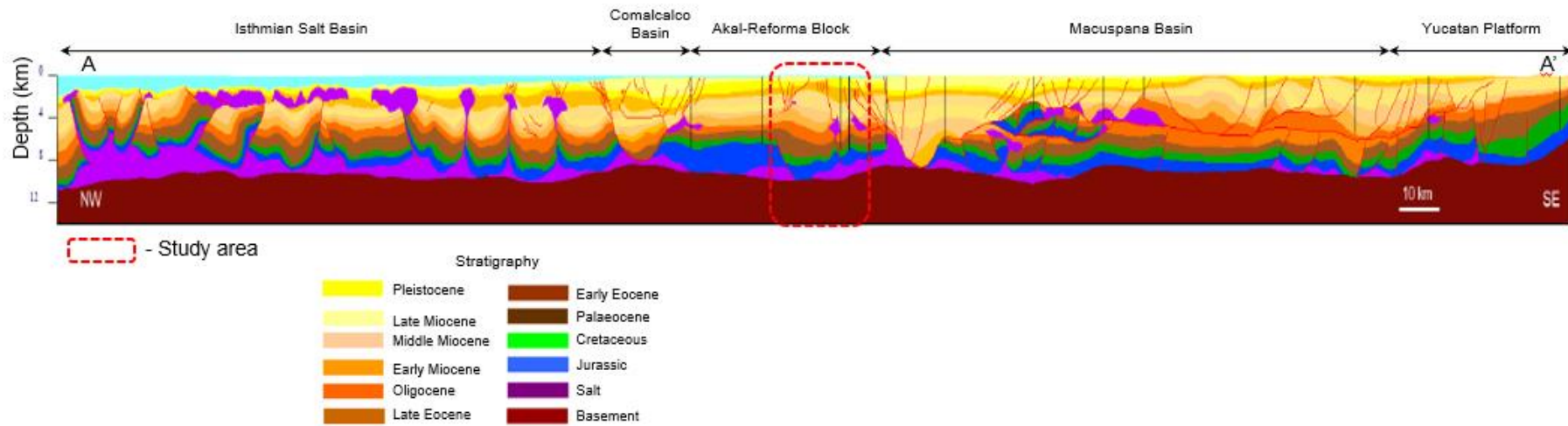


Figure 4.7. Regional cross-section A-A'. Dashed rectangle shows the location of the study area. (Modified from Sanchez-Rivera et al., 2011).

Linea B-B': This line has a length of 122 km, it is oriented NW-SE and the interpretation is well constrained by several boreholes. Also, this section crosses through the Akal-Reforma Block and a portion of Comalcalco Basin (Figure 4.8). The study area is located towards the SW end of the section, inside the Akal-Reforma Block, where deformation in the Mesozoic section was directly controlled by salt movement very soon after its deposition (D1 event). Also, allochthonous salt was emplaced during Palaeogene times (D2) and re-deformed in Neogene times (D3). Finally, trans-tension during Pliocene times (D4) resulted in intense normal faulting of the Neogene section with a strike-slip component; however, this faulting is not always restricted to Neogene section, but occasionally cuts down to the Mesozoic section perhaps retaking pre-existent normal faults, as is the case of the major normal fault bounding the salt diapir which is interpreted to have this origin. The graben at the centre of the section corresponds to Comalcalco Basin and it is interpreted to have developed from a salt diapir that collapsed by gravitational extension during Neogene times (D4 event). Supporting evidence includes the thickness of Pliocene sediments, which in this graben reach up to 8 km. Comalcalco Basin is bounded by major regional and counter-regional normal faults which also show some strike-slip component. To the NE, the section cuts parallel to the regional strike of the Akal-Reforma Block, which close to Comalcalco Basin is affected by diapirism and salt canopies, whereas to the NE end of the section salt is restricted to core relatively low-relief pillows/anticlines. Salt diapirs also seemed to have been affected by contractional deformation (D2 and D3) during Cenozoic times, according to the analysis of growth strata.

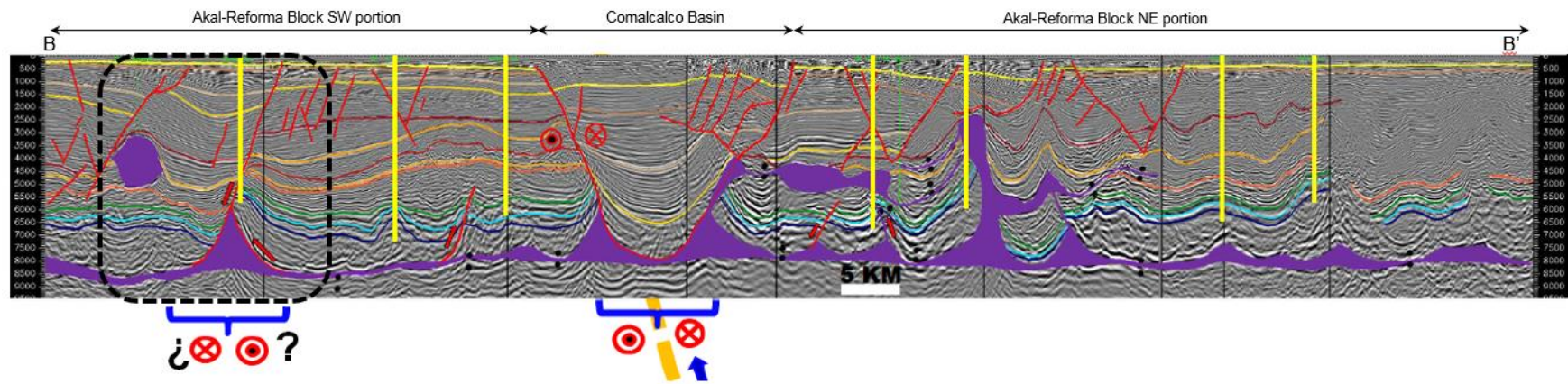
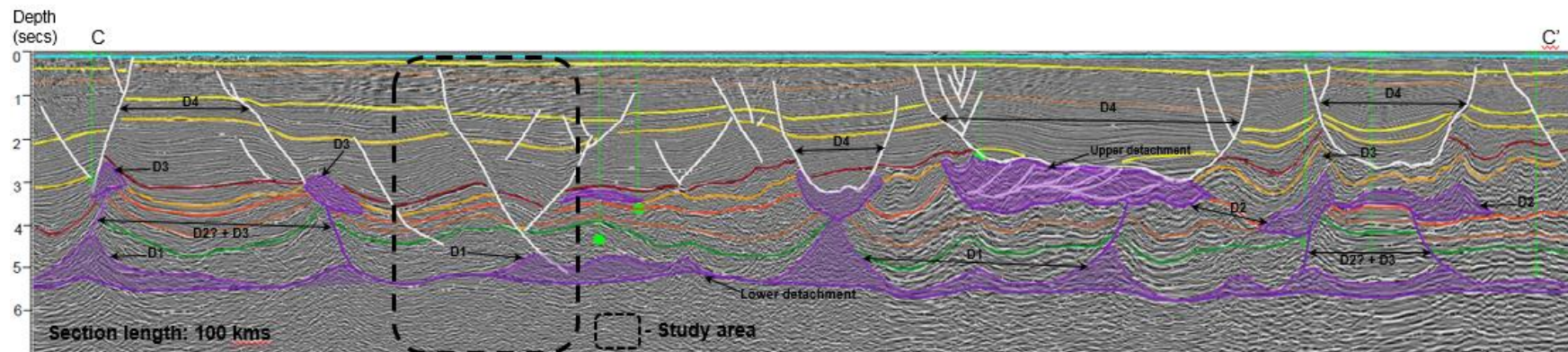


Figure 4.8. Regional cross-section B-B'. Dashed rectangle shows the location of the study area (PEMEX, 2013).

Line C-C': This line has a length of 122 kms, it is oriented WSW-NE and runs through the southern portion of the Akal-Reforma Block (Figure 4.9). The study area is located at the center of the section where the Mesozoic section is gently folded and the Tertiary column is affected by late normal faulting (D4 event). In this section, it is clear the presence of two detachment levels: the lower at the autochthonous salt; and the upper, in Tertiary section, which in some places coincides with the top of allochthonous salt and where most of later Neogene normal faults sole. Regional deformation events are identified and labelled in this section. Event D1 resulted in development of passive salt diapirs, pillows and anticlines, which core prospective structures. Allochthonous salt emplacement and development of salt canopies took place between Palaeocene-Oligocene and seemed to be related to D2 event, which is also related with re-deformation of pre-existent salt bodies (Peterson Rodriguez et al., 2013). Pinching of salt diapirs feeders along with active diapirism were triggered by D3 contractional event during Middle-to-Late Miocene. Finally, gravitational extension associated to D4 event produced not only extensive normal faulting but also transtensional faulting. This was likely to be the result of the differences in velocity of displacement between individual blocks, thus creating lateral ramps that accommodated this differential displacement. The location of these ramps seems to be controlled by pre-existent salt structures. Although deformation related to D4 event is mostly restricted to the stratigraphy above the upper detachment, in some areas faulting cuts down to the Mesozoic section.



Stratigraphy			
	Seafloor		Early Miocene
	Late Pliocene		Oligocene
	Middle Pliocene		Middle Eocene
	Early Pliocene		Late Cretaceous
	Late Miocene		Late Jurassic
	Middle Miocene		Salt

Figure 4.9. Regional cross-section C-C'. Dashed rectangle shows the location of the study area (modified from CNH, 2014).

In summary, analysis of regional cross-sections suggest that salt tectonics has played a fundamental role in structural evolution of Southern Gulf of Mexico and also on the structural style of its different tectonic elements. Four main deformational events (D1 to D4) can be identified and associated to the development of prospective structural and stratigraphic hydrocarbon traps. In the study area, specifically, structural traps for Mesozoic targets are associated with salt-cored anticlines and diapirs, which may indicate a transitional domain between up-dip extensional domain and down-dip contractional domain during the main stage of trap development in Mesozoic times (D1). These traps seemed to have formed simultaneously to the development of salt structures (anticlines, pillows and diapirs) during Mesozoic times (D1) and subsequently re-deformed during Cenozoic times (D2/D3). Trap preservation is conditioned by different factors such as closeness to active faults and/or squeezed diapirs, and most of Mesozoic structures are not affected by late Neogene extensional event (D4), which indicates a good potential for hydrocarbon exploration. This chapter takes advantage of using high-quality 3D seismic data, which may help to refine the structural model of the study area as well as to increase the understanding of the influence of salt in trap development.

4.2 Dataset and Methods

4.2.1 Seismic Data

The available seismic dataset consists of a 3D OBC multicomponent onshore-offshore survey, Tsimin-Tojual 3DTZ, which covers an area of 3,990 km², including the study area which has an area of 220 km² (Figure 4.10). A summary of acquisition and processing parameters is shown in Table 4. 1. The version available for this project is a pre-stack depth-migrated (PSDM) using the RTM algorithm and a TTI anisotropic model. Tilted Transverse Isotropy (TTI) is a velocity model that characterizes anisotropy in the subsurface around an arbitrary tilted axis instead of a vertical one like in Vertical Transverse Isotropy (VTI) model (Audebert and Pettenati, 2006) or Horizontal Transverse Isotropy (Figure 4.11), which are associated mainly to horizontal bedding and vertical fractures respectively. As a result, TTI models provide better imaging of the subsurface in structurally complex areas, like those involving salt-related deformation (Figure 4.13). The aims of this survey were: 1) to confirm the extension of Mesozoic oilfields and, 2) support the assessment of petroleum potential of Kimmeridgian and Cretaceous Plays in the south and south-eastern portions of South Eastern Basins.

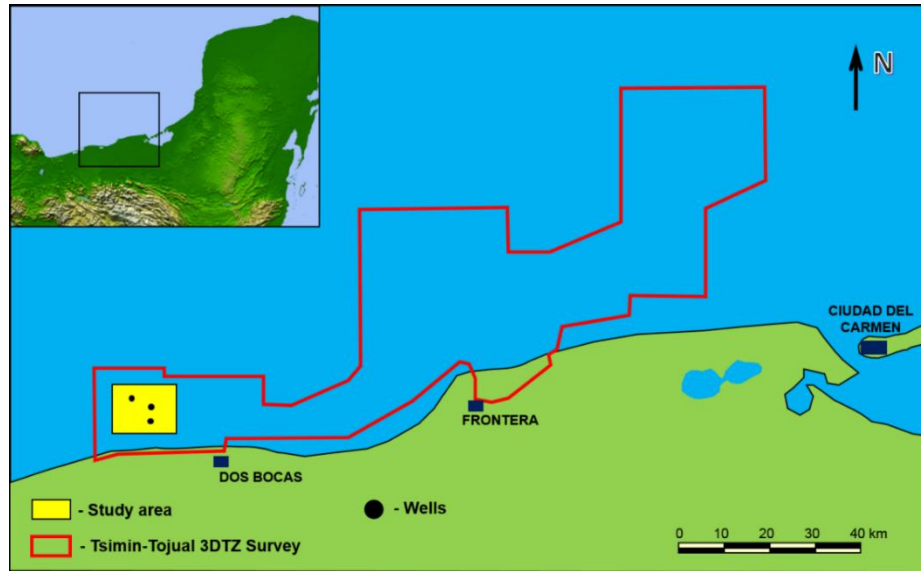


Figure 4.10. Location map of the 3D seismic survey and the study area.

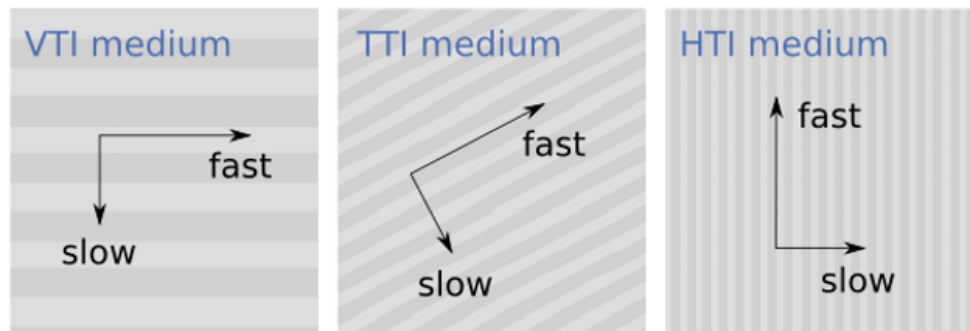


Figure 4.11. Schematic illustration of differences in subsurface velocities in Vertical, Tilted and Horizontal Transverse Isotropy models respect to bedding orientation (horizontal, tilted and vertical, respectively) (Hall, 2015).

Figure 4.12 shows a cross-section displaying the velocity model used for depth migration superimposed on the conventional amplitude section. For Tertiary section, vertical and lateral variations are more abrupt and range from 2000 m/s in the shallowest portion to 4000 m/s at 5-6 km depth, whereas for Mesozoic section velocities are fairly constant and ranging between 4500 and 550 m/s, characteristic of carbonate rocks. For salt sediments, a constant velocity of 4500 m/s was used.

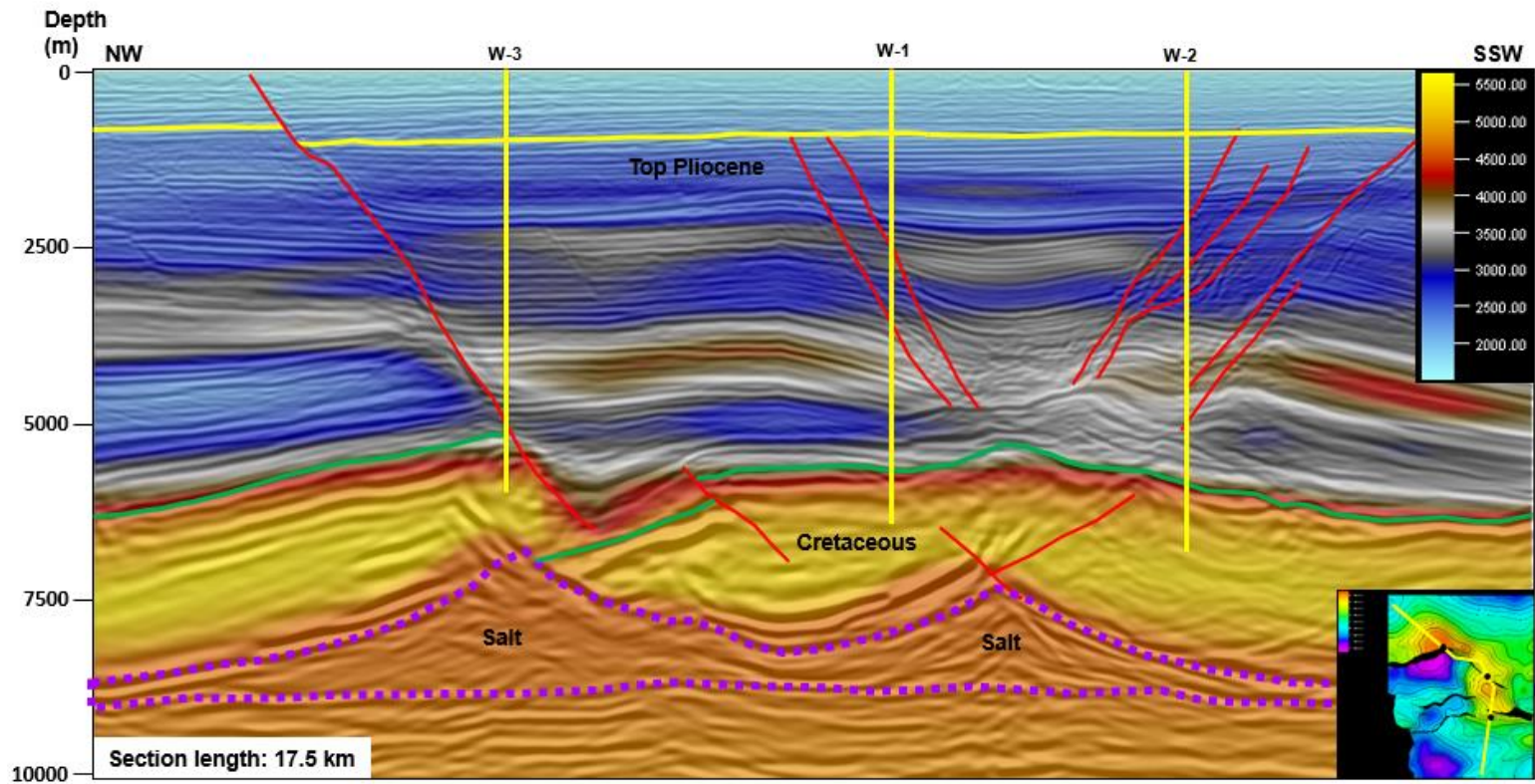


Figure 4.12. Random cross-section showing the distribution of velocities used for depth migration. No vertical exaggeration.

Figure 4.13 shows a comparison between a PSTM seismic dataset previously used for interpretation in the study area and the most recent PSDM survey, used for this study. The latter offers many advantages in terms of imaging quality and definition of structural features: A) Significant improvement in signal-to-noise ratio with important reduction of coherent noise (migration smiles); B) better definition of Mesozoic seismic stratigraphy; C) Enhancement in definition of top and base of autochthonous salt and geometry of salt bodies; D) Improved imaging of Tertiary-aged sequence known as *chaotic*, which represents possible mass-transport sediments; E) Better definition of the Pliocene trans-tensional fault system.

Seismic Survey	Tsimin-Tojual 3DTZ
Interpreted seismic version	MIGPSDMRTM_M35_2017
Acquisition Parameters	
Company	Geokinetics
Area	3,990m km ²
Recording length	10 s
Offset Length	11 km
Type of acquisition	Ocean Bottom Cable (OBC)
Bin size	50 m
Year	2011-2013
Type of source	Air Guns
Processing Parameters	
Company	ION GX Technology
Area	1000 km ²
Type of Processing	RTM TTI
Bin size	25 x 15 m
Year	2015
Visual Quality Control	
Tertiary	Good
Mesozoic	Regular to Good
Allochthonous salt bodies	Good
Autochthonous salt	Good

Table 4. 1. Summary of acquisition and processing parameters of Tsimin-Tojual 3DTZ seismic survey.

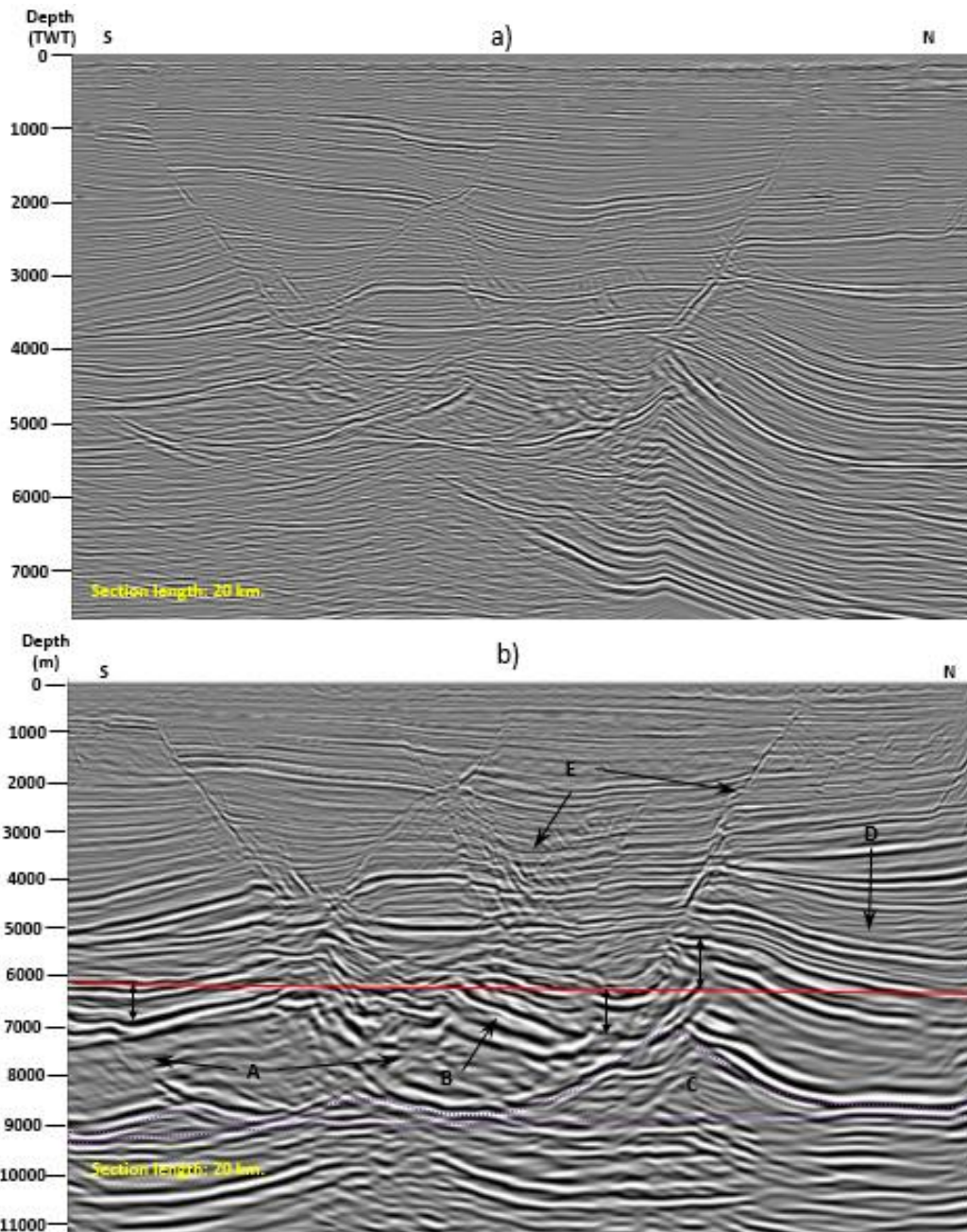


Figure 4.13. Visual comparison between (a) PSTM and (b) PSDM seismic datasets in the study area. Imaging quality improves significantly with the PSDM dataset, resulting in a more reliable interpretation. Purple dashed line in PSDM section represents the interpreted top and base of autochthonous salt. Horizontal red line at 6 km is the regional of Top Cretaceous in the study area. Double head arrows show the vertical difference between the regional and Top Cretaceous. No vertical exaggeration.

4.2.2 Well Data

Information from three productive wells drilled in the study area includes final reports, petrographic descriptions of cores and cutting samples, and complete sets of well logs (Table 4. 2). Final reports consist of geological background, description of stratigraphy, mud logging information, analysis of tested intervals and a resume of drilling and termination operations. These wells, along with others wells outside of the study area, were used to create the velocity model for depth migration of the seismic survey used for this project. The location of the wells is shown in

Figure 4.10. The three wells found hydrocarbon accumulations in Mesozoic targets at different stratigraphic levels (Late Cretaceous and Kimmeridgian) with an oil density of 32-33° API. Table 4. 3 summarizes the stratigraphy found in the wells, which ranges from Late Jurassic Kimmeridgian to Pleistocene.

	W-1	W-2	W-3
Operations report	✓	✓	✓
Core description	1	1, 1C, 2, 3, 4	3, 4, 5
Fracture analysis in core samples	1	1, 3, 4	3, 4
Biostratigraphic appendix	✓	✓	✓
Well logs	AIT-GR-LDL-CNL-DSI (6476-5762 m)	AIT-GR-LDL-CNL-DSI, SS (6880-5836 m)	AIT-GR (5715-5295 m)
	FMI (6473-5795 m)	FMI (6425-5836 m)	LDL-CNL-DSI, OBMI (5552-5295 m)

AIT= Array Induction Manager Tool

GR= Gamma Ray

LDL= Litho Density Log

CNL= Compensated Neutron Porosity Log

DSI= Dipole Shear Sonic Imager

SS= Sonic Scanner

FMI= Fullbore Formation MicroImager

OBMI= Oil-Base Micro Imager

Table 4. 2. Inventory of borehole information used for this study.

	W-1				W-2				W-3			
	KB=34 m Water Depth=30 m				KB= 42 m Water Depth=22 m				KB=30 m Water Depth=28 m			
	Oil Producer				Oil and gas Producer				Oil Producer			
	Top (m)	Thickness (m)	Core samples	Production tests	Top (m)	Thickness (m)	Core samples	Production Tests	Top (m)	Thickness (m)	Core samples	Production tests
Pleistocene	64	1096			64	1431			58	952		
Late Pliocene					1495	440			1010	100		
Middle Pliocene	1160	1050			1935	390			1110	1185		
Early Pliocene	2210	690			2325	650			2295	905		
Late Miocene	2900	1400			2975	1175			3200	825		
Middle Miocene	4300	480			4150	315			4025	635		
Early Miocene	4780	320			4465	720			4660	200		
Late Oligocene					5185	70			4860	180		
Middle Oligocene	5100	230			5255	65			5040	60		
Early Oligocene	5330	60			5320	55			5100	50		
Late Eocene	5390	50			5375	70			5150	20		
Middle Eocene	5440	80			5445	140			5170	45		
Early Eocene	5520	200			5585	150			5215	105		
Late Palaeocene	5720	30			5735	180						
Early Palaeocene	5750	10										
Late Cretaceous	5760	166	Core 1	Test 3 (5892-5975 m)= Oil producer	5915	110	Core 1	Test 2 (6015-6075 m)= Oil Producer	5320	35		
Middle Cretaceous	5926	50		Test 3= Oil Producer	6025	170	Core-1C	Test 2= Oil Producer	5355	20		
Early Cretaceous	5976	84			6195	105			5375	65	Core-3	
Late Jurassic Tithonian	6060	257			6300	235	Core-2		5440	200		
Late Jurassic Kimmeridgian	6317	163		Test 1 (6377-6408 m)= Oil and water; Test 2 (6319-6350 m)= Water invaded	6535	345	Cores 3 and 4	Test 1 (6510-6640 m)= Water invaded	5640	340	Cores 4 and 5	Test 4 (5610-5655 m)= Oil Producer
Total Depth	6480				6880				5980			
*Depth referred to Kelly Bushing												

Table 4. 3. Summary of results of production tests in the boreholes within the study area.

4.2.3 Methodology

Figure 4.14 illustrates the methodology developed in order to define a structural evolution model and its implications for fracture development in Mesozoic rocks. First, a review of existing literature and previous studies in order to understand the regional geological setting was carried out. Secondly, 3D seismic interpretation provided structural and thickness maps as well as cross-sections, whose combined study constitute the framework for a structural analysis. Third, 2D structural restoration was performed using properly orientated cross-sections in order to define the timing of deformational events that affected the analysed structures. Finally, all this information was integrated in order to define the structural style of deformation, propose an evolutionary model of the study area, understand the salt-overburden interaction through time and, finally, define its implications as hydrocarbon traps.

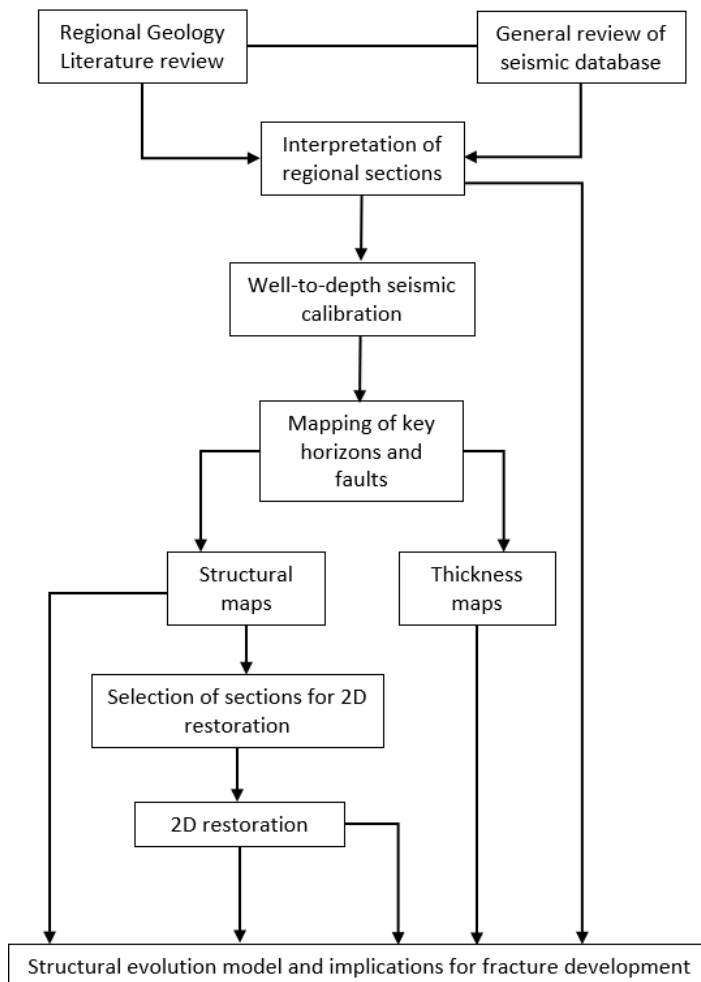


Figure 4.14. Methodology workflow.

4.2.3.1 Seismic Interpretation

First, an extensive literature review was done in order to understand the tectono-stratigraphic setting of the study area. Also, a visual inspection of the PSDM seismic survey was carried out in order to assess imaging quality and the corresponding uncertainty in interpretation as well as recognize the structural style of the study area. A qualitative analysis of certainty and confidence on interpretation of the Mesozoic section was carried out, based on criteria such as: imaging quality, difficulty to identify structural and stratigraphic features and lack of correlation with nearby wells (Figure 4.15). For Tertiary section, confidence is high in almost all of the area, whereas in the Mesozoic section confidence is medium to low in the central portion of the area due mainly to low seismic resolution, imaging issues (low signal-to-noise ratio in specific areas, migration smiles) in spite of the state-of-the-art imaging techniques applied during processing as well as lack of boreholes in the central area that difficult horizon correlation. Moreover, depth of Mesozoic column (at least 6 km) influences directly in loss of resolution, thus affecting negatively the imaging quality and adding difficulty to interpretation (Figure 4.16). Additionally to the previously analysed regional sections contained in PEMEX's technical reports, local sections across the study area were constructed in order to identify the structural deformation style and characterize the structural traps.

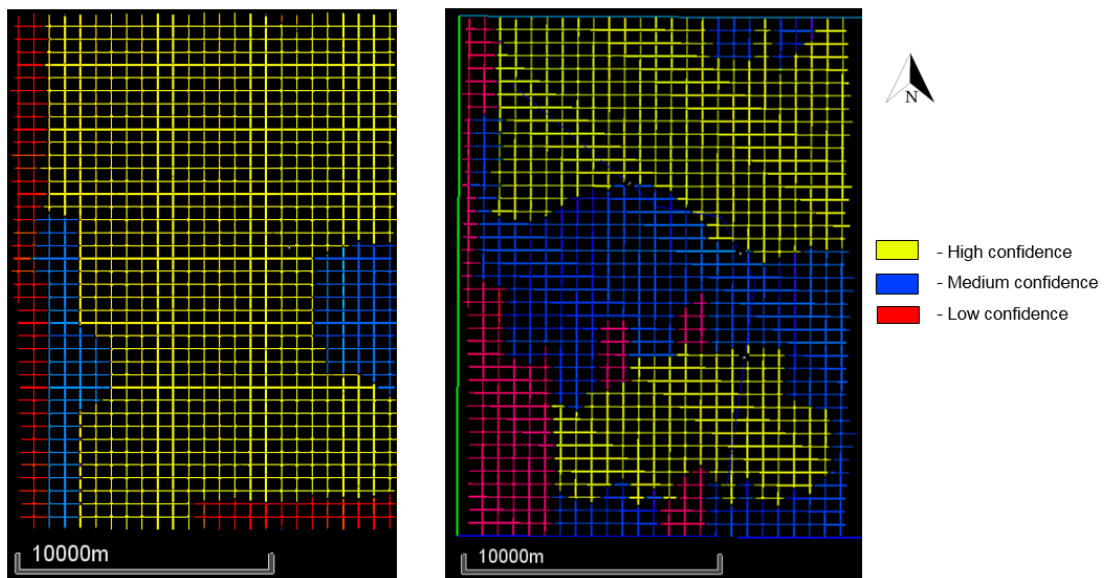


Figure 4.15. Confidence map on seismic interpretation for Mesozoic section. Left panel: Tertiary; Right panel: Mesozoic.

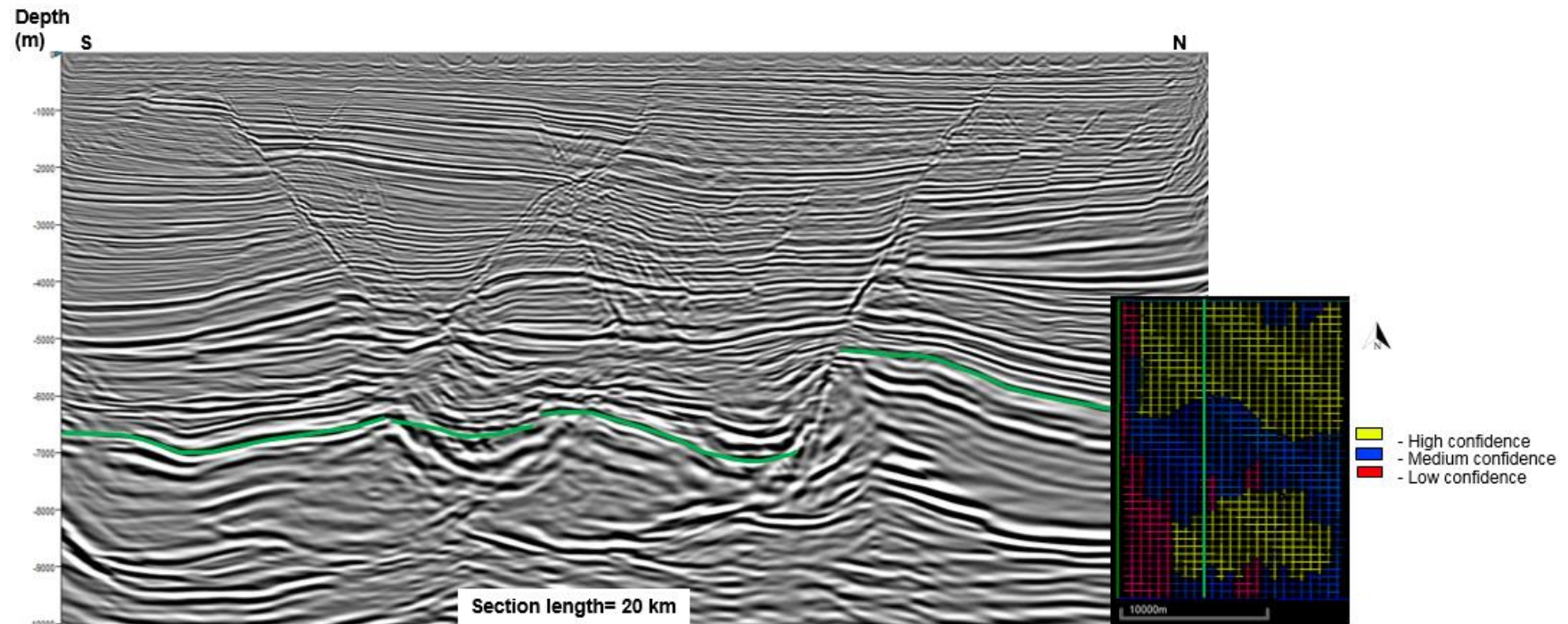


Figure 4.16. Seismic cross-section showing the differences in quality image in the Mesozoic section between the central portion, where image is not very good and confidence in interpretation is low, and the northern and southern, where image is better as well as the confidence in interpretation. Green horizon corresponds to Top Cretaceous. No vertical exaggeration.

Well-to-depth seismic calibration

Information from the boreholes within the study area was used to build and calibrate the velocity model for depth migration; however, in order to corroborate the well tie as well as to have a better certainty of the seismic interpretation, synthetic seismograms for each well were created before carrying out seismic interpretation. Sonic (DTCO) and Density (RHOB) logs from each borehole were used as input in order to generate synthetic seismograms as well as a Ricker wavelet, whose central frequency was determined by the following procedure:

1. The wave number (k) was obtained from an analysis window of 640 m (32 samples) directly picked from the corresponding seismic section, and then graphed to obtain a more precise value.
2. With the value k already known, wavelength value (λ) was obtained substituting k in the formula $\lambda=2\pi/k$.
3. Finally, frequency (f) was obtained with the formula $f= V/\lambda$, where V is the seismic velocity of carbonate rocks (4500-5500 m/s).

Table 4. 4 summarizes the values obtained for each borehole. Vertical resolution is very low, ranging between 157 and 262 m due to the very low frequencies predominant at Mesozoic depths, which range between 5 and 7 km. Figure 4.17-4.19 illustrate the results of the synthetic seismograms and the degree of correlation with PSDM seismic. In all cases, Top Cretaceous shows a very good match between synthetic and PSDM seismic, both coinciding with a positive peak. It should be noted that Top Cretaceous is an often good controlled pick associated with the top of the carbonate column, and is usually used as the top for migration of carbonate sediments during PSDM processing. In the other hand, for Top Tithonian and Top Kimmeridgian matching is low, even showing opposite polarities. This is due possibly to very low seismic resolution, and a non-detailed velocity model used for PSDM migration, which may influence on the positioning of seismic reflectors.

	W-1	W-2	W-3
k (m ⁻¹)	0.01	0.006	0.01
λ	628.3	1047.2	628.3
V (m/s)	5500	5500	5500
f (Hz)	9	5	9
Wavelet length (ms)	504	504	504
Vertical Resolution (m)	157	262	157

Table 4. 4. Parameters used to calculate the dominant frequency (f) in the seismic data for each borehole in the study area.

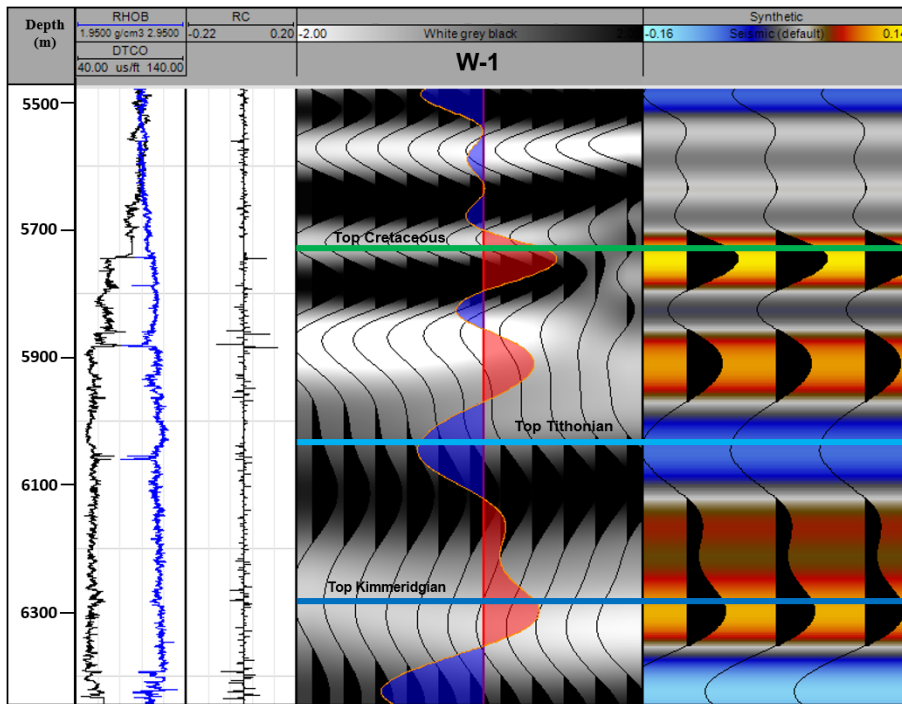


Figure 4.17. Synthetic seismogram from W-1 and correlation along a seismic line crossing the borehole. Correlation for Top Cretaceous is good (positive peak), although matching accuracy decreases for Top Tithonian and Kimmeridgian.

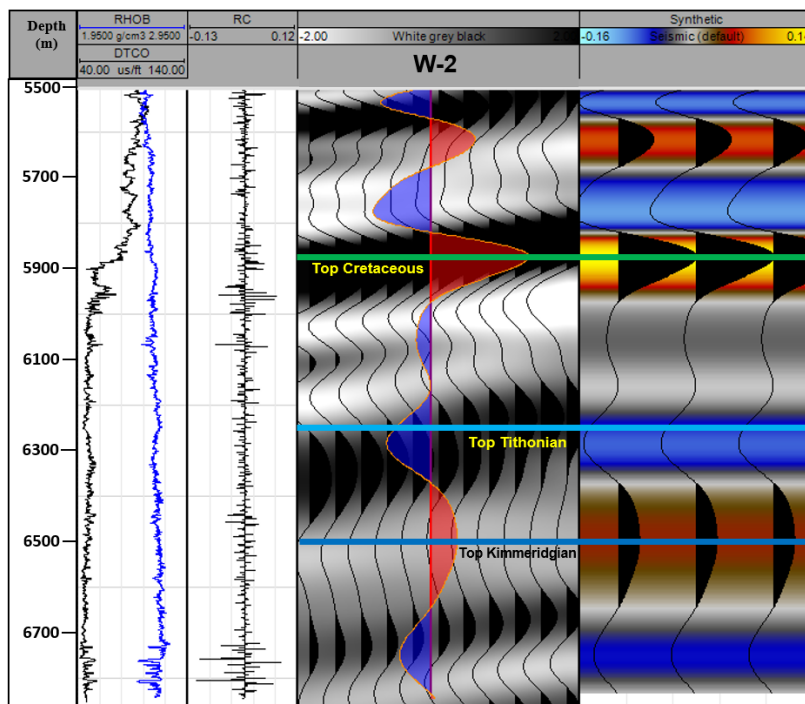


Figure 4.18. Synthetic seismogram from W-2 and correlation along a seismic line crossing the borehole.

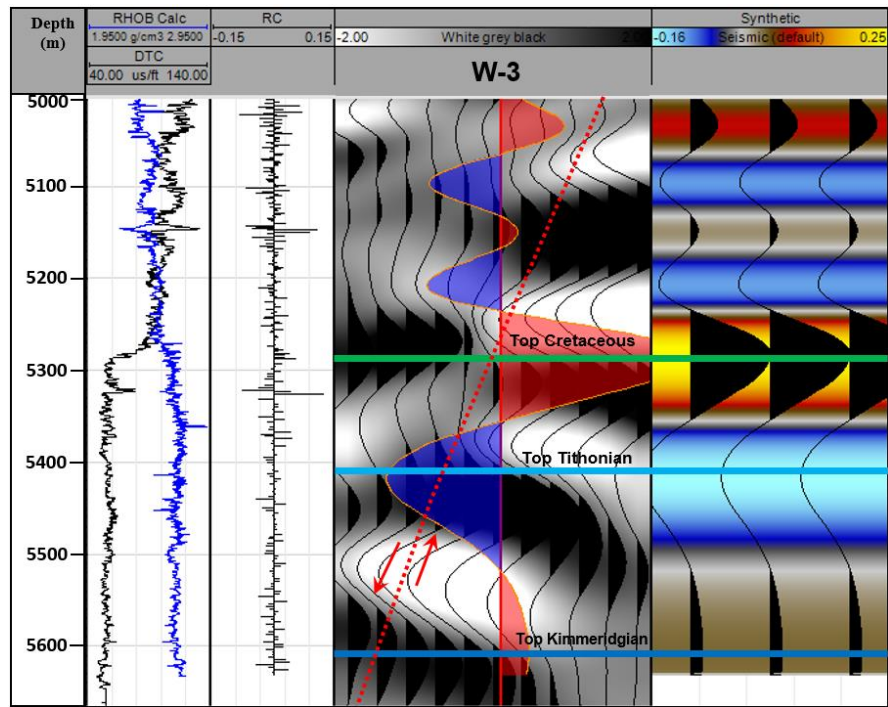


Figure 4.19. Synthetic seismogram from W-3 and correlation along a seismic line crossing the borehole. Although the presence of a normal fault (dashed red line) difficults correlation, this is good for Top Cretaceous.

Horizons and Fault Mapping

The first step in seismic interpretation consisted of regular grids where inlines and crosslines were interpreted at equidistant intervals intersecting boreholes all over the study area (220 km²). Additionally, random lines and depth slices were used in order to constrain the interpretation of grids. For each surface, two horizons were merged: one well-constrained with the suffix “*observation*”, which extended over an area with high confidence in correlation and interpreted using auto-pick where possible. The second horizon was no well-constrained with the suffix “*interpretation*”, which was picked over an area with low confidence in correlation due to low image quality, no wells, or structural complexity and was interpreted mostly manually. For this project, a total of 16 horizons were interpreted; 7 correspond to Neogene and 2 to Paleogene, which were interpreted in grids of 40 x 40 lines (1.2 km x 1.2 km). The remaining 6 horizons correspond to Mesozoic and were interpreted in more closely spaced grids of 20 x 20 lines (600 m x 600 m). Figure 4.20.

The American SEG Convention was used for horizon interpretation. Reflections corresponding to an increase in acoustic impedance are considered positive and displayed as a peak (black), whereas reflections corresponding to decrease in acoustic impedance are considered negative and displayed as a through (white). Figure 4.21

illustrates the seismic stratigraphy of the study area. Traditionally, Tertiary horizons in the study area are not associated to characteristic seismic reflectors, so biostratigraphic information from boreholes is required to identify and map these horizons. In the other hand, key Mesozoic horizons are associated with specific reflectors. For example, Late Cretaceous is associated with a high amplitude positive reflector derived from the contrasting contact between Paleogene siliciclastic sediments and Mesozoic carbonates; however, in some areas Palaeocene sediments comprise mudstone and/or marls, which may cause confusion and lead to misidentify the top of Late Cretaceous with the top of carbonate sediments. In those cases, well logs and biostratigraphy are required to identify Top Cretaceous. Top Tithonian is associated to a high amplitude negative reflector, and Late Kimmeridgian is associated to a high amplitude positive reflector. Although this represent a general trend in South-Eastern Basins, there are areas where particular stratigraphy conditions may cause different seismic responses and therefore, a deviation from the general trend.

Similarly to horizon interpretation, nine faults were interpreted and mapped manually in crosslines and inlines in a grid of 20 x 20 lines (600 x 600 m) following the next criteria: 1) Faults affecting Mesozoic sequences, 2) To show clear offset or evidences of possible reactivation and, 3) To display a lateral continuity of 20 lines (600 m) as a minimum (that is, at least two lines with the selected grid mapping). Then, a surface was created for each interpreted fault. From these, six show normal relationships and the other three can be considered as reverse faults according to their present-day geometries (Figure 4.22). Low vertical resolution at depths below 5 km make fault interpretation difficult without additional borehole data to support a more constrained interpretation.

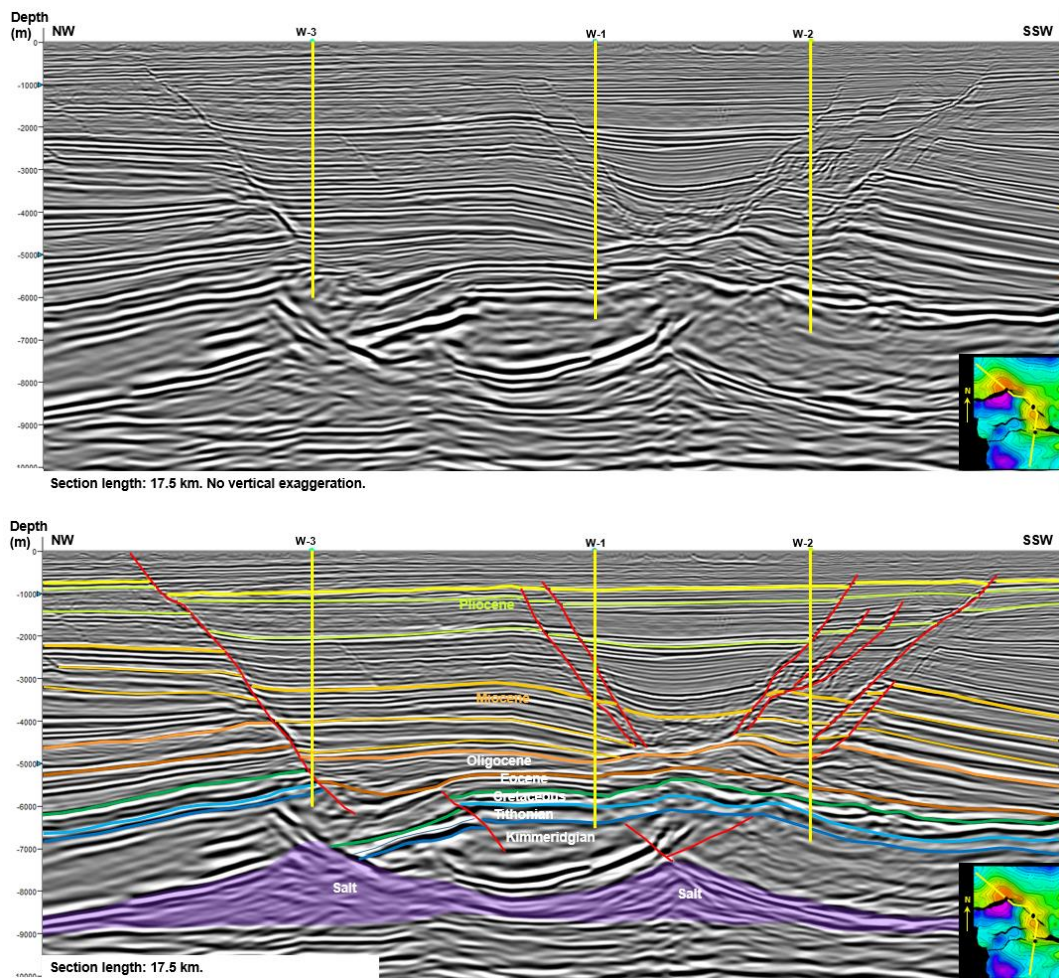


Figure 4.20. Random sections crossing the three boreholes in the study area. Above: uninterpreted section; below: Interpreted section showing all the horizons and their correlation between the boreholes.

Thickness maps

These maps display the distribution of either vertical (apparent) or true (measured perpendicular to bedding) thickness between two particular horizons. For this project, 12 maps of true thickness (perpendicular to bedding) were generated in order to describe the variations in spatial distribution of depocenters with time, which enables to define and constrain the tectonostratigraphic evolution of the study area (Figure 4.23).

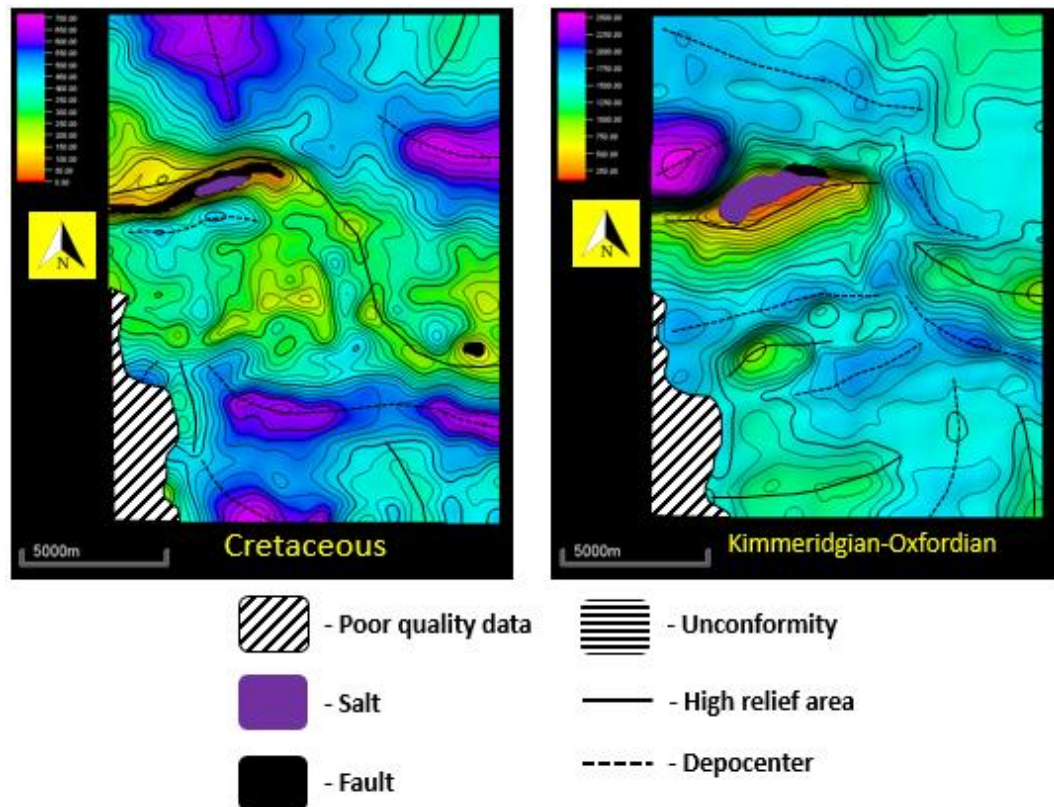


Figure 4.23. Thickness maps for the two stratigraphic packages that constitute the main economic targets in the study area.

4.2.3.2 2D Kinematic Modelling

Cross section restoration is a technique that allows geoscientists to determine the temporal evolution of geological structures (Rowan, 1993) by reversing deformation progressively from a deformed state to an initial undeformed state. Originally, it was developed to predict subsurface trap geometry in fold-and-thrust belts (Dahlstrom, 1969). Since then, it has been extensively applied successfully to extensional regimes (Rowan and Kligfield, 1989; Nunns, 1991) and even to salt terrains (Rowan, 1993; Hossack, 1995; Macaulay, 2017). Technological advances in specialized software have made possible to carry out three-dimensional restoration when enough data is available. Its application in oil industry is relevant mainly in exploratory stages, where information

provided is critical to make accurate decisions involving the design of exploration strategies. Information provided by structural restoration includes:

- Evolution of basin architecture through time.
- Timing of formation and re-deformation of potential hydrocarbon traps.
- Timing of burial and/or uplift of source rocks.
- Constrains about synchronicity of the different elements of Petroleum systems.

The basic assumptions of cross-section restoration are: 1) cross-sectional area conservation during deformation and, 2) Deformation is plane-strain, which implies that no material can move into or out from the cross-section plane (Woodward et al., 1985) and that the cross-section must be properly oriented parallel to the direction of maximum deformation. The procedure of restoration involves the removal and reversing of the effects produced by geological processes such as sedimentation, compaction, eustasy, fault-related deformation, isostasy, salt movement (if applicable) and thermal subsidence (Rowan, 1993). To achieve this, a series of algorithms are applied during the different steps in the restoration process and the choice of each of them depends on factors such as length of cross-section, type of folding, fault geometries and presence of salt.

For this project, three cross-sections were selected for 2D restoration, which are oriented parallel to the direction of tectonic transport and therefore, perpendicular to the main axis of the structure of interest; however, the occurrence of late strike-slip deformational events of Neogene age along with the presence of two levels of salt detachment (one autochthonous and the other allochthonous), represent major issues that hindered the restoration process and brought some artifacts and quantitative inaccuracies. For example, movement into and out of the section planes may explain that faulted blocks above the upper detachment do not fit after restoration. Also, geometric issues arise if exceeding sediment load in Pliocene times is accommodated by subsidence in the upper salt detachment alone.

4.2.3.3 Integration and Analysis of Results

Finally, all the inputs generated previously (local and regional cross-sections; structural, thickness and strain maps and 2D restored sections) were integrated and analysed in order to define a structural evolution model which provided information about the time of formation of structural traps and its implications for fracture development and the subsequent analysis of reservoir rock quality.

4.3 Results

4.3.1 Seismic interpretation

4.3.1.1 Structure maps

Structure maps in depth for every interpreted horizon were generated from 3D seismic interpretation. For Mesozoic targets (Top Cretaceous and Top Kimmeridgian), grid spacing used was 20 x 20 lines (600 m x 600 m), which is a standard spacing for a semi-detailed prospect mapping. Due to low seismic resolution in Mesozoic, intra-Cretaceous, hydrocarbon-producing target horizons (tops of Middle and Early Cretaceous) were not mapped. In the study area, thickness of these intervals ranged from 20-216 m and 65-135 m, respectively. Moreover, thickness of Late Cretaceous ranged from 35 to 160 m, which also made difficult to map Middle Cretaceous across the entire study area.

Mapping of Top of Autochthonous salt reflects the distribution of withdrawal basins, which have a semi-circular to elliptical geometries, and are delimited by a polygonal pattern of salt ridges and diapirs (Figure 4.24a). Base of Autochthonous salt is relatively flat and location of salt diapirs do not seem to be related to basement structural highs, thus suggesting a thin-skinned deformation (Figure 4.24b). Top Cretaceous and Top Kimmeridgian are the two main economic Mesozoic targets and their structure maps show remarkable similarities in terms of the location and orientation of the main structural features such as anticlines, synclines and main faults (Figure 4.25a-c). Moreover, these maps are also very similar to Top Autochthonous salt, since the location and orientation of the two main anticlines correlate with those of salt diapirs. Eocene and Oligocene maps show structural configurations similar to the Mesozoic maps as well (Figure 4.25d-e), which suggests that these horizons were deformed similarly to the Mesozoic horizons as the result of the continuing influence of salt distribution and associated diapirism; additionally, individual effects of contraction during Paleogene times (D2 event) are likely to be overprinted by later D3 folding and therefore, difficult to quantify in structure maps. In contrast, effects of contractional D3 event (Miocene) are not visible in structure maps due mainly to the overprinted effects of later D4 event. However, D3 effects can be identified by analysing thickness maps.

Oligocene map is the first one where allochthonous salt is mapped in the western edge of the study area. The geometry of this allochthonous salt body is dome-shaped and its complete plan view geometry could not be defined because it extends out of the study area, although it may range from semi-circular to elliptical (Figure 4.26). The configuration of the base of salt could indicate that in a possible feeder may be located at its central portion; however, this could not be confirmed due to poor seismic imaging. From the relationship between salt and the Tertiary stratigraphy, it can be deduced a possible age of emplacement during the interval from Oligocene to Late Miocene (

Figure 4.27).

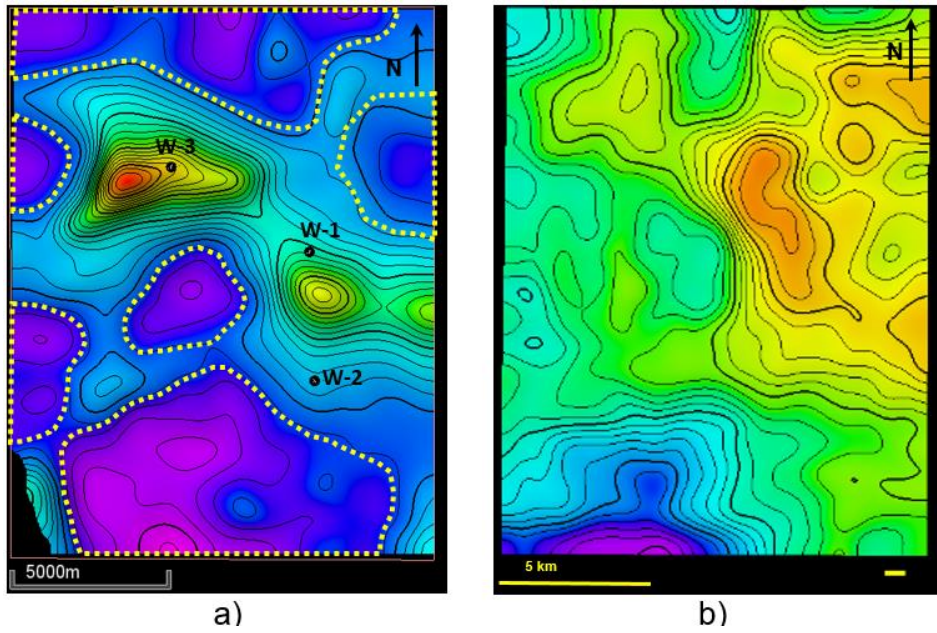


Figure 4.24. Structure maps showing the distribution of autochthonous salt. a) Top salt (primary minibasins delimited with yellow dotted lines); b) Base of salt. Black dots represent the location of boreholes.

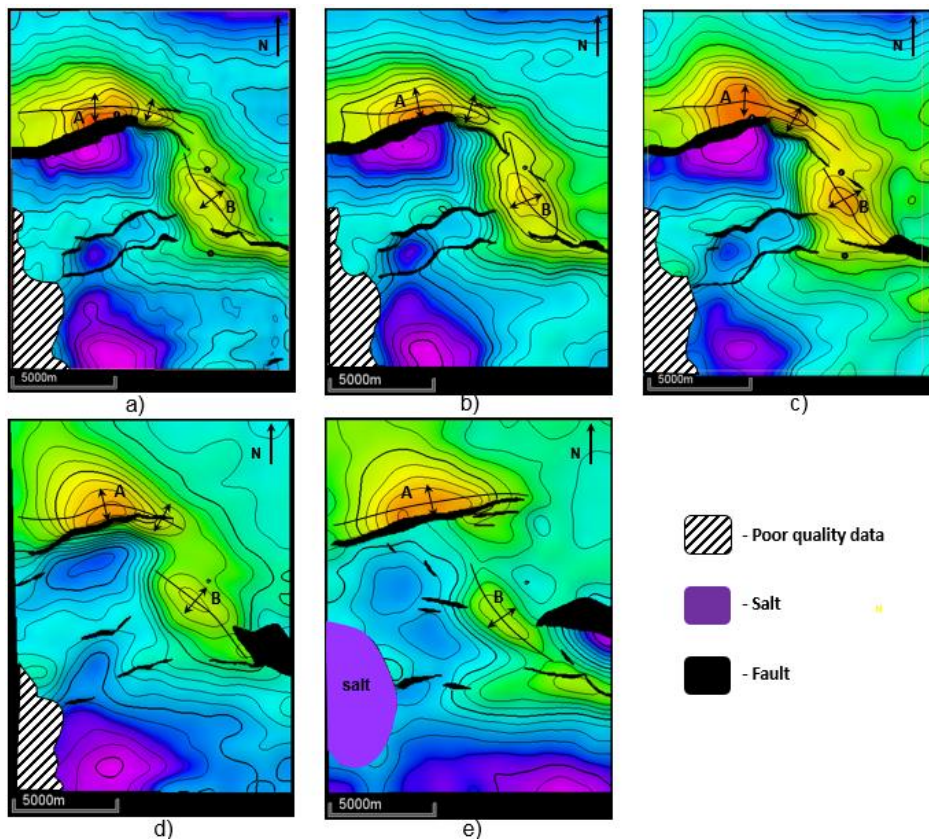


Figure 4.25. Structure maps illustrating the contouring similarity between Mesozoic and Paleogene horizons as a result of salt distribution (Figure 4.24). a) Top Kimmeridgian, b) Top Tithonian, c) Top Cretaceous, d) Top Palaeocene, e) Top Oligocene.

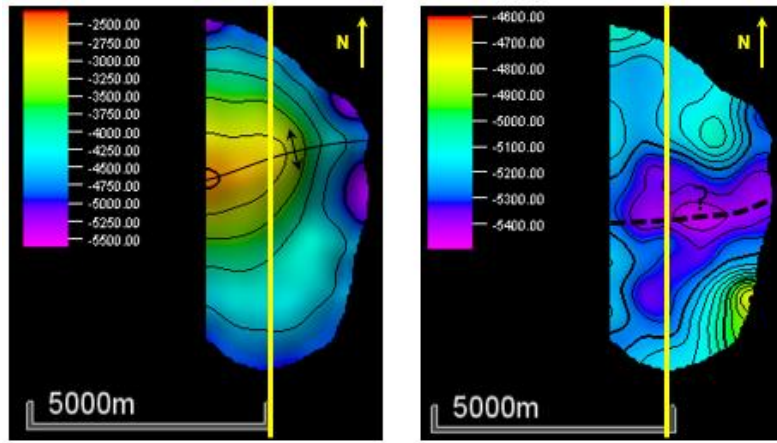


Figure 4.26. Structure maps of allochthonous salt. Left: Top, Right: Base. Black dashed line and question mark represent a possible location of a feeder for this salt sheet. Yellow line indicates location of cross-section from

Figure 4.27.

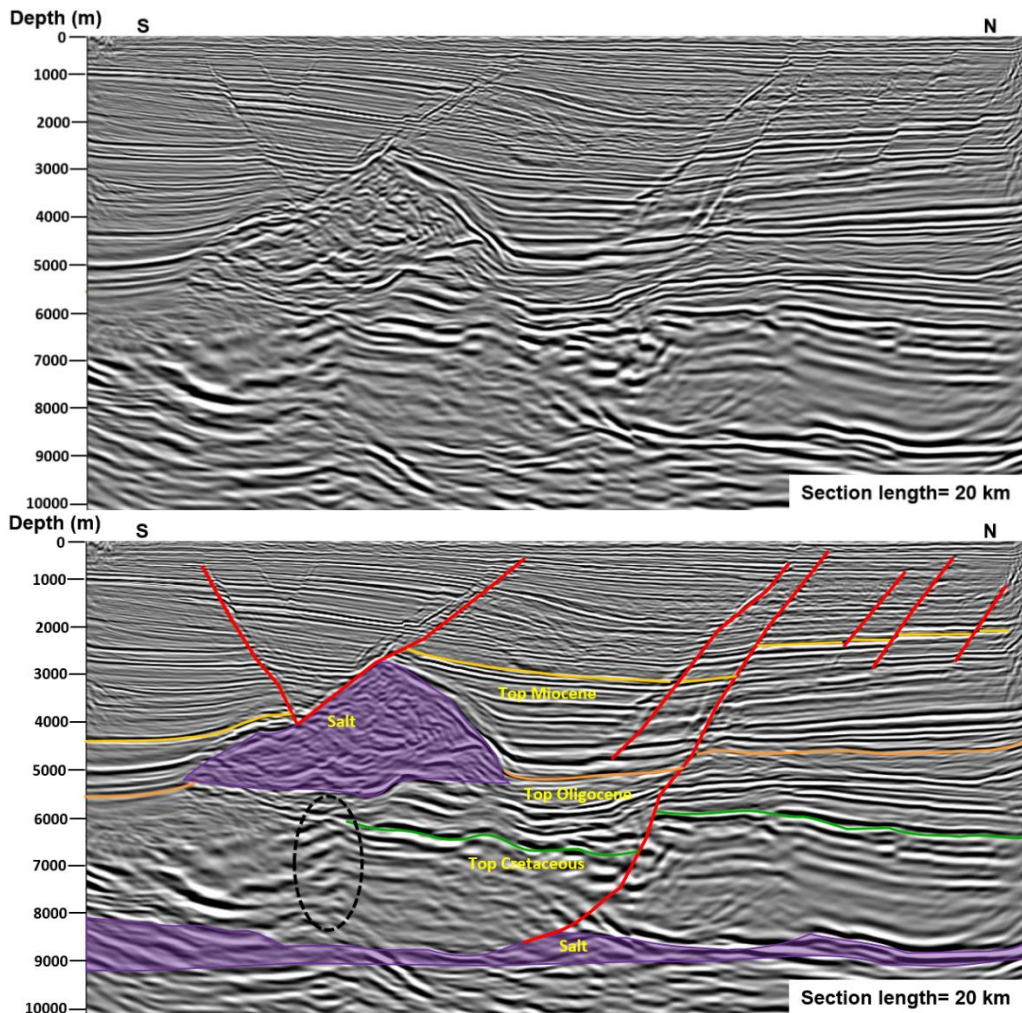


Figure 4.27. Uninterpreted and interpreted cross-section from Figure 4.26 showing the allochthonous salt body emplaced in the SW portion of the study area. Relationship with stratigraphy constrain the age of emplacement from Oligocene to Late Miocene. Moreover, the salt sheet was deformed by D2/D3 contraction and D4 extension. Dashed oval below the sheet represents an uncertain area where a salt feeder could be

interpreted or, alternatively, it may correspond to a velocity pull-up. No vertical exaggeration.

Structure maps from Middle Miocene to Late Pliocene show the effects of heavy normal faulting associated to the extensional D4 event (Figure 4.29). In the northern and southern portions, a series of ENE-WSW striking, en-echelon faults are present dipping towards the south and north, respectively; whereas in the central portion, a pull-apart trough striking NW-SE was developed and bounded by major normal faults with a right-lateral component (Figure 4.28). This event affected mainly the section above the upper detachment level, with the exception of main faults NF1 and NF4 (Figure 4.30), which penetrate below the detachment level and seem to merge with pre-existent faults, thus possibly causing a reactivation.

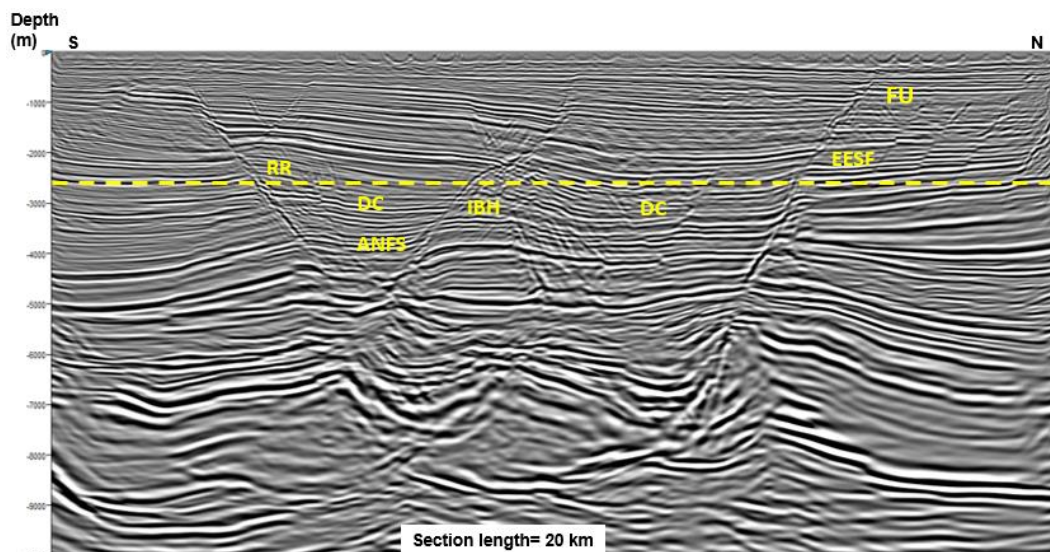
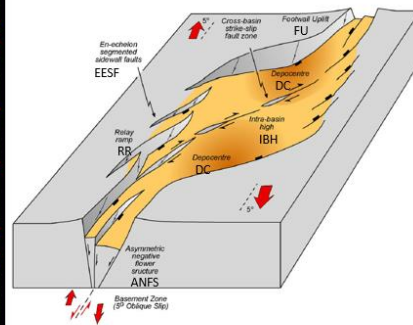
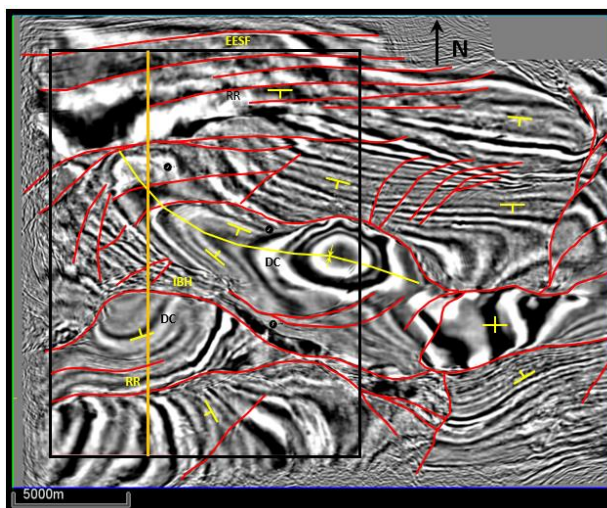


Figure 4.28. Top Left: Slice of the amplitude volume at 2500 m extending outside the limits of the study area (black rectangle) to the west, illustrating the location and geometry of an interpreted trans-tensional basin system. Top Right: Conceptual model of a trans-tensional basin based on analogue modelling (Wu et al., 1999). Bottom: Uninterpreted cross-section showing the trans-tensional system and their main components at 2500 m depth.

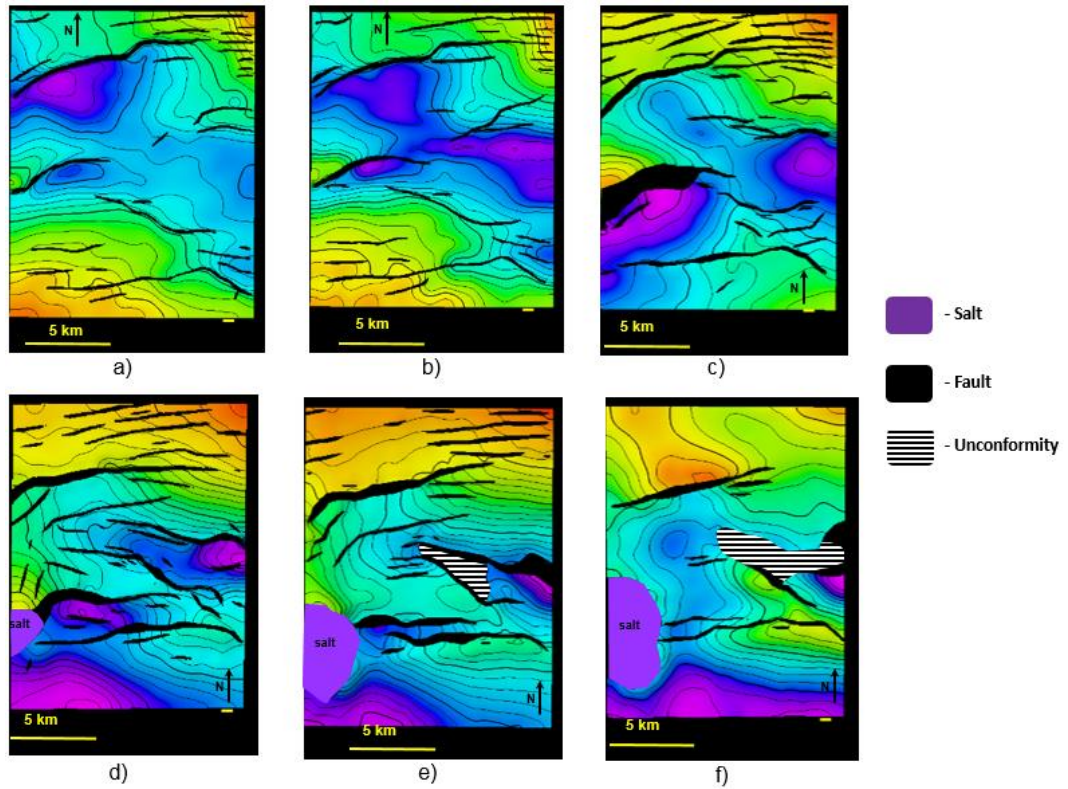


Figure 4.29. Structure maps showing the effects of D4 event in the study area. a) Top Late Pliocene; b) Top Middle Pliocene; c) Top Early Pliocene; d) Top Late Miocene; e) Top Middle Miocene; f) Top Early Miocene.

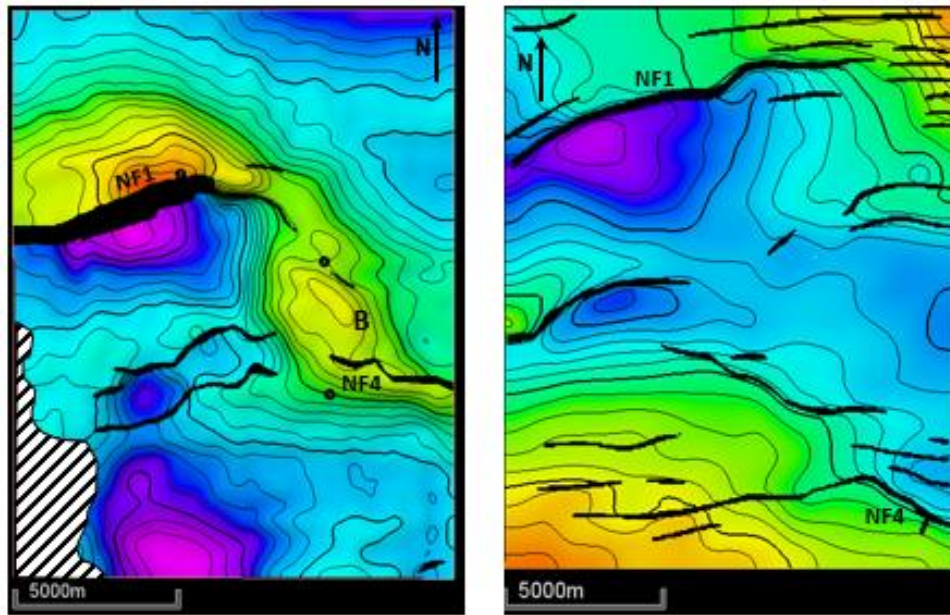


Figure 4.30. Structure maps of Top Kimmeridgian (left) and Top Pliocene showing the locations of normal faults NF1 and NF4, which cut through the entire stratigraphy and now form a single segment with pre-existent Mesozoic faults.

4.3.1.2 Thickness maps

Autochthonous salt (163?-165? Ma): These sediments are oddly distributed throughout the study area. Maximum thickness values are located in the Northwest and East where salt diapirs B (>2000 m) and A (1300 m) developed respectively, whereas lowest values (<100 m) are distributed in the peripheries of such diapirs (Figure 4.31f). Presence of primary salt welds is very likely, especially in the northern and southern portions, although vertical resolution of the seismic survey makes difficult to determine welds.

Top Kimmeridgian-Top Autochthonous salt (152-163? Ma): During this time, withdrawal basins started to develop as a result of early salt movement; consequently, thickness is highly variable in the study area. Location and orientation of these depocenters are directly controlled by autochthonous salt, where maximum thickness values (up to 2500 m) are located. Inversely, lower thickness values are located directly above salt diapirs (Figure 4.31e). Because the study area was not located on the basin's updip extensional domain at this time, D1 deformational event distinctive features are absent; however, salt diapirism can be considered as an expression of D1 in the linked system's transitional domain.

Late Jurassic Tithonian (145-152 Ma): Thickness of sediments deposited during this time is much more uniform and variations are not as remarkable as in Kimmeridgian-Oxfordian package. Average thickness ranges from 150 to 300 m, with maximum values

(up to 450 m) located in the western side and lowest values (> 100 m) located in the Diapir B area and in the northern side (Figure 4.31d). This uniformity reflects the stability and continuity of tectonostratigraphic conditions inherited from Late Kimmeridgian.

Cretaceous (66-145 Ma): Thickness variations are greater than in Tithonian. Maximum values (up to 700 m) are present in depocenters located in the northern and southern portions of the study area, whereas minimum values (< 150 m) are located above the Diapir B. In a general sense, the central portion of the area shows a thinning of this sequence, which may have been associated to the presence of a relatively salt-inflated area that controlled sediment distribution within the basin (Figure 4.31c). This salt probably was withdrawn from up-dip areas in the basin (and/or neighbouring areas) and accumulated in the study area during this period of time.

Palaeocene-Eocene (33.9-66 Ma): This sequence show significant thickness variations within the study area (Figure 4.31b). It thickens towards the north limit in a uniform way, probably due to an uplift of the central area associated to D2 compressional event and the consequent regional tilting towards the south, which caused salt withdrawal and accumulation of thicker sedimentary sequences. Also, a local depocenter (with a maximum thickness of 1 km) developed in the central portion of the study area, which seems to be associated with sedimentation derived from erosion of the uplifted footwall and its corresponding salt evacuation. And it is bounded by the following structural elements: To the north, the south-dipping normal fault NF1 bounding the Diapir B and the north-dipping reverse fault RF1; to the south, the south dipping normal fault NF2; to the East, the western limb of the Anticline A.

Oligocene (23-33.9 Ma): Thickness distribution is irregular and new depocenters, with maximum thickness of up to 1100 m were formed; at the same time, the depocenter inherited from Eocene-Palaeocene times still remains but with a lesser areal distribution (Figure 4.31a). Lower thickness values are located in structural highs probably inherited as well as newly formed ones during this time.

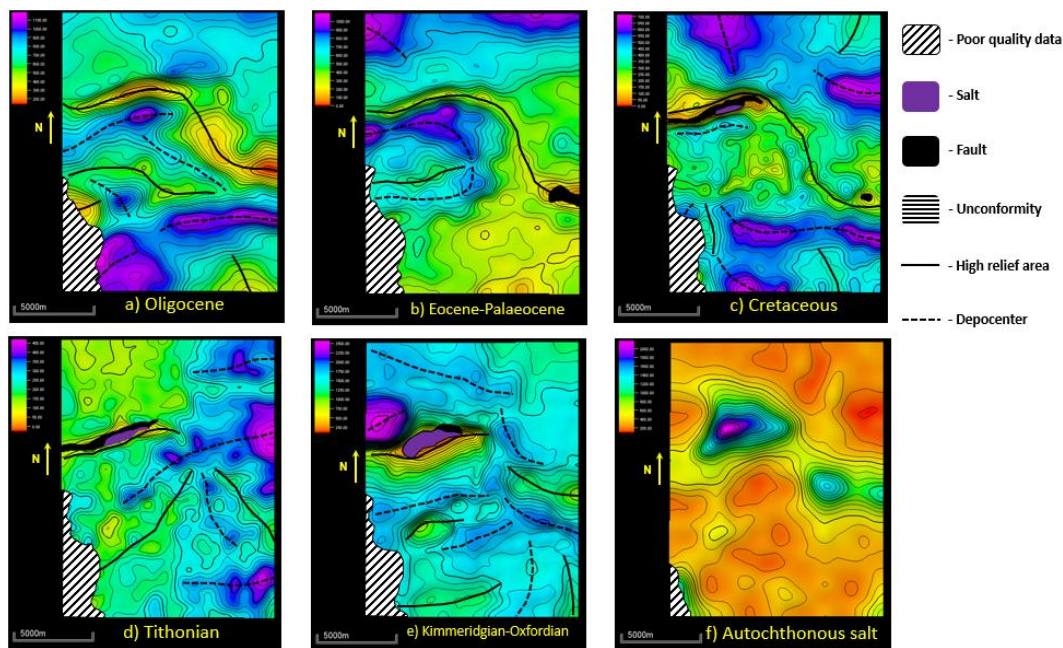


Figure 4.31. Thickness maps for Mesozoic and Palaeogene packages.

Early Miocene (16-23 Ma): Thickness distribution is irregular and four zones are clearly differentiated: 1) The northernmost zone, thickness values are the highest (up to 900 m) and increase regularly towards the north; 2) In the central portion, there is a zone with zero thickness, which is associated with an unconformity (Figure 4.36f). Flattening of this horizon in seismic cross-sections shows the onlap of Early Miocene horizon against Oligocene sediments (Figure 4.32), reflecting the paleo-topography at this time; 3) The southwestern zone also has absence of Early Miocene sediments due to the presence of allochthonous salt emplaced during this time, and 4) Central and southern portions where thickness distribution is relatively uniform with lower thickness values and two depocenters are identified.

Allochthonous salt is restricted to the SW portion of the area; however, tridimensional analysis of seismic data shows the presence of a detachment level of age Early Miocene-Oligocene, which suggests that allochthonous salt could have been emplaced more extensively across the study area, and later evacuated by sediment loading mainly (Figure 4.33).

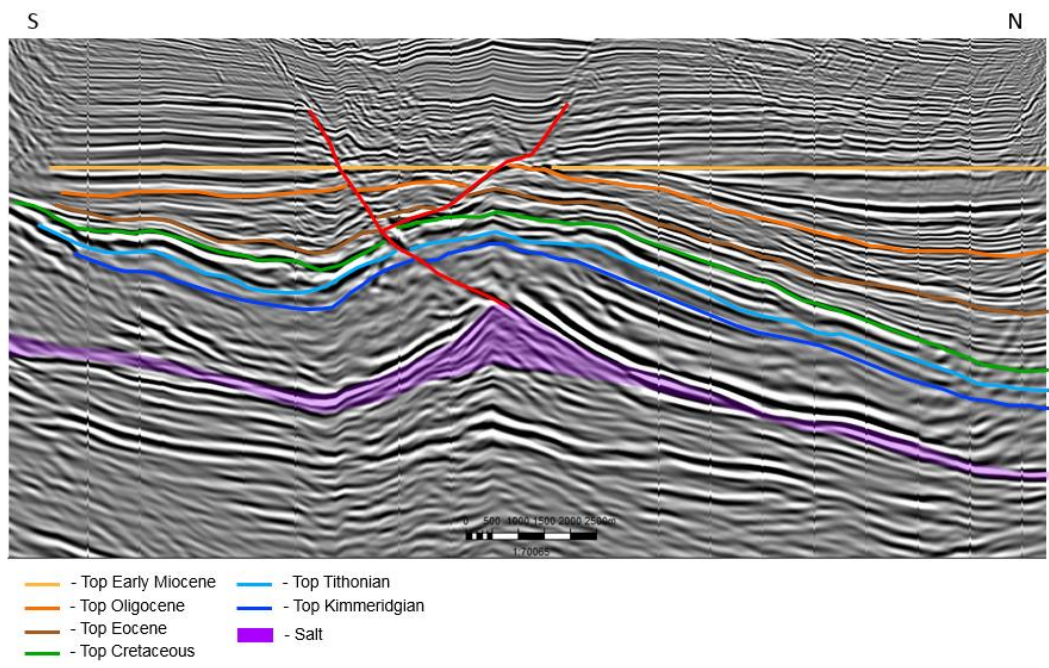


Figure 4.32. Seismic cross-section flattened at Top Early Miocene.

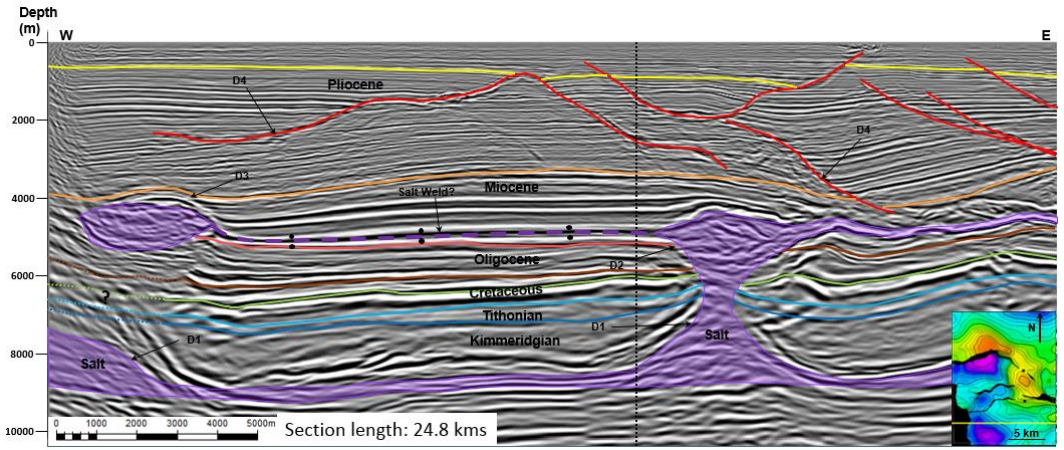


Figure 4.33. Cross section between two salt diapirs. Vertical dotted black line marks the limit of the study area. Miocene stratigraphy it is inverted probably by salt withdrawal from the surface interpreted as a welding (dashed purple line), which implies the presence of a paleo salt canopy.

Tectonic activity continued during this time, thus controlling thickness distribution in the study area. As in previous stages, structures associated to salt distribution were re-deformed and exerted a primary control on sediment distribution and, therefore, defining the location of depocenters. N-S tectonic contraction associated to D2 and/or D3? events originated folding orientated WNW-ESE and basin tilting towards the north, which caused salt evacuation due to both gravitational forces and loading of sediments coming from the South thus creating accommodation space and where maximum thickness values of this sequence are located. Also, uplifting could have caused submarine exposure and localized erosion in the central portion of the area.

In the SW portion of the study area, emplacement of allochthonous salt prevented deposition of Early Miocene-aged sediments. Although it is not clear the provenance of this salt (due to it is located in the limits of the study area), two mechanisms, proposed by Hudec and Jackson (2006) can be proposed a priori to explain this emplacement (Figure 4.34). From these, the plug-fed thrust seem to fit more with the available data.

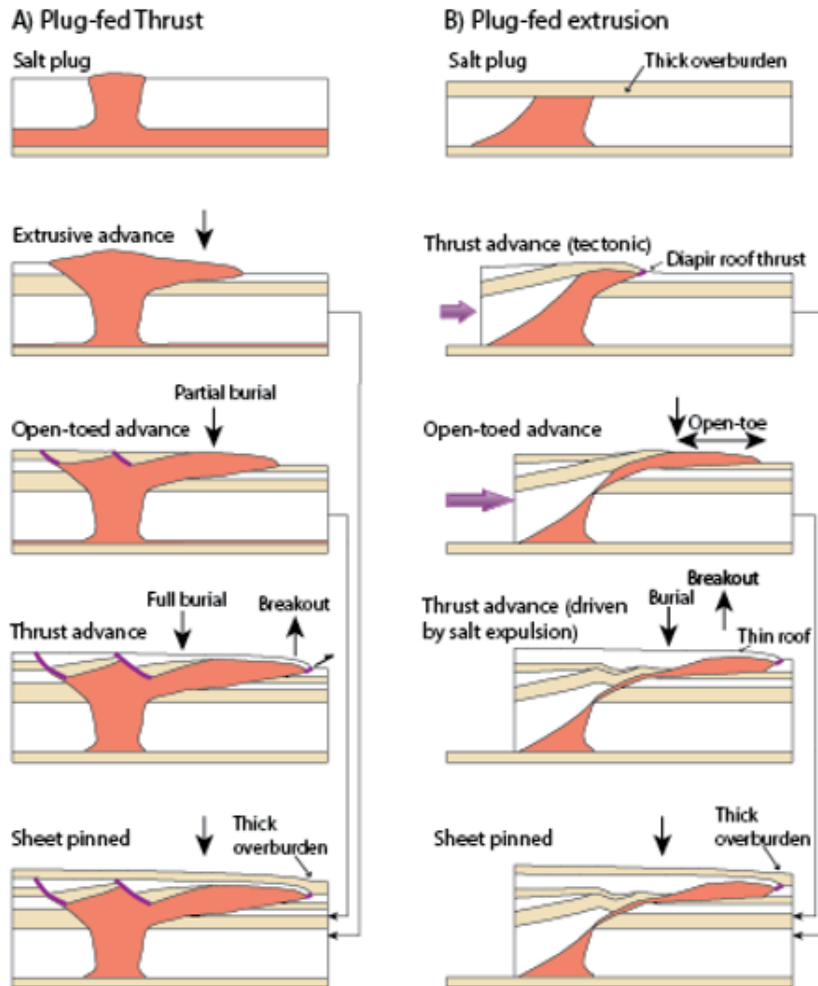


Figure 4.34. Different scenarios for emplacement of allochthonous salt (Hudec and Jackson, 2006).

Middle Miocene (11.6-16 Ma): Similarly to Early Miocene, thickness distribution is irregular and similar zones can be identified. Higher thickness values (up to 1 km) are associated to depocenters orientated NW-SE and located in the west-central and south eastern portions of the area (Figure 4.36e) whereas zero values are located where allochthonous salt was emplaced as well as in the unconformity zone. Lower values distributed in NE-SW and E-W trends are partially artifacts originated by truncation of the horizon with later normal faults, which can be identified in maps as very closely spaced

contour lines adjacent to abrupt changes in the gradient steep; however, it is also possible that paleo-topography played a role on the sequence's thinning.

During this time, contractional D3 event continued to fold pre-existing structures, thus influencing on sediment distribution. A depocenter orientated WNW-ESE developed in the west and centre of the study area, due probably as a combined response to greater allochthonous salt evacuation and paleo-topography controlled by tectonic activity (Figure 4.36e). Absence of this sequence in the centre of the area may be the result of original non-deposition because that area could have been occupied by a salt body that was collapsed and evacuated by later extension, since there is no onlapping of Mid-Miocene horizon over older structures but they truncate against normal faults.

Late Miocene (5.3-11.6 Ma): Thickness distribution within the study area is relatively uniform and it was mainly controlled by subsidence related to salt withdrawal in the upper detachment level. Highest thickness values (up to 1.1 km) correspond to two depocenters in the eastern edge of the area, which are separated by a south-dipping counter-regional fault whereas lowest thickness values show different orientation trends associated to terminations against normal faults (Figure 4.36d). Allochthonous salt emplacement still took place during this time, causing zero thickness values and thinning of Late Miocene sequence around the edges of the allochthonous salt, which seemed to have folded by D3 event, thus promoting active diapirism and preventing sediment deposition above it as well as controlling sediment distribution around the diapir (Figure 4.35).

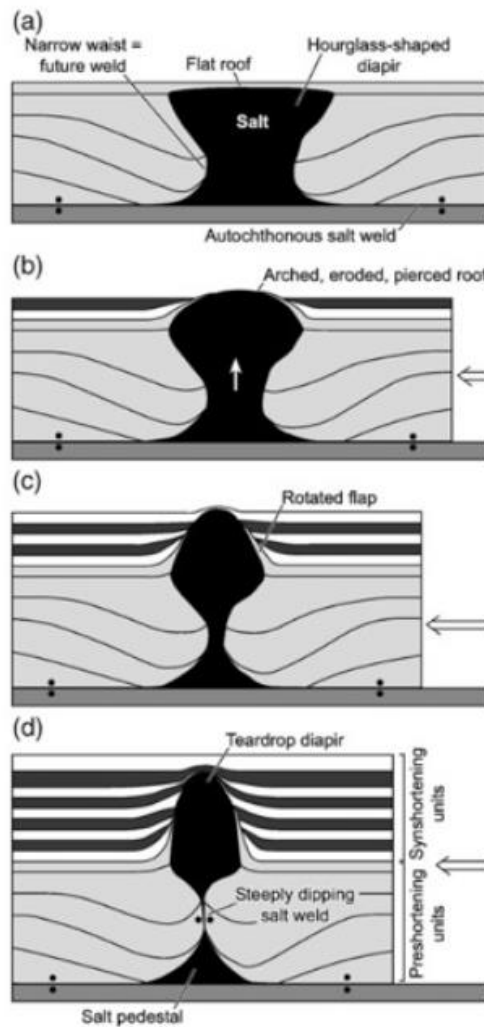
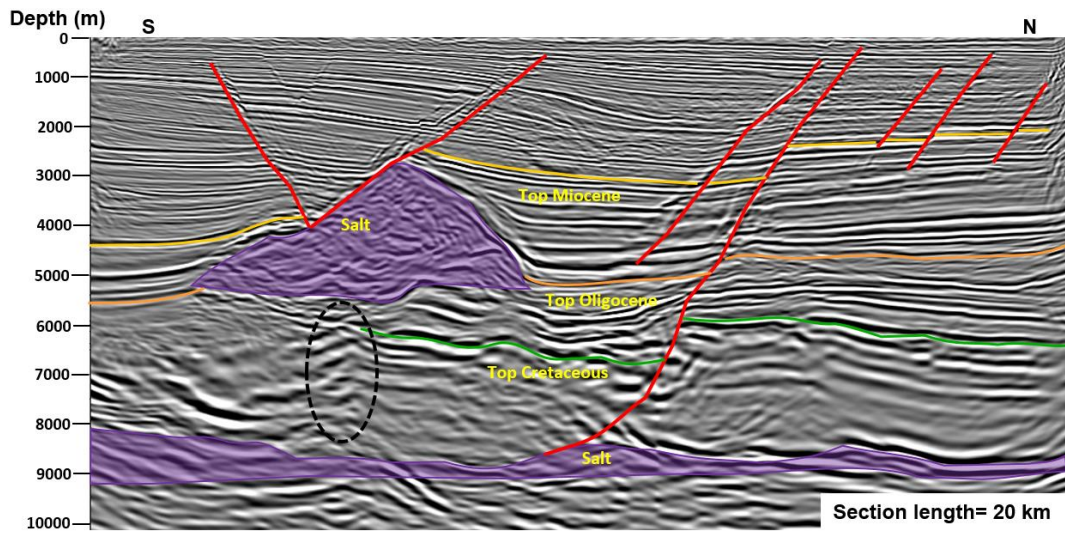


Figure 4.35. Top: Interpreted section showing the allochthonous salt sheet in the study area. Bottom: Conceptual model illustrating the concept of diapir rejuvenation by contraction (Hudec and Jackson, 2007). Later normal faults above the sheet could have been originated as a keystone graben and control salt withdrawal during D4 event.

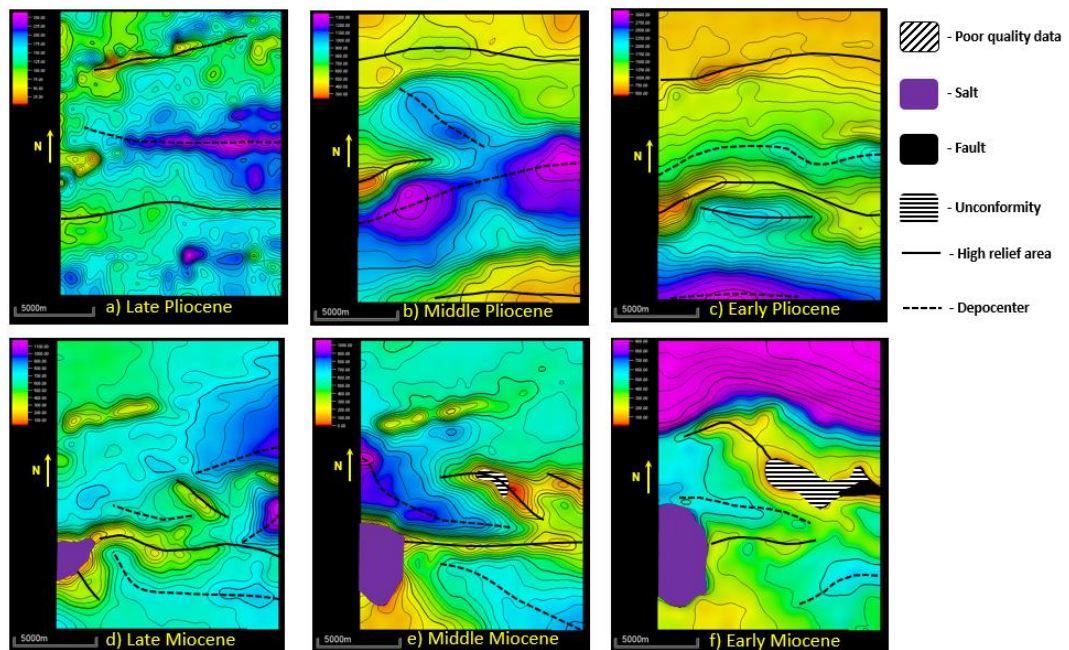


Figure 4.36. Thickness maps for Neogene packages.

Early Pliocene (3.5-5.3 Ma): This sequence shows a progressive thinning from south to north (Figure 4.36c) due to prograding siliciclastic sedimentation. Highest thickness values (up to 3 km) are located in the south associated to accommodation space created by salt withdrawal whereas lowest values (500 m) are located in the northern portion, which was located in a more distal area from the sediment source. No zero values are present; however lowest values are related to a structural high associated with the allochthonous salt emplaced and truncations against faults. Also, extensional event D4 started to generate normal faulting and control sediment distribution within individual blocks in the central portion.

Middle Pliocene (2.56-3.5 Ma): Prograding siliciclastic sedimentation towards the north continued during this time, and therefore, thickest depocenters (up to 1300 m) developed in the central portion of the area (Figure 4.36b). Lowest thickness values are distributed in the northern and southern portions of the area, which may correspond to by-passed and distal zones respectively. Areas where contour lines are closely spaced represent zones where syn-sedimentary faults act as depocenter boundaries.

Strong similarities between structure map of this sequence and corresponding thickness map suggest that location and extension of these depocenters were also controlled by a complex interaction between sedimentation and trans-tensional faulting associated to gravitational collapse above the upper detachment level (D4 event) along with differential salt evacuation from this same level (Figure 4.37). Differences in the speed of movement

between individual blocks originated a complex array of trans-tensional faults, most of them with a right-lateral component.

Late Pliocene (1.7-2.56 Ma): During this time, sedimentation rate decreased in the study area as progradation continued towards the north. As a result, thickness is relatively uniform throughout the area and thickest accumulation (up to 250 m) are much lesser than in Early (3000 m) and Middle (1300 m) Pliocene (Figure 4.36a). Similarly to Middle Pliocene, these sediments are syntectonic to D4 event and thickest accumulations are located in the central portion in an E-W trend and were controlled by localized trans-tensional faulting.

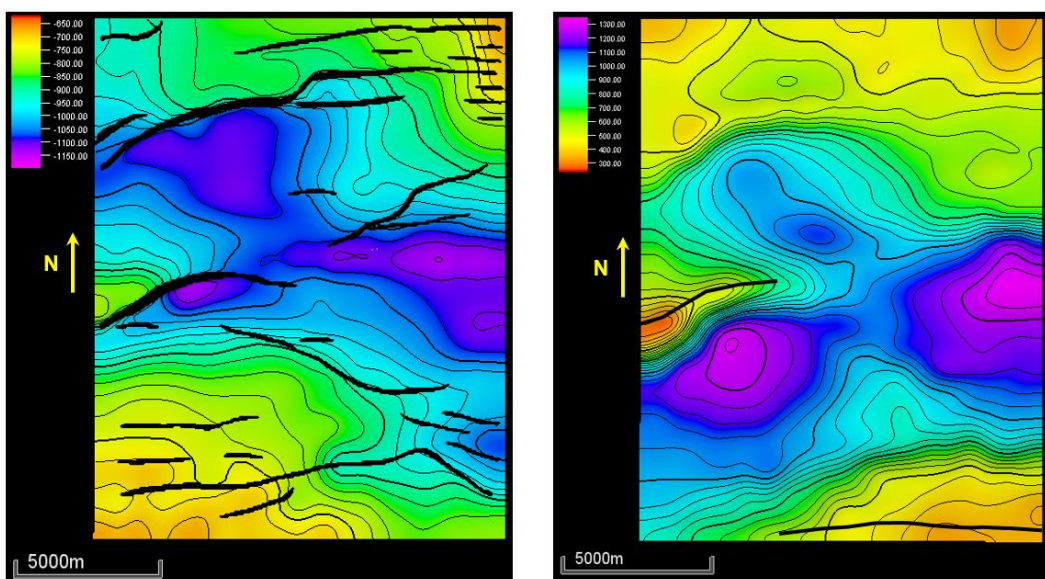


Figure 4.37. Similar contour configurations between structure map (left) and thickness map (right) suggest that location of depocenters is directly controlled by D4 normal faulting.

4.3.1.3 Structural Restoration of 2D Seismic Cross-Sections

For this project, three cross-sections were restored in order to show the structural evolution of Anticlines A and B (Figure 4.38), which are structural traps for hydrocarbons. Although the restoration process is performed going back in time, results will be described in a forward sense for a better understanding of their evolution. The cross-sections were oriented perpendicular to the main axes in order to best represent the plane-strain deformation. Since input seismic data is already depth-migrated, there is no need for a depth conversion of the analysed seismic cross-sections. Table 4. 5 shows the parameters used as an input for the restoration process, which are constrained by borehole data in the study area.

Horizon	Age (Ma)	Lithology	Initial Porosity	Young's Modulus (Gpa) / Poisson Ratio			Density (kg/m ³)	Bathymetry (m)		
				W-1	W-2	W-3		W-1	W-2	W-3
Pleistocene	0	Shaly Sand	0.83	23.7 / 0.3			2250	0-30	0-30	30-100
Late Pliocene	2.58	Shaly Sand	0.7	23.7 / 0.3			2300	0-30	0-30	30-100
Middle Pliocene	3.1	Shaly Sand	0.67	23.7 / 0.3			2350	30-100	100-200	30-100
Early Pliocene	3.6	Shaly Sand	0.67	23.7 / 0.3			2400	100-200	100-200	100-200
Late Miocene	5.3	Shaly Sand	0.65	23.7 / 0.3			2450	200-500	200-500	100-200
Middle Miocene	11.6	Shaly Sand	0.7	23.7 / 0.3			2500	200-500	200-500	100-200
Early Miocene	15.9	Shaly Sand	0.65	23.7 / 0.3			2550	500-1000	200-500	200-500
Oligocene	23	Shale	0.65	23.7 / 0.3			2600	500-1000	500-1000	200-500
Eocene	33.9	Siltstone	0.65	23.7 / 0.3			2550	1000-2000	1000-2000	1000-2000
Late Cretaceous	66	Limestone	0.48	38 / 0.31	55 / 0.28	51 / 0.31	2700	2000-3000	2000-3000	2000-3000
Tithonian	145	Shaly Limestone	0.45	61 / 0.18	61 / 0.18	61 / 0.18	2750	2000-3000	2000-3000	2000-3000
Kimmeridgian	152.1	Limestone	0.48	69 / 0.3	69 / 0.3	36.3 / 0.15	2700	100-200	0-30	0-30
Callowian	163.5	Salt	0	5.8 / 0.4			2200	< 30	< 30	< 30

Table 4. 5. Parameters used for structural restoration.

Each section was restored to 11 intermediate stages and top of salt using the following sequence for each stage: 1) Remove the top layer and decompact the underlying sequences using the decompaction curve by Sclater and Christie (1980). Where growth packages are involved, decompaction is applied in two steps in order to avoid artifacts and unrealistic geometries. The first step is decompaction of the regional load and the second one is the decompaction of the growth package in the hanging-wall; 2) Isostatic adjustment using the Airy Isostasy algorithm, which is adequate for cross-sections lengths less than 25 km that also contains salt masses; 3) Structural restoration of movement on faults matching hanging-wall and footwall cut-offs using Simple Shear algorithm for growth faults and Fault Parallel Flow algorithm for planar faults; 4) Unfolding of horizons using Flexural slip and Simple Shear algorithms depending of the stage of restoration. The template line for unfolding is located at the depth of bathymetry at each stage, which is constrained by borehole data.

As expected given the closeness between them, in general terms the three sections share many similarities and the structural evolution of the two anticlines is also similar; however, the differences between them are important and critical in order to understand the role of salt in the development of structural traps. In the other hand, there are important limitations inherent to the structural complexity of the study area such as the presence of salt masses, two detachment levels and strike-slip movement above the upper detachment level that hinder the restoration process and prevent obtaining reliable quantitative results in terms of total amount of shortening and/or extension; however, they can be interpreted in a qualitative way in order to understand the structural evolution. Although our proposed interpretation can be considered as admissible, the inherent geological difficulties mentioned above make enough room for alternative interpretations that can be considered equally valid.

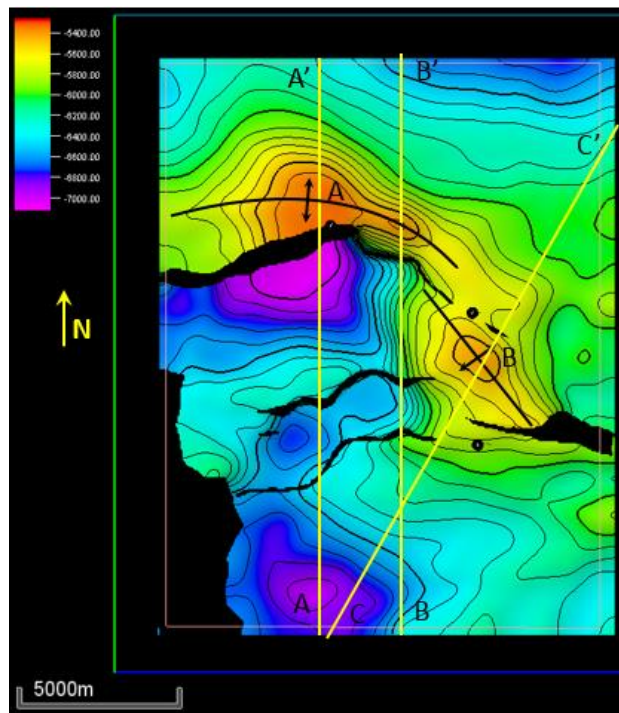


Figure 4.38. Structure map of Top Cretaceous showing the orientations of the three cross-sections that were restored.

Section A-A'

This section is oriented N-S, has a length of 20 km and crosses the central portion of the anticline A (Figure 4.38). Figure 4.39a-b show relevant structural features in the present day section that provide insights of the deformational processes involved: 1) a salt-cored anticline bounded by a major normal, counter-regional south-dipping fault; 2) A crest-faulted anticline probably associated to flank collapse by salt withdrawal and some buckle folding; 3) a very thin, probably welded in some parts, autochthonous salt level; 4) intense normal faulting in the Tertiary section detaching on Top Oligocene horizon. Mesozoic horizons are relatively gently folded and few major faults can be interpreted. Seaward direction is towards the North (right) in every stage and pin line is in the left side (landwards) for every section.

Although is very difficult to estimate the original thickness of salt in areas where it has flowed or bulged, an estimated thickness between 2 and 3 km, deposited during Callovian times, is considered as reasonable (Salvador, 1991; Hudec et al., 2013) for the study area and was used for the three sections (Figure 4.39n). Late Jurassic may be considered the onset of passive diapirism associated to early salt movement and differential loading, resulting in development of diapir A. North-South oriented gravitational extension associated to a linked system of up-dip extension and down-dip contraction (D1 event) generated normal faulting in the Mesozoic column with a south-

dipping, counter-regional normal listric fault NF1 and north-dipping regional faults from Late Jurassic until Palaeocene times as a continuous process (Figure 4.39j-m). Diapir A developed as a salt-roller structure associated to NF1 fault during Mesozoic times. During Palaeocene, increasing displacement on the main listric fault (NF1) could have built topography; as a result, a wedge composed of a series of slumps coming off the footwall fault scarp filled the hanging-wall during Palaeocene-Eocene time interval.

In the study area, shortening began around Eocene times (D2 event) and seemed to continue until Middle Miocene (D3 event), although no typical shortening structures can be identified above the upper detachment level (post-Oligocene section). Moreover, if contraction is considered as a continuous process between two separately identified events, then it becomes too difficult to quantify the individual effects of each event separately in the Mesozoic section. Both contractional events re-deformed the pre-existent structures by buckle folding and also could have reactivated normal faults in a reverse sense (Figure 4.39i) It is also likely that tectonic fracturing of Mesozoic carbonates associated to buckle folding had taken place.

Three-dimensional analysis of seismic data, along with regional geology information, suggest the possibility of allochthonous salt emplacement during this time. However, the areal extent where salt emplaced and, specially, the volume of salt emplaced are almost impossible to know, but its presence has been inferred from the existence of a detachment level aged Early Miocene-Oligocene over the whole study area. Given the limitations of restoration in terrains with multiple detachment levels and the presence of late strike-slip faulting, the total area of allochthonous salt shown in the southern portion of the restored cross-section can be considered as an artefact of the restoration process (Figure 4.39g); however, this author considers that at least a fraction of that volume was effectively emplaced. Another possible solutions are that accommodation may be provided by both salt levels and thus thickness in the upper level would diminish, but thickness in the lower level would increase; conversely, if accommodation is considered to have occurred only on the lower level, then an unrealistic excess of salt thickness would appear.

Pliocene times are characterized by intense normal faulting associated to D4 event, which additionally may have a strike-slip component. This implies movement in and out of the section plane, which results in different thickness at both sides of faults and the mismatch of horizons during the restoration process. D4-related faulting linked with pre-existent south-dipping D1 fault (NF1), which may have been reactivated, to become a single fault that generated a dextral off-set between the hanging-wall and footwall in

Mesozoic section (Figure 4.39d). This later reactivation of the fault can have implications not only on fracture development close to the fault but also on integrity of the trap. Finally, sediment loading may have caused evacuation of salt canopy, leaving a tertiary weld.

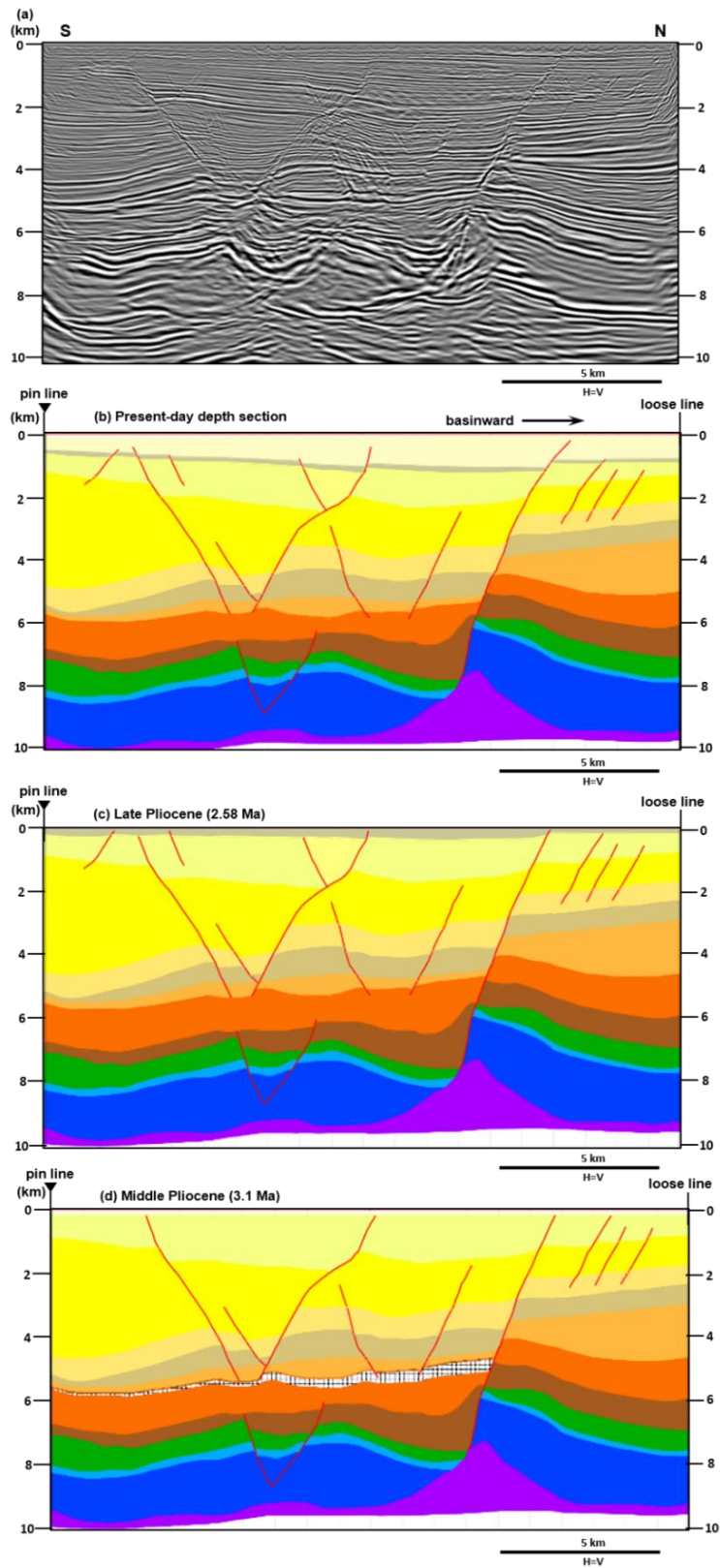


Figure 4.39. Sequential restoration of cross-section A-A', across Anticline A (Figure 4.38). a) uninterpreted seismic section. Length of present-day section is 20 km. No vertical exaggeration.

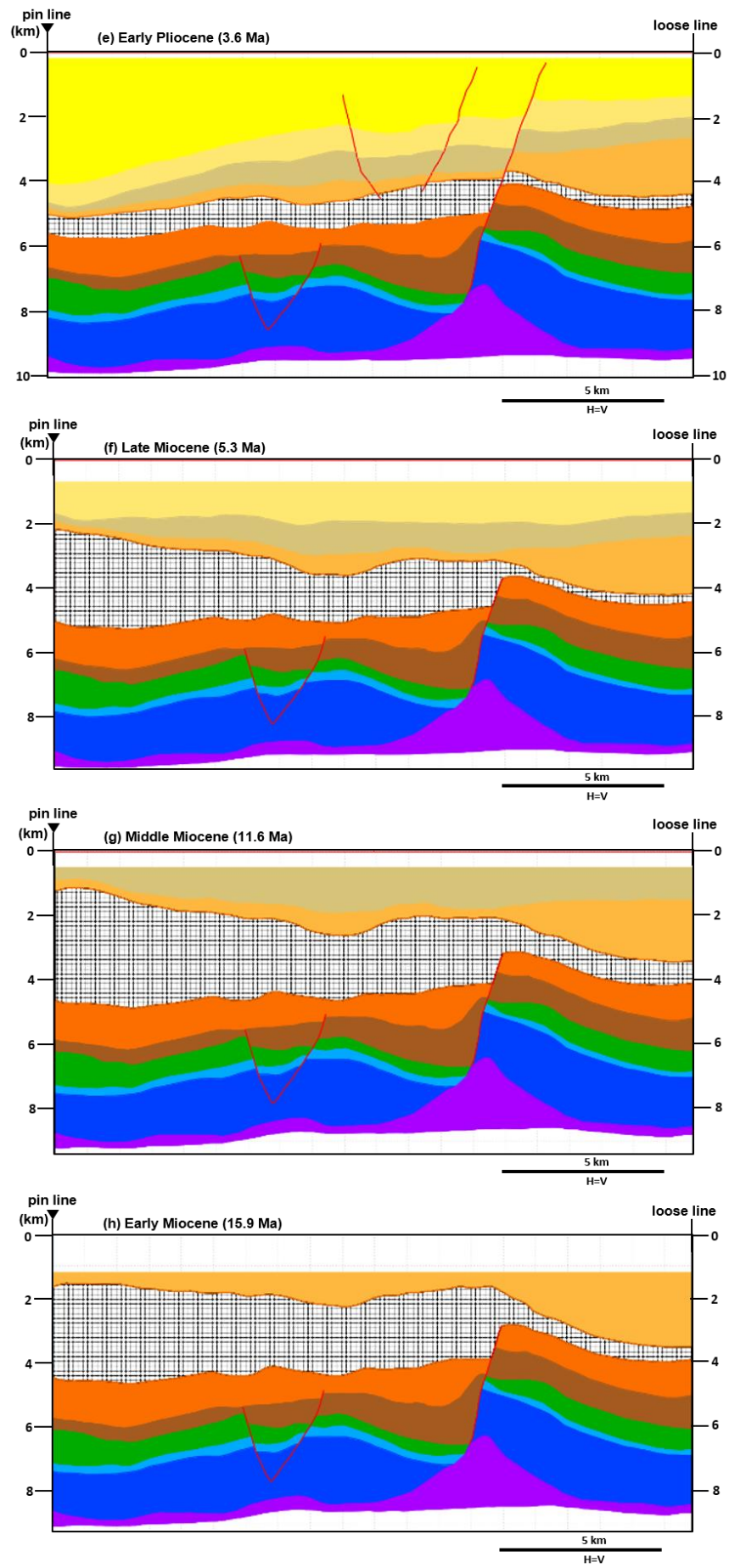


Figure 4.39 (continued)

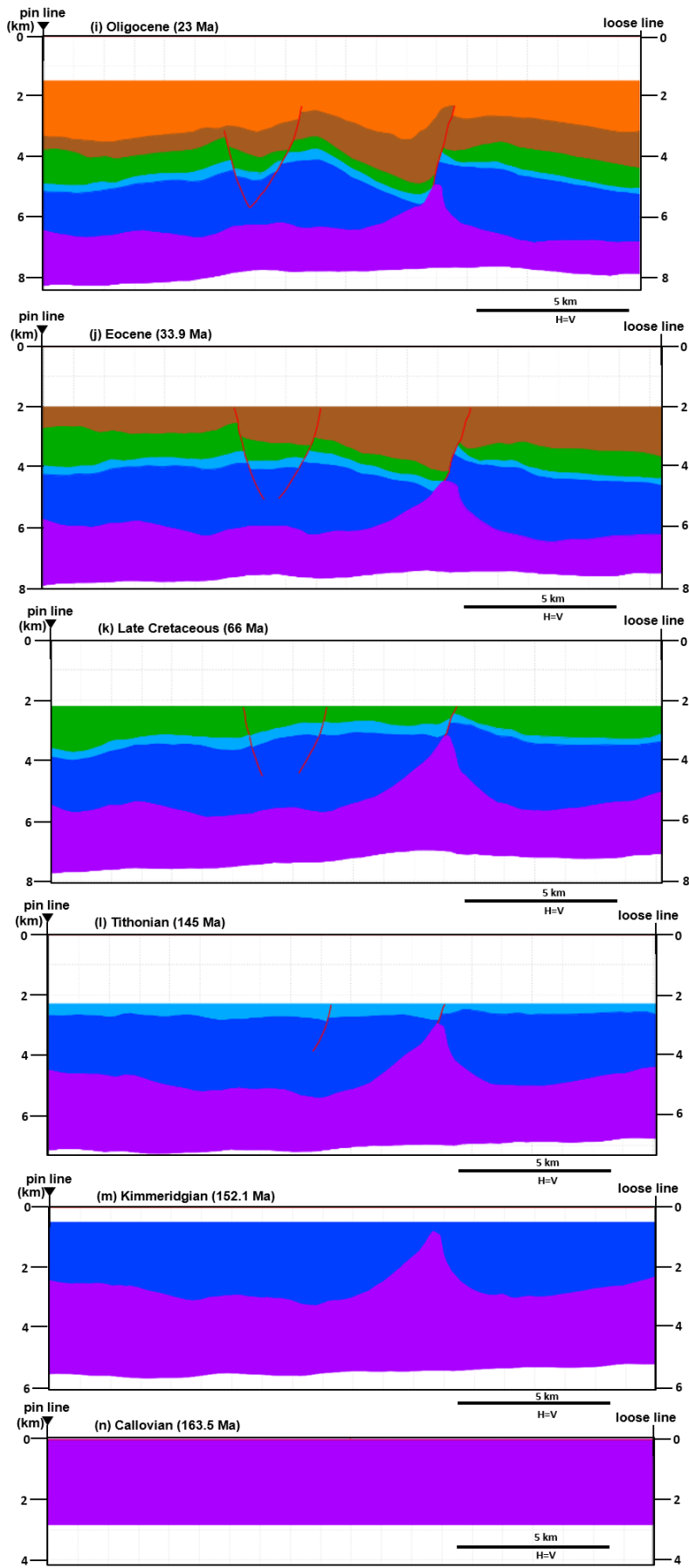


Figure 4.39 (continued)

Section B-B'

This section is located 2.5 km to the east of section A-A'. It is also oriented N-S and has a length of 20 km but crosses the eastern flank of Anticline A (Figure 4.38). As a result, they are very similar, share the same basic assumptions and the same restoration issues apply; therefore, these sections together help to constrain Anticline A's structural evolution. However, the main difference consists in the along-strike variation of Anticline A's geometry in both sections, which provide insights on the role of salt in the development of structural traps.

The interpreted present day section (Figure 4.40a-b) shows that geometry of Anticline A consists of a salt-cored Pop-up anticline, whose flanks are limited by steeply dipping reverse faults. Another difference respect to section A-A' is the presence of an inversion structure (turtle anticline) above the upper detachment level, which may be associated to flank collapse due to salt withdrawal. In order to avoid repetitive information, only relevant differences between both sections will be described below:

Evolution of Anticline A during Mesozoic times along this line (eastern edge) is also associated to a salt core, whose 3D geometry corresponds to a salt ridge. A regional north-dipping fault started to develop during Tithonian and continued as a syn-sedimentary fault during Cretaceous (Figure 4.40k-l) as a result of D1 event. Effects of D2 and D3 contractional events are more evident in this section, creating a Pop-up anticline by buckle folding as well as inverting the pre-existent NW-SE striking, NE-dipping synthetic fault as a reverse fault (RF1) in the southern flank, whereas in the northern flank, a similarly NW-SE striking, SW dipping reverse fault RF2 was developed.

Irregular emplacement of allochthonous salt, during Miocene times could have prevented deposition of Early-Middle Miocene sediments in localized areas (Figure 4.40g), thus creating an unconformity whose areal extent is defined in the correspondent thickness maps.

D4 extensional event effects are more intense in this section and heavy trans-tensional normal faulting is evident; however, this event did not seem to affect the Anticline A Mesozoic section. In the northern side of the section, Miocene sediments seemed to collapse towards the south in response to salt evacuation due to a combined effect of sediment load and gravitational extension detaching on the upper level (Figure 4.40c-e).

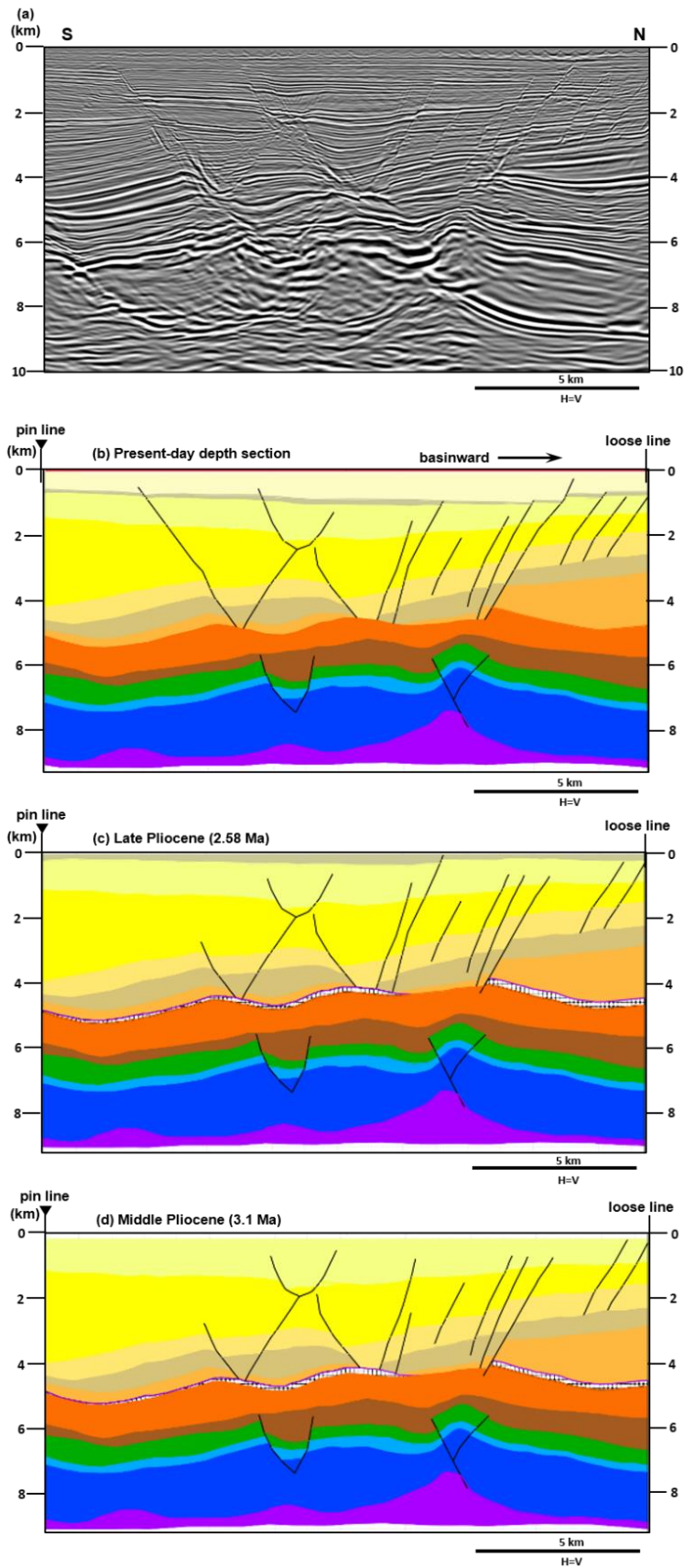


Figure 4.40. Sequential restoration of cross-section B-B', across Anticline A (Figure 4.38). a) uninterpreted seismic section. Length of present-day section is 18.5 km. No vertical exaggeration.

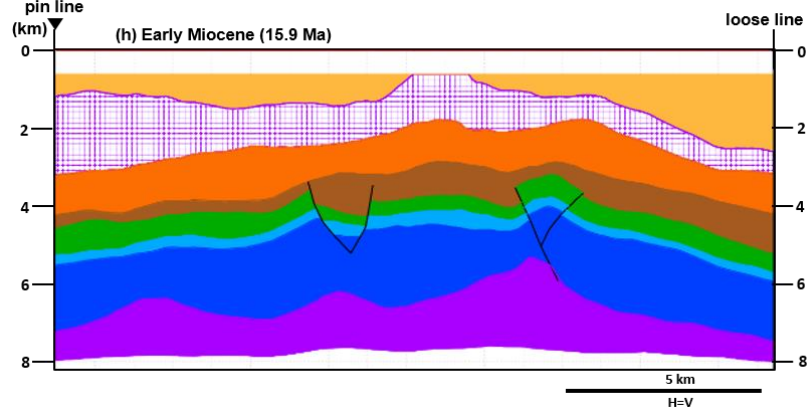
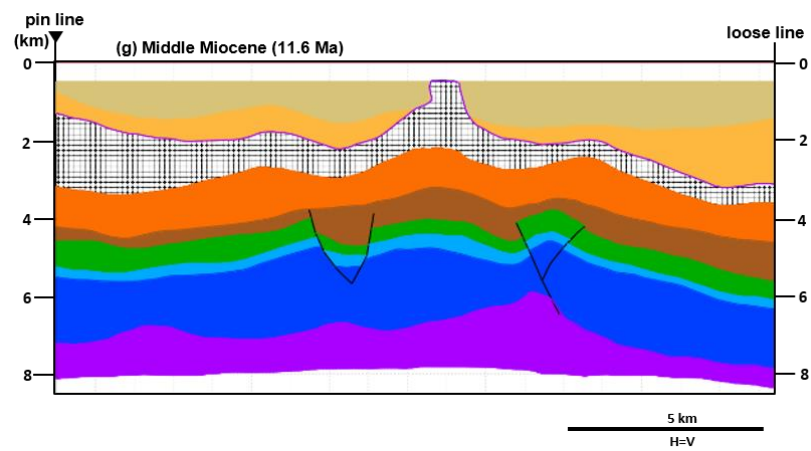
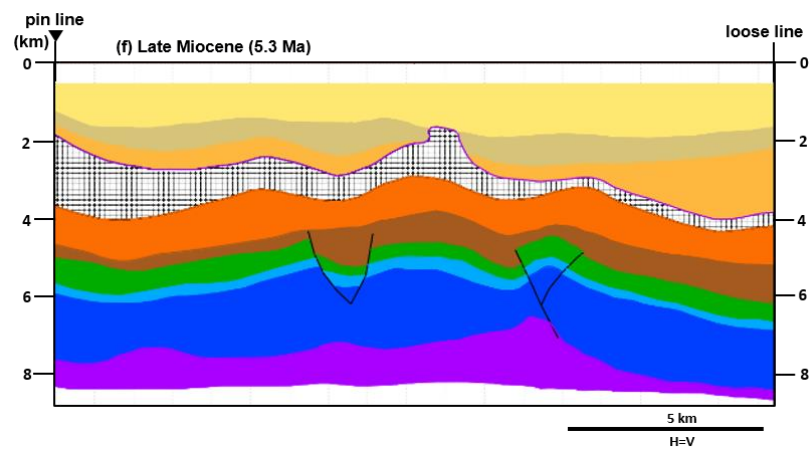
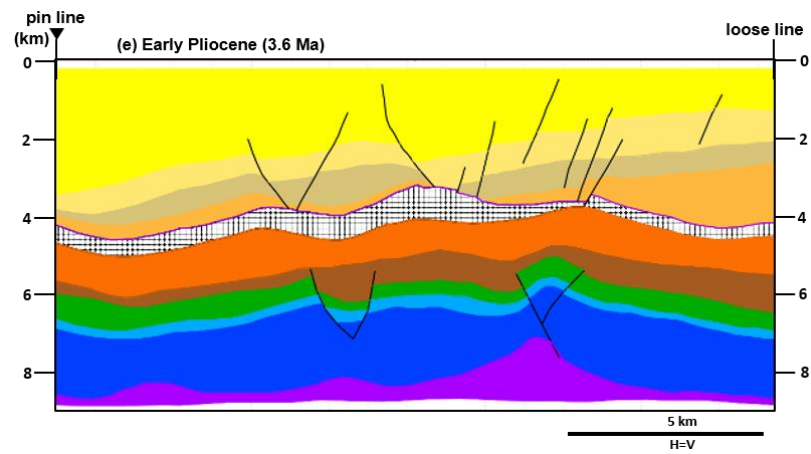


Figure 4.40 (continued)

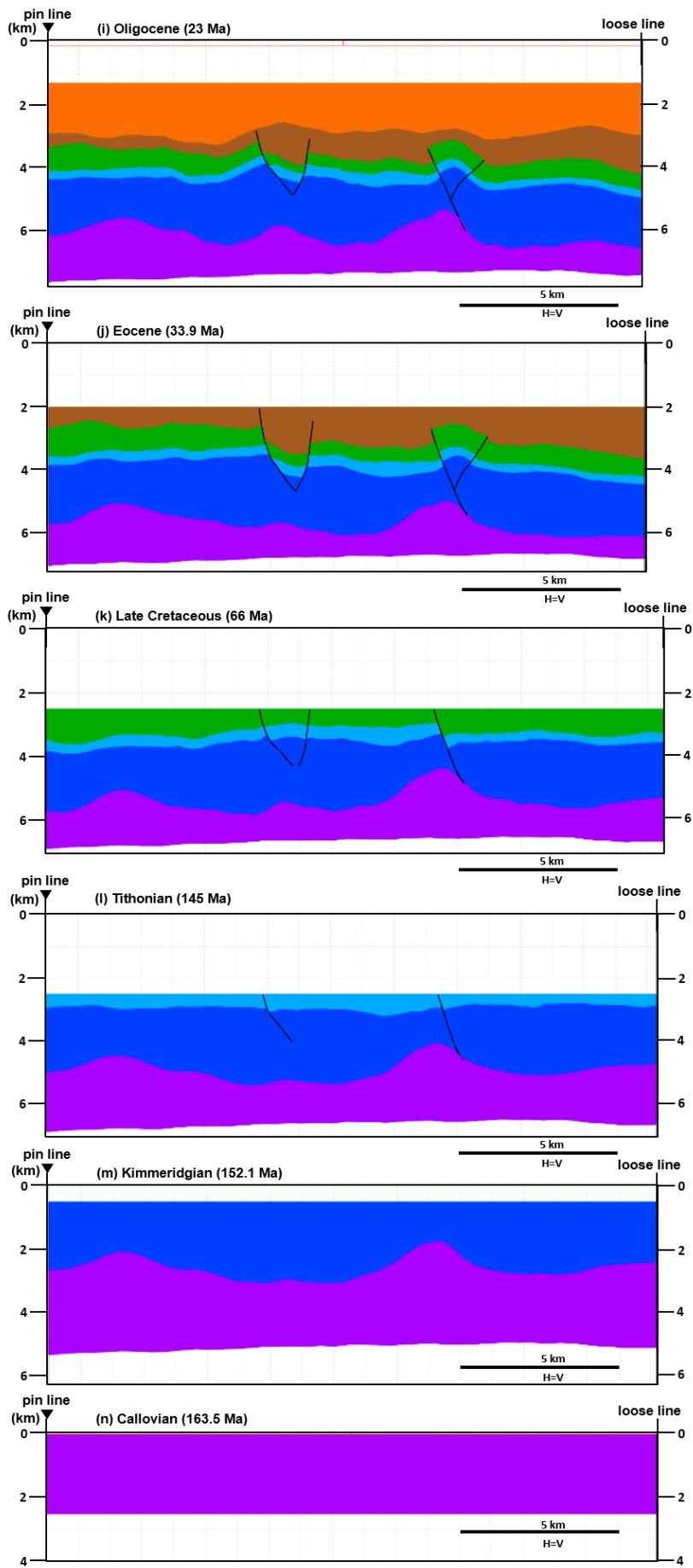


Figure 4.40 (continued)

Section C-C'

This section is orientated NE-SW 31° , perpendicular to the Anticline B strike, has a length of 16 km and crosses the Anticline through its hinge zone (Figure 4.38). The present day section (Figure 4.41a-b) shows the geometry of Anticline B as a relatively gently folded salt-cored anticline bounded in its NE flank by a SSW, steeply dipping reverse fault. Right above the anticline, in the Tertiary section, the graben and the inverted, SW dipping flank is the same as in the section B-B'. The salt diapir coring the anticline, conversely, corresponds to diapir B, which is orientated NW-SE identically to Anticline B.

Similarly to diapir A, diapir B started to develop very soon after salt deposition during Oxfordian-Kimmeridgian times (Figure 4.41m) probably as a passive diapir, simultaneously to surrounding withdrawal minibasins as a result of D1 event. The passive diapir stage may have been short-lived and was soon buried by the overburden; however, the continuing influx of salt into the diapir may have folded the overburden enough to create topography in a continuing the process until Paleogene times (Figure 4.41j-l). D2 and D3 events resulted in folding and creating the anticline geometry as well as steeply SSW dipping reverse faulting (detaching on autochthonous salt), that seemed to affect only the Mesozoic section (Figure 4.41g-j).

Allochthonous salt emplacement prevented localized sedimentation of Early Miocene sequence only unlike Section B-B' where non-deposition included Middle Miocene sequence (Figure 4.41g-h). D4 event had the same effects seen in Section B-B' with allochthonous salt withdrawal and trans-tensional faulting, which did not affect Anticline B (Figure 4.41c-e).

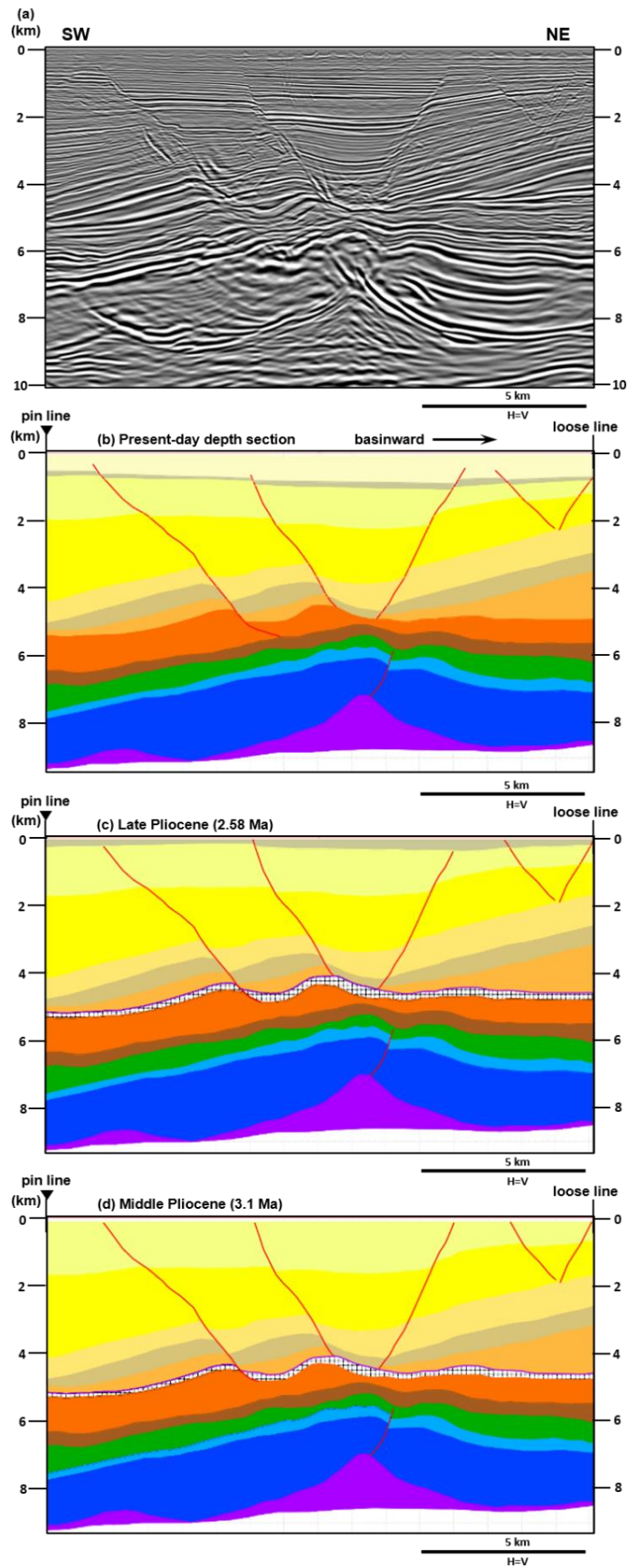


Figure 4.41. Sequential restoration of cross-section C-C', across Anticline A (Figure 4.38). a) uninterpreted seismic section. Length of present-day section is 16 km. No vertical exaggeration.

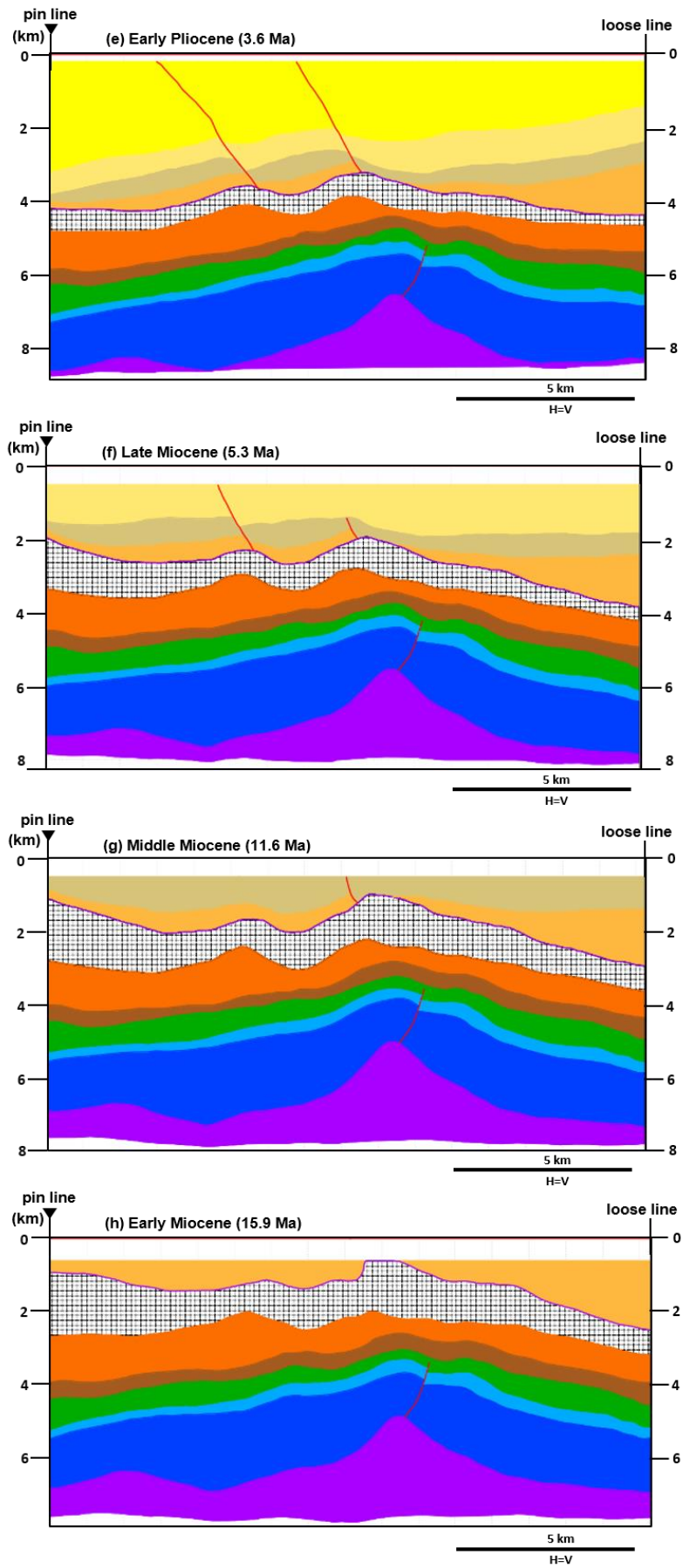


Figure 4.41 (continued)

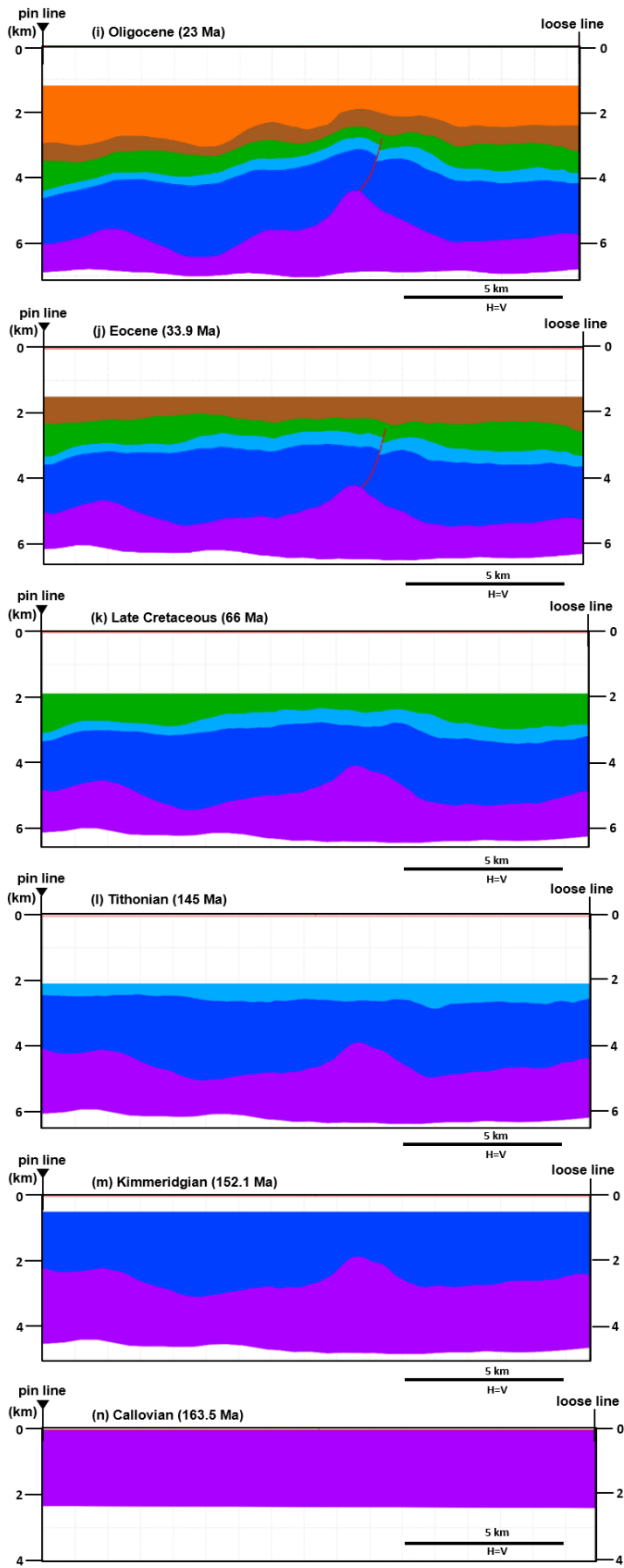


Figure 4.41 (continued)

4.3.1.4 Characterization of structural traps

Structural characterization of hydrocarbon traps with Mesozoic target in the study area was defined by the 3D interpretation and analysis of the available seismic survey. Interpretation was constrained by picks from three hydrocarbon-producing boreholes in the area. Analysis of key individual cross-sections, whose average length is 20-25 km corresponding to inlines, crosslines and random lines, combined with depth slices and structure maps allowed to recognize the effects of deformational events, characterize structural traps and constrain the structural evolution in the study area. Figure 4.42 shows the location of different lines selected for analysis.

Two structural traps with Mesozoic targets were identified and named *Anticlinal A* and *Anticlinal B*. Present day geometry of these anticlines is directly influenced by the presence of salt and, therefore, they exemplify the role of salt in the development of structural hydrocarbon traps. Several boreholes have drilled both structures and hydrocarbon accumulations in different Mesozoic stratigraphic levels have been discovered.

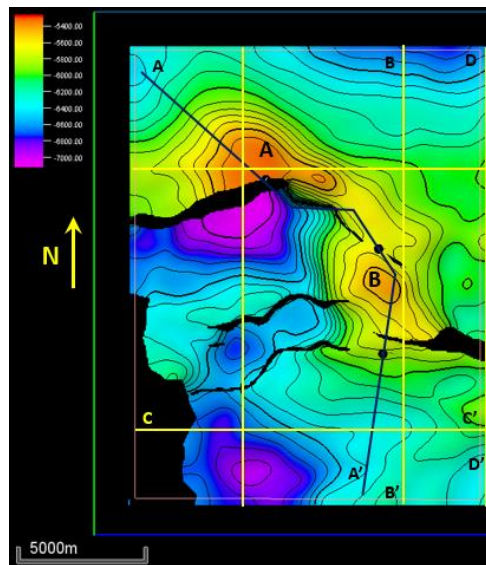


Figure 4.42. Top Cretaceous structure map showing the different cross-sections analysed to characterize the structural traps.

Anticline A

From a descriptive point of view, for Top Cretaceous and Top Kimmeridgian this structure is a salt-cored, faulted anticline, oriented WSW-ESE and WNW-ESE in its eastern flank, with a three-way closure and bounded in its southern limb by a south-dipping normal fault, which is relieved by a north-dipping, high angle reverse fault towards the east (Figure 4.43-4.44). In cross-section view, it displays great variability in geometry along strike, which is typical from salt-related deformation (Figure 4.45). From West to East,

the salt body varies from a low relief pillow which progressively increases in vertical size becoming a salt-roller in the anticline's central portion; towards the east, it decreases its vertical size again and becomes a salt anticline. Similarly, Mesozoic stratigraphy also shows along-strike variation. In the western and central portions, stratigraphy in the footwall is gently folded keeping the geometry of a salt-roller without great variations; however, towards the eastern flank, folding becomes progressively more intense with decreasing of the fold wavelength and the occurrence of reverse faulting bounding the northern and southern flanks of Anticline A. The hanging-wall stratigraphy in the west and centre of the anticline shows a north-dipping, roll-over geometry truncating against the salt diapir; additionally, vertical offset respect to the footwall cut-off increases from west to the centre (700 to 1700 m) progressively. This offset decreases again towards the east in the transition from salt roller to pop-up anticline as stratigraphy becomes folded and the hanging-wall becomes the southern footwall of the pop-up anticline.

Deformation in the Tertiary section is mostly decoupled from Mesozoic due to the presence of a detachment level. Later normal faulting associated to D4 event does not cut across this level. However, main normal fault NF1 propagated below the detachment level and hard-linked with the pre-existent listric fault associated to the salt-roller. This relationship is present in the western and central portions of the Anticline and separates where reverse faulting and folding become more prominent towards the east.

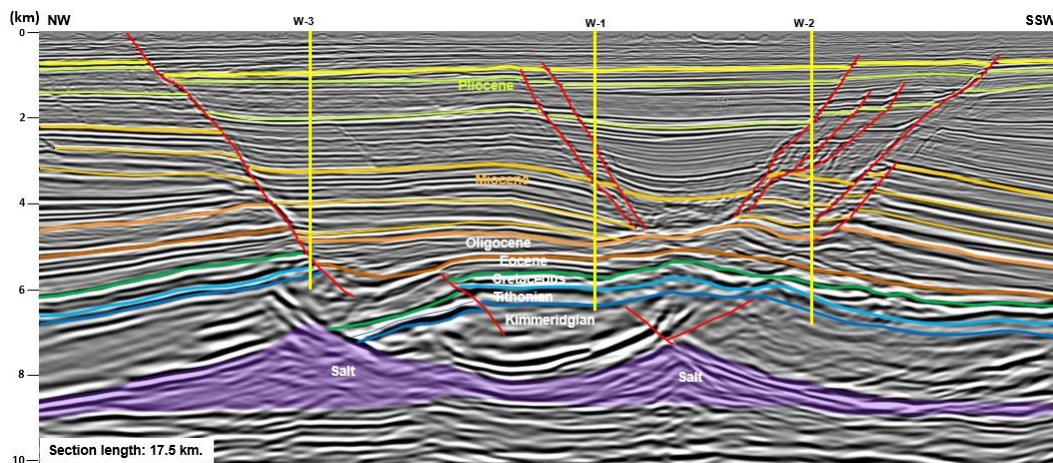


Figure 4.43. Cross section A-A' from Figure 4.42 showing the structural style in the study area and the Anticlines A (left) and B (right).

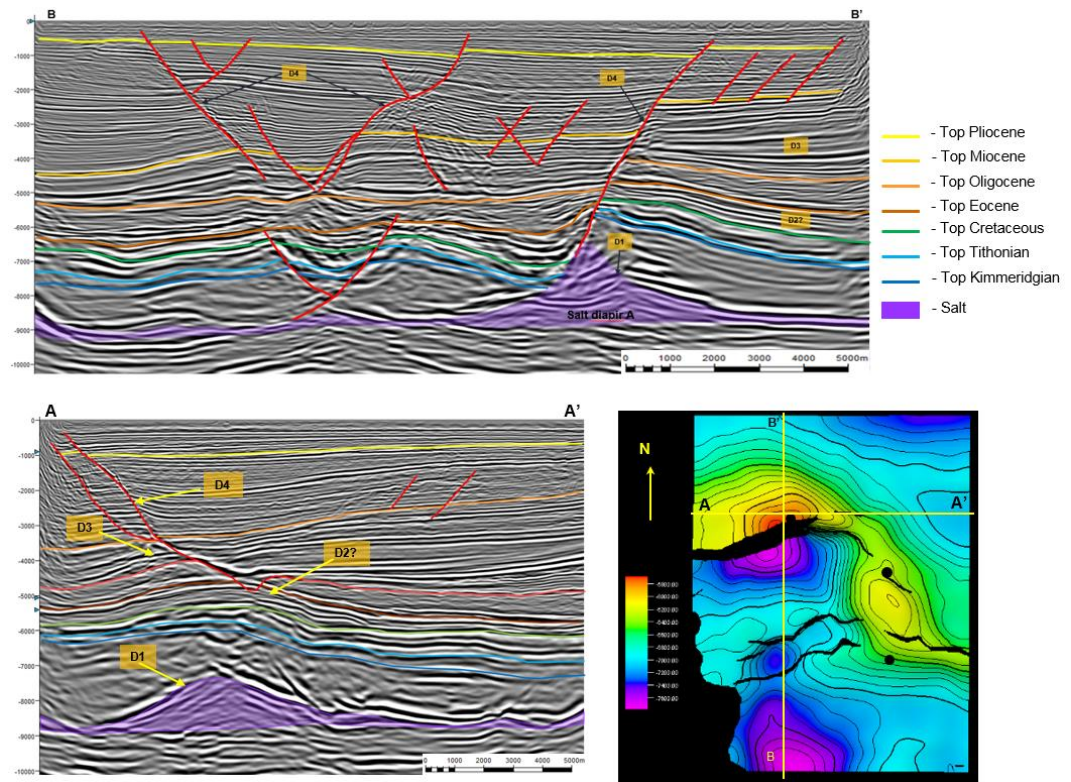


Figure 4.44. Interpreted seismic Inline (B-B') and Cross-line (A-A') showing the geometry of Anticline A. Structure map of Top Kimmeridgian (right below).

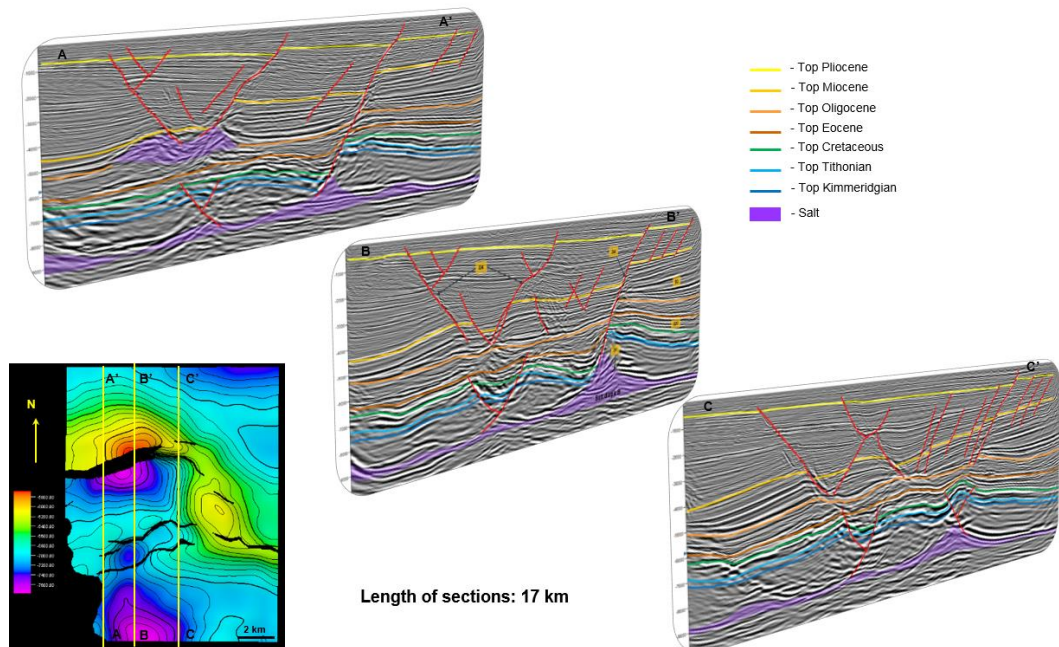


Figure 4.45. Parallel interpreted seismic cross-sections showing the variability in geometry along strike of Anticline A. Structure map of Top Kimmeridgian.

Anticline B

For Mesozoic horizons, it is a salt-cored anticline orientated NW-SE with a four-way closure. The southern and northern limbs are affected by a normal fault and a reverse fault oriented NW-SE and WNW-ESE respectively (Figure 4.46-4.47). Likewise Anticline A, Anticline B also shows variability in geometry along strike (Figure 4.48). The salt core shows variations in vertical size only, which increases progressively from the northern (600 m) and southern flanks (1000 m) to the centre (1600 m). Its geometry is constant along-strike resembling a symmetric anticline. Similarly, Mesozoic stratigraphy does not show great variation in geometry along-strike and basically it is gently folded and mostly parallel to the top of salt towards the flanks. In its centre, folding is more intense and due to the presence of high-angle reverse faults in its northern and southern flanks (RF3 and NF4, respectively) can be considered as a pop-up anticline.

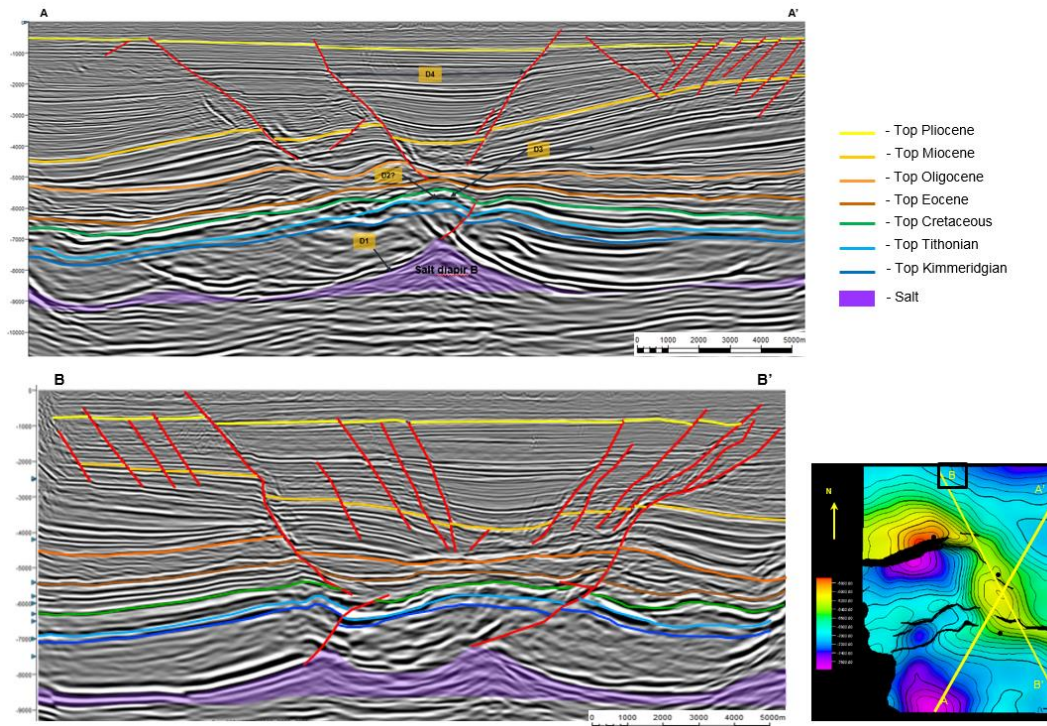


Figure 4.46. Interpreted seismic Inline (above) and Cross-line (left below) showing the geometry of Anticline B and the effects of the different deformational events. Structure map of Top Kimmeridgian (right below).

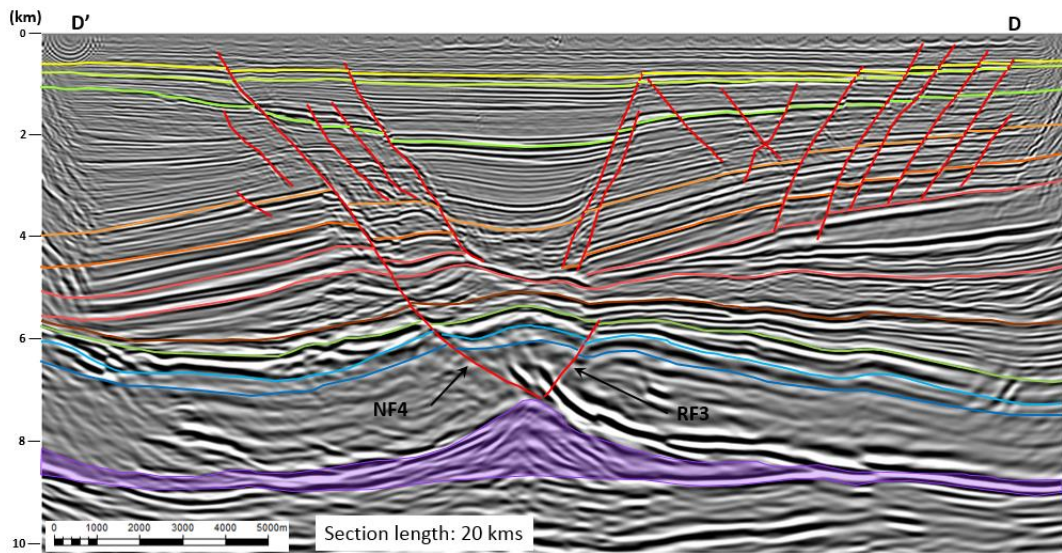


Figure 4.47. Interpreted seismic cross-section showing the geometry of Anticline B. Structure map of Top Kimmeridgian (right below).

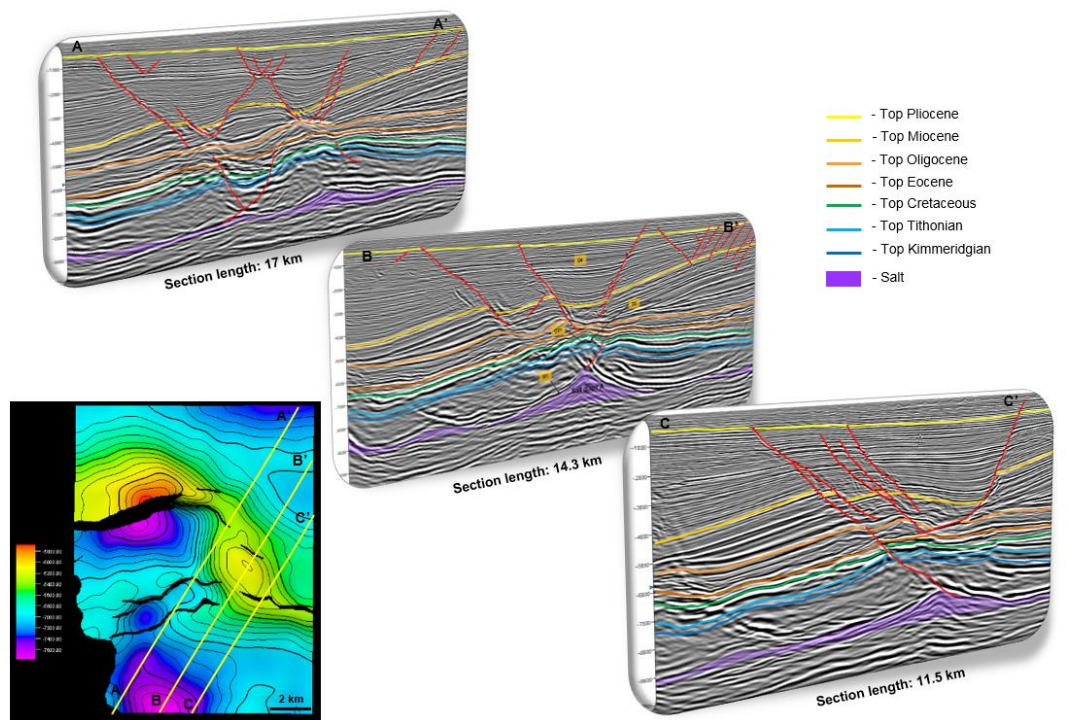


Figure 4.48. Parallel interpreted seismic cross-sections showing the variability in geometry along strike of Anticline B. Structure map of Top Kimmeridgian.

Similarly to Anticline A, a major counterregional normal fault NF4 associated to D4 event seems to have hard-linked with a pre-existent reverse fault detaching on diapir B thus forming a single segment in the southern limb showing a very small offset (Figure 4.47). This reverse fault could have been reactivated as normal fault during Pliocene times. At the south-eastern limb, Mesozoic stratigraphy becomes gently folded and NE-dipping

whereas the graben above Anticline B becomes more prominent. This graben is bounded by main normal faults NF4 and NF5 (Figure 4.48), the latter becoming progressively from planar to listric in order to accommodate a bigger volume of Late Miocene-Pliocene sediments deposited during extension associated to D4 event and its corresponding salt withdrawal from the upper detachment level (Figure 4.49).

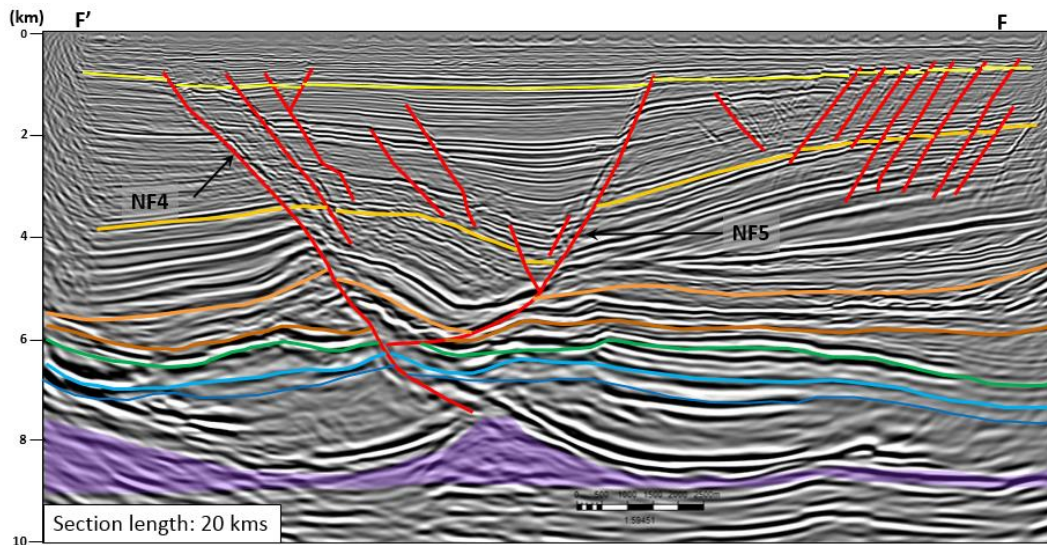


Figure 4.49. Cross section F-F' from Figure 4.42 showing the geometry of the Tertiary graben with roll-over structure bounded by normal faults NF4 and NF5 to the east of Anticline B.

4.4 Discussion

4.4.1 Structural style of traps

Anticlines A and B are two structural hydrocarbon traps whose geometries are directly influenced by the presence of salt in the geologic column. Their present day geometries are the result of the superimposed effects of different deformational events during their structural evolution. These traps show different degrees of variability in geometry along-strike of their salt cores and Mesozoic overburden, which is typical of salt-cored structures (Grando et al., 2004; Rowan and Vendeville, 2006; Brun and Fort, 2004). This variability can be attributed mainly to the thickness of the salt layer (Stewart, 1999; Hudec and Jackson, 2007), which favours faulting preceded of folding when salt is thin and, conversely, detachment folding with only minor faulting predominates where salt is thick. Eastern limb of Anticline A and Anticline B show this tendency where highest deformation in overburden is located above thinner salt and less deformation above thicker salt. Geometry variation between Anticline A's centre and western limb are not too great, where vertical amplitude of the salt diapir diminishes gradually towards the west as well

as the vertical offset between footwall and hanging-wall. A similar example is observed in the Espirito Santo Basin, Brazil (Figure 4.50).

Considering their present-day geometries we can conceptualize and characterize Anticlines A and B as follows: Anticline A is a mixed-styled, salt-cored structure whose geometry in its centre and western limb is associated mainly to extensional deformation detaching on autochthonous salt (roll-over anticline), which are common in the up-dip extensional domain but they are also present in the transitional domain (Kr zsek C. et al., 2007) whereas in its eastern flank the geometry corresponds to a typical contractional style that can be defined as a pop-up anticline, which is a type of detachment fold (Mitra, 2002). Anticline B, in the other hand, is an anticline cored by a salt-anticline/pillow with a typical contractional structural style characterized by symmetric buckle folding and high-angle thrust faults detaching on salt similar to those observed in the Sierra Madre Oriental, Mexico (Marrett and Aranda-Garcia, 2001), the Spanish Pyrenees (Sans and Verges, 1995) and the Prebetics, Spain (Roca et al., 2006) as well as in physical models (Sans and Koyi, 2001). This anticline, therefore, can be defined as a symmetric detachment fold. Both anticlines were drilled by boreholes that found important hydrocarbon accumulations in different Mesozoic stratigraphic levels, which reinforces the importance of the presence of salt and its influence in the development of structural traps.

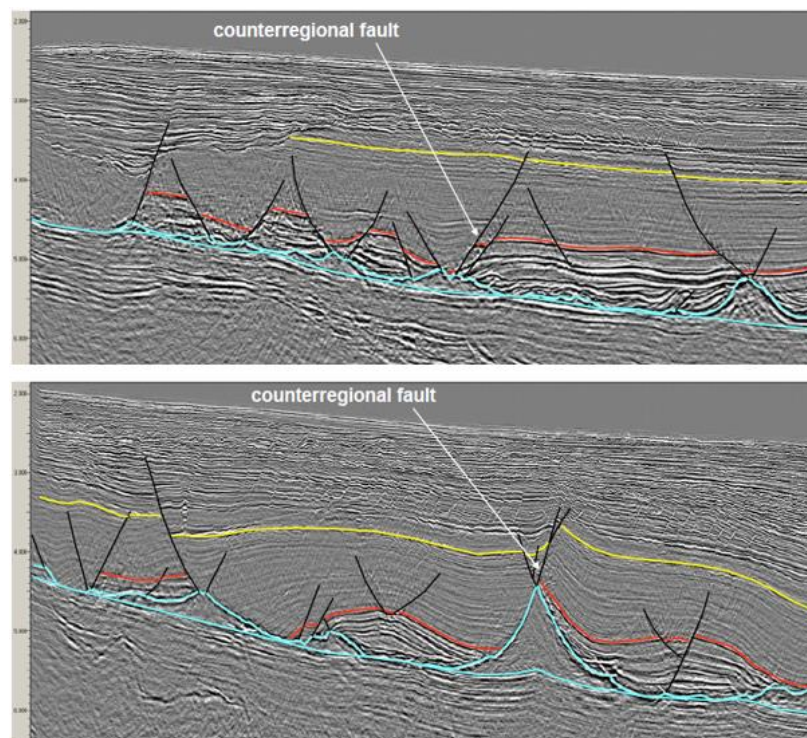


Figure 4.50. 3D, time migrated seismic cross-sections illustrating the lateral variation in geometry of a counterregional fault associated to salt-cored structure in the Espirito Santo Basin, Brazil.

Uncertainty in the interpretation derived from seismic imaging and the reduced number of boreholes drilled in the area makes room for multiple alternative interpretations, which may modify the structural style, propose different evolution histories, and most importantly, they may have a critical impact on relevant aspects regarding to hydrocarbon exploration such as: Exploratory risk, correct locations of well proposals, estimation of size and volume of reservoir and well design.

4.4.2 Structural evolution

Anticlines A and B are the result of a complex structural evolution involving different deformational events from Late Jurassic to Pliocene times where salt sediments have played a fundamental role in development of structural traps. The combined analysis of thickness maps, structure maps and 2D restoration allowed to propose an evolutionary model for both structures, which share some general similarities but also remarkable differences that will be discussed below.

4.4.2.1 Anticline A

Figure 4.52 shows a conceptual model of the structural evolution of this anticline, which can be summarized as follows:

a) The onset of autochthonous salt movement occurred during Late Jurassic (Oxfordian-Kimmeridgian), soon after its deposition at some point between the distal extensional domain and the transitional domain of a linked system (Figure 4.52-b). Figure 4.51 shows a comparison between present-day distribution of autochthonous salt with semi-circular minibasins separated by polygonal salt ridges and diapirs and an experimental model by Rowan and Vendeville (2006); location of these diapirs is coincident with those of Anticlines A and B, so this close relationship may evidence the control of salt. N-S oriented gravitational extension associated to D1 event originated a counter-regional (landwards), south-dipping, NE-SW striking, normal listric fault NF1 (Section A) and north-dipping (seawards), NW-SE striking, listric faulting RF1 in the eastern edge of the anticline (Section B). Continuity of D1 event during Cretaceous time allowed the development of roll-over structures whereas fault segments probably propagated laterally until they hard-linked and acted as a single fault since then (Figure 4.52-c).

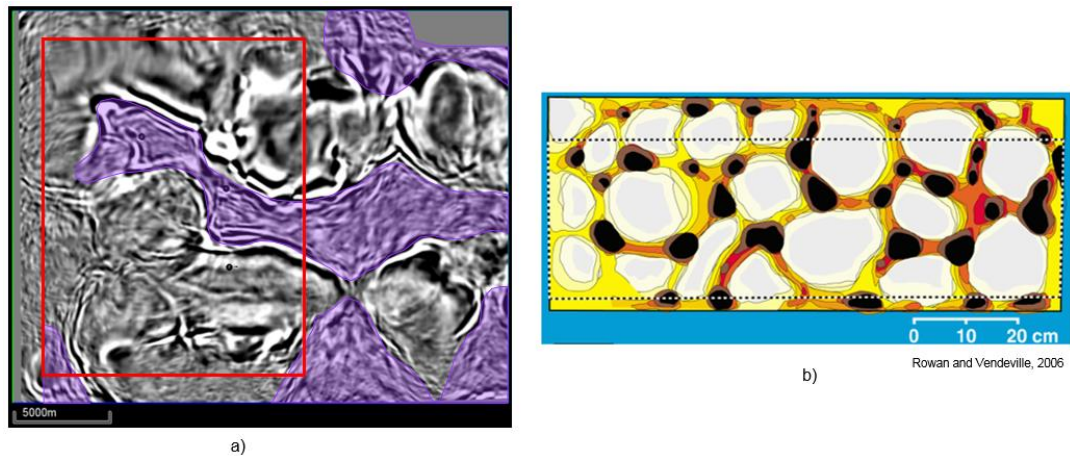


Figure 4.51. a) Depth slice from the amplitude volume at 8300 m illustrating the present-day distribution of autochthonous salt, which corresponds to the purple-coloured area (Study area delimited by red rectangle); b) Experimental model showing minibasin and salt distribution (Rowan and Vendeville, 2006).

b) Tectonic inversion occurred during Palaeocene-Oligocene and the extensional phase was followed by a contractional event (D2). Structural variability along-strike led to two different evolutions on the Anticline A's edges. In western and central portions, contraction could have reactivated the NF1 fault in a reverse sense and folded the sedimentary sequence, whereas in the eastern limb, contraction was accommodated by buckle folding and reverse faulting resulting in a pop-up structure (Figure 4.52-d). This can be explained as a consequence of the lesser amount of salt coring this limb, causing that most of deformation was accommodated by the overburden (Stewart, 1999; Hudec and Jackson, 2007). Shortening seemed to continue until Middle Miocene, although no typical shortening structures can be identified above the upper detachment level (post-Oligocene section) although it is possible that some deformation in the Mesozoic had occurred. Shortening events D2/D3 may have had a very important impact on Mesozoic carbonate rocks, by fracturing them and therefore, increasing permeability and secondary porosity, which turns these anticlines in prospective structures for hydrocarbon exploration.

c) During Pliocene, D4-related normal faulting linked with pre-existent south-dipping D1 fault (NF1), which may have been reactivated, to become a single fault that generated a dextral off-set between the hanging-wall and footwall in Mesozoic section (Figure 4.52-e). This later reactivation of the fault can have implications not only on fracture development close to the fault but also on integrity of the trap. Conversely, towards the east, NF1 progressively dies out, being relieved by reverse fault RF1, and only affects the post-Eocene section, so there is no risk for trap integrity on this flank of the anticline.

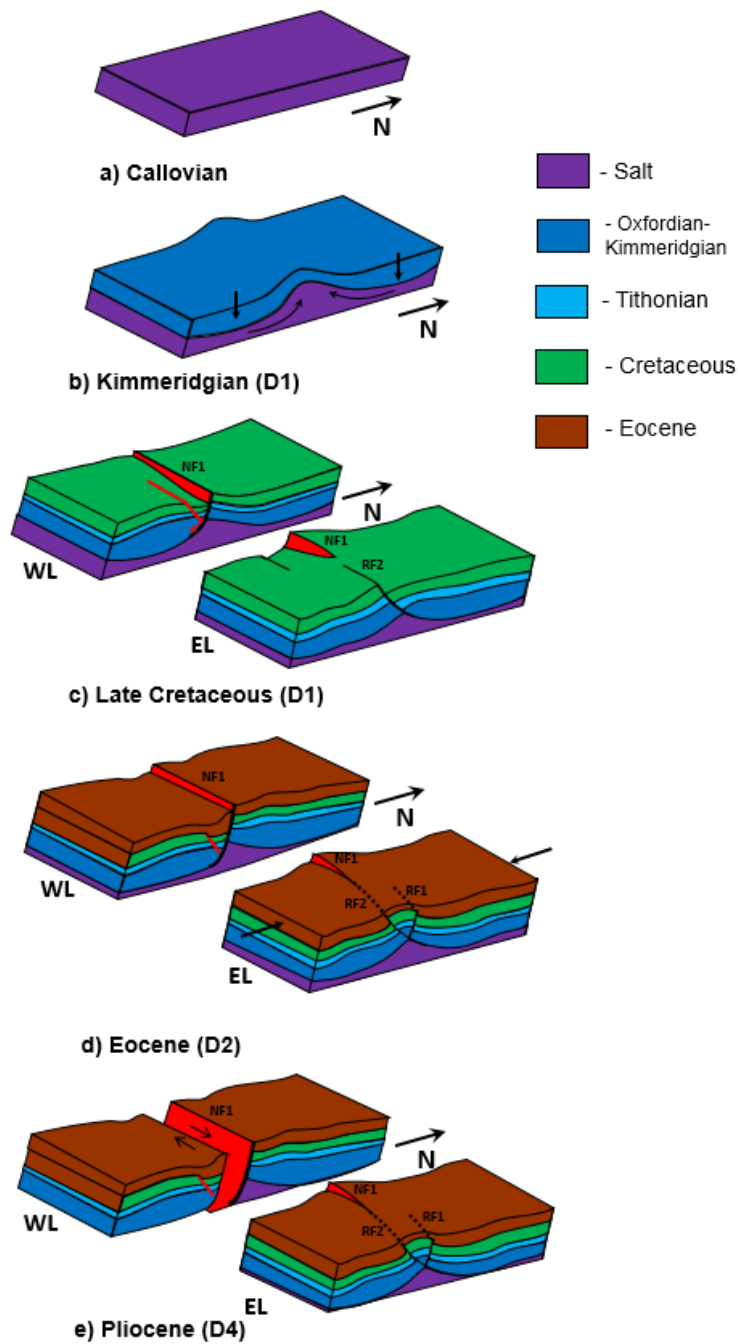


Figure 4.52. Conceptual model of Anticline A's structural evolution, which evolved from two originally separated structures that hard-linked into a single one. WL= Western limb, EL= Eastern limb.

4.4.2.2 Anticline B

Figure 4.55 shows an evolutionary model proposed for Anticline B. Evolution of this structure shares similarities with Anticline A: 1) it is salt-cored; 2) Salt inflation is also related to the development of adjacent minibasins during D1 event; 3) D2 and D3 events re-deformed the pre-existent structure and, 4) D4 normal faulting reactivated pre-existent Mesozoic faults; therefore, to avoid repetitive information, only relevant differences between both structures will be discussed below:

- 1) Anticline B is cored by a salt anticline/pillow, which developed as salt flowed into it from the adjacent minibasins and thus acted as a site for salt accumulation during Late Jurassic and Mesozoic times when its constant growth could have caused drape folding of the overburden and the formation of halokinetic sequences prior to shortening (Figure 4.54), similarly to those observed around salt diapirs in La Popa Basin, Mexico (Giles and Rowan, 2011).
- 2) During D2/D3 contraction, the amount of salt coring the anticline did not allow intense folding of the overburden, thus favouring a relatively larger wave-length folding (Hudec and Jackson, 2007), although reverse faults developed in the northern and southern limbs. Anticline B, thus, is a structure representative of the effects of shortening where no precursor salt structures (diapirs) exists (Figure 4.53).

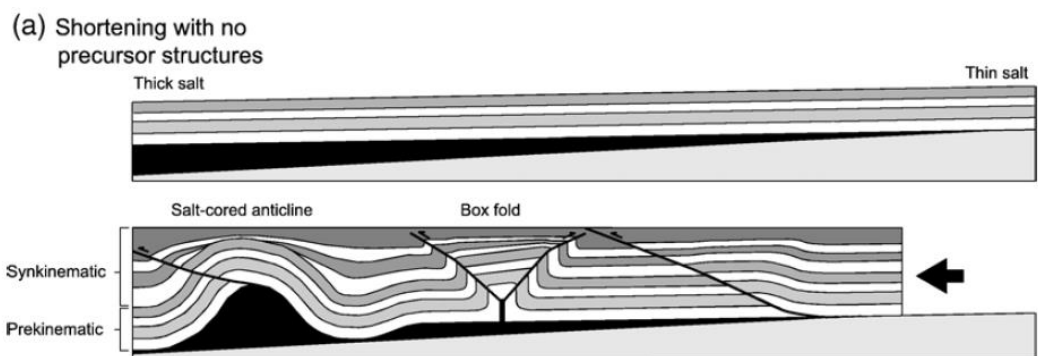


Figure 4.53. Models of salt tectonics showing effects of regional shortening (Hudec and Jackson, 2007).

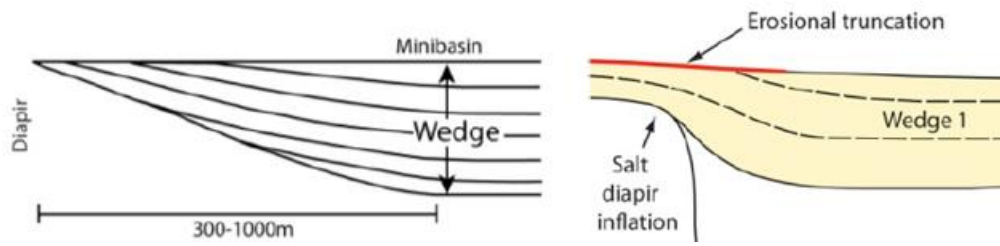


Figure 4.54. Development of wedge (left) and tapered (right) halokinetic sequences during salt diapirism (Giles and Rowan, 2011).

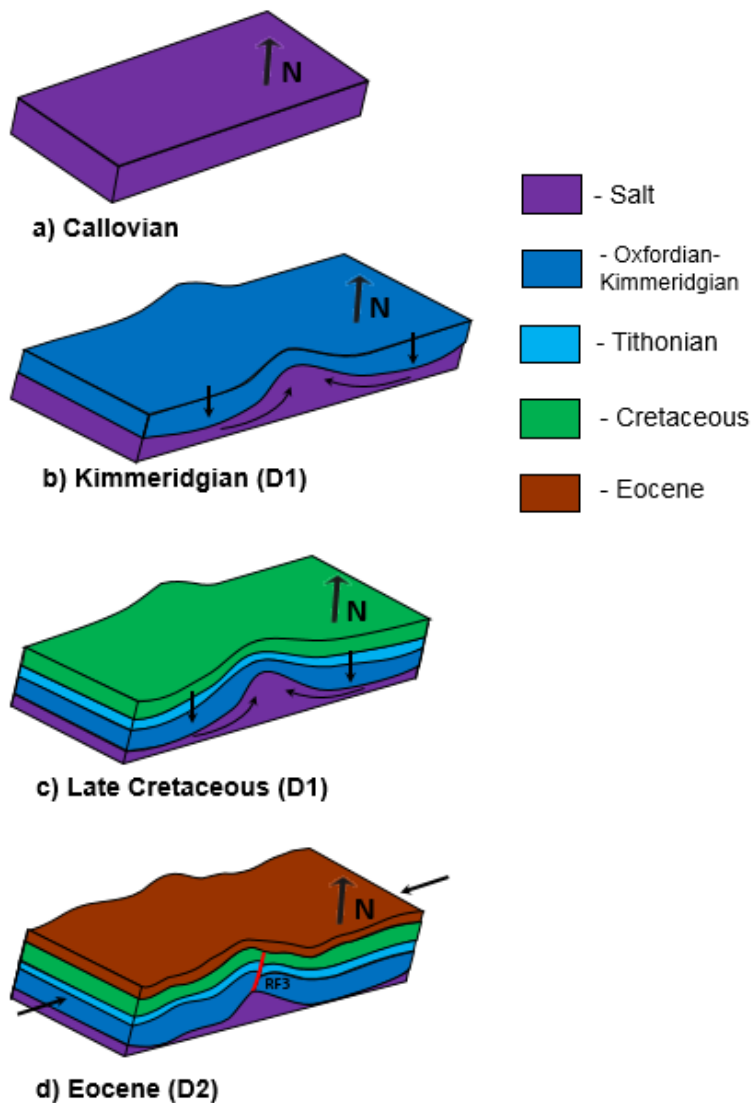


Figure 4.55. Conceptual model of Anticline B's structural evolution.

4.5 Conclusions

Knowledge of evolution of structural traps is crucial to estimate fracture intensity, which in turn, is a parameter used for assessment of quality of reservoir rock. This information is particularly useful in exploratory stages where little or no information of well data is available. For this project we have combined 3D seismic interpretation, isopach maps and cross-sections restoration analysis in order to define the evolution of structural traps within the study area. The obtained results can be summarized as follows:

- Four deformational events that generated structural traps for hydrocarbons were identified in the study area: Early passive diapirism and listric faulting during Late Jurassic-Late Cretaceous (D1); Tectonic inversion characterized by folding, reverse faulting and reactivation of pre-existent faults during the period Eocene-Middle Miocene (D2 and D3), and finally, trans-tensional faulting (D4).
- Early distribution of autochthonous salt (development of withdrawal minibasins and salt ridges-diapirs) soon after its deposition was the main controlling factor over the location and orientation of Anticlines A and B at the early stages of their development.
- Folding associated to deformational events D2 and D3 not only contributed to shape the geometries of both Anticlines A and B, but also may have caused tectonic fracturing in Mesozoic carbonate rocks, thus increasing their potential as reservoir rocks. Moreover, orientation of both anticlines respect to direction of main stress vectors influenced the differences in deformation observed.
- Deformational event D4 had different influence and implications on each Anticline. In Anticline B, it had not influence on later re-deformation, thus resulting in good trap preservation and therefore, better prospectivity. Also, it is very unlikely that fracture development had taken place in Mesozoic rocks as a result of this deformational event, since its associated deformation was accommodated mainly above the Oligocene-Early Miocene upper detachment level. In the other hand, D4 could reactivate the pre-existent normal fault due to linking of Tertiary and Mesozoic segments into a single one, which may have an impact on trap preservation but also it may contribute positively on fracture formation in the vicinity of the fault plane.

Chapter 5

Analysis of well data for fracture interpretation

5.2. Introduction

A good understanding of how natural fracturing in carbonate rock is controlled by different geological factors is critical in order to assess the quality of prospective reservoir rocks and define exploratory strategies in undrilled areas where petroleum plays are associated with naturally fractured reservoirs and fracture systems may provide essential reservoir porosity and/or permeability.

Existing knowledge of the individual effects of different geological factors, such as lithology, texture, porosity, structural position and bed thickness on natural fracturing has been provided by extensive fieldwork and laboratory experiments, from which some general assumptions have been made. For example, lithologies with a higher percentage of brittle particles (i.e., dolomite, quartz, feldspar) tend to have higher fracture densities (Nelson, 2001). For carbonate rocks, some authors have found that dolomites are more prone to fracture than limestones (Schmoker et al., 1985; Hughman and Friedman, 1979); however other studies suggest that dolomitization may in fact have little effect on fracture density (Wennberg et al., 2006). When considering the texture of carbonate rocks, mud supported carbonates have higher fracture density than grain supported (Wennberg et al., 2006) and fine-crystalline dolomites are more fractured than coarse-crystalline dolomites (Giorgioni et al., 2016). Furthermore, it has been widely recognized that thinner beds will have a higher fracture density than thicker beds (Nelson, 2001; W. Ding et al., 2012; Awdal et al., 2016). Contradictory results for each of these general assumptions would however suggest more complex spatial and temporal interactions and each case study may have different results depending on their specific geological conditions, thus making generalisations difficult to apply.

Here, the effects of geological factors that can be defined through the analysis of well data, such as lithology, texture, bed thickness and brittleness in the study area are investigated. For this, the results of analysis from different sources (Petroleos Mexicanos, Instituto Mexicano del Petroleo, Schlumberger) such as well reports, image logs, petrographic description from core and cutting samples have been compiled, integrated and analysed. Also, Cumulative Fracture Intensity (CFI) plots have been constructed in order to integrate some of this information. These findings are presented here, and are subsequently integrated with a structurally-focused analysis in the

following chapter in order to get a more complete knowledge of the effects of geological controls in natural fracturing.

5.3 Dataset and Methods

Well logs

Sets of different well logs from three existing wells in the study area were available for this project, including standard logs such as Gamma Ray (GR), Array Induction (AIT), Lithodensity (LDL), Compensated Neutron (CNL), Image log (FMI, OBMI) and Dipole Sonic (DSI), among others (Table 5.1). Although the combined analysis of these logs provides useful information about the petrophysical characteristics of the drilled rocks, this work placed greatest emphasis on image logs in order to identify geologic controls on natural fracturing.

	W-1	W-2	W-3
AIT-GR	6476-5762	6880-6420, 6425-5836	5715-5550, 5552-5295
LDL-CNL			5552-5295 (OBMI)
DSI			
FMI	6473-6177, 6183-5795	6425-5836	
Sonic Scanner		6880-6420, 6425-5836	

Table 5.1. Summary of well logs from the boreholes within the study area.

Lithological descriptions

Complete lithological and petrographic descriptions from cutting and core samples (hand specimen and thin sections) from three wells within the study area were used for this project. These descriptions were carried out by personnel from PEMEX and Instituto Mexicano del Petroleo (IMP). Table 5.2 summarizes the basic information from the core samples obtained from the Mesozoic section.

Biostratigraphic analysis

Assignment of ages and definition of depositional environments of the stratigraphy in the study area was possible through biostratigraphy analysis of cutting samples and cores from the boreholes undertaken by PEMEX and IMP personnel. These analyses are based on identification of biozones and subzones of different Mesozoic and Cenozoic fossils groups, mostly planktonic foraminifera in order to assign ages of cutting and core

samples. Benthic foraminifera, in the other hand, is used to define depositional environments and paleo-bathymetries. Results used in this study are included in PEMEX's reports from each well and in IMP reports.

Well	No.	Depth (m)	Recovery (m/%)	Age	Environment	Lithology
W-1	1	5892-5895	2.8/94	Late Cretaceous (Turonian)	Basinal	Shaly, light gray, fossiliferous Mudstone- Wackestone.
	1C	6023-6025.5 6025.5-6034	1.36/54 4.56/59	Late Cretaceous (Coniacian-Santonian)	Basinal	Light gray, fossiliferous Wackestone-Packstone
W-2	2	6325-6334	8.6/96	Late Jurassic Tithonian	Basinal	Shaly, dark gray, Mudstone- Wackestone interbedded with black, bituminous, calcareous shale.
	3	6595-6604	9/100	Late Jurassic Kimmeridgian	Basinal	Shaly, light/dark brown, Mudstone
	4	6683-6688.3	3.7/41	Late Jurassic Kimmeridgian	Inner platform	Shaly, dark brown, bioclastic Mudstone - Wackestone
W-3	3	5376-5379	1/33	Early Cretaceous (Valanginian)	Basinal	Light brown, gray Mudstone - Wackestone
	4	5651-5660	9/100	Late Jurassic Kimmeridgian	Inner platform	Light gray Grainstone (oolites, pellets, intraclasts and bioclasts)
	5	5815-5824	9/100	Late Jurassic Kimmeridgian	Inner platform	Dark brown, brechoid, micro-mesocrystalline Dolomite

Table 5.2. Summary of descriptions from the core samples available for this study.

5.3.1 Methods

For this study, borehole data (FMI well logs and cutting/core samples descriptions) available from the study area were compiled, compared, analysed and integrated in order to investigate the role of different geological factors such as lithology, texture, bed thickness and brittleness on natural fracturing. Lithological descriptions taken from well reports were compared against gamma ray and image logs in order to establish a correlation between these two data sets, and also to calibrate logs' responses. Image logs were provided already interpreted by Schlumberger Service Company whereas lithological descriptions and fracture analysis from core samples were undertaken by PEMEX and IMP personnel.

5.3.1.1 Cutting/core samples analysis

Collection of fracture data, as well as lithological descriptions from core samples used in this study, were undertaken by PEMEX and IMP personnel following standard procedures approved by PEMEX that are also of common use in oil industry. First, the core is recovered, conditioned and oriented properly (Zaldivar, 1998). Secondly, geological features (bed limits, fractures, stylolites, etc) are identified, measured and logged. Then, thin sections are processed and analysed according to a procedure developed by Monroy (2011) in order to define fracture sets and their attributes such as fracture porosity, aperture, connectivity between different sets, paragenesis, etc. Petrographic descriptions and fracture analysis of the thin sections taken from core samples were undertaken by IMP personnel using standard microscopy techniques such

as natural and polarized light and, occasionally, cathodoluminescence to define cross-cutting relationships.

5.3.1.2 Well log data

A well log is a continuous recording of a geophysical parameter along a borehole (Rider, 1996). The obtained measurements are usually plotted against depth, and the most common formation parameters measured include: natural radioactivity, resistance to electrical current, conductivity of electrical current, velocity of sound propagation, reaction to gamma ray and neutron bombardments, among others.

Geophysical well logging is a good complement to geological cutting sampling during drilling, which provides a very imprecise record of the formations encountered although usually covers entirely the target formations. In the other hand, core sampling provides more accurate information about the geological characteristics of particular intervals of interest, but it is expensive, slow and spatially limited to a few meters long.

Traditionally, well logs are used mainly to make correlations between wells, to define lithologic facies, stratigraphic sequences and even to establish depositional environments. However, the more extended use of well logging is to define the petrophysical properties of rocks in the borehole vicinity, by performing both qualitative and quantitative calculations of parameters such as porosity, shale content, water saturation, moveable hydrocarbons, hydrocarbon density, etc, all of which allow a characterization of the reservoir rock as well as an estimate of hydrocarbon reserves.

5.3.2 Image well logs

Image logs are a very useful tool to visualize rocks in situ and determine formation properties such as lithologic heterogeneity, sedimentary conditions, fractures, faults and folds where core information is absent, thus being the closest geophysical source for subsurface vision. (Brown et al., 2015).

The Fullbore Formation Microlmager (FMI) tool consists of four orthogonal arms each containing 48 electrodes distributed within a pad and a flap (24 electrodes each), making a total of 192 electrodes which provide nearly 80% coverage in an 8.5" diameter borehole of high quality images (Figure 5.1). FMI's operating principle is based on the measurement of variations of electrical current density across the formation, which are directly related to variations in formation's resistivity, which in turn, are related to formation's geological characteristics. The input current injected into the formation is provided by the four pads and the current density is sampled by the tool's button array (Rider, 1996).

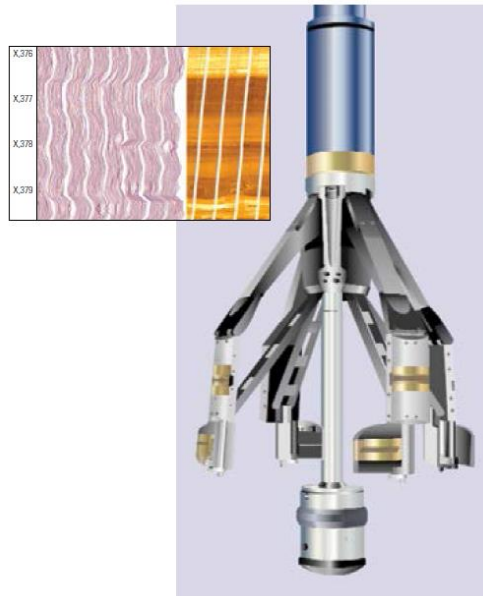


Figure 5.1. Imaging tool for FMI-HD log. The close spacing between the sensors buttons provide a high-resolution data from which images are generated (inset) (Brown et al., 2015).

Resistivity measurements are sampled vertically every 0.2 inches by each electrode, thus providing 192 readings at any depth with a high vertical resolution. Due to the fact that the borehole is sampled regularly in both vertical and horizontal intervals, the obtained information can be pixelated and, as a result, an image can be created and analysed by geoscientists. The standard colour coding used for FMI log presentation usually assigns light colours to high resistivity (low conductivity) measurements and dark colors to low resistivity (high conductivity) measurements (Figure 5.2). High conductivity may be associated to the presence of conductive minerals such as pyrite, certain types of shales or non-resistive mud filtrate within porous spaces.

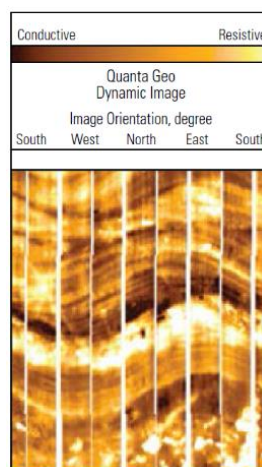


Figure 5.2. FMI log image. Standard color code assigns dark colors to high conductivities and light colours to high resistivities (Brown et al., 2015).

Bed limits, faults and fractures are geological features that are displayed in the image log as sinusoids, which correspond to the unwrapped projection of a planar event in the borehole. In a vertical borehole, the amplitude of the sinusoid is proportional to the angle between the planes and the tool axis. The apparent dip's azimuth of these events is defined by the orientation of the line that connects the sinusoid's peak and through (Figure 5.3).

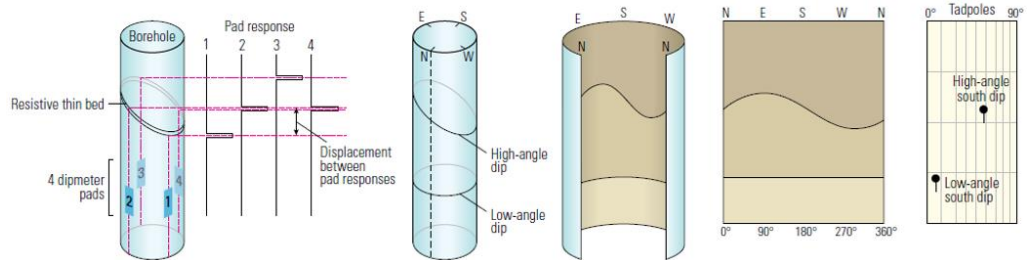


Figure 5.3. Illustration of detection and plotting of bedding planes and fractures in the FMI log (Brown et al., 2015).

Image logs were obtained, processed and interpreted by Schlumberger Service Company. All of the logs used for this study were obtained from boreholes drilled vertically with oil-based mud, but only in log W-3 was OBMI logging tool used. The standard processing procedure that had been applied to these consists of different corrections for several factors such as speed logging, depth, logging tool stuck inside the borehole, magnetic declinations, among others. Then, the images are oriented with respect to magnetic North and different filters are applied in order to eliminate noise and improve image quality. Interpretation by Schlumberger personnel was undertaken manually following standard procedures and comprised the identification of geologic features such as textural features, bed limits, fractures, microfaults or possible induced fractures and breakouts. Orientation and frequency of fractures and beds were also quantified in order to characterize the different fracture sets and their relationship with bedding.

5.4 Stratigraphy

This section summarizes the stratigraphy from the boreholes within the study area. For this, lithological descriptions (cutting and core samples) from well reports were compiled and summarized. For practical purposes, the stratigraphy for each well is described in the drilling direction starting with Late Cretaceous and finishing with Late Jurassic Kimmeridgian-Oxfordian? sediments. Lithologic descriptions in this work use the

Dunham (1962) classification of carbonate rocks, which has also been used as standard by PEMEX geologists.

Traditionally, PEMEX has considered the Albian-Cenomanian stages as Middle Cretaceous due to its economic importance in several oilfields. Here, the same subdivision is used when describing the stratigraphy as well as to consider possible Cretaceous targets. Figure 5.4 illustrates a stratigraphic section which correlates the Mesozoic columns from the three boreholes in the study area showing the thickness variations between them.

Although sediments' ages were mostly constrained from existing biostratigraphic analysis, occasionally well log correlation and even lithologic variations helped to establish stratigraphic tops when biostratigraphy did not provide conclusive information. High resolution biostratigraphic analysis reported the absence of several biozones in the Cretaceous columns, which may have resulted from either erosion/non deposition, absence of index microfossils or because those biozones may be condensed and thinner than the usual sampling interval (5 m) while drilling.

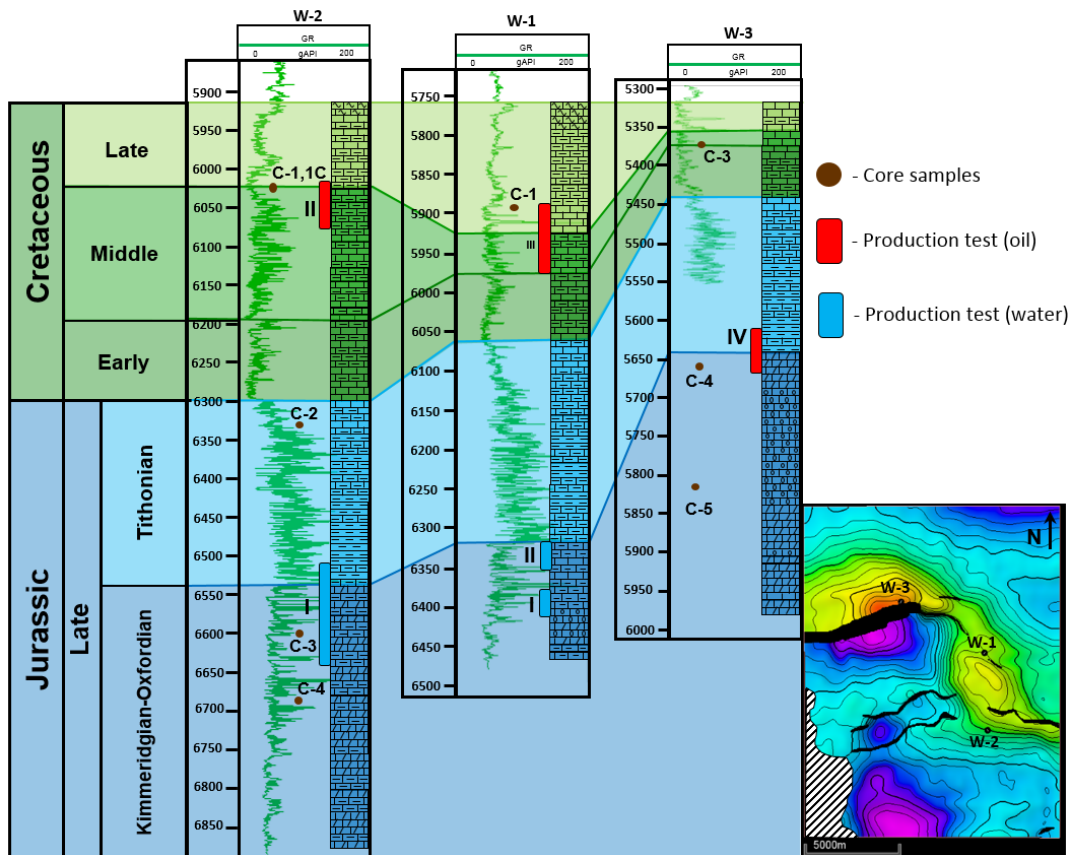


Figure 5.4. Correlation between the stratigraphic columns from the boreholes in the study area. Location of core samples and production tests are also indicated. Right: Top Kimmeridgian structure map with locations of boreholes.

5.4.1 Late Cretaceous (93-66 Ma)

From top to base, this sequence can be subdivided into three different members according to lithologic criteria: a) light grey, reddish marls interbedded with calcareous shale and shaly mudstone; b) light brown, bioclastic wackestone-packstone interbedded with white, recrystallized mudstone; and c) dark grey, shaly mudstone with flint nodules interbedded with dark gray, bituminous, calcareous shale (Figure 5.5). Depositional environment corresponds to basinal according to biostratigraphic analysis. Thicknesses in the study area range between 110-160 m. However, local variations due to erosion/non deposition occur as it is the case of borehole W-3, where only 35 m were drilled.

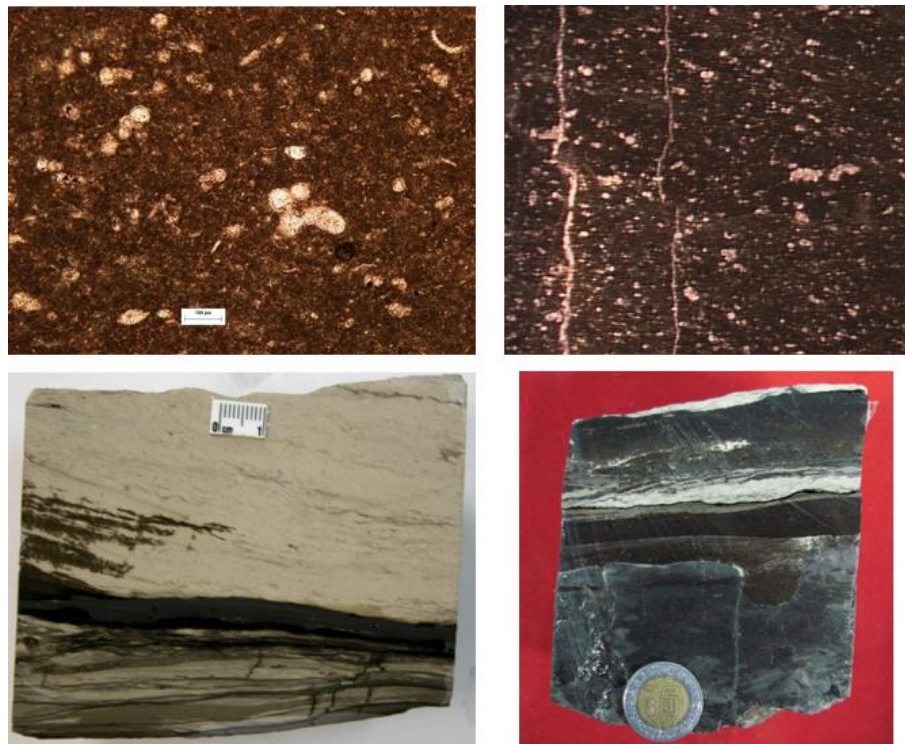


Figure 5.5. Foraminifera wackestone. W-1, Late Cretaceous, C-1, Top: thin sections, 2.5X. Polarized light. Bottom: Hand samples from C-1.

5.4.2 Middle Cretaceous (113-93 Ma)

W-2 has the thickest section in the study area (150 m) whereas W-1 and W-3 have much thinner sections (50 and 20 m, respectively). Given the high lithologic similarities between the boreholes, the W-2 section may be considered as representative and is described below.

The upper section consists of dark grey, shaly mudstone and flint nodules interbedded with light/dark brown foraminifera mudstone-wackestone (

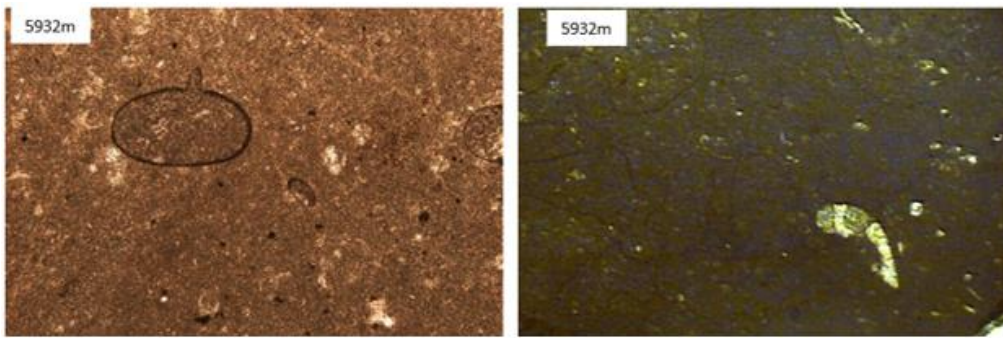


Figure 5.6), whereas the lower section consists mostly of dark/light gray foraminifera mudstone-wackestone with flint nodules. The interpreted depositional environment is basinal according to biostratigraphic analysis.

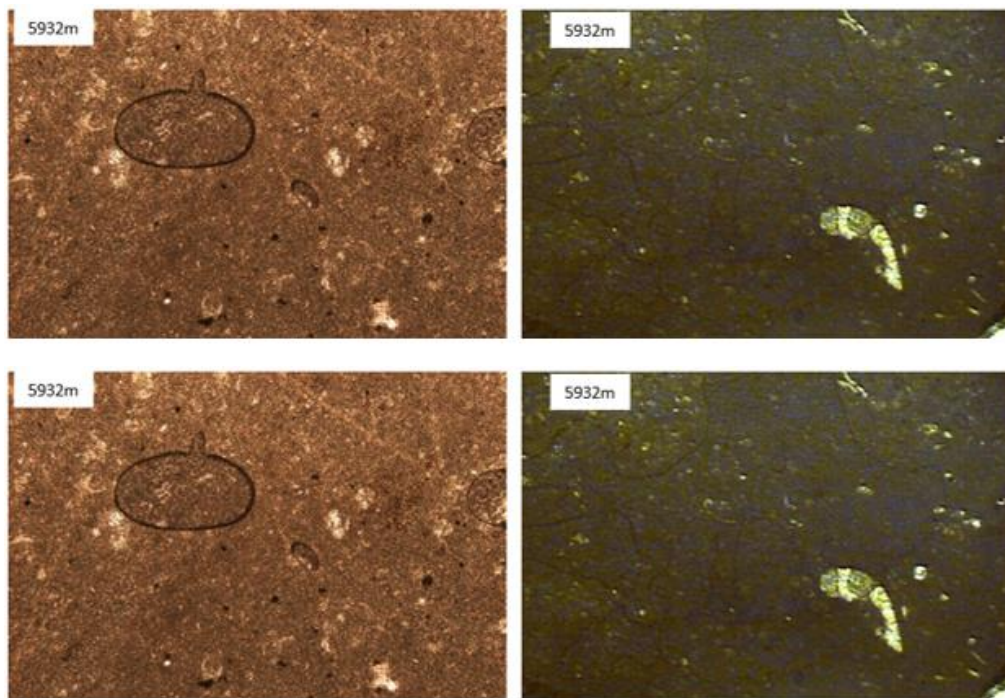


Figure 5.6. Foraminifera mudstone-wackestone. W-1, Middle Cretaceous, 2.5X. Polarized light.

5.4.3 Early Cretaceous (145-113 Ma)

Dark/light grey, foraminifera mudstone-wackestone interbedded with dark grey, bituminous, shaly mudstone and thin beds of dark grey calcareous shale (Figure 5.7). Thickness ranges between 65 m in W-3 to 105 m in W-2. The depositional environment is basinal according to biostratigraphic analysis.

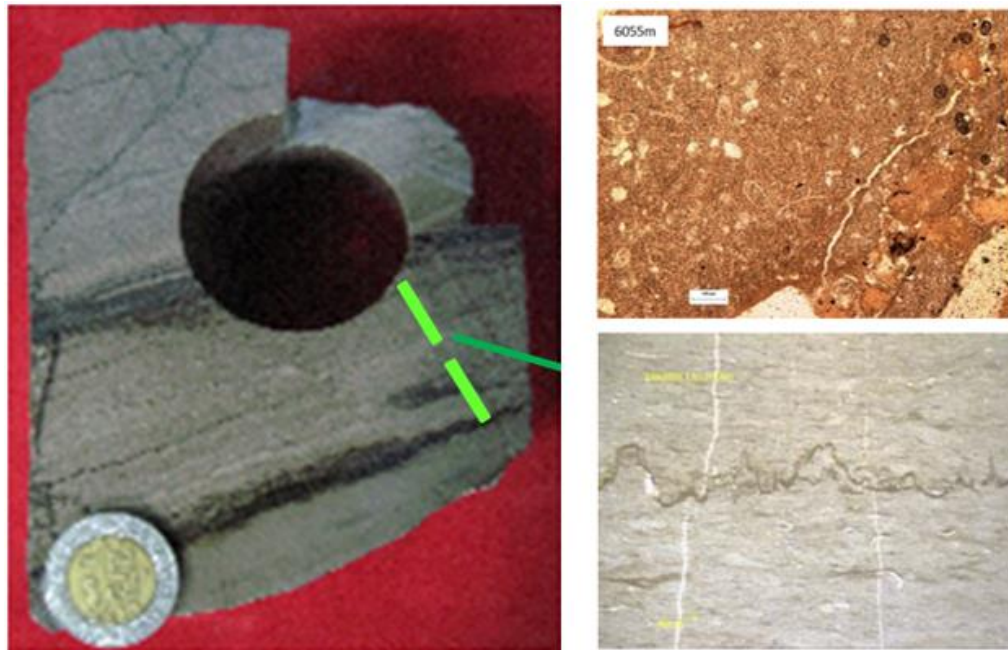


Figure 5.7. Left: Hand sample from W-3, C-3. Top right: Foraminifera Mudstone-wackestone. W-1. Bottom right: Stylolite and sealed fractures in Mudstone, W-3, C-3. 2.5X. Polarized light.

5.4.4 Late Jurassic Tithonian (152-145 Ma)

The upper section (40 m) consists of light brown, foraminifera mudstone-wackestone interbedded with dark brown, shaly Mudstone. Below this section, lithology consists of dark grey to black, bituminous, shaly mudstone-wackestone with abundant organic matter interbedded with black, bituminous calcareous shale (Figure 5.8). Thickness of this sequence is quite uniform in the study area and ranges between 200 and 260 m, once more biostratigraphy indicates that these were deposited in a basinal environment.

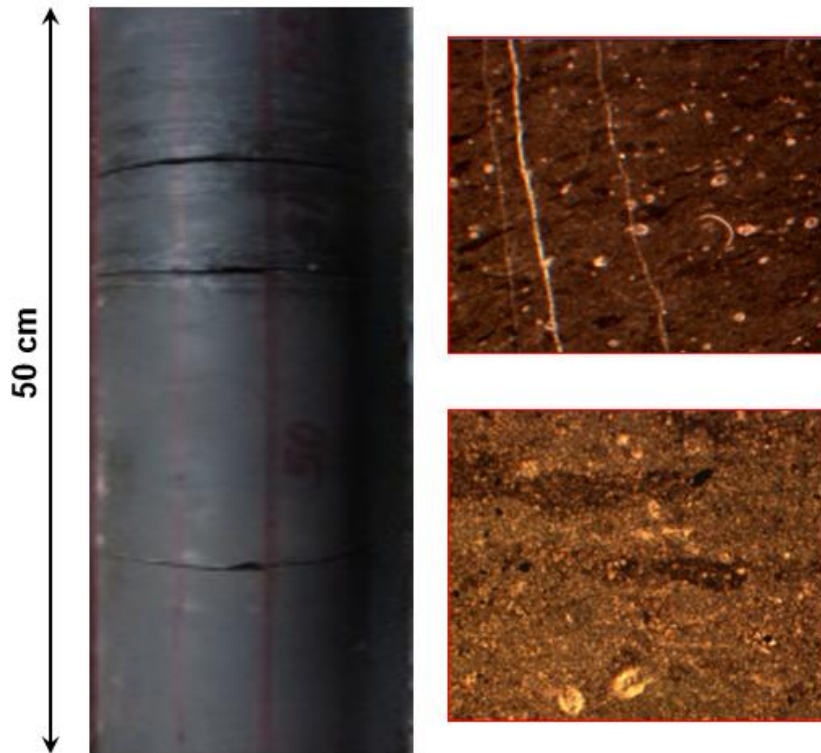


Figure 5.8. Left: Fragments from W-2, C-2. Right: shaly foraminifera mudstone-wackestone with microfractures. W-2, C-2. 2.5X, Natural light.

5.4.5 Late Jurassic Kimmeridgian-Oxfordian? (163?-152 Ma)

Lateral facies variations that occur within this interval across the study area are associated with variations in depositional environments whose distribution, in turn, was controlled by salt diapirism during this time. As a result, areas located above the crest of active diapirs were paleo-highs with shallow (inner platform) sedimentation (W-3) whereas deeper carbonate facies (outer platform) were deposited in surrounding areas (W-1, W-2). Due to this, different stratigraphic columns in the study area will be described.

- W-1, W-2: Two major sequences can be defined in these boreholes (Figure 5.9). The upper sequence (130 m) consists of light grey, shaly mudstone interbedded with light grey, partially dolomitized, intraclastic wackestone. The lower sequence consists of pellets and oolitic packstone interbedded with light grey, shaly, dolomitized mudstone-wackestone (W-1), whereas in W-2, dolomitized mudstone-wackestone is more predominant than oolitic packstone. Thicknesses drilled in these wells are 345 m (W-2) and 163 m (W-1) for this interval. The depositional environment for this interval corresponds to inner ramp (W-2) and outer ramp (W-1) according to biostratigraphic analysis.

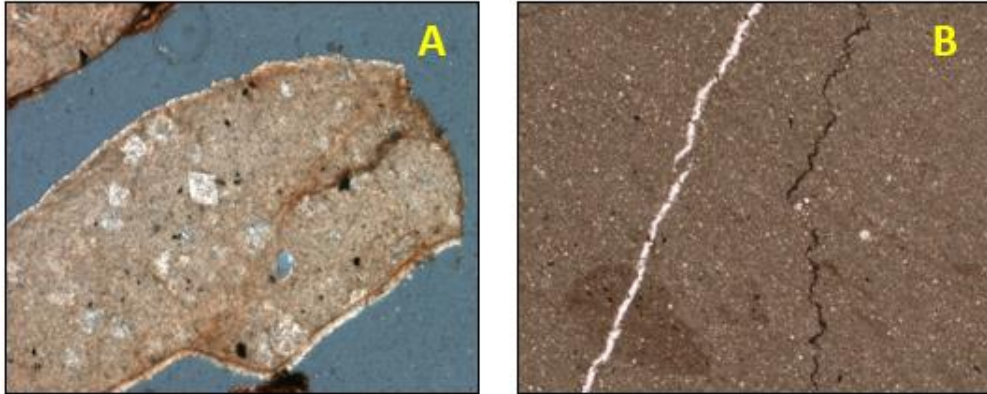


Figure 5.9. Late Jurassic Kimmeridgian thin sections. A) Dolomitized mudstone, W-1; B) shaly mudstone, W-2, C-3.

- W-3: Three major sequences were defined: upper sequence (50 m) consists of light grey, dolomitized intraclastic wackestone-packstone (Figure 5.10). The middle sequence consists of light grey, ooids, pellets and intraclasts grainstone. The lower sequence consists of dark brown, micro to meso-crystalline dolomite whose original texture possibly corresponded to oolitic packstone interbedded with dolomitized wackestone (Figure 5.11). The drilled thickness of this sequence in this well is 380 m and the depositional environment corresponds to inner ramp according to biostratigraphic analysis.

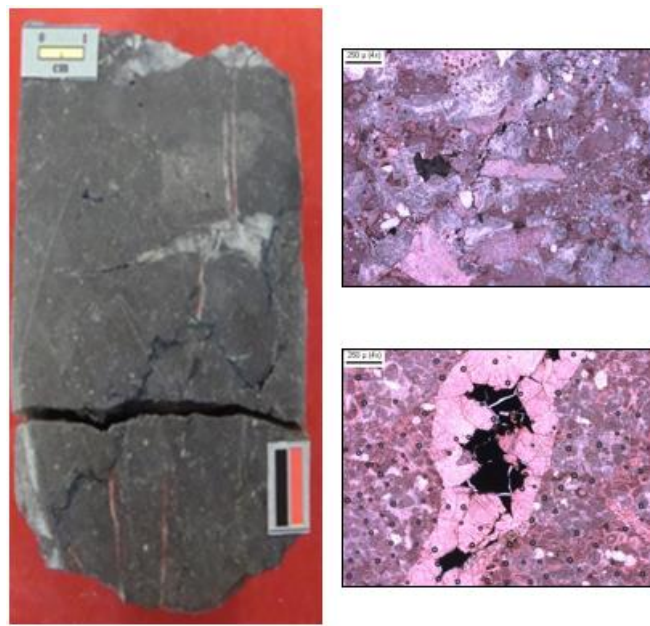


Figure 5.10. Left: Fragment from W-3, C-4. Top right: dolomitized oolitic grainstone, W-3, C-4. Bottom right: dissolution cavity in dolomitized grainstone, W-3, C-4.

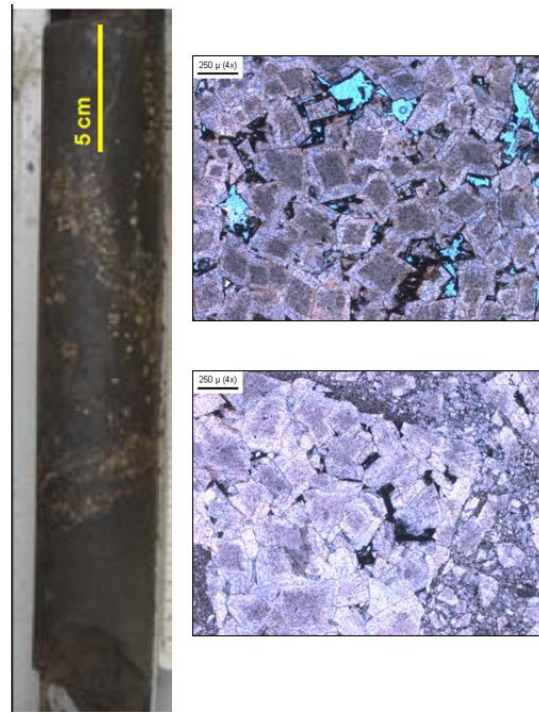


Figure 5.11. Left: Fragment from W-3, C-5. Right: Micro-mesocrystalline dolomite, W-3, C-5.

5.5 Fracture analysis in core samples

Analyses were performed in both hand samples and thin sections in order not only to identify and characterize the fracture systems in the rock but also to define a sequence of diagenetic events that have altered rock properties through geologic times and may shed a light on the role of diagenesis on fracture development. These diagenetic events were dated in a relative way, since no absolute ages could be defined in the petrographic studies; thus, the terms “early” and “late” used in the paragenetic charts indicate the relative position of the events in the sequence. Due to the fact that each core was analysed independently, identical nomenclature of fracture sets was used for each core (f1, f2, etc.); however, orientations of these fracture sets are unique for each core and may differ or not from other cores. For this study, analyses results were compiled from different sources, integrated and interpreted in terms of their quality as reservoir rocks.

W-1, C-1 (5892-5895 m, Late Cretaceous): Lithologically consists of light grey, fossiliferous wackestone-packstone with flint nodules and thin beds. To the naked eye, stylolites are visible and a relatively small number of fractures were with an inclination between 70° and 90° to bedding in hand samples; however, analysis of thin sections parallel to bedding from Fragment 14 reveals a more intense and interconnected microfracturing with two main orientations: f1) NNE-SSW, these fractures are extensional (Type I), sealed with syn-kinematic calcite and apertures fairly constant ranging from

0.01 to 0.03 mm. f2) *E-W (278°)*, these are the most abundant fractures in the thin sections and are also extensional (Type I) in origin. All fracture sets occur at a high angle and/or perpendicular to bedding and apertures are highly variable, ranging from 0.01-0.02 mm to 0.63 mm. Most fractures show two stages of calcite cementation, completely covering the fracture area (Figure 5.12B). Cross-cutting relationships between f1 and f2 were determined by cathodoluminescence and suggest that f1 pre-dates f2.

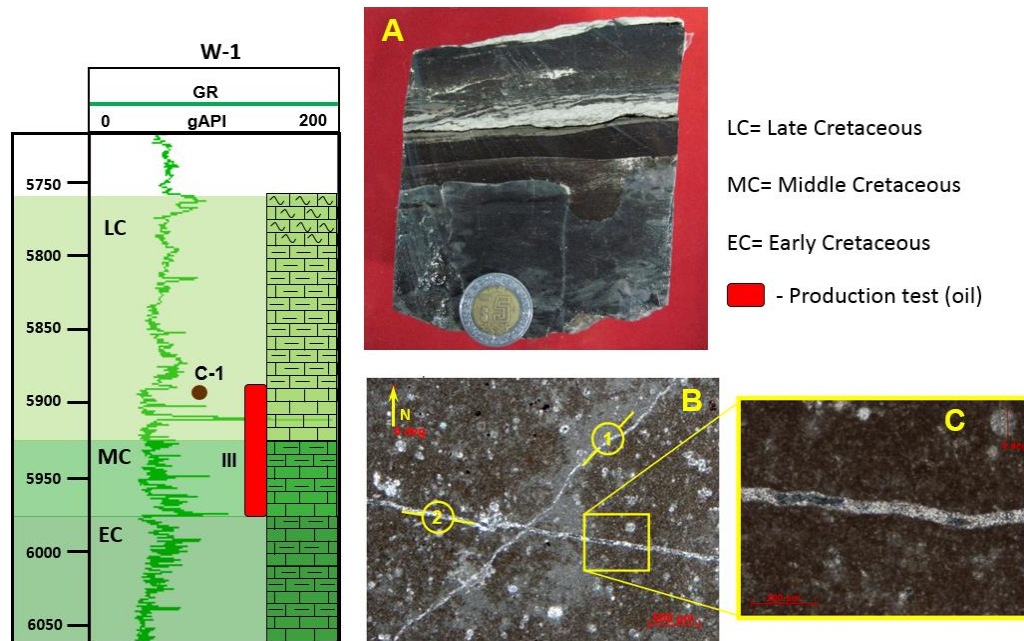


Figure 5.12. A) fragment from C-1; B) cross-cut relationship between f1 and f2 fractures (2.5x); C) close-up from f2 fracture in B showing calcite cementation (10x). W-1, C-1.

Petrographic analysis revealed a relatively simple paragenetic evolution (Table 5.3. Paragenetic chart from Core-1, W-1.). Defined events consist of two stages of fracture developments, each with syn-kinematic calcite cementation (f2 with a 2nd post-kinematic cementation) which almost completely closed the fracture-related porosity. Pyritization was also identified as well as hydrocarbon migration, which started to charge Mesozoic rocks during Middle Miocene according to geochemical modeling (CNH, 2014) coinciding in time with D3 event which may correspond to a fracturing episode. Pressure-solution is evidenced by the presence of stylolites in both hand sample and thin sections.

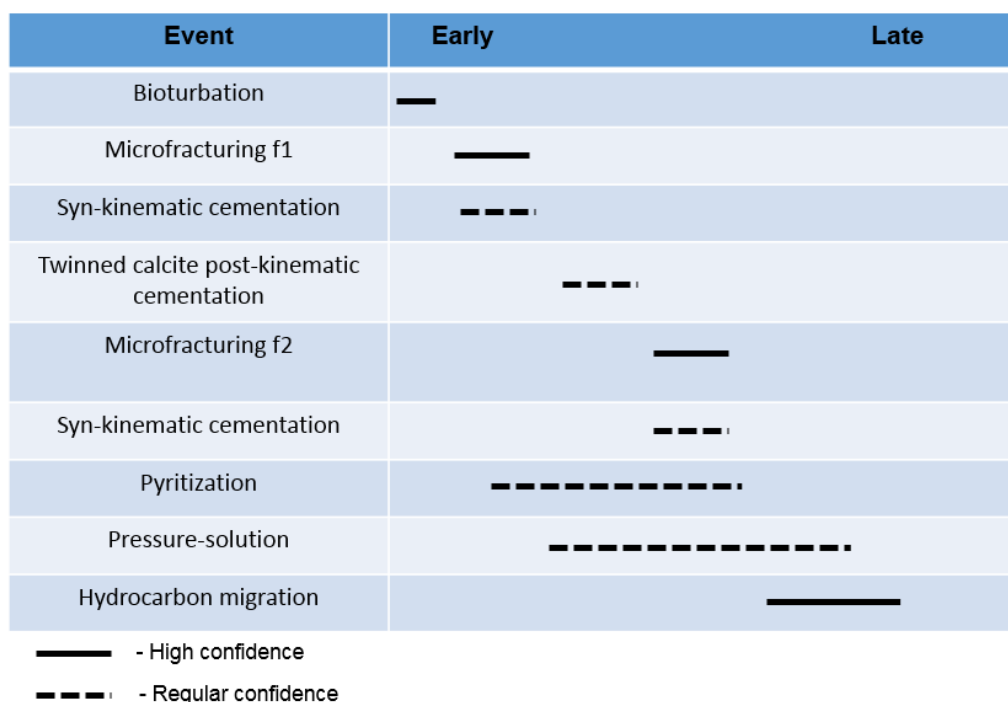


Table 5.3. Paragenetic chart from Core-1, W-1.

W-2, C-1C (6023-6025 m, Late Cretaceous): Lithologically comprises light grey, fossiliferous partially silicified wackestone-packstone. Microfractures are relatively abundant all along the core, and a fracture analysis was carried out in Fragment 6, which is highly silicified; thin sections were taken parallel to bedding. Three fracture sets (f1, f2 and f3) that are oriented NW-SE 80°, NW-SE 20° and NE-SW 35° respectively, were identified and analysed. f1 fractures are the most abundant, with an average aperture of 0.04 mm, cemented with syn-kinematic silica partially replaced by dolomite such that remnant porosity is lacking. f2 is represented by only one fracture, with an aperture of 0.06 mm, which is cemented by post-cinematic calcite with very low remnant porosity with hydrocarbon stains. f3 fractures have apertures from 0.02 up to 2 mm, and are cemented with post-cinematic calcite partially replaced by dolomite. All fracture sets are at a high angle and/or perpendicular to bedding and remnant porosity is variable (poor to regular) with residual hydrocarbon stains. Cross-cut relationships suggest that f2 and f3 are synchronous and postdate f1, which show a left-lateral offset where cut by f2 and f3 fractures (Figure 5.13).

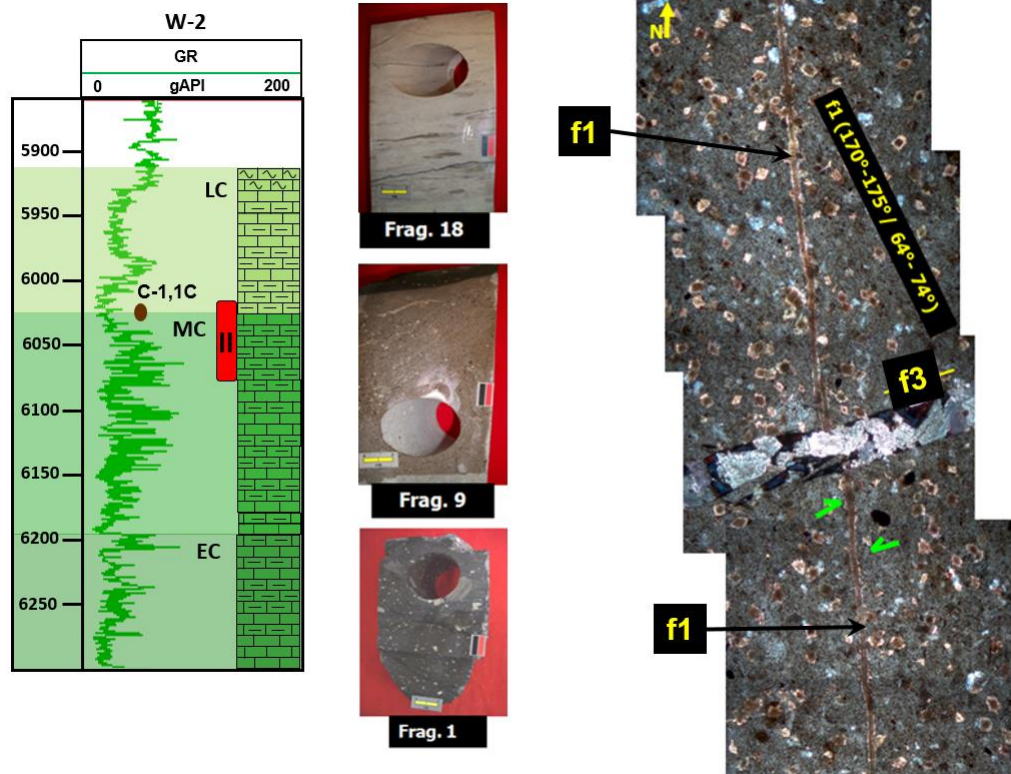


Figure 5.13. Centre: three fragments from base, middle and top of W-2, C-1. Right: close-up from fragment 1 showing lateral offset of f1 fracture caused by cross-cutting of a later f3 fracture, W-2, C-1. LC= Late Cretaceous, MC= Middle Cretaceous, EC= Early Cretaceous.

Table 5.4 illustrates the paragenetic sequence defined from the petrographic analysis of core fragments. Paragenetic evolution is more complex than in W-1 C-1, with more events identified. Early silicification and partial dolomitization are processes which may have influenced the mechanical properties of the rock soon after its deposition. Two episodes of fracturing generated at least 3 sets of fractures with their corresponding syn and post-cinematic cementation. Finally, late hydrocarbon migration occurred, pervading primary and secondary porosities.

W-2, C-3 (6595-6604 m, Late Jurassic Kimmeridgian): Lithologically, consists of dark grey, shaly foraminifera mudstone-wackestone interbedded with partially dolomitized shale. Fracturing is of moderate intensity, with fractures sealed with calcite and very low remnant porosity. Bedding-parallel and tectonic stylolites are relatively abundant along the core. Petrographic analysis of Fragment 3 identified 3 fracture sets (f1, f2, f3) oriented NW-SE 10°, NE-SW 20-40°, and E-W, respectively. f1 set is represented by one fracture, which is sealed by calcite and truncates against a tectonic stylolite. f2 and f3 sets are considered to be formed simultaneously due to their crosscutting relationships, so they can be considered as shear fractures and post-date f1 (Figure 5.14). All fracture sets are at a high angle and/or perpendicular to bedding and apertures range between 0.2 and 1

mm, they are sealed by syn-kinematic calcite and lack of remnant porosity. Paragenetic evolution is characterized by dolomitization, pressure-solution, two episodes of fracturing with syn-kinematic cementation and hydrocarbon migration (Table 5.5).

Event	Early	Late
Matrix and bioclasts silicification	—	
Microfracturing f1	—	
Syn-kinematic silica cementation	- - -	
Microfracturing f2	—	
Microfracturing f3	—	
Syn-kinematic silica cementation	- - -	
Post-kinematic calcite cementation	- - -	
Dolomitization	—	—
Pressure-solution	—	- - -
Hydrocarbon migration		—

—	Fractures with regular to good conductivity	—	- High confidence
—	Fractures with regular to low conductivity	- - -	- Regular confidence
—	Fractures with null conductivity		

Table 5.4. Paragenetic chart from Core-1C, W-2.

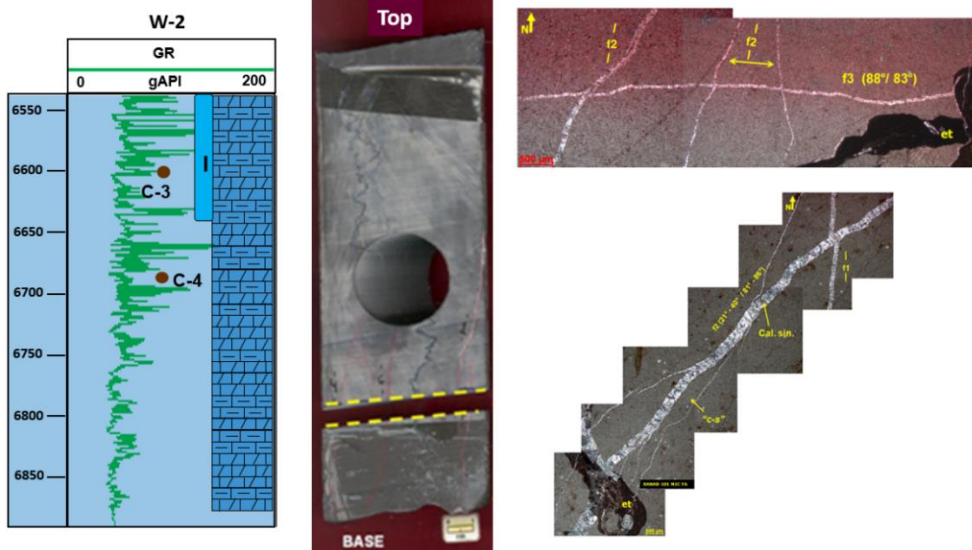


Figure 5.14. Centre: Shaly mudstone-wackestone with vertical stylolites, Fragment 3, C-3. Right: thin sections showing cross-cutting relationships between f2 and f3 fractures (top) and f1 and f2 fractures (bottom), W-2, C-3 (Top).

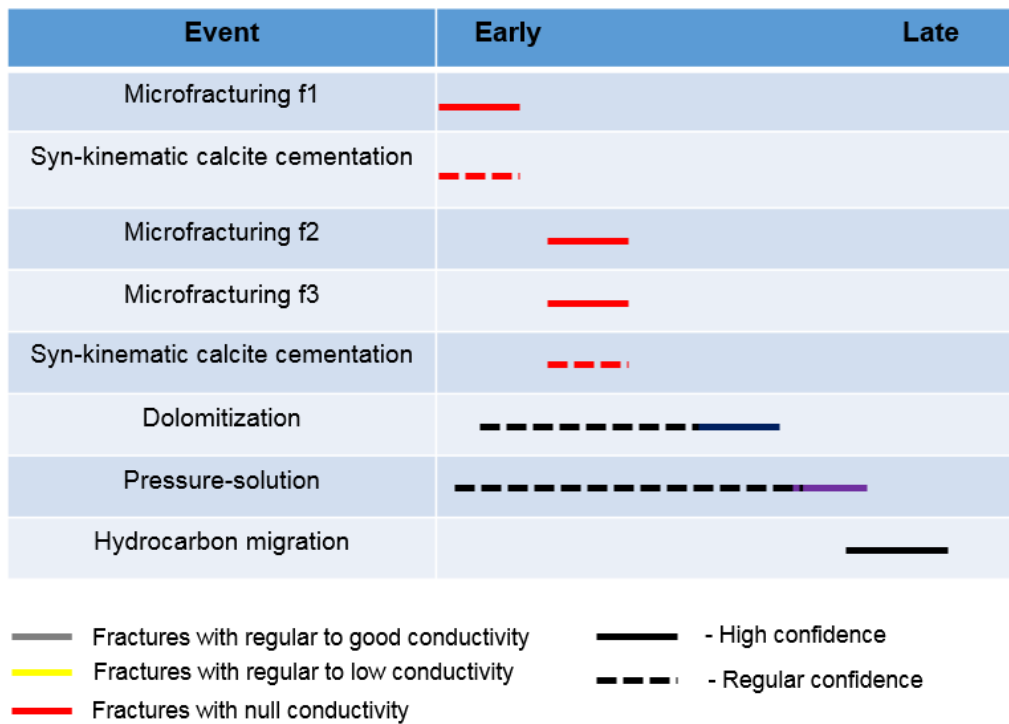


Table 5.5. Paragenetic chart from Core-3, W-2.

W-2, C-4 (6683-6688 m, Late Jurassic Kimmeridgian): Lithologically consists of dark brown, shaly, bioclastic mudstone-wackestone, slightly dolomitized. Silty micro-flows are observed in thin section and micro-fractures are relatively abundant, sealed with calcite and with very low remnant porosity. Petrographic analysis on Fragment 31 identified 4 fracture sets (f1, f2, f3 and f4) oriented WNW-ESE, NE-SW 60°, NW-SE 50°, and NW-SE 80°, respectively which are at high angle and/or perpendicular to bedding. Apertures range from 0.01 mm (f2, f4) up to 0.13 mm (f4) and most fractures are sealed with syn-kinematic calcite. Dolomitization is present sealing f3 fractures and replacing the original matrix (Figure 5.15). Cross-cutting relationships between fracture sets determine that f3 and f4 occurred synchronously and postdate f1 and f2.

Paragenetic evolution is characterized mainly by porosity reduction (pressure-solution, dolomitization, and cementation) rather than porosity enhancing events (fracturing). Both matrix and fracture porosities are very low or zero and therefore, this lithology can be considered as poor-quality reservoir rock (Table 5.6).

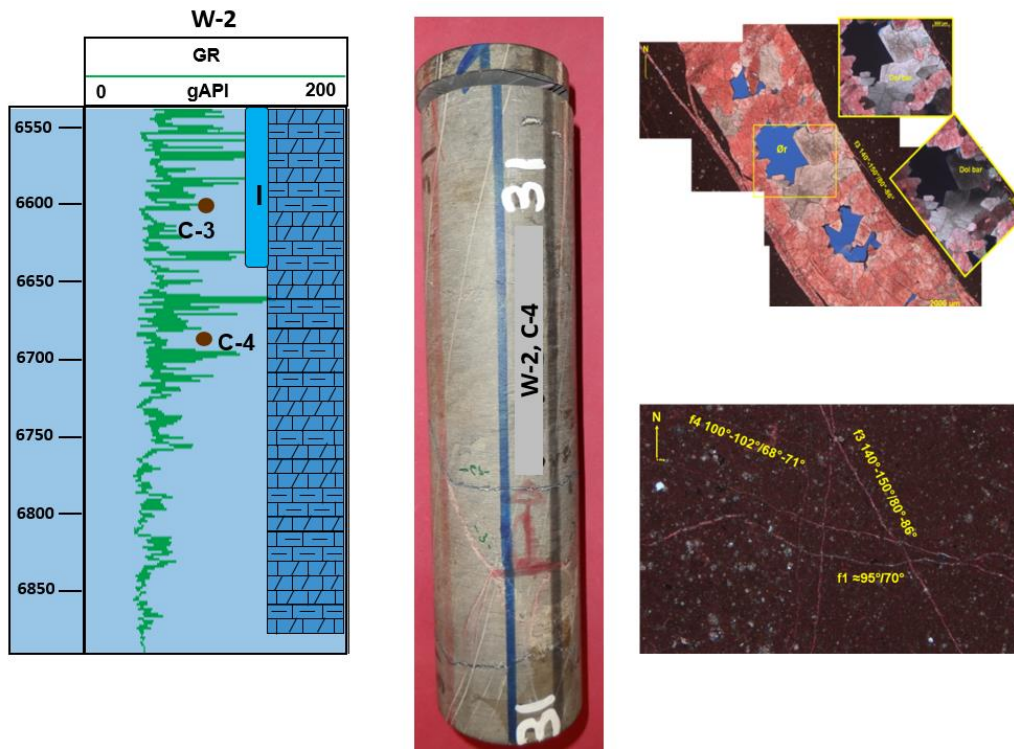


Figure 5.15. Centre: Fragment 31, C-4. Top right: Dolomite partially cementing fractures with remnant porosity. Bottom right: cross-cutting fractures from different families. Thin sections from fragment 31, C-4.

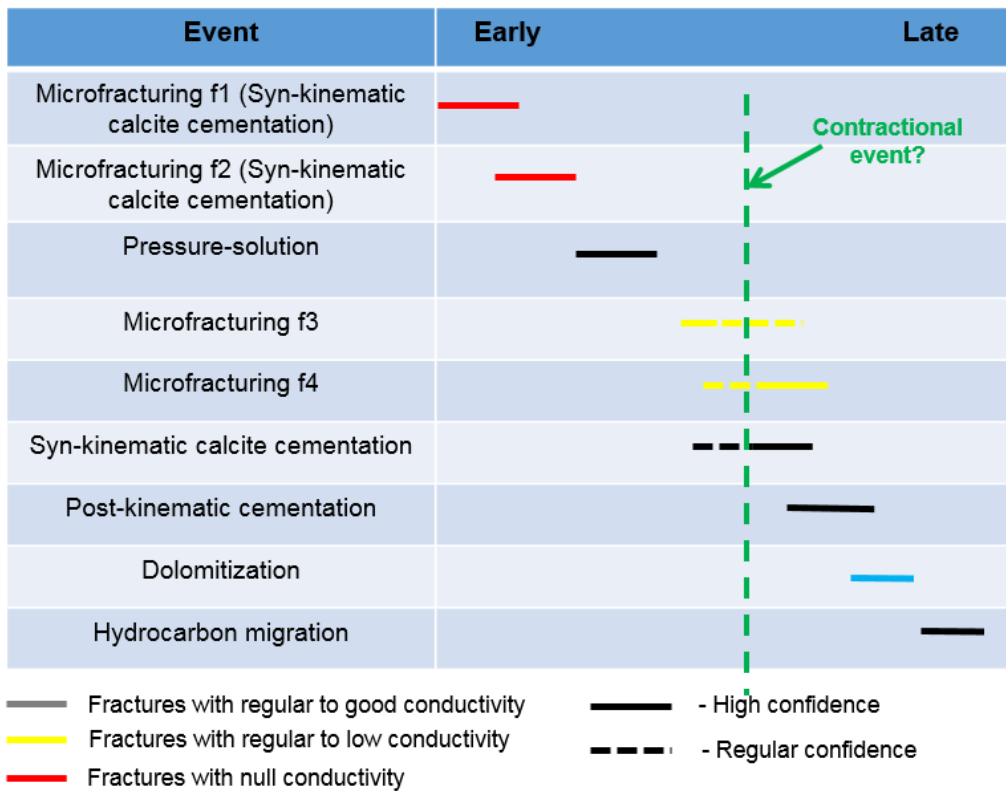


Table 5.6. Paragenetic chart from Core-4, W-2.

W-3, C-3 (5375-5381 m, Early Cretaceous): Lithologically consists of gray foraminifera mudstone-wackestone interbedded with gray mudstone with organic matter laminations. Abundant stylolites (both perpendicular and parallel to bedding) are present and perpendicular-to-bedding fracturing is also intense in core sample (Figure 5.16). Petrographic analysis on fragment 3 identified five fracture sets (f1, f2, f3, f4, f5) oriented NW-SE 60°, NE-SW 50°, NW-SE 30°, NE-SW 70° and NE-SW 50°, respectively. Fractures are mostly sealed with calcite and residual hydrocarbon and occasionally with dolomite (f5). Remnant porosity in fractures is very low and apertures range from 0.01 mm (f4) to 0.36 mm (f3). Cross-cutting relationships between fractures sets are complex and represent the superimposed effects of different deformational events with similar orientations; however, a fracturing sequence can be defined. Moreover, f3 fractures are considered as synchronous to the tectonic stylolites; whereas f4 fractures post-date those same stylolites. Although fracturing is relatively abundant in this interval, the diagenetic evolution resulted in porosity reduction (due to pressure-solution, dolomitization, cementation, compaction) and therefore, this lithologic facies can be considered as poor-quality reservoir rock (Table 5.7).

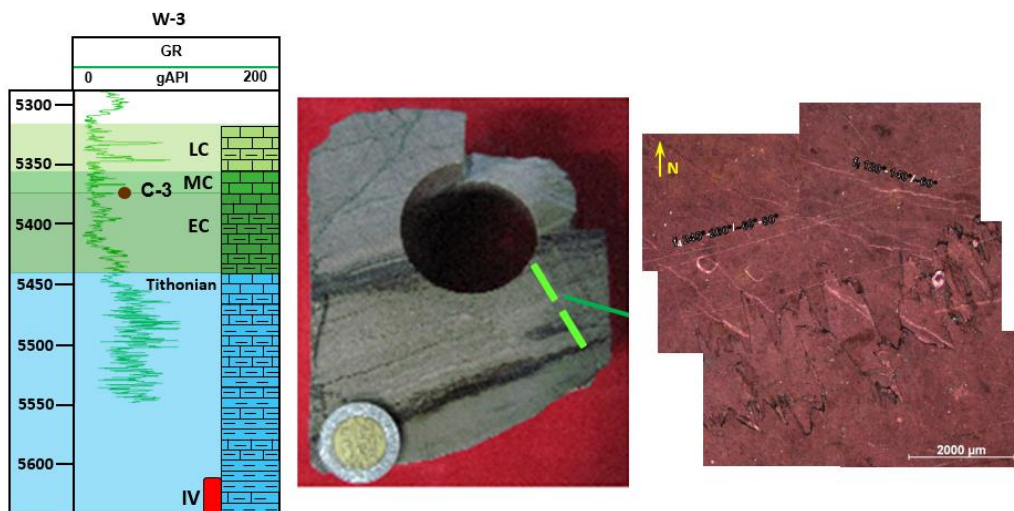


Figure 5.16. Centre: Fragment 3 from C-3. Right: cross-cutting relationships between fractures from f1, f4 families and stylolites. W-3, C-3.

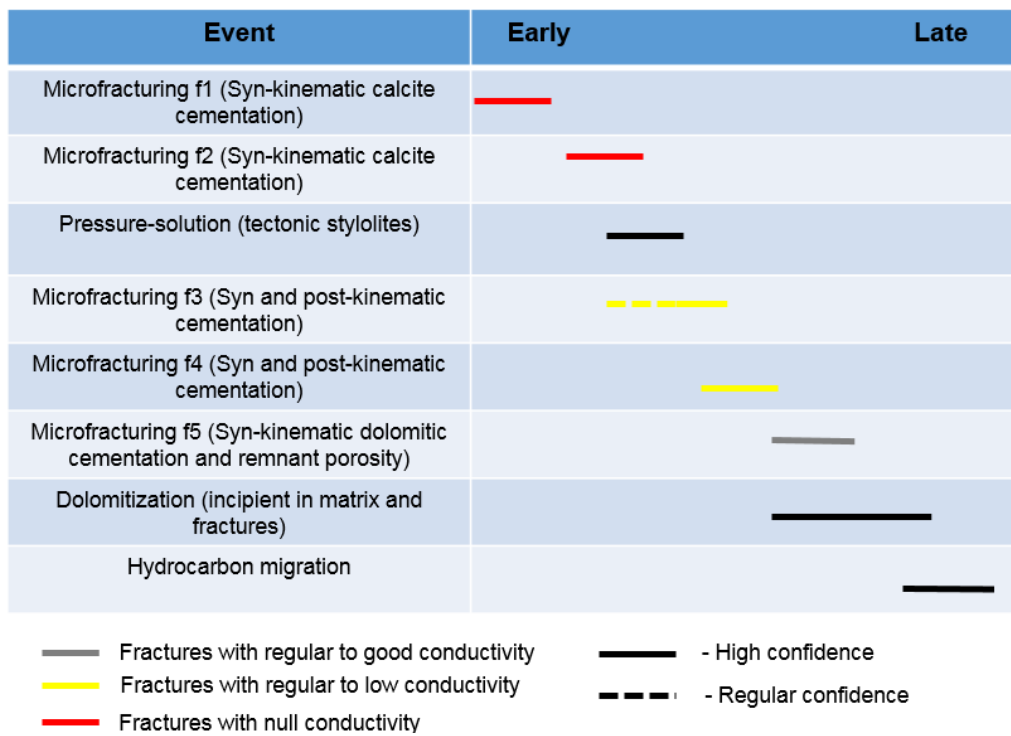


Table 5.7. Paragenetic chart from Core-3, W-3.

W-3, C-4 (5651-5660 m, Late Jurassic Kimmeridgian): Lithologically consists of light gray, dolomitized, oolitic and bioclastic packstone-grainstone with the presence of dissolution cavities, abundant tectonic stylolites and moderate fracturing (Figure 5.17). Polycrystalline quartz is also abundant in the nucleus of oolites and present as disseminated quartz. Petrographic analysis on fragment 7 identified four fracture sets (f1, f2, f3, f4) oriented NW-SE 70°, NE-SW 30°, NE-SW 50°, and NE-SW 40°. Apertures range from 0.01 mm (f4) to 0.5 cm (f3), and fractures are sealed with syn-kinematic calcite and dolomite (f4). Fracture remnant porosity is null in f1 and f2, whereas f3 shows porosity by dissolution and f4 has good remnant porosity connected with matrix. Cross-cutting relationships between fracture sets were defined using cathodoluminescence techniques establishing that f1 and f2 formed synchronously, whereas f3 and f4 resulted from different fracturing episodes and post-date f1 and f2. The diagenetic evolution is relatively complex and, unlike the earlier examples, porosity-enhancing processes were more prominent through microcrystalline dolomitization and dissolution which produced solution cavities and remnant porosity within f3 and f4 sets (Table 5.8). As a result, this facies can be considered to be a good quality potential reservoir rock.

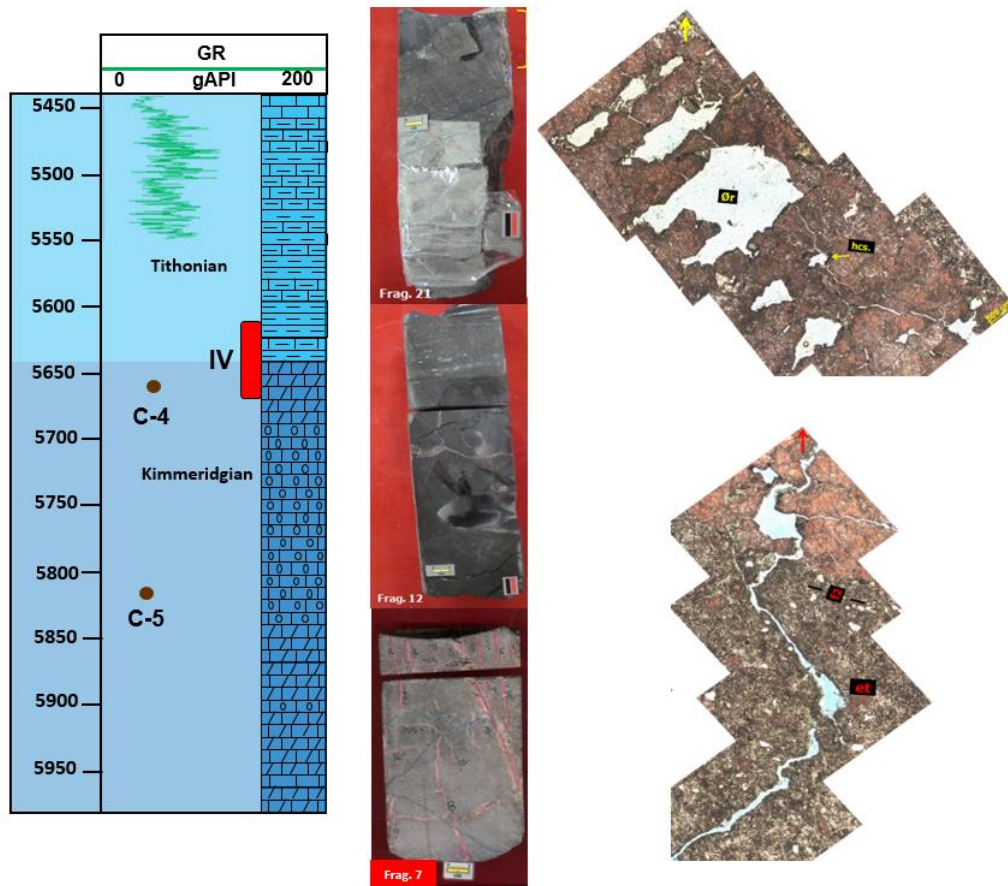


Figure 5.17. Centre: fragments from bottom, middle and top C-4. Top right: dissolution cavities and fractures. Bottom right: stylolite with some dissolution.

Event	Early	Late
Microfracturing f1	—	
Microfracturing f2	—	
Syn-kinematic calcite cementation (f1, f2)	- - - -	
Dolomitization	—	
Microfracturing f3 (Syn-kinematic calcite cementation)		—
Microfracturing f4 (Syn-kinematic calcite cementation)		—
Pressure-solution		—
Dissolution		—
Hydrocarbon migration		—

— Fractures with regular to good conductivity — High confidence
 — Fractures with regular to low conductivity - - - - Regular confidence
 — Fractures with null conductivity

Table 5.8. Paragenetic chart from Core-4, W-3.

5.6 Image log analysis

Image logs were run in the three wells used for this project. However, some Mesozoic sections were not logged and therefore, information is incomplete. Nonetheless, valuable information can be obtained from the available information and each well will be described individually with relevant information from the image logs. Analysis was performed in two different scaled logs, 1:20 for detailed interpretation, and 1:500 for a quick review of the main structural and stratigraphic features (fractures and bed limits, respectively) as well as to define zones with higher fracture densities. These boreholes were drilled vertically using resistive oil-based mud, which makes the interpretation of open fractures difficult, since these may be filled with resistive mud-filtrate and therefore, indistinguishable from sealed fractures (resistive). However, analysis of processed DSI, where available, allowed zones with probable open fractures to be inferred. Image logs available for this study were already interpreted by the company service by defining bed limits and fractures with their corresponding fracture intensity, orientation and true dip. For this section, image logs were compiled, described and integrated with lithological descriptions in order to investigate the relationship between lithology and bed thickness versus fracture intensity.

5.6.1 W-1

Late Cretaceous (5760-5926 m): Three different sequences can be defined according to characteristics such as bed thickness, fracture density and vertical variations of conductivity/resistivity as a response of lithological changes (Figure 5.18). For this study, bed thickness description is based on the classification of Blatt et al., (1980).

- Sequence A (5790-5830 m): Lithologically, comprises marls interbedded with calcareous shale. Fracture density is low, bedding is thin to medium (3-30 cm) in the shaly intervals and thick to very thick (>30 cm) in the more carbonate beds. Bedding dip orientation is consistent towards W-SW, whereas dip angle is relatively low (5-10°).
- Sequence B (5830-5890 m): Bioclastic wackestone-packstone interbedded with white, recrystallized mudstone. Fracturing is scarce and bedding is mostly massive with very few bed limits interpreted.
- Sequence C (5890-5925 m): Shaly mudstone interbedded with bituminous, calcareous shale. Fracture density shows the higher values for this interval (3-4 f/m) in medium resistivity beds (5900 m) and bed thickness is mostly thin in shaly beds. Bedding dip orientation is also consistent towards W-NW (although local variations exist) and low dip angles are also consistent (5-10°).

Fractures show preferential orientations E-W and NNW-SSE throughout this interval; however, in sequences A and B fractures dip at angles between 40-60°, whereas in sequence C they dip at higher angles (70-80°).

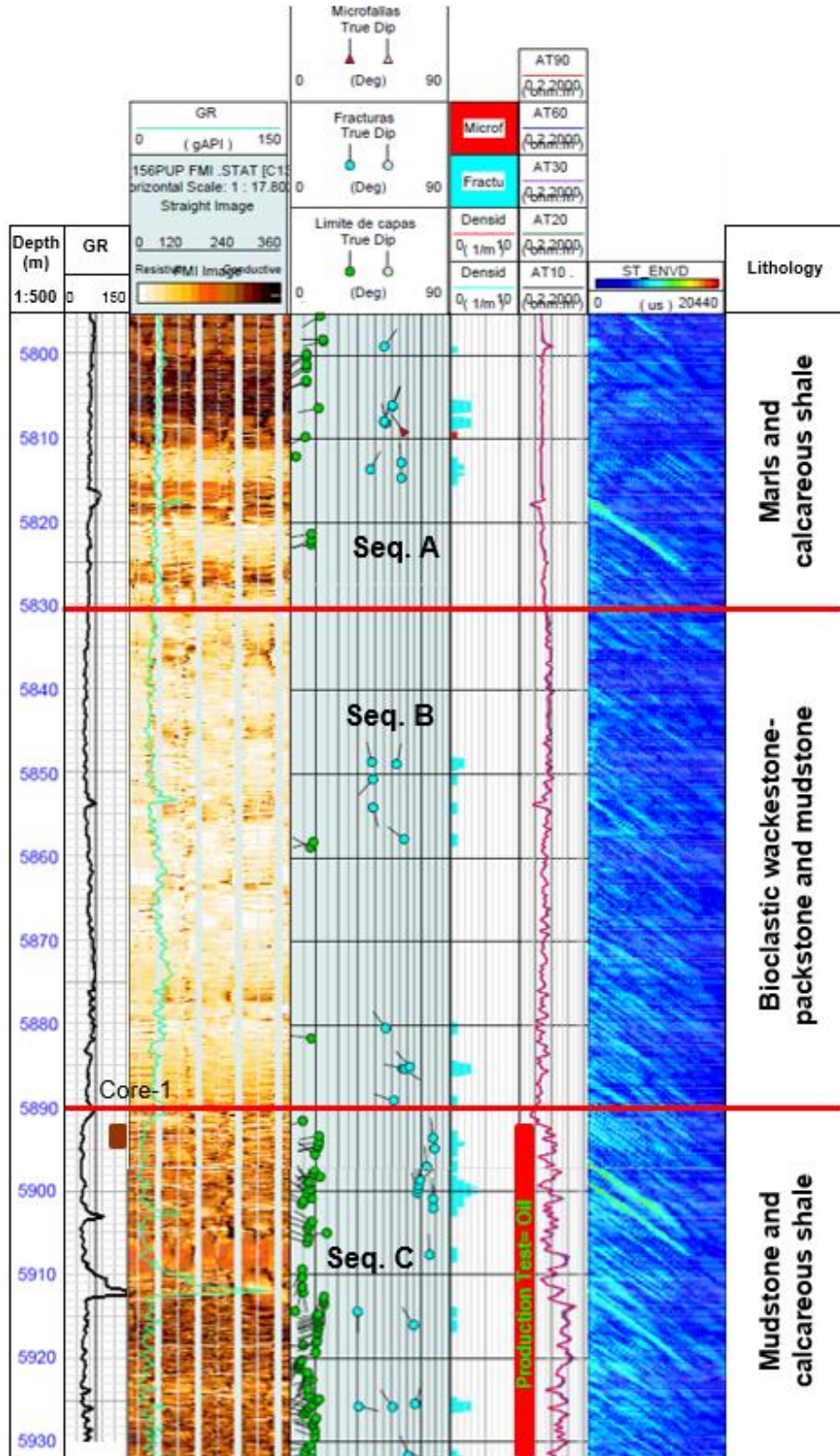


Figure 5.18. Composite log. W-1, Late Cretaceous.

Middle Cretaceous (5925-5976 m): Lithologically, this interval is very homogeneous and consists of shaly mudstone interbedded with foraminifera mudstone-wackestone. Fracture density is higher in shaly beds (most conductive), with most fractures dipping at high angles (70-80°) and orientated NE-SW. Bed thickness is highly variable, but medium to thick values (20-40 cm) are predominant. Bedding orientation and dipping are very consistent and similar to Late Cretaceous trends (Figure 5.19).

Early Cretaceous (5976-6060 m): Lithologically consists of foraminifera mudstone-wackestone interbedded with bituminous, shaly mudstone and thin beds of dark grey calcareous shale towards the base. Fracture density is low and high-angle dipping, except at the interval 5995-6000 m, where interpreted fractures show a relatively high fracture density (3-4 f/m), with no preferential orientations although a some dominance toward NE-SW and NNE-SSE and dips as low as 20° (Figure 5.19). Bedding is predominantly thick to massive but gradually becomes thinner towards the base of the interval. Bedding dip orientations are consistent with Middle and Late Cretaceous trends (W-SW and 5-10° respectively).

Late Jurassic Tithonian (6060-6317 m):

Three major sequences were defined for this interval according to fracture density, bed thickness and vertical changes in resistivity/conductivity. These are:

- Sequence A (6060-6110 m): Consists of foraminifera mudstone-wackestone, which becomes more shaly towards the base. Fracture density is low; however, dipmeter tadpoles suggest the presence of a fault in the interval 6080-6090 m, which is likely to be causing some observed fracturing orientated WNW-ESE (Figure 5.20). Bedding is mostly thin to medium (<30 cm), dipping at low angles (5-10°) towards NW preferentially.
- Sequence B (6110-6230 m): Consists of alternations between of bituminous, shaly mudstone-wackestone with abundant organic matter and bituminous calcareous shale. Fracture density values in the FMI log (up to 7-8 f/m) are the highest that occur in this borehole and are present in the interval with highest values of conductivity (most shaly). Fractures display different orientations and their dips are generally high (>70°). Dipmeter readings suggest the likely presence of a sub-seismic fault at 6150 m (similar to the fault within Sequence A), which may also be contributing to increased fracture density at this depth (Figure 5.20). Bed thickness is thick (> 30 cm) except in shaly intervals where bedding is thin to medium (< 30 cm). Bedding dips at low angles (5-10°) towards different orientations (NW, W, SW and SE).

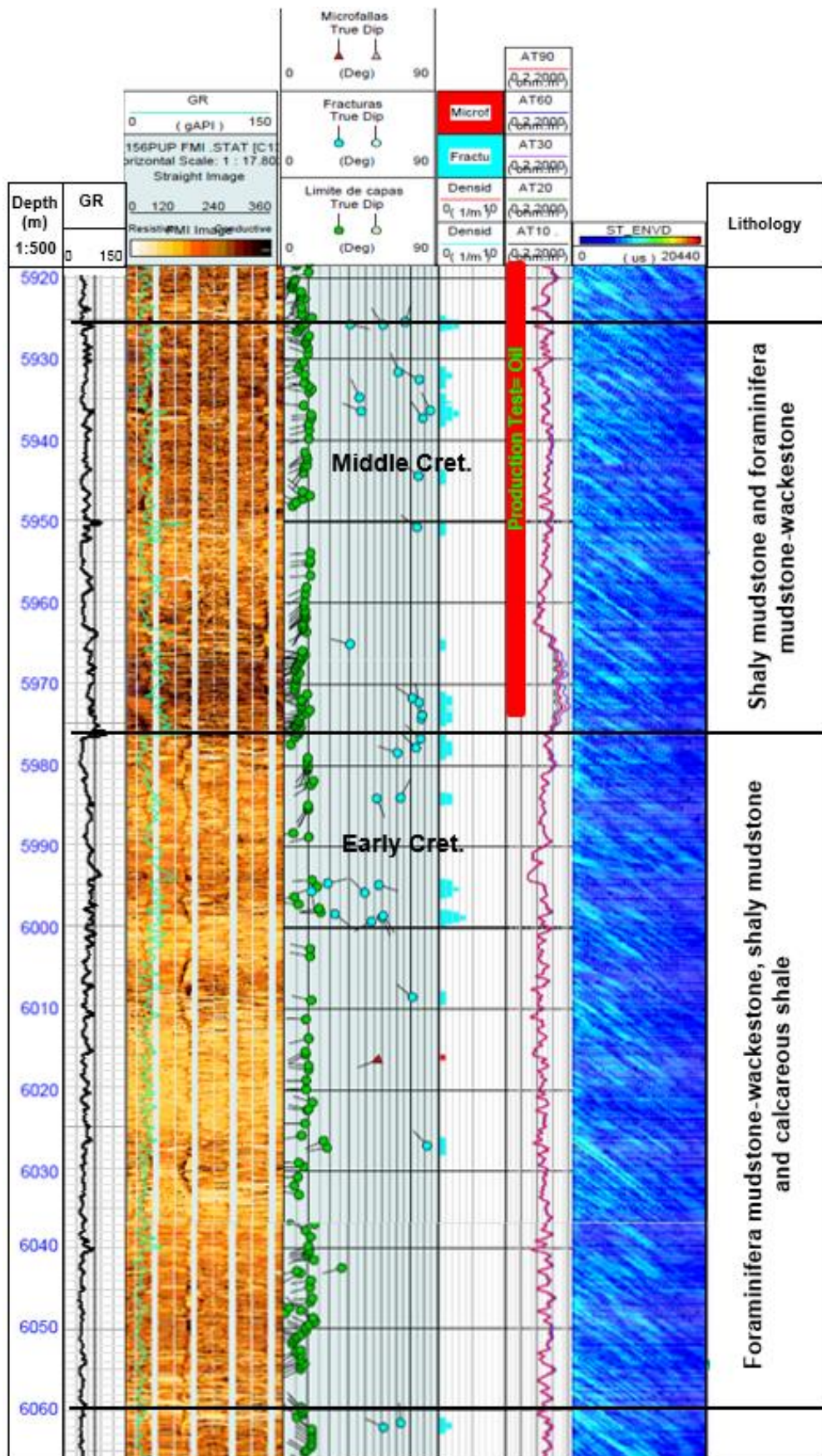


Figure 5.19. Composite log. W-1, Middle and Early Cretaceous.

- Sequence C (6230-6317 m): Lithologically this sequence is very similar to Sequence B; however, Sequence C is more resistive, perhaps reflecting differences in mineralogy. Bedding is generally medium to thick, dipping at low angles towards SSE and SE. Fracture density is low to medium (maximum 3-4 f/m in some parts), fracture dips are sub-vertical and almost perpendicular to bedding with different dip azimuths (N, NW and NE, mainly).

For the interval 5795-6183 m, some breakouts were observed, thus defining the present stress state, where σ_H (maximum horizontal stress favouring fracture re-opening) is oriented ENE-WSW and σ_h (minimum horizontal stress) is oriented NNW-SSE.

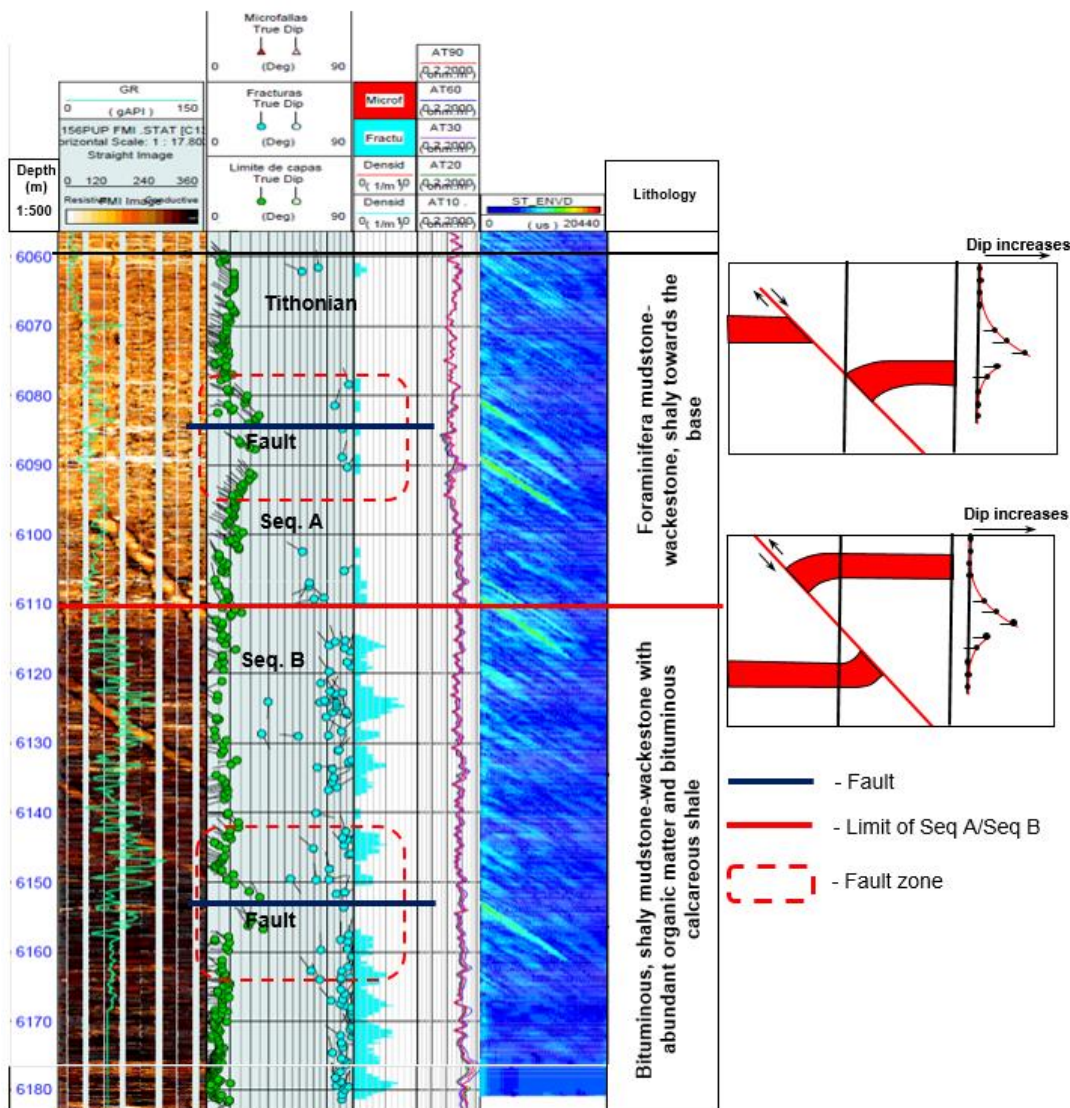


Figure 5.20. Left: Composite log from W-1, Late Jurassic Tithonian. Red dashed lines represent areas of probable sub-seismic fault zones according to the pattern of tadpoles, whereas dark blue lines represent the location of such faults. DSI log response seems to confirm the presence of faults. Right: Interpretation of tadpoles suggest the presence of faults with drag adjacent to fault; however, ambiguity prevents to define the sense of the faults (reverse/normal). Modified from Bengtson (1982).

Late Jurassic Kimmeridgian (6317- 6480 m): Sequences A and B, which were described lithologically in section 5.4.5, will now be described according to their observed characteristics in the image logs.

- Sequence A (6320-6450 m): Bed thickness is generally thin and medium (3-30 cm) from 6317 to 6383 m, and progressively becomes thick, even massive down to 6450 m. Fracture intensity can be considered relatively high, with average values of 3-4 f/m (Figure 5.21). Fractures dip at high angles and orientations are highly variable; however, in the interval 6400-6450 m, fracture density is too low or null to be recorded, except for a high fracture density at 6426-6428 m (5-6 f/m values). This decrease in fracture density seems to be associated with a progressive increase in both the conductivity of the rock (texture/lithological composition) and overall bed thickness.

- Sequence B (6450-6480 m): For this interval, fracture density is so low that only few fractures were interpreted in the image log (Figure 5.21). Likewise, few bed limits were interpreted thus suggesting massive bedding inherent to sedimentation, which consisted mainly of oolitic packstone.

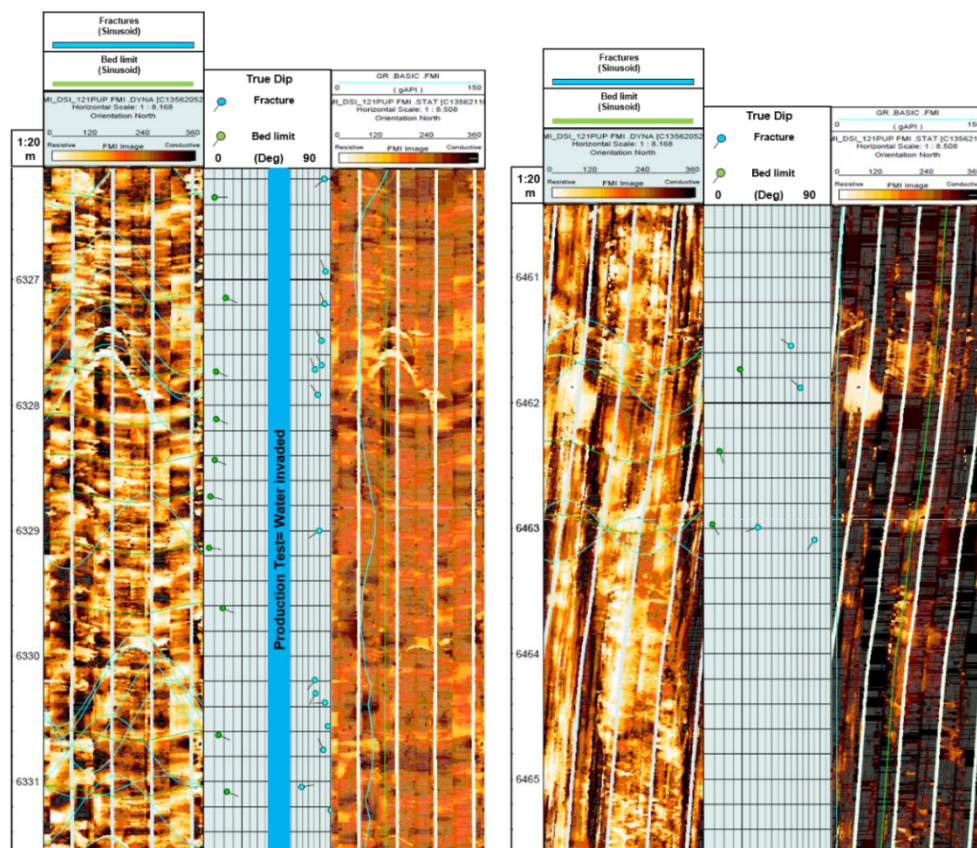


Figure 5.21. Image logs for W-1, Late Jurassic Kimmeridgian. Left: Sequence A; Right: Sequence B.

5.6.2 W-2

Imaging quality in the interval 6426-6880 m is poor and was affected mainly by the high content of solids within the drilling mud as well as mud salinity and borehole conditions such as ovalization, which caused poor contact and occasional sticking of the logging tool.

Late Cretaceous (5915-6025 m): Lithologically comprises mudstone interbedded with foraminifera mudstone-wackestone and shaly mudstone. Fracture intensity is low, even null, in the entire interval. Bedding is thick to massive and consistently dipping SW at an average angle of 10°.

Middle Cretaceous (6025-6195 m): Lithologically consist of foraminifera mudstone-wackestone lithology that is interbedded with shaly mudstone and shale. Fracture density is low, with the exception of layers at the top and bottom of this interval where fracture intensity values are up to 2-3 f/m, which can be considered as mechanical layers. No preferential orientation of fractures is observed, although at the interval 6175-6180 m fracture orientation is predominantly NE-SW 10° with high angle dips recorded (75-80°). Bedding thickness is thick to massive throughout the interval.

Early Cretaceous (6195-6300 m): Lithologically consists of foraminifera mudstone-wackestone interbedded with shaly mudstone and calcareous shale. Fracture density values are consistently low and null, except for a mechanical layer between 6265-6270 m where a few fractures were interpreted with an orientation of NE-SW 40-50° and dipping at high angles. Bedding thickness is generally thick to very thick.

Late Jurassic Tithonian (6300-6535 m): This consists of a broadly homogeneous lithology through the interval comprising a bituminous, shaly mudstone-wackestone with abundant organic matter interbedded with bituminous calcareous shale. Bedding ranges from medium to thick, even massive towards the top, dips from 10-15° and has a constant dip orientation of SSW-NNE (Figure 5.22). Fracture intensity is low (1-2 f/m) except at some intervals interpreted as mechanical layers (6330-6340, 6410-6425 and 6525-6540 m) where FI values reach up to 5 f/m (Figure 5.22). Dipmeter tadpoles show a possible sub-seismic fault event at 6485 m which could be associated with some fracturing immediately above.

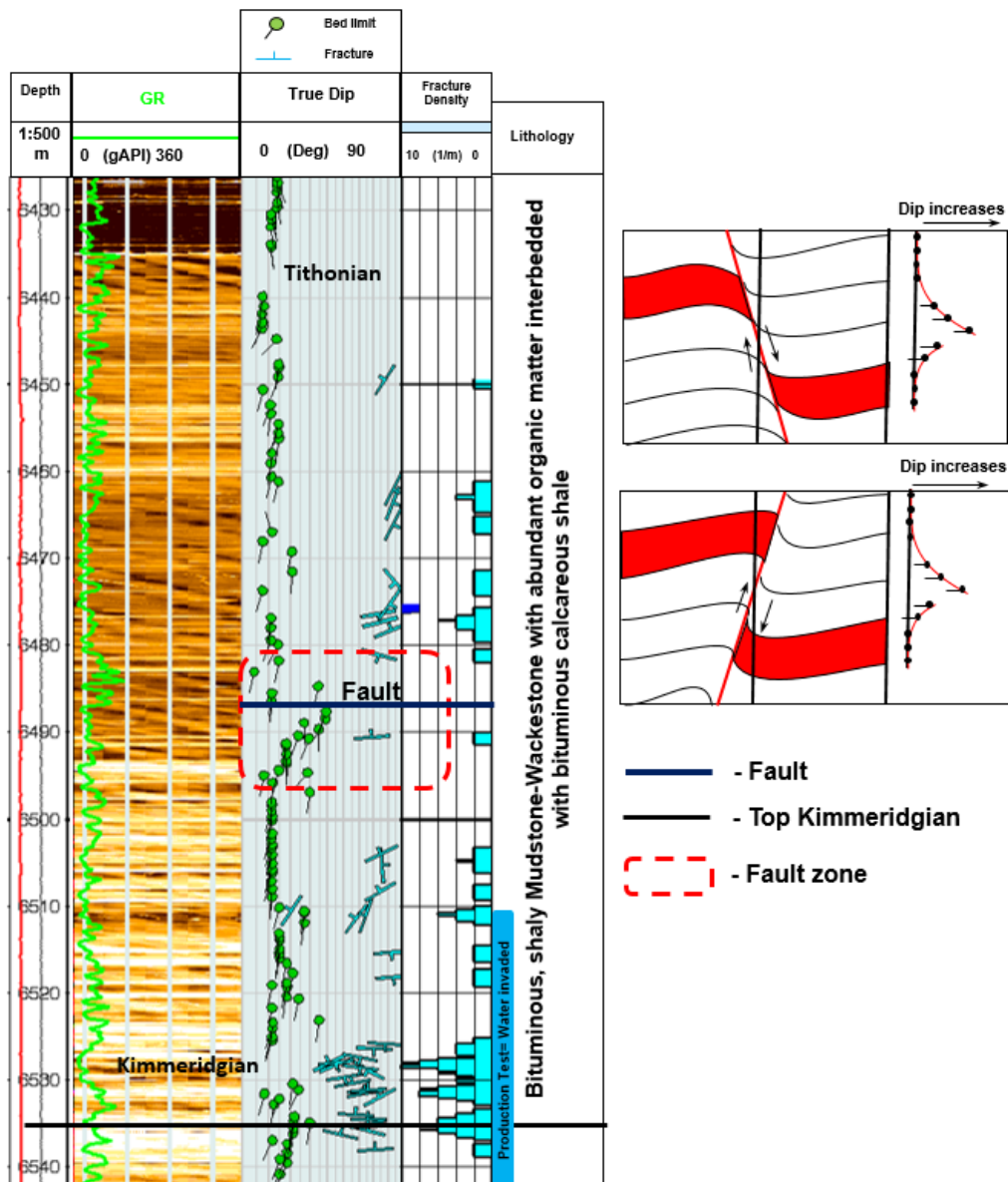


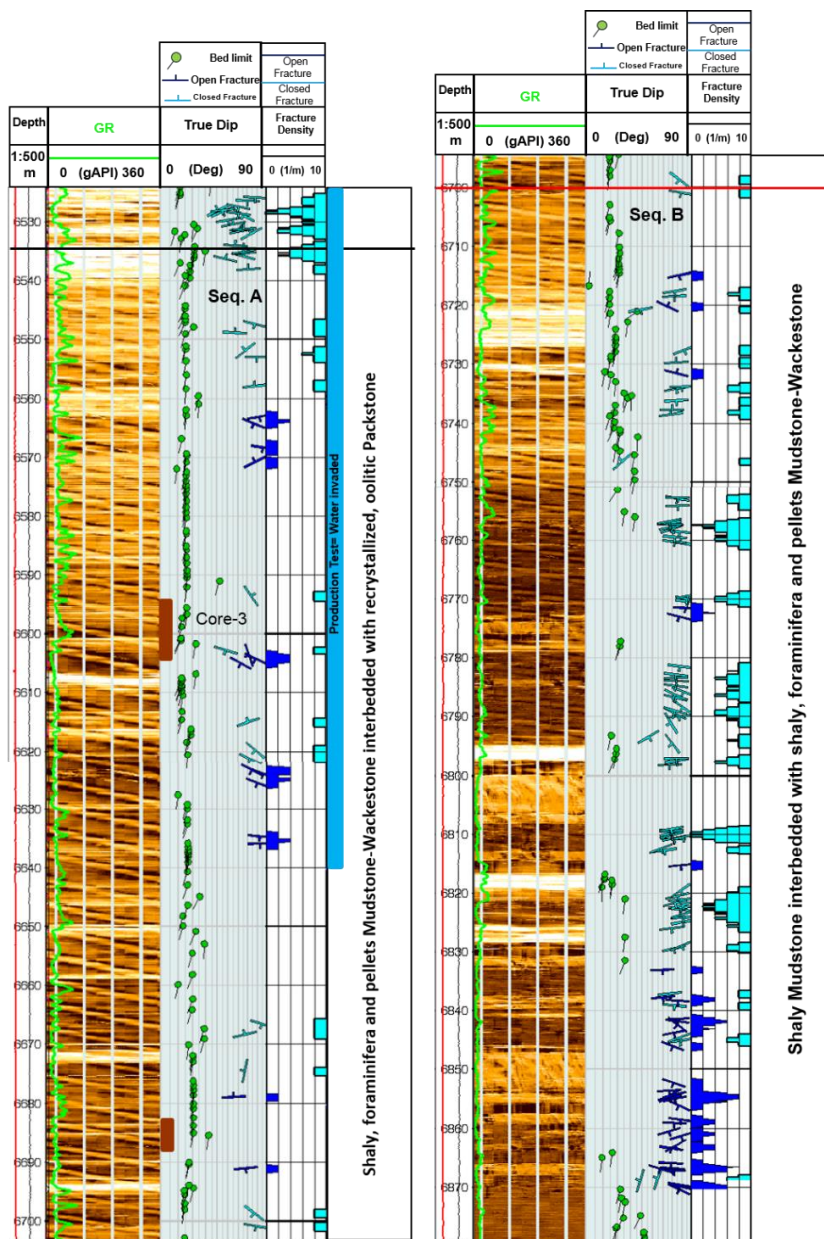
Figure 5.22. Composite log from W-2, Late Jurassic Tithonian. A fault (dark blue line) is interpreted at 6485 m according to the pattern of tadpoles. Right: Similarly to Figure 5.20, ambiguity in interpretation of tadpoles prevents to define the sense of the fault (reverse/normal). Modified from Bengtson (1982).

Late Jurassic Kimmeridgian (6535-6880 m): This interval was subdivided into two main sequences (A and B) based upon lithological characteristics, which also show well defined and differentiated bed thickness and fracture intensity.

- Sequence A (6535-6700 m): Lithologically consists of shaly mudstone interbedded with shaly, foraminifera and pellets mudstone-wackestone. Fracture intensity is low (average 1 f/m), and even null in thick intervals (Figure 5.23). However, high fracture intensity is located in the interval 6525-6540 m (up to 5-6 f/m). Fracture preferential orientations are E-W and NNW-SSE. Bed thickness ranges from medium to

thick towards the base and dip orientation is constant to the SW with angles of mostly 10-15°.

- Sequence B (6700-6880 m): Lithologically comprises shaly, foraminifera and peloidal mudstone-wackestone interbedded with recrystallized, oolitic packstone. Fracture intensity is higher than that of Sequence A (4 f/m average) with an increase in the number of potentially open fractures in the interval 6830-6880 m (Figure 5.23). Also, fracture orientations are similar to Sequence A. Bed thickness is medium to thick in the interval 6700-6760 m and becomes massive from 6760 m downwards. Bedding dip orientation in this sequence is similar to sequence A, but angles are slightly higher (20-25°).



- **Figure 5.23.** Composite log. W-2, Late Jurassic Kimmeridgian. Left: Sequence A; Right: Sequence B.

5.6.3 W-3

The interval 5300-5550 m was the only one to be logged in this borehole, containing information from the whole Cretaceous sequence but only 110 m from Late Jurassic Tithonian due to 7" casing cementation. An OBMI logging tool was used for this borehole, allowing the interval to be imaged but with a reduced coverage of only 35% of the area in an 8" borehole. Also, this type logging tool cannot image small features as other tools do, and, consequently, only major features can be interpreted. No distinction between open and closed fractures was made due to the type of oil used in this borehole.

Late Cretaceous (5320-5355 m): Consists of mudstone lithology interbedded with shaly mudstone, flint nodules and calcareous shale towards the base. Fracture intensity is relatively high with an average of 3-4 f/m in the image log and preferential orientations NE-SW and NW-SE (Figure 5.24). Bedding thickness is thick in the upper part of the interval and progressively thins toward the base. Bedding dips mostly to the SE at angles of 20-25°.

Middle Cretaceous (5355-5375 m): Is lithologically very similar to the Late Cretaceous except for the lack of interbedded shale. Fracture intensity is slightly lower than Late Cretaceous (average of 2-3 f/m) with preferential orientations NNW-SSE and NE-SW. Bed thickness is medium to thick through the interval and constantly dipping to the SE at 15-20° (Figure 5.24).

Lower Cretaceous (5375-5440 m): Lithologically identical to Middle Cretaceous. In terms of fracture intensity, this is higher in the interval 5375-5410 m (average of 2-3 f/m) whereas in the interval 5410-5440 m average fracture intensity is 0-1 f/m (Figure 5.24). Preferential fracture orientations are E-W and SSE-NNW. Bed thickness is highly variable, but generally is thick to massive, specifically in the interval 5390-5410 m.

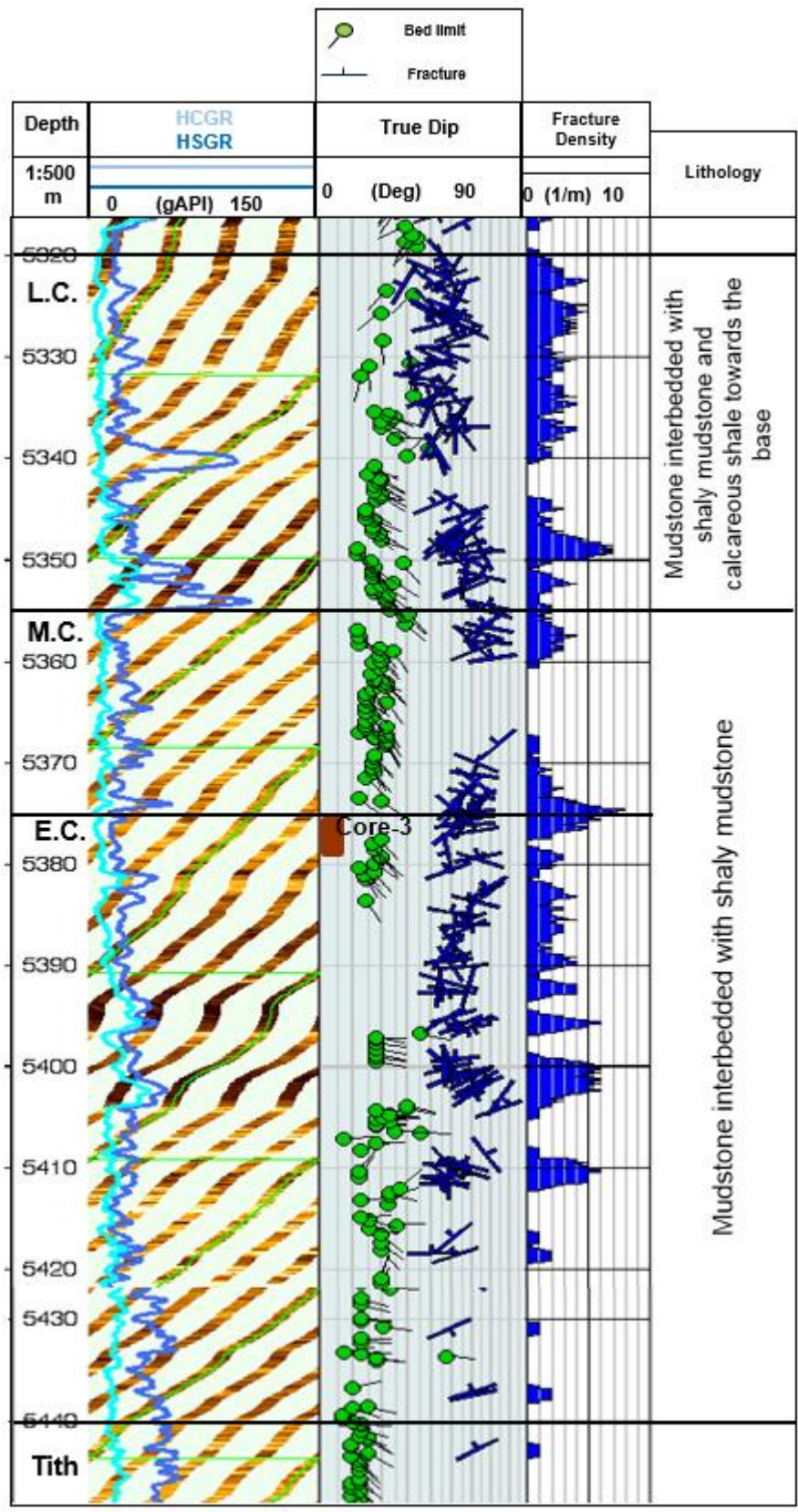


Figure 5.24. Composite log. W-3, Cretaceous. L.C.= Late Cretaceous; M.C.= Middle Cretaceous; E.C.= Early Cretaceous; Tith=Tithonian.

Late Jurassic Tithonian (5440-5640 m): Lithologically consists of bituminous mudstone interbedded with calcareous shale. Fracture intensity is very low and only a few fractures were interpreted within this interval (Figure 5.25) in spite of the possible presence of a fault at 5465 m. By contrast, bedding is highly developed and thickness is low to medium through the whole interval with a constant, preferential dipping orientation towards the East at angles of 15-20°.

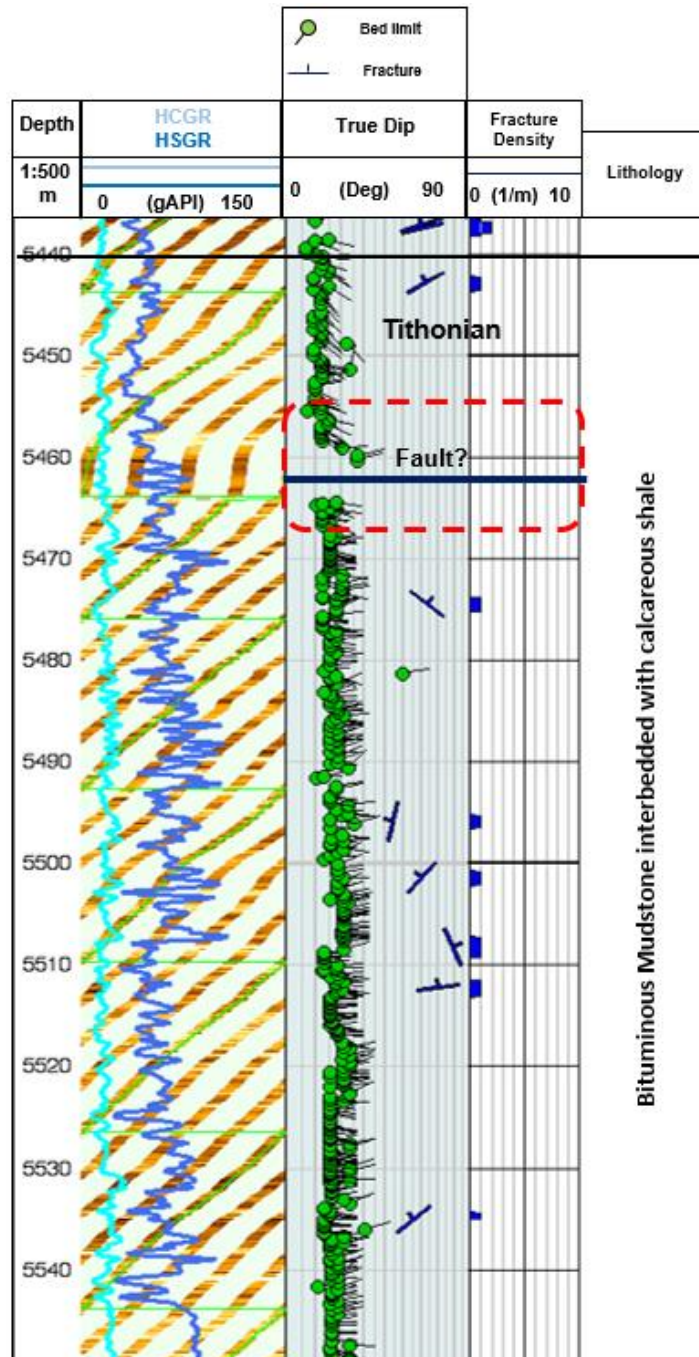


Figure 5.25. Composite log from W-3, Late Jurassic Tithonian. Very low fracture intensity characterizes this interval even when a fault (dark blue line) is interpreted at 5465 m.

5.7 Discussion

This study investigated the relationship between different geologic controls (lithology, texture, bed thickness and faulting) and natural fracture intensity. General tendencies and relationships were observed. First, original rock texture seems to be the primary control in natural fracturing, and mud supported textures show higher fracture intensities than grain supported textures. Second, the effect of lithology is that pure limestones are more fractured than dolomitized limestones or dolomites, although the opposite effect also occurs. Third, thin to medium thickness beds have higher fracture densities than thick or massive beds. However, contradictory observations for each of the analysed factors suggest a complex interaction between them, so no rules of thumb should be assumed. Finally, a strong correlation between fracture orientations measured in core samples and image logs was found, thus suggesting a fractal relationship at two different scales of observation.

Well	No.	Depth (m)	Age	Lithology/Environment	Texture	Fracture intensity in core sample	Fracture intensity in image logs (f/m)	Young's Modulus (Gpa)
W-1	1	5892-5895	Late Cretaceous (Turonian)	Shaly, light gray, fossiliferous Mudstone- Wackestone / Basinal	Micritic	Moderate to high	1-2	52
	1C	6023-6025.5 6025.5-6034	Late Cretaceous (Conacian-Santonian)	Light gray, fossiliferous Wackestone-Packstone / Basinal	fine-grained	High	No data available	58
W-2	2	6325-6334	Late Jurassic Tithonian	Shaly, dark gray, Mudstone-Wackestone interbedded with black, bituminous, calcareous shale/ Basinal	fine-grained	No data available	No data available	
	3	6595-6604	Late Jurassic Kimmeridgian	Shaly, light/dark brown, Mudstone / Basinal	Micritic	Moderate	2-3	69 (correlation with W-1)
	4	6683-6688.3	Late Jurassic Kimmeridgian	Shaly, dark brown, bioclastic Mudstone – Wackestone / Inner platform	Micritic	Low	0-1	80 (correlation with W-1)
	3	5376-5379	Early Cretaceous (Valanginian)	Light brown, gray Mudstone - Wackestone / Basinal	Micritic	High	3-4	57
W-3	4	5651-5660	Late Jurassic Kimmeridgian	Light gray Grainstone (oolites, pellets, intracasts and bioclasts) / Inner platform	Microcrystalline dolomitization	Low to moderate	No logs run	67 (correlation with Kb-1)
	5	5815-5824	Late Jurassic Kimmeridgian	Dark brown, brechoid, micro to meso-crystalline Dolomite / Inner platform	Micro to meso-crystalline	Low to moderate	No logs run	67 (correlation with Kb-1)

Table 5.9. Comparison between lithology from cores, fracture intensity and Young's modulus for the study area.

5.7.1 Fracture intensity vs lithology

A summary of the results from the analysis of cores, thin sections and well logs is listed on Table 5.9. Comparison between lithology from cores, fracture intensity and Young's modulus for the study area. In general terms, for the study area, limestones (mudstone-wackestone) deposited in a basinal environment show higher fracture densities than partially dolomitized limestones or dolomites deposited in shallow environments (inner platform); however, in borehole W-2, for Kimmeridgian aged rocks, FI values observed in partially dolomitized limestones (Seq. A) are higher than those observed in pure limestones (Seq. B). These contradictory results support the idea that lithology may not

be a primary control on natural fracturing but secondary to other parameters such as rock texture, bed thickness, the presence of faults, or structural position (Giorgioni et al., 2016). It is worth mentioning that the values of Fracture Intensity (FI) in core samples column (low, moderate and high) are of qualitative nature and obtained from visual inspection from different geologists and no numerical references are indicated for such values. Conversely, quantitative FI values from image logs obtained in this study seems to support this relationship, where higher and lower FI values (fractures per meter) match with visual FI values obtained during core analysis; however, only four cores could be correlated with the image log due to lack of log runs and available data.

Analysis of image logs also show that intervals with higher FI values tend to have a more conductive response, which may be related to electric conductor mineralogical composition (some types of clay, pyrite) or another factors such as water-based mud in fractures, dissolution cavities or porous space (Mantilla et al., 2015). With this in mind, mineralogical composition of any given lithology may exert a major control on fracturing rather than the lithological texture, since different FI values are present in intervals with similar lithology (e.g., Tithonian in wells W-1 and W-3) but different conductive/resistive responses (conductive in W-1 and resistive in W-3) as shown in figures 5.20 and 5.25.

5.7.2 Fracture intensity vs Texture

Texture is not only associated with depositional conditions but it is also the result of diagenetic processes through time, which impact on reservoir rock quality, either by creating porosity/permeability (dissolution, fracturing) or destroying it (cementation, compaction) as well as modifying mechanical rock properties.

In general terms, for the study area, the mud-supported textures (mudstone-wackestone) that were deposited in a basinal environment show higher fracture densities than grain-supported textures (packstone-grainstone) deposited in shallow environments (inner platform) as shown in Table 5.9. Paragenetic charts show a similar diagenetic evolution for the different core samples, where in most cases, diagenesis didn't substantially modify the original mineralogy and texture of the rock; moreover, syn-kinematic cementation during the initial fracturing episodes could have increased rock stiffness and brittleness, thus making it more prone to fracturing during later tectonic deformational events. In the case of borehole W-2 Core1, early silicification along with dolomitization, may have contributed to making this rock interval prone to the observed higher fracture density. Conversely, where diagenesis modified the original texture by early dolomitization of the rock's grain components (e.g. oolitic packstone from W-3, Cores 4 and 5), FI visual values are reported as low to moderate. These results suggest that the

original texture may exert a primary control on natural fracturing, rather than lithology or diagenetic changes.

5.7.3 Fracture intensity vs Bed thickness

Cumulative Fracture Intensity (CFI) plots are a valuable tool to identify mechanical stratigraphy from image logs as well as to define relationships between fracture intensity and geological parameters such as bed thickness, stratigraphy and structural features, among other applications (La Pointe, 2010).

For this study, CFI plots were constructed for every chronostratigraphic unit from the three boreholes in the study area. The vertical axis corresponds to depth whereas the horizontal axis is the normalized number of fractures and bed limits interpreted from image logs. Lithostratigraphic boundaries and faults were also plotted as horizontal lines as a reference to relate these two factors to fracture intensity (FI). Non-fractured intervals can be identified as intervals where fractures are not plotted; likewise, massive-bedded intervals are identified as intervals where no bedding limits are plotted.

Some mechanical layering has developed in the Mesozoic sequence at different stratigraphic levels. In the CFI plots, these features are characterized by sub-horizontal slopes of lines connecting fractures which are separated from other layers with different FIs (different slopes) or bounded by non-fractured layers (Figure 5.26). No relationship seems to exist between mechanical layering and bedding thickness at this scale of observation, thus suggesting that heterogeneity of rock properties between different facies and within individual facies associated to sedimentary cycles may be controlling the vertical and horizontal distribution of such mechanical layers. In other words, mechanical stratigraphy (which in turn, is controlled by diagenesis) may be controlling fracture stratigraphy (Laubach et al., 2009).

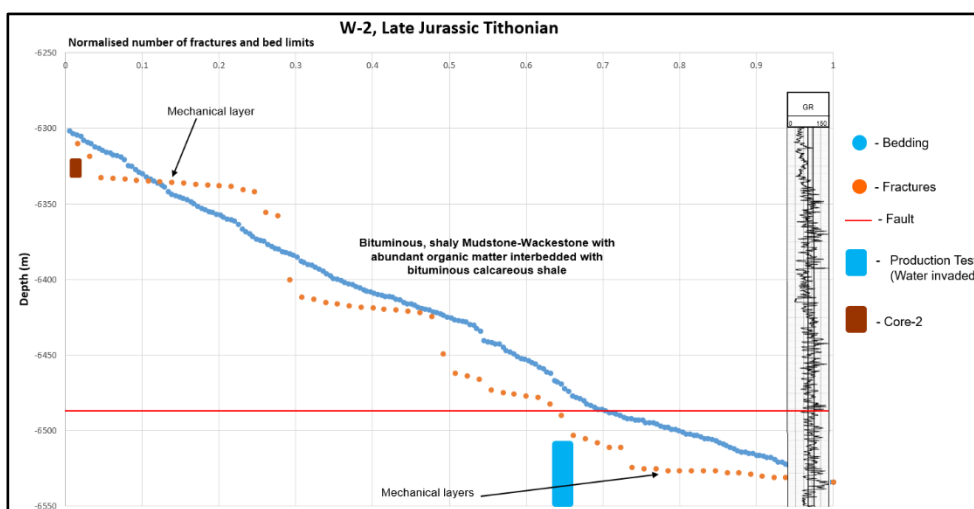


Figure 5.26. CFI plot showing the presence of mechanical layers in Tithonian sediments from borehole W-2.

Carbonate rocks can show strong and complex vertical and lateral variations at every scale of observation, and so a correlation of their properties can be difficult in order to define a more generic set of relationships. However, some similarities in the fracturing patterns exist between Cretaceous (W-1 and W-3) intervals, which can be correlated, and even extrapolated to undrilled localities with similar characteristics to some extent and taking into account other geological controls as well (Figure 5.27).

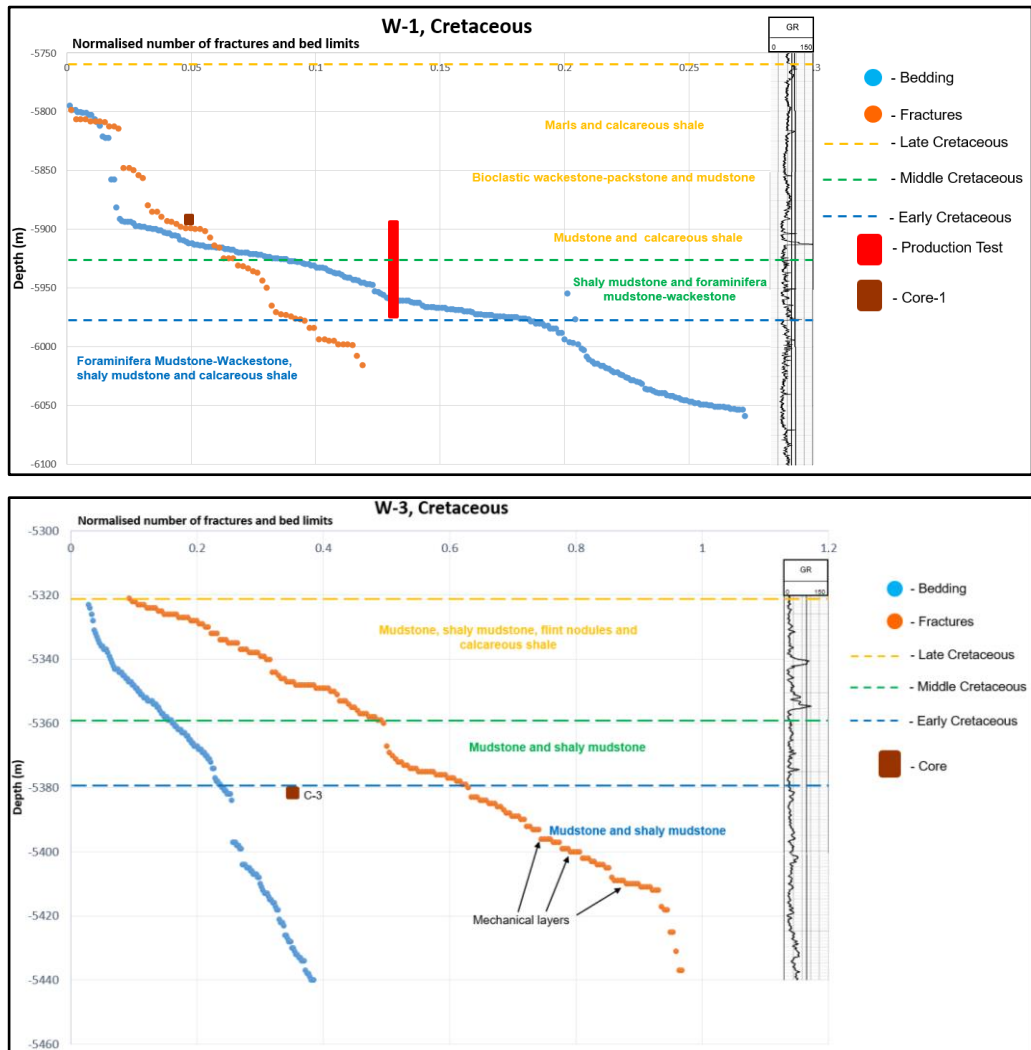


Figure 5.27. Comparison of fracture patterns (orange dots) in Cretaceous rocks between boreholes W-1 (top) and W-3 (bottom). These patterns show similarities in slope angles and shapes and could be extrapolated to undrilled areas with similar characteristics.

Generally, FI has been found to decrease in intervals where bedding is poorly developed or massive. Conversely, higher FI values are mostly located in intervals where bedding is well developed (thin to medium), thus suggesting that bed thickness may exert a control (probably secondary to lithology) on FI at least at a meso-scale (>10 m). On the other hand, there are some intervals shown in Figure 5.27 (Early Cretaceous, W-3) and

Figure 5.28 (Seq. B, Kimmeridgian, W-2; Seq. A, Kimmeridgian, W-1) where bedding is poorly developed but yet relatively high FI values are recorded, and intervals with well-developed bedding that have low or null FI, indicating that while fracturing is controlled partially by bed thickness, this may be subordinated to another factors.

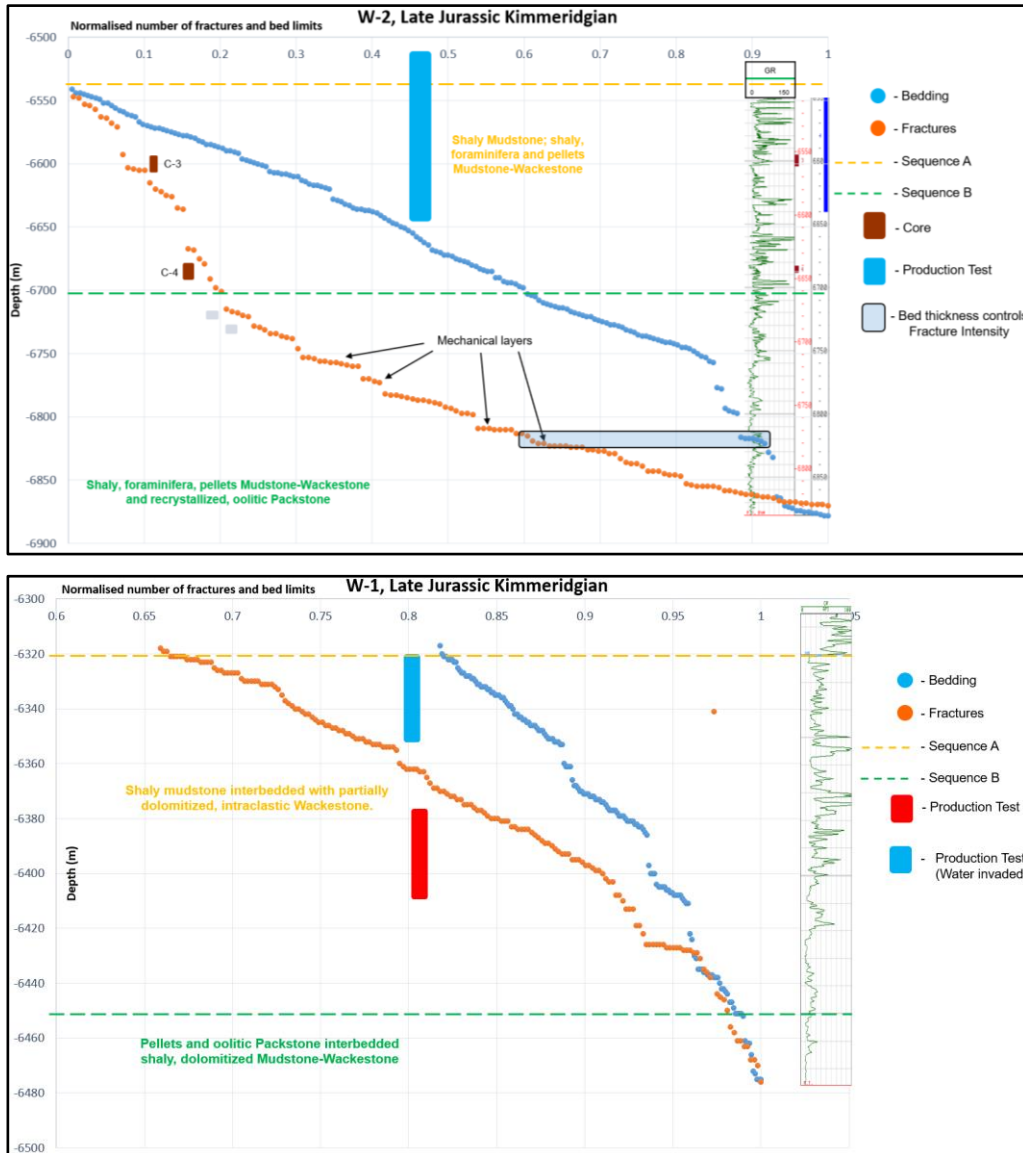


Figure 5.28. Relationship between FI and bed thickness from Kimmeridgian sequences in boreholes W-2 (top) and W-1 (bottom). Although the expected inverse relationship (thicker beds=less fractures) can be defined, some intervals show the opposite tendency, evidencing the secondary influence of bed thickness on FI.

At a smaller scale (<10 m); however, no relationship seems to exist between FI and bed thickness (BT), since high FI values can be present in both thin and massive beds. Nevertheless, some specific intervals show some direct association between FI and BT, and these are identifiable in the CFI plots where bedding and fracture layers start and finish at the same depth and their respective slopes are the same (Figure 5.29).

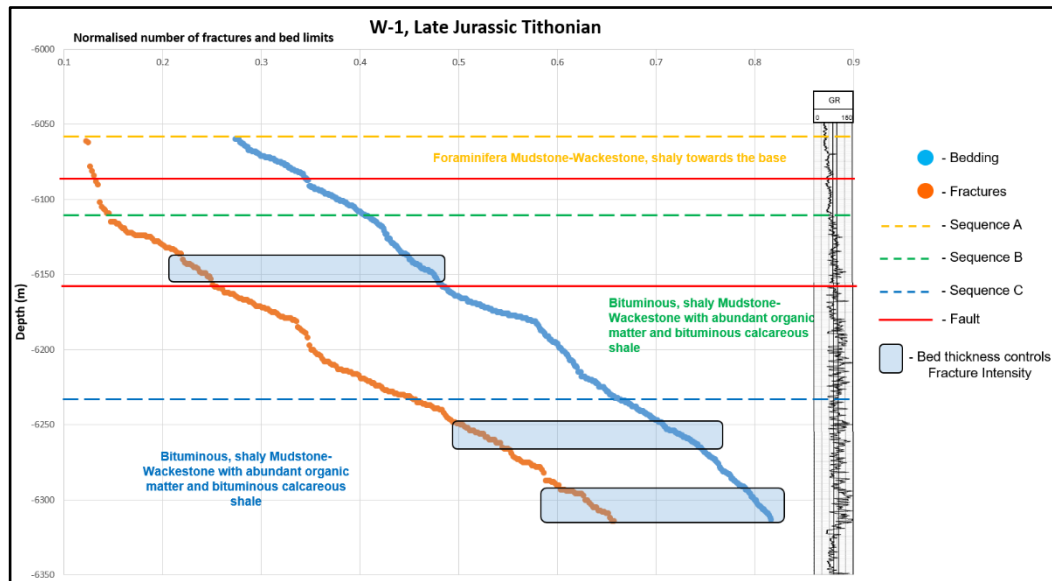


Figure 5.29. CFI plot showing the presence of intervals where bed thickness seems to control FI. These intervals (shaded rectangles) are characterized by identical slopes in both fracture and bed limits lines.

5.7.4 Fracture intensity vs faulting

This relationship is a function of several factors such as lithology, distance from the fault plane, the amount of fault displacement, total strain in the rock mass, and depth of burial (Nelson, 2001). Moreover, a predominance of any of these factors is variable from fault to fault. From image log analysis, four possible sub-seismic faults intersect the Tithonian interval in boreholes W-1 (6085 and 6155 m), W-2 (6485 m) and W-3 (5465 m). These faults were also plotted in the corresponding CFI plots. In borehole W-1, both faults seem to be associated with some minor fracturing on both sides of the fault (Figure 5.29). Conversely, in borehole W-2 very few fractures are present adjacent to the fault (Figure 5.26), whereas in W-3 the zone adjacent to the fault is non-fractured (Figure 5.30). This suggests that particular characteristics of the faults that cannot be quantified here, such as size and/or displacement, may control fracture intensity at those particular intervals, since their lithologic characteristics are very similar and bedding is well developed. Another explanation is that diagenesis may have modified selectively these intervals and, therefore, making them less prone to fracturing.

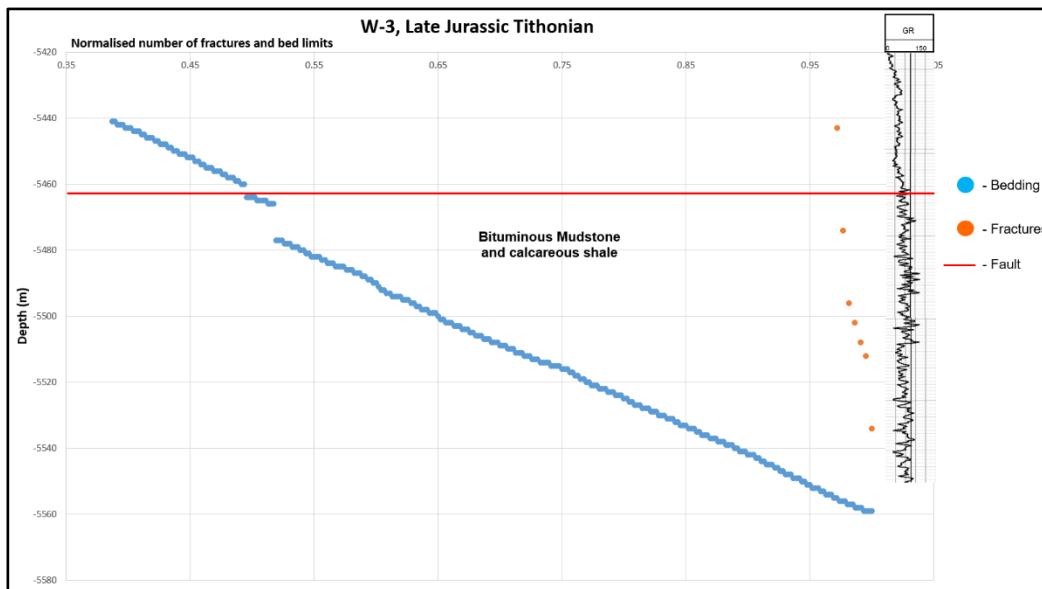


Figure 5.30. CFI plot from borehole W-3. No fractures are present adjacent to the interpreted fault from Figure 25.

5.8 Integration of core and well log data

A combined analysis of information from these two sources results in a more reliable interpretation of the fracture systems by linking two different scales of observation, although they have limitations in sampling since they are not vertically continuous (except for core samples, but these do not exceed 9 m) or laterally continuous (as image logs normally are not able to fully register larger than borehole diameter fracture lengths). The orientation of microfractures observed in thin sections (Section 1.3) and cores show a strong correlation with orientations of fractures interpreted in image logs for the three boreholes in the study area (Figure 5.31). Also, fracture densities in cores and well logs show a positive correlation. This supports the concept of a fractal relationship (similar patterns at different scales of observation) characterized by a power-law distribution (Nicol et al., 1996; Bour and Davy, 1999), although in this case only fracture density and orientation, not fracture length, are considered. The matching of results from well data at different scales, together with other structurally-focused analysis, can be very useful to use as analogues during exploratory stages in hydrocarbon exploration. Estimation of fracture density and orientation in undrilled areas could be more confidently defined if geological conditions are considered to be similar.

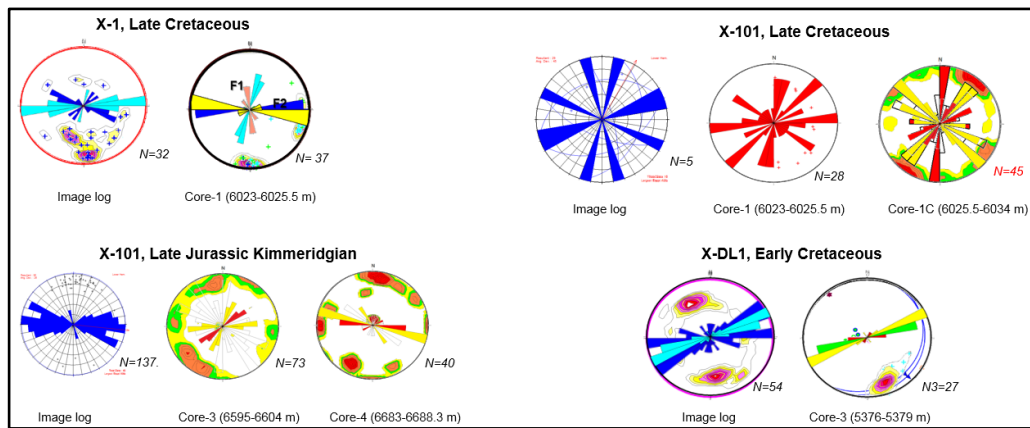


Figure 5.31. Rose diagrams showing a comparison between fracture orientations obtained from image logs and core samples.

5.9 Conclusions

Analysis and integration of well data allowed this study to identify some of the geological controls on natural fracturing of carbonate Mesozoic rocks from the Southern Gulf of Mexico. Conclusions from this chapter are summarized as follows:

- A complex interaction of different geologic factors such as texture, lithology, bed thickness, rock brittleness and fault presence influenced natural fracturing in carbonate rocks.
- The original texture of the rock seems to exert the primary role in natural fracturing. Mud supported textures (mudstone-wackestone) deposited in a basinal environment show higher fracture densities than grain supported textures (grainstone-packstone) deposited in shallow environments.
- Lithology seems to exert a secondary role in natural fracturing. For the study area, limestones generally show higher fracture densities than partially dolomitized limestones or dolomites, except for Kimmeridgian rocks in W-2 where the opposite occurs, maybe as a result of the influence of another factors.
- Bed thickness seems to exert a secondary role in natural fracturing. Although the well-known inverse relationship between bed thickness and fracture intensity was observed in a first-order scale, a direct relationship was also observed at some specific intervals.
- The superimposed effect of several geological factors, their strong lateral, vertical and temporal variations, along with the fractional nature of information sampling makes difficult to define accurately the individual effects of each factor. However, some general assumptions can be made and used as analogues to extrapolate to undrilled areas.

Chapter 6

Analysis of structural seismic attributes and geomechanical modelling for fracture interpretation

6.1 Introduction

The development of natural fracture systems in the subsurface results from the complex interaction of applied stresses and diagenetic processes during the burial history. Likewise, the relationship between fractures and folding when formed simultaneously is widely acknowledged and conceptual models have been proposed where fracture sets show predictable symmetric orientations with respect to the fold geometry (Nelson, 1985; Price, 1966; Stearns, 1968; Liu et al., 2016) and intensity also varies according to the structural position; moreover, if sets of pre-folding and/or post-folding fractures are also present these may enhance the ability of carbonate rocks to host fluids of economic importance in the subsurface. An accurate prediction of the orientation and intensity of fracture sets in the subsurface during the exploration stage in undrilled areas is crucial in order to assess the quality of a prospective reservoir rock in hydrocarbon exploration, due to their important role in enhancing porosity and permeability of tight carbonate reservoirs (Anjaneyulu et al., 2011). Moreover, fault mapping also helps to determine the size, geometry and the level of compartmentalization of hydrocarbon reservoirs (Jibrin, 2009).

Structural attributes within seismic reflection data sets (coherency/variance, curvature, ant-tracking) are commonly used to interpret the smaller-scale tectonic features that are easy to overlook in the conventional amplitude volume such as fault/fracture zones, small flexures and folds (Marfurt and Alves, 2015). On the other hand, geomechanical modelling is a relatively new analysis that allows us to visualize the effects of deformation of a given surface by calculating the strain needed to deform it. A direct relationship between fracture intensity and strain is generally acknowledged (Nelson 1985; Price, 1966); moreover, as strain increases with structural deformation, the structural position relative to a developing fold may be related to fracture intensity; however, factors such as lithology, bed thickness and the rock's brittleness makes this relationship very complex (Watkins et al., 2015; 2018; Price, 1966). This approach of the curvature radius/strain/fracture intensity is the theoretical background for structural seismic attributes (Roberts, 2001; Marfurt, 1998).

Extensive research on the use of different structural attributes in seismic data sets to detect fracture zones (Blumentritt et al., 2006; Chopra and Marfurt, 2007; Ngeri et al., 2015; Odoh et al., 2014; Maleki et al., 2015; Jibrin et al., 2009; Kalid et al., 2016) and its integration with borehole data (Hunt et al., 2009; Arasu et al., 2011; Astratti et al., 2012) contrasts with the few investigations about strain and fracturing (Watkins et al., 2015; 2018).

This chapter has two aims: 1) to investigate the influence of structural position and the mechanism of deformation on the development of natural fracture systems in three anticlines within the study area (Figure 6.1), which are the result of contractional events that folded and faulted the Mesozoic column (the main targets for hydrocarbon exploration) and their geometries and evolution are strongly influenced by salt tectonics; 2) to predict the orientations of fracture sets and qualitative fracture intensities in undrilled areas. To achieve this, this study is focused on the integration of two independent analyses, specifically: structural seismic attributes and geomechanical modelling. The results of these combined analyses will also be tested and calibrated with the available borehole data in order to define a model of sequential fracture development as well as to investigate its potential as a tool for estimating fracture intensity and orientation in undrilled areas.

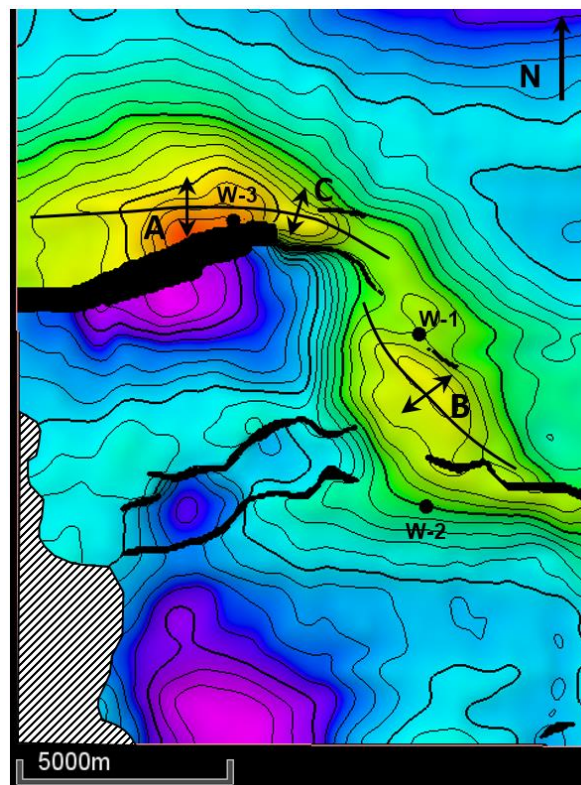


Figure 6.1. Top Kimmeridgian structure map showing the locations of the three analysed anticlines (A, B and C) and locations of boreholes used for this study.

6.2 Background

6.2.1 Seismic Data

In order to understand the nature and characteristics of the seismic data used for this project, it is necessary to highlight some aspects that are relevant for the analysis carried out in this chapter, such as fundamentals of Reverse Time Migration (RTM), Processing sequence and seismic resolution, which impact directly on quality of seismic image, and consequently, on analysis results. Structural complexity, strong presence of allochthonous and autochthonous salt are some other important issues that strongly affects seismic imaging.

6.2.2 Reverse Time Migration (RTM)

Seismic surveying is not only the most effective method to obtain indirect images from the subsurface, but also the information obtained from it is the best source to map structures, sedimentary features and different properties of the subsurface (Zhou et al., 2018). Continuous advances on computational capacity, along with the interest from the oil industry to obtain higher resolution and image quality, have made possible the development of imaging algorithms that allow to improve seismic imaging (Kirchhoff, Beam, Wave Equation, RTM), and therefore, reduce the risk on petroleum exploration. The seismic volume used for this project was depth-migrated using the Reverse Time Migration (RTM) algorithm, which has several advantages including: superior amplitude preservation, higher signal-to-noise ratio, the ability to handle steep dips (>70 degrees) and improved sub-salt imaging (Figure 6.2). These two latter in particular make RTM the most efficient method for seismic imaging in areas with high structural complexity and/or high lateral velocity complexity (Boechat et al., 2007; Jones et al., 2007). Although there is no way to quantify the term “structural complexity” since it is a rather subjective concept, for seismic imaging purposes, it is related to the presence of geological features such as steep dips, folding, intense faulting and presence of salt bodies, all of which are associated to imaging issues such as complex raypaths, seismic velocity anisotropy, P- and S-wave mode conversions, and reflected refractions (Jones and Davison, 2014).

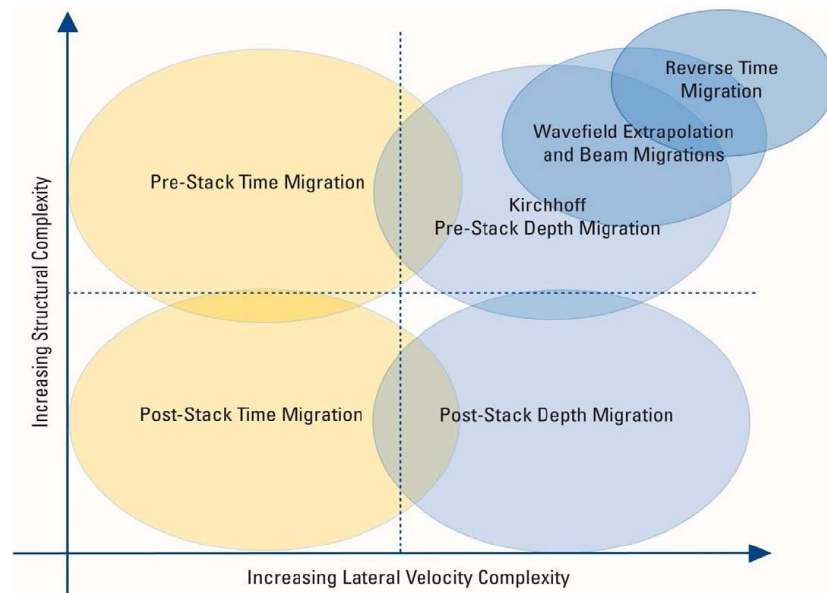


Figure 6.2. Comparison between different migration algorithms. NExT Training course notes (2011).

6.2.3 Structural Seismic Attributes

A seismic attribute is a measurement obtained from seismic data that highlight features associated with the amplitude, phase and frequency variations of the seismic signal (Espinoza Carrasco, 2016). As a result, seismic attributes provide a very valuable aid to seismic interpretation, since these variations in seismic signal may be associated with structural and stratigraphic features and, therefore, help to define both the geologic characteristic and evolution of a specific area (Chopra and Marfurt, 2007). Seismic attributes are grouped into two classes; physical and geometric. The latter includes dip, azimuth, curvature, coherence, variance, chaos and ant-tracking, all of which enhance the visibility of the geometrical characteristics or shape of seismic reflectors, while physical attributes (amplitude, phase, and frequency) are related to the lithologic characteristics in the subsurface (Jibrin, 2009).

Structural attributes that are most useful in structural analyses (coherency/variance, curvature), are commonly used to interpret tectonic features that are easy to overlook in the conventional amplitude volume such as fault/fracture zones (coherence, variance), small flexures and folds (curvature), and differential compaction features involving lateral changes in thickness and lithology (spectral components) (Marfurt and Alves, 2015).

Curvature

Mathematically, it can be defined as the rate of change of direction of a curve (Roberts, 2001) or as the radius of a circle tangent to a curve (Chopra and Marfurt, 2007). For conventional purposes, a *positive curvature* is considered for anticlines, *negative curvature* for synclines, and *zero curvature* for planar surfaces (Figure 6.3). Three dimensional shapes of a surface can be described by the combination of *mean curvature* (the average of two orthogonal normal curvatures) and *Gaussian curvature* (the product of the principal curvatures), thus making it possible distinguish between differently shaped surfaces such as spherical and elongated domes, cylindrical ridges, elongated and perfect saddles (Roberts, 2001, Figure 6.4). Figure 6.5 illustrates the effect of the quadratic approximation of surfaces in curvature calculation, where high curvature values correspond to the upthrown side and high negative curvatures to the downthrown side. Consequently, faulted rock blocks may be identified using the most positive and most negative curvature attributes respectively (Roberts, 2001).

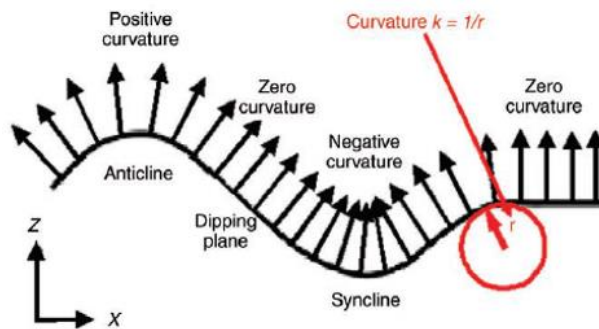


Figure 6.3. Definition of 2D curvature (Chopra and Marfurt, 2007.)

		GAUSSIAN CURVATURE		
		$K_g < 0$	$K_g = 0$	$K_g > 0$
MEAN CURVATURE	$K_m > 0$			
	$K_m = 0$			
	$K_m < 0$			

Figure 6.4. Curvature shape classification (Roberts, 2001).

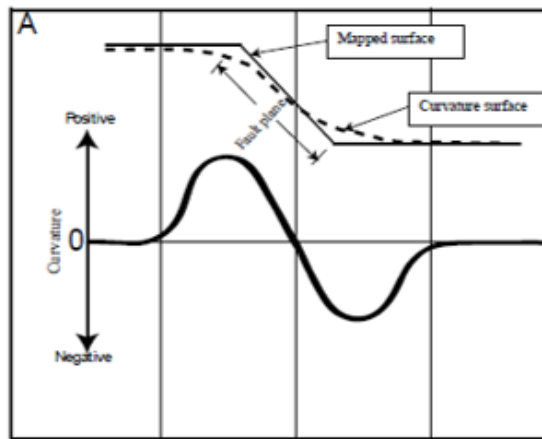


Figure 6.5. Application of curvature attribute in fault interpretation. (Roberts, 2001).

The relationship between curvature and stress has been studied (e.g., Lisle, 1995; Murray, 1968) and observed a correlation between curvature and fracture density in folded beds, which experience different stresses throughout the layers (Figure 6.6). Price and Cosgrove (1990) proposed that for rocks with similar Young's modulus, the amount of stresses within a layer depends on the amount of curvature and the distance of the neutral surface. However, geological curved features can result not only from folding, but also from sedimentary depositional processes such as dunes and clinoforms, in which case, curvature alone cannot be associated with fracture density. Curvature attributes should be calibrated with well data such as core samples, image logs, VSP, etc (Roberts, 2001) in order to improve the confidence on the seismic attribute information as an accurate representation of the present-day subsurface conditions (Chopra and Marfurt, 2007). The software used for this study offers a suite of different curvature attributes (Figure 6.7), which provide very useful information in order to predict fracture density variations.

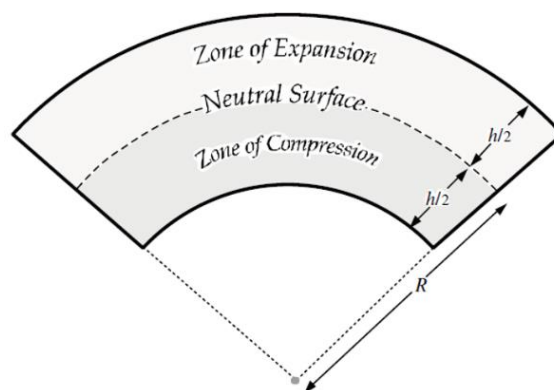


Figure 6.6. Relationship between stress and curvature. (Roberts, 2001).

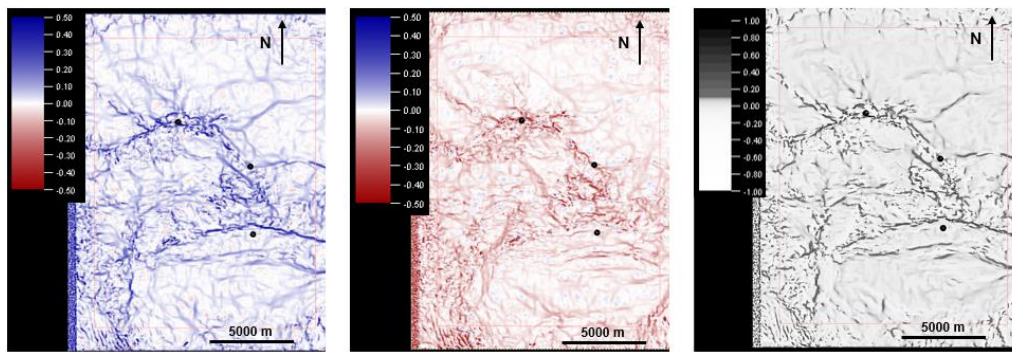


Figure 6.7. Different curvature attributes. From left to right: Most Positive curvature, Most Negative Curvature and Most Extreme Curvature.

Variance

Variance is a discontinuity attribute that measures the similarity between waveforms of seismic traces in vertical and lateral windows (Chopra and Marfurt, 2007). These waveform variations are commonly associated with changes in lithology, porosity and fluid content, making it a valuable tool in mapping structural and sedimentary features in subsurface. Mathematically, variance is the reciprocal of semblance estimate of coherence (1 minus coherence), which calculates the energy of different traces inside a window search and generates an average trace; then, compares the similarity between this average trace and each of the traces inside the window (Figure 6.8). If all traces are equal, then variance=0 and coherence=1; however, this is not the case if amplitudes are different and coherence is calculated with semblance algorithm. In contrast, with the cross-correlation algorithm, coherence=1 independently of the amplitude traces but only if the waveform is the same (Chopra and Marfurt, 2007).

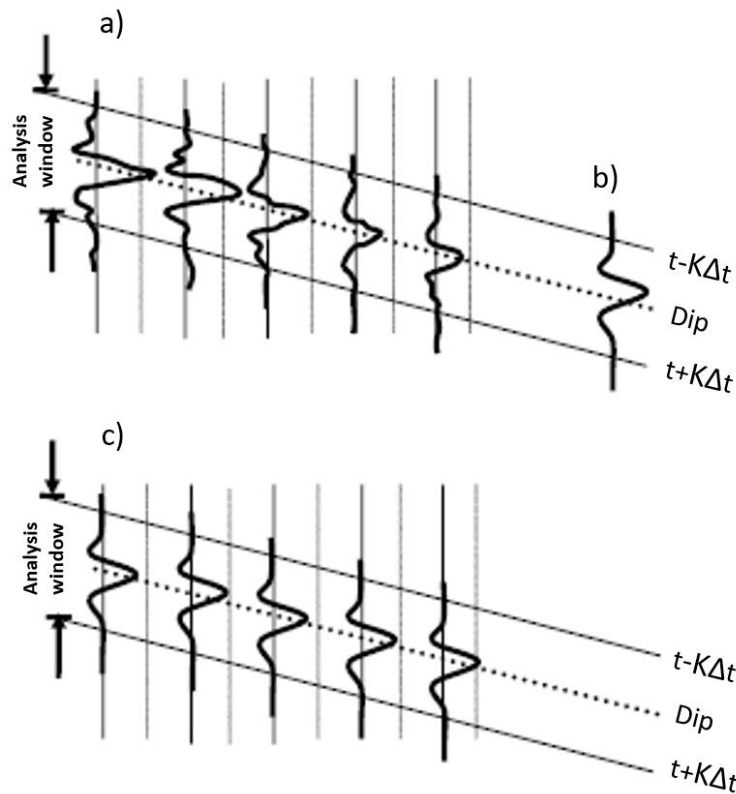


Figure 6.8. Semblance estimation of coherence. a) The energy from 5 input traces in the analysis is calculated and (b) an average trace is calculated; c) The semblance is calculated by the ratio of the energy of the average trace to the energy of each of the input traces. If all the traces in a) are equal, then semblance=1. If not, it is less than 1. (Chopra and Marfurt, 2007).

Coherence and/or variance volumes are useful in imaging and delineating structural (vertical or near vertical faults/fractures, salt and shale diapirs) and stratigraphic (deltas, submarine canyons, karst collapse, mass transport complexes) features, which in turn might define the extent of reservoirs and help to plan development wells and production design. Usually, stratigraphic features are shown best on horizon slices whereas structural features are best seen on constant-time (or depth) slices (Figure 6.9), which lack the interpreter bias that would be present on horizon-based extractions (Chopra and Marfurt, 2007). Discontinuity attributes, in spite of their robustness, are sensitive to factors such as structural dip and algorithmic limitations, which must be taken into account in order to avoid the generation of artifacts and pitfalls during attribute calculation and interpretation, respectively (Marfurt and Alves, 2015).

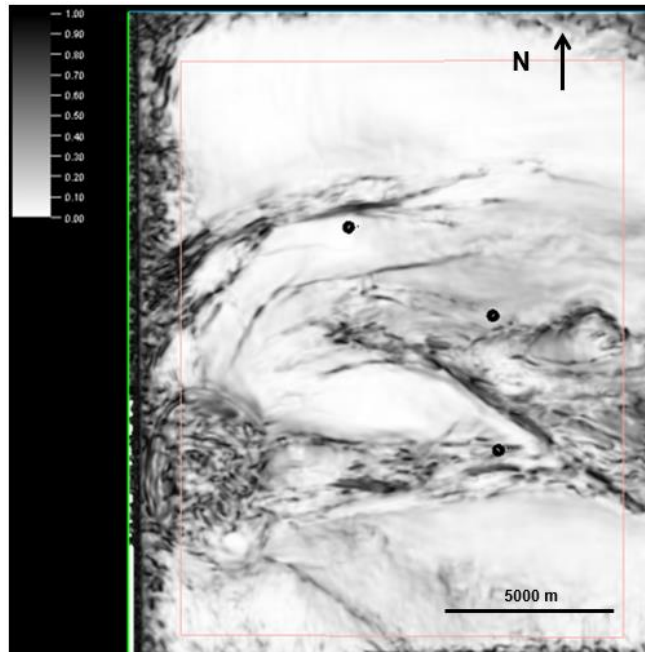


Figure 6.9. Variance slice at a depth of 4000 m. Major faults are clearly delineated as well as a salt diapir in the southwest edge of the survey.

Given the algorithmic limitations of both curvature and coherence attributes to identify different types of faults, a more accurate interpretation is gained by using them together either in time/depth slices or in surfaces (Figure 6.10), although in the latter case experiences a greater uncertainty due to geological complexity, lack of constrained correlation and poor seismic imaging.

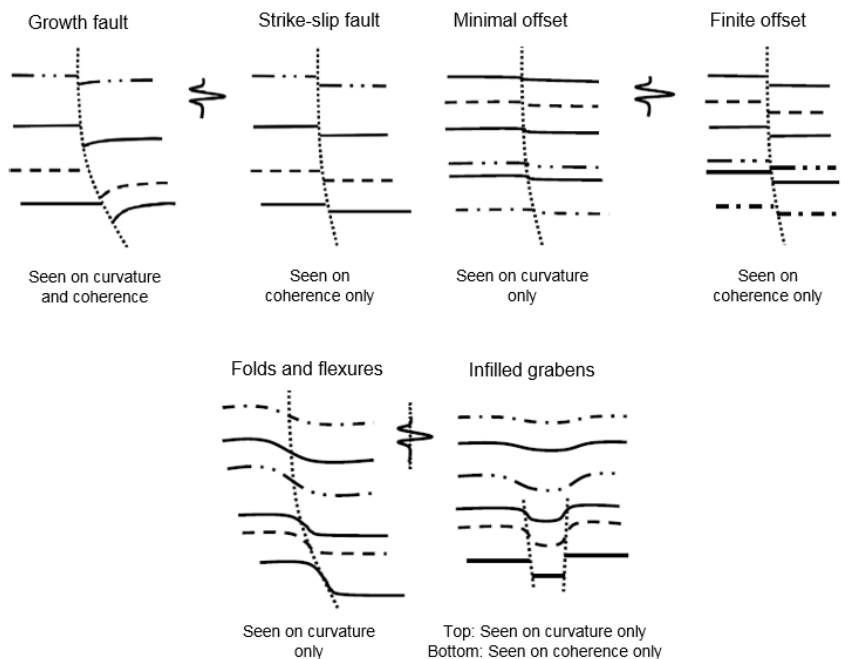


Figure 6.10. Attribute sensitivity to faults, folds and flexures (Chopra and Marfurt, 2007).

Ant-tracking

This attribute has been proven to be very useful in enhancing fault/fracture interpretation in 3D seismic data (Ngeri et al., 2015; Chopra and Marfurt, 2007). It uses the principles of swarm intelligence, which explains the collective behaviour of social insects in communicating to others using pheromone trails to find the shortest, most efficient path between the nest and food (Ngeri et al., 2015). The ant-tracking algorithm is an iterative scheme that progressively tries to connect adjacent zones of low coherence, which have been filtered to eliminate horizontal features associated with stratigraphy by distributing electronic ants in the seismic-discontinuity attribute volume that are allowed to follow different paths. Ants deployed at different positions traverse the fault surface by following an electronic equivalent of a pheromone. As these ants traverse different surfaces in the discontinuity volume, they estimate the orientation of those surfaces (Chopra and Marfurt, 2007).

Figure 6.11 illustrates a conventional workflow used in commercial software packages. First, the seismic data must be conditioned by reducing noise in the signal. Then, an edge enhancing volume (variance, chaos), which delineates spatial discontinuities (faults) must be generated. Finally, the Ant-tracking volume is generated using the enhancing volume as an input, resulting in an attribute volume that shows very sharp and detailed fault zones. Figure 6.12 shows a comparison between the response of ant-tracking attribute and fault interpretation from the amplitude volume a depth slice at 2500 m. Ant-tracking provides a more detailed definition of the major faults, and visualizes minor faults that are difficult to interpret in the amplitude volume. However, some minor lineaments oriented N-S (parallel to regional N-S extension) correspond to variations in the seismic traces associated to dipping beds and do not actually represent fractures, which can lead to pitfalls during interpretation.

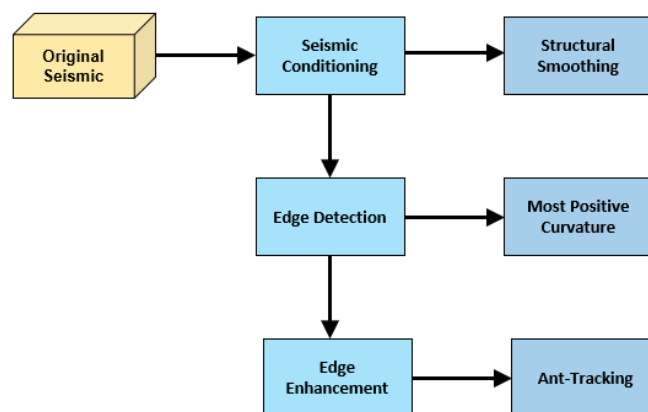


Figure 6.11. Standard Workflow used to generate an ant-tracking attribute volume.

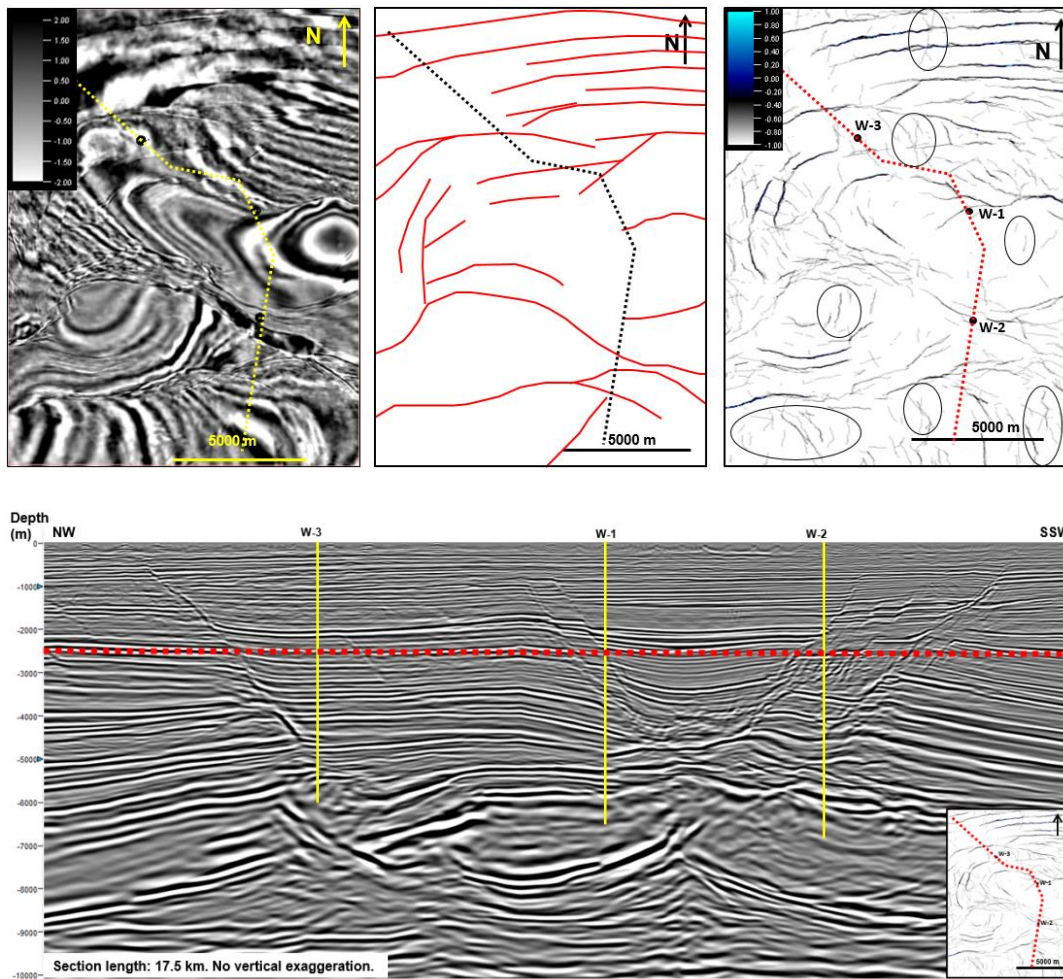


Figure 6.12. Depth slice at 2500 m. Top left: amplitude volume. Top Centre: fault interpretation (red lines) from amplitude volume. Top right: ant tracking attribute calculated from Variance showing subtle faulting that it is not visible in the amplitude volume. Lineaments inside ovals represent lineaments associated with dipping beds instead of fractures. Bottom: seismic cross-section through the study area. Dotted red line indicates the position of the depth slices.

6.3 Methods

6.3.1 Seismic attributes

For structural seismic attributes, the Schlumberger Petrel software was used to extract information from seismic volumes. Attributes including coherency, curvature and ant-tracking were calculated following standard workflows included in the software. First, the input seismic data must be conditioned in order to increase the continuity of seismic reflections by applying a structural smoothing using a dip-guided filter based on the local dip and azimuth. Secondly, this conditioned data was used as an input to calculate the edge detection attributes, namely curvature and variance. Finally, these attribute volumes were used as the input to generate an ant-tracking volume.

For each step in the process, calculation parameters were adjusted depending on the response of the seismic data, selecting those that provided the best visual and geologically reasonable information (Figure 6.13-6.15). The response of the attributes is negatively influenced by the depth of the Mesozoic column in the study area (deeper than 5.5 km), where frequencies are very low and image quality decreases respect to shallower depths where the response of the attributes is considerably better (Figure 6.16). Table 6.1 summarizes the parameters used for each attribute calculated.

	Sigma X, Y, Z	Vertical radius	Inline/Crossline radius	Inline/Crossline range	Vertical smoothing	Aggressive/Passive Ants	Stereonet Azimuth/Dip
Structural smoothing (dip-guided)	1.5						
Most Positive Curvature		30	2				
Most Negative Curvature		40	3				
Most Extreme Curvature		30	2				
Variance				5/5	33		
Ant tracking						Aggressive	Unfiltered

Table 6.1. Parameters used for seismic attribute calculations.

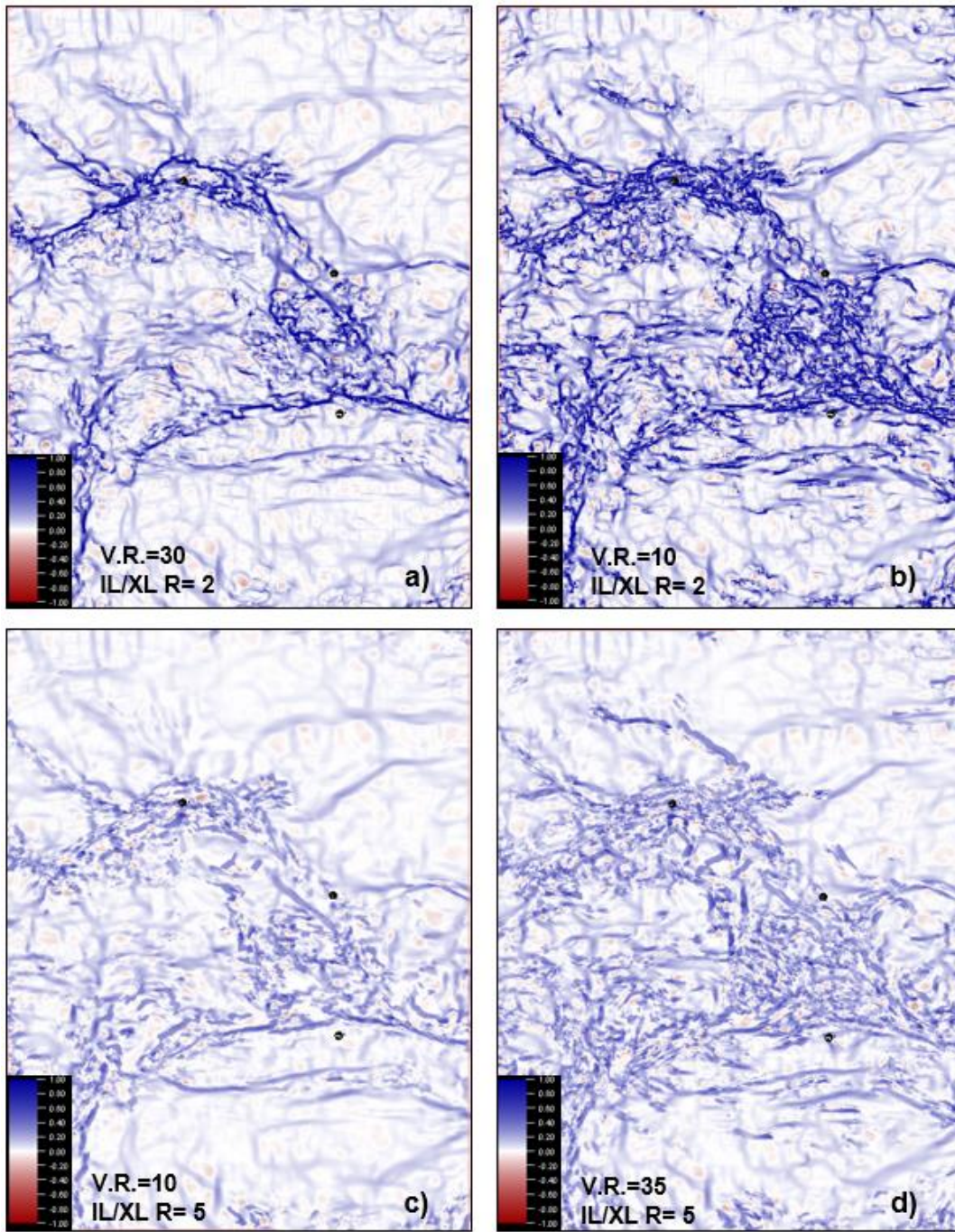


Figure 6.13. Depth slices at 6100 m of most positive curvature attribute calculated with different values of input parameters (V.R= vertical radius, IL/XL R=IL/XL Range) in order to analyse lineaments associated with faults and fracture zones. For this study, the attribute in a) provided the best visual information.

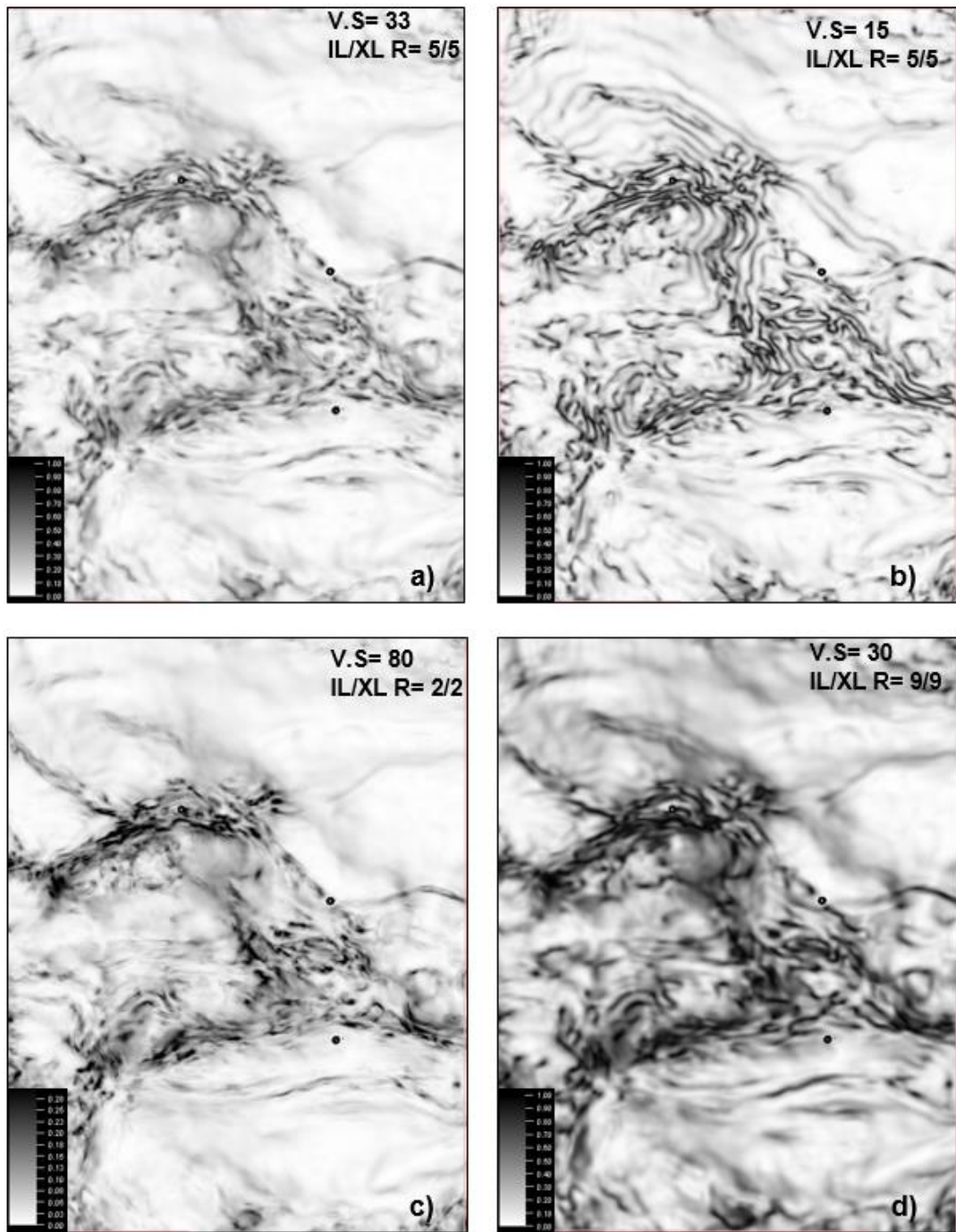


Figure 6.14. Depth slices at 6100 m of variance attribute calculated with different values of input parameters (V.S= vertical smooth, IL/XL R=IL/XL Radius). Image from a) provided the best visual information. For this attribute, reduction in horizontal analysis window IL/XL R (b image) caused lineaments follow contour lines, which is not associated with faults/fractures.

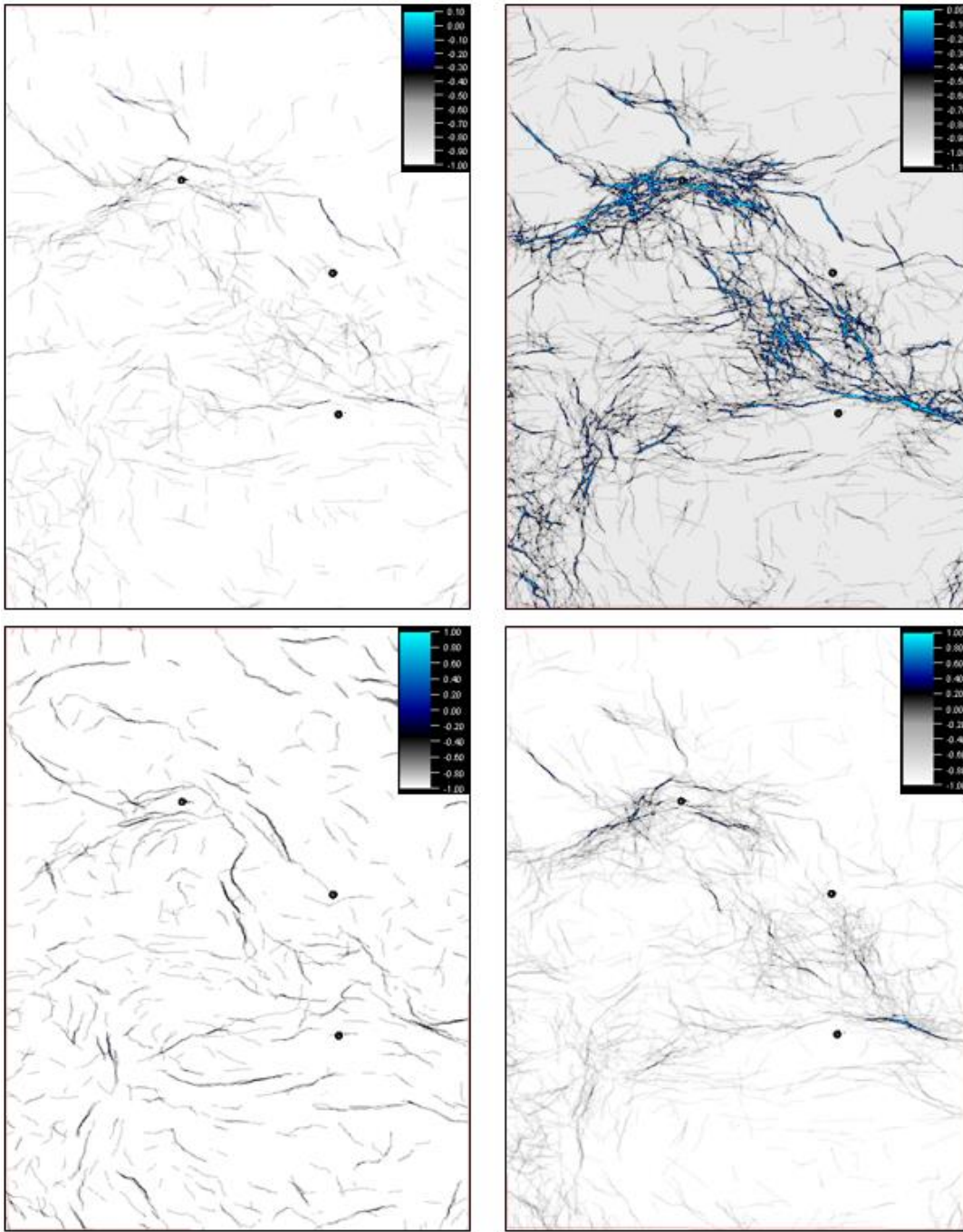


Figure 6.15. Depth slices at 6100 m of Ant-tracking attribute calculated from different edge detection attributes. Top left: most positive curvature (MPC) with *passive* configuration (best for detection of major faults); top right: MPC with *aggressive* configuration (best for detection of subtle faults); bottom left: variance and, bottom right: most extreme curvature.

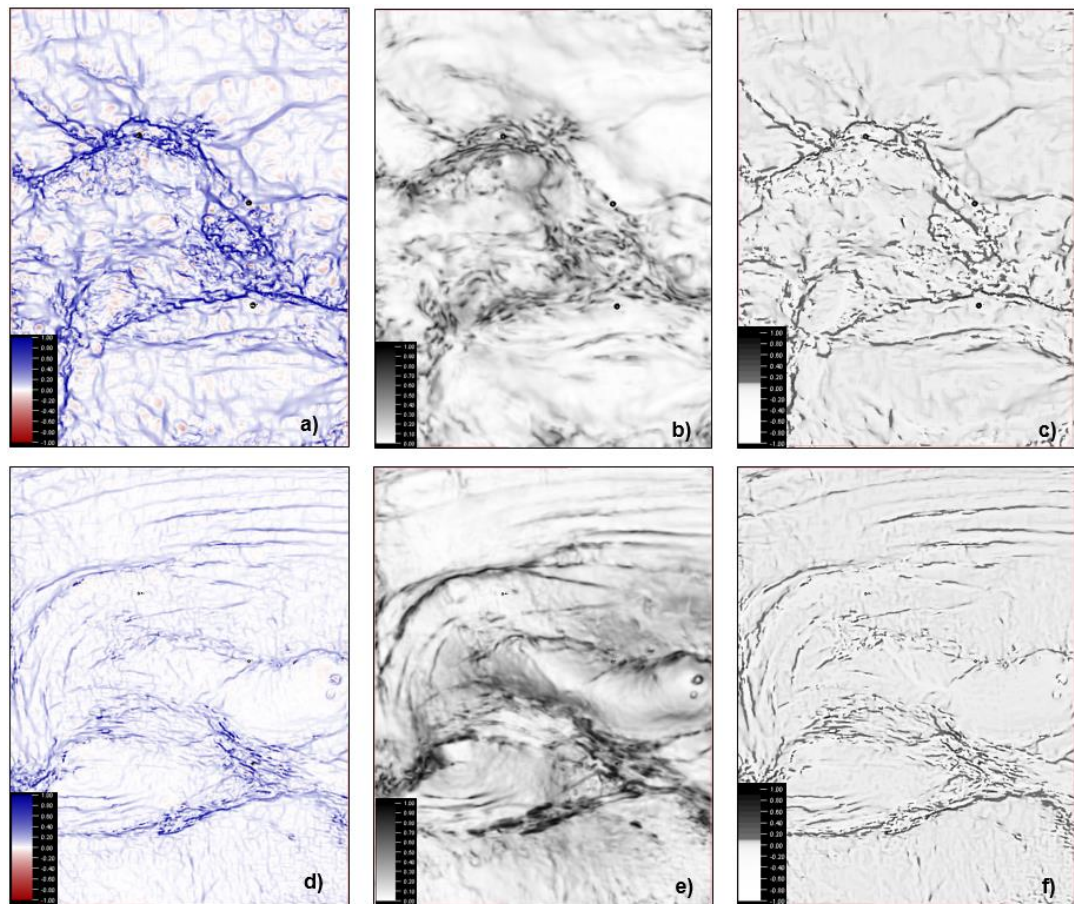


Figure 6.16. Comparison in the response of different seismic attributes calculated at different depths (6100 m in top row and 3000 m in bottom row). From left to right column: Most positive curvature, variance, and most extreme curvature. Although geologically structural conditions are different at each depth, a well-developed system of normal faulting is visible at 3000 m whereas at 6100 m faults are less abundant and lineaments associated with faults are less defined than at shallower depths.

6.3.2 Geomechanical Modelling

Strain, which can be defined as “a distortion or change in shape of a body related to the displacement of inner particles from their original position to a new position” (Gudmundsson, 2011), is a parameter that can be associated fracture intensity, since brittle deformation is present at shallow levels of earth’s crust. Moreover, strain calculation in a deformed mapped surface provides a representation of the areal distribution of strain and, therefore, can be used as a proxy in order to consider areas with higher strain values (usually more deformed areas by folding and/or faulting) as more likely to have higher fracture intensities.

Strain maps were calculated from interpreted Mesozoic surfaces in order to visualize the effect of the total deformation in each one of them and compared to the results of structural seismic attributes. Input data consisted of the interpreted surfaces and faults and mechanical properties (Young’s Modulus, Poisson’s Ratio) which were obtained

from well logs analysis and PEMEX's database. For the strain calculation, two different modules from the Move© software suite were used, namely: Geomechanical Modelling and Fault Response Modelling. For practical purposes, the term Geomechanical Modelling encompasses the results of these two modules.

Geomechanical Modelling module can restore 3D surfaces from a deformed state to an initial non-deformed state, or viceversa, and capture its corresponding strain by simulating heterogeneous (non-plane strain) displacement. This module is particularly useful when deformation is related to folding rather than faulting. The theory principle is based on a Mass-Spring approach that uses pre-defined rock properties (Young's Modulus, Poisson's Ratio). For surfaces, the process takes a template mesh and deforms it to a target mesh or datum. The template mesh is discretised into masses and springs, which are traditionally placed along the edges of mesh triangles and masses replace the vertices. The "boundary condition" of the model is the projection of a surface to a target. Projection changes the shape of the surface, which changes the length of triangle edges, "loading" the model springs. The springs are used to calculate forces on the point masses, which governs the point mass trajectories and simulates physical behaviour of the surface during heterogeneous strain. The Mass-Spring solver iteratively moves the point masses in the template surface and calculates resulting spring forces in very small time steps. At each step it minimizes the energy in the springs and converges on the target surface to a predefined percentage tolerance or error.

Fault Response Modelling module calculates and visualizes fault-related displacements, strain and stress in an elastic medium by using elastic dislocation theory with defined elastic and mechanical properties (Poisson's Ratio, Young's Modulus and different friction settings). The module uses a boundary element approach whereby calculations are only performed at observation points, which correspond to the vertices of meshes from surfaces. When the material is deformed in an elastic medium, it creates a displacement field from which a stress and strain field will automatically be calculated.

Since deformation in the study area is related to faulting and folding, the two modules were used and their results compared. These results were subsequently integrated with seismic attribute maps and, finally, compared with well data in order to find a correlation that allows an estimation of fracture intensity in undrilled areas.

6.4 Results

In this section, results from analysis of different structural seismic attributes are presented across a series of depth slices and surface maps from the different Mesozoic targets in the study area in order to identify orientation and density of fracturing. Then, these results are compared to those obtained from well data and thus determine a possible relationship involving different scales of observation.

6.4.1 Curvature/Variance analysis

Figure 6.17-19 illustrate the interpreted surfaces of Top Cretaceous, Top Tithonian and Top Kimmeridgian with Most Positive Curvature, Most Negative Curvature, Variance and Ant-Tracking attributes together with their corresponding structure maps. Depth to surfaces varies from 5300 to 6535 m, where seismic resolution is low and image quality decreases in some areas, which affect negatively in the response of seismic attributes, although ant-tracking provides a more detailed image.

Most Positive (MPC) and Most Negative (MNC) Curvatures were calculated using the parameters shown on Table 6.1, which were selected after several tests with different values until the best results were obtained. Figure 6.17-19a-b show both attributes with almost identical qualitative and quantitative results, thus either could be selected for fracture analysis; however, a combined analysis of both attributes provides useful information to identify up-thrown (blue colour in MPC) and downthrown blocks (red colour in MNC). In the three surfaces it is observed that higher density of most positive and negative values are distributed around anticline structures A, B and C and major fault traces. No preferential orientations are observed as a result of different superimposed deformational events; however, some lineaments seem to be related to folding/faulting processes since they tend to be parallel to the axis of the anticlines, suggesting a possible influence of structural position on orientation and density of fractured zones. Some background noise and acquisition footprint is visible on the surfaces as lineaments showing regular grid patterns, which can lead to pitfalls in structural interpretation (Figure 6.17-19a-b).

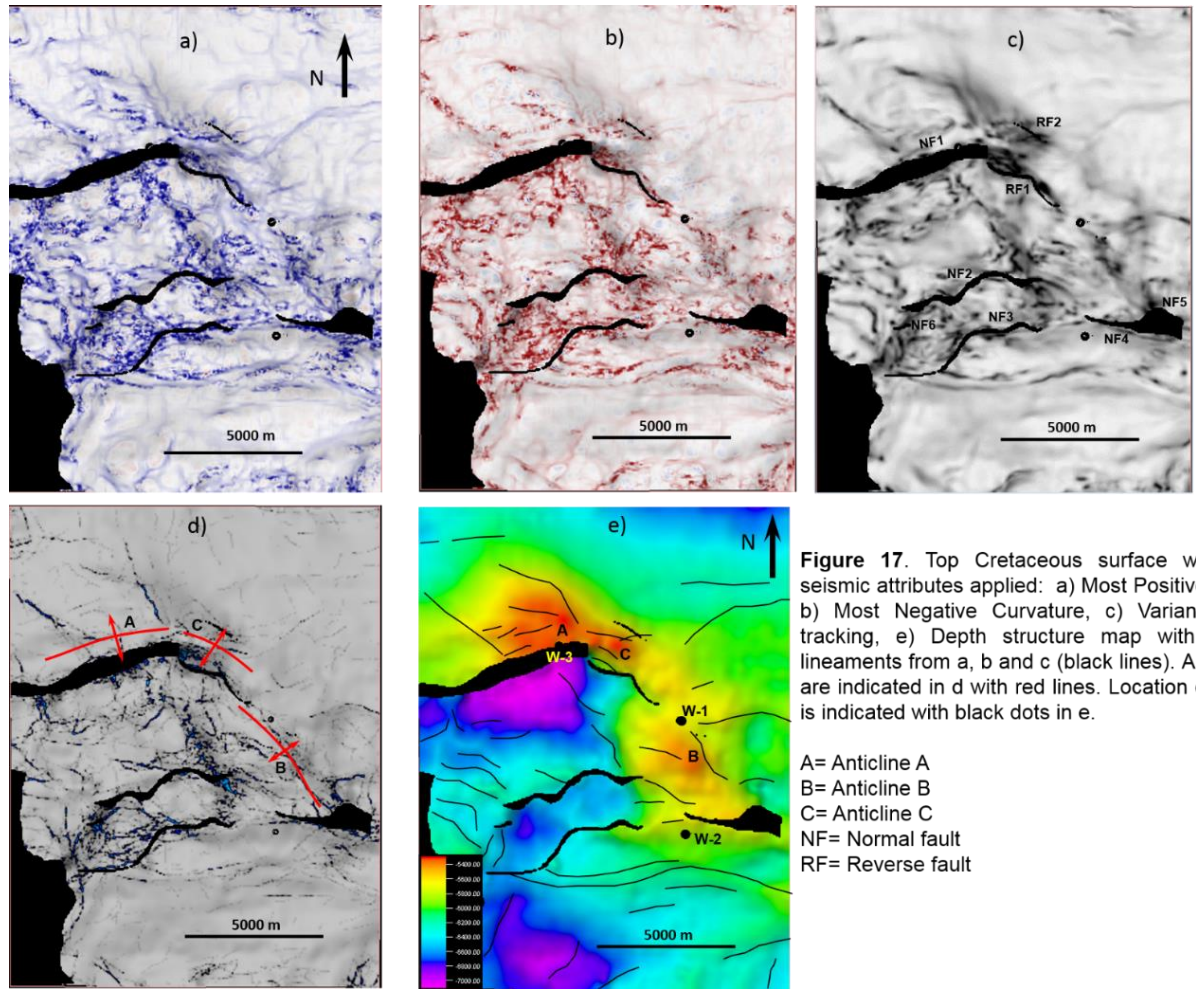


Figure 6.17. Top Cretaceous surface with different seismic attributes applied.

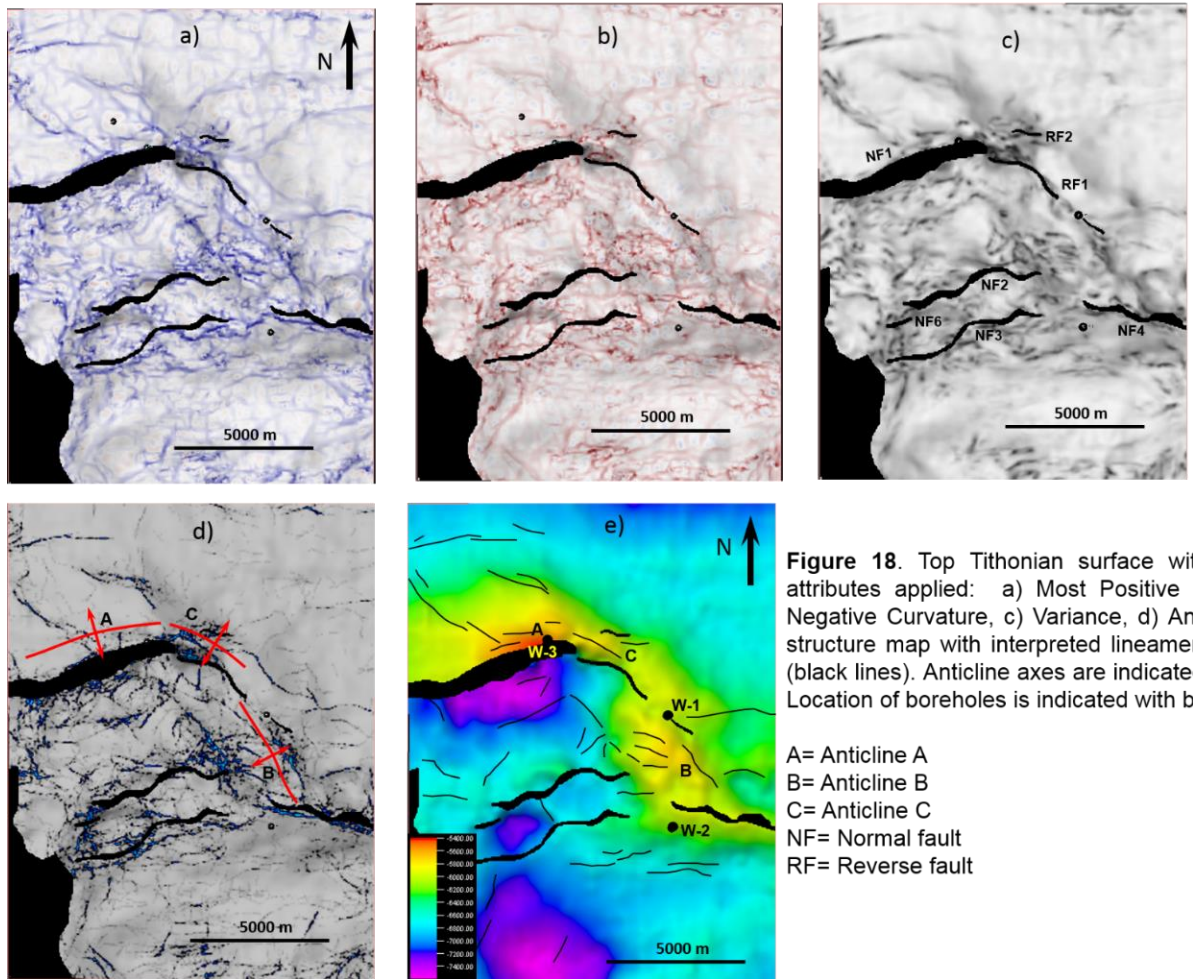


Figure 6.18. Top Tithonian surface with different seismic attributes applied.

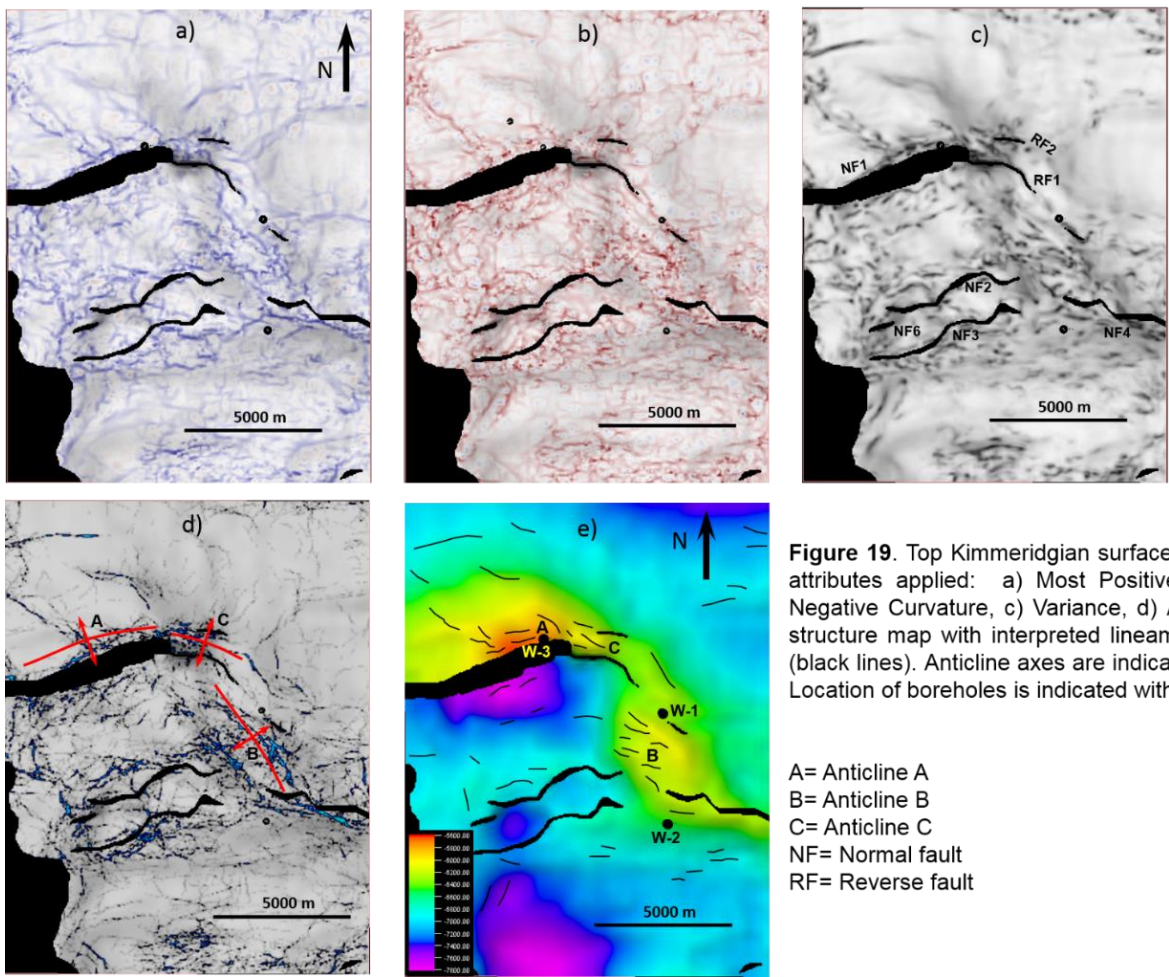


Figure 19. Top Kimmeridgian surface with different seismic attributes applied: a) Most Positive Curvature, b) Most Negative Curvature, c) Variance, d) Ant-tracking, e) Depth structure map with interpreted lineaments from a, b and c (black lines). Anticline axes are indicated in d with red lines. Location of boreholes is indicated with black dots in e.

A= Anticline A
 B= Anticline B
 C= Anticline C
 NF= Normal fault
 RF= Reverse fault

Figure 6.19. Top Kimmeridgian surface with different seismic attributes applied.

Similarly to curvature attributes, different parameter values were tested before selecting the definitive values shown on Table 1. Variance attribute (Figure 6.17-19c) show similar characteristics to curvature (Figure 6.17-19a-b) regarding the density and orientation of lineaments; however, fewer lineaments are present and are mostly sharper and more clearly defined. Moreover, their interpretation is, in principle, less ambiguous than curvature, since variance lineaments are typically associated with faults rather than folds. For this work, both attributes were combined in order to identify and interpret possible subtle faults and fracture zones.

For each of the three interpreted surfaces, subtle faults were interpreted as black lines superimposed on the structure maps (Figure 6.17-19e) based on lineaments visible on both curvature and variance volumes, which were later verified and calibrated on amplitude volume cross-sections. Each lineament must be visible on both curvature volumes with different polarity appearing together but with a small lateral shift, which evidences either up-thrown/downthrown pairs or an anticline/syncline axis. In order to exclude potential folds from the fracture analyses, these lineaments are also interpreted in the variance volume, since the presence of fault planes with a finite offset may cause variations in adjacent seismic traces, resulting in locally high values of variance. Figure 6.14-16d show the three interpreted Mesozoic surfaces with the ant-tracking attribute, which was extracted from the Most Positive curvature volume. This attribute provides the best, least noisy and most detailed extraction of sharp lineaments, which are easier to interpret than in coherence and curvature attributes as well as more subtle lineaments. Parameters used for ant-tracking correspond to the “aggressive” configuration, which can capture smaller discontinuities in the data set, and is therefore more effective in detecting more subtle faults. Comparison between lineaments from the ant-tracking attribute and the lineaments interpreted from curvature/variance show a good correlation, thus adding certainty to interpretation of subtle faults. Figure 6.20 show enlargements of variance depth slices and cross-sections corresponding to the three anticline structures with interpreted lineaments indicated on each by arrows. These lineaments have maximum absolute values in curvature and variance volumes and are associated with lateral changes in amplitude or polarity probably due to the presence of faults whose vertical offset is small enough to be resolved seismically, especially at depths where low frequencies are predominant. Furthermore, lineaments with relatively low values of curvature and variance are associated with small flexures in the interpreted horizons and, therefore, are not interpreted as faults in a conventional amplitude volume.

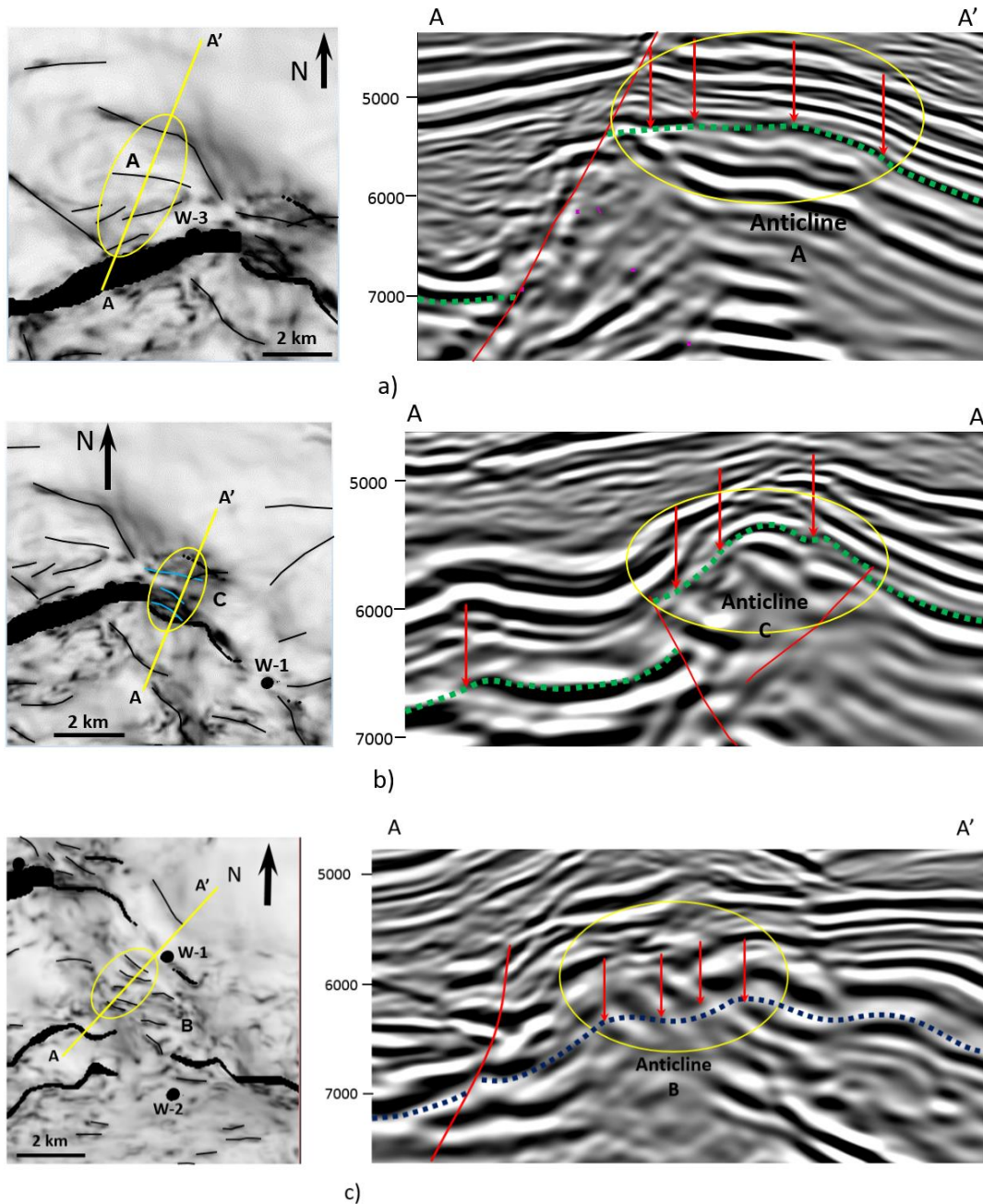


Figure 6.20. Interpreted faults in Mesozoic surfaces with variance attribute (left) and their character in seismic cross-section (right). Red arrows indicate the location of the lineaments, which are related with lateral changes in amplitude and polarity associated with the presence of faults. a) and b) Top Cretaceous; c) Top Kimmeridgian. In c), lack of lateral continuity of horizons increases uncertainty in mapping of the horizon, and can lead to pitfalls in the interpretation of subtle faults using attributes.

6.4.2 Ant-tracking analysis

This attribute was extracted from two previously conditioned attribute volumes: Most Positive Curvature (MPC) and Variance. Figure 6.21 shows a N-S inline from the conventional amplitude volume and the two ant-tracking extracted volumes crossing Anticline B. In the MPC ant-tracking volume, the central graben is better defined and more detailed faulting can be interpreted. Also, the salt anticline in the middle of the section can be more easily identified and interpreted whereas major faulting in the Mesozoic section above the salt anticline can be defined although some noise is also present; however, the south-dipping en-echelon faults located in the northern edge of the section is not well defined.

The variance ant-tracking volume, in the other hand, shows less detail in identifying major faulting and delimiting salt bodies and the central graben is not clearly defined; conversely, the en-echelon fault system is well defined. Also, south-dipping reflectors between 4 and 5 km deep with a high contrast of acoustic impedance appear as lineaments in this volume which may lead to pitfalls in interpretation. Each ant-tracking attribute (MPC and variance) has limitations and advantages respect to one another and, therefore, an integrated analysis of these attributes along with the conventional amplitude volume provides more robust information for structural interpretation.

Figure 6.22 shows a merge between the structure maps (from the amplitude volume interpretation); the interpreted curvature/variance lineaments (black lines) that may be associated with subtle faults; and the ant-tracking attribute, where a good match between the lineaments can be observed.

Ant-tracking also may provide a relatively good confidence to predict the orientation of fractures in undrilled areas. Figure 6.23 show close-ups from each of the three Mesozoic surfaces in the vicinity of the boreholes W-1, W-2 and W-3 where orientations of fractures obtained from FMI logs are compared to ant-tracking lineaments that occurs close to the boreholes. In all cases, there is a relatively good matching at least in one orientation between the two scales of observation.

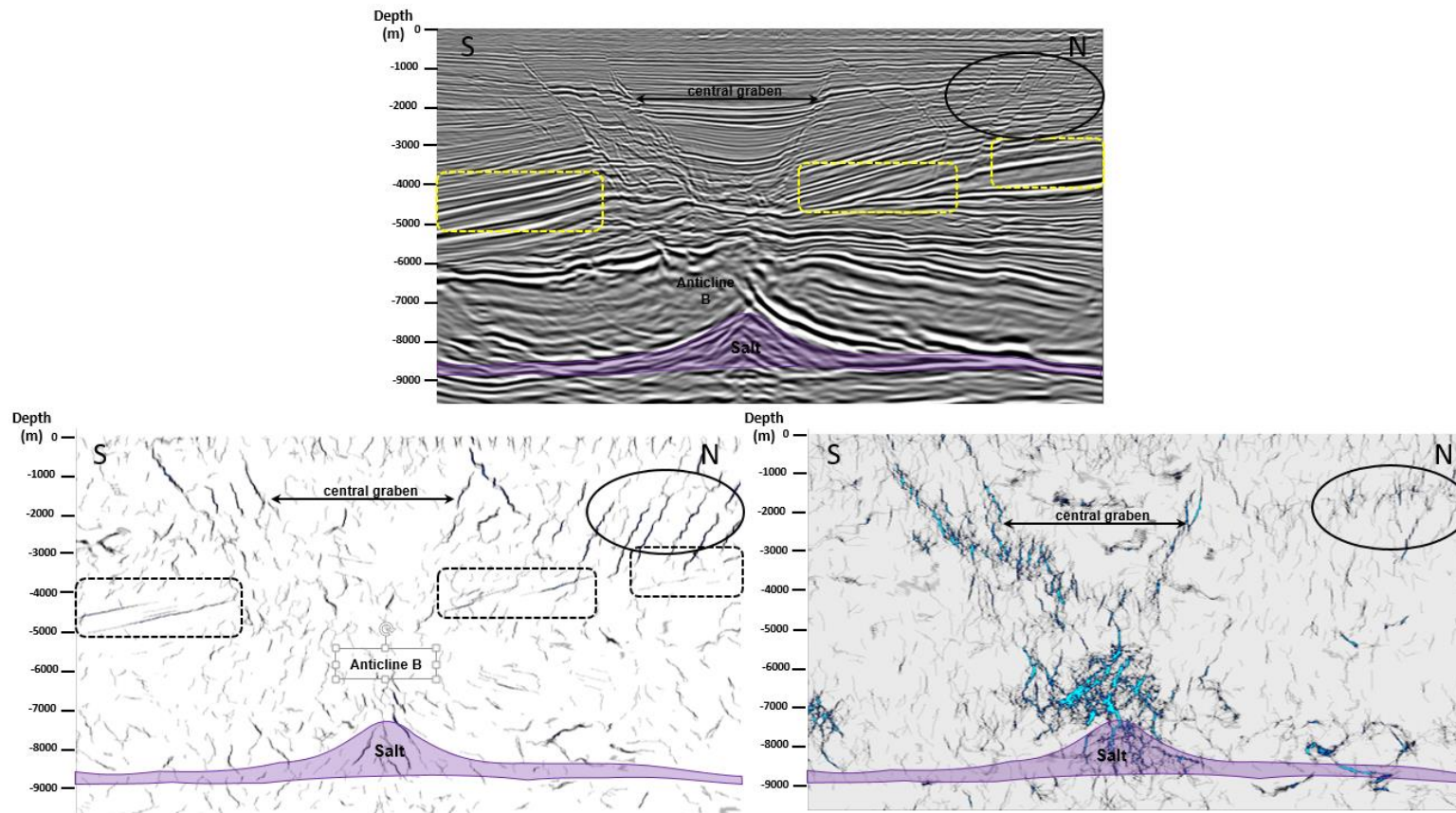


Figure 6.21.Top: Cross-section in amplitude volume. Bottom left: Ant-tracking from variance volume. Bottom right: Ant-tracking from Most Positive Curvature. Dashed rectangles indicate south-dipping lineaments that are related to reflectors with high contrast of acoustic impedance and not to faults. No vertical exaggeration.

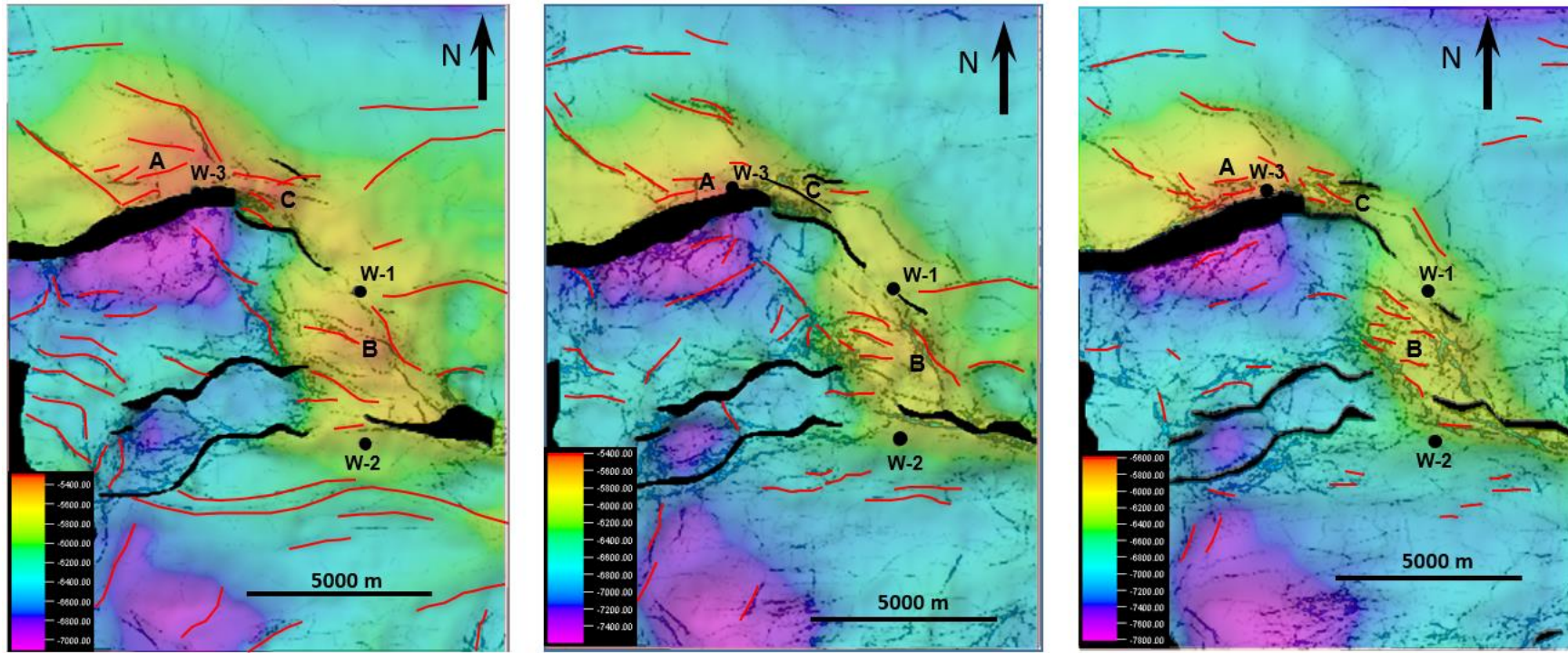


Figure 6.22. Ant-tracking/structure surfaces from Top Cretaceous (left), Top Tithonian (center) and top Kimmeridgian (right) showing lineaments interpreted from curvature/variance attributes (red lines) and their correlation with ant-tracking lineaments. A= Anticline A; B= Anticline B; C= Anticline C.

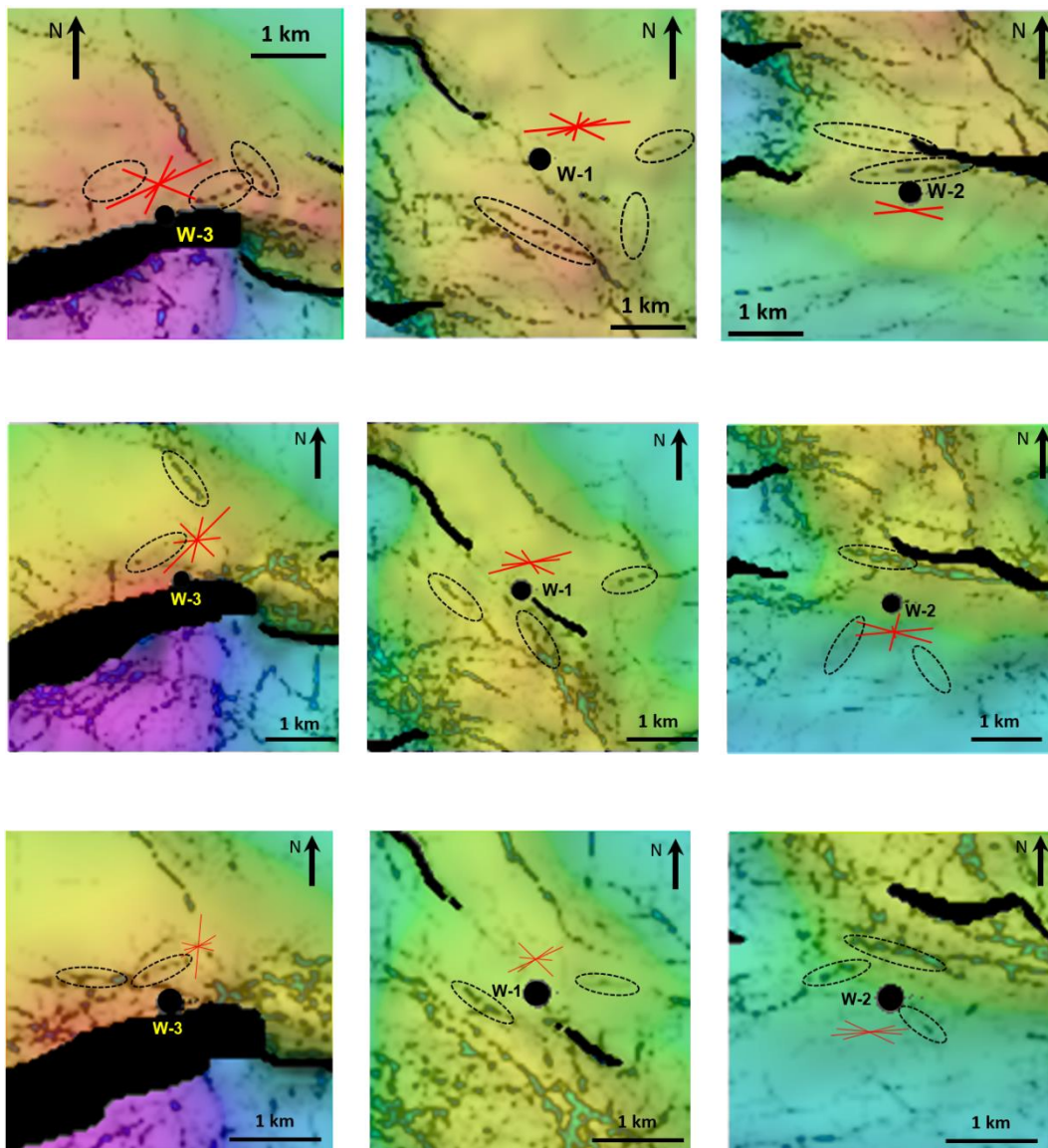


Figure 6.23. Close-ups from Fig. 22 showing a comparison between the ant-tracking lineaments adjacent to the boreholes with similar orientations (inside black dashed ovals) to fracture orientations measured in FMI logs (red lines). From top to bottom rows: Top Cretaceous, Top Tithonian and Top Kimmeridgian.

6.4.3 Cross-Section Analysis

This section investigated the correlation between ant-tracking lineaments in seismic cross-sections and FMI logs values of fracture density obtained from the three boreholes within the study area. Although results are variable, in general terms, the correlations presented below can be considered as good. In order to avoid confusions with the correlation between depths within the seismic data and within the boreholes, depth in seismic is referred to sea level (mbsl) whereas borehole depth is referred to Kelly bushing (mbkb).

W-1

For the Cretaceous, the interval between 5900-6000 m on seismic data correlates to the Middle Cretaceous and the upper part of Early Cretaceous, which in the FMI data shows a presence of fractures and mechanical layers. Production test III was undertaken at this interval, which resulted in an oil producer (red). This fractured interval may be associated with a south-dipping normal fault located very close to the borehole (

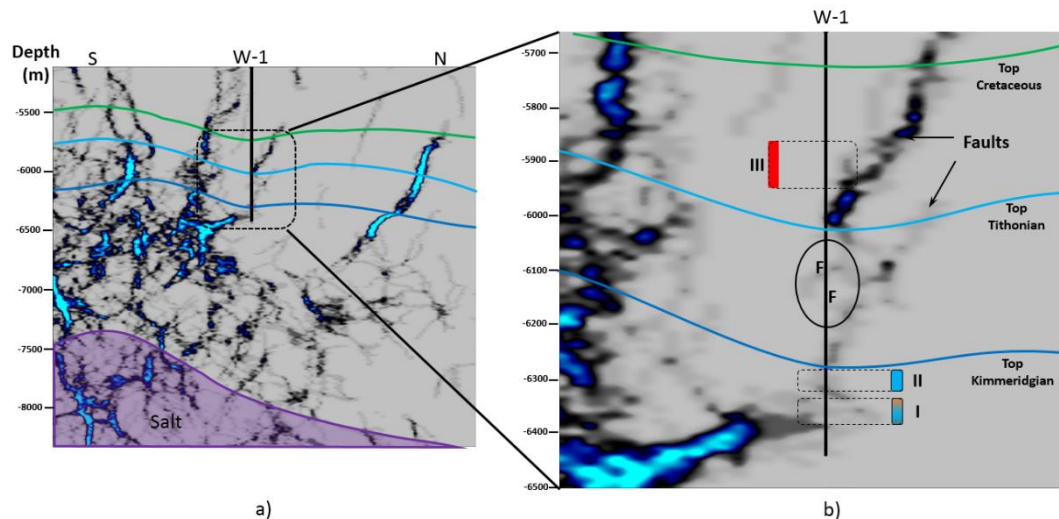


Figure 6.24). The Tithonian interval in the seismic is characterized by the presence of lineaments probably associated a subtle south-dipping faults adjacent to the borehole. The FMI results shows this interval with high fracture density and also two faults were interpreted at 6050 and 6130 mbsl and can be associated to lineaments in seismic. Bottom of Tithonian section in seismic is intersected by lineaments and correlates with high fracture density values in FMI logs. Kimmeridgian interval it is also intersected in seismic by lineaments from the top to the borehole's bottom depth, which has a good correlation with the FMI values. Production tests I and II were undertaken, resulting in oil production (red/blue) and water invaded (blue), respectively.

W-2

The Cretaceous interval in seismic shows no lineaments across the borehole (Figure 6.25), which correlates with FMI log values; however, Production test II was carried out in a fractured interval that is not detected with ant-tracking probably due to the reduced thickness of that interval, the small size of the fractures and a relatively low fracture density. For Tithonian, the interval 6400-6500 mbsl shows a good correlation with FMI log values. The same interval is intersected by a lineament associated with a subtle fault, which was interpreted in FMI at 6450 mbsl. Production test I was carried out at the bottom of this interval resulting as water invaded. For Kimmeridgian, only the top 50 m shows a moderate correlation between seismic and FMI, where the bottom part of the lineament

also present in Tithonian mentioned above correlates with FMI values. The interval 6620-6850 mbsl in seismic shows no lineaments whereas in FMI log it was interpreted as a fractured interval, thus no good correlation exists between the two data sets.

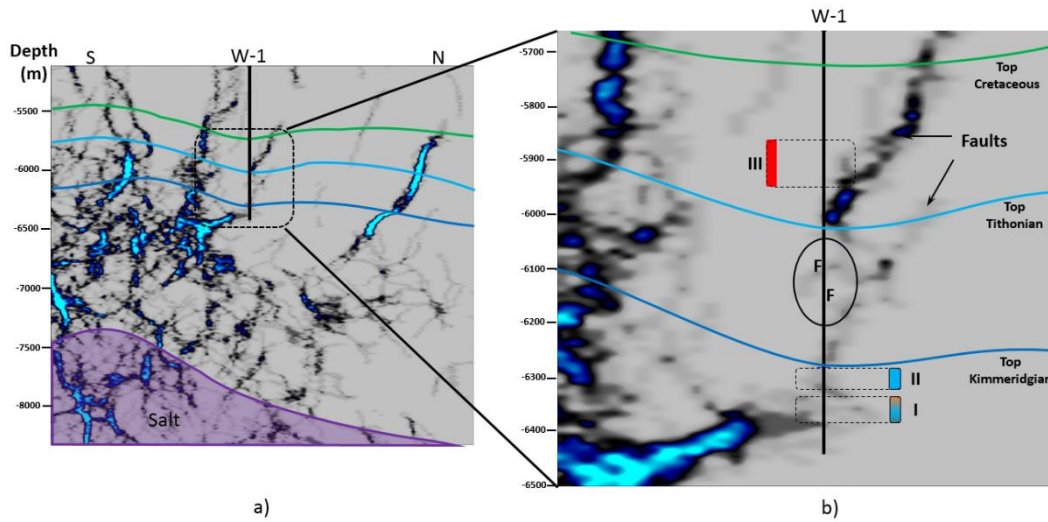


Figure 6.24. (a) Cross-section with ant-tracking attribute shown. (b) Close-up in the Well-1 showing the location of production tests (dashed rectangles) and faults interpreted in FMI logs (F). No vertical exaggeration.

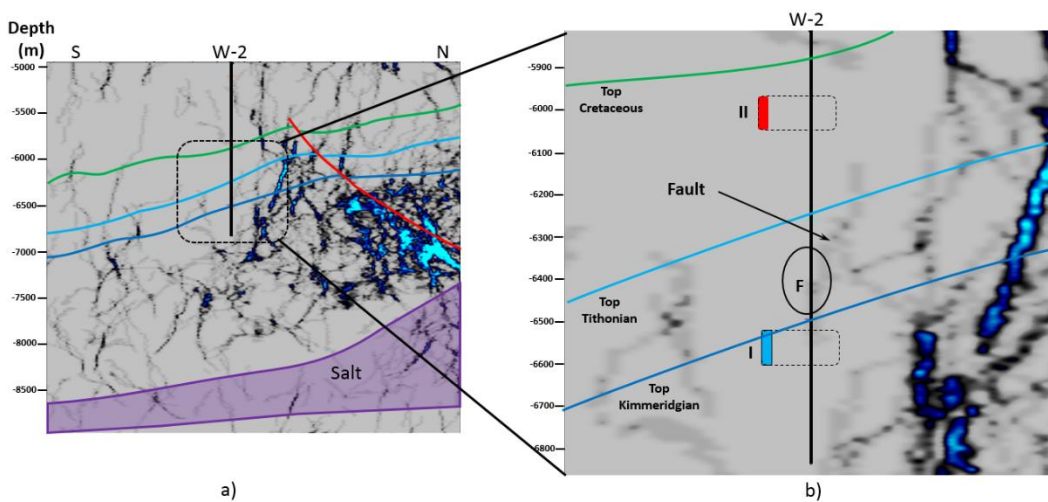


Figure 6.25. (a) Cross-section with ant-tracking attribute shown and, (b) close-up in Well-2 showing the Production tests and fault interpreted in FMI logs (F). No vertical exaggeration.

W-3

Here, the Cretaceous interval in seismic is intersected by lineaments associated with the adjacent major south-dipping normal fault (NF1), which indeed limits the anticline at its southern limb (Figure 6.26). The entire interval has a good correlation with FMI log values which show relatively high fracture density. Tithonian's top half interval (5410-5510 mbsl) also seems to be intersected by ant-tracking lineaments; however, FMI shows very few fractures across the logged interval (5410-5530 mbsl) and no fracture-associated

indicators were observed while drilling this interval. The lower half of the Tithonian interval (5530-5610 mbsl), conversely, is not intersected by ant-tracking lineaments; however, the presence of fractures across this interval are suggested by high gas shows at 5550 and 5587mbsl, oil stains in cutting samples and volume increase in mud pits.

Additionally, production test I that included the base of this interval (5580-5610 msbl) resulted with oil production. Because of this, correlation between ant-tracking and FMI may be considered regular to poor. The Kimmeridgian interval is affected in its top section (5610-5660 msbl) by subtle ant-tracking lineaments, where a production test (5610-5635 mbsl) resulted in oil production in wackestone, oolitic grainstone and packstone facies with relatively abundant fractures (Figure 6.27). Drilling reports show that mud losses, high gas values in mud and oil stains in cutting samples were constant in the interval 5610-5780 mbsl (blue dashed line rectangle), which may indicate presence of fractures Figure 6.26). In seismic data, this interval is partially intersected by an adjacent lineament, which may be related to a fault that could be influencing fracturing in the borehole due to its closeness. The interval 5780-5950 mbsl (red dashed line rectangle) is intersected by several ant-tracking lineaments, which correlates positively with fractures reported in cutting samples in dolomitized wackestone (Figure 6.28). Although no FMI logs were run for this interval, drilling reports seem to confirm the presence of fractures and thus, correlation with ant-tracking attribute can be considered as good.

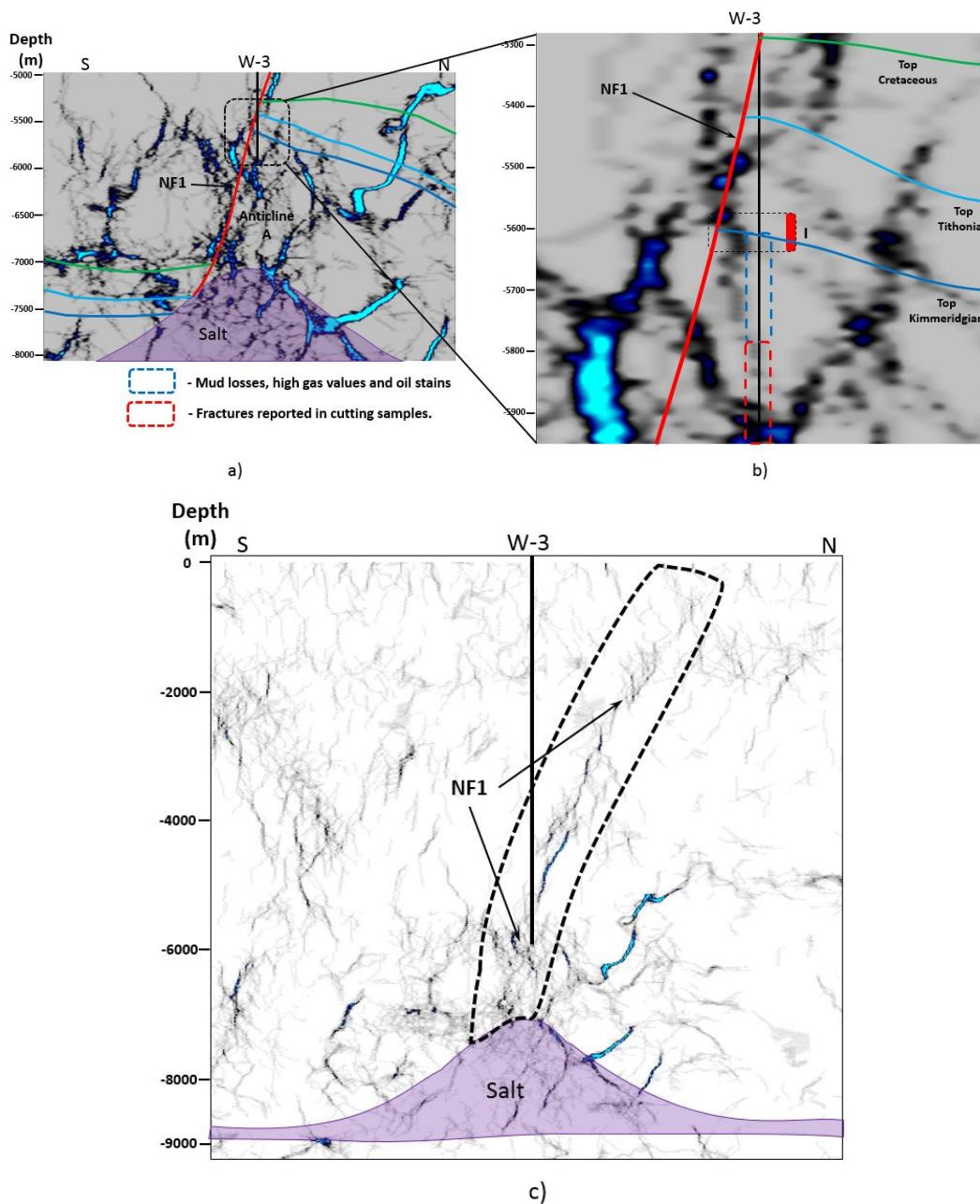


Figure 6.26. (a) Cross-section with ant-tracking attribute shown and, (b) close-up in Well-3 showing the Production tests and zones associated to presence of fractures in Kimmeridgian section. Although the attribute is designed to highlight faults as lineaments, NF1 major fault does not look as a single continuous lineament, but rather as several interconnected segments in (a), whereas in (b) is more difficult to interpret due to the scale of observation. In (c), conversely, NF1 is easier to interpret. No vertical exaggeration.

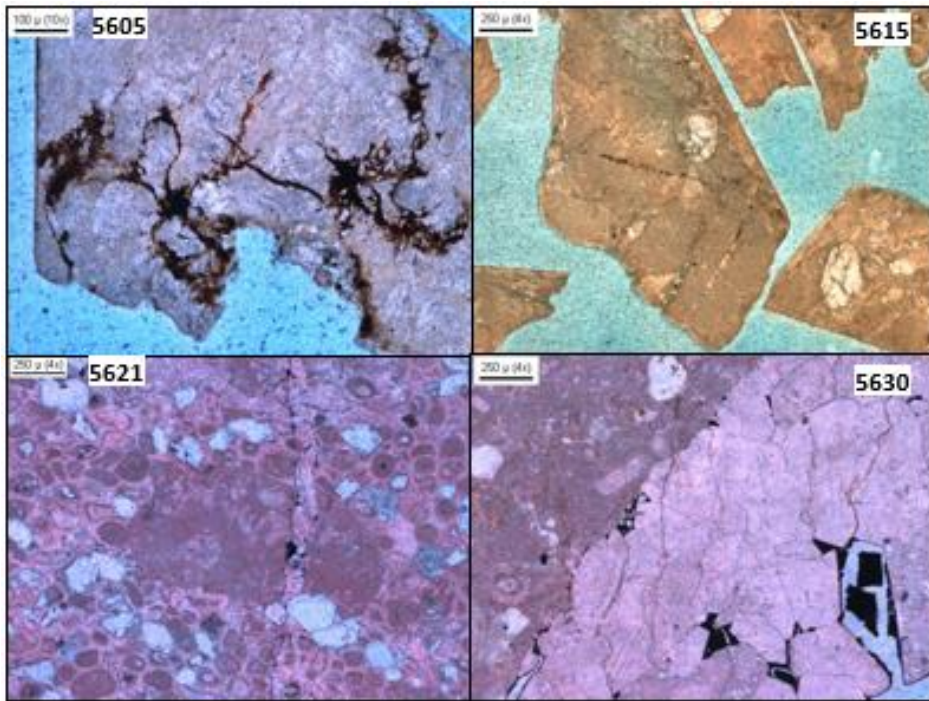


Figure 6.27. Thin sections from the Production test I interval, showing the different oil-prone carbonate facies. Late Kimmeridgian, Well-3.

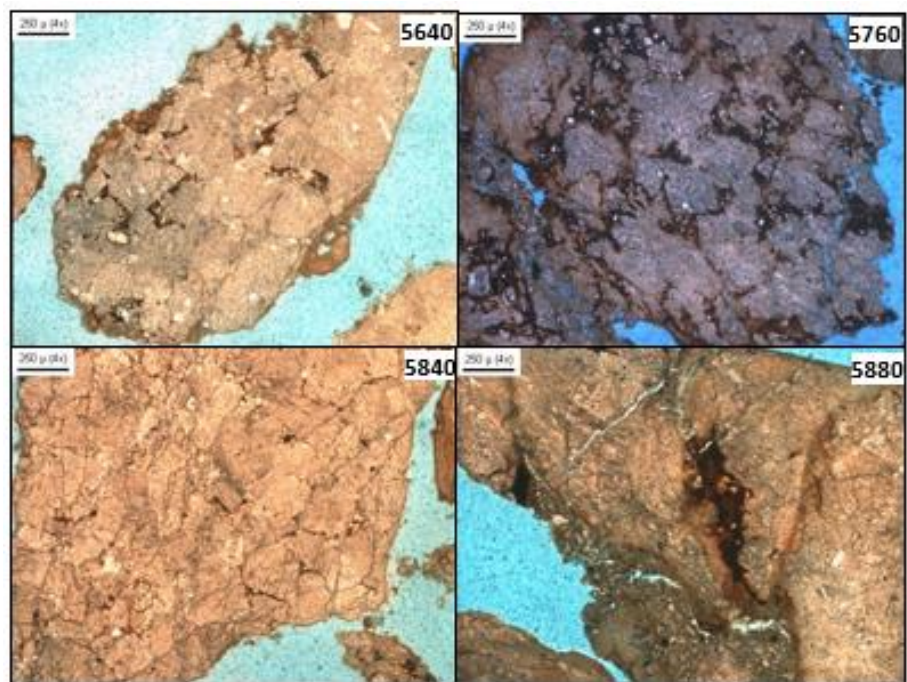


Figure 6.28. Thin sections from the interval 5640-5950 mbsl. Fractures are reported in cutting samples in addition to mud losses and high gas values. Late Kimmeridgian, Well-3.

6.4.4 Depth slices analysis

The same analysis was carried out in depth slices (Figure 6.29). Depth slices are preferred over interpreted surfaces due to their better flexibility for 3D analysis and better correlation results. Since depth slices represent flat surfaces and may include lithologic sequences above or below the interval of interest (depending on the amount of deformation), a comparison squared-window of 500 m length per side (yellow dashed lines) was used as a reference with boreholes located at the centre, so the comparison radius is approximately 250 m, which includes the interval of interest for every case.

Rose diagrams of FMI orientation measurements elaborated for this analysis include fractures from the top of each formation down to 30 m into the selected formations but in some cases, a longer depth window analysis was required in order to identify more representative orientations with a larger data population. In the case of Top Kimmeridgian from W-3, the rose diagram was taken from available core fracture analysis since no FMI logs were run in this interval. In general terms, a good correlation exists between the orientations of ant-tracking lineaments within the analysis window and the fracture orientations measured in FMI logs, so this analysis can be considered potentially predictive of fracture orientations in undrilled areas.

6.4.5 Geomechanical Modelling (GM)

Table 6.2 shows values of rock properties used in the strain calculation for each of the three Mesozoic surfaces in both the Geomechanical and Fault-Response Modelling. These values were obtained from calculated logs, with the exception of Top Kimmeridgian in the W-3 borehole, where a database was used to correlate these rock properties with similar lithologies drilled in another borehole. The lithological characteristics of these rocks are described in detail in Chapter 5.

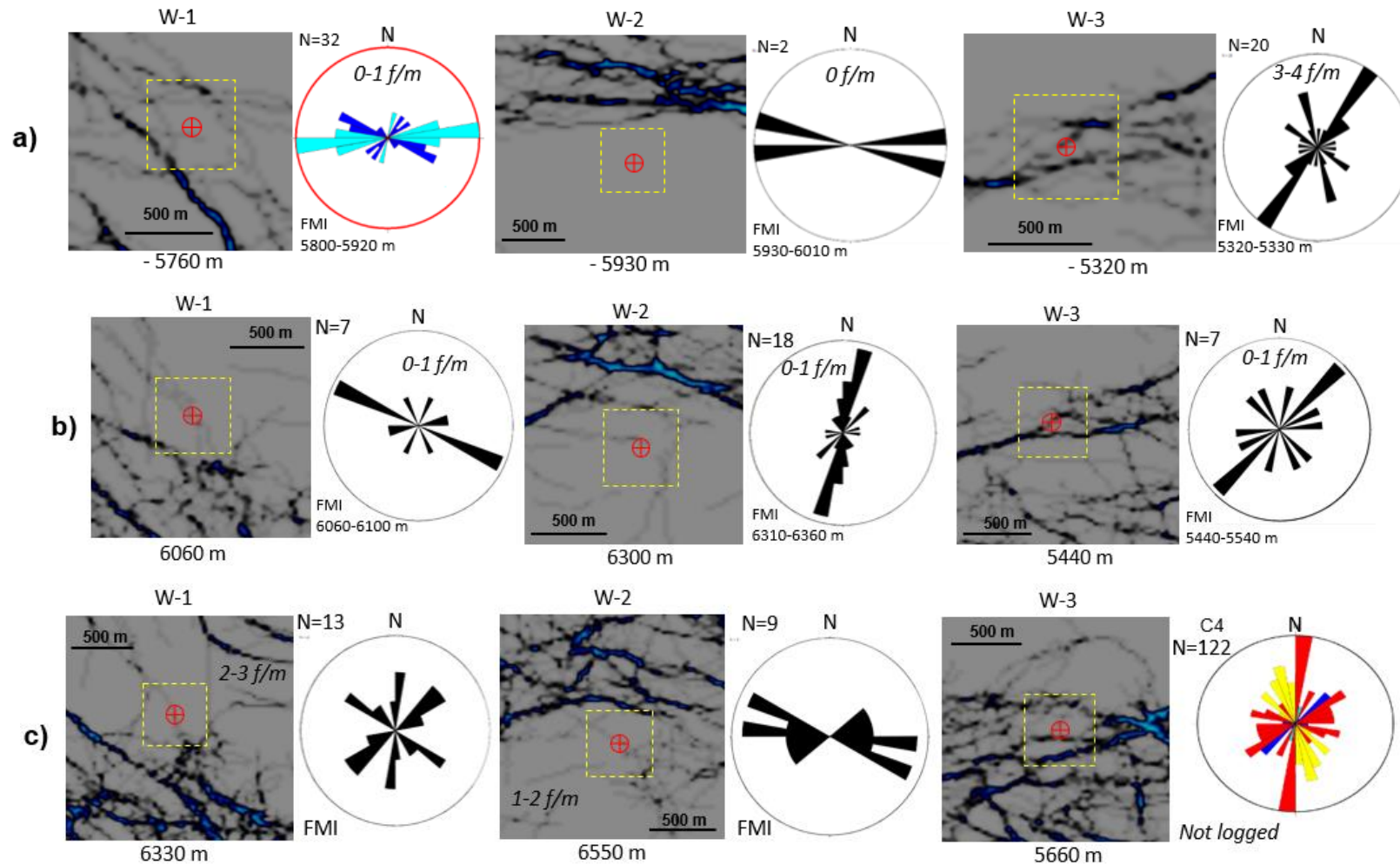


Figure 6.29. Depth slices showing the comparison between the orientations of lineaments interpreted in ant-tracking attribute and orientations measured in FMI logs and core samples. (a) Top Cretaceous, (b) Top Tithonian and, (c) Top Kimmeridgian.

Figure 6.30-32 show the strain maps for each of the three Mesozoic surfaces. Mapped strain corresponds to finite strain 1 (ϵ_1), which represents the maximum strain component. Warm colours correspond to high values in the colour scale, whereas cold colours represent low strain values. The Eulerian calculation method was used because the starting and ending geometries correspond to the undeformed and deformed states, respectively and the attributes are displayed in the deformed state. Different values of Young's Modulus (E) and Poisson's ratio (ν) were assigned for each structure analysed according to the lithology drilled in nearby boreholes. One limitation of this method is that only one pair of values of E and ν can be used for every surface, which may be inaccurate in areas where strong variations of lateral facies exist (Top Cretaceous in Anticline A and Top Kimmeridgian in Pop-Up anticline). In these cases, a sensitivity analysis was conducted by testing the modelling with different parameters and compare the results.

	Young's Modulus (Gpa)			Poisson's Ratio			Density (kg/m3)
	W-3	W-1	W-2	W-3	W-1	W-2	
Top Cretaceous	51	38	55	0.31	0.31	0.28	2700
Top Tithonian	57	59	59	0.3	0.3	0.3	2750
Top Kimmeridgian	36	69	69	0.15	0.3	0.3	2700

Table 6.2. Parameters used for strain calculation in Geomechanical Modelling.

Anticline A

Figure 6.30 shows the strain distribution in Anticline A. In general terms, regions of high strain values are more widely distributed in the hanging-wall, where the highest values are concentrated next to the fault plane. In the footwall, areas with high strain are smaller and located in the hinge and next to the fault plane as well, with low strain dominating the back limb. Fracture density values obtained from FMI logs at borehole W-3 are higher in Top Cretaceous (4-5 f/m) than in Top Tithonian (0-1 f/m), whereas for Top Kimmeridgian no logs were run; however, indirect indicators of presence of fractures while drilling, and a production test, suggest a relatively high FI. Strain values, however, are slightly higher in Top Tithonian, probably because this surface has a greater curvature than Top Cretaceous, which is relatively flat next to the borehole. Moreover, Cretaceous section in the borehole is closer to the fault plane, probably within its damage zone, than Tithonian section (Figure 6.26b). Some artefacts derived from the restoration process are visible mostly in the hanging-wall as evenly spaced, N-S oriented, straight lines.

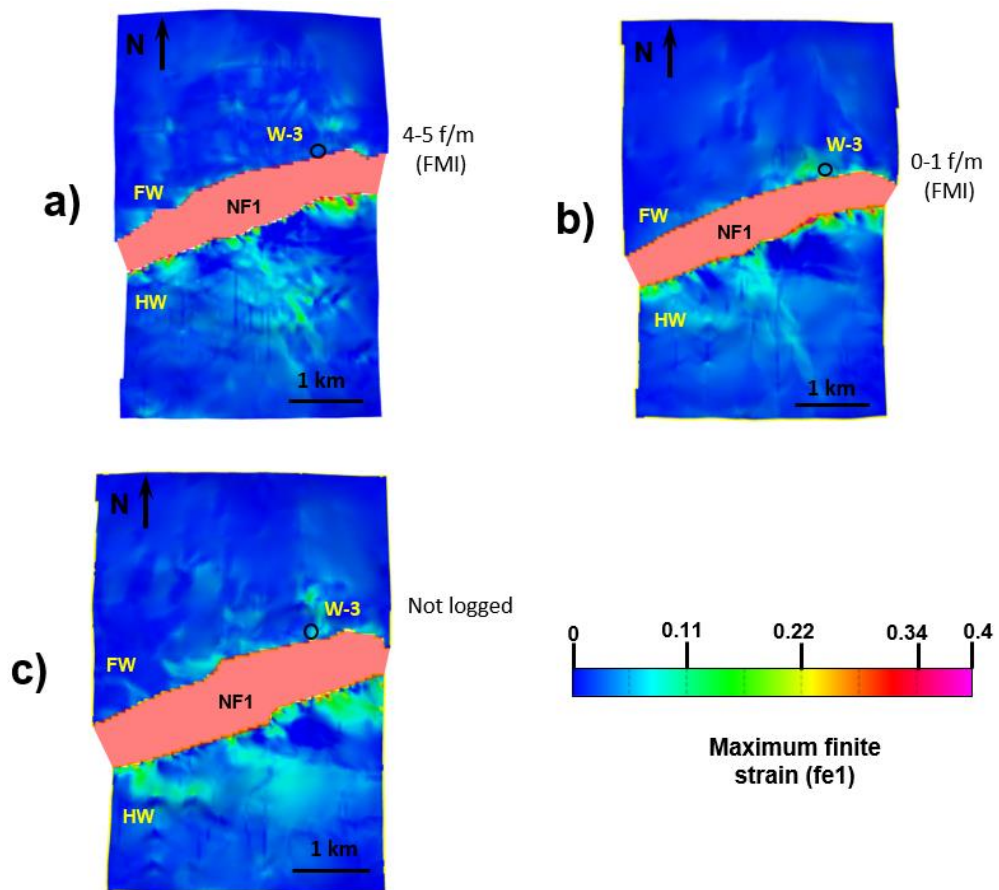


Figure 6.30. Fe1 strain (maximum finite strain) distribution calculated from GM Module displayed on the Anticline A deformed state. (a) Top Cretaceous; (b) Top Tithonian; (c) Top Kimmeridgian. Red polygon indicates the NF1 fault plane. FW= footwall, HW= hanging-wall. Values of fracture density obtained from FMI logs are indicated for comparison.

Anticline C

This anticline is oriented NW-SE and it is delimited in its northern and southern limbs by two reverse faults oriented E-W and WNW-ESE, respectively. Development of this anticline, which is described in detail in Chapter C, is closely related to Anticline A. Figure 6.31 shows the distribution of three zones of high strain located in the hanging-wall hinge and the northern and southern foot-walls right next to reverse fault planes in a similar way as Anticline A. In this area no borehole data are available, so two tests were carried out with different geomechanical parameters from nearby wells W-3 and W-1 for Top Kimmeridgian surface. High strain zones have a wider distribution in the footwalls with higher YM (69 GPa from W-1), whereas strain values are slightly higher in the hanging wall when using W-3 values (36.3 GPa). Values of W-3 correspond to inner platform, oolitic facies, which are restricted to small areas corresponding to paleo-highs associated with salt diapirism, whereas W-1 values correspond to outer platform, dolomitized mudstone-wackestone. A more realistic geomechanical model, based on 2D restoration,

for Top Kimmeridgian would consist of using W-3 strain values in the hanging-wall and W-2 strain values in both footwalls, which is not possible to do due to software limitations.

Anticline B

Figure 6.32 shows the strain distribution for each of the three surfaces. Top Cretaceous and Top Tithonian have similar strain distributions, with highest strains localized in the footwall sides of the fault planes. Also, high strain zones are located in the hanging-wall, where maximum folding has taken place. For Top Kimmeridgian, high strain zones are distributed mostly in the southern limb and are related to gently folded zones. Another high strain zone is located in the footwall adjacent to the northern reverse fault. FMI values seem to have a degree of positive correlation with strain values in the three surfaces.

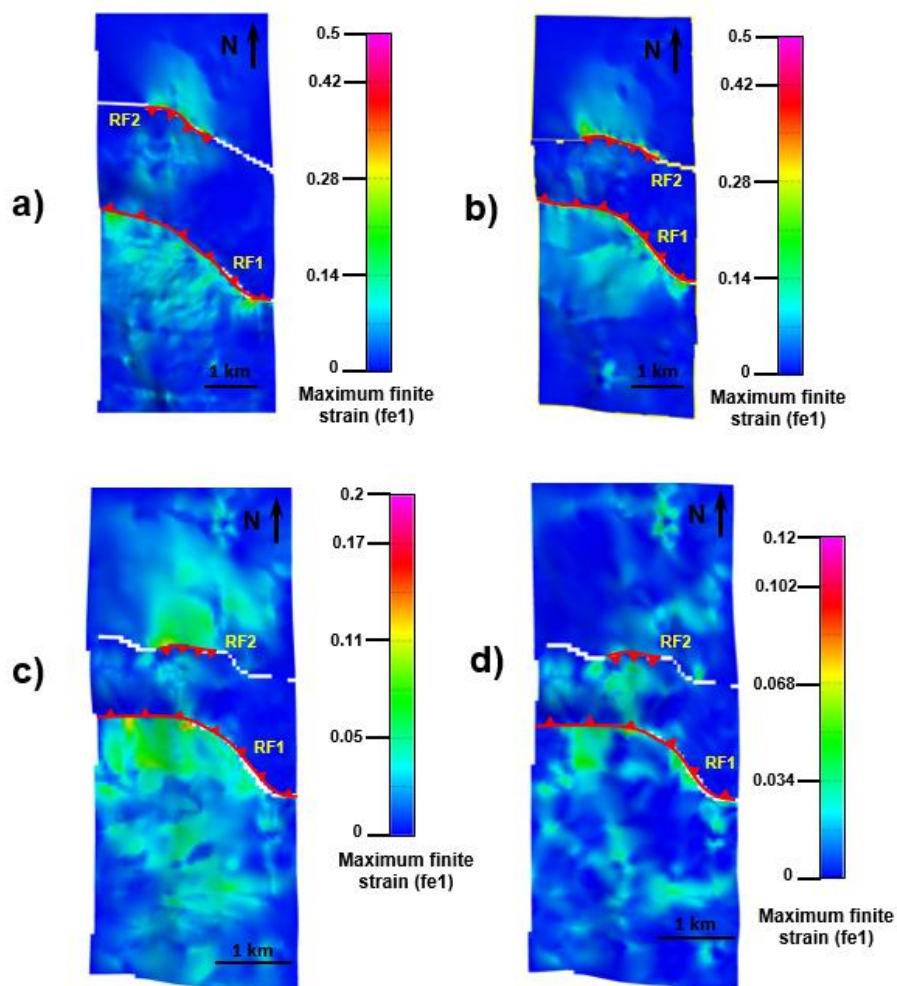


Figure 6.31. Sensitivity analysis of Fe1 strain (maximum finite strain) distribution calculated from Geomechanical Modelling Module displayed on Anticline C deformed state. (a) Top Cretaceous; (b) Top Tithonian; (c) Top Kimmeridgian calculated using W-1 parameters; (d) Top Kimmeridgian using W-3 parameters. RF1 and RF2 correspond to reverse faults.

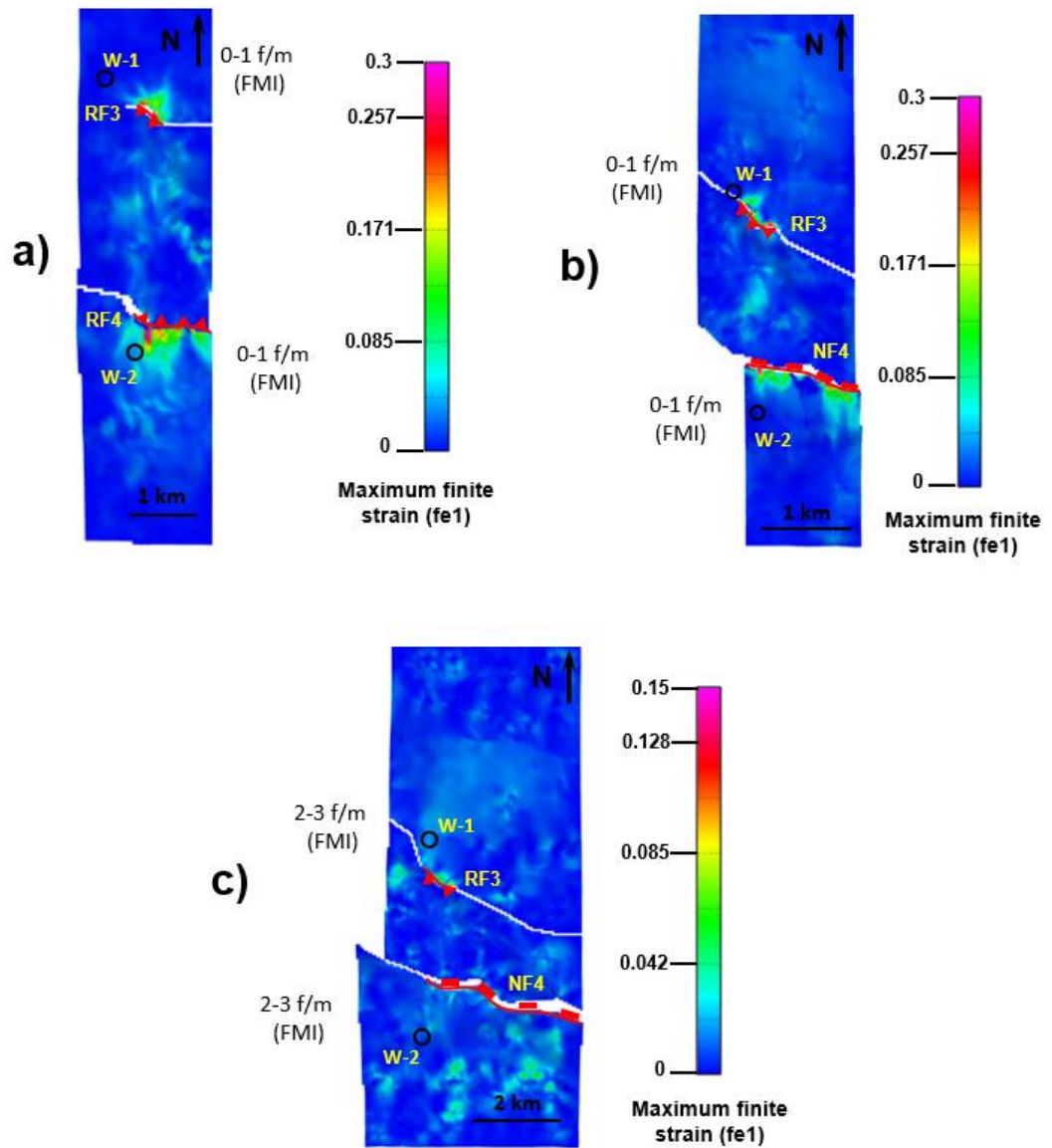


Figure 6.32. Fe1 strain (maximum finite strain) distribution calculated from GM Module displayed on the Anticline B deformed state. (a) Top Cretaceous; (b) Top Tithonian; (c) Top Kimmeridgian. RF3, RF4 and NF4 correspond to reverse and normal faults, respectively. Values of fracture density obtained from FMI logs are indicated for comparison.

6.4.6 Fault Response Modelling (FRM)

Figure 6.33-35 shows the distribution of calculated total strain for each of the three anticlines within the study area using the FRM approach. Mapped strain corresponds to the maximum stretching direction (E1) and the same values of rock strength parameters shown in Table 6.2 were used; however, maximum strain maps show some differences with respect to those produced with GM as in the FRM approach, the calculation of high strain zones is emphasized in areas adjacent to the fault planes, whereas fold-related strain is not taken into account.

For Anticline A, high strain zones are located along the fault plane and extending irregularly towards the hanging wall and gradually decreasing in the footwall back limb whereas in the GM strain maps, high strain zones are patchy and have a more irregular distribution (Figure 6.33).

For the Anticline C, a zone of high strain in the hanging-wall is associated with the interaction of individual reverse faults and can be considered as a potential area for fracture development in the Top Tithonian and Top Kimmeridgian surfaces (Figure 6.34). In contrast, in the Top Cretaceous surface the hanging-wall is a low strain zone and high strain zones are located next to the fault planes.

For Anticline B, both Top Cretaceous and Kimmeridgian surfaces exhibit low strain zones in the hanging-wall, which differs from the GM strain maps (Figure 6.35). The Top Tithonian surface, however, shows a high strain zone that extends towards the north of the southern fault into the hanging-wall in a similar way to the GM strain map.

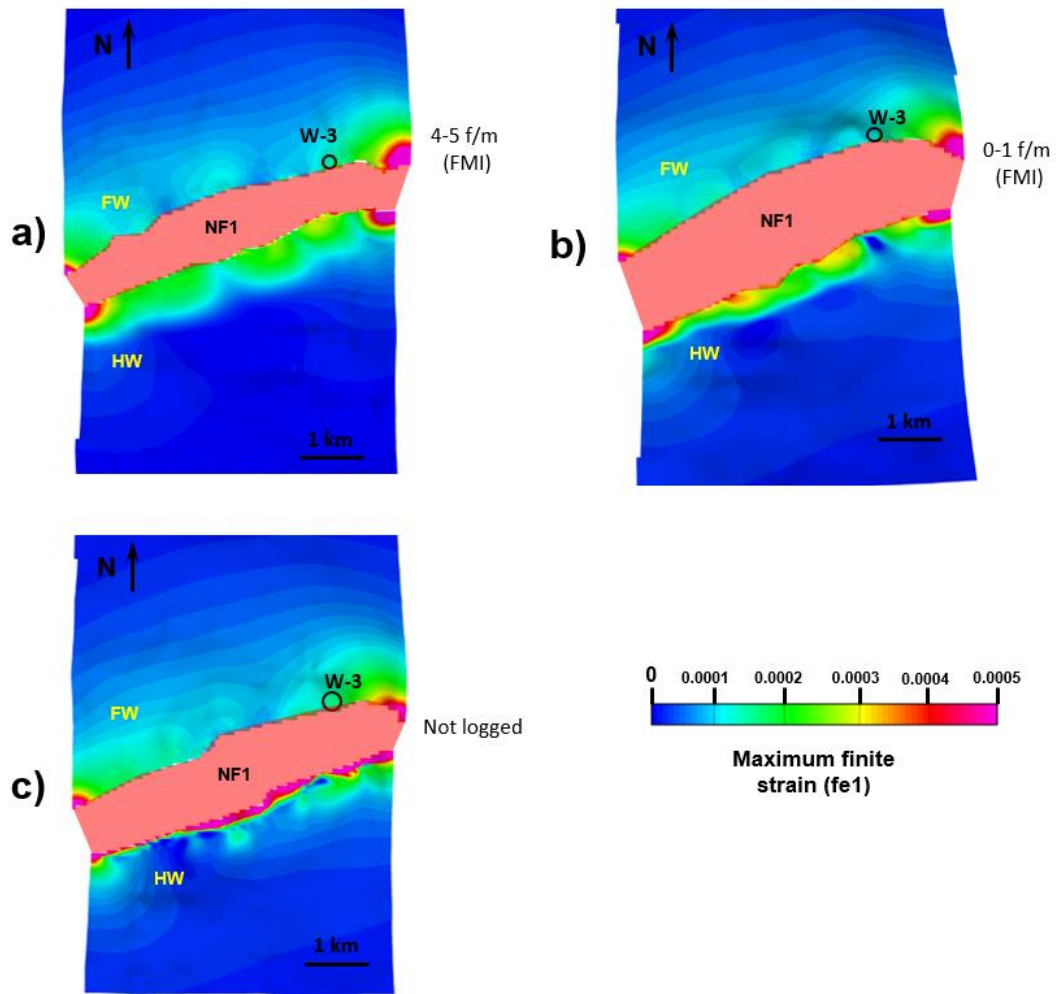


Figure 6.33. E1 Strain (maximum stretching) distribution calculated from FRM Module displayed on the Anticline A deformed state. (a) Top Cretaceous; (b) Top Tithonian; (c) Top Kimmeridgian. Red polygon indicates the NF1 fault plane. FW= footwall, HW= hanging-wall. Values of fracture density obtained from FMI logs are indicated for comparison.

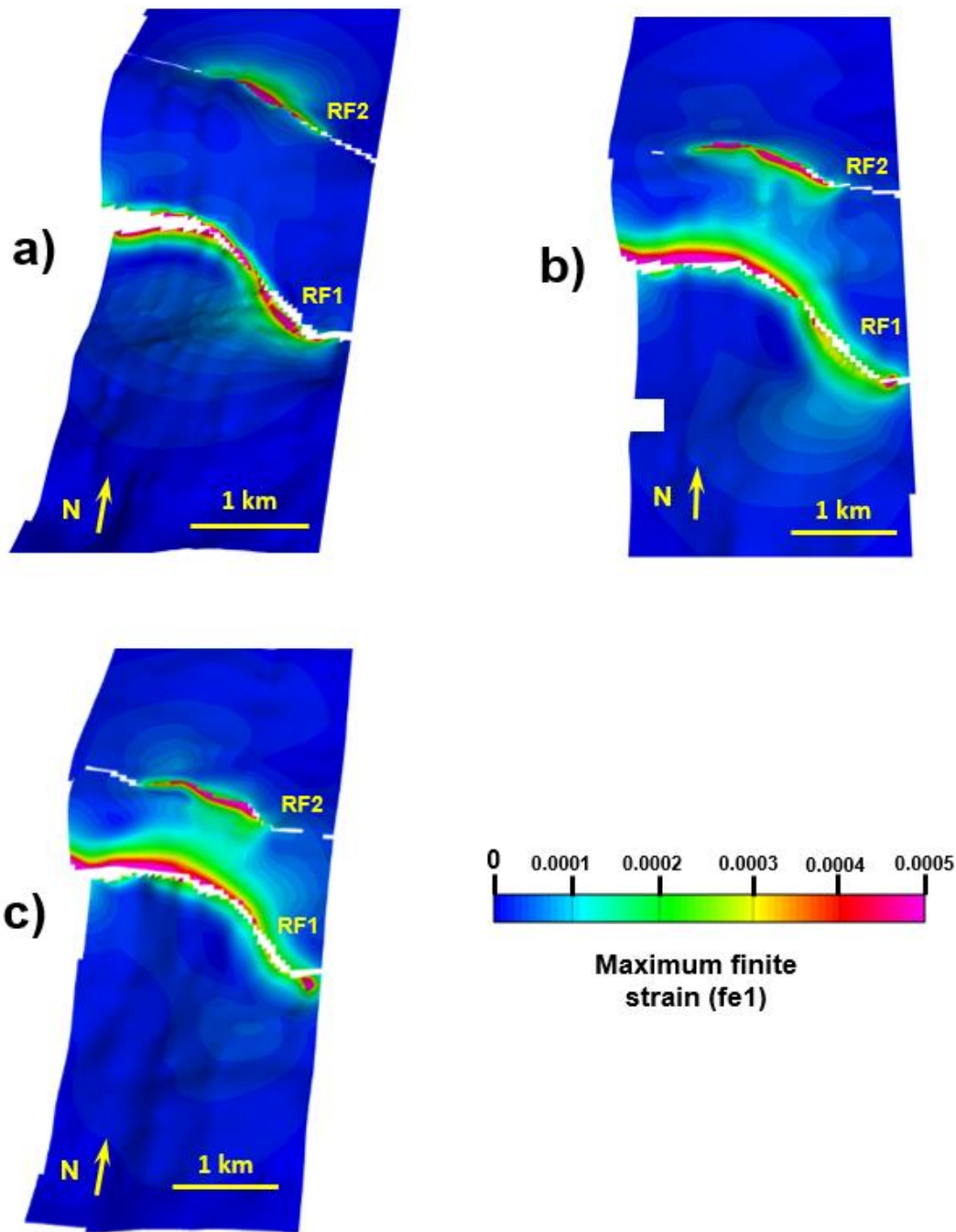


Figure 6.34. E1 Strain (maximum stretching) distribution calculated from FRM Module displayed on the Poo-Up Anticline deformed state. Top left: Top Cretaceous; top right: Top Tithonian. Bottom Top Kimmeridgian. RF1 and RF2 correspond to reverse faults.

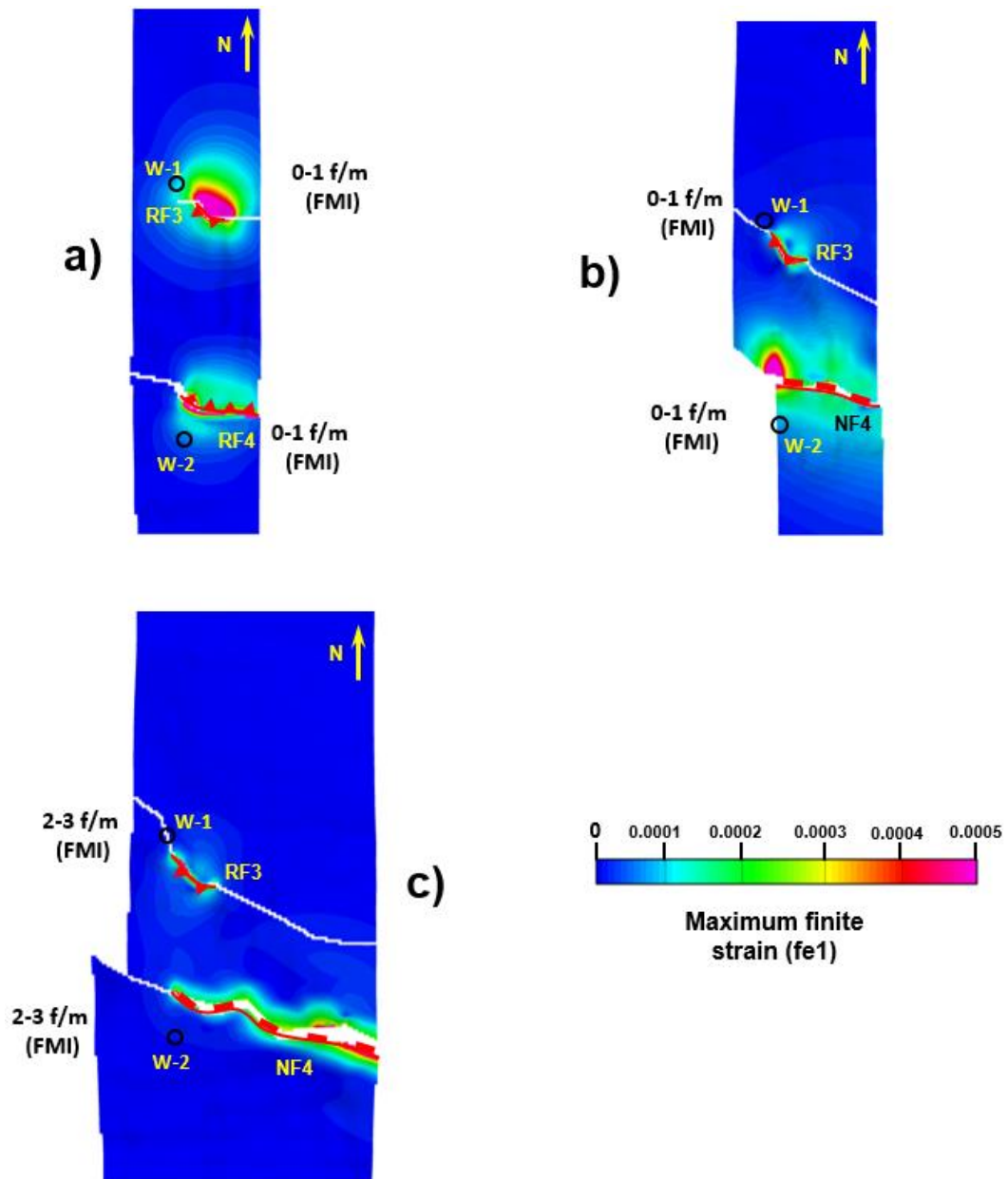


Figure 6.35. E1 Strain distribution calculated from FRM Module displayed on the Anticline B deformed state. Top left: Top Cretaceous; top right: Top Tithonian. Bottom Top Kimmeridgian. RF3, RF4 and NF4 correspond to reverse and normal faults, respectively. Values of fracture density obtained from FMI logs are indicated for comparison.

6.5 Integration of strain and attribute maps

A comparison of strain and structural attribute maps is essential to establish a correlation between structural position and fracture density and orientation within the study area. Both analyses are independent and correspond to indirect indicators of the possible presence of fractures based on different principles:

- 1) Geomechanical modelling calculates strain in a surface from an undeformed state to a deformed state and vice versa. Deformation is accommodated by folding and/or fracturing, whose intensities can be related directly to strain (Price, 1966; Nelson, 1985).
- 2) Structural attributes are based on variations between adjacent seismic traces, which can be caused, among other reasons, by the presence of folds and/or fault/fractures (Marfurt and Alves, 2015). Therefore, a highly deformed rock mass is more likely to have a higher fracture density than a relatively undeformed one.

A visual comparison between the strain maps obtained with GM and their corresponding ant-tracking maps which also have the structural maps superimposed is shown in Figure 6.36, 6.37 and 6.38. GM maps were selected for comparison over FRM maps as they provide a better visual correlation to the ant-tracking maps. For Anticline A, high strain zones have a similar distribution to that of lineaments observed in the ant-tracking maps for the three Mesozoic surfaces. The density of lineaments is generally higher in the hanging-wall, although for Top Kimmeridgian the footwall area next to the fault plane also shows numerous lineaments. In the case of Anticline C, high strain zones have a good correlation with ant-tracking lineaments in all three surfaces, particularly in the hanging-wall, where deformation has been accommodated by folding and the corresponding associated fracturing. High values of strain are also located next to the fault planes in the footwalls as anticipated. For Anticline B, high strain zones in the hanging-wall show a good correlation with ant-tracking lineaments. Conversely, high strain zones adjacent to the fault planes in the footwalls do not have a good correlation with ant-tracking lineaments.

In anticlines B and C, the density of ant-tracking lineaments generally increases with depth, whereas the folding intensity and calculated strain decrease, especially in the areas with higher structural deformation. This apparent contradiction may be explained as a product of bad imaging at depths below 6 km, where very low frequencies are predominant and therefore, low seismic resolution prevails, thus generating more lineaments that may not be associated with faults or/fractures. Another explanation may be that presence of fractures in rock masses increases with depth due to the increase of vertical lithostatic loading, which alters the amplitude and travel times of the seismic waveform, thus affecting seismic velocities and consequently, negatively affecting the quality of seismic imaging (Boadu and Long, 1996).

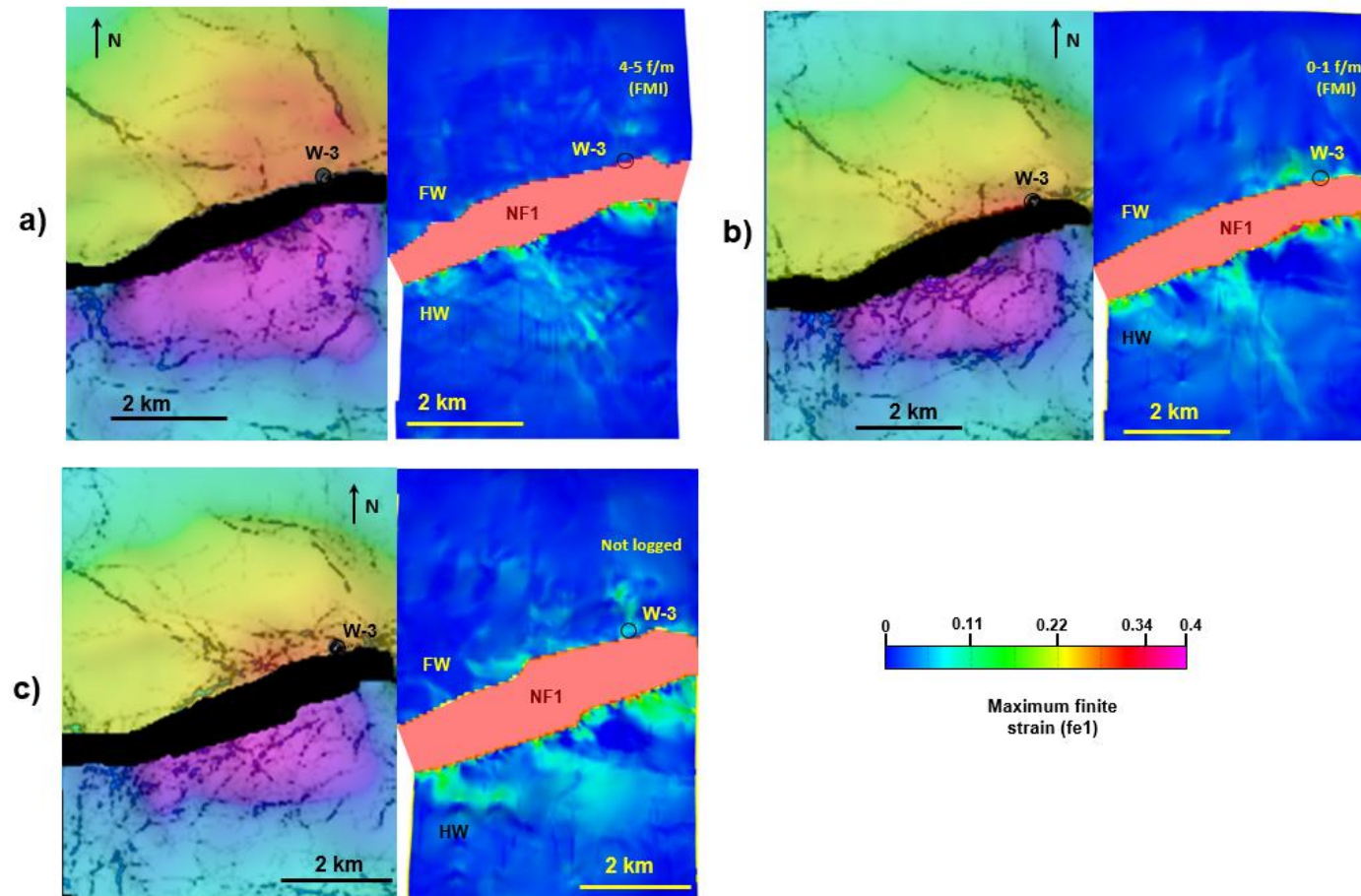


Figure 6.36. Comparison between strain calculated with Geomechanical Modelling and structural position for Anticline A using ant-tracking attribute superimposed on structure map. A) Top Cretaceous; (b) Top Tithonian; (c) Top Kimmeridgian. NF1= Normal fault 1; FW= Footwall; HW= Hanging-wall.

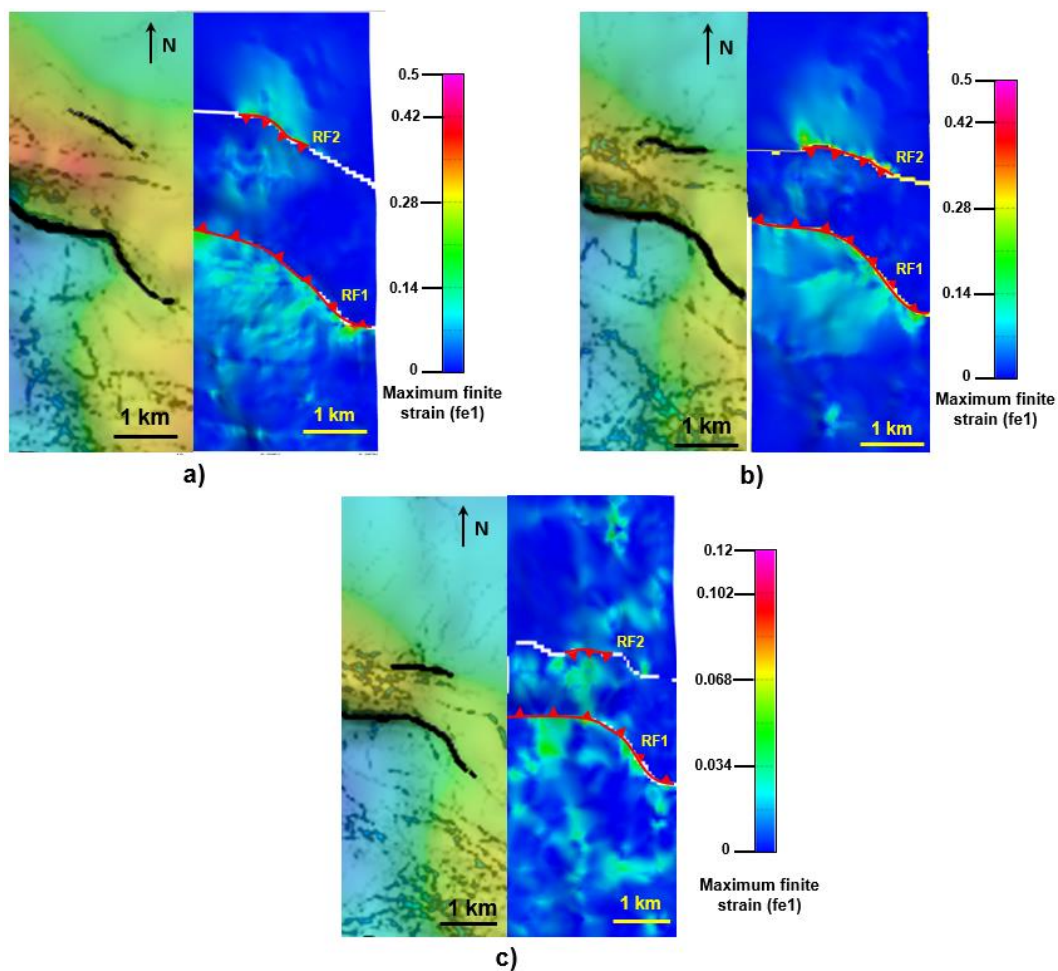


Figure 6.37. Comparison between strain calculated with Geomechanical Modelling and structural position for Anticline C using ant-tracking attribute superimposed on structure map. A) Top Cretaceous; (b) Top Tithonian; (c) Top Kimmeridgian. RF1 and RF2= Reverse faults.

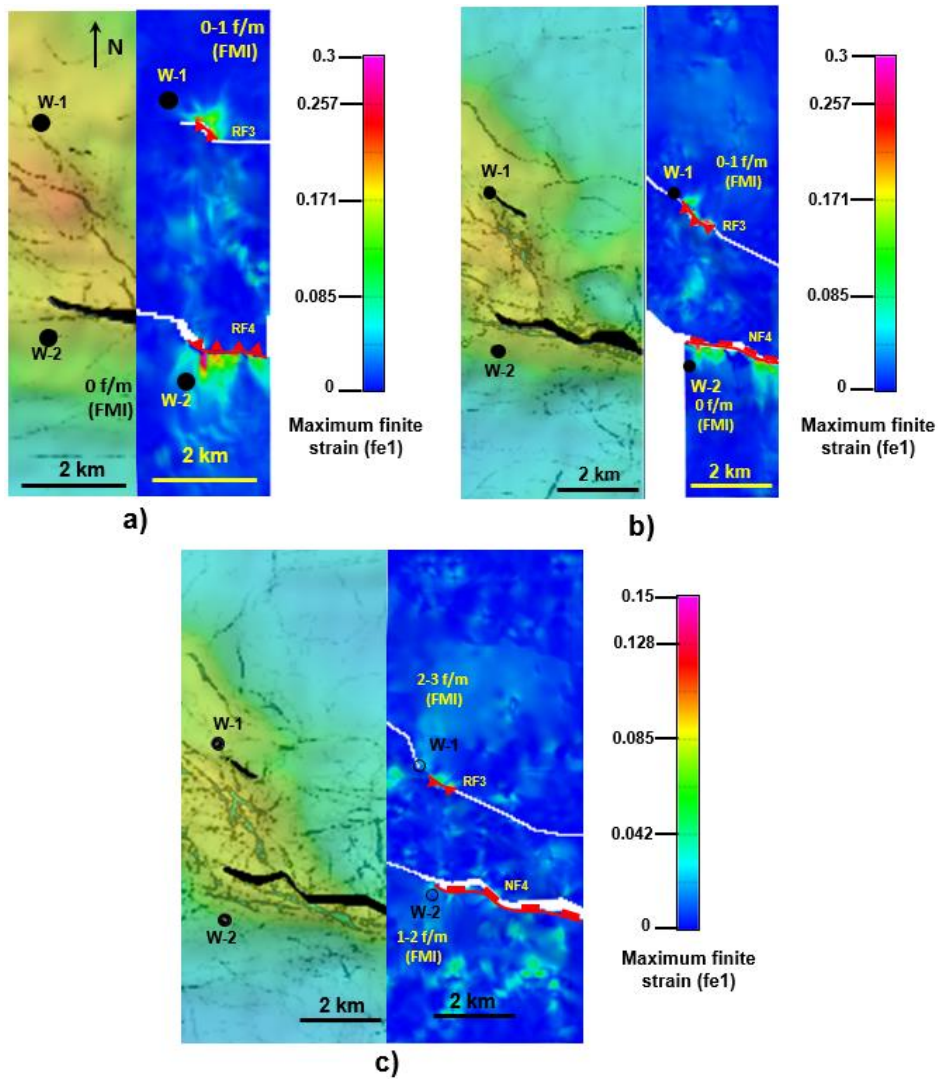


Figure 6.38. Comparison between strain calculated with Geomechanical Modelling and structural position for Anticline B using ant-tracking attribute superimposed on structure map. A) Top Cretaceous; (b) Top Tithonian; (c) Top Kimmeridgian. Values of fracture density from FMI logs are annotated as reference. RF3, RF4 = Reverse faults; NF4= Normal fault.

6.6 Discussion

Structural position and mechanisms of deformation are important controls on fracture development and distribution associated with geological structures. Quantitative and qualitative knowledge of fracture distribution is crucial during hydrocarbon exploration, due to its economic impact on an adequate assessment of reservoir rock and the correct choice of locations for exploratory boreholes. The results obtained from a combined analyses of seismic attributes and geomechanical modelling increase our current understanding about the influence of these factors in fracture development. Furthermore, the integration of these analyses with well data allowed to propose an evolutionary model of fracture development.

6.6.1 Role of structural position

In this study, structural seismic attributes analyses (variance, curvature, ant-tracking) show that areas with higher density of lineaments related to faulting are directly associated with structural position. In the three major structures investigated: Anticlines A, B and C, higher densities of ant-tracking lineaments that can be associated with subtle faults are observed in their hinges. Additionally, areas adjacent to major faults exhibit high densities of what are considered to be possible faults. This observation is reinforced by the geomechanical modelling, which yields similar results from strain maps calculated on the Mesozoic surfaces, where higher strains are distributed predominantly on highly deformed areas and adjacent to fault planes. Fracture Intensity (FI) values obtained from FMI indicate that FI for the three Mesozoic surfaces are slightly higher in borehole W-3, which is located in the hinge of Anticline A, whereas the boreholes W-1 and W-2 are located in opposite limbs of Anticline B. This supports the hypothesis that structural position is a primary control on FI, rather than lithology, since the lithological facies are very similar in the three boreholes for the Cretaceous and Tithonian. In contrast, for the Kimmeridgian, lithological variation is greater (inner platform vs outer platform carbonates) within the study area; however, the same tendency in FI can be observed. These results are in agreement with similar previous studies showing how structural position influences FI (e.g., Watkins et al., 2015; Watkins et al., 2018); however, those studies were conducted from fieldwork, whereas this work utilises limited borehole data, which are mostly unidimensional and may not be fully representative of a greater rock volume.

Strain maps calculated by the Geomechanical Modelling show a distribution of high strain zones in areas adjacent to fault planes and anticlinal hinges. This strain distribution can be directly correlated to the ant-tracking maps, and so the density of lineaments associated with fractures in the ant-tracking attribute can be associated with high strain zones. Conversely, low strain zones are associated with low deformation areas and, therefore, areas where FI is likely to be lower than in high strain zones.

6.6.2 Role of mechanism of deformation

The mechanism of folding is also another controlling factor for fracture development; however, another factors such as lithology, mechanical properties of rocks and fold strain history influence fracture orientation and distribution within a geological structure (Eckert et al., 2014). In the study area, the analysed anticlines A and B have undergone a complex geological history involving several deformational events (and therefore, different mechanisms of deformation), which is reflected in well and seismic data. Although it is very complex to define a detailed and accurate sequence of fracturing through time with the available data, it is possible to propose a simplified model for the

Mesozoic carbonate rocks based on the analysis of the geometrical relationship between fracture and fold geometry according to conceptual models by Price (1966) and Stearns (1968) and the deformational history of each anticline.

6.6.2.1 Anticline A

Anticline A consists of a three-way closure, salt-cored anticline oriented NE-SW 70° bounded by a normal fault. Its deformational history (Figure 6.39) commenced with early syn-folding, extensional fractures sets that may have developed during the early stages of active salt diapirism along the salt anticline axis, whereas in the adjacent withdrawal minibasins, pre-folding fracture sets and bed-parallel stylolites developed due mainly to vertical lithostatic pressure (σ_1), which in turn caused salt withdrawal and subsequent bending of the overburden developed (Figure 6.39a). Fracture sets f1 and f2 observed in Core 4 (W-3, Late Kimmeridgian) are perpendicularly oriented each other (NW-SE 70° and NE-SW 30°, respectively) and slightly oblique to the fold axis, and possibly developed during a pre-folding stress regime, and thus not related to the final fold geometry (Figure 6.40).

During the D1 event (Late Jurassic- Late Cretaceous), Anticline A developed initially in a relatively undeformed footwall of a roll-over structure associated with a listric normal fault; fractures developed mainly in the hanging wall due to the higher strain generated by the formation of antithetic faults and folding of layers in order to accommodate extension (Bose and Mitra, 2009), whereas fracturing in the footwall may have been restricted to the damage zone associated with the listric normal fault, which acted as an isolated fault and therefore, no relay ramps or overlapping with other faults influenced fracture development in the footwall (Figure 6.39b). Later, tectonic compressional events D2 and D3 re-deformed this structure by buckle folding and layer-parallel shortening associated with a horizontal principal stress (σ_1), thus generating sets of conjugate shear fractures and vertical stylolites in both the hanging-wall and footwall. Fracture sets f5 (W-3, Core-3, NE-SW 50°, Early Cretaceous) and f3, f4 (W-3, Core-4, NE-SW 50° and 40°, Late Kimmeridgian) are 20-30° oblique to the fold axis and have very similar orientation to pre-existent fracture sets, which could have conditioned the orientation of these new fracture sets during D2-D3 events; however, no conjugate fractures were identified (Figure 6.39c) to support these assumption. Finally, extensional event D4 probably reactivated this fault with a dextral strike-slip component (σ_1 and σ_3 horizontal) and generating new fracture sets, resulting in multiple fracture orientations close to the main fault plane as reported in core samples and FMI logs from borehole W-3 (Figure 6.39d).

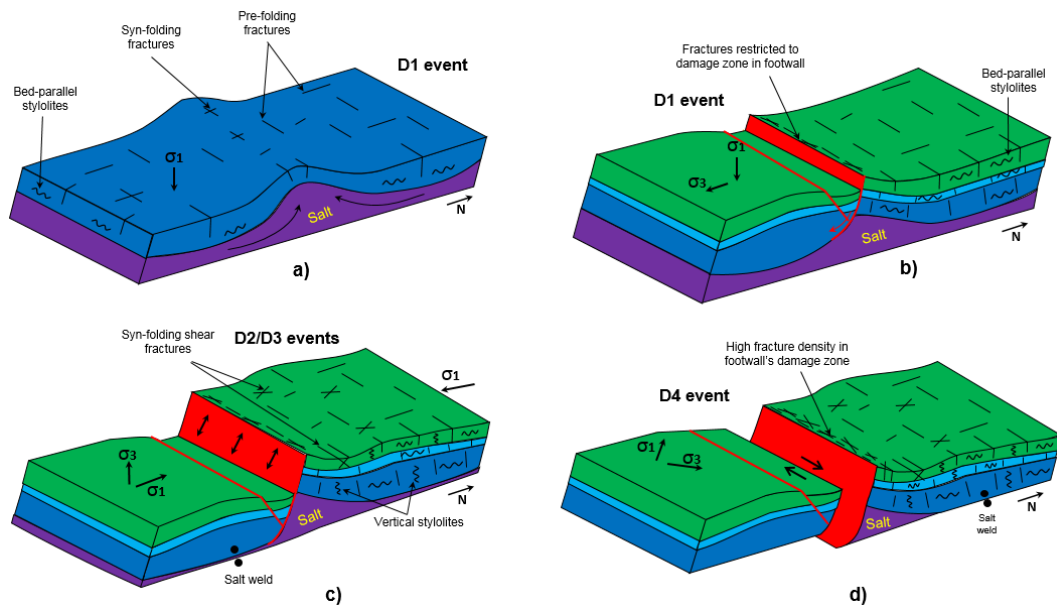


Figure 6.39. Schematic evolution of fracture development in Anticline A. (a) Late Kimmeridgian; (b) Late Cretaceous; (c) Oligocene-Miocene; (d) Pliocene.

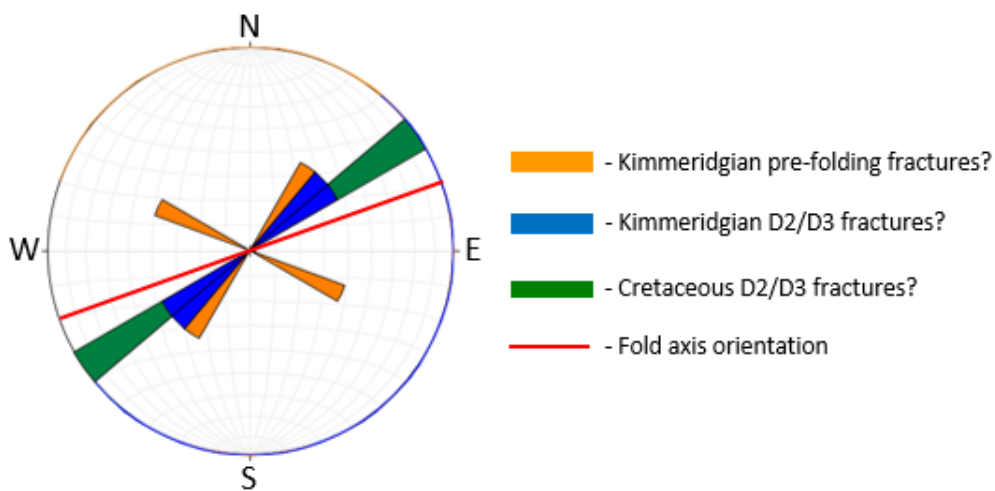


Figure 6.40. Rose diagram from Anticline A showing different fracture sets measured in W-3.

6.6.2.2 Anticline B

Anticline B (Figure 6.41) consists in a salt-cored anticline orientated NW-SE 40° with a four-way closure. The southern and northern limbs are affected by a normal fault and a reverse fault orientated NW-SE 40° and WNW-ESE respectively. Folding related to salt diapirism was of low intensity, although diapirism controlled bathymetry during Mesozoic times (Figure 6.41a). Early extensional fractures and bed-parallel stylolites developed during D1 event may result from lithostatic load, with a vertical σ_1 (Figure 6.41b). These fractures seem to show a consistent, oblique orientation (lack of asymmetry) respect to the fold axis and may correspond to f1 (NW-SE 10°, W-2 Core 3,

Kimmeridgian), f1 (WNW-ESE, W-2 Core 4, Kimmeridgian), f1 (NW-SE 80°, W-2, Core 1C, Late Cretaceous) and f1, f2 (NNE-SSW and E-W, W-1, Core 1, Late Cretaceous; Figure 6.42). The almost identical orientations of these fracture sets in Cretaceous and Kimmeridgian levels, which have similar lithology is striking, and may be due to a single non-tectonic fracturing event that simultaneously affected the Mesozoic column; alternatively, it is possible that there were two different events but with similar stress regimes.

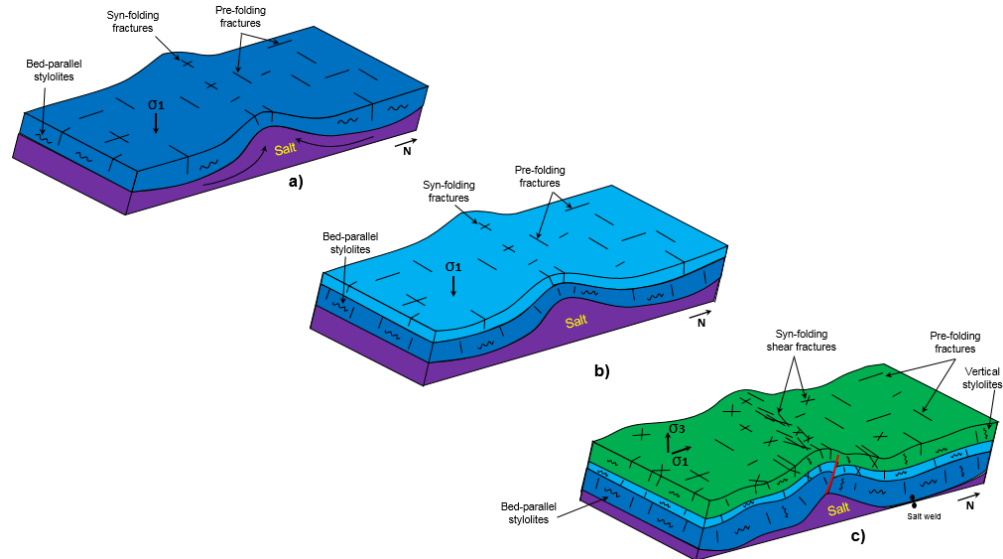


Figure 6.41. Schematic evolution of fracture development in Anticline B. (a) Late Kimmeridgian; (b) Late Tithonian; (c) Oligocene-Miocene.

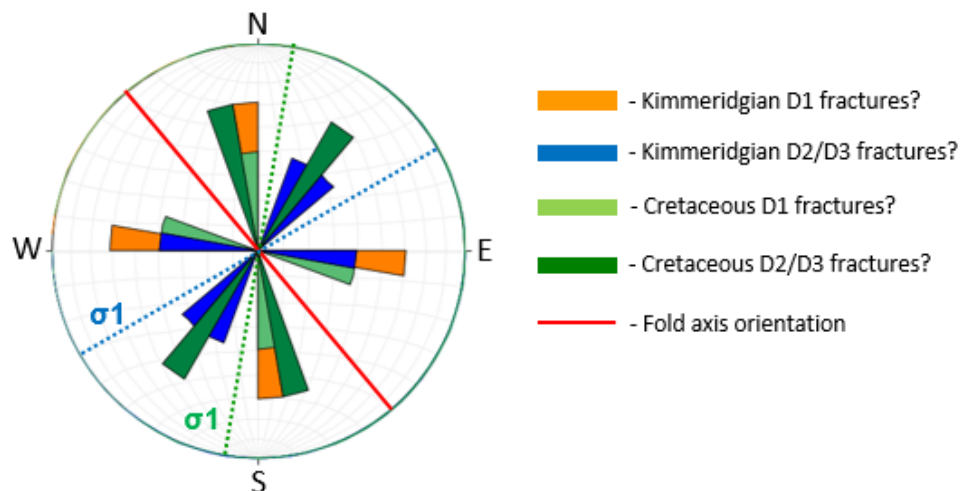


Figure 6.42. Rose diagram from Anticline B showing different fracture sets measured in W-2 and possible σ_1 stress orientations of D2/D3 events.

Similarly to Anticline A, contractional events D2 and D3 folded Anticline B by buckling and layer-parallel shortening, and forming new sets of fractures (Figure 6.41c). For Late Kimmeridgian, f2 and f3 sets (NE-SW 20-40° and E-W, W-2, Core-3) are reported to be

synchronous, and their orientations are perpendicular and oblique to the fold axis, respectively. If they are conjugate shear fractures related to D2 or D3, then a possible orientation of horizontal σ_1 would be NE-SW 60°, which is almost perpendicular to the fold axis (Figure 6.42), and thus geologically consistent. FMI also shows fractures that trend E-W and slightly oblique orientations, which seem to support the hypothesis that they correspond to D2 or D3 events.

For Late Cretaceous, f2 and f3 sets (NW-SE 20° and NE-SW 35°, W-2, Core 1C) are reported as synchronous and oriented oblique and perpendicular to the fold axis, respectively. If they are the result of the same deformational event (D2 and/or D3), then a possible horizontal σ_1 orientation would be NE-SW 10°, which is also consistent with regional geology in the study area (Figure 6.42). This correlation shows that a symmetry between fracture and fold orientations exists, and therefore, fracture orientations in undrilled areas can be deduced if fold orientations are known from seismic interpretation. Although most of fracture orientations within the borehole data show a relatively good symmetry with fold geometry, some fracture orientations measured in core samples and FMI logs show a lack of symmetry with respect to the anticlines axis. This may be the result of local stress variations related to pre-existent fractures, which may control the orientation of new fractures (Bergbauer and Pollard, 2004).

6.6.3 Fracture intensity

A correlation between FI values from FMI and ant-tracking/strain maps is difficult to establish since FMI results are representative only of the sampled volume (i.e., the boreholes), which is a very small area with a maximum diameter of 8 in (20 cm), while the ant-tracking encompasses much wider areas. Moreover, larger fractures are also difficult to sample in boreholes due to the low probability of intersecting them and, if that happens, mechanical problems while drilling and/or low core recovery may happen if associated fracturing is intense. The ambiguous results of FMI vs Ant-tracking depth slices clearly shows that the number of lineaments inside the window analysis around the boreholes cannot be associated directly to the FI values obtained from FMI logs, even if these lineaments seem to have geologically consistent orientations and correspond to subtle faults or fractured zones. Watkins et al., (2018) showed that lateral variability in FI at outcrop scale in the Torridon Group sandstone, Scotland represents a high degree of uncertainty for FI prediction; however, qualitative estimations of FI based on ant-tracking and strain maps may be more reliable when enough well data are available for calibration, as is the case of mature, well developed oilfields. If no well data were available, or these are scarce (like in this study), FI qualitative estimations should be considered with high degree of uncertainty, especially if carbonate rocks are involved,

which may show great lateral and vertical variability related to lithological heterogeneity derived from their high sensitivity to diagenetic changes.

The observed strain distribution follows expected patterns since high strain zones are located in the anticlines hinges and next to the fault planes and low strain zones are located in areas of low-deformation; however, strain distribution also shows a weak correlation with FI values from FMI logs probably due to the difference in the scale of observation and resolution of modelling, which cannot detect small-scale strain variations. Moreover, strain is calculated along a 2D surface and the value at each point is representative of a single vertical depth whereas FI from FMI logs are considered as an average of vertical intervals which may include the value corresponding to the depth of strain calculation. Additionally, interpreted surfaces used as an input could be affected by smoothing during the mapping process, which may slightly vary the depth at some points. Another explanation is that the drilled section in the borehole lies within the damage zone given the proximity to the fault plane, thus intersecting a larger number of fractures even if strain is relatively low due to a low curvature of the modelled surface (e.g., the Cretaceous section in Anticline A).

As demonstrated here, on a prospect scale (areas of up to tens of square km), qualitative FI estimation from the combined analysis of Ant-tracking attribute and geomechanical modelling can be considered reasonably useful in hydrocarbon exploration to assess the quality of reservoir rock; on the other hand, quantitative FI is much more difficult to predict at the smaller scale due to the reasons explained above; however, an integral approach including a greater number of boreholes may help to reduce the degree of uncertainty.

6.6.4 Fracture orientation

The importance of predicting the fracture orientation lies in the fact that it is closely related to permeability anisotropy, and consequently, in the quality of reservoir rock. Thus, several cross-cutting fracture orientations are most likely to increase the fracture connectivity and percolation potential than a single orientation where fractures are parallel. The interpreted orientation of lineaments within the ant-tracking attribute in surfaces and depth slices provided a relatively good matching with fracture orientations obtained from FMI logs and core samples (section 1.5.4, Figure 6.29). Depth slices seem to provide a better correlation between ant-tracking and FMI orientations and therefore, it may be more suitable to be used in the prediction of fracture orientations at a borehole scale; whereas ant-tracking in surfaces seems to be more suitable for larger scale analysis of fracture orientations and in helping to define paleo-stress orientations.

Anticlines in the study area show lineaments orientations that are consistent with models by Price and Cosgrove (1990) and appear to be related to pre-folding and syn-folding stages (Figure 6.43); however, the relationship between fold geometry and fracture orientation may not always follow pre-established and generally accepted concepts since folding can reactivate pre-existent fractures whose orientations may not match the resulting fold symmetry (Bellahsen et al., 2006). Also, different tectonic regimes during deformational history generate orientations that may be difficult to relate to the final fold geometry (Casini et al., 2011). Finally, pre-existent fractures can generate local stresses around them, depending on their mechanical properties, and thus control the orientation of new fracture sets which may be asymmetrical respect to the principal stress that generated them (Gudmundsson, 2011).

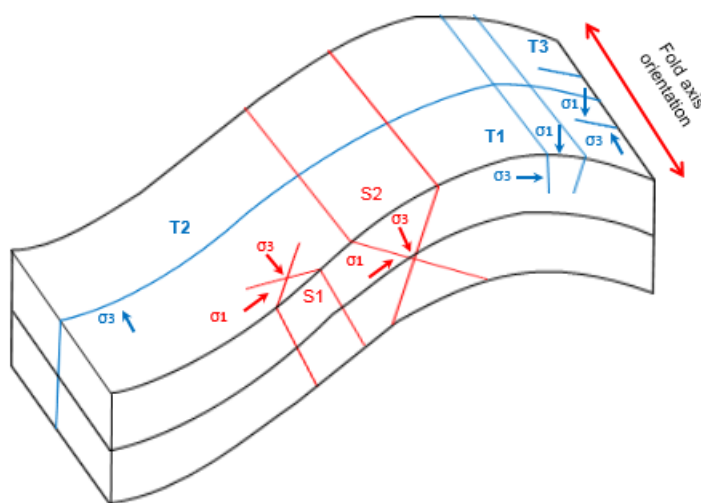


Figure 6.43. Fold-related fracture sets observed in the study area and their associated orientations of maximum and minimum stresses (Modified from Liu et al., 2016).

Lineaments parallel to the fold axis in the crest (T1) and limbs (S2) in Anticlines A and B may correspond to tension and shear fractures, respectively, which probably developed during buckling stages (D2/D3); lineaments perpendicular to the fold axis in the crest (T3) and backlimb (T2) may correspond to pre-folding tension and/or early diapir-related bending-fold fractures; and lineaments oblique to the fold axis (S1) may correspond to shear fractures developed during buckling (Figure 6.44-6.45). Rose diagrams from FMI and core samples show that the orientations of fractures in the boreholes are similar to the ant-tracking lineament orientations shown on the surfaces. These orientations are consistent in the three surfaces; however, a larger number of lineaments and orientations appear at deeper surfaces, which may be the combined result of factors such as lower seismic resolution, decreasing seismic signal-noise ratio and more abundance of fractures at depth due to a longer deformation history.

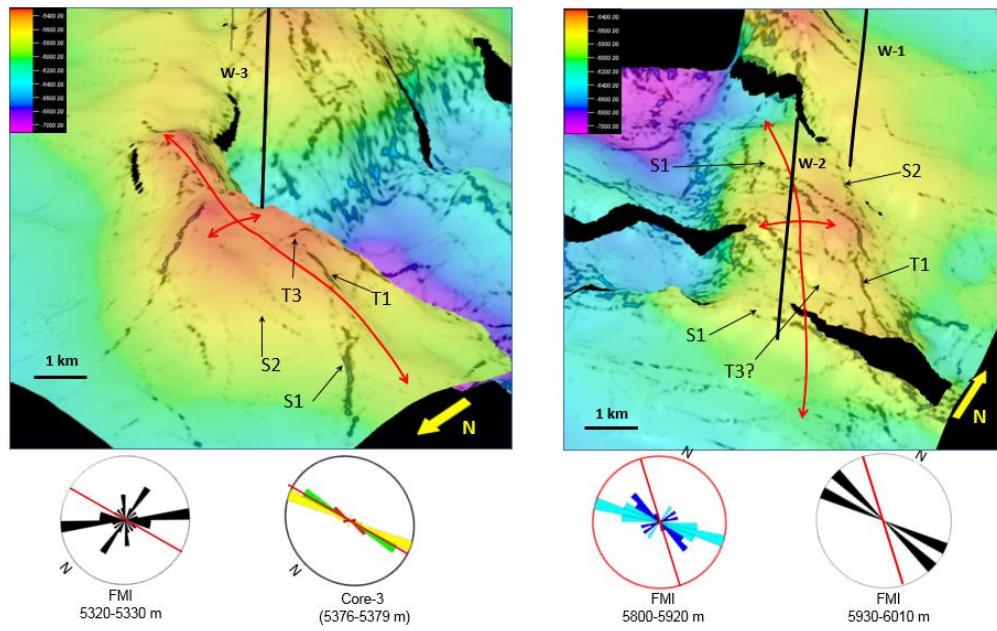


Figure 6.44. Combination of structure with ant-tracking attribute for Top Cretaceous surface. Left: Anticline A; Right: Anticline B. Nomenclature of lineaments are referred to Fig. 42. Rose diagrams show fracture orientations from FMI logs and core samples, where red line indicates fold axis orientation.

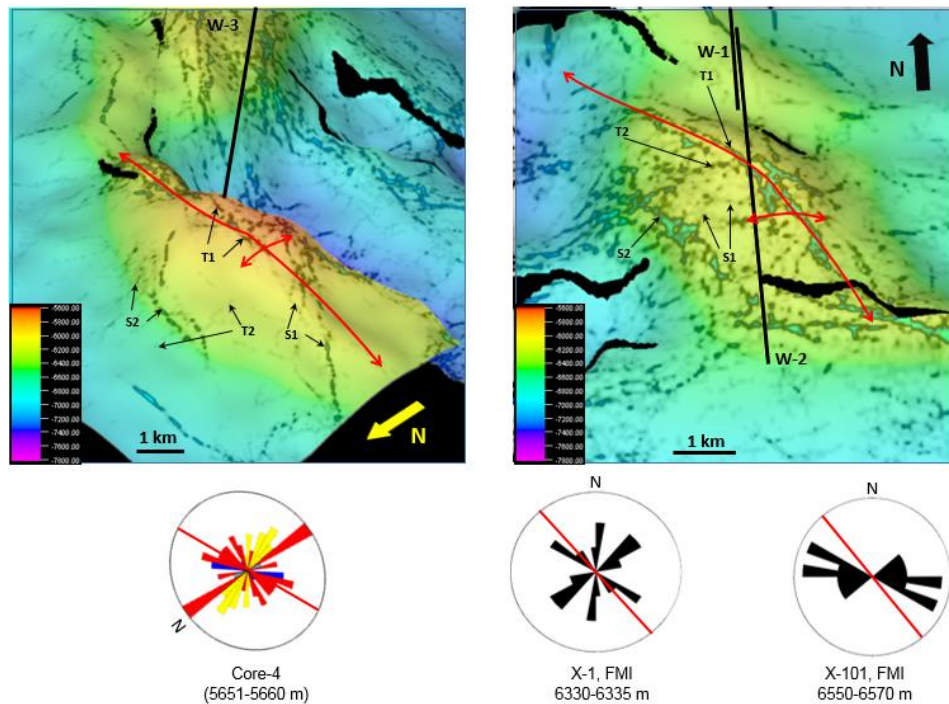


Figure 6.45. Combination of structure with ant-tracking attribute for Top Kimmeridgian surface. Left: Anticline A; Right: Anticline B. Rose diagrams show fracture orientations from FMI logs and core samples, where red line indicates fold axis orientation.

6.7 Conclusions

This study shows the advantage of the combined analysis of structural seismic attributes and geomechanical modelling as a helpful tool to identify the influence of structural position as a primary control on fracture orientation and intensity in folds. Although other geological factors such as lithology, texture and bed thickness also control fracture development, they seem to be secondary to structural position.

In spite of limitations in seismic resolution at depth in the study, the ant-tracking attribute calculated from the Most Positive Curvature volume provided better results for fracture interpretation and showed a relatively good correlation with borehole data, thus proving its predictive potential for undrilled areas. Surfaces and cross-sections provide essentially qualitative information about fracture location and intensity, whereas depth slices are more useful in defining fracture orientations.

Geomechanical modelling results also show the influence that structural position exerts on strain distribution, which in turn, may be directly associated with higher fracture intensities in areas with greater deformation such as fold hinges and faults' damage zones; however, strain analysis alone should not be considered as a potential predictor of fracture intensity, since this is the result of a complex interaction between other controls such as lithology, texture, bed thickness, pore pressure and porosity, so that it is also possible for relatively little deformed areas to have high fracture intensities.

Different mechanisms of deformation were identified in the evolution of the analysed anticlines including salt diapirism, salt-related extension, layer-parallel shortening and trans-tension. Each mechanism generates different fracture sets with their own specific characteristics, which may potentially be predicted if the tectonic history is accurately defined and combined with seismic attribute and geomechanical modelling analysis.

The amount of available borehole data provides the limitation for this study, and naturally, a greater amount of data would provide more detailed information about the spatial variations in fracture distribution and characteristics, and therefore, a better calibration of seismic attribute and geomechanical analyses. Likewise, this study would be improved upon with better age constraints on fracture development and diagenetic evolution obtained from core analysis.

Chapter 7

Modelling of sub-seismic fractures in Southern Gulf Of Mexico.

7.1 Introduction

Prediction of location and orientation of sub-seismic fractures in subsurface rock masses is difficult due to the scale gap between seismic and borehole data sources. Elastic dislocation (ED) theory assumes that strain distribution around larger faults (mappable on seismic data) is the main control on medium-to-small-scale faulting, which has an offset of a few dm to 30 m (Gauthier and Lake, 1993) and is usually not recognizable on seismic data. Larger faults are modelled as dislocations in an elastic medium and boundary-element numerical methods using the equations of Okada (1992) must be applied in order to calculate the strain tensors in the rock volume (Thomas, 1993). As a result, this approach is useful as a first order approximation to predict fracture intensity and orientation in a reservoir scale (Bourne et al., 2001; Maerten et al., 2002).

In recent years, the application of a geomechanical approach based on elastic dislocation (ED) theory for prediction of subsurface strain and therefore, intensity and orientation of sub-seismic fractures, has been the subject of research oriented to characterize subsurface hydrocarbon reservoirs as well as to increase the understanding of the role of faults in strain distribution at subsurface. Maerten et al., (2002) showed that stresses associated with major mapped faults can be used to predict the orientation of minor mapped faults in the northern North Sea. Dee et al., (2007) found similar results for contractional and extensional structures in Venezuela and the North Sea, respectively. Freeman et al., (2015) demonstrated a good correspondence between observed and modelled fracture orientation and densities in the Gorm field, North Sea for a chalk reservoir with salt-diapirism related deformation.

Integration of different analyses for sub-seismic fracture prediction have been documented in literature; Lohr et al., (2008) integrate 3D seismic data and well data with 3D structural restoration in order to predict sub-seismic fractures in the Lower Permian sandstones, NW German Basin. Jenkins et al., (2009) use a Continuous Fracture Modeling (CMF) approach integrating fracture drivers (facies types, porosity, proximity to faults, etc) from borehole and seismic data sets and relate them to fracture indicators in boreholes using neural networks in order to predict fracture distribution within a reservoir; however, this methodology relies heavily on the availability of abundant

borehole data and high-quality 3D-seismic data, which is not the case in early exploration stages.

The importance of this study is that it undertakes theoretical ED-based models of fracture development and compares the obtained results with quantitative observations of fracture orientation and relative intensity from borehole data (FMI and core samples). Moreover, ED-models are compared with ant-tracking attribute maps and strain maps derived from structural restoration in order to assess their potential as a predictive tool during early stages of hydrocarbon exploration where borehole data are sparse or null.

7.1.1 Elastic Dislocation Background

Fracture prediction presented in this chapter is based on Elastic Dislocation (ED) theory, in which faults interpreted from 3D seismic data are used as main inputs and represent dislocations within an elastic medium. The equations of Okada (1992) are used in the Badley's L7 © software to calculate the response of the surrounding elastic medium (strain) to the slip in these large faults, which are subdivided into an array of rectangular or triangular panels (Figure 7.1), as a function of the fault parameters (strike, dip, dimensions, slip vector) and the elastic constants of the medium (Young's modulus and Poisson's ratio). A calculated stress tensor is then used in conjunction with a failure envelope to calculate mode of failure and the orientation of sub-seismic fracture planes, at each observation point on the observation grid. Fracturing is deemed to have occurred if the failure envelope is exceeded. The mode of failure may be shear or tensile depending on which part of the failure envelope is first exceeded by the fault-induced stresses (Figure 7.2). Where shear failure is predicted, shear fractures are oriented as a conjugate pair intersecting along the σ_2 axis and making an angle θ with the σ_1 axis, where $\tan 2\theta = - (1/\mu)$. Where tensile fractures are predicted, their orientation is perpendicular to the σ_1 axis (Dee et al., 2007).

A limitation of this method is that it cannot predict the size or scale of the fractures, but only the fracture type and orientation that may be present at a specific location. Fracture density can be associated to the maximum Coulomb shear stress attribute (MCSS), but that is only a proxy and not an actual measure (Maerten et al., 2002; Dee et al., 2007). This relationship can be established if the predicted fractures can be calibrated with actual observations made from wells and/or from surface exposures. However, like all models, it is not a 100% accurate description of all the factors that influence medium-to-small-scale fractures. In particular, vertical variations of rock properties in the sedimentary sequences are not considered in the strain modelling. Also, because the ED theory only models fault-related fracturing, fractures associated with vertical lithostatic load (background), hydrofractures and folding cannot be modelled.

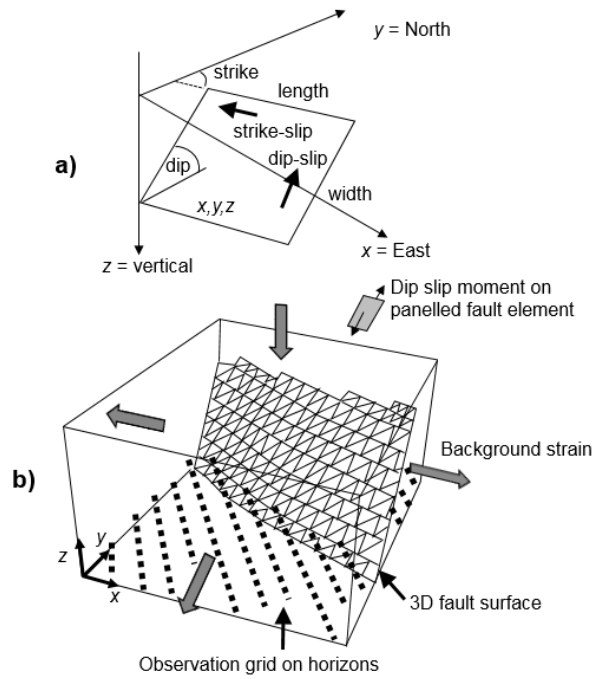


Figure 7.1. a) the basic input for the ED solution is a rectangular fault panel with a constant slip and a position defined by xyz coordinates; b) A fault surface is modelled as an array of small rectangular panels similar to a). The horizontal observation grid comprises a series of points where strains, displacements and stresses are calculated (Dee et al., 2007).

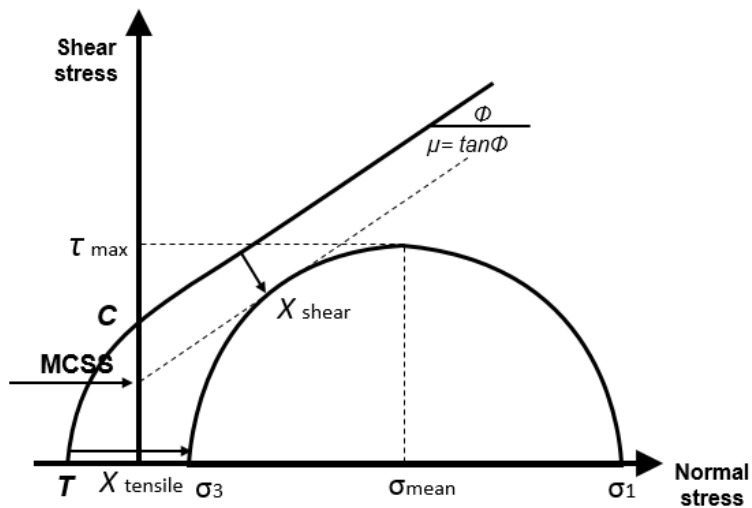


Figure 7.2. Mohr-Coulomb diagram illustrating definitions of failure criterion. MCSS is the shear stress measured in the y axis for a tangent line to the Mohr-circle of a given stress state parallel to the slope of the failure envelope. X_{shear} and $X_{tensile}$ are perpendicular distances from the Mohr circle to the failure envelope that define the failure mode. C is the rock's cohesive strength or shear strength (Dee et al., 2007).

7.2 Methods

7.2.1 Elastic dislocation (ED) modelling

This section describes the ED methodology used to calculate the strain distribution in the different horizons of the study area. The method assumes that the modelled horizons have isotropic properties and that strain accumulated during different deformational events (elastic processes) become permanent after stress relaxation (Freeman et al., 2015).

a) **Data input.** For this work, the main input for fracture modelling consist of horizon surfaces and faults previously mapped on 3D seismic data (see Chapter 4). These surfaces correspond to Top Cretaceous, Top Tithonian and Top Kimmeridgian whereas 6 major faults, three normal and three reverse, were also interpreted (Figure 7.4). These faults were interpreted manually as segments on cross-lines and in-lines and then correlated to create fault surfaces. In order to analyse each of the geological structures independently, each horizon was split into different subsets (Figure 7.3), each comprising an area that includes a single anticline.

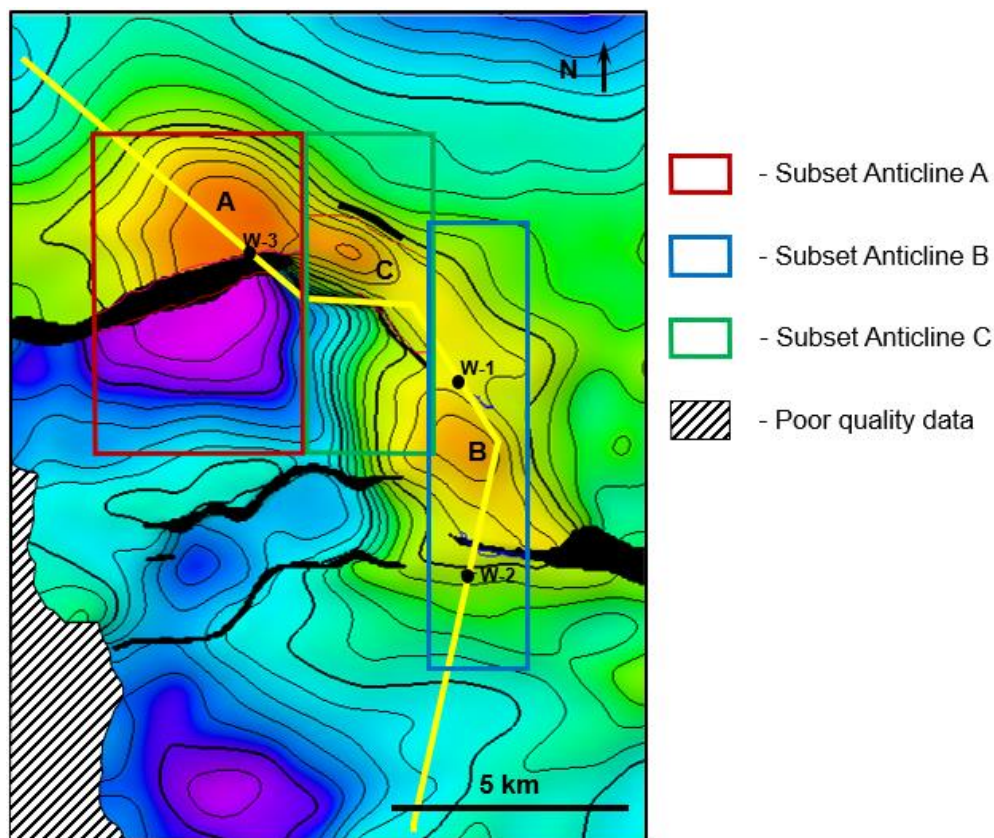


Figure 7.3. Data subsets used to model the three anticlines within the study area. Top Late Cretaceous structure map.

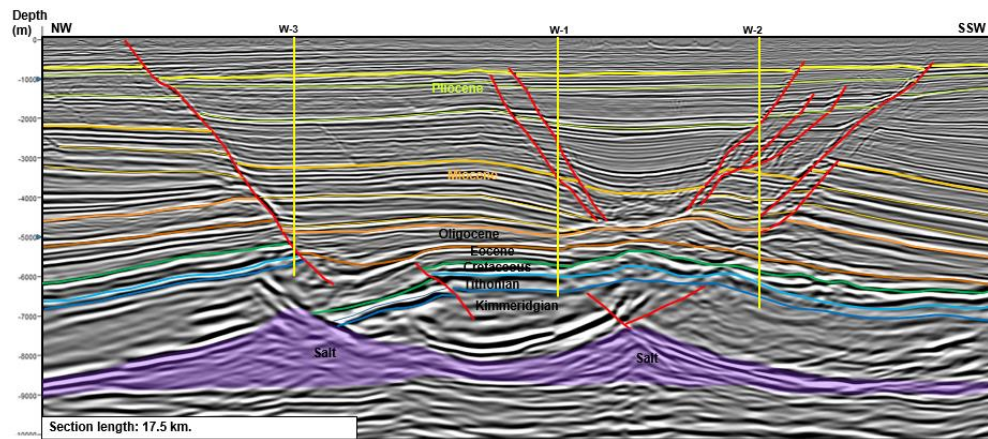


Figure 7.4. Interpreted cross-section from Figure 3 showing the structural style of the Mesozoic structural traps.

b) **Modelling parameters.** In this step, a scenario is created for every horizon investigated, which includes different modelling parameters for faults and horizons. Geomechanical parameters are the following:

- **Poisson's ratio:** is the ratio of the contraction or transverse strain (normal to the applied load) to the extension or axial strain (in the direction of the applied load).
- **Young's Modulus:** is the ratio of stress (which has units of pressure) to strain.

Values for these two parameters, along with rock density, were obtained from previously calculated well logs and average, representative values corresponding to the predominant lithology were selected, since they show great vertical variability related to lithological changes (Table 7.1).

- **Coefficient of internal friction:** It is the stress required to overcome internal frictional resistance and, therefore, to trigger movement along the fracture plane. A typical value of 0.6 was used for all the different scenarios (Crider and Pollard, 1998).
- **Cohesive (shear) strength:** It is the inherent shear stress in a rock when it ruptures and forms or reactivates a shear fracture when no normal stress is applied. No data obtained from tests carried out in core samples from the study area were available for this work; however, values obtained from triaxial tests to rock samples with similar lithologies and depth of burial in offshore Southern GOM show a range between 15 and 34 MPa; also, Karaman et al. (2015) obtained values of this parameter between 15-23 MPa from tests performed on carbonate rock samples. Based on this information, a constant value of 20 MPa was used for every modelled scenario in this work.

	Young's Modulus (Gpa)			Poisson's Ratio			Cohesive strength (Mpa)	Density (kg/m ³)
	W-3	W-1	W-2	W-3	W-1	W-2		
Top Cretaceous	51	38	55	0.31	0.31	0.28	20	2700
Top Tithonian	57	59	59	0.3	0.3	0.3	20	2750
Top Kimmeridgian	36	69	69	0.15	0.3	0.3	20	2700

Table 7.1. Geomechanical parameters used for ED modelling.

Fault elements were modelled as discretized triangular elements by using their surfaces tri-meshes (Figure 7.1). The slip magnitude was calculated from offsets in the interpreted horizons by using the average direction of dip of the entire fault, thus implying that the movement along the fault plane is pure dip-slip and not affected by any strike-slip component. The ED formulation of Okada (1992) describes the displacement field at any given point in the elastic medium as a function of the fault parameters (strike, dip, dimensions, slip vector) and the elastic constants of the medium (Young's modulus and Poisson's ratio).

c) **Observation grid.** This is a set of points distributed evenly within a grid, where ED parameters are modelled and the displacement vector and strain tensor at any arbitrary set of observation points in the surrounding rock volume are calculated. In this work, the observations grids were horizontal and placed at the top of the different horizons assuming that the rock properties do not vary significantly throughout the same lithological unit.

d) **Generation of an Elastic Model:** After a scenario is fed with the modelling parameters, the elastic dislocation equations of Okada (1992) are used to calculate the response of an elastic medium to the fault slip on the fault panels as well as to compute the displacement caused by the total fault slip. At each observation point, the Okada equations combine the effect of fault slip on every panel in the model in order to provide a 3D displacement (deformation) vector.

Prediction of rock fracturing is based on the comparison between the total stress computed and the state of stress to a standard Mohr–Coulomb failure envelope, defined by appropriate coefficient of internal friction (μ) and cohesive strength (C) (Figure 7.2). If the failure envelope is exceeded then fracturing will occur, which may be shear or tensile depending on which part of the failure envelope is first exceeded by the fault-induced stresses. Fracture orientations are calculated relative to the principal stress axes at every node in the observation grid, where shear fractures are oriented as a conjugate pair intersecting along the σ_2 axis and making an angle θ with the σ_1 axis and tensile fractures are oriented perpendicular to the σ_1 axis (Figure 7.5). Another boundary

condition for Elastic Modelling consists of the background strain, which is the regional scale deformation responsible for the formation of the large-scale geological structures (e.g. rift basins or thrust belts). This strain is added to the fault-related strain to give a net perturbed stress/strain at each observation point and compensate the extension/compression induced by movement on fault-blocks (Maerten et al., 2002).

Although fracture density cannot be predicted directly, certain calculated properties can be used as a proxy for this result. The most commonly used is the maximum Coulomb shear stress (MCSS), which is represented by the intersection of the shear stress axis and a tangent line to the Mohr-circle of a given stress state parallel to the slope of the failure envelope (Figure 7.2). MCSS is applicable in areas where the failure mode is shear, which is expected if $MCSS > C$, where C is the cohesive strength of the rock (Jaeger and Cook, 1979).

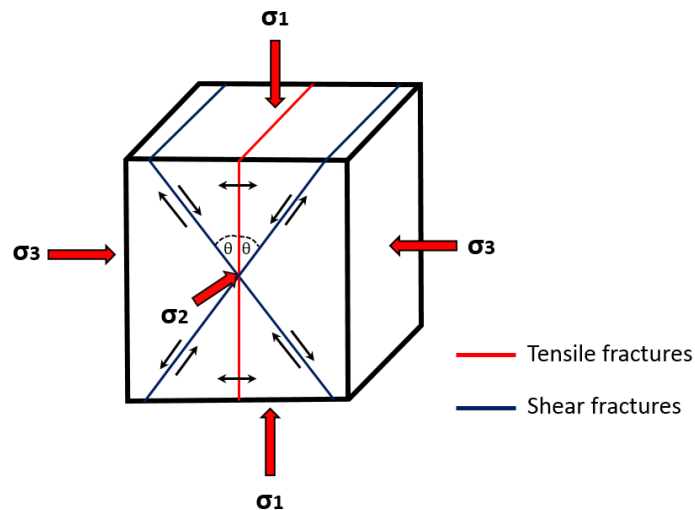


Figure 7.5. Orientation of shear and tensile fractures respect to the orientation of applied stresses (Hunt et al., 2009).

7.2.2 Seismic interpretation

For the purposes of this work, seismic interpretation was done using a 3D PSDM offshore survey acquired in 2013. Horizon interpretation is well constrained in most of the study area due to the presence of three boreholes, although in other areas interpretation is less reliable (see Chapter 4). The inclusion of Top Cretaceous, Top Tithonian and Top Kimmeridgian horizons are useful to constrain the displacement of Mesozoic faults, which in turn, provides constraints for the ED modelling (Figure 7.6). Also, these horizons represent the economic targets for hydrocarbon exploration in the study area. For Mesozoic horizons, a grid spacing of 20 x 20 lines (600 m x 600 m) was used, which is a standard spacing for a semi-detailed prospect mapping. Fault interpretation used the

same spacing as the Mesozoic horizons following the next criteria: 1) Faults affecting Mesozoic sequences, 2) To show clear offset or evidences of possible reactivation and, 3) To display a lateral continuity of 20 lines (600 m) as a minimum (that is, being visible at least on two lines within the selected grid mapping). Preferential orientation of these faults are NE-SW and NE-SW, although their orientations are controlled mainly by the location of salt diapirs. The structural evolution of these anticlines (Chapter 4.5.2) reveals that some of these faults have undergone several phases of deformation often with reversal in sense of movement. This represents a limitation for the ED modelling, since it considers that the present geometry of faults and the amount of displacement on their planes is the result of a single deformational event.

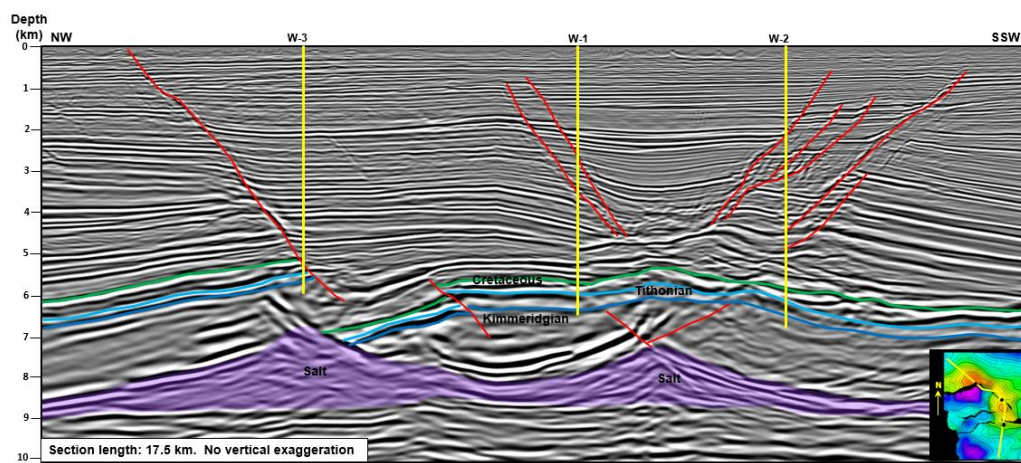


Figure 7.6. Interpreted cross-section showing the modelled Mesozoic horizons: Top Cretaceous, Top Tithonian and Top Kimmeridgian.

7.3 Results

In this section, ED modelling results from each of the Mesozoic surfaces of Anticlines A and B are presented and compared with borehole data, strain maps and seismic attribute results in order to test theoretical models of fracture development with quantitative observations. Furthermore, the integration of these different analyses will allow an assessment of their combined predictive potential of density and orientation of medium-scale faults and fractures in exploratory areas.

Modelled fractures shown in Figures 7.10 to 7.13 and 7.22 to 7.24 represent fracture type and orientation at each location while size and scale of the fractures cannot be predicted by ED. Rose diagrams from ED comprise the fracture orientations observed within squares of 500 m of length per side, whose centres are set at each borehole location. These orientations were compared with the orientations obtained from FMI logs, core samples (when available) and ant-tracking attribute applied to depth slices and top

surfaces. Rose diagrams from FMI include fractures observed in intervals with variable thickness ranging from 10 m (Top Cretaceous, W-3) up to 120 m (Top Cretaceous, W-1) starting from the top of the sequence. Thickness of the sampled intervals is inversely proportional to their fracture density, so intervals with low fracture density needed more vertical sampling thickness in order to obtain a representative value for fracture orientation.

The degree of correlation for fracture orientation is considered as poor if there is no match between the orientations of modelled and borehole data (FMI and core samples) or ant-tracking lineaments considered as fractures, regular if there is matching in one predicted orientation, and good if there is matching in more than one predicted orientation.

Another limitation of ED modelling is that it does not predict directly the fracture density; however, Maximum Coulomb Shear Stress (MCSS) attribute can be used as a proxy in order to get an idea of the fracture density, where higher values of MCSS represent areas with a higher probability of more intense fracturing. Due to this, MCSS maps were compared with fracture density values obtained from FMI logs or core samples (when available) and strain maps from geomechanical modelling in order to determine a correlation between direct and indirect indicators of fracture density.

The estimation of the degree of correlation between ED and geomechanical modelling is based on the similarities between the areal distribution of MCSS (the modelled proxy for fracture intensity) and strain in any given surface, so the more similar the distributions, the higher degree of correlation. In the other hand, the degree of correlation between ED and borehole data can be estimated by relating the values of MCSS with fracture density values observed in FMI logs, with qualitative estimations of fracture density in core samples, and even with indicators observed during drilling/completion of boreholes (drilling mud loss/gain, gas shows, sudden increase in rate of penetration, high readings of gas in mud and flow of formation fluids during production tests). It should be noted that a single value of MCSS may correspond to more than one single value of fracture density obtained from FMI logs, and vice versa, so the key point is to observe the distribution of these values within a specific area in order to establish a correlation. Finally, correlation between ED and ant-tracking attributes is based on the relation of values of MCSS and the density of lineaments associated to subtle faults.

Figures 7.7 and 7.8 illustrate the distribution of MCSS in all Mesozoic mapped surfaces for anticlines A and B and their comparison with the ant-tracking attribute applied to the same surfaces. Areas in warm colours indicate higher shear stresses and therefore, areas with higher probability of having higher intensities of medium-scale faulting/fracturing. Highest values of MCSS are located usually in the vicinity of fault planes and fault tips.

Despite some issues related to seismic quality and geological complexity, ED had reasonably good results when applied to the Mesozoic horizons in the study area. The following sections describe the relationships between the modelled data, borehole data, geomechanical modelling and ant-tracking for anticlines A and B. For each anticline, in turn, subsections will show the differences between the ED predicted orientations and the observed in the different datasets as well as how all these techniques can be combined in order to qualitatively estimate fracture density and their comparison with borehole data for calibration of ED results.

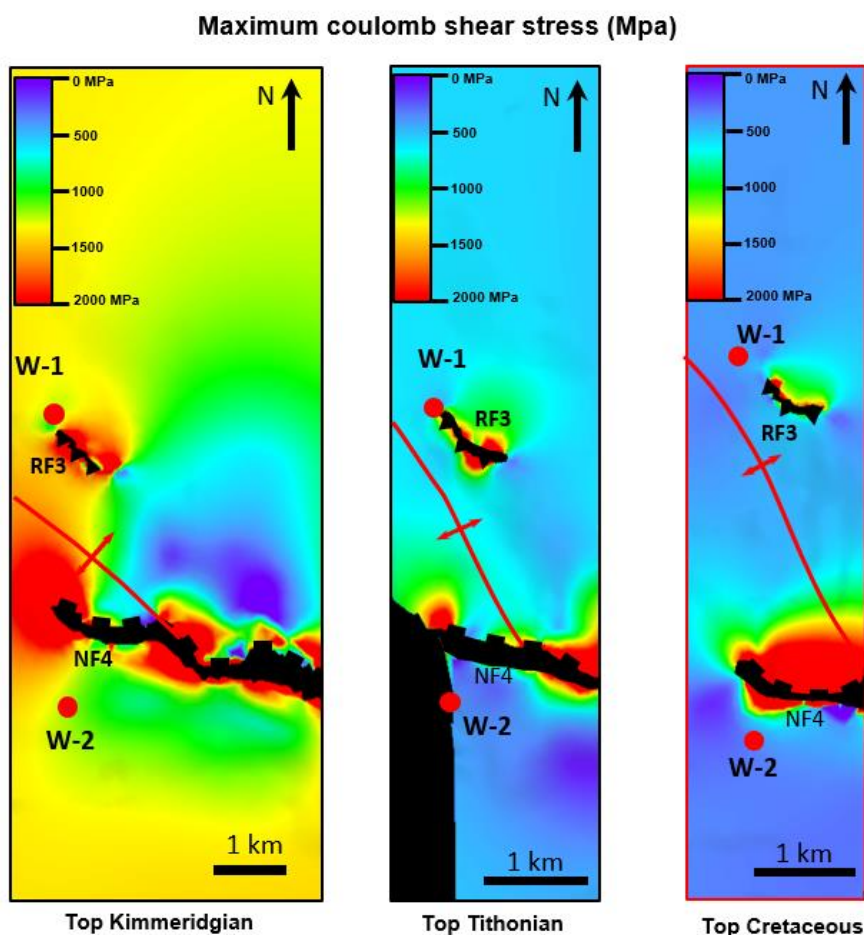


Figure 7.7. Distribution of MCSS at each of the three Mesozoic mapped surfaces in anticline B.

Maximum coulomb shear stress (Mpa)

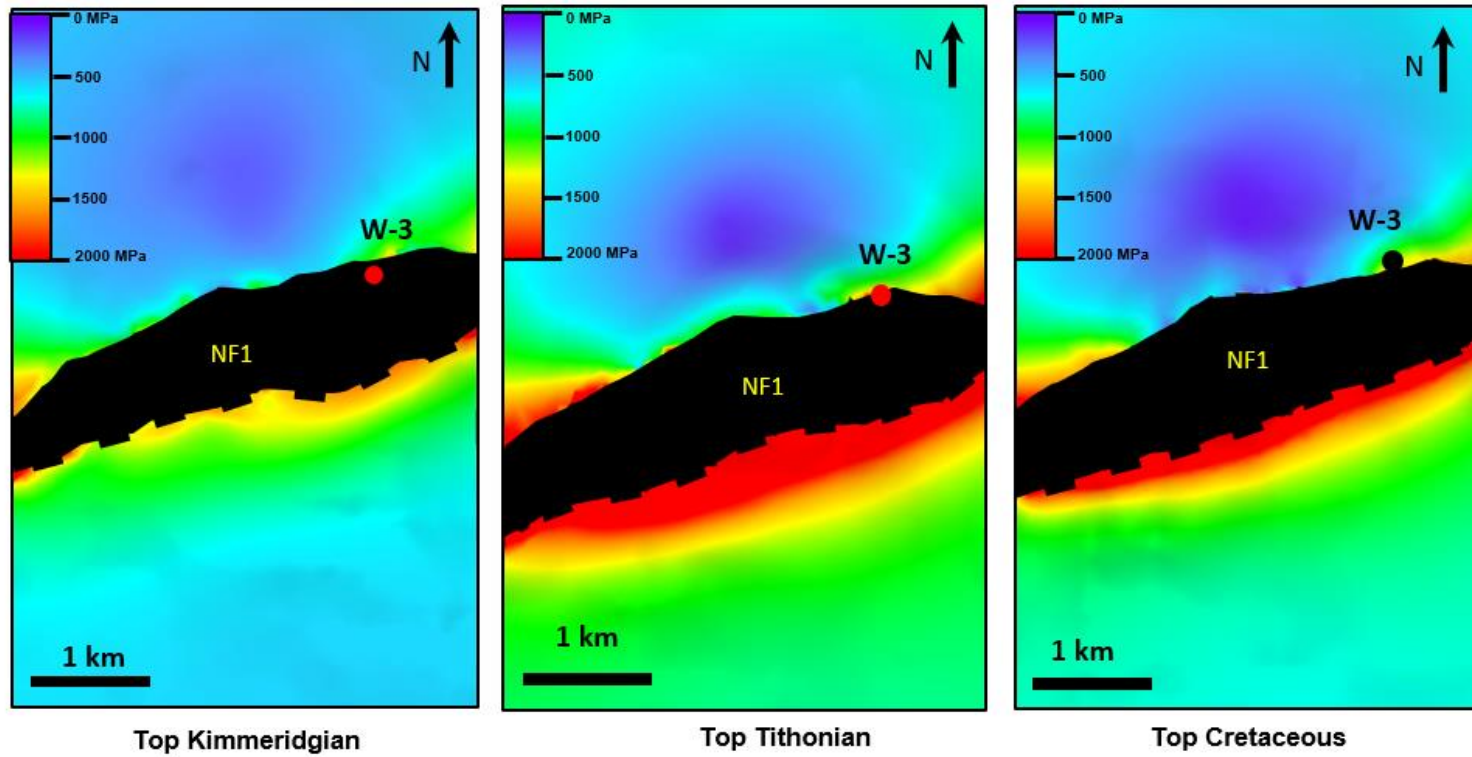


Figure 7.8. Distribution of MCSS at each of the three Mesozoic mapped surfaces in anticline A. Black areas represent the fault plane.

7.3.1 Anticline B

This structure can be defined as a salt-cored anticline oriented NW-SE characterized by symmetric buckle folding and high-angle thrust faults oriented NW-SE (RF3) and WNW-ESE (NF4) detaching on salt similar on its northern and southern flanks (Figure 7.9). Any strike-slip component on these faults cannot be constrained directly; however, it is possible that NF4 have been affected by some minor strike-slip movement during Pliocene times although this is difficult to quantify (see Chapter 4). Displacement on reverse fault RF3 diminishes laterally towards the fault edges and upwards and the maximum vertical displacement (200 m) is located at the centre of the fault plane. Fault NF4, on the other hand, shows a normal offset for Top Tithonian and Top Kimmeridgian horizons all along the fault plane and a reverse offset for Top Cretaceous, which may indicate a possible reactivation of the fault in a reverse sense or even a strike-slip movement. For modelling purposes, displacement on these faults is considered as pure dip-slip. The maximum vertical displacement is 160 m and is located towards the western edge of the fault plane. However; low seismic resolution, lack of continuity of reflectors and regular imaging increase the uncertainty of the interpretation in this particular area.

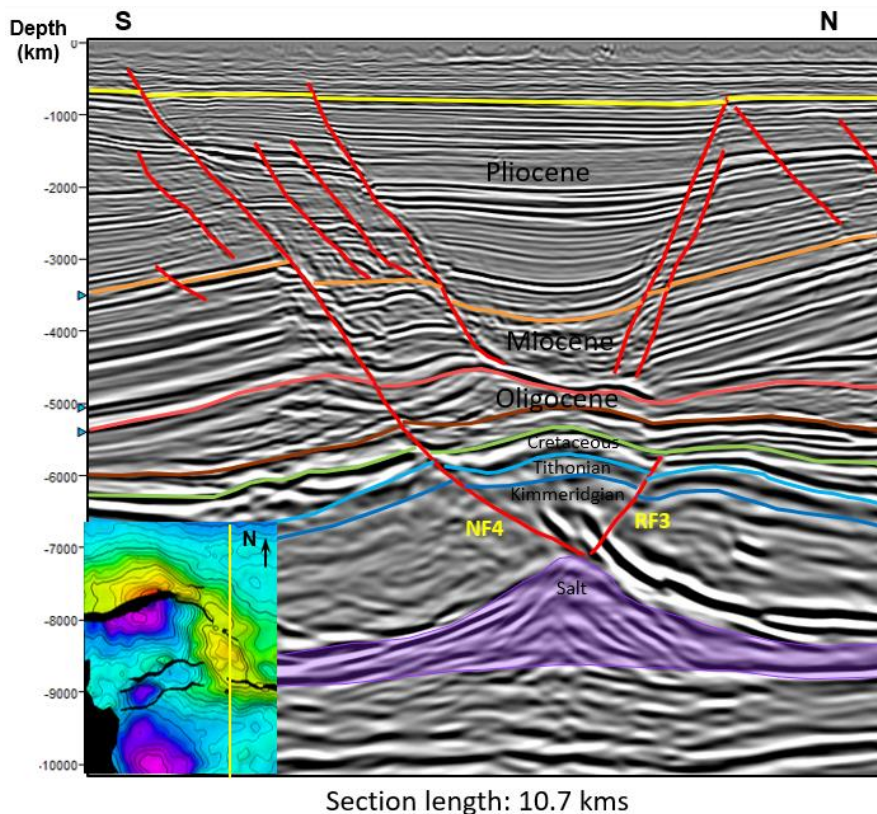


Figure 7.9. Interpreted cross-section showing the geometry of anticline B, which is bounded by faults NF4 and RF3 in its southern and northern flanks, respectively.

The tectonic history of this area indicates that different deformational events are superimposed, which poses a limitation for modelling this structure, since one assumption of the modelling is that faults and folding formed during a single deformational event (see Chapter 4). A solution for this problem consists in a 3D back-stripping of the dataset, which was not possible to carry out due to the geological issues of the study area discussed in Chapter 4; however, the contractional phase of deformation can be considered as the dominant one for generation of the main fracture sets.

For this structure, values of Young's modulus, Poisson's ratio and rock density from boreholes W-1 and W-2 shown in Table 7.1 were used for each Mesozoic modelled scenario. Additionally, values for coefficient of internal friction (μ) and cohesive strength of 0.6 and 20 MPa respectively, were used.

7.3.1.1 Fracture orientation

Top Kimmeridgian

The predominant orientations predicted by ED in the vicinity of borehole W-1 are NW-SE 60-80° and correspond mainly to fractures with normal displacement, almost parallel to the anticline's strike (NW-SE 50°). These orientations are also present in both depth slice and mapped top surface in the immediate vicinity of the borehole as well as in FMI well log (Figure 7.10).

For borehole W-2, predicted ED predominant orientations range from NE-SW 10° to NW-SE 10°, which are oblique to the anticline's strike. Correlation with ant-tracking attributes is considered as regular to good, although the predicted orientations are present in both depth slice and mapped top surface around the borehole (Figure 7.11). Correlation with FMI is good, although in FMI the ED orientations are not predominant. ED orientations were also compared with fracture orientations measured in Core-3, whose depth (6595-6604 m) is located 60 m below the Kimmeridgian top but, in the other hand, lithology is similar to the surface as well as other factors such as texture, bed thickness and structural position. Correlation between predicted ED orientations and those observed in Core-3 is considered as good, since they have a good matching in more than one orientation (ENE-WSW and NE-SW 10-20°).

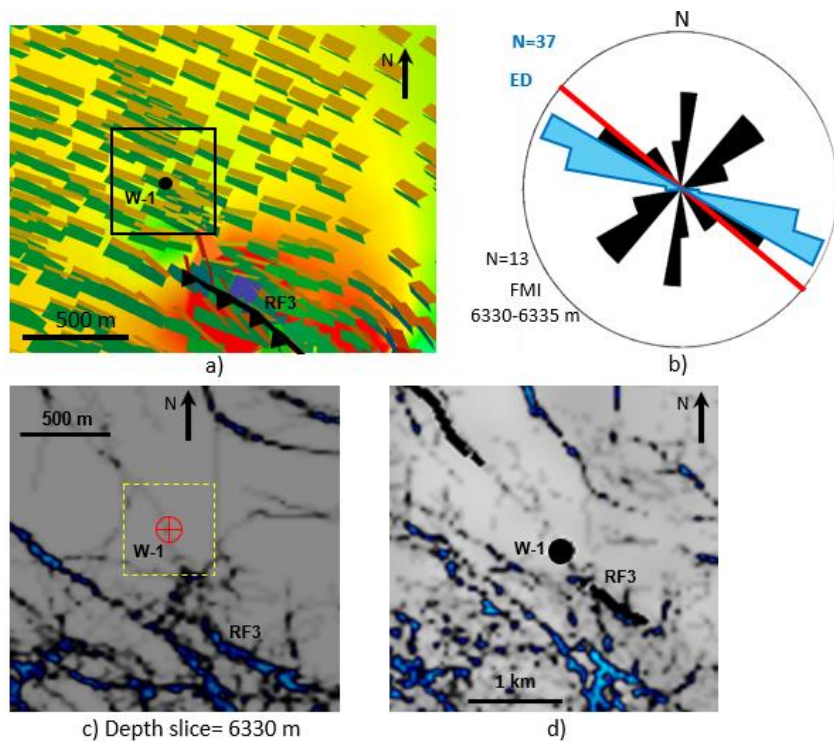


Figure 7.10. a) Predicted orientations of fractures around borehole W-1 superimposed on MCSS distribution (RF3 is the input reverse fault for fracture modelling); b) rose diagram comparing the predicted orientations (blue) with FMI orientations measured in FMI log (black), red line corresponds to the anticline axis; c) Depth slice and, d) Top Kimmeridgian surface with ant-tracking attribute showing the lineaments around W-1.

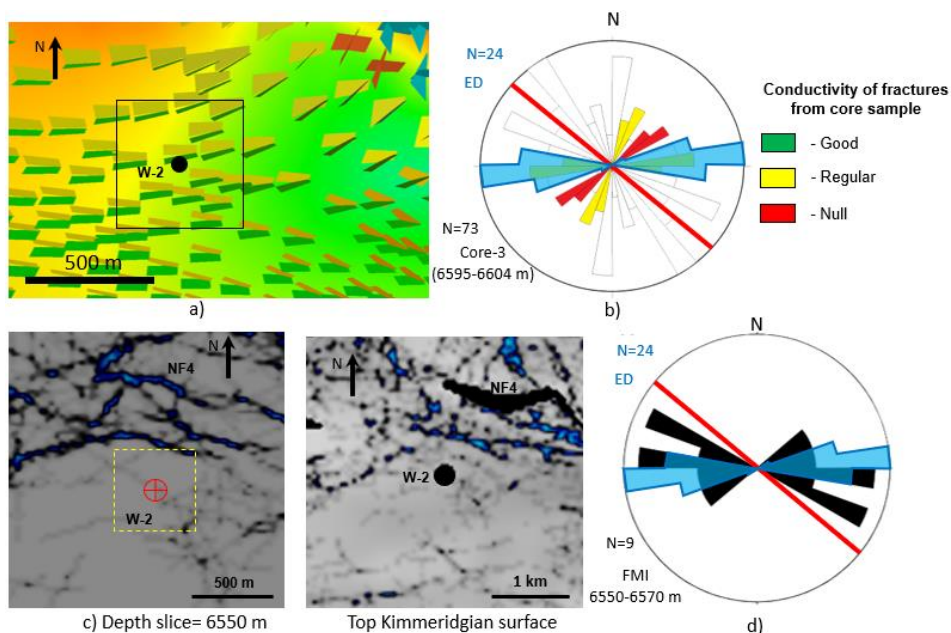


Figure 7.11. a) Predicted orientations of fractures around borehole W-2 superimposed on MCSS distribution (NF4 is the input normal fault for fracture modelling); b) rose diagram comparing the predicted orientations (blue) with orientations measured in Core-3; c) Depth slice and Top Kimmeridgian surface with ant-tracking attribute showing the lineaments around W-2; d) rose diagram comparing the predicted orientations (blue) with FMI orientations measured in FMI log (black), red line corresponds to the anticline axis.

Top Tithonian

ED modelling predicted fracture orientations around borehole W-1 (NW-SE 50°) are parallel to anticline's strike, and very similar to the predominant orientations measured in FMI logs ((NW-SE 30°). Also, secondary ED predicted orientations show a good matching with FMI secondary orientations (Figure 7.12). ED predominant orientations also show a good matching with orientations of lineaments observed in depth slice and top surface around the borehole, where ant-tracking attribute was applied.

For W-2, predicted ED fractures have two main orientations, NW-SE 70-80° and NW-SE 50-60° (parallel to anticline's strike). Predominant orientations measured in FMI log are NE-SW 10° and NE-SW 30-40°, which are perpendicular to predicted ED orientations; therefore, correlation between the two data sets can be considered as poor (Figure 7.13). In the other hand, ant-tracking depth slice and mapped top surface show lineaments similarly oriented as ED predicted fractures, so correlation can be considered as regular to good.

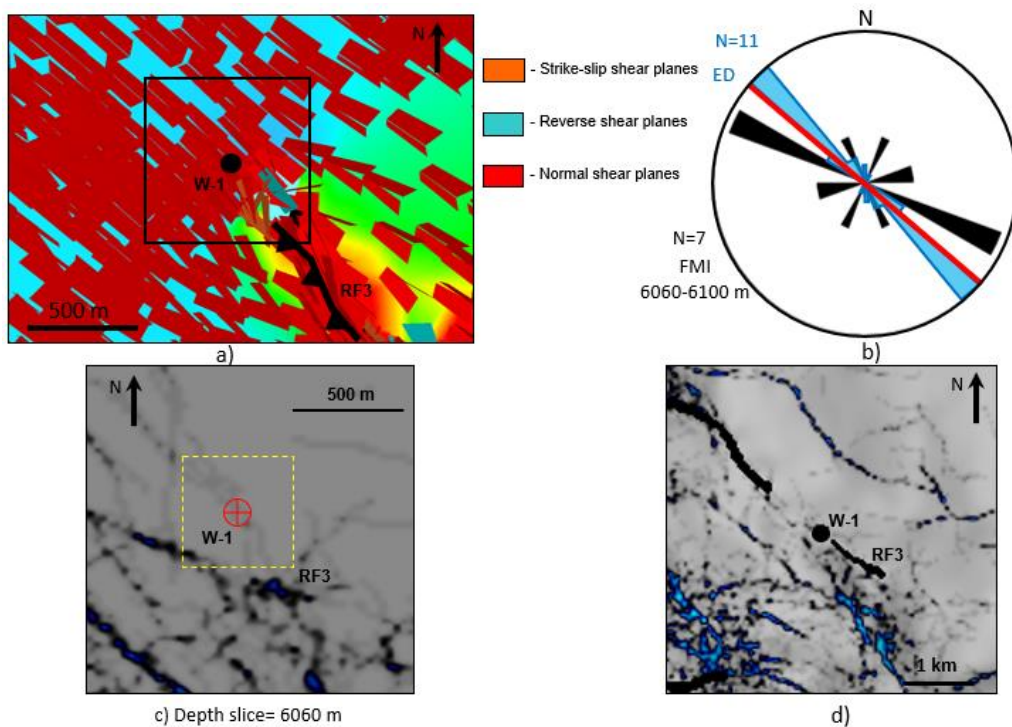


Figure 7.12. a) Predicted orientations of fractures around borehole W-1 superimposed on MCSS distribution; b) rose diagram comparing the predicted orientations (blue) with FMI orientations measured in FMI log (black), red line corresponds to the anticline axis; c) Depth slice and, d) Top Tithonian surface with ant-tracking attribute showing the lineaments around W-1.

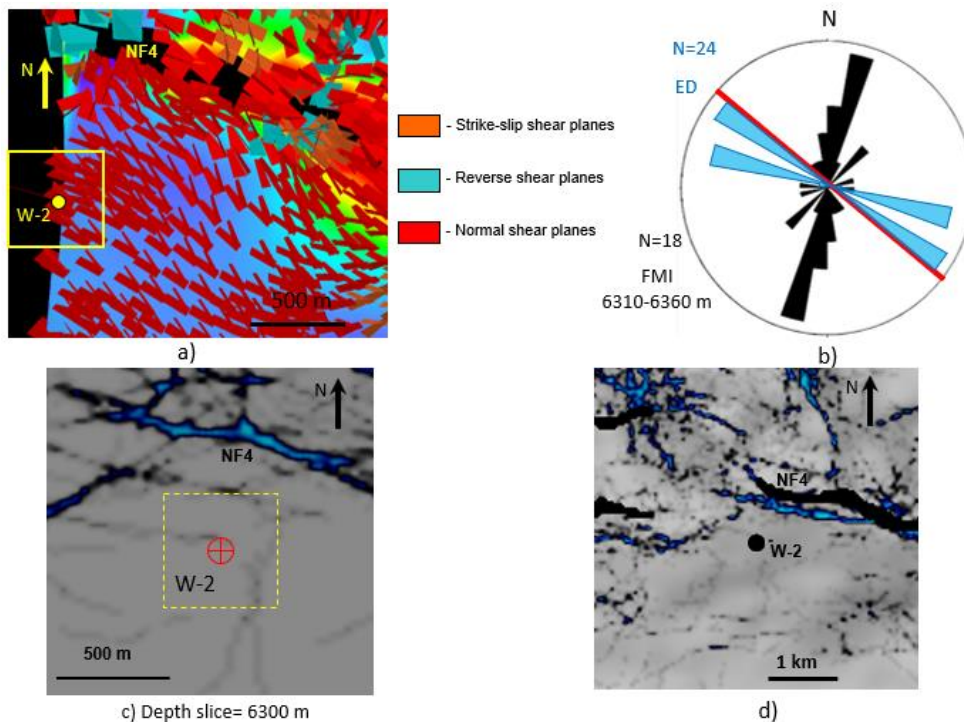


Figure 7.13. a) Predicted orientations of fractures around borehole W-2 superimposed on MCSS distribution; b) rose diagram comparing the predicted orientations (blue) with FMI orientations measured in FMI log (black), red line corresponds to the anticline axis; c) Depth slice and, d) Top Tithonian surface (right) with ant-tracking attribute showing the lineaments around W-2.

Top Cretaceous

ED predicted predominant orientations around W-1 range from NW-SE 10° to NW-SE 50° (parallel to anticline's strike), which are almost perpendicular to predominant FMI orientations (ENE-WSW); however, they show very similar values to secondary FMI orientations (NW-SE $50-65^\circ$). Based on this, degree of correlation between fracture orientations from ED and FMI can be considered as regular to good (Figure 7.14). Ant-tracking lineaments observed in depth slice and mapped surface around W-1 show similar orientations to ED predicted orientations, so the degree of correlation is considered as good.

For W-2, ED predicted predominant orientations close to the borehole range from N-S to NE-SW 20° , which are highly oblique to anticline's strike and almost perpendicular to predominant FMI orientations ENE-WSW and NW-SE $10-20^\circ$; however, the latter matches a secondary ED predicted orientation. Therefore, correlation between the two data sets is considered as regular to good (Figure 7.15). Ant-tracking lineaments are absent around the borehole in the depth slice at 5930 m and are very scarce in the mapped top surface, although a single lineament is oriented similarly to a secondary ED predicted orientation (NE-SW $20-30^\circ$).

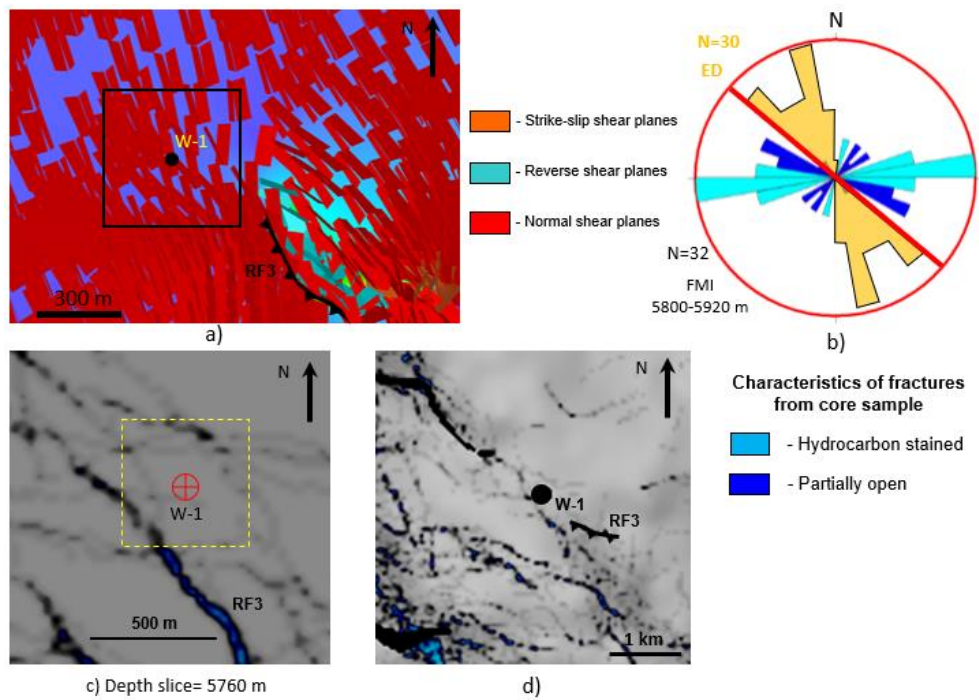


Figure 7.14. a) Predicted orientations of fractures around borehole W-1 superimposed on MCSS distribution; b) rose diagram comparing the predicted orientations (orange) with FMI orientations measured in FMI log (blue), red line corresponds to the anticline axis; c) Depth slice and, d) Top Cretaceous surface with ant-tracking attribute showing the lineaments around W-1.

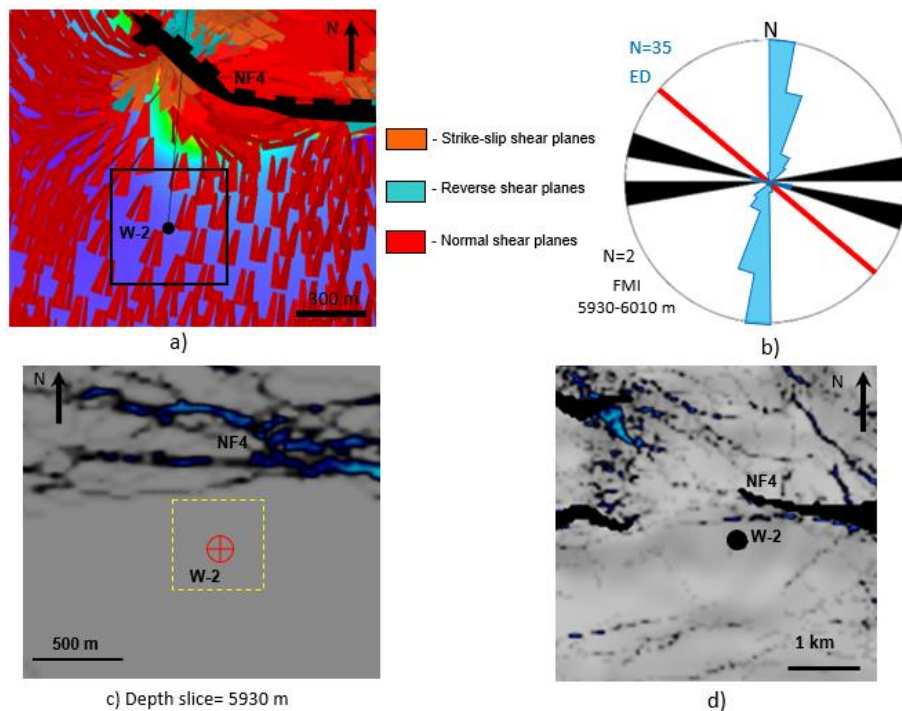


Figure 7.15. a) Predicted orientations of fractures around borehole W-2 superimposed on MCSS distribution; b) rose diagram comparing the predicted orientations (blue) with FMI orientations measured in FMI log (black), red line corresponds to the anticline axis; c) Depth slice and, d) Top Cretaceous surface with ant-tracking attribute showing the lineaments around W-2.

7.3.1.2 Fracture Intensity

Figures 7.16 and 7.17 illustrate the distribution of Maximum Coulomb Shear Stress (MCSS) for each Mesozoic mapped surface on anticlines A and B, respectively. Higher values (warm colours) represent areas where is more likely to have higher density of medium-scale faulting/fracturing. Also, the same surfaces with the ant-tracking attribute applied are shown for comparison. Subtle faults interpreted from curvature/variance (C/V) attributes (black lines) and later verified on the amplitude volume are superimposed on the MCSS and ant-tracking maps in order to define a correlation. Correlation between areas with high values of MCSS and location/orientation of these lineaments is relatively good; for anticline B, most of these lineaments are located in zones with higher MCSS, more noticeably in the inter-wells area, and in some cases they are even aligned to MCSS trends (Figure 7.14). Also, density of C/V lineaments has a good correlation with MCSS values. For Anticline A, C/V lineaments are more numerous in the foot-wall than in the hanging-wall; moreover, it is remarkable the absence of ant-tracking and C/V lineaments in the area with lowest MCSS values in the footwall, especially in Top Tithonian and Top Kimmeridgian surfaces.

Top Kimmeridgian

Borehole W-1 is located close to the NW tip of a reverse fault in an area with high values of MCSS and relatively high values of strain, which indicates a good degree of correlation and a good probability of having a high density of medium-scale fracturing (Figure 7.18). Analysis of FMI logs shows relatively high fracture density in the uppermost Kimmeridgian sequence, where two production tests were performed, thus providing a good degree of correlation between ED modelling and FMI logs.

Similarly to borehole W-1, W-2 is located in an area with high values of MCSS and relatively high values of strain; however, the degree of correlation with FMI logs is considered as regular since FMI log shows a relatively low fracture density, although a production test was performed and resulted as water invaded. Core-3 provided an opportunity to calibrate ED results; fracture intensity was reported as moderate, which agrees with the values of MCSS in the borehole's location for this surface, thus the degree of correlation is considered as good.

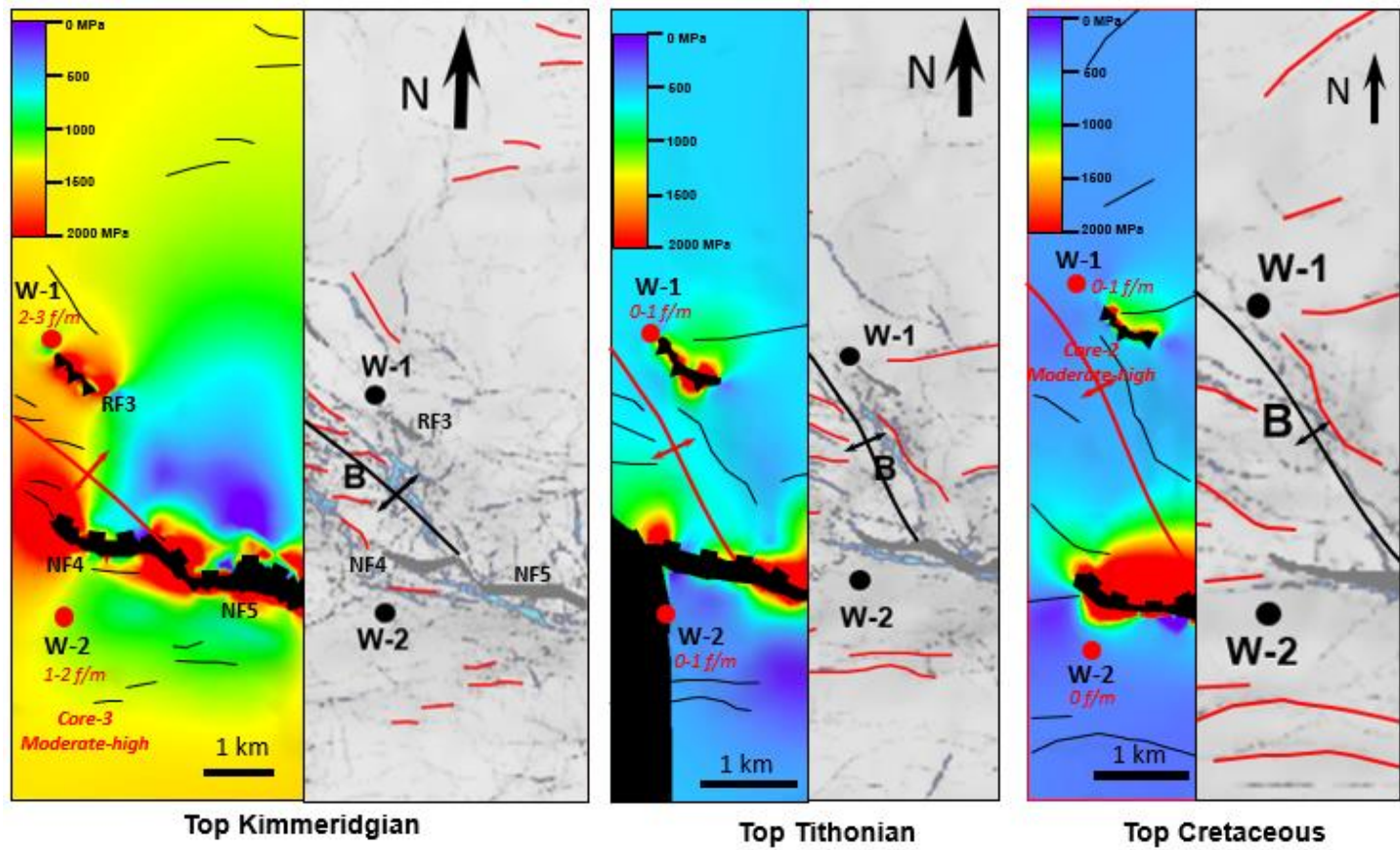


Figure 7.16. Comparison between the distribution of MCSS and ant-tracking for Mesozoic surfaces in anticline B. Superimposed black lines correspond to subtle faults interpreted from curvature/variance attributes. Values of fracture density from FMI logs for boreholes W-1 and W-2 seem to have a relatively good correlation with MCSS values.

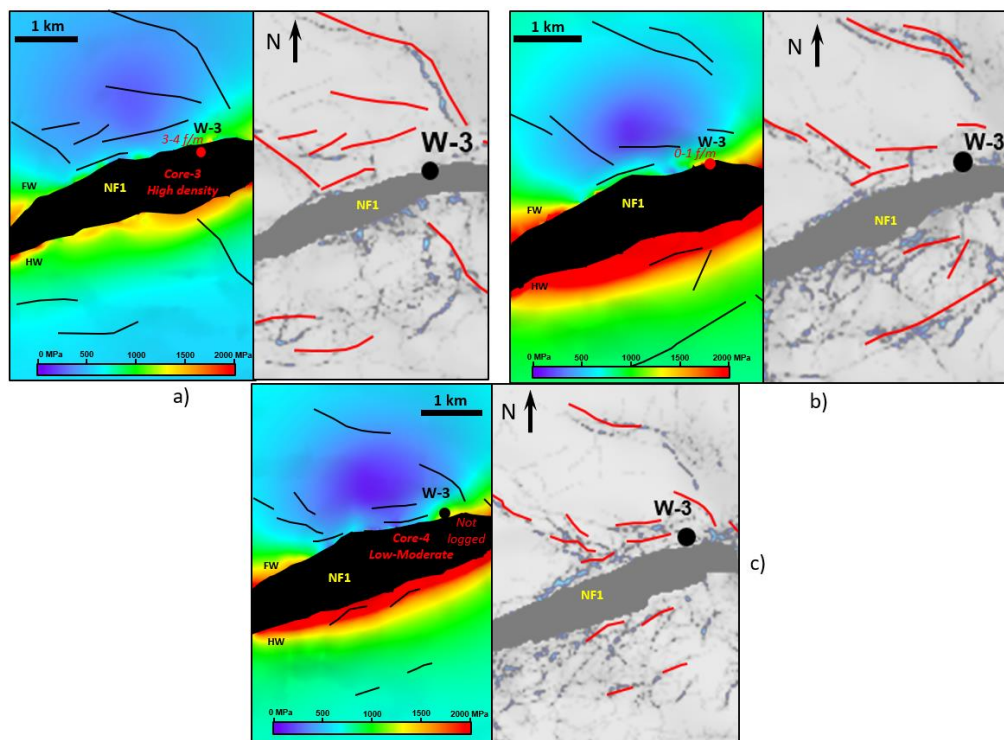


Figure 7.17. Comparison between the distribution of MCSS and ant-tracking for Mesozoic surfaces in Anticline A. Superimposed black lines correspond to subtle faults interpreted from curvature/variance attributes. Values of fracture density from FMI logs for boreholes W-1 and W-2 seem to have a relatively good correlation with MCSS values. a) Top Cretaceous; b) Top Tithonian; c) Top Kimmeridgian. HW=Hanging wall; FW=Footwall.

Top Tithonian

For borehole W-1, high values of MCSS show a good correlation with relatively high strain values; however FMI log shows relatively low fracture density in the uppermost Tithonian sequence, so this correlation is considered as regular (Figure 7.19). Borehole W-2 shows a good correlation between ED modelling and geomechanical modelling, with low values of MCSS and strain in the borehole's location; likewise, correlation with FMI log is also good since FMI log shows low values of fracture density, except for a thin interval where Core-2 was obtained which shows high fracture density.

Top Cretaceous

Borehole W-1 is located in an area with relatively low values of MCSS and low strain values, thus existing a good correlation between ED modelling and geomechanical modelling (Figure 7.20). Correlation with FMI log is regular since the uppermost Cretaceous sequence shows alternate intervals of high and low fracture density.

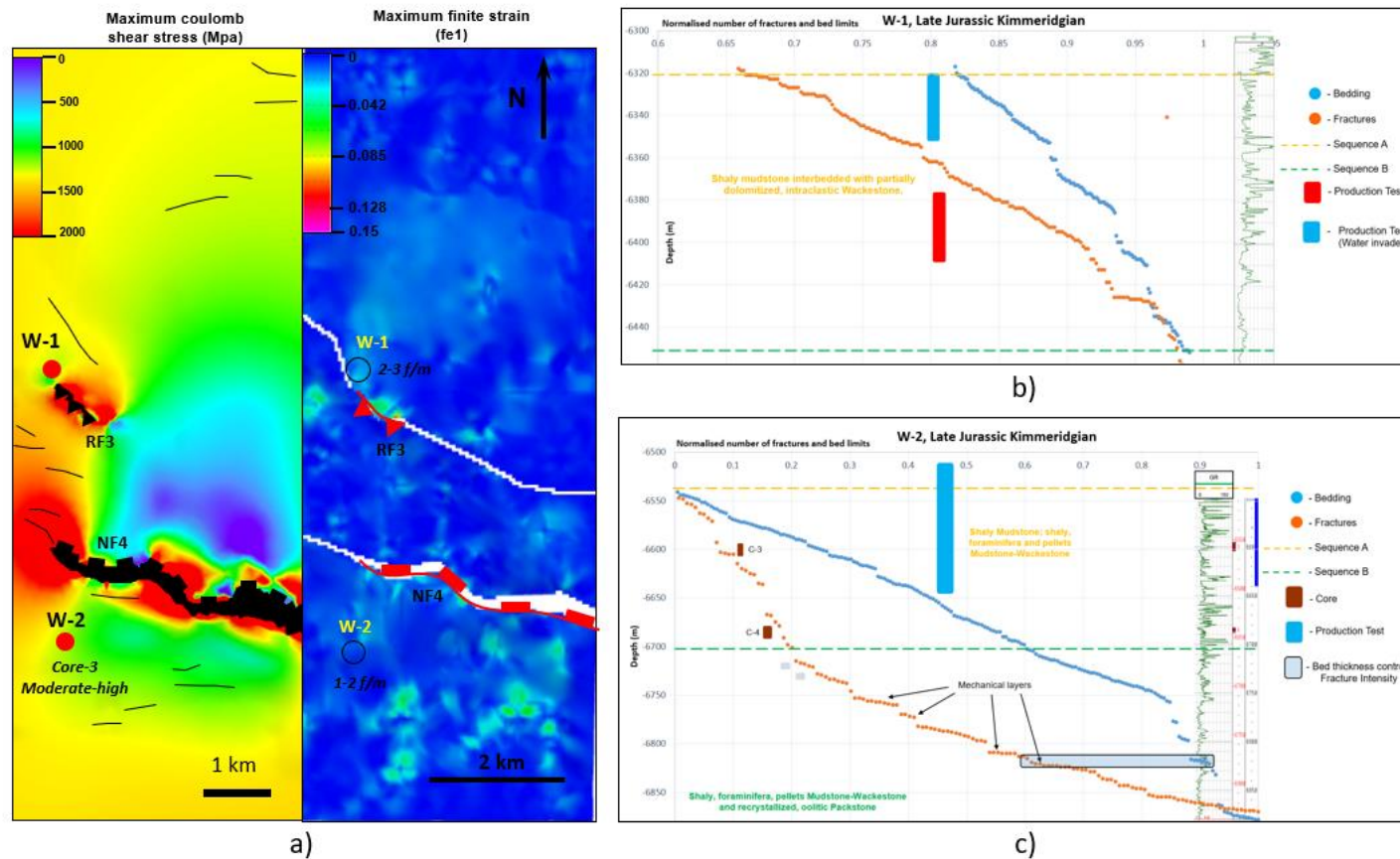


Figure 7.18. a) distributions of MCSS and strain in Top Kimmeridgian show some similarities around reverse fault RF3 and a low strain zone to the north of normal fault NF4; b) Cumulative Fracture Intensity (CFI) plot show high fracture density in the Kimmeridgian uppermost sequence for borehole W-1, confirmed by a production test that resulted water invaded thus indicating good permeability; c) Similarly to borehole W-1, CFI plot shows relatively high fracture density in the Kimmeridgian uppermost sequence for borehole W-2. Another water invaded production test confirmed good permeability, probably assisted by interconnected fracture sets.

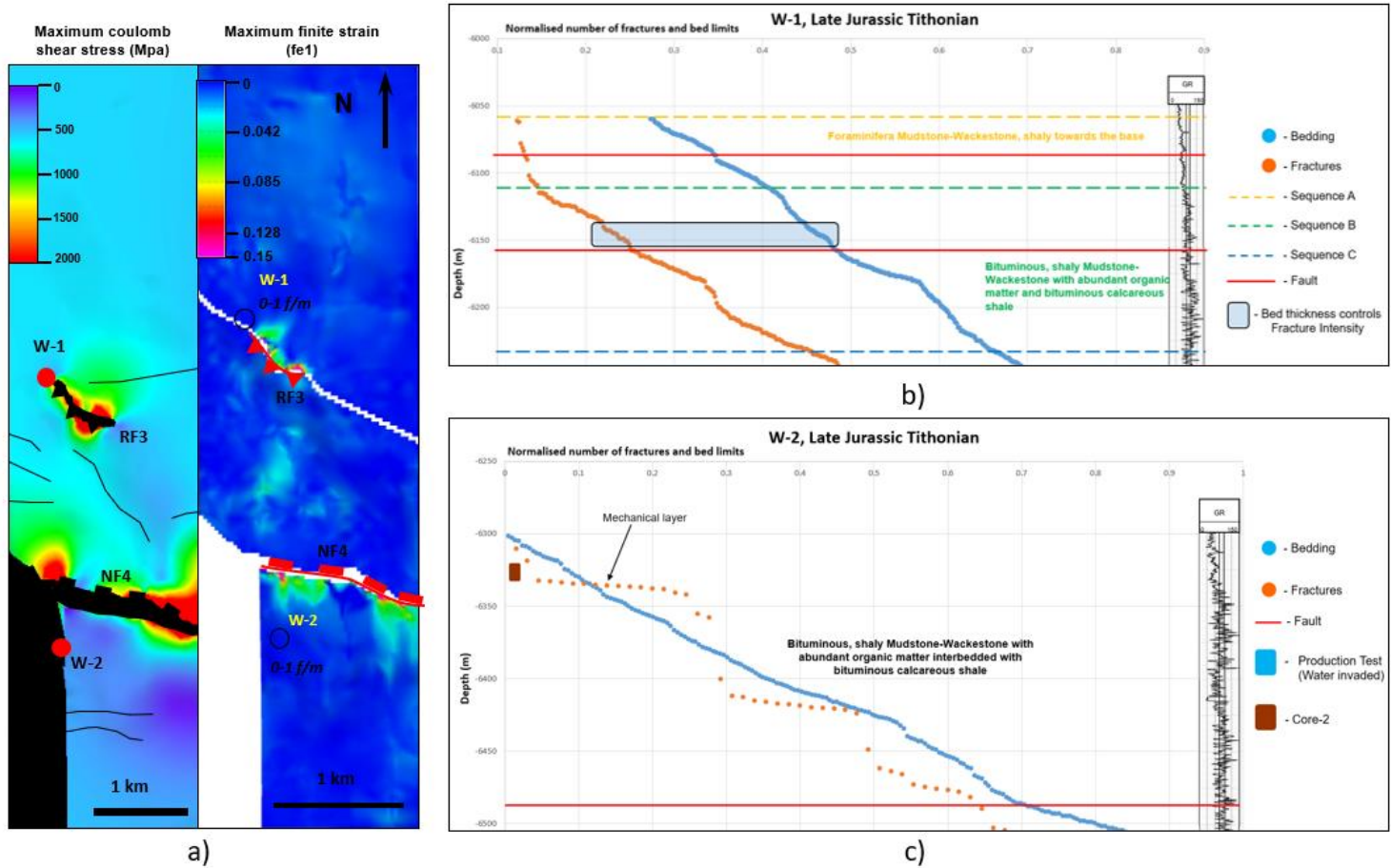


Figure 7.19. a) MCSS and strain in Top Tithonian show similar distributions of high strain zones around fault planes and the anticline's hinge; b) CFI plot showing a moderate fracture intensity in the Tithonian uppermost sequence; c) CFI plot showing low fracture density but with the presence of an interval with high fracture density in the Tithonian uppermost sequence for borehole W-2.

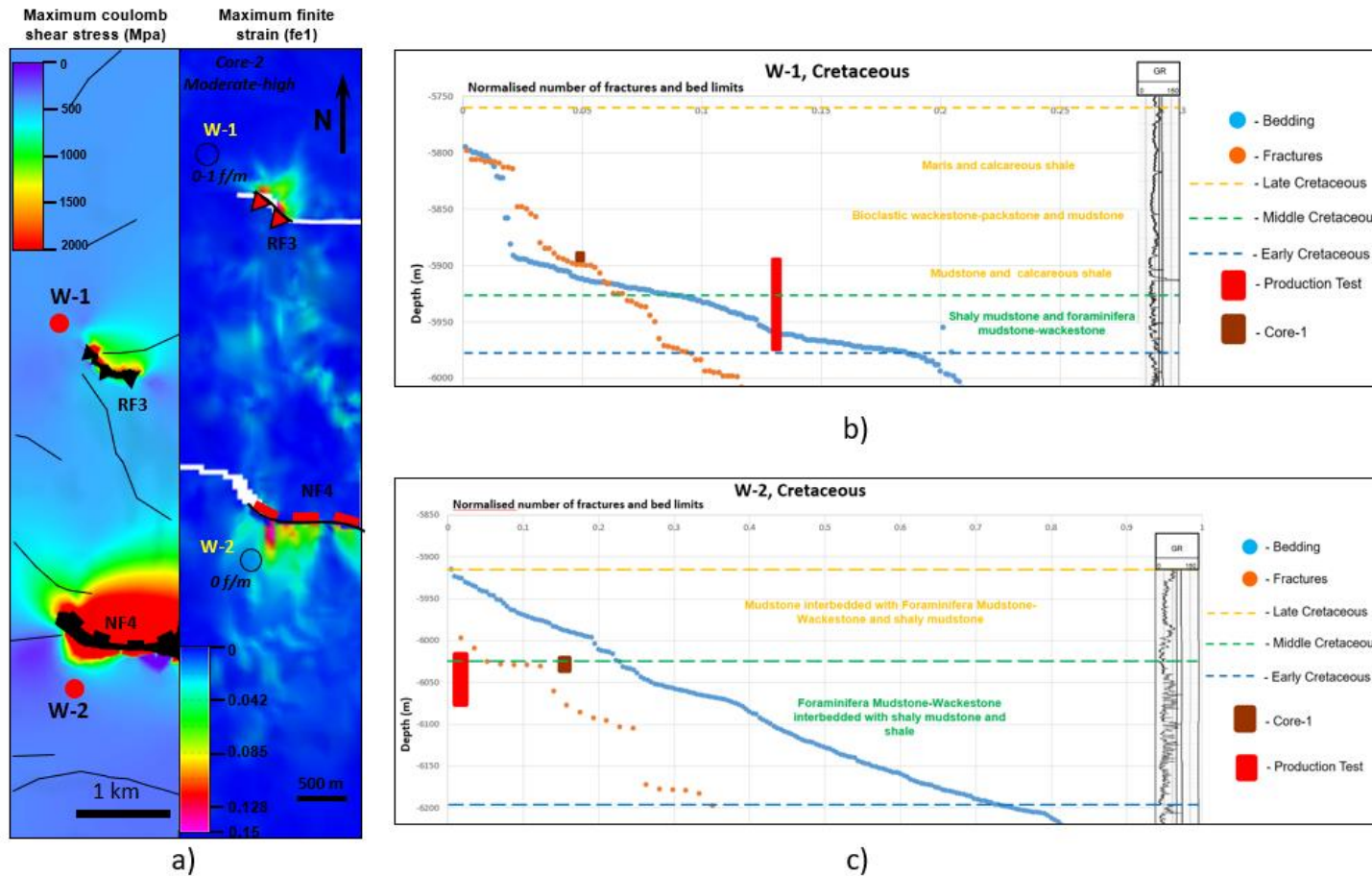


Figure 7.20. a) distribution of MCSS and strain in Top Cretaceous follow similar patterns with high strain zones around the fault planes and the fold hinge and relatively low strain values in the borehole locations; b) CFI plot shows intervals of low and relatively high fracture density in the Late Cretaceous uppermost sequence for borehole W-1; c) CFI plot showing absence of fractures in the Late Cretaceous uppermost sequence for borehole W-2.

7.3.2 Anticline A

This structure is a salt-cored anticline oriented NE-SW bounded in its southern flank by a similarly oriented normal fault NF1, whose vertical offset diminishes gradually towards the western edge as well as the amplitude of the salt diapir (Figure 7.21). Similarly to other faults in the study area, maximum vertical displacement (1900 m) is located at the centre of the fault plane. The structural evolution of this anticline suggests that this fault had a normal displacement during Mesozoic event D1, then it could have been reactivated with a reverse displacement during contractional events D2/D3 and finally another reactivation as a normal fault with a strike-slip component during D4 event (see Chapter 4). The amount of displacement during each deformational event cannot be quantified with accuracy, and the present-day total offset is the result of the individual displacements. For modelling purposes, the fault is assumed to be generated during a single event and considered as a pure-dip displacement.

For this structure, values of Young's modulus, Poisson's ratio and rock density from boreholes W-3 were used for each Mesozoic modelled scenario. Also, values for coefficient of internal friction (μ) and cohesive strength of 0.6 and 20 MPa were used.

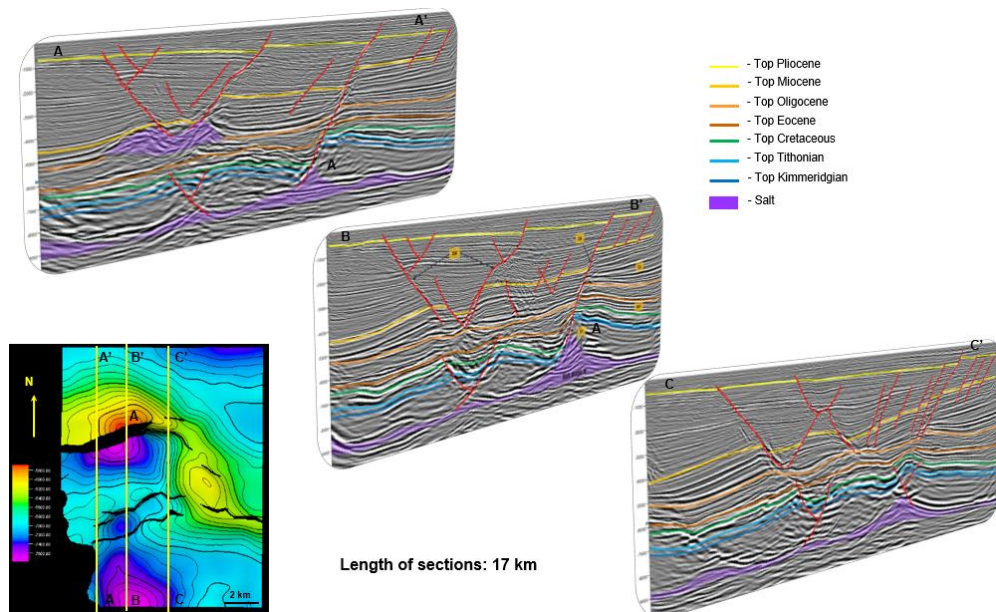


Figure 7.21. Series of interpreted cross-sections illustrating the along-strike variability of anticline A's geometry associated to the variations in the thickness of autochthonous salt.

7.3.2.1 Fracture orientation

Top Kimmeridgian

Predicted ED predominant orientations in the vicinity of borehole W-3 are NW-SE 50-60°, WNW-ESE and correspond mainly to fractures with normal displacement, oblique to the anticline's strike (NE-SW 60°). These orientations are perpendicular to the predominant orientations measured in Core-4; however, they match some secondary orientations measured in the same core, thus providing a relatively good degree of correlation. Likewise, ant-tracking lineaments observed in both depth slice and mapped top surface show similar orientations to predicted ED orientations, so correlation is considered as good (Figure 7.22). No logs were run at this interval, so a correlation with ED modelling was not possible to define.

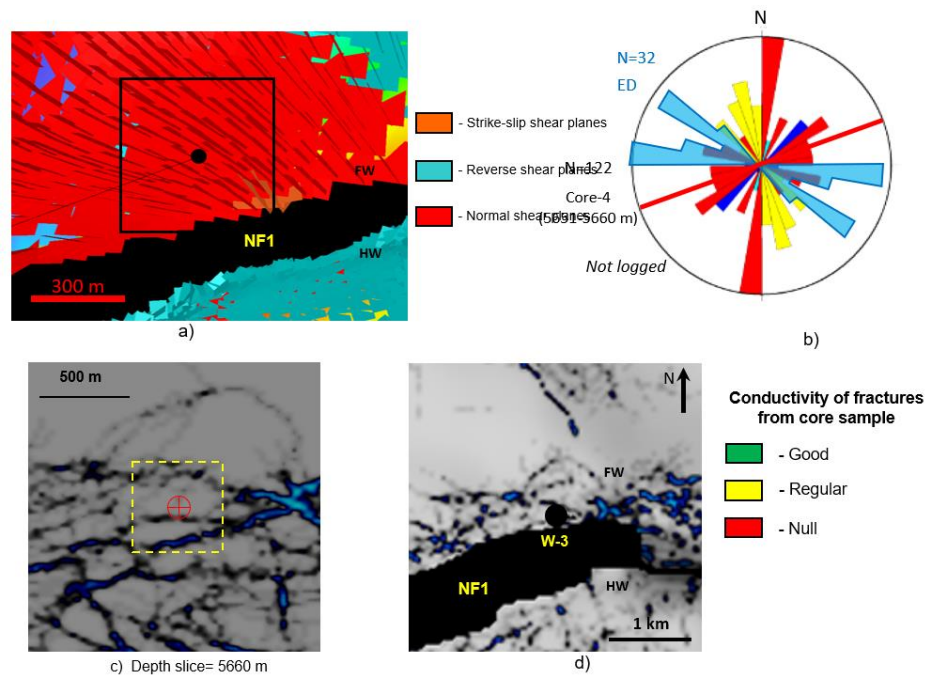


Figure 7.22. a) Predicted fractures around borehole W-3, anticline A; b) rose diagram comparing the predicted orientations (blue) with orientations measured in Core-4, red line corresponds to the anticline axis; c) Depth slice and, d) Top Kimmeridgian surface with ant-tracking attribute showing the lineaments around W-3. Normal fault NF1 was used as input for fracture modelling. HW=Hanging wall; FW= Footwall. Conductivity of fractures was determined in previous studies (unpublished PEMEX internal reports) by analysing thin sections and considering parameters such as fracture porosity, degree of cementing, connectivity and evidence of fluids (Monroy Santiago, 2011).

Top Tithonian

ED predicted orientations for this surface are NW-SE 50-70°, with normal displacement and highly oblique to anticline's strike. These orientations are similar to secondary orientations measured in FMI logs, so correlation can be considered as good (Figure 7.23). In the other hand, ED predicted orientations are not observed on lineaments of ant-tracking depth slice and mapped surfaces, although the difference in orientation between them is not too great so the degree of correlation can be considered as poor to regular.

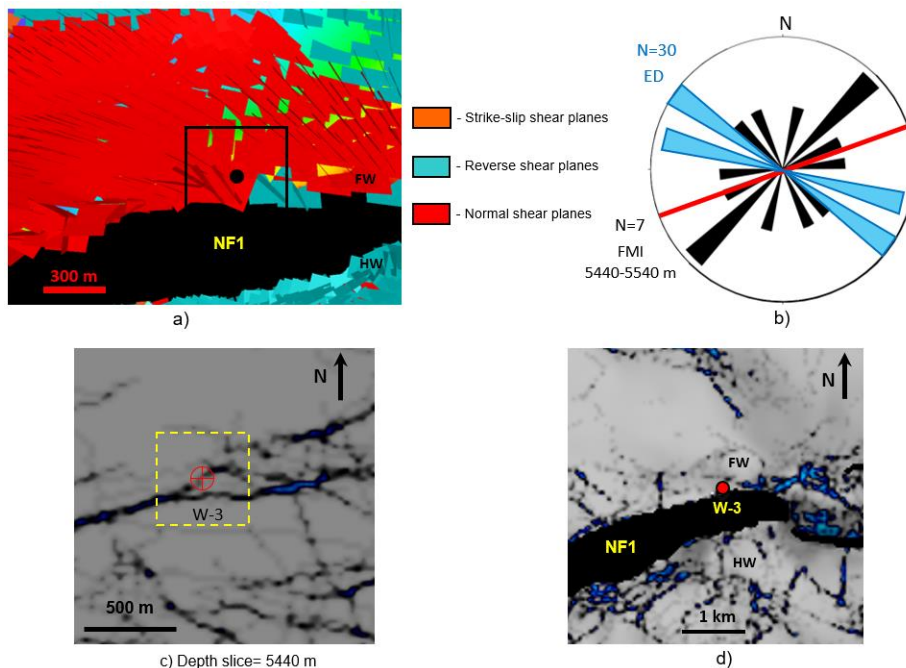


Figure 7.23. a) Predicted fractures around borehole W-3, anticline A; b) rose diagram comparing the predicted orientations (blue) with orientations measured in FMI logs (black), red line corresponds to the anticline axis; c) Depth slice and, d) Top Tithonian surface with ant-tracking attribute showing the lineaments around W-3. HW=Hanging wall; FW= Footwall.

Top Cretaceous

ED predicted orientations show a range between NW-SE 50-80°, which are almost perpendicular to orientations observed in FMI log and the anticline's strike (Figure 7.24); conversely, secondary ED predicted orientations NNE-SSW and ENE-WSW show a good matching with secondary orientations from FMI logs, so the degree of correlation between these data sets can be considered as regular to good.

Predominant ED predicted orientations do not match the orientations of lineaments in ant-tracking depth slice and mapped surface; however, secondary ED orientations this,

the degree of correlation between fracture orientations of ED modelling and ant-tracking orientations in depth slice within the window analysis whereas in the mapped surface they are not clearly observed in the vicinity of borehole W-3. Based on tracking is considered as poor to regular.

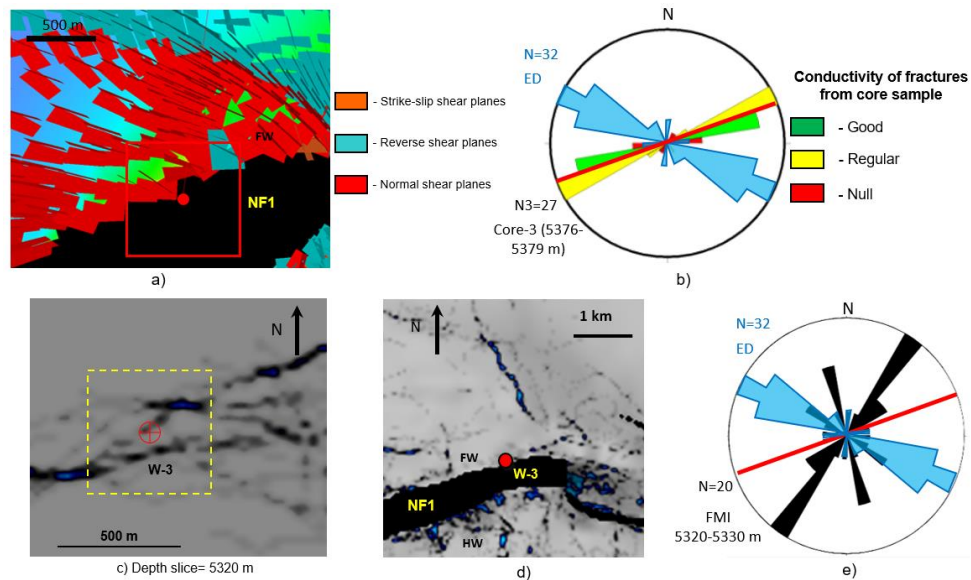


Figure 7.24. a) Predicted fractures around borehole W-3, anticline A; b) rose diagram comparing the predicted orientations (blue) with orientations measured in Core-3, red line corresponds to the anticline axis; c) Depth slice, d) Top Cretaceous surface with ant-tracking attribute showing the lineaments around W-3; e) rose diagram comparing the predicted orientations (blue) with orientations measured in FMI logs (black). HW=Hanging wall; FW= Footwall.

7.3.2.2 Fracture intensity

Top Kimmeridgian

Borehole W-3 is located very close to the fault plane of a major normal fault, in an area where values of MCSS are typically high. Similarly, values of strain obtained from geomechanical modelling are high at the borehole's location, thus providing a good degree of correlation and a good probability of having a high density of medium-scale fracturing (Figure 7.25). This interval was not logged and, therefore, no correlation between ED modelling and FMI log was possible to define; however, Core-4 is reported to show a moderate qualitative fracture intensity, which implies a relatively good degree of correlation with the MCSS values from ED modelling.

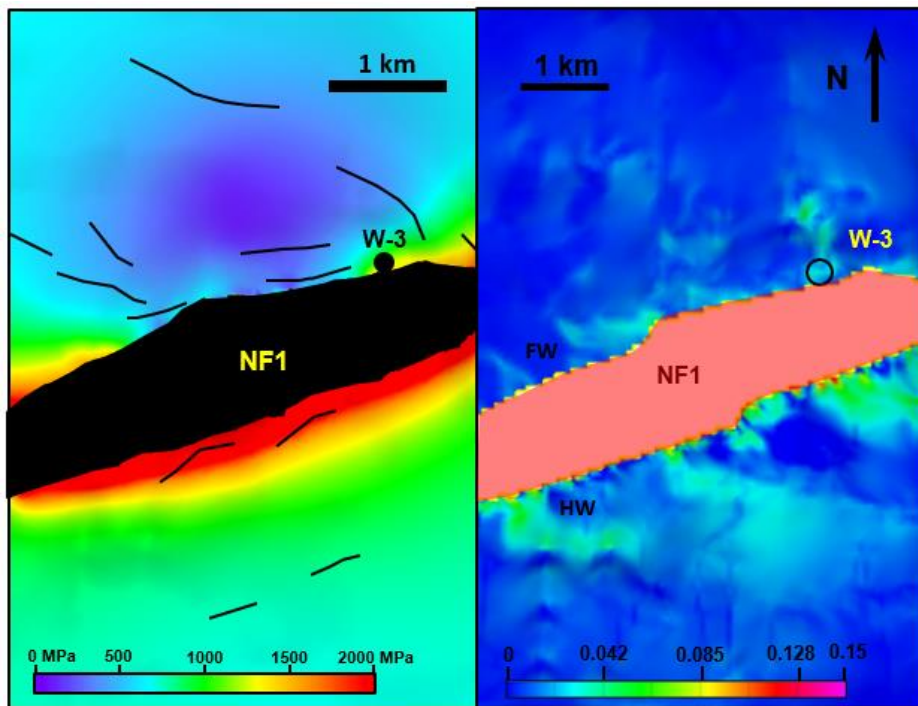


Figure 7.25. Distribution of MCSS (left) and strain (right) in Top Kimmeridgian show similar patterns for anticline A.

Top Tithonian

Similarly to Top Kimmeridgian, values of MCSS and strain show a good correlation with high values distributed in the borehole's location; however, FMI log shows a very low fracture density across the entire sequence, thus providing a poor degree of correlation between ED modelling and FMI log (Figure 7.26); the same situation is observed in anticline B, so it is possible that factors such as lithology and texture may be playing a primary role in fracture development rather than structural position.

Top Cretaceous

This sequence is virtually on the fault plane and values of MCSS are high whereas strain values are relatively high, so the degree of correlation is considered as regular to good. FMI log shows a high fracture density in the entire Cretaceous sequence, thus providing a good degree of correlation with MCSS values from ED modelling (Figure 7.27).

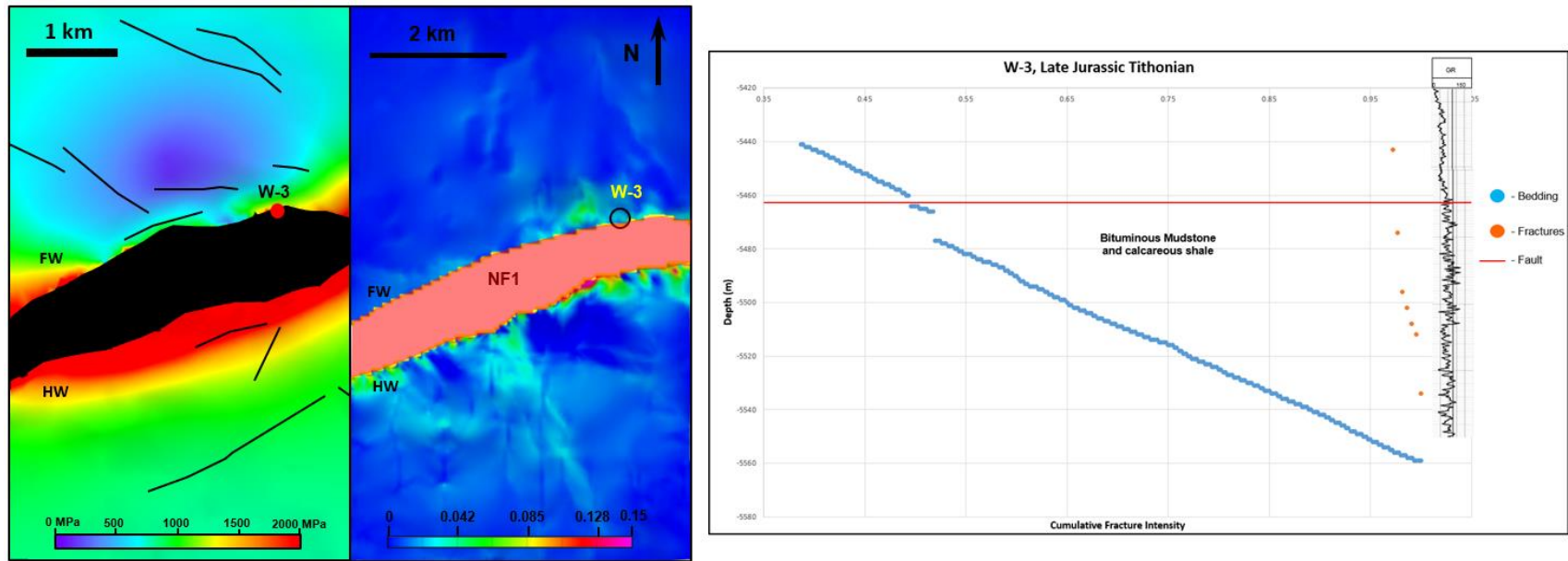


Figure 7.26. Left: Comparison between distribution of MCSS and strain in Top Tithonian, anticline A; Right: Cumulative Fracture Intensity (CFI) plot..

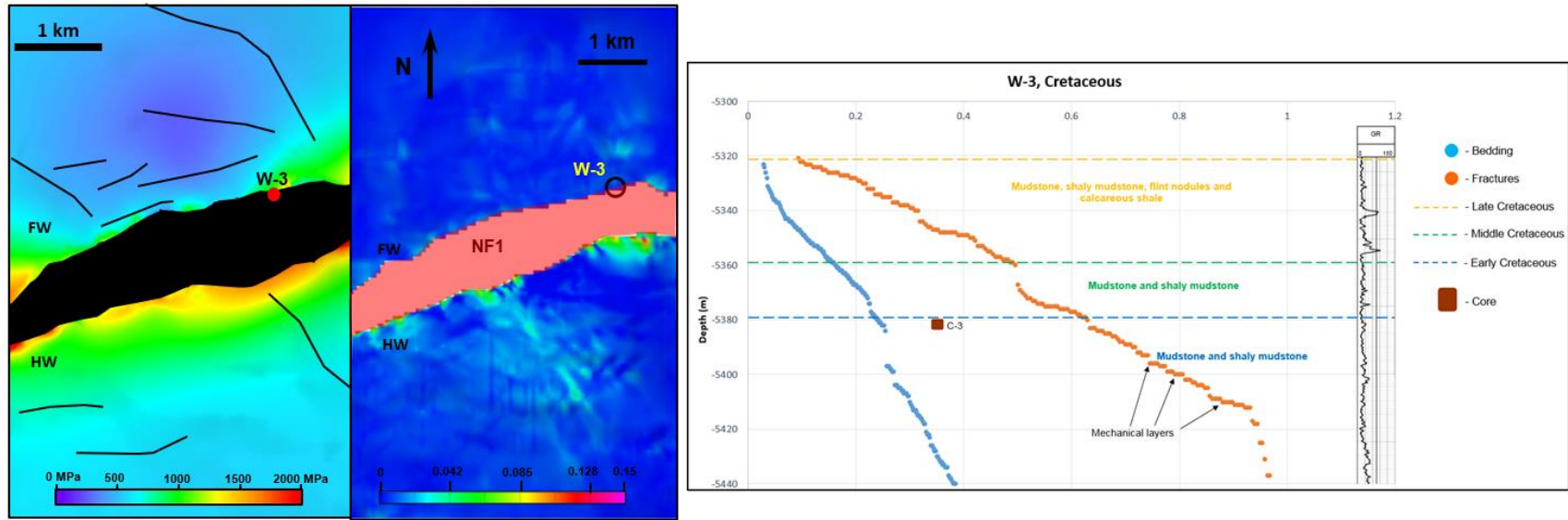


Figure 7.27. Left: Comparison between distribution of MCSS and strain in Top Cretaceous, anticline A; Right: Cumulative Fracture Intensity (CFI) plot.

7.4 Discussion

For this chapter, Elastic Dislocation modelling was used in order to test its potential as a predictive tool for fracture orientation and intensity within the study area. To achieve this, three Mesozoic mapped surfaces from Anticlines A and B were modelled and their results compared against geomechanical modelling, seismic attributes and calibrated with borehole data.

7.4.1 Comparison between modelled, seismic attributes and well data

7.4.1.1 Fracture orientation

Although ED modelling results show variable degrees of correlation with borehole data, seismic attributes and geomechanical modelling for fracture orientation and intensity in the study area (Table 7.2), its predictive potential can be considered as good, so it can be applied not only in frontier areas with little or no borehole data, but also in areas with high density of boreholes, which allows a better calibration between predicted data and borehole data.

In most cases, ED predicted fracture orientations that are slightly oblique and/or parallel to the anticline's axis. When compared with orientations from FMI logs, predicted orientations in some cases match the predominant orientations and in other cases they are perpendicular, thus implying a poor correlation; in contrast, ED predicted orientations match at least one secondary orientation in all modelled cases, implying a good correlation.

For anticline B, orientation of ant-tracking lineaments observed in mapped surfaces provides the best correlation with ED predicted fracture orientations whereas FMI orientations provided the lowest degree of correlation (Cretaceous and Tithonian, borehole W-2, Figures 7.12 and 7.13). For anticline A, the opposite situation occurs, and the best correlation is observed between ED and FMI orientations (Cretaceous and Tithonian, borehole W-3, Figures 7.23 and 7.24) whereas the lowest correlation is with ant-tracking lineaments in surfaces. The higher number of orientations observed in borehole data from both anticlines relative to the number of ED predicted orientations, as well as the discrepancy between the predicted orientations and borehole data may be explained as the result of a combination of the following factors: 1) Difference in the scale of observation, since the number of fracture orientations observed in borehole data is generally greater than those predicted by ED; 2) Under sampling of sub-horizontal fracture sets due to geometrical limitations of FMI logging; 3) Lack of information about a crucial control of fracture formation such as fluid pressure, which reduces the effective confining pressure and leads to shear or extension fracturing, depending if differential stress is small or large, respectively (Twiss and Moores, 1992); 4) Rock anisotropy, 5)

Presence of multiple deformational events, which poses a limitation to ED modelling, which uses a single-event approach; 6) Stress perturbations around larger faults/fractures may promote variations in orientations of smaller, newly formed fracture sets (Maerten et al., 2002; Bergbauer and Pollard, 2004) observed only in borehole data and not predicted by ED, and, 7) fractures predicted by ED correspond only to fault-related fractures whereas fractures observed in borehole data may be also related to folding, overpressure and vertical load.

In summary, ED proved to be effective to predict orientation of fracture sets in the study area; however, it must be used along with other techniques such as ant-tracking attributes and geomechanical modelling and borehole data (if available) in order to calibrate the modelled results and provide more accurate and confident results. In this work, variability in the correlation between predicted and borehole orientations indicate the influence of different geologic factors, so it is not possible to associate the degree of predictability of ED to a single factor; in other words, the accuracy of ED predictions may vary from one area to another and will depend on the particular geological characteristics of each area.

7.4.1.2 Fracture density

With respect to fracture intensity, two basic assumptions must be considered: 1) most of strain in the study area is accommodated by brittle fracturing, and; 2) the curvature of a folded bed is directly related to the amount of stress and strain (Price and Cosgrove, 1990) as long as curvature is not associated to sedimentary depositional processes. Maximum Coulomb shear stress (MCSS) is a parameter that measures the propensity for failure of surfaces under compression or shear and has been used as a proxy for fracture density and near-fault deformation (Jaeger and Cook, 1979, Crider and Pollard, 1998; Maerten et al., 2002). In this work, strain, MCSS and fracture density values from FMI and core samples are compared in order to define a relationship. The best correlation is observed between modelled MCSS and strain calculated from geomechanical modelling in both anticlines. These two parameters show similar distributions in map view, thus indicating a direct correlation between them; moreover, this correlation can be used as a proxy to define zones where higher fracture densities are more likely to occur, which are characterized by high values of both strain and MCSS; however, this assumption should not be considered as a rule of thumb, since it is possible that areas with low strain and MCSS may be highly fractured due to diagenetic processes; conversely, it is also possible that rock sequences within tight folds may not be highly fractured due to their particular mechanical properties. With these considerations in mind, it is crucial to include the geological knowledge of the study area in any analysis aimed for fracture prediction.

A visual comparison between map distributions of MCSS and ant-tracking attribute show similar patterns, where the density of lineaments is higher in areas with high values of MCSS; moreover, subtle faults interpreted from a combined analysis of curvature/variance attributes are more concentrated in areas with high MCSS and, in some cases, they are aligned with trends of high MCSS values. A similar relationship is also observed by Dee et al., (2007) in a fault-related fold in Venezuela. These lineaments are superimposed in the ant-tracking surfaces (Figures 7.16 and 7.17), showing a good degree of correlation with ant-tracking lineaments. It is very likely that more ant-tracking lineaments correspond to subtle faults; however, the low seismic resolution prevents faults to be resolved and, therefore, to make a reliable confirmation in the conventional amplitude volume. This good correlation suggests that a combined analysis of MCSS and structural seismic attributes can be used as a more robust proxy for medium-scale fracture intensity in undrilled areas rather than if they are used alone or separately.

Availability of borehole data provided the possibility to compare modelled data against fracture density observed in FMI logs and core samples. In most cases, a regular to good direct correlation was observed with fracture intensity from FMI logs in both anticlines, with the exception of Top Tithonian in anticline A where high values of strain and MCSS are in contrast with almost no fractures observed in FMI logs in the uppermost Tithonian section. This may indicate that factors such as lithology and texture exert a primary role in fracture development rather than structural position, thus highlighting the complex interplay between different geological factors that control fracturing in carbonate rocks. Correlation of ED with fracture density reported in core samples is also good, although only in two cases they were compared: boreholes W-2 (Core-3, Kimmeridgian) and W-3 (Core-3, Cretaceous). In both cases, high values of strain and MCSS correspond to reported qualitative high fracture densities in core samples.

Boreholes W-1 and W-2 located in the flanks of anticline B show a higher degree of correlation between ED results and geomechanical modelling, seismic attributes and borehole data than borehole W-3 located in anticline A. This difference may be associated to the location of W-3 within the damage zone of a major fault plane, which has been reactivated with different senses of displacement thus generating multiple fracture sets not predicted by ED modelling. Conversely, W-1 and W-2 are located in the flanks of an anticline that has undergone a less complex structural evolution, which is easier to model and therefore, more likely to have a good correlation with predicted results from ED modelling.

Fracture orientation									
Anticline B						Anticline A			
	W-1			W-2			W-3		
	JSK	JST	KS	JSK	JST	KS	JSK	JST	KS
FMI	Regular-good	Regular-good	Regular	Good	Poor	Regular	N/A	Good	Regular-good
Core	N/A	N/A	N/A	Good (Core-3)	N/A	N/A	Good (Core-4)	N/A	Poor-regular (Core-3)
Ant-tracking slice	Good	Good	Good	Regular	Regular-good	Poor	Good	Poor-Regular	Regular
Ant-tracking surface	Good	Good	Good	Regular	Good	Good	Regular-good	Poor-Regular	Poor
Fracture intensity									
Anticline B						Anticline A			
	W-1			W-2			W-3		
	JSK	JST	KS	JSK	JST	KS	JSK	JST	KS
FMI	Regular-good	Regular	Regular-good	Good	Good	Good	N/A	Poor	Good
Core	N/A	N/A	N/A	Good (Core-3)	N/A	N/A	Good	N/A	Good (Core-3)
Geomechanical modelling	Good	Good	Good	Good	Good	Good	Good	Good	Regular-Good

Table 7.2. Comparison of the degree of correlation between predicted fracture orientation and intensity and results obtained from borehole data, ant-tracking attribute and geomechanical modelling for anticlines A and B.

7.5 Conclusions

This study shows the application of ED modelling as a predictive tool for orientation and intensity of medium-scale faults/fractures, which are geological features that play an important role in low-matrix porosity and permeability and are usually not detected neither by borehole data or seismic data. At the same time, it combines ED modelling with ant-tracking analysis and geomechanical modelling and compare their results with borehole data in order to test its potential as a predictive tool in undrilled areas.

Predicted fracture orientations from ED modelling match some of the orientations of lineaments observed in mapped surfaces and depth slices where ant-tracking attribute was applied; moreover, orientations observed in FMI and core samples also have a good degree of correlation with predicted orientations.

Prediction of fracture intensity is of a qualitative nature, so calculated parameters are used only as proxy to determine the relative fracture intensity for a given location. In the study area, MCSS and strain distributions obtained from ED modelling and geomechanical modelling respectively show a relatively good degree of direct correlation; likewise, MCSS distribution has a regular to good degree of correlation with borehole data.

Although the degree of correlation between the results observed in this work are varied, they can be considered as good; however, there is a number of important limitations to take into account in order to explain the observed discrepancies and variability of the degree of correlation between modelled data and borehole data, or when attempting fracture prediction in areas with little or no borehole data: 1) Difference between the scales of observation of the datasets; 2) Under sampling of fracture sets in core samples and FMI logs; 3) Lack of information about pore-pressure, which may control natural fracturing; 4) Rock anisotropy, 5) Presence of multiple deformational, and 6) software limitations.

In summary, predicted ED modelling results show a good degree of correlation with borehole data, seismic attributes and geomechanical modelling for fracture orientation and intensity. An adequate combined analysis of the results of these different datasets constitute an improved methodology with good potential to estimate location, orientation and intensity of medium-scale fracture sets in exploratory areas where borehole data is scarce or null. Reliability of fracture prediction at subsurface, however, can be affected mainly by the amount and quality of borehole and seismic data, complexity of structural geology, the three-dimensional variations in rock properties and the inherent limitations of the different analytical techniques.

Chapter 8

Integration and testing of a multidisciplinary methodology for fracture prediction

8.1 Introduction

Traditionally, fracture characterization in the oil industry has been focused mainly at reservoir scale for production purposes. Due to the increasing complexity and the high costs associated with non-conventional hydrocarbon exploration, it has become necessary to more accurately assess the quality of reservoir rock in new prospective areas with little or no available well data, in order to reduce the exploratory risk. This represents a highly complex problem due to most of the fractures and faults that increase fluid flow and/or compartmentalize a reservoir are below seismic resolution (Lohr et al., 2008; Endres et al., 2008); also, core samples and well logs only provide information at very small scale (Ameen et al., 2009; Sagi et al., 2014). Due to this, it is necessary to adopt a multidisciplinary approach by combining geological and geophysical data and techniques in order to predict the presence and distribution of small scale from larger structures.

This chapter has two main aims: 1) to integrate the different analyses discussed in previous chapters into a multidisciplinary methodology and apply it in the study area to predict fracture sets within the subsurface, and, 2) to test the validity of this methodology by assessing the presence and quality of a potential reservoir rock for a proposed borehole within the study area. To achieve this, the study proposes some improvements to the traditional assessment of the presence and quality of the reservoir rock element currently used in the petroleum industry by including additional sub-elements derived from the different analyses described in previous chapters in order to provide a more robust prediction of the characteristics of the fracture sets at the subsurface.

Availability of data from three boreholes within the study area offered an opportunity to compare the results obtained and assess the viability of this methodology as a predictive tool in exploratory areas with little or no borehole data available.

8.2 Background

8.2.1 Integration of techniques

The methodology for fracture prediction proposed in this work is illustrated in Figure 8.1. Its multidisciplinary approach incorporates different data sources, which provides a more robust estimation of the presence and characteristics of fracture sets in the subsurface. It provides additional analysis that are not included in the standard methodologies proposed by Endres et al., (2008), Lohr et al., (2007). Also, it differs from the model proposed by Jenkins et al., (2009) in that it does not rely as heavily on the amount and quality of borehole data, so it can be applied to the exploratory stages during hydrocarbon exploration. The two main datasets are 3D seismic data and borehole data. From these, seismic data represents the main source of subsurface information and provides the primary input for most of the analyses (which are independent from each other) and their correspondent results, but with the limitation of the poor seismic resolution at the depth of investigation, whereas borehole data provide very spatially limited, direct information about the presence and characteristics of fractures as well as the opportunity to calibrate the results obtained from the geophysical analyses. Regional geology information represents the bridge between global geology and local geology (Roberts and Bally, 2012) and provides a very useful first-order context to guide exploration in oil and gas industry. Finally, results obtained from these sources are integrated into a final model which needs to be assessed and included in the evaluation of proposed prospects for drilling. In order to get a better understanding of the proposed methodology workflow for fracture prediction, the following sections summarize the results and the individual contributions of each of the analyses involved in this methodology.

8.2.1.1 Seismic Interpretation

The first step during the early stages of the hydrocarbon exploratory process consists of the mapping of the prospective area in order to: 1) identify the presence and define the geometry of potential structural hydrocarbon traps; and, 2) define the geological evolution of the traps including the timing of deformational events that affected their geometries with respect to hydrocarbon maturation and migration. The degree of certainty in the interpretation is related to different factors such as quality of seismic imaging, amount of available borehole data and geological complexity. For this work, seismic imaging is considered as good at the depth of investigation (5-7 km) although

resolution is low (no greater than 150 m). Information from three boreholes in the area was available, which provided good control of the interpretation in the majority of the study area.

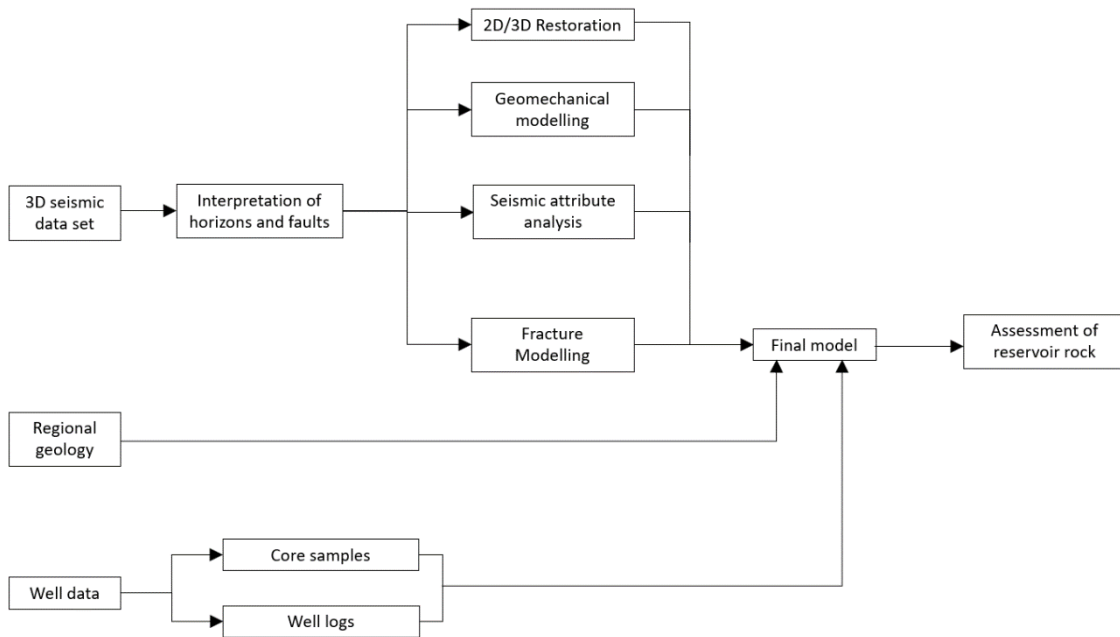


Figure 8.1. Flow diagram illustrating the developed methodology for fracture prediction.

The structure maps in depth from the two main economic Mesozoic targets (Top Cretaceous and Top Kimmeridgian) reveal the presence of three anticlines (A, B and C) that represent structural hydrocarbon traps. Their geometries show different degrees of variability in geometry along-strike of their salt cores and Mesozoic overburden, which is typical of salt-cored structures (Chapter 4). Considering their present-day geometries we can conceptualize and characterize these anticlines as follows: Anticline A is a salt-cored structure whose geometry is associated mainly to extensional deformation detaching on autochthonous salt (roll-over anticline); Anticlines B and C are cored by salt-anticline/pillows with a typical contractional structural style characterized by symmetric buckle folding and high-angle thrust faults detaching on salt, so they can be defined as pop-up anticlines (Chapter 4).

As discussed in Chapter 4, the combined analysis of thickness maps and 3D interpretation allowed the identification of not only the structural style of deformation of the study area but also its tectonostratigraphic evolution, including the effects of different regional deformational events (Peterson Rodriguez et al., 2013). Thickness maps suggest that the location and orientation of these anticlines is controlled primarily by the early distribution of underlying autochthonous salt. Also, the combined analysis of these maps and seismic cross-sections allowed to define the changes in the tectonic regime

through time. During Mesozoic and early Palaeogene, deformation was mainly driven by a combination of gravitational process combined with salt diapirism within a passive margin context (D1 event). From Palaeogene to Middle-Late Miocene buckle folding and faulting of the structural traps associated to regional tectonic contraction (D2/D3 events). Another effect of this tectonic regime is the emplacement of allochthonous salt in the study area. During Pliocene, intense trans-tensional faulting related to both gravitational process and progradational sedimentation from south to north affected mainly the stratigraphic column above the upper detachment level (see Chapter C).

Although the analysis of seismic facies and stratigraphy is beyond the scope of this work, it also provides valuable information about the lithological characteristics of the target stratigraphy, and therefore, should be integrated into any predicted geological model that will be applied to an undrilled area.

8.2.1.2 2D Restoration

After the mapping of the Mesozoic targets, the next step in the workflow consisted of defining properly oriented cross-sections from each of the structural traps in order to carry out 2D restorations, which provided information about the timing of deformation of each analysed structure (Chapter 4); however, important limitations inherent to the structural complexity of the study area that hindered the restoration process such as the presence of salt bodies, two detachment levels and strike-slip movement above the upper detachment level made 3D restoration unfeasible. Some similarities in the structural evolution of these anticlines are: 1) They are salt-cored structures; 2) Salt inflation is related to the development of adjacent mini-basins during D1 event; 3) D2 and D3 events re-deformed the pre-existent structure and, 4) D4 normal faulting reactivated pre-existent Mesozoic faults in anticlines A and B. The main differences in their structural evolutions are summarized as follows:

- Anticlines A and C initially developed as salt-roller structures associated to counter-regional and regional faults respectively and subsequently hard-linked into a single segment, whereas anticline B developed as an isolated salt anticline/pillow cored structure during Mesozoic times.
- During contractional events D2/D3, the geometry of Anticline A was not re-deformed substantially, whereas anticlines B and C were re-deformed as pop-up anticlines.
- D4 event caused reactivation of the normal faults bounding Anticlines A and C with the correspondent implications for both fracture generation and trap integrity, whereas faulting associated to D4 did not affect the Mesozoic section in Anticline C. New fracture sets with multiple orientations may have been generated within the

- damage zone around the main fault plane (see Chapter 5) bounding Anticline A, which increases permeability and the quality of potential reservoir rocks; however integrity of the trap may be affected negatively due to the breaching of the seal rock associated to fault's reactivation.

In summary, 3D seismic interpretation and 2D restoration defined the presence and geometry of potential structural traps in the study area as well as their structural evolutions, which are characterized by the presence of deformational events (D2/D3) that very likely caused fracture development in Mesozoic carbonate rocks. This information confirms its high potential for hydrocarbon exploration, so further analyses must be carried out in order to assess more accurately the potential of the Mesozoic targets as reservoir rocks.

8.2.1.3 Analysis of borehole data

Borehole data represent the only direct source of information about not only the characteristics of the geologic column (lithology, porosity, and permeability) and its diagenetic evolution but also about the presence and characteristics of hydrocarbon in the subsurface as well as confirms the accuracy of the predicted geological model in an area. As a result, availability of any borehole data during the early stages of hydrocarbon exploration in frontier areas, where borehole data are scarce or even absent, is of critical importance since they provide possible geologic scenarios that can be extrapolated to undrilled and/or unknown areas. For this work, borehole data were used as a source of information in order to investigate the influence of geologic controls on natural fracturing. Limitations of these analyses are the fractional nature of information sampling (under-sampling of fracture sets), the superimposed effect of several geological factors and their strong lateral, vertical and temporal variations, which difficult an accurate definition of the individual effects of each geologic factor on fracturing; however, the relationships observed can be integrated into the predicted geological scenarios and extrapolated to undrilled areas.

The results obtained from the analysis of borehole data shown in Chapter 5 suggest the following relationships between geologic controls and fracturing within the study area: a) the original texture of the rock seems to exert the primary role in natural fracturing. Mud-supported textures (mudstone-wackestone) deposited in a basinal environment show higher fracture densities than grain-supported textures (grainstone-packstone) deposited in shallow environments; b) On the other hand, lithology seems to exert a secondary role in natural fracturing. For the study area, limestones generally show higher fracture densities than partially dolomitized limestones or dolomites; c) bed thickness seems to exert a secondary role in natural fracturing. The well-known inverse relationship between

bed thickness and fracture intensity was observed in a first-order scale; however, some specific intervals show either direct or null relationship (see Figures 5-27 and 5-28), was also observed at some specific intervals.

Reports of paragenetic analyses (Instituto Mexicano del Petroleo, 2011) performed in core samples provided qualitative information about fracture intensity, the relative timing of fracturing by the analysis of cross-cutting relationships of the different fracture sets observed, as well as the relative timing of the different diagenetic processes observed in the study area such as dolomitization, pressure-solution, cementation, silicification, etc. This provides critical information about the evolution of the lithological characteristics of carbonate rocks, since the presence of diagenetic events may have enhanced and/or destroyed porosity/permeability, thus affecting their potential as reservoir rocks. Due to its importance, this information must be integrated into the predicted geological model for undrilled areas with additional borehole data (texture, lithology, bed thickness and fracture intensity) as part of the assessment of reservoir rock quality.

8.2.1.4 Structural seismic attributes

After defining: 1) the presence of structural traps, 2) their structural evolution and, 3) a predicted geological model, it is necessary to assess the quality of the potential reservoir rock. To achieve this, structural seismic attributes (curvature, variance and ant-tracking) provide valuable information about the location, relative density and orientation of fracture sets and subtle faults that are often overlooked in the conventional amplitude seismic volume due mainly to they are not imaged at depths where seismic vertical resolution is too low (see Chapter 6). This information can be compared and calibrated with borehole data in order to strengthen a predicted geological model; however, the low seismic vertical resolution at the depth of investigation (estimated to be between 157 and 260 m) and low image quality represent the main limitations of this analysis by not imaging, or poor imaging of, subtle faults.

In the study area, the ant-tracking attribute calculated from the Most Positive Curvature volume provided better results for fracture interpretation (Basir et al., 2013) and showed a relatively good correlation with borehole data. When applied to the three Mesozoic mapped surfaces, density of lineaments possibly associated to subtle faults is higher in the hinges of the three anticlines and in the areas adjacent to major faults, thus suggesting that structural position exerts a primary control on fracture distribution (Watkins et al., 2015; Watkins et al., 2018; Gosh and Mitra, 2009; Hanks et al., 1997; Nelson, 2001). In cross-sections, the correlation between the results of ant-tracking and

FMI logs, although variable in some intervals, can be considered as good. Furthermore, the analysis of depth slices showed, in general terms, a good correlation between the orientations of ant-tracking lineaments within the analysis window and the fracture orientations measured in FMI logs.

In summary, analysis of ant-tracking attribute showed the location of subtle faults and/or fractured zones in mapped surfaces and cross sections, which in general terms, have a good correlation with borehole data (see Chapter 6). This represents a positive indicator of intervals with good quality reservoir rock in the Mesozoic column and, therefore, reinforces the potential prospectivity of the study area, and of the structural traps in particular, for hydrocarbon exploration.

8.2.1.5 Geomechanical Modelling

This analysis predicts the strain distribution on mapped surfaces, which in turn, may be directly associated with higher fracture intensities in areas with greater deformation such as fold hinges and faults' damage zones (see Chapter 6); therefore, it can be considered as an indirect indicator of the possible presence of fractures. When combined with analysis of seismic attributes, it provides information about the influence that structural position exerts on fracture intensity through the correlation between the number of ant-tracking lineaments and the amount of strain in a specific location; however, limitations of this analysis include: 1) the horizontal resolution is not small enough to detect small-scale strain variations, 2) strain values are representative of a single vertical depth at every point of a surface and, 3) It is not possible to model areas with high lateral variations in rock properties, although sensitivity analyses can be performed. For the study area, sensitivity analysis was performed in order to compare the strain distribution of Late Kimmeridgian in Anticline C. Results showed some qualitative and quantitative differences between the two modelled scenarios using rock parameters from W-1 (shaly mudstone) and W-3 (dolomitized wackestone-packstone).

In the study area, the results obtained from this analysis (Chapter 6) show zones of higher strains are distributed predominantly on folded areas and adjacent to fault planes, following a similar pattern of the distribution of lineaments in the ant-tracking attribute, thus suggesting that structural position plays a primary role in fracture intensity (Figure 8.2). This is supported by fracture intensity values obtained from FMI logs, which are higher in anticline hinges than in the limbs for similar lithological facies. The correlation between these two independent analyses provides validation of the techniques to predict good quality fracture reservoir rock within structural traps.

8.2.1.6 Elastic Dislocation (ED) Modelling

This analysis provides a qualitative prediction of the orientation and the nature of sub-seismic fractures (normal, reverse or strike-slip) that are expected to be found at any given location, which are related to folding and movement on major fault planes as a result of different deformational events. Also, it provides the distribution of Maximum Coulomb Shear Stress (MCSS), which can be used as a proxy for fracture intensity, since this parameter cannot be calculated directly. As it happens with other types of modelling, there are some limitations that prevent this technique to reproduce accurately the fracturing of rock masses, since this is the result of a complex interaction of multiple factors through time. Some of these limitations include: presence of multiple deformational events (complex tectonic history), influence of fluid pore-pressure and rock anisotropy.

For the study area, results of ED modelling show a moderately strong, qualitative, correlation with borehole data, seismic attributes and geomechanical modelling for fracture orientation and intensity. The strength of correlation between modelled and borehole data seems to be inversely related to the complexity of the tectonic evolution of the modelled structural trap and the location of the borehole. The observed results show that the degree of correlation between modelled and borehole data is lower for anticline A, which has a more complex tectonic evolution than anticline B, where the degree of correlation is higher (see Chapter 7).

All the techniques and analyses outlined above provide useful insights about the relationships between different geological factors (texture, lithology, structural position, bed thickness) and natural fracturing, which can be combined in order to estimate fracture orientation and intensity at subsurface in undrilled areas. This estimation is, in turn, crucial to assess the quality of potential reservoir rocks at early stages of hydrocarbon exploration. The next sections explain and discuss the methodology for assessment of reservoir rock and how the results of the geological-geophysical analyses can be used.

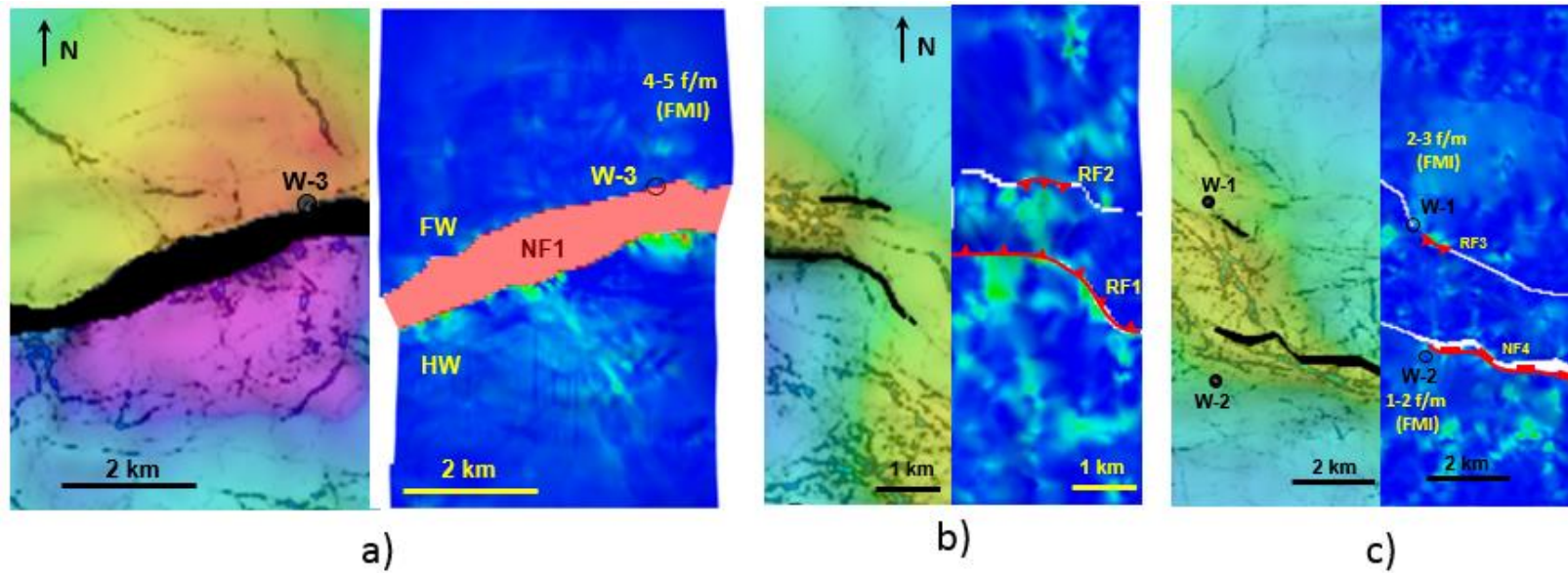


Figure 8.2: Comparison between strain distribution and ant-tracking lineaments applied to mapped surfaces. Areas with high strain correspond to areas with high density of lineaments probably associated to subtle faults, which may indicate that structural position exerts a primary control on natural fracturing. a) Anticline A, Late Cretaceous; b) Anticline C, Late Kimmeridgian; c) Anticline B, Late Kimmeridgian.

8.2.2 Methodology for assessment of reservoir rock

Current tendencies in hydrocarbon exploration are focused on plays where production relies greatly on fracture permeability; from these, tight carbonates with low-matrix permeability (<0.1 mD, Rashid et al., 2015; Nelson, 2001) and naturally-fractured contain large volumes of hydrocarbon reserves (Nelson, 2001; Akbar et al., 2000; Bourbiaux, 2010; Ahr, 2008), which makes necessary to predict more accurately the presence and characteristics of natural fracture sets at early stages of exploration. However, this remains a major challenge for the oil industry, due to the complex interaction of multiple factors that influence natural fracturing including the spatial variability of rock properties inherent to carbonates, and its correspondent sensitivity to diagenetic processes. Additionally, information about fracture characteristics and distribution at the subsurface is limited by spatially restricted and often non-representative volumes in borehole sampling (core samples, FMI logs) and, in the case of geophysical techniques, by limitations in resolution and their inherent ability to provide enough information about 3D geometry of fractures at subsurface. All these limitations result in simplified models with varying degrees of inaccuracy in their attempts to represent the true characteristics of fractures at subsurface.

The presence and characteristics of natural fracture sets are crucial in order to increase the quality of the reservoir rock, which is an element of the petroleum system that is assessed during the estimation of probability of geological success (PoS) of exploratory boreholes; therefore, availability of more complete information from fractures combined with a proper assessment methodology will allow a more efficient ranking of prospects and management of exploration portfolios and, consequently, redeem the high costs associated with hydrocarbon exploration and maximize the profits.

8.2.3 Estimation of probability of geological success (PoS)

In petroleum exploration, decisions about drilling are based upon the results of several subsurface studies as well as economic evaluations. The outcome of subsurface studies are commonly prospect inventories, which are ranked according to their prospective resources and the probability of making a discovery (PoS), or geological success (Milkov, 2015). From these two parameters, assessment of PoS is more challenging and critical in exploration, since there is no equation or method that can calculate it in a precise and accurate way (Rose, 1987). PoS can be considered simply as 1 minus risk (Schwade, 1967), which in turn, is an inherently subjective parameter in explorers' minds and is completely independent of the occurrence of hydrocarbon accumulations.

The oil industry requires that explorers can identify and differentiate low-risk prospects from high-risk prospects by assigning PoS values to those prospects. To achieve this, these values should be based on scientific methods applied to available datasets, expertise and deliberation. Nowadays, the most common way to obtain PoS for any given prospect is by serially multiplying the probabilities of each independent risk factor (trap, seal, reservoir, etc) (Gotautas, 1963; Rose, 2001; Rezic and Veranina, 2017; Salleh et al., 2007); however, this method is limited by the following issues: 1) the correct identification of the truly independent risk factors and, 2) the subjectivity when calculating the probability of risk factors, since this can vary from one person to other depending mainly on their level of expertise and biased judgement. Milkov (2015) summarizes several common biases when estimating values of PoS: overestimation of the probability of the events; tendency to interpret the data in order to fit the results to the dominant expertise and knowledge (Bond et al., 2007); interpret the information to confirm preconceptions and hypothesis, independently of the truth (Oswald and Grosjean, 2004); underestimation of high values and overestimation of low ones (Fischhoff et al., 1977); to overestimate favourable or pleasing results (Baron, 2007) and, excessive subjective confidence in judgement (Hoffrage, 2004). Milkov (2015) also proposes risk tables in order to assess more effectively each risk factor by reducing the bias and subjectivity thus increasing the consistency of PoS assessment by different exploration teams. In these tables, PoS is primarily dependent on the amount and closeness of borehole data. Although these risk tables reduce substantially the subjectivity of PoS estimations, it cannot be removed completely.

This section addresses the second aim of this chapter, which is to improve the assessment of the presence and quality of the reservoir rock element by including additional sub-elements derived from the different analyses described in the previous section. The methodology proposed in this work is based on the Format for Registration and Assessment of Exploratory Opportunities (CEROE for its acronym in Spanish) method, which is used institutionally in PEMEX E&P and is based on models proposed by Rose (2001); Johns et al. (1998) and Gotautas (1963). In this method, the probability of geological success (the chance to find an economic hydrocarbon accumulation, PoS, is calculated by multiplying the values obtained from each of the five elements of the Petroleum systems that are assessed individually, which are considered to be independent (trap, seal, reservoir rock, source rock and synchrony/migration). Each element, in turn, comprises sub-elements that are assessed according to criteria such as amount, quality and confidence on available data; commonly, the lowest value of the sub-elements is assigned as the value of each element. Assigned values represent the level of confidence in the data and vary from 0.1 (including no data available) to 1.0. PoS values range from 0 to 1.0 and can be expressed as percentages if multiplied by 100.

Usually, PoS values between 0.25 – 0.30 (25-30%) are considered the minimum cut-off values in order to consider a proposal with good chances to be successful. Table 8.1 illustrates this methodology; in this example, a final PoS value of 0.25 (25%) was obtained by multiplying the values of each element (orange cells) of the petroleum system.

Table 8.2 shows the proposed improved assessment format, which will be used to assess the reservoir rock element in a well proposal within the study area. Here, the element reservoir rock is subdivided into two main sub-elements, Presence and Quality; unlike the traditional assessment method (Table 8.1), Quality is subdivided into 6 different categories, which in turn, can contain one or more sub-components to be evaluated. When a category has more than one sub-component, each of these is weighted according to their relevance within that category. Values for each sub-component result from multiplying the assigned value V (based on amount and quality of available data, analysis results, etc.) by its correspondent weight. Then, the values of all the sub-components are added in order to obtain the final value for their category. Finally, the values of all the categories are averaged in order to obtain the value for the sub-element Quality of reservoir rock which, along with the value obtained for Presence of reservoir rock, will be used for the assessment of a given prospect. For parameters such as amount and quality of data, level of confidence on data and rock quality, values from 0 to 0.4 are considered as low/poor, 0.5 to 0.7 as regular/moderate and 0.8 to 1.0 as high/good. The main limitation derived from using this system of values is the high degree of subjectivity inherent to the assigning of values, since they do not specify guidelines and do not contain geological information, which leaves significant uncertainty and also may cause that different values can be assigned to the same data by different exploration teams (White, 1993; Watson, 1998).

On the other hand, this improved assessment provides several elements in order to describe in a more detailed way the characteristics of the reservoir rock based on the results of the different analyses included in the proposed methodology, which is not the case of the traditional assessment method. Also, by including numerous sub-elements, the final values of both Presence and Quality of reservoir rock are not dependent of a single criteria, since the presence of natural fracture sets results from the interaction of different geological controls; so, if one sub-element has a low value, its impact on the final value will be minimum.

Well name		
Probability of geological success (Pg)		Play fractured carbonates (Late Cretaceous)
Trap	Value	0.7
Presence / Characteristics	0.8	
Mapping confidence and data control	0.7	
P90 area (km2)	3	
Seal		0.7
Upper seal	0.8	
Lateral seal / Fault	0.7	
Base seal / Other	0.8	
P90 area (km2)	3.0	
Reservoir rock		0.8
Presence	0.9	
Characteristics of the porous system	0.8	
P90 Net thickness (m)	50	
Source Rock		0.8
Capacity of Initial Charge	0.8	
Maturity of source rock	0.9	
Synchrony and Migration		0.8
Synchrony	0.9	
Migration pathways	0.8	
Preservation	0.8	
Probability of geological success		0.25

Table 8.1. Example of a CEROE format used to calculate the probability of geological success of an exploratory well proposal.

Well Name			
Reservoir rock	Play: fractured carbonates		
Presence		Weighing (%)	0
Correlation with borehole data		30	
Regional geology analysis		25	
Confidence on mapping		25	
Seismic facies analysis		20	
Quality			
Seismic interpretation			0.0
Trap geometry		50	
Proximity to faults		50	
2D/3D Restoration			0
Deformational events		100	
Borehole data			0.0
Texture		20	
Lithology		15	
Diagenetic evolution		35	
Bed thickness		5	
Fracture intensity and orientations (FMI)		25	
Structural seismic attributes			0.0
Quality of seismic data input		30	
Borehole calibration		40	
Attribute analysis (ant-tracking)		30	
Geomechanical modelling			0.0
Strain maps		100	
Fracture modelling			0.0
MCSS (proxy for density)		40	
Fracture connectivity		60	
Reservoir rock			0.0

	Amount of data	Quality of data	Confidence level	Reservoir rock quality
0 - 0.4	Scarce	Low	Low	Poor
0.5 - 0.7	Regular	Moderate	Moderate	Regular
0.8 - 1.0	Abundant	High	High	Good

The amount of available correlation boreholes is essential for a more confident definition of the presence of reservoir rock
Regional geology constitutes a first-order approach to define the presence of reservoir rock
This refers to the confidence on the representation of the areal distribution of the potential reservoir rock within an specific are
This analysis provides an indirect prognosis about the lithological characteristics of the potential reservoir rock

This parameter refers to the amount of folding of the trap.
Closeness to faults increase the probability of a borehole to intersect fracture sets.

The number of deformational events that formed and/or re-deformed the trap

Texture is a primary control on fracture development
Lithology is a secondary factor on fracture development
Availability of diagenetic studies is crucial to understand the evolution of the reservoir rock characteristics through time
Bed thickness is a secondary factor on fracture development. Thin beds are more prone to fracture than thick beds
Availability of this information is essential to calibrate seismic attributes as well as for correlation

This parameter is essential in order to obtain reliable information from structural seismic attributes
Availability of boreholes is crucial for calibration of seismic attributes
This analysis provides information about the location and orientation of possible subtle faults and fracture zones

Provide the distribution of areas where intensity of strain is related to folding, and the probability of fracture generation is higher

This parameter can be interpreted as an indirect indicator of relative fracture density
This analysis provides the orientations of predicted fracture sets, which may have and impact on their connectivity and therefore, on the quality of the reservoir rock.

Table 8.2. Proposed format for assessment of reservoir rock, where the main elements, Presence and Quality, are subdivided into different categories and sub-elements. Numerical values are assigned according to the amount, type, quality and level of confidence of data (top right).

8.3 Methodology Test

In order to test its validity as a predictive tool, the proposed workflow is applied to the well location W-4, which was specifically proposed for this work within the study area; then, assessment of the presence and quality of the reservoir rock will be carried out by using the proposed format shown in Table 8.2. Finally, the results are compared with the information from the nearby well W-5, which was not used neither for PSDM processing nor for seismic mapping. W-4 is located in the north-western flank of Anticline C, whose geometry makes it a highly prospective structural trap for hydrocarbon exploration (Figure 8.3). Values assigned to the different categories corresponding to the sub-elements Presence and Quality are mostly conservative rather than overoptimistic in order to get a final minimum value, which can be considered as a “base” to have in mind when assessing the reservoir rock element along with other elements of the petroleum system where Plays are associated to fractured reservoirs.

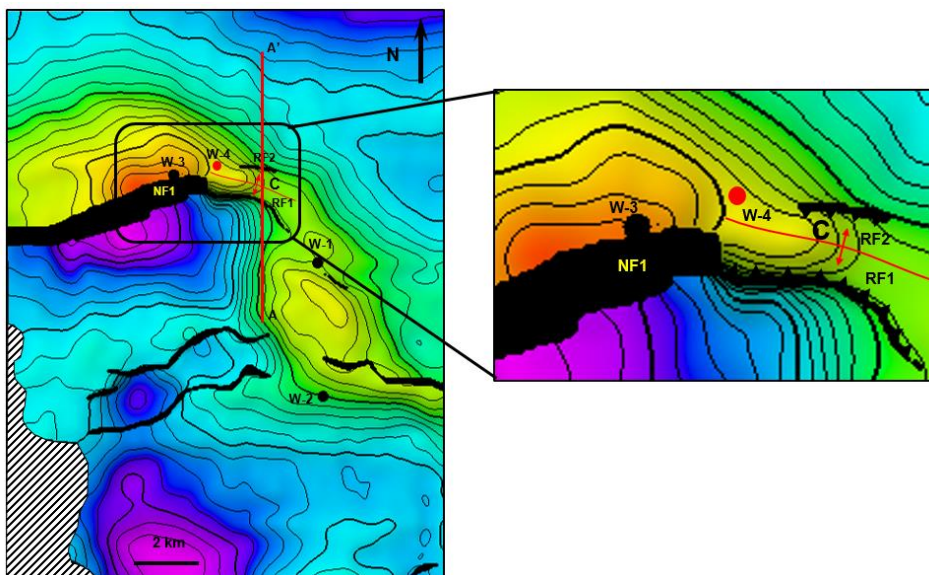


Figure 8.3. Location of borehole W-4 within the study area. Top Kimmeridgian structure map. RF1= reverse fault 1, NF1= normal fault 1. Section A-A' is shown in Figure 3.

Anticline C

This anticline offers the opportunity to test the proposed methodology due to its relative geometric simplicity, closeness to boreholes, and because no boreholes drilled on it were available for this study, which allowed the chance to propose a blind well. This structure is a salt-cored pop-up anticline oriented WNW-ESE characterized by buckle folding and bounded by high-angle reverse faults RF1 and RF2 oriented WNW-ESE and NW-SE, respectively (Figure 8.4). No strike-slip component seemed to affect these faults since they are not connected to the Pliocene-aged trans-tensional fault system; however RF2

is conceptualized as a listric normal reactivated as a reverse by the contractional deformational events during Cenozoic times. For practical purposes, this fault is modelled as a result of a single contractional event.

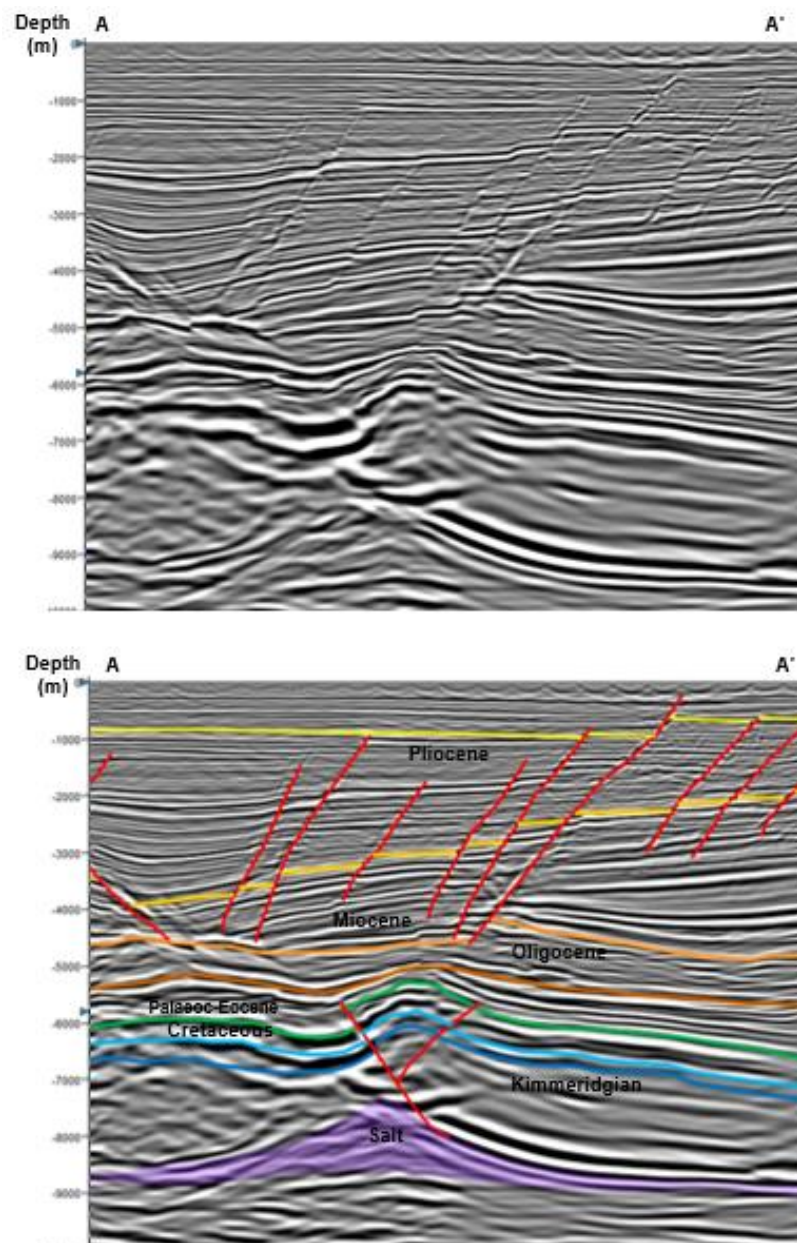


Figure 8.4. Uninterpreted and interpreted cross-section A-A' from Figure 2 showing the pop-up geometry of Anticline C.

Maximum vertical displacement on reverse fault RF1 is located close to the western edge of the fault (700 m) and diminishes laterally towards the eastern edge, which may be related to the amount of salt coring the structure as well as to the orientation of the structure relative to the direction of the principal compressive stress. For fault RF2, the maximum vertical displacement is 150 m and is located at the centre of the fault plane and diminishes gradually towards the edges.

No information from boreholes drilled on this structure were available for this work, so values of Young's modulus, Poisson's ratio and rock density from nearby boreholes W-1 and W-3 were used to model two different scenarios for Top Cretaceous and Top Kimmeridgian targets (Table 8.3). Also, values of 0.6 and 20 MPa were used for coefficient of internal friction (μ) and cohesive strength, respectively.

	Young's Modulus (Gpa)		Poisson's Ratio		Coefficient of internal friction (μ)	Cohesive strength (Mpa)	Density (kg/m3)
	W-3	W-1	W-3	W-1			
Top Cretaceous	51	38	0.31	0.31	0.6	20	2700
Top Kimmeridgian	36	69	0.15	0.3	0.6	20	2700

Table 8.3. Geomechanical parameters used for fracture modelling of borehole W-4.

8.3.1 Assessment of reservoir rock

Table 8.4 summarizes the results obtained from the assessment of the presence and quality of reservoir rock from Mesozoic targets of W-4 prospect. The assignment of values for sub-components entailed a degree of inherent subjectivity, so it was decided to follow a conservative approach by selecting the lowest values within a limited range when the available data and/or the results from the different analysis allowed the assignment of higher values that could be considered equally valid. This approach also allows the explorers to consider the obtained results as a "probable minimum", which may not be a definitive value, but it may serve as a reference for further assessments.

8.3.1.1 Presence of reservoir rock

Presence of reservoir rock is assessed by considering elements such as: amount of correlation boreholes, analysis of regional geology, confidence on seismic-based mapping and seismic facies analysis; from these, only the latter was not performed for this study.

- Due to the fact that nearby boreholes W-1 and W-3 found hydrocarbon accumulations in Late Cretaceous and Late Kimmeridgian intervals, the probability of the presence of potential reservoir rocks in W-4 is high, so a value of 0.8 was assigned to both plays.

Name: W-4							
Reservoir rock	Play fractured carbonates (Late Cretaceous)			Play fractured carbonates (Late Kimmeridgian)			Observations
	Value	Weighing (%)	0.7	Value	Weighing (%)	0.7	
Correlation with borehole data	0.8	35		0.8	35		- Abundant information from three nearby boreholes was available for correlation
Regional geology analysis	0.7	25		0.8	25		- Regional lithofacies maps propose the presence of carbonate rocks within the study area at stratigraphic levels of economic importance
Confidence on mapping	0.8	25		0.7	25		- Nearby boreholes provided a good degree of correlation in the area around the proposed well
Seismic facies analysis	0	15		0	15		- This analysis was not carried out for this work.
Quality			0.6			0.7	
Seismic interpretation			0.7			0.7	
Trap geometry	0.6	50		0.6	50		- The anticline shows a shortening of approximately 3% in the area of the proposed well
Proximity to faults	0.7	50		0.7	50		- The proposed well is located relatively close to major faults and subtle faults interpreted from seismic attributes
2D/3D Restoration			0.8			0.8	
Deformational events	0.8	100		0.8	100		- Three deformational events (D1-D3) may have been involved in fracture generation
Borehole data			0.6			0.7	
Texture	0.8	20		0.8	20		- For Late Cretaceous, textures are likely to be deep marine, mud-supported. For Late Kimmeridgian, textures may be either inner platform, grain-supported or outer platform, mud-supported
Lithology	0.6	15		0.7	15		- For Late Cretaceous, predicted lithology consists of marls and shaly mudstone - For Late Kimmeridgian, two possible scenarios are predicted: 1) dolomitized wackestone-packstone and, 2) Shaly mudstone interbedded with dolomitized wackestone
Diagenetic evolution	0.6	30		0.7	30		- Diagenetic events were dated in a relative way; however, these events suggest that diagenesis played a positive role in fracture development in Late Cretaceous and Late Kimmeridgian
Bed thickness	0.6	10		0.7	10		- Bed thickness is expected to be generally well developed in both Late Cretaceous and Late Kimmeridgian intervals
Fracture intensity and orientations (FMI)	0.5	25		0.8	25		- For Late Cretaceous, fracture intensity from FMI are relatively low - For Late Kimmeridgian, fracture intensity from FMI are moderate to relatively high with several orientations
Structural seismic attributes			0.7			0.6	
Quality of seismic data input	0.6	30		0.6	30		- Seismic resolution is low and imaging quality is regular to good at the depth of study in the area around the proposed well
Borehole calibration	0.8	30		0.8	30		- Calibration of borehole information with seismic attributes provided a regular to good degree of correlation
Structural attributes analysis	0.7	40		0.5	40		- For Late Cretaceous, the probabilities of crossing possible fractured zones are moderate to good - For Late Kimmeridgian, the probabilities of crossing fractured zones are moderate
Geomechanical modelling			0.5			0.5	
Strain maps	0.5	100		0.5	100		- Although the proposal is located in a favourable structural position close to the anticline's crest, strains are low in both targets
Fracture modelling			0.6			0.6	
MCSS (proxy for density)	0.6	40		0.7	40		- Relatively high values of MCSS
Fracture connectivity	0.6	60		0.6	60		- Two different trends of fracture orientations are predicted, which may provide a moderate fracture connectivity.
Reservoir rock			0.6			0.7	

	Amount of data	Quality of data	Confidence level	Reservoir rock quality
0 - 0.4	Scarce	Low	Low	Poor
0.5 - 0.7	Regular	Moderate	Moderate	Regular
0.8 - 1.0	Abundant	High	High	Good

Table 8.4. Assessment of the presence and quality of reservoir rock in the proposed borehole W-4 for Late Cretaceous and Late Kimmeridgian targets. Calculated values of 0.7 indicate a moderate/regular probability of finding a potential reservoir rock, which in turn, is more likely to be of a regular quality.

- Regional lithofacies maps (Figure 8.5) propose the presence of mudstone-wackestone and marls for the uppermost sections of Late Kimmeridgian and Late Cretaceous, respectively, so that values of 0.8 and 0.6 were assigned to these plays.

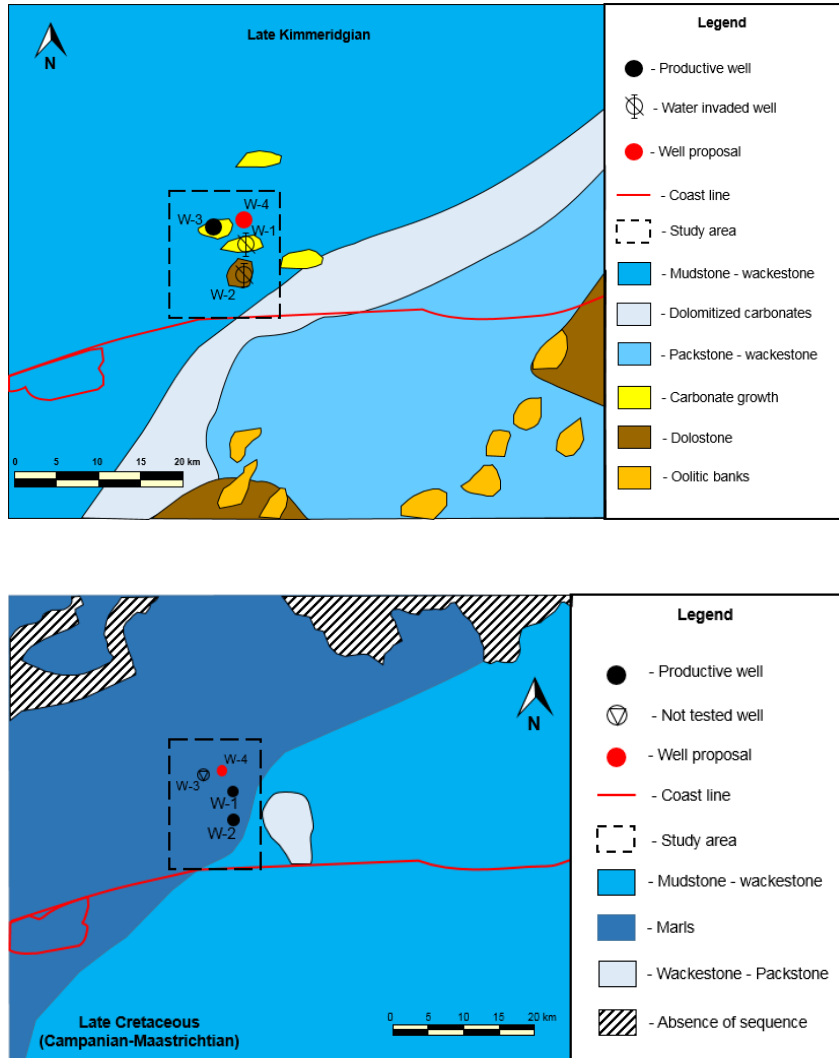


Figure 8.5. Regional maps illustrating the distribution of lithofacies for Late Kimmeridgian (top) and Late Cretaceous (bottom). Modified from PEMEX (2015).

- Proximity of boreholes W-1 and W-3 to W-4 allowed a good seismic correlation and, therefore, provides a good degree of confidence on mapping of the target surfaces, so values of 0.8 and 0.7 were assigned to Late Cretaceous and Late Kimmeridgian, respectively.

Based on the available information, values of 0.7 were calculated for presence of reservoir rock in both Top Cretaceous and Top Kimmeridgian targets respectively, which represents a moderate-to-good probability.

8.3.1.2 Quality of reservoir rock

Quality of reservoir rock section was subdivided into the following six categories for its assessment, which in turn, contained different elements:

- 1) **Seismic interpretation:** This category includes the information obtained from seismic interpretation that can be related to reservoir rock quality. Anticline C is a structural trap with dip closure on its eastern flank and closure against reverse faults on northern and southern flanks. The fold type can be considered as a detachment fold and the folding style corresponds to buckle folding, whose deformation could have been accommodated also by faulting and fracturing of the carbonate sequence (Figure 8.6). Also, the proposed well is relatively close to the tips of major faults (480 m from NF1 and 780 m from RF2 for Late Kimmeridgian and 330 m from NF1 and 900 m from RF2 for Late Cretaceous), around which high stresses tend to concentrate. Based on this, a value of 0.7 was calculated for this category, which is considered as moderate.

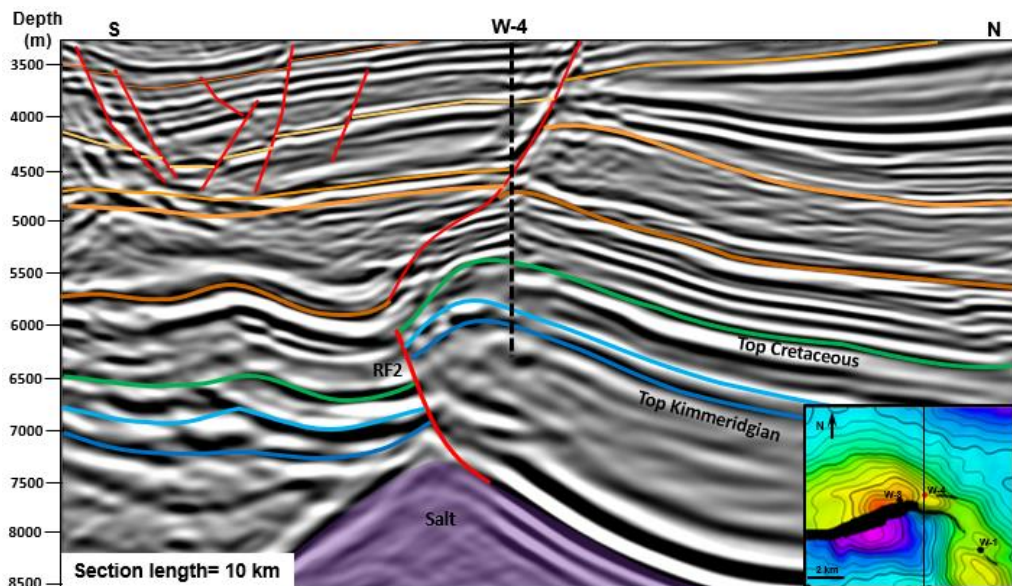


Figure 8.6. Seismic cross-section across the proposed W-4 well illustrating its folding style. Top Kimmeridgian structure map.

- 2) **2D restoration:** This analysis (see Chapter 4, section 4.4.1.3) suggests that contractional events D2/D3 may have produced fold-related fracturing that post-date possible pre-existent fracture sets which resulted from mostly vertical lithostatic load, thus increasing the possibility of more connectivity between fracture sets. Estimation of maximum shortening perpendicular to the anticline's strike is around 5-6%, which produced buckle folding and probably may have induced enough strain to produce natural fracturing on Mesozoic carbonate rocks; however, shortening diminishes towards the flanks of the anticline, so in the proposed well area shortening is around 2-3% only. Based on this information, a value of 0.8 was assigned, which is considered as good.

3) **Borehole data:** Availability of nearby borehole data offered the possibility of predict with more confidence the presence of fracture controls such as texture, lithology and bed thickness as well as to estimate their effects on the potential reservoir rock in the proposed well. For Late Cretaceous, the lowest assigned value (0.5) corresponds to fracture intensity from FMI logs whereas the highest value (0.8) corresponds to texture. For Late Kimmeridgian, the lowest value (0.7) corresponds to diagenetic evolution, lithology and bed thickness, whereas the highest value (0.8) corresponds to texture and fracture intensity from FMI logs. Calculated values for this category are 0.6 for Late Cretaceous and 0.7 for Late Kimmeridgian, which can be considered as moderate.

4) **Structural seismic attributes:** Given the utility of applying multi-attribute ant-tracking analysis for fault/fracture detection (Basir et al., 2013; Khair et al., 2012), ant-tracking attributes extracted from Variance, Most Positive Curvature and Most Extreme Curvature volumes were applied and compared in depth slices located close to the top of the mapped targets as well as in cross-sections. For Late Cretaceous target, the proposed well W-4 intersects lineaments that could be related to fractured zones or subtle faults in the curvature/variance analysis, which are oriented E-W and WNW-ESE (Figure 8.7); a similar lineament intersecting W-4 was interpreted in the curvature/variance analysis applied to the mapped surface (Figure 8.9). Furthermore, analysis of cross-sections shows that almost the entirety of the Cretaceous interval is intersected by more lineaments (Figure 8.11), which suggests that not only the Late Cretaceous interval may represent a potential target but also Middle and Early Cretaceous can be considered as potential fractured reservoirs.

For the Late Kimmeridgian target, low vertical resolution (150 m and dominant frequencies of 9 Hz) and regular seismic imaging affect negatively the response of the attributes and therefore, hinders interpretation. Analysis of depth slices close to the top surface (Figure 8.8) shows lineaments oriented WNW-ESE, similarly to Late Cretaceous, inside the window around W-4, which has a length of 250 m per side. The curvature/variance analysis also shows that W-4 is located very close to possible subtle faults (Figure 8.10). In cross-sections, few lineaments intersect the well trajectory; however, a strong north-dipping lineament, which may be associated to a subtle fault, is closely located to W-4 (Figure 8.11). Based on these considerations, values of 0.7 and 0.6 were assigned to this category for Late Cretaceous and Late Kimmeridgian targets, respectively.

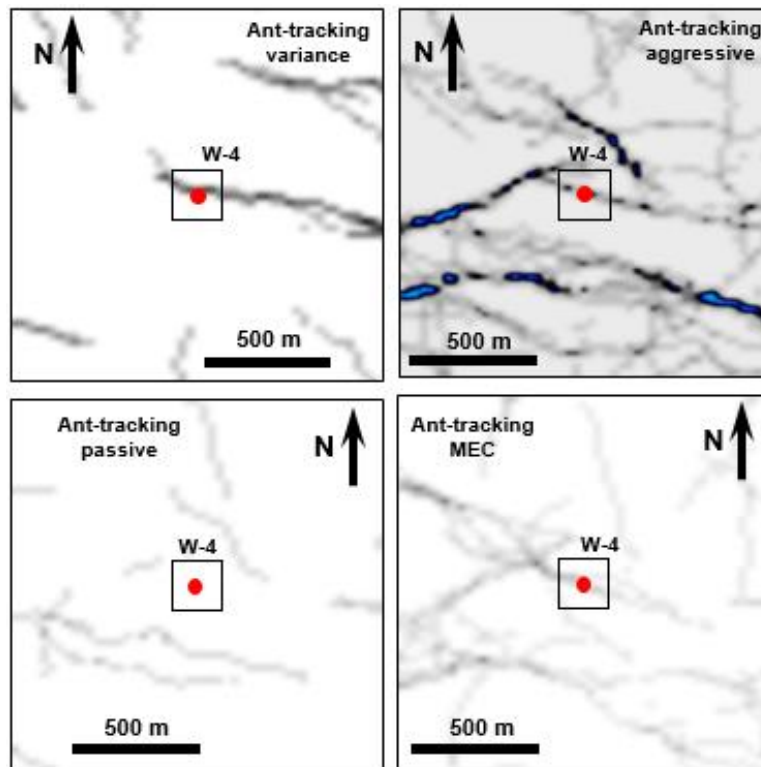


Figure 8.7. Depth slice at 5400 m showing the distribution of lineaments around borehole W-4 for Late Cretaceous target. Ant-tracking attributes are calculated from Most Positive Curvature, except bottom-right (Most Extreme Curvature).

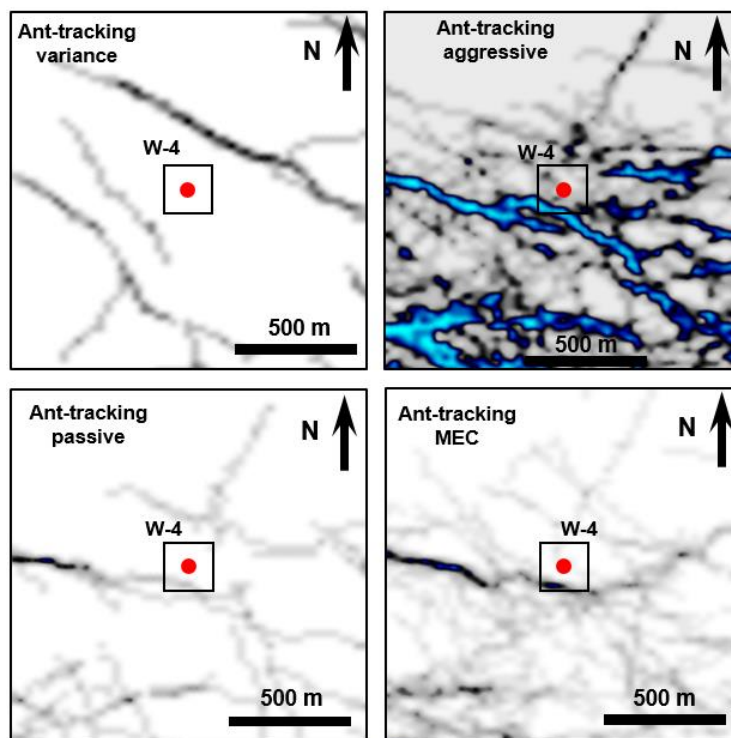


Figure 8.8. Depth slice at 6100 m showing the distribution of lineaments around borehole W-4 for Late Kimmeridgian target. Ant-tracking attributes are calculated from Most Positive Curvature, except bottom-right (Most Extreme Curvature).

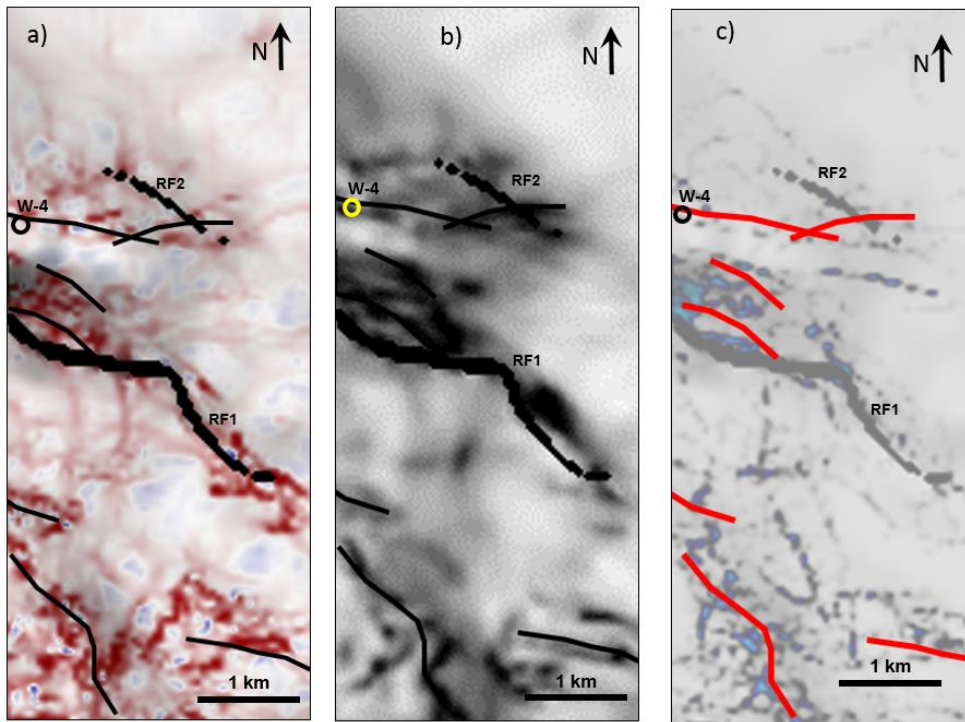


Figure 8.9. Top Cretaceous surface with different attributes applied. A) Most negative curvature, b) variance and, c) Ant-tracking from Most Positive Curvature. Interpreted lineaments represent subtle faults, one of which intersects the proposed borehole W-4.

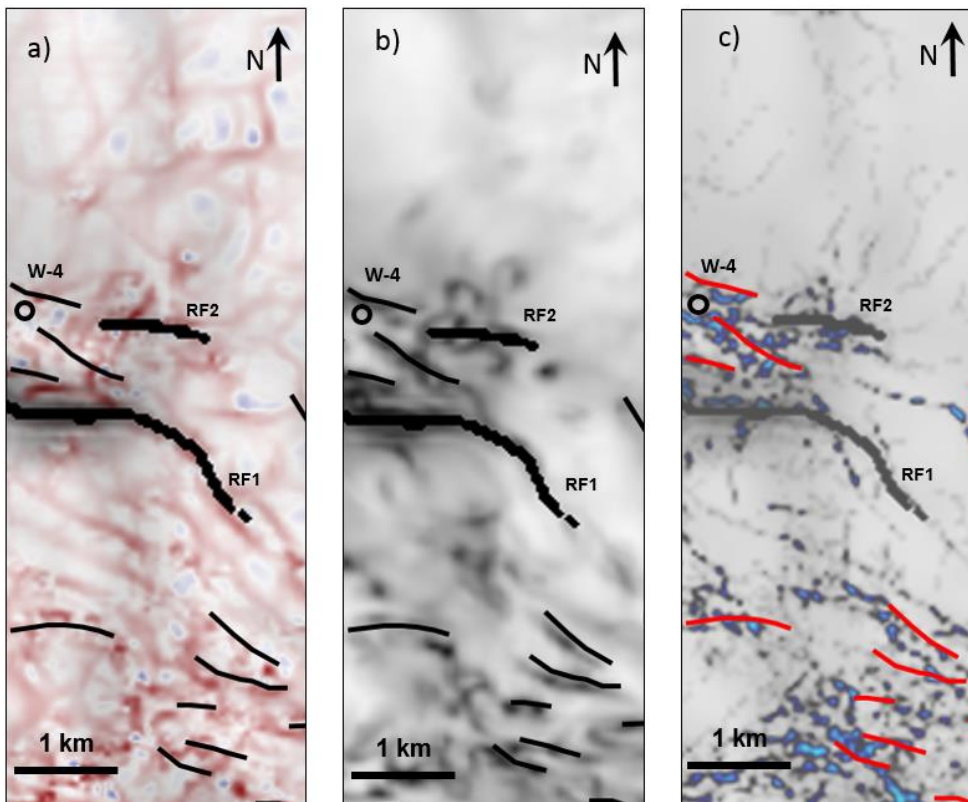


Figure 8.10. Top Kimmeridgian surface with different attributes applied. A) Most negative curvature, b) variance and, c) Ant-tracking from Most Positive Curvature. Interpreted lineaments represent subtle faults, which were calibrated with the amplitude volume.

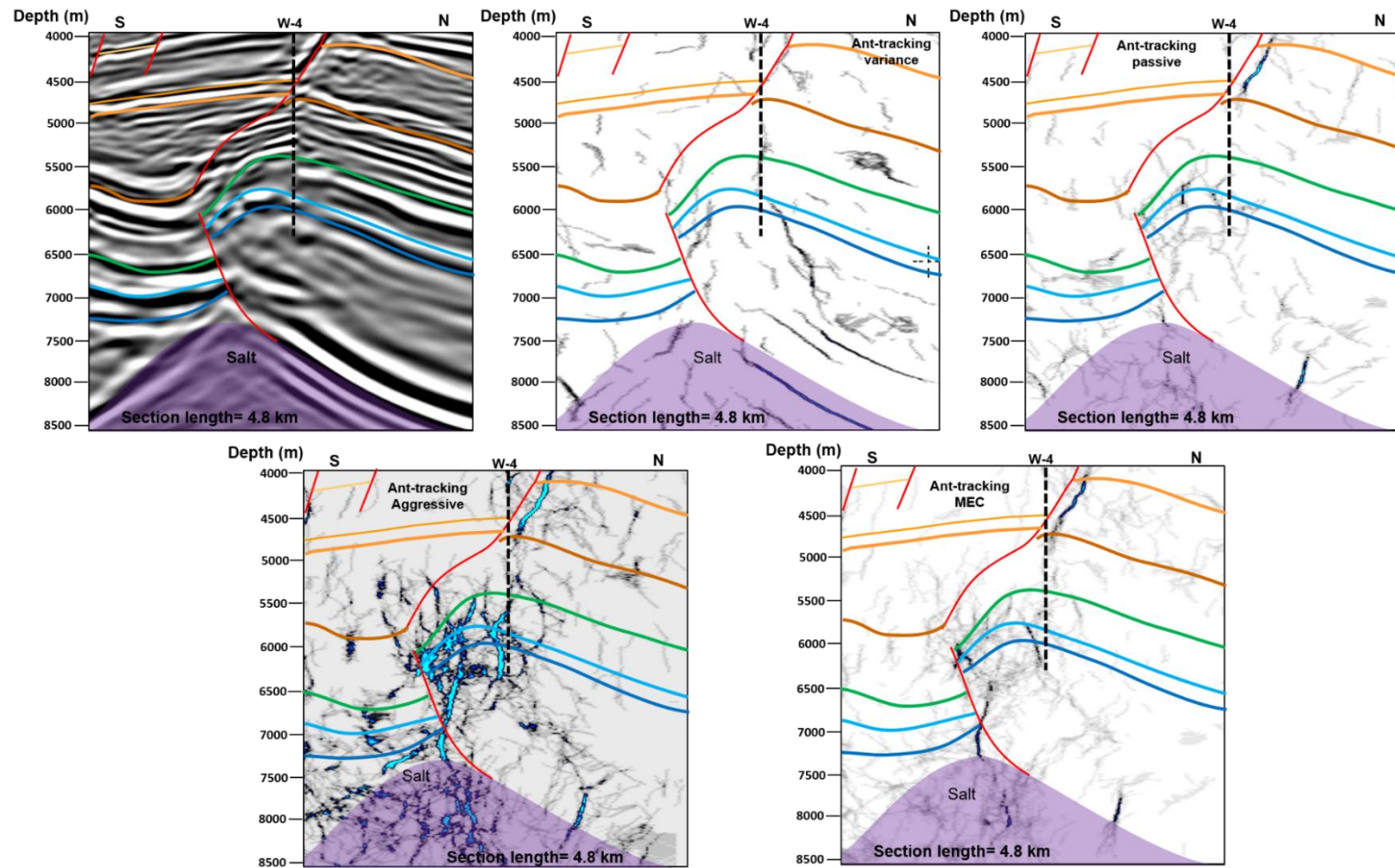


Figure 8.11. Cross-sections showing the distribution of lineaments around borehole W-4 in the Mesozoic section. The Cretaceous section has more lineaments intersecting the borehole's proposed trajectory.

5) **Geomechanical modelling:** The proposed well is located in a favourable structural position close to the anticline's crest; however, mapped strains are low in both targets (Figure 8.12), probably due to the relatively low curvature in a parallel direction to the anticline's axis. A value of 0.5 was assigned to this category, which can be considered as moderate to low.

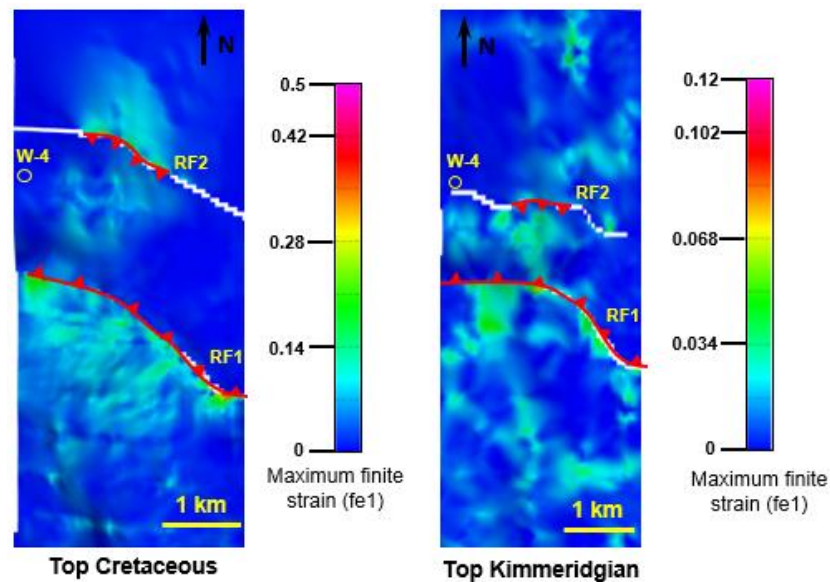


Figure 8.12. Distribution of strain around the proposed borehole W-4.

6) **Fracture modelling:** Distribution of Maximum Coulomb Shear Stress (MCSS) shows that the proposed borehole W-4 is located in an area of relatively high values of MCSS, although the absolute values for Late Kimmeridgian are higher than the values observed in Late Cretaceous (Figures 13-14). Two scenarios for each target were tested using different geomechanical parameters (Young's modulus and Poisson's ratio) from nearby boreholes W-1 and W-3. From these, the scenarios using parameters from W-3 shows higher values of MCSS than the W-1 scenarios for both targets. Based on this, values of 0.6 and 0.7 were assigned to Late Cretaceous and Late Kimmeridgian, respectively.

Predicted orientations of reverse-shear fracture sets within a 500 m per-side square centred in borehole W-4 were plotted in rose diagrams for both targets (Figures 15-16); these predicted sets are oriented WNW-ESE, ESE-WNW and NW-SE 25-30° and are very similar in both targets, which may provide a moderate degree of fracture connectivity. Similar results were obtained in the other anticlines within the study area, where a similar number of predicted orientations matched borehole data and production tests were performed in some of those intervals confirming the existence of good fracture connectivity. Based on this, values of 0.6 were assigned to both Late Cretaceous and Late Kimmeridgian targets.

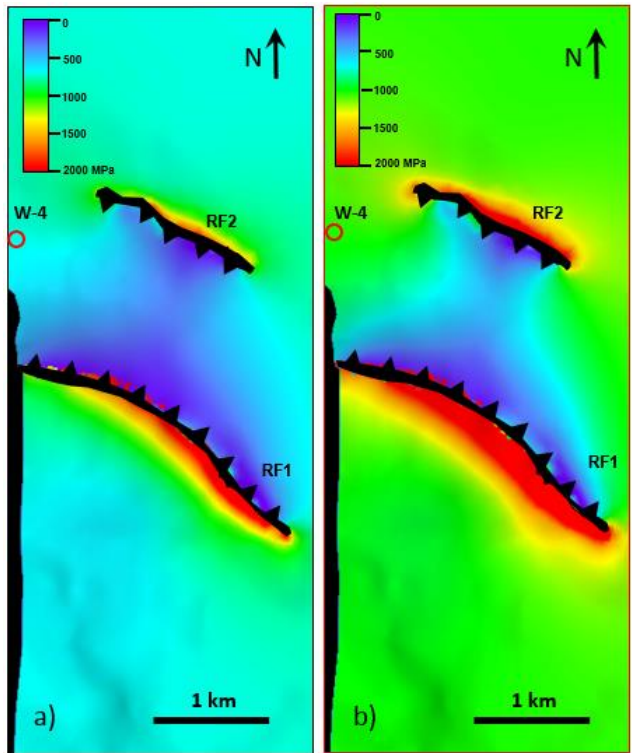


Figure 8.13. Distribution of MCSS in Top Cretaceous surface calculated with geomechanical parameters from W-1 (left) and W-3 (right).

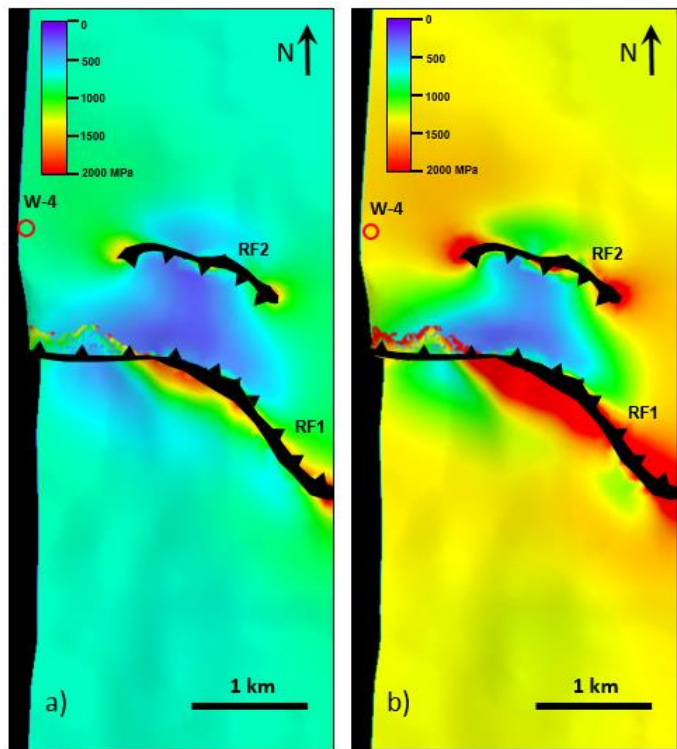


Figure 8.14. Distribution of MCSS in Top Kimmeridgian surface calculated with geomechanical parameters from W-1 (left) and W-3 (right).

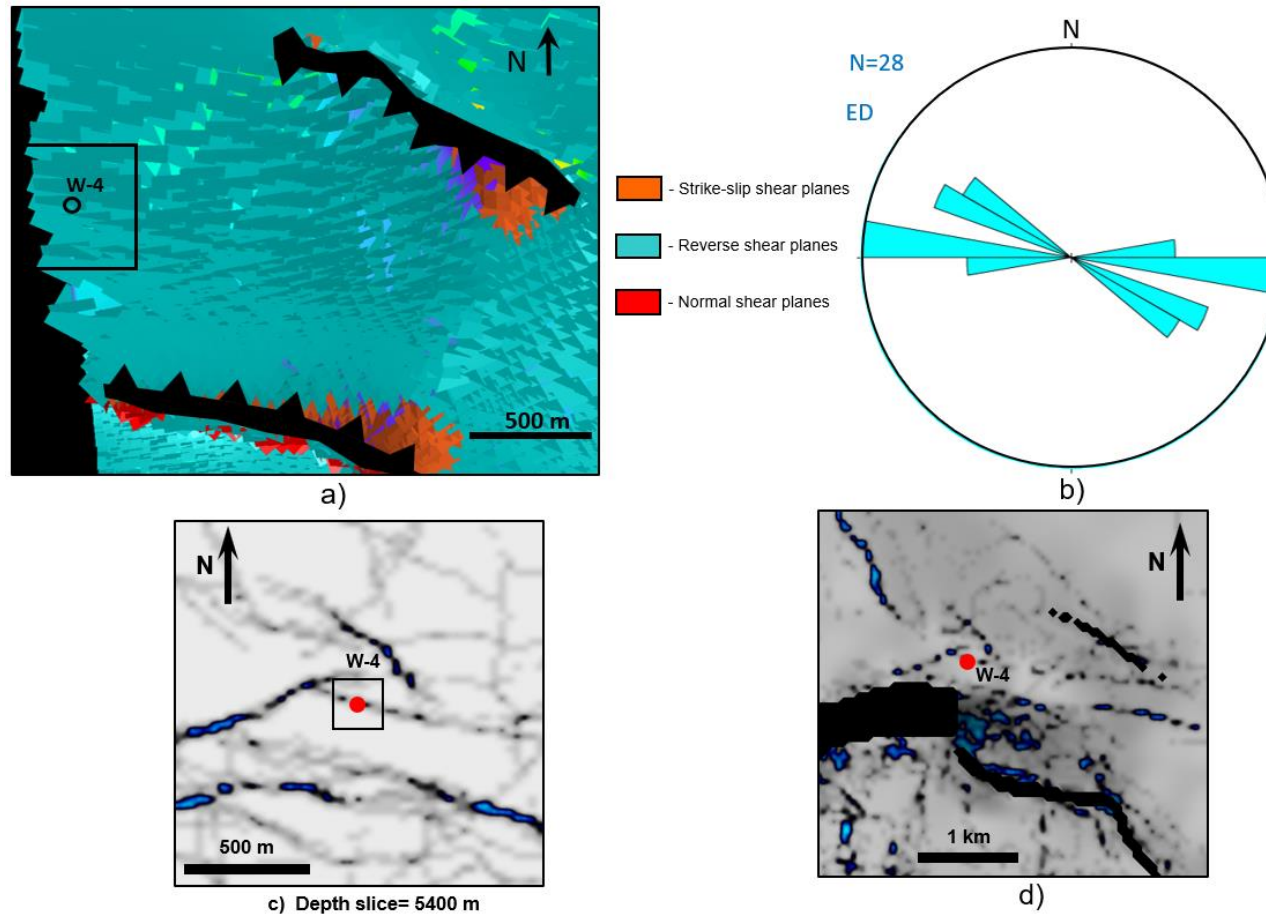


Figure 8.15. a) Predicted fractures around proposed borehole W-4; b) rose diagram showing the predicted orientations of fractures inside the square window around W-4; bottom: c) Depth slice= 5400 m and, d) Top Cretaceous surface with ant-tracking attribute showing the lineaments around W-4.

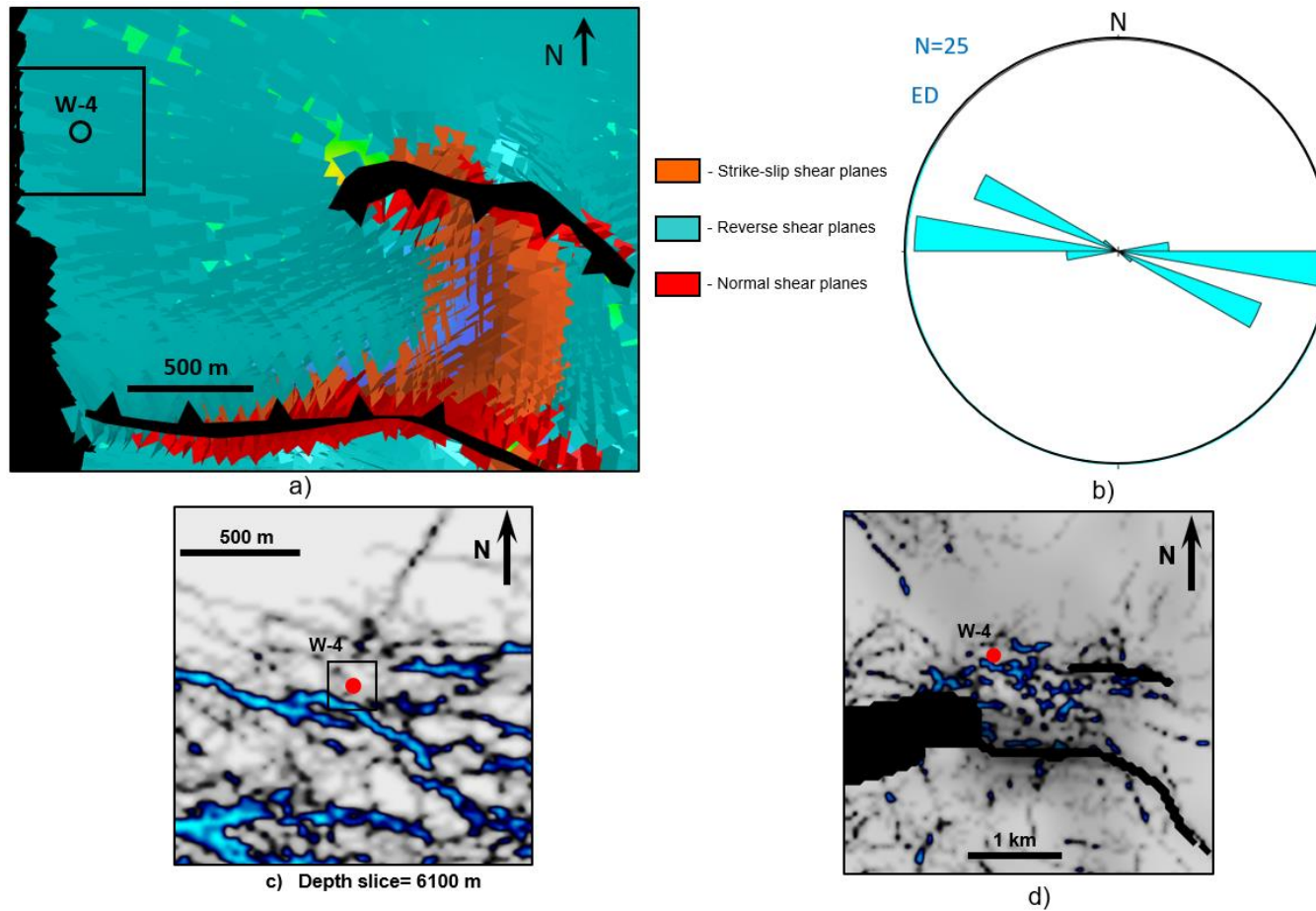


Figure 8.16. a) Predicted fractures around proposed borehole W-4; b) rose diagram showing the predicted orientations of fractures inside the square window around W-4; c) Depth slice and, d) Top Kimmeridgian surface with ant-tracking attribute showing the lineaments around W-4.

8.3.2 Comparison with borehole data

The proposed borehole W-4 is located 240 m to the SW of the well-head of borehole W-5, which is a blind well and was not used neither for PSDM processing nor for mapping of the Mesozoic surfaces (Figure 8.17). Information available from this borehole is fragmentary and included only formation tops, trajectory survey and results of a production test; no information from well logs, lithology or fractures was available for this study. This represented a unique opportunity to test not only the workflow for fracture prediction but also the proposed methodology for assessment of reservoir rock.

Both wells are located in the hinge of anticline C, which is traditionally an area where boreholes are placed in structural traps. The seismic cross-section shown in Figure 8.18 illustrates the closeness between the two wells; the section is oriented parallel to the trajectory of deviated well W-5 and also intersects the proposed well W-4. There is a remarkable difference between the depth of the Mesozoic picks from W-5 and the mapped Mesozoic picks from W-4. This discrepancy may be due to the following reasons: borehole W-5 was not included in the velocity model during PSDM processing, low seismic resolution may prevent an accurate imaging of subtle faults, which affects the accuracy of mapping by not detecting the fault throws.

A production test was performed in the blind well W-5 in the interval 5819-5893 md, which resulted in oil and gas production from Top Kimmeridgian. No information about lithology of the tested interval was available; however, correlation with nearby borehole W-3 suggests that partially dolomitized, intraclastic wackestone-packstone interbedded with oolitic packstone-grainstone may constitute the reservoir rock in W-5 (Figure 8.19). Figure 8.20 illustrate the response of different ant-tracking attributes at the depth of the production test; the curvature-based attributes show lineaments with different orientations intersecting W-5 well's trajectory, which in turn, intersects W-4 at 5850 m. In the other hand, the variance-based attribute is the only one that does not show any lineaments intersecting any of the two wells. The combined results of the production test and the ant-tracking response suggest that natural fracturing may provide enough reservoir porosity and permeability.

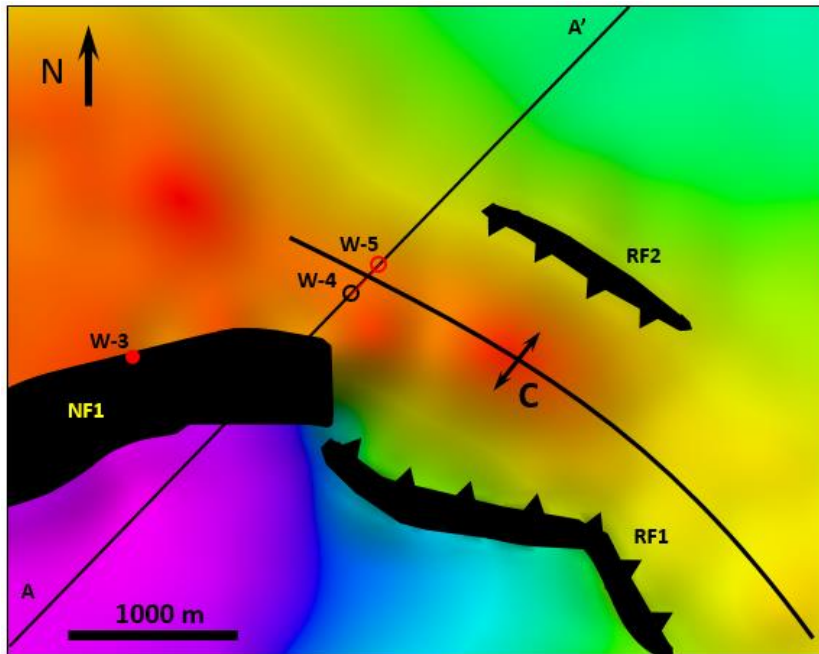


Figure 8.17. Top Cretaceous map showing the location of boreholes W-4 and W-5 in anticline C.

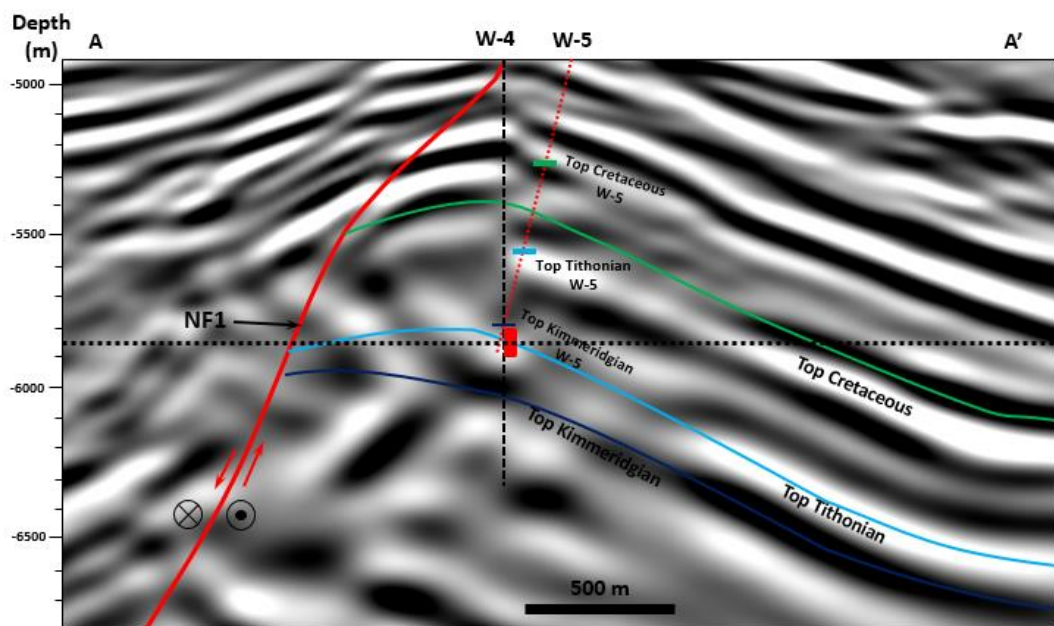


Figure 8.18. Cross section A-A' from Fig. 15 showing the trajectories of boreholes W-4 and W-5. Red rectangle represents the interval tested in W-5 which had oil and gas production. Horizontal dashed line represents the depth of the slices shown in Figure 18.

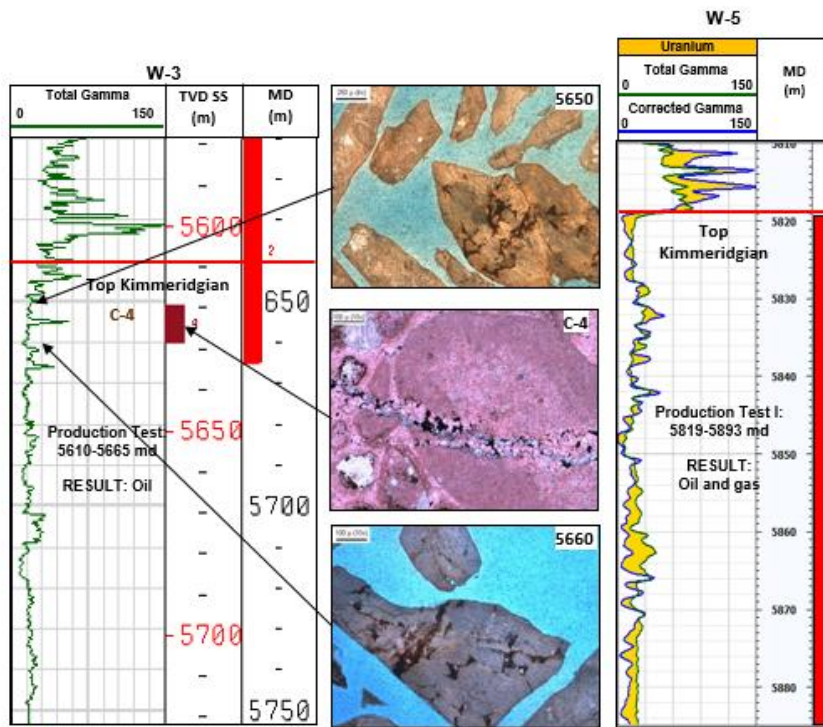


Figure 8.19. Well log correlation between wells W-3 and W-5. Reservoir rock in W-3 consists of partially dolomitized, intraclastic wackestone-packstone. Similarity of the gamma ray response in both wells suggests that lithofacies may also be similar (PEMEX internal report).

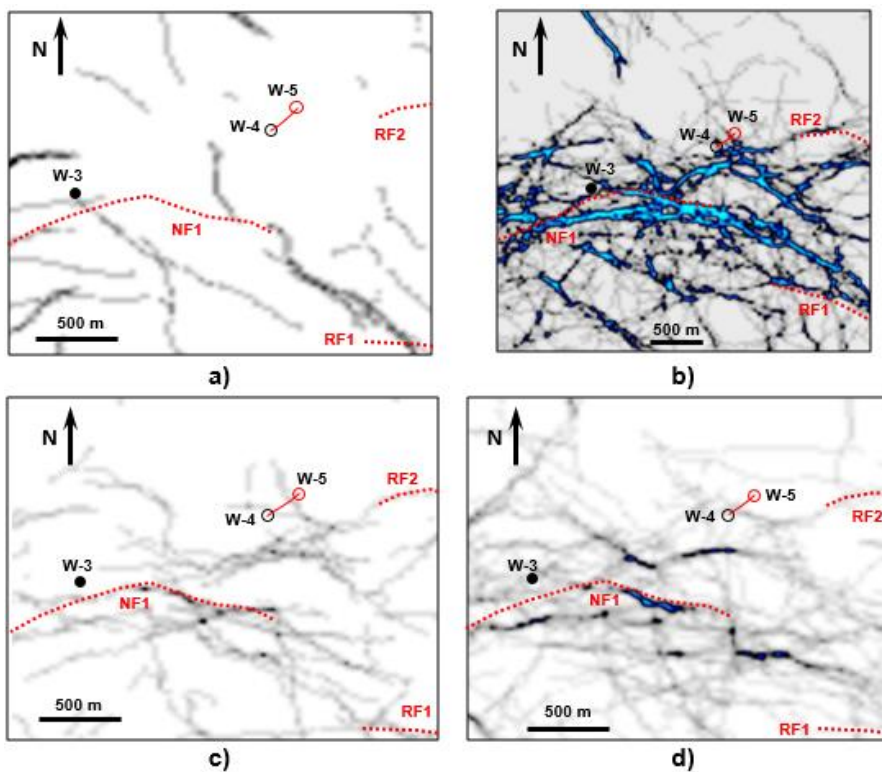


Figure 8.20. Depth slices at 5850 m showing the distribution of ant-tracking lineaments in the vicinity of boreholes W-4 and W-5. a) variance, b) most positive curvature aggressive, c) most positive curvature passive and, d) most extreme curvature. RF= Reverse fault; NF= Normal fault.

8.4 Discussion

Analysis of the results obtained from the case study shows that the proposed multidisciplinary workflow integrating different analytical techniques, regional geology and borehole data has a good potential for estimating location, orientation and relative intensity of sub-seismic fracturing in undrilled areas; however, its applicability and reliability of results can be strongly limited by several factors such as complex geology, depth of investigation, quality of seismic data and the amount of borehole data available. This case study offered an opportunity to test this workflow in an ideal setting: a structural trap (anticline C) with a relatively simple geometry and structural evolution, presence of nearby correlation boreholes with abundant data, low-resolution and relatively good seismic imaging. The relative simplicity of the structural trap allowed a good confidence of seismic mapping and the subsequent 2D restoration and geomechanical and fracture modelling. Table 8.5 shows the parameters taken into account for fracture prediction in borehole W-4 and its comparison with boreholes W-1, W-2 and W-3, which were used to calibrate the modelled parameters. The degree of correlation between the results of seismic ant-tracking, strain distribution and fracture modelling for proposed borehole W-4 is somewhat different to the degree of correlation observed in the other boreholes due to the low strain values; however, similarities with the geological controls, MCSS and ant-tracking counteract this mismatch, thus avoiding this well proposal to be discarded and, most importantly, keeping a good predictive potential.

Prediction of fracture orientations based on interpretation of ant-tracking lineaments in mapped surfaces and depth slices provided a relatively good matching with fracture orientations obtained from FMI logs and core samples, so it is expected a similar degree of matching for proposed borehole W-4. These results are similar to those obtained by Lohr et al. (2007) and Endres et al. (2008), who used coherency algorithms for fracture prediction and obtained a good matching with FMI orientations. Moreover, ant-tacking obtained from the most-positive and most-extreme curvature attributes provided better definition and enhancement of fracture and subtle faults, thus confirming their value for structural interpretation (Basir et al., 2013). Suardana et al., (2013) also obtained a good matching between ant-tracking based interpretation and well data for identification of fractures in basement rocks at NW Java Basin. In the other hand, prediction of fracture intensity combining ant-tracking and strain maps within the study area provided ambiguous matching with borehole data, which can be explained mainly by the difference in the scales of observation and resolution of modelling. Prediction of fracture intensity based on strain distribution can be only qualitative if borehole data are sparse or null; however, higher strains have been related to areas with high density of mapped faults in

seismic data (Ziesch et al., 2019), and to zones with highest curvature in folds where highest production rates have been reported (Luneburg, 2017). Feng et al., (2018) made an accurate quantitative prediction of fracture intensity for tight sandstones from the Kuqa Depression, China, by integrating mechanical tests, X-ray CT scanning, finite element method (FEM) and failure criterion into a numerical model that was tested against borehole data. For this, a direct relationship between strain energy density and fracture volume density was established.

Regarding to MCSS, this modelled parameter is considered as a proxy to estimate fracture intensity (Maerten et al., 2002; Dee et al., 2007), had a good correlation with strain and ant-tracking maps. Also, FMI values showed a regular to good degree of correlation with MCSS, thus confirming its importance as fracture intensity predictor although the lack of enough core samples prevented to define the degree of correlation more accurately. These results are in agreement with a study by Maerten and Maerten (2006) where modelled high MCSS values in cross-sections matched areas with higher fracture intensity observed in extensional analogue models and contractional folds in outcrop.

Summarizing, different tectonic styles show distinctive patterns of fracture distribution and orientation, either extensional (Price and Cosgrove, 1990), contractional (Stearns, 1968; Bergbauer and Pollard, 2004) or salt tectonics related (Tuncay et al., 2003; Rowan et al., 2003) so if the tectonic style of a given structural trap can be characterized, it is possible to predict the fracture distribution and orientation; moreover, the combined analysis of widely accepted geometric relationships between fold geometry and fracture orientation (Price, 1966; Stearns, 1968; Price and Cosgrove, 1990; Liu et al., 2016) along with the relationships between structural position, mechanisms of deformation and distribution of fracture intensity (Watkins et al., 2015; Watkins et al., 2018), provides additional useful information for fracture prediction. Finally, the accuracy of this prediction may improve considerably with the integration of borehole data which provides information about the contribution of other geological factors that also control the natural fracturing (lithology, texture, porosity, diagenesis).

Parameters		Late Cretaceous			Late Kimmeridgian			
		W-1	W-2	W-3	W-1	W-2	W-3	W-4
Seismic attribute	<i>Ant-tracking surface</i>	regular	low	medium	high	medium	medium	High
Modelled	<i>MCSS</i>	medium	medium	high	high	high	high	High
	<i>Strain</i>	low	medium	high	high	medium	medium	Low
Geological controls	<i>Structural position</i>	limb	limb	Hinge/fault	limb	limb	Hinge/fault	Hinge
	<i>Lithology</i>	Marls, shaly Mdst	Marls, shaly Mdst	Marls, shaly Mdst	Shaly Mdst, wkcst	Shaly Mdst, wkcst	Oolitic grstn	Wcks-pckst dol
	<i>Texture</i>	micritic	micritic	micritic	fine-grained	fine-grained	microcrystalline	grain-supported
	<i>Deformational events</i>	2	2	3	2	2	3	2
Relationships	<i>MCSS vs ant-tracking</i>	regular-good	regular	regular-good	good	regular	good	regular-good
	<i>MCSS vs strain</i>	good	good	regular-good	good	good	good	poor
	<i>strain vs ant-tracking</i>	regular	regular	good	good	good	good	regular-poor

Table 8.5. Summary of the different parameters used for fracture prediction and comparison between their relationships in the boreholes within the study area.

This work also offered an opportunity to test the proposed methodology for assessment of reservoir rock and compare the results with borehole information. The assessment was performed using a conservative approach and the results indicated a moderate probability (0.7) for both Presence and Quality of reservoir rock in both Mesozoic targets (Late Cretaceous and Late Kimmeridgian) of the W-4 proposed prospect; however, the value of the category Borehole Data (0.6) and the values of its correspondent assessed sub-components are slightly lower for the Late Cretaceous target, which may suggest that, although the values of the sub-element Quality are identical for both targets (0.7), the importance of borehole data must be taken into account in order to consider the Late Cretaceous target as more risky for this prospect. The successful production test performed in the adjacent correlation borehole W-5 confirmed the presence of a reservoir rock for the Late Kimmeridgian target, for which a value of 0.7 was calculated for the sub-elements Presence and Quality of reservoir rock.

This methodology represents an improvement to the traditional assessment of the reservoir rock element, since it incorporates additional sub-elements derived from different geophysical and geological analyses, which provides a more detailed and robust characterization of sub-seismic fractures. Even when the proposed assessment is not free from a certain degree of subjectivity, the inclusion of different categories and sub-components allows the reservoir rock element to be assessed from different perspectives, so that low values in a single category or sub-component may not affect considerably the final value of the sub-elements or the main element as it would be the case if the final value relied on one or two categories only, which reduces the interpretation bias, although not removing it completely. Furthermore, this assessment can be applied at different stages of the exploration process, since its multidisciplinary approach includes analyses that are independent of borehole data; this represents an advantage over risk tables proposed by Milkov (2015), which can be applied only in already drilled, relatively well-known areas; however, the certainty of their results is higher as opposed to the proposed methodology, whose certainty in results is affected negatively by the lack of borehole data for correlation and calibration.

Another limitation of the proposed assessment method is the relatively high level of subjectivity needed for the assignment of the probability values of the sub-components as well as for the definition of their weighing. Limitations inherent of the geophysical techniques inevitably derive in different ranges of uncertainty, since it is very difficult to establish precise limits with numerical values that fit every single geological possible scenario. In the case of borehole data, measurements are direct but fragmentary and representative of a small rock volume only; additionally, natural fracturing results from a

complex combination of multiple factors, whose effects can be difficult to quantify individually and, more importantly, they are not subject to rules of thumb, thus creating ambiguity and therefore, difficult to predict in unknown areas.

In summary, the mostly qualitative nature of fracture prediction in exploratory areas implies a relatively high degree of subjectivity during the assessment of potential reservoir rock. Conversely, if prospects need to be assessed in areas with numerous boreholes, the prediction will tend to be more quantitative and less subjective (Lohr et al, 2008; Jenkins et al., 2009).

8.5 Conclusions

Estimation of location, orientation and intensity of fracture sets is crucial in order to assess areas with potential as reservoir rock at early stages of hydrocarbon exploration. This chapter showed the application of an integrated methodology for fracture analysis as well as an example of an improved assessment of the presence and quality of the reservoir rock element, which includes additional sub-elements derived from the different analyses involved in fracture prediction.

The results obtained show, in general terms, a good degree of correlation between modelled data (MCSS and strain distribution) and borehole data, thus indicating its potential as a predictive tool, which can be applied in a variety of structural settings as well as in different trap geometries. Also, ant-tracking attribute applied to mapped surfaces and slices showed a good correlation with fracture orientations obtained from FMI and core samples.

The validity of the proposed reservoir rock's assessment was tested in the well proposal W-4 by using the results of a nearby blind well (W-5). The result of the assessment agrees with the confirmed presence of a good-quality reservoir rock for Late Kimmeridgian play in the area. However, the certainty of these assessments will depend greatly on the amount of available borehole data.

The relatively high level of subjectivity needed for the assignment of the probability values represents another limitation of this assessment method. The difficulty to establish precise limits with numerical values that fit every single geological possible scenario, additionally to ambiguous results provided by the different analyses, may result in that different work teams will evaluate the same dataset and give different answers.

Chapter 9

Conclusions and Further Work

9.1 Conclusions

The work developed in this research was aimed not only to increase in the understanding of natural fracturing, but also to propose a methodology with a multidisciplinary approach designed to predict the location, orientation and relative intensity of sub-seismic fracturing that can be applied in early stages of the oil and gas exploratory process. This section presents the conclusions of the project, which answer the main questions posed at the introduction chapter.

1. What is the influence of structural evolution on natural fracturing of carbonate rocks?

Present-day geometry of structural traps is the result of the combined effects of one or more different episodes of deformation associated to local or regional tectonics. Four different deformational events (D1-D4) were identified within the study area, ranging in age from Late Jurassic to Pliocene. From these, contractional events D2 and D3 may have caused tectonic fracturing in Mesozoic carbonate rocks, thus increasing their potential as reservoir rocks. Whilst events D1-D3 affected the three anticlines, event D4 affected only anticline A, which has important implications for hydrocarbon exploration: good trap preservation is considered for anticlines B and C since they were not affected by late event D4. In the other hand, event D4 could have reactivated the pre-existent Mesozoic normal fault due to linking of Tertiary and Mesozoic segments into a single one, which may have a negative impact on trap preservation but also it may contribute positively on fracture formation in the vicinity of the fault plane.

1. What are the geological factors that control natural fracturing within the study area?

Analysis and integration of borehole data (core samples and FMI logs) allowed this study to identify the following general tendencies and relationships between geological controls and fracturing intensity in carbonate Mesozoic rocks: Original rock's texture seems to exert the primary role in natural fracturing. Mud-supported textures (mudstone-wackestone) deposited in a basinal environment show higher fracture densities than grain-supported textures (grainstone-packstone) deposited in shallow environments; Lithology seems to exert a secondary role in natural fracturing. In the study area, limestones generally show higher fracture densities than partially dolomitized limestones or dolomites; Bed thickness also exerts a secondary role in natural fracturing and fracture densities tend to be higher in thinner beds whereas presence of faults seem to be

associated with higher fracture density in their vicinity. However, contradictory results for each of the analysed factors were observed, which can be attributed mainly to a complex interaction between them derived from diagenesis, the fractional nature of information sampling in boreholes and/or structural position. Finally, structural position seems to exert a primary role when other controls such as lithology, texture or bed thickness are very similar. In such cases, locations very close to major faults and/or with high strain/MCSS show higher fracture intensities.

2. How can geological and geophysical data be integrated for fracture prediction?

A more accurate characterization of fracture sets (including location, orientation and intensity) at subsurface is crucial in order to assess potential reservoir rocks at early stages of hydrocarbon exploration. This work provides a multidisciplinary methodology that combines different data sources (including borehole data) and analytical methods widely used in the industry; moreover, each of these methods contribute with their own criteria to an overall understanding of fracture distribution at subsurface. The results obtained show, in general terms, a good degree of correlation between modelled data and borehole data, thus indicating its potential as a predictive tool, which can be applied in a variety of structural settings as well as in different trap geometries; however, its main limitations consist of the quality of seismic data, amount of borehole data for correlation and calibration, depth of investigation and structural complexity.

3. Assessment of reservoir rock during prospect evaluation.

This work proposes an improved assessment of the presence and quality of the reservoir rock element by including additional sub-elements derived from the different analyses involved in fracture prediction. The validity of this assessment was tested in the proposed location W-4, for which a value of 0.7 for reservoir rock was calculated for the Kimmeridgian Play. The results of the adjacent blind well W-5 (oil producer), which was not considered for the assessment, confirmed the presence of a good-quality reservoir rock for that play. However, the certainty of the results will depend greatly on the amount and quality of available borehole data. Also, the relatively high level of subjectivity needed for the assignment of the probability values represents another limitation of this assessment method. Finally, the difficulty to establish precise limits with numerical values that fit every single geological possible scenario, additionally to ambiguous results provided by the different analyses, may result in that different work teams will evaluate the same dataset and give different answers.

9.2 Recommendations for future work

1. Influence of diagenesis on natural fracturing.

This work investigated the effect of different geological controls on natural fracturing; however, some of the primary factors (lithology, texture, porosity) are affected by diagenetic processes through time which, in turn, modify the quality of reservoir rock. Paragenetic charts used in this work provided only a relative chronology of the diagenetic processes, resulting in an incomplete understanding of the relationship between the diagenetic processes and natural fracturing. The application of investigation techniques like cathodoluminescence and fluid inclusions are crucial in order to provide an absolute timing of the diagenetic events as well as an improved and more complete understanding of their influence on natural fracturing.

2. Definition of mechanical and fracture stratigraphy from borehole data.

This work shows a first-order relationship between fracture intensity and factors such as lithology, texture and porosity. A more complete understanding of these relationship can be defined with a detailed characterization of the mechanical and fracture stratigraphy by obtaining UCS values from uniaxial tests and define different mechanical groups in the stratigraphy based on the calibration of UCS values with well logs and cutting samples.

Bibliography

- Aarre, V., Astratti, D., Dayyni, T.N.A.A., Mahmoud, S.L., Clark, A.B.S., Stellas, M., Stringer, J.W., Toelle, B., Vejrbæk, O.V., White, G., 2012, "Seismic detection of subtle faults and fractures", *Oilfield Review*, Vol. 24, pp. 28-43.
- Ahr, Wayne M., 2008, "*Geology of Carbonate Reservoirs- The Identification, Description, and Characterization of Hydrocarbon Reservoirs in Carbonate Rocks*", Hoboken, New Jersey, John Wiley and Sons, Inc.
- Akbar, M., Vissapragada, B., Alghamdi, A.H., Allen, D., Herron, M., Carnegie, A., Dutta, D., Olesen, J.R., Chourasiya, R.D., Logan, D., Stief, D., Netherwood, R., Russell, S.D., Saxena, K., 2000, "A Snapshot of Carbonate Reservoir Evaluation", *Oilfield Review*, No. 12, pp. 20-41.
- Alsop, G.I., Weinberger, R., Levi, T., Marco, S., 2016, "Cycles of passive versus active diapirism recorded along an exposed salt wall", *Journal of Structural Geology*.
- Ameen, M.S., Smart, B.G.D., Somerville, J., Hammilton, S., Naji, N.A., 2009, "Predicting rock mechanical properties of carbonates from wireline logs (A case study: Arab-D reservoir, Ghawar field, Saudi Arabia)", *Marine and Petroleum Geology*, No. 26 (2009), pp. 430–444.
- Anderson, E.M., 1951, "*The Dynamics of faulting and dyke formation with applications to Britain*", 2nd edition, Edinburgh, Oliver and Boyd.
- Angeles-Aquino, F. J., Reyes-Nunez, J., Quezada-Muneton, J. M. and Meneses-Rocha, J. J. 1994, "*Tectonic evolution, structural styles, and oil habitat in Campeche Sound, Mexico*", Gulf Coast Association of Geological Societies, Austin, TX (United States).
- Ángeles-Aquino, F. J. and Cantú-Chapa A., 2001, "*Subsurface Upper Jurassic Stratigraphy in the Campeche Shelf, Gulf of Mexico*", AAPG Memoir, Vol. 75, pp. 343-352.
- Ángeles-Aquino, F. J., 2006, "*Monografía Petrolera de la Zona Marina*", Edited by AMGP, Special Volume, 77 pages.
- Anjaneyulu S., Singh, S., Al-Ajmi, A., Dey, A., Al-Busairi, A., Al-Azmi, K., Roy, M., 2011, "Integrated seismic-attribute analysis to characterize Tertiary Rus/Radhuma reservoirs: An emerging exploration play in Kuwait", *SEG Technical Program Expanded Abstracts 2018*, pp. 1768-1772.
- Arasu, R., Singh, S., Khan, B., Al-Adwani, T., Nath, P., Abu-Ghneej, A., Bader, S., 2011, "*Sub-seismic discontinuity mapping to infer fracture potential of tight carbonate reservoirs of the early Cretaceous Makhul Formation in Kuwait*", *SEG Technical Program Expanded Abstracts 2011*, pp. 1113-1117

- Audebert, F., Dirks, V., Pettenati, A., “TTI anisotropic depth migration: What tilt estimate should we use?”, *SEG Technical Program Expanded Abstracts 2006*, pp. 2382-2386.
- Awdal, A., Healy, D., Alsop, I., 2016, “Fracture patterns and petrophysical properties of carbonates undergoing regional folding: A case study from Kurdistan, N Iraq”, *Marine and Petroleum Geology*, Vol. 71, pp. 149-167.
- Barbier, M., Hamon, Y., Callot, J.-P., Floquet, M. and Daniel, J.-M., 2012, “Sedimentary and diagenetic controls on the multiscale fracturing pattern of a carbonate reservoir: The Madison Formation (Sheep Mountain, Wyoming, USA)”, *Marine and Petroleum Geology*, 29, pp. 50-67.
- Baron, J., 2007, “*Thinking and Deciding*”, 4th edition, Cambridge University Press, New York, 600 pp.
- Basir, H.M., Tavakoli, M., Javaherian, A., 2013, “Multi-attribute ant-tracking and neural network for fracture detection: A case study of an Iranian oilfield”, *Journal of Geophysics and Engineering*”, No. 10, 10 pp.
- Bellahsen, N., Fiore, P. and Pollard, D.D., 2006, “The role of fractures in the structural interpretation of Sheep Mountain Anticline, Wyoming”, *Journal of Structural Geology*, Vol. 28, pp. 850–867.
- Bengtson, C. A., 1982, “Structural and stratigraphic uses of dip profiles in petroleum exploration”, in M. T. Halbouty, ed., *The deliberate search for the subtle trap: AAPG Memoir 32*, 351 pp.
- Bergbauer, S., and Pollard, D. D., 2004, “A new conceptual fold-fracture model including prefolding joints, based on the Emigrant Gap anticline, Wyoming”, *Geological Society of America Bulletin*, Vol. 116, Issue (3-4), pp. 294–307, doi:10.1130/B25225.1.
- Bird, D.E., Burke, K., Hall, S.A., Casey, J.F., 2005, “Gulf of Mexico tectonic history: Hotspot tracks, crustal boundaries, and early salt distribution”, *AAPG Bulletin*, Vol. 89, No. 3, pp. 311–328.
- Blatt, H., Middleton, G.V. and Murray, R.C., 1980, “*Origin of Sedimentary Rocks*”, 2nd Edition, Prentice-Hall, New Jersey, 634 pp.
- Blumentritt, Ch., Marfurt, K., Sullivan, E., “Volume-based curvature computations illuminate fracture orientations — Early to mid-Paleozoic, Central Basin Platform, West Texas”, *Geophysics*, Vol. 71, No. 5 (September-October 2006); pp. B159–B166.
- Boadu, F., Long, L., 1996, “Effects of fractures on seismic-wave velocity and attenuation”, *Geophysical Journal International*, Vol. 127, Issue 1, pp. 86-110.
- Bourbiaux, B., 2010, “Fractured Reservoir Simulation: a Challenging and Rewarding Issue”, *Oil & Gas Science and Technology – Rev. IFP*, Vol. 65, No. 2, pp. 227-238.

- Boechat, J. B., Bulcao, A., Filho, D. M. S., Cunha, P. M., Mansur, W. J., and Moreira, T., 2007, "A 3D reverse-time migration scheme for offshore seismic data", *SEG Technical Program Expanded Abstracts*, No. 26, pp.2427-2431.
- Bond, C.E., Gibbs, A., Shipton, Z.K., Jones, S., 2007, "What do you think this is? 'Conceptual uncertainty' in geoscience interpretation", *GSA Today*, 17, pp. 4–10.
- Bose, S., Mitra, Sh., 2009, "Deformation along oblique and lateral ramps in listric normal faults: Insights from experimental models", *AAPG Bulletin*, Vol. 93, No. 4 (April 2009), pp. 431–451.
- Bour, O., and Davy, P., 1999, "Clustering and size distributions of fault patterns: theory and measurements", *Geophysical Research Letters*, Vol. 26, No. 13, pp. 2001-2004.
- Bourne, S. J., Rijkels, L., Stephenson, B. J. and Willemse, E. J. M., 2001, "Predictive modelling of naturally fractured reservoirs using geomechanics and flow simulation", *GeoArabia*, Vol. 6, pp. 27–42.
- Brown, J., Davis, B., Gawankar, K., Kumar, A., Li, B., Miller, C., Laronga, R., Schlicht, P., 2015, "Imaging: Getting the Picture Downhole", *Oilfield Review* 27, No. 2 (September 2015).
- Brun, J.-P., Fort, X., 2004, "Compressional salt tectonics (Angolan margin)", *Tectonophysics*, 382, pp. 129-150.
- Caine, J.S., Evans, J.P., Forster, C.B., 1996, "Fault zone architecture and permeability structure", *Geology*, Vol. 24 (11), pp. 1025–1028.
- Casini, G., Gillespie, P. A., Verges, J., Romaine, I., Fernandez, N., Casciello, E., Saura, E., Mehl, C., Homke, S., Embry, J. C., Aghajari, L. and Hunt, D. W., 2011, "Sub-seismic fractures in foreland fold and thrust belts: insight from the Lurestan Province, Zagros Mountains, Iran", *Petroleum Geoscience*, Vol. 17, 2011, pp. 263–282.
- Chopra, S., Marfurt, K., 2007, "Seismic curvature attributes for mapping faults/fractures, and other stratigraphic features", *CSEG Recorder*, No. 32, pp. 37-41.
- Chopra, S and Marfurt, K.J., 2007, "*Seismic attributes for prospect identification and reservoir characterization*", SEG Geophysical Developments Series No. 11.
- Casini, G., Gillespie, P. A., Verges, J., Romaine, I., Fernandez, N., Casciello, E., Saura, E., Mehl, C., Homke, S., Embry, J. C., Aghajari, L. and Hunt, D. W., 2011, "Sub-seismic fractures in foreland fold and thrust belts: insight from the Lurestan Province, Zagros Mountains, Iran", *Petroleum Geoscience*, Vol. 17, 2011, pp. 263–282.

- Cooke, M. L., Simo, J. A., Underwood, C. A. and Rijken, P., 2006, "Mechanical stratigraphic controls on fracture patterns within carbonates and implications for groundwater flow", *Sedimentary Geology*, 184, pp. 225-239.
- Comision Nacional de Hidrocarburos (CNH), 2014, "Cuencas del Sureste Aguas Someras: Sintesis Geologico Petrolera", Available from: <http://rondasmexico.gob.mx/wp-content/uploads/2015/09/AguasSomeras.pdf>, (Accesed 30th-October-2016).
- Crider, J.G. and Pollard, D., 1998, "Fault linkage: Three-dimensional mechanical interaction between echelon normal faults", *Journal of Geophysical Research*, Vol. 103, No. B10, pp. 24,373-24,391.
- Cruz-Mercado, M. A., Flores-Zamora J. C., León-Ramírez R., López-Céspedes H. G., Peterson-Rodríguez R. H., Reyes-Tovar E., Sánchez-Rivera R., Barrera-González D., 2011, "Salt provinces in the Mexican portion of the Gulf of Mexico—Structural characterization and evolutionary model", *Gulf Coast Association of Geological Societies Transactions*, Vol. 61, pp. 93–103.
- Dahlstrom, C. D. A., 1969, "Balanced Cross-Sections," *Canadian Journal of Earth Sciences*, Vol. 6, No. 4, pp. 743-757. doi:10.1139/e69-069
- Davison, I., Alsop, G.I., Evans, N.G., Safaricz, M., 2000, "Overburden deformation patterns and mechanisms of salt diaper penetration in the Central Graben, North Sea", *Marine and Petroleum Geology*, Vol. 17 (2000), pp. 601-618.
- Dee, S., Yielding, G., Freeman, B., Healy, D., Kuszniir, N., Grant, N. and Ellis, P., 2007, "Elastic dislocation modelling for prediction of small-scale fault and fracture network characteristics" In Lonergan, L., Jolly, R. J. H., Rawnsley, K. and Sanderson, D. J. (eds) *Fractured Reservoirs*, Geological Society, London, Special Publications, Vol. 270, pp. 139–155.
- Díaz G. T., Mixon, R., and Murray, G.E., 1959, "Mesozoic Stratigraphy and Structure, Saltillo-Galeana Areas, Mexico", *South Tex. Geol. Soc. Field Trip Guidebook*, p. H1-H6.
- Dickinson, W.R., Lawton, T.F., 2001, "Carboniferous to Cretaceous assembly and fragmentation of Mexico", *GSA Bulletin*, Vol. 113; No. 9, pp. 1142–1160.
- Di Naccio, D., Boncio, P., Cirilli, S., Casaglia, F., Morettini, E., Lavecchia, G. and Brozzetti, F., 2005, "Role of mechanical stratigraphy on fracture development in carbonate reservoirs: Insights from outcropping shallow water carbonates in the Umbria–Marche Apennines, Italy", *Journal of Volcanology and Geothermal Research*, Vol. 148, (2005), pp. 98-115.
- Ding, W. L., Fan, T. L., Yu, B. S., Huang, X. B. and Liu, C., 2012, "Ordovician carbonate reservoir fracture characteristics and fracture distribution forecasting in the Tazhong area of Tarim Basin, Northwest China", *Journal of Petroleum Science and Engineering*, 86-87, pp. 62–70.

- Eckert, A., Connolly, P, and Liu, X., 2014, “Large-scale mechanical buckle fold development and the initiation of tensile fractures”, *Geochemistry, Geophysics, Geosystems*, 15, pp. 4570 - 4587.
- Eddy, D. R., Van Avendonk, H. J. A., Christeson, G. L., Norton, I. O., Karner, G.D., Johnson, C. A., and Snedden, J. W., 2014, “Deep crustal structure of the North-eastern Gulf of Mexico: Implications for rift evolution and seafloor spreading”, *Journal of Geophysical Research: Solid Earth*, Vol. 119, pp. 6802–6822, doi:10.1002/2014JB011311.
- Eguiluz, S., Aranda-Garcia, M., Marrett, R., 2000, “Tectonica de la Sierra Madre Oriental, Mexico”, *Boletín de la Sociedad Geologica Mexicana*, Vol, LIII, pp. 1-26.
- Endres, H., Lohr, T., Trappe, H., Samiee, R., Thierer, P. O., Krawczyk, C. M., Tanner, D. C., Oncken, O. and Kukla, P. A., 2008, “Quantitative fracture prediction from seismic data”, *Petroleum Geoscience*, Vol. 14, 2008, pp. 369–377.
- Espinoza Carrasco, E., 2016, “Cálculo de Atributos Sísmicos con Datos Migrados en Tiempo y en Profundidad”, BsC Thesis, Universidad Nacional Autonoma de Mexico.
- Feng, J., Ren, Q., Xu, K., 2018, “Quantitative prediction of fracture distribution using geomechanical method within Kuqa Depression, Tarim Basin, NW China”, *Journal of Petroleum Science and Engineering*, Vol. 162, pp. 22- 34.
- Fischhoff, B., Slovic, P., Lichtenstein, S., 1977, “Knowing with certainty: the appropriateness of extreme confidence”, *J. Exp. Psychol. Hum. Percept. Perform*, 3, pp. 552–564.
- Foltinek, D., Quiring, S., Durocher, M., Yoshida, Y., 2013, “Reverse Time Migration: A case study of GPU / CPU hybrid computing”, *Rice Oil and Gas HPC Workshop*.
- Fort, X., Brun, J.P. and Chauvel, F., 2004, “Salt tectonics on the Angolan margin, synsedimentary deformation processes”, *AAPG Bulletin*, 88, pp. 1523–1544.
- Fossen, H., 2004, “Structural Geology”, New York, Cambridge University Press.
- Freeman, B., Quinn, D. J., Dillon, C.G., Arnhild, M., and Jaarsma, B., 2015, “Predicting subseismic fracture density and orientation in the Gorm Field, Danish North Sea”, Geological Society, London, Special Publications, 421.
- Friedman, M., Kwon, O., French, V.L., 1994, “Containment of natural fractures in brittle beds of the Austin Chalk, rock mechanics, models and measurements challenges from industry”. In: Nelson, P.P., Laubach, S.E. (Eds.), *Proceedings of the 1st North American Rock Mechanics Symposium*, Balkema, Texas, Austin, pp. 833–840.

- Gartner, J. and Suau, J., 1980, "Fracture Detection From Well Logs", *Society of Petrophysicists and Well-Log Analysts*.
- Gauthier, B.D.M., and Lake, S.D., 1993, "Probabilistic Modeling of Faults Below the Limit of Seismic Resolution in Pelican Field, North Sea, Offshore United Kingdom", *AAPG Bulletin*, Vol. 77, No. 5, pp. 761-777.
- Ghosh, K. and Mitra, S., 2009, "Structural controls of fracture orientations, intensity, and connectivity, Teton anticline, Sawtooth Range, Montana", *AAPG Bulletin*, 93, pp. 995-1014.
- Giles, K.A., and Rowan, M.G., 2011, Concepts in halokinetic-sequence deformation and stratigraphy, in I. Alsop et al., eds., *Salt, Sediments and Prospectivity: Geological Society London Special Publication*.
- Gillam, D., 2004, "*Structural and Geomechanical Analysis of Naturally Fractured Hydrocarbon Provinces of the Bowen and Amadeus Basins: Onshore Australia*", PhD Tesis, The University of Adelaide, Australia.
- Giorgioni, M., Iannace, A., D'amore, M., Dati, F., Galluccio, L., Guerriero, V., Mazzoli, S., Parente, M., Strauss, C. and Vitale, S., 2016, "Impact of early dolomitization on multi-scale petrophysical heterogeneities and fracture intensity of low-porosity platform carbonates (Albian-Cenomanian, southern Apennines, Italy)", *Marine and Petroleum Geology*, Vol. 73, pp. 462-478.
- Gotautas, V.A., 1963, "Quantitative analysis of prospect to determine whether it is drillable", *AAPG Bulletin*, Vol. 47, pp.1794–1812.
- Grando, G., McClay, K., 2004, "Structural evolution of the Frampton growth fold system, Atwater Valley-Southern Green Canyon area, deep water Gulf of Mexico", *Marine and Petroleum Geology*, 21, pp. 889–910.
- Gray, D. and Zheng, Y., 2003, "*Analyzing fractures from seismic for improved drilling success*", Houston, Gulf Publishing Co.
- Griffith, A.A., 1920, "The phenomena of rupture and flow in solids", *The Philosophical Transactions of the Royal Society London, Series A* 221, pp.163-198.
- Griffith, A.A., 1924, "Theory of rupture. In: Biezeno C.B. and Burgers, J.M. (eds), *Proceedings of the 1st international Congress of applied mechanics*. Delft: Waltman, pp. 55-63.
- Gross, M.R., 1993, "The origin and spacing of cross joints: example from the Monterey Formation, Santa Barbara Coastline, California", *Journal of Structural Geology*, 15, pp. 737–751.
- Gudmundsson, A., Fjeldskaar, I. and Brenner, S. L., 2002, "Propagation pathways and fluid transport of hydrofractures in jointed and layered rocks in geothermal fields", *Journal of Volcanology and Geothermal Research*, 116, 257-278.

- Gudmundsson, Agust, 2011, “*Rock Fractures in Geological Processes*”, Cambridge, Cambridge University Press.
- Gudmundsson, A., 2012, “*Fracture propagation, linkage and arrest*”, lecture notes, Advanced Structural Analysis GL5701, Royal Holloway University of London, delivered March 2012.
- Guzmán, A. E., and Márquez-Domínguez, B., 2001, “The Gulf of Mexico Basin south of the border”, in M.W. Downey, J. C. Threet, and W. A. Morgan, eds., *Petroleum provinces of the twenty-first century: AAPG Memoir*, Vol. 74, pp. 337–351.
- Halbouty, M.T., 1979, “*Salt Domes – Gulf Region, United States and Mexico*”, 2nd Edition: Houston, Gulf Publishing Co., 561p.
- Hanks, C. L., Lorenz, J., Teufel, L. W. and Krumhardt, A. P., 1997, “Lithologic and structural controls on natural fracture distribution and behavior within the Lisburne Group, Northeastern Brooks Range and North Slope subsurface, Alaska”, *AAPG Bulletin*, Vol. 81, pp. 1700-1720.
- Hoek, E. and Martin, C.D., 2014, “Fracture initiation and propagation in intact rock - A review”, *Journal of Rock Mechanics and Geotechnical Engineering*, Vol. 6, 287e300287-300.
- Hoffrage, U., 2004, “Overconfidence”, In Pohl, R. (Ed.), “Cognitive Illusions: A Handbook on Fallacies and Biases in Thinking, Judgement and Memory”, Psychology Press Hove, UK, pp. 235–254.
- Hossack, J.R., 1995, “Geometrical rules of section balancing of salt structures”, In: Jackson, M.P.A., Roberts, D.G., Snelson, S. (Eds.), *Salt Tectonics: A Global Perspective*, AAPG Memoir 65, pp. 29-40.
- Hudec, M.R., and Jackson, M.P.A., 2006, “Advance of allochthonous salt sheets in passive margins and orogens”, *American Association of Petroleum Geologists Bulletin*, Vol. 90, No. 10, pp. 1535–1564, doi: 10.1306/05080605143.
- Hudec, M. R., and Jackson, M. P. A., 2007, “Terra infirma: Understanding salt tectonics”, *Earth-Science Reviews*, Vol. 82, pp.1-28, doi:10.1016/j.earscirev.2007.01.001.
- Hudec, M., Norton, I., Jackson, M.P.A., Peel, F., 2013, “Jurassic Evolution of the Gulf of Mexico salt basin”, *AAPG Bulletin*, Vol. 97, No. 10, pp. 1683–1710.
- Hugman, R.H.H., Friedman, M., 1979, “Effects of texture and composition on mechanical behavior of experimentally deformed carbonate rocks”, *AAPG Bulletin*, Vol. 63, Issue 9, pp.1478-1489.
- Hunt, Lee et al., 2009, “On Calibrating Curvature Data to Fracture Density: Causes”, *CSEG RECORDER*, Vol. 34, No. 10, pp. 27-32.

- Instituto Mexicano del Petroleo, 2011, “Actualización e Integración De Plays Mesozoicos, Terciarios Y Fracturamiento 2011”, Unpublished (Property of PEMEX).
- Jackson, M. P. A., 1995, “Retrospective salt tectonics”, *in* M. P. A. Jackson, D. G. Roberts, and S. Snelson, eds., *Salt tectonics: a global perspective: AAPG Memoir 65*, p. 1-28.
- Jaeger, J.C., and Cook, N.G.W., 1979, “*Fundamentals of rock mechanics*”, 3rd edition, London, Chapman and Hall.
- Jenkins, C., Ouenes, A., Zellou, A., and Wingard, J., 2009, “Quantifying and predicting naturally fractured reservoir behavior with continuous fracture models”, *AAPG Bulletin*, V. 93, No. 11, pp. 1597–1608.
- Jibrin, B.W, Turner, J.P., Westbrook, G., Huck, A., 2009, “Application of volumetric seismic attributes to delineate fault geometry: Examples from the outer fold and thrust belt, deepwater Niger Delta (Joint Development Zone”, http://static.dgbes.com/images/PDF/fault_attributes_niger_delta_aapg.pdf.
- Johns, D.R., Squire, S.G., Ryan, M.J., 1998, “Measuring exploration performance and improving exploration predictions — with examples from Santos’s exploration program 1993–96”, *APPEA J.* 38, pp. 559–569.
- Jones, I. F., Goodwin, M. C., Berranger, I. D., Zhou, H. and Farmer, P. A., 2007, “Application of anisotropic 3D reverse time migration to complex North Sea imaging”, *SEG Technical Program Expanded Abstracts*, No. 26, pp.2140-2144.
- Jones, I. and Davison, I., 2014, “Seismic imaging in and around salt bodies”, *Interpretation*, Vol. 2, Issue 4, pp. 2324-8858.
- Kalid, N., Hmzah, U., Samsudin, A., 2016, “ Seismic Attributes And Their Application In Faults Interpretation of Kupe Field, Taranaki Basin, New Zealand”, *Electronic Journal of Geotechnical Engineering*, Vol. 21, Issue 6, pp. 2169-2184.
- Karaman, K., Cihangir, F., Ercikdi, B., Kesimal, A., Demirel, S., 2015, “Utilization of the Brazilian test for estimating the uniaxial compressive strength and shear strength parameters”, *The Journal of The Southern African Institute of Mining and Metallurgy*, Vol. 115, (3), pp. 185-192.
- Keppie, J. D., and Moran-Zenteno, D. J., 2005, “Tectonic implications of alternative Cenozoic reconstructions for southern Mexico and the Chortis Block”, *Int. Geol. Rev.*, 47, 473–491, doi:10.2747/0020-6814.47.5.473.
- Khair, H. A., Cooke, D., Hand, M., 2013, “Natural Fracture Networks Enhancing Unconventional Reservoirs’ Producibility: Mapping & Predicting”, *Search and Discovery Article #41182*, (2013)
- Kopf, A.J., 2002. “Significance of mud volcanism”, *Rev. Geophys.* 40 (2), 52 pp.

- Krézsek C., Adam J., and Grujic D., 2007, "Mechanics of fault and expulsion rollover systems developed on passive margins detached on salt: Insights from analogue modelling and optical strain monitoring", *Geological Society, London, Special Publications 2007*, Vol. 292; pp. 103-121.
- Lamarche, J., Lavenu, A. P. C., Gauthier, B. D. M., Guglielmi, Y. and Jayet, O., 2012, "Relationships between fracture patterns, geodynamics and mechanical stratigraphy in Carbonates (South-East Basin, France)", *Tectonophysics*, 581, pp. 231-245.
- La Pointe, P.R., 2010, "Techniques for Identification and Prediction of Mechanical Stratigraphy in Fractured Rock Masses", *American Rock Mechanics Association*.
- Larsen, B., Grunnaleite, I., Gudmundsson, A., 2010, "How fracture systems affect permeability development in shallow-water carbonate rocks: An example from the Gargano Peninsula, Italy", *Journal of Structural Geology*, Vol. 32, pp. 1212–1230.
- Laubach, S.E., 1988, "Subsurface fractures and their relationship to stress history in east Texas basin sandstone", *Tectonophysics*, Vol. 156, pp. 495-503.
- Laubach, S.E., Olson, J.E., Gross, M.R., 2009, "Mechanical and fracture stratigraphy", *AAPG Bulletin*, Vol. 93, pp. 1413-1426.
- Lavenu, A. P. C., Lamarche, J., Gallois, A. and Gauthier, B. D. M., 2013, "Tectonic versus diagenetic origin of fractures in a naturally fractured carbonate reservoir analog (Nerthe anticline, southeastern France)", *AAPG Bulletin*, Vol. 97, pp. 2207-2232.
- Lawton, T. F., Vega, F. J., Giles, K. A., and Rosales Domínguez, C., 2001, "Stratigraphy and origin of the La Popa basin, Nuevo Leon and Coahuila, Mexico", in: C. Bartolini, Buffler, R. T. and Cantú-Chapa, A., eds., "Mesozoic and Cenozoic evolution of the western Gulf of Mexico Basin: tectonics, sedimentary basins and petroleum systems", *American Association of Petroleum Geologists Memoir*, Vol. 75, pp. 219–240.
- Lisle, R. J., 1992, "Constant bed-length folding: three-dimensional geometrical implications", *Journal of Structural Geology*, Vol. 14, Issue 2, pp. 245–252.
- Lisle, R. J., 1995, "The Mohr circle for curvature and its application to fold description", *Journal of Structural Geology*, Vol. 17, Issue 5, pp. 1811-1819.
- Liu, X., Eckert, A., Connolly, P., 2016, "Stress evolution during 3D single-layer visco-elastic buckle folding: Implications for the initiation of fractures", *Tectonophysics*, Vol. 679, pp. 140–155.
- Lohr, T., Krawczyk, C. M., Tanner, D. C., Samiee, R., Endres, H., Thierer, P. O., Oncken, O., Trappe, H., Bachmann, R. & Kukla, P. A., 2008, "Prediction of subseismic faults and fractures: Integration of three-dimensional seismic data,

three-dimensional retrodeformation, and well data on an example of deformation around an inverted fault”, *AAPG Bulletin*, Vol. 92, Issue 4, pp. 473-485.

- Luneburg, C., 2017, “Using Structural Restoration Techniques and Strain Tracking to Predict Fracture Distributions”, *Search and Discovery Article*, No. 42089, Adapted from poster presentation given at AAPG 2017 Annual Convention and Exhibition, Houston, Texas, United States, April 2-5, 2017.

- Macaulay, E., 2017, “A new approach to backstripping and sequential restoration in subsalt sediments”, *AAPG Bulletin*, Vol. 101, No. 9 (September 2017), pp. 1385–1394.

- Maerten, L., Gillespie, P. & Pollard, D. D., 2002, “Effects of local stress perturbation on secondary fault development”, *Journal of Structural Geology*, Vol. 24, pp. 145–153.

- Maerten, L., and Maerten, F., 2006, “Chronologic modeling of faulted and fractured reservoirs using geomechanically based restoration: Technique and industry applications”, *AAPG Bulletin*, Vol. 90, pp. 1201-1226.

- Maleki, S., Ramazi, H., Gholami, R., Sadeghzadeh, F., 2015, “Application of seismic attributes in structural study and fracture analysis of DQ oil field, Iran”, *Egyptian Journal of Petroleum* (2015), Vol. 24, pp. 119–130.

- Maltman, A., 1994, “*The Geological Deformation of Sediments*”, 362 pp., Chapman and Hall, New York.

- Mandujano-Velazquez, J., and Keppie, D., 2009, “Middle Miocene Chiapas fold and thrust belt of Mexico: A result of collision of the Tehuantepec Transform/Ridge with the Middle America Trench”, *Memory of Geological Society*, 327, pp. 55–69, doi:10.1144/SP327.4.

- Mantilla, M., Davila, D., 2015, “Interpretation of Microresistivity Image Logs and Core Tomographic Images in a Natural Fractured Reservoir Evaluation, Upper Magdalena Valley, Colombia”, *Society of Petroleum Engineers Latin American and Caribbean Petroleum Engineering*, Quito, Ecuador, 18-20 November, 2015.

- Marfurt, K., Kirilin, R., Farmer, S., Bahorich, S., 1998, “3-D seismic attributes using a semblance-based coherency algorithm”, *Geophysics*, Vol. 63, No. 4 (July-August 1998); pp. 1150-1165.

- Marfurt, K., Alves, T., 2015, “Pitfalls and limitations in seismic attribute interpretation of tectonic features”, *in Interpretation*, Vol. 3, No. 1 (February 2015); pp. SB5–SB15.

- Marin, B. A., Clift, S. J., Hamlin, H. S. and Laubach, S. E., 1993, “*Natural fractures in Sonora Canyon sandstones, Sonora and Sawyer fields, Sutton County, Texas*”, Society of Petroleum Engineers Paper, No. 25895, pp. 523–531.

- Marrett, R., and Aranda-García, M., 2001, “Regional structure of the Sierra Madre Oriental fold-thrust belt, Mexico”, *in* R. Marrett, ed., *Genesis and controls*

of reservoir-scale carbonate deformation, Monterrey salient, Mexico: Bureau of Economic Geology, Austin, Guidebook 28, pp. 31-55.

- Martini, M., Ortega-Gutiérrez, F., 2016, "Tectono-stratigraphic evolution of eastern Mexico during the break-up of Pangea: A review", *Earth-Science Reviews* (2016), <http://dx.doi.org/10.1016/j.earscirev.2016.06.013>.
- Marton, G., and Buffler, R. T., 1994, "Jurassic reconstruction of the Gulf of Mexico Basin", *International Geology Review*, Vol. 36, pp. 545–586, doi:10.1080/00206819409465475.
- Marton, L.G., Tari, G.C. and Lehmann, C.T., 2000, "Evolution of the Angolan passive margin, West Africa, with emphasis on post-salt structural styles", *In: Atlantic Rifts and Continental Margins* (Ed. by W. Mohriak & M. Talwani) Am. Geophys. Union Geophys. Monogr, 115, pp. 129–149.
- McCaleb, J.A. and Wayhan, D.A., 1969, "Elk Basin Madison heterogeneity: its influence on performance", *Journal Petroleum Technology*, pp. 153-159.
- Milkov, A.V., 2015, "Risk tables for less biased and more consistent estimation of probability of geological success (PoS) for segments with conventional oil and gas prospective resources", *Earth-Science Reviews*, 150, pp. 453–476.
- Mitra, S., 2002, "Structural models of faulted detachment folds", *AAPG Bulletin*, Vol. 86, No. 9 (September 2002), pp. 1673–1694.
- Mitra, S., Figueroa, G. C., Garcia, J. H. and Alvarado, A. M., 2005, "Three-dimensional structural model of the Cantarell and Sihil structures, Campeche Bay, Mexico", *AAPG Bulletin*, Vol. 89, pp. 1-26.
- Mitra, S., Duran Gonzalez, J. A., Hernandez, J. G., Garcia, S. H. and Banerjee, S., 2006, "Structural geometry and evolution of the Ku, Zaap, and Maloob structures, Campeche Bay, Mexico", *AAPG Bulletin*, Vol. 90, pp. 1565-1584.
- Mitra, S., Gonzalez, J. D. A., Garcia, J. H. and Ghosh, K., 2007, "Ek-Balam field: A structure related to multiple stages of salt tectonics and extension", *AAPG Bulletin*, Vol. 91, pp. 1619-1636.
- Monroy-Santiago, F., 2011, "Methodology for static characterization of natural fractures: Implementation in Pemex projects and its application in oil and gas field development", *Gulf Coast Association of Geological Societies Transactions*, Vol. 61, p. 787.
- Montgomery, S.L., Walker, T.H., Wahlman, P., Tobin, R.C. and Ziegler, D., 1999, "Upper Jurassic "Reef play, East Texas Basin: an updated overview: Part 1 – background and outboard trend", *AAPG Bulletin*, Vol. 83, pp. 707-728.
- Morán-Zenteno, D. J., Cerca, M. and Keppie, J. D., 2007, "The Cenozoic tectonic and magmatic evolution of southwestern México: Advances and

problems of interpretation”, in Alaniz-Álvarez, S.A., and Nieto-Samaniego, Á.F., eds., *Geology of México: Celebrating the Centenary of the Geological Society of México: Geological Society of America Special Papers*, 422, 71.

- Mount, V.S., Dull, K. and Mentemeier, S., 2007, “Structural style and evolution of traps in the Paleogene play, deepwater Gulf of Mexico”, in Kennan, L., Pindell, J., and Rosen, N.C., eds., *The Paleogene of the Gulf of Mexico and Caribbean Basins: 27th Annual GCSSEPM Foundation Bob F. Perkins Research Conference*, CD-ROM.

- Murray, G.H. Jr., 1968, “Quantitative Fracture Study-Sanish Pool, McKenzie Co., North Dakota”, *AAPG Bulletin*, Vol. 52, pp.57-65.

- Narhari, S. R., Al-Qadeeri, B., Dashti, Q., Silva, J., Dasgupta, S., Hannan, A., Walz, M., Lu, L., Wagner, C. and Sayers, C. M., 2015, “Application of pre-stack orthotropic AVAz inversion for fracture characterization of a deep carbonate reservoir in northern Kuwait”, *Leading Edge*, Vol. 34, pp. 1488-1493.

- Nelson, R. A., 2001, “*Geologic analysis of naturally fractured reservoirs*”, 2nd edition, Boston, Gulf Professional Publishing.

- Nelson, R.A., Ward, B.J. et al., 1993, “*Vertical and lateral variations in fracture spacing in several carbonate sections*”, In Proc. Tunisian Fractured Reservoir Seminar (ETAP), Tunis, pp. 79-89.

- Ngeri, A.P.; Tamunobereton-ari, I., and Amakiri, A.R.C., 2015, “Ant-Tracker Attributes: An Effective Approach To Enhancing Fault identification And Interpretation”, *IOSR Journal of VLSI and Signal Processing (IOSR-JVSP)*, Volume 5, Issue 6, Ver. II (Nov -Dec. 2015), pp. 67-73.

- Nguyen, L. and Mann, P., 2016, “Gravity and magnetic constraints on the Jurassic opening of the oceanic Gulf of Mexico and the location and tectonic history of the Western Main transform fault along the eastern continental margin of Mexico”, *Interpretation*, Vol. 4, No. 1, pp. SC23–SC33.

- Nichols, Gary, 2009, “*Sedimentology and Stratigraphy*”, 2^{dn} edition, Hoboken, NJ, Wiley-Blackwell.

- Nicol, A., Walsh, J.J., Watterson, J., and Gillespie, P.A., 1996, “Fault size distributions m are they really power-law?”, *Journal of Structural Geology*, Vol. 18, No. 2/3, pp. 191 m 197.

- Norbeck, J. H., 2011, “*Identification and Characterization Of Natural Fractures While Drilling Underbalanced*”, MSc Thesis, Colorado School of Mines.

- Nunns, Alan, 1991, “Structural Restoration of Seismic and Geologic Sections in Extensional Regimes”, *AAPG Bulletin*, Vol. 75, No. 2, (February 1991), pp. 278-297.

- Odoh, B., Ilechukwu, J., Okoli, N., 2014, “The Use of Seismic Attributes to Enhance Fault Interpretation of OT Field, Niger Delta”, *International Journal of Geosciences*, Vol. 5, pp. 826-834.

- Okada, Y., 1992, "Internal deformation due to shear and tensile faults in a half-space", *Bulletin of the Seismology Society of America*, Vol. 82, pp. 1018–1040.
- Ortega, O. and Marrett, R., 2000, "Prediction of macrofracture properties using microfracture information, Mesaverde Group sandstones, San Juan basin, New Mexico", *Journal of Structural Geology*, Vol. 22, pp. 571-588.
- Ortega, O. J., Gale, J. F. W. and Marrett, R., 2010, "Quantifying diagenetic and stratigraphic controls on fracture intensity in platform carbonates: An example from the Sierra Madre Oriental, northeast Mexico", *Journal of Structural Geology*, 32 (2010), pp. 1943-1959.
- Oswald, M.E., Grosjean, S., 2004, "Confirmation bias", *In Pohl, R.F. (Ed.), "Cognitive Illusions: A Handbook on Fallacies and Biases in Thinking, Judgement and Memory"*, Psychology Press, Hove, UK, pp. 79–96.
- Ouenes, A., 2000, "Practical application of fuzzy logic and neural networks to fractured reservoir characterization", *Computers & Geosciences*, Vol. 26, pp. 953-962.
- Padilla y Sanchez, R.J., 1986, "Post-Paleozoic tectonics of Northeast Mexico and its role In the evolution of the Gulf Of Mexico", *Geofísica Internacional*, Vol. 25, No. 1, pp. 157-206.
- Padilla y Sánchez, R., 2007, "Evolución geológica del sureste mexicano desde el Mesozoico al presente en el contexto regional del Golfo de México", *Boletín de la Sociedad Geológica Mexicana*, Tomo LIX, No. 1, 2007, pp. 19-42.
- Peel, F. J., Travis, C. J. and Hossack, J. R., 1995, "Genetic structural provinces and salt tectonics of the Cenozoic offshore U.S. Gulf of Mexico: a preliminary analysis", *in Jackson, M. P. A., Roberts, D. G. and Snelson, S., eds., "Salt tectonics: a global perspective"*, AAPG Memoir 65, pp. 153–175.
- PEMEX-Paradigm, 2005, "Identificación y Análisis de Plays y Prospectos en el Área Bolol", Unpublished report.
- PEMEX-IMP, 2008, "Integración y Correlación de Eventos del Jurásico Superior-Cretácico en las Cuencas del Golfo de México", Unpublished report.
- PEMEX-Exxon Mobil, 2008, "Análisis Regional de Sincronía y Estilos Estructurales", *Convenio Específico de Colaboración, Estudio Conjunto en Temas Exploratorios Pemex – ExxonMobil*, Unpublished (Property of PEMEX).
- PEMEX, 2009, "Informe Final Tectónica Salina y sus Implicaciones en la Exploración Petrolera", Unpublished report.
- PEMEX, 2013, "Interpretación Sísmica-Estructural Play Fairway Yaxche-Kuzam-Bolol", Unpublished report.

- PEMEX, 2014, “Interpretación Sísmica-Estructural Play Fairway Yaxche-Kuzam-Bolol”, Unpublished report.
- Peterson, R., Hernández Peñaloza, J.J., Heyn, T., Jiménez, M., Ibáñez, D., Garza, C., Ortiz, N., Méndez, A., Zuzek, A., Peña, P., Rojas, R., 2013, “Modelo de evolución estructural para entender el desarrollo de las trampas estructurales de hidrocarburos en la zona costa afuera de la porción occidental en la sonda de Campeche, México”, *Congreso Mexicano del Petróleo*, Riviera Maya, Mexico, June 5-8, 2013, E-poster Session.
- Peterson, R., Ortiz, D., Portillo, R., Rodríguez, U., Abarca, J., Ruiz, J.C., 2017, “Eventos de deformación que formaron trampas estructurales en las Cuencas del Sureste, México”, PEMEX unpublished report.
- Pilcher R. S. et al, 2011, “Primary basins and their boundaries in the deep-water Northern Gulf of Mexico: Origin, trap types, and petroleum system implications”, *AAPG Bulletin*, Vol. 95, No. 2, pp. 219–240.
- Pindell, J. L., 1985, “Alleghenian reconstruction and subsequent evolution of the Gulf of Mexico, Bahamas, and proto-Caribbean”, *Tectonics*, Vol. 4, pp. 1–39, doi:10.1029 /TC004i001p00001.
- Pindell, J. L., Cande, S. C. W., Pitman, W. C., Rowley, D. B., Dewey, J. F., Lebreque, J. and Haxby, W., 1988, “A plate-kinematic framework for models of Caribbean evolution”, *Tectonophysics*, 155, 121–138.
- Pindell, J., and Kennan, L., 2001, “Kinematic evolution of the Gulf of Mexico and Caribbean”, in R.H. Fillon, N.C. Rosen, P. Weimer, A. Lowrie, H. Pettingill, R. L. Phair, H. H. Roberts, and B. van Hoorn, eds., *Petroleum systems of deep-water basins: Global and Gulf of Mexico experience: 21st Annual Gulf Coast Section-SEPM Foundation Bob F. Perkins Research Conference*, Houston, Texas, December 2–5, 2001, pp. 193–220.
- Pindell, J., Kennan, L., Stanek, K.P., Maresch, W.V., and Draper, G., 2006, “Foundations of Gulf of Mexico and Caribbean evolution: Eight controversies resolved”, *Geologica Acta*, Vol. 4, No. 1-2, pp. 303–341.
- Pindell, J. and Kennan, L. 2009, “Tectonic evolution of the Gulf of Mexico, Caribbean and northern South America in the mantle reference frame: an update”, *Geological Society of London, Special Publications*, 328, pp. 1-55.
- Pollard, D.D., Segall, P., 1987, “Theoretical displacements and stresses near fractures in rock: with applications to faults, joints, veins, dikes, and solution surfaces”. In: Atkinson, B.K. (Ed.), *Fracture Mechanics of Rock*. Academic Press, London, pp. 277–349.
- Pollard, D.D., Aydin, A., 1988, “Progress in understanding jointing over the past century”, *Geological Society of America Bulletin*, 100, pp.1181– 1204.
- Price, N. J., 1966, “*Fault and joint development in brittle and semi-brittle rock*”, Oxford, Pergamon Press, 176 p.

- Price, N. J. and Cosgrove, J. W., 1990, "*Analysis of geological structures*", Cambridge, Cambridge University Press.
- Rashid, F., Glover, P.W.J., Lorinczi, P., Collier, R., Lawrence, J., 2015, "Porosity and permeability of tight carbonate reservoir rocks in the north of Iraq", *Journal of Petroleum Science and Engineering*, No.133, pp. 147–161
- Renshaw, C.E., Myse, T.A., Brown, S.R., 2003, "Role of heterogeneity in elastic properties and layer thickness in the jointing of layered sedimentary rocks", *Geophysical Research Letters*, 24, doi:10.1029/2003GL018489.
- Reyer, D., Bauer, J. F. and Philipp, S. L., 2012, "Fracture systems in normal fault zones crosscutting sedimentary rocks, Northwest German Basin", *Journal of Structural Geology*, Vol. 45, pp. 38-51.
- Rezic M. and Veranina, A., 2017, "A new freeware program for the Probability of Success calculation of new gas discoveries within the Croatian part of the Po depression", *Rudarsko-geološko-Naftni Zbornik*, Vol. 32, No. 2, pp. 49-55.
- Rider, Malcom, 2002, "*The Geological Interpretation of Well Logs*", Second edition.
- Rijken, P., Cooke, M.L., 2001, "Role of shale on vertical connectivity of fractures in the Austin Chalk, Texas: application of crackbridging theory", *Tectonophysics*, 337, pp. 117– 133.
- Rijken, P., 2005, "*Modeling naturally fractured reservoirs: from experimental rock mechanics to flow simulation*", Ph.D. dissertation, University of Texas at Austin, Austin, Texas, p. 239.
- Roberts, A., 2001, "*Curvature attributes and their application to 3D interpreted horizons*", *First Break*, 19, pp. 85-99.
- Roberts, D.G., Bally, A.W., 2012, "Regional geology and tectonics of sedimentary basins: A Prologue", *in* "Regional Geology and Tectonics: Phanerozoic Passive Margins, Cratonic Basins and Global Tectonic Maps", Elsevier, pp. 0-15.
- Roca, E., Sans, M. and Koyi, H.A., 2006, "Polyphase deformation of diapiric areas in models and in the eastern Prebetics (Spain)", *AAPG Bulletin*, Vol. 90, pp. 115-136.
- Rose, P.R., 1987, "Dealing with risk and uncertainty in exploration: how can we improve?", *AAPG Bulletin*, No. 71, pp. 1–16.
- Rose, P.R., 2001, "Prospect should be portfolio fit", *AAPG Explorer* 8.
- Rowan, M.G. and Kligfield, R., 1989, "Cross section restoration and balancing as an aid to seismic interpretation in extensional terranes", *AAPG Bulletin*, 73, pp. 955-966.

- Rowan, Mark, 1993, "A systematic technique for the sequential restoration of salt structures", *Tectonophysics*, No. 228 (1993), pp.331-348.
- Rowan, M.G., Lawton, Timothy F., Giles, Katherine A., Ratliff, Robert A., 2003, "Near-salt deformation in La Popa basin, Mexico, and the northern Gulf of Mexico: A general model for passive diapirism", *AAPG Bulletin*, Vol. 87, No. 5 (May 2003), pp. 733–756.
- Rowan, M. et al., 2004, "*Gravity-driven fold belts on passive margins*", in K. R. McClay, ed., "Thrust tectonics and hydrocarbon systems: AAPG Memoir", 82, pp. 157– 182.
- Rowan, M.G., and Vendeville, B.C., 2006, "Foldbelts with early salt withdrawal and diapirism: physical model and examples from the northern Gulf of Mexico and the Flinders Ranges, Australia", *Marine and Petroleum Geology*, Vol. 23, pp. 871-891.
- Rowan, M.G., Lawton, Timothy F., Giles, K.A., 2012, "Anatomy of an exposed vertical salt weld and flanking strata, La Popa Basin, Mexico", *Geological Society, London, Special Publications* 2012, Vol. 363; pp. 33-57.
- Sagi, D.A., Arnhild, M., Karlo, J.F., 2014, "Quantifying fracture density and connectivity of fractured chalk reservoirs from core samples: implications for fluid flow", *from: Spence, G. H., Redfern, J., Aguilera, R., Bevan, T. G., Cosgrove, J. W., Couples, G. D. and Daniel, J.M. (eds), 2014, "Advances in the Study of Fractured Reservoirs"*, Geological Society, London, Special Publications, No. 374, pp. 97–111.
- Salleh, S.H., Rosales, E., Flores de la Mota, I., 2007, "Influence of different probability based models on oil prospect exploration decision making: a case from southern Mexico", *Revista Mexicana de Ciencias Geológicas*, Vol. 24, No. 3, pp. 306-317.
- Salvador, A., 1987, "Late Triassic–Jurassic paleogeography and origin of Gulf of Mexico basin", *AAPG Bulletin*, Vol. 71, pp. 419–451.
- Salvador, A., 1991a, "Introduction", *in Salvador, A., The Gulf Of Mexico Basin: Boulder, Colorado, Geological Society of America, The Geology of North America*, v.J.
- Salvador, A., 1991b, "Triassic–Jurassic", *in Salvador, A., ed., The Gulf of Mexico Basin: Boulder, Colorado, Geological Society of America, The geology of North America*, v. J, pp. 131–181.
- Sánchez-Montes de Oca, R., 1980, "Geología Petrolera de la Sierra de Chiapas", *AMGP Bulletin*, Vol. 31, Issues 1-2, pp. 67-77.
- Sánchez, R., Cruz, M. Á., Reyes, E., López, H. G., Peterson, R., Flores, J. C., Ramirez R., and Barrera, D., 2011, "Tectonic evolution of the South Gulf Salt Province in the Gulf of Mexico", *Gulf Coast Association of Geological Societies Transactions*, Vol.. 61, pp. 421–427.

- Sandwell, D. T., Müller, Smith, W. H. F., Garcia, E. and Francis, R., 2014, "New global marine gravity model from CryoSat-2 and Jason-1 reveals buried tectonic structure", *Science*, Vol. 346, pp. 65–67, doi: 10.1126/science.1258213.
- Sans, M., and Vergés, J., 1995, "Fold development related to contractional salt tectonics, southeastern Pyrenean thrust front, Spain", in M. P. A. Jackson, D. G. Roberts, and S. Snelson, eds., *Salt tectonics: a global perspective: AAPG Memoir 65*, p. 369-378.
- Sans, M.R. and Koyi, Hemin, 2001, "Modeling the role of erosion in diapir development in contractional settings", *Memoirs-Geological Society Of America*, Vol. 193, pp. 111-122.
- Santamaria Orozco, D.M., 2008, "La Formacion del Petroleo en el Sur del Golfo de Mexico: Prediccion de su calidad", *Academia de Ingenieria de Mexico*, Available from: <http://www.ai.org.mx/presentacion/la-formaci%C3%B3n-del-petr%C3%B3leo-en-el-sur-del-golfo-de-m%C3%A9xico-predicci%C3%B3n-de-su-calidad>.
- Schmoker, J.W., Krystinik, K.B., Halley, R.B., 1985, "Selected characteristic of limestone and dolomite reservoirs in the United States", *AAPG Bulletin*, Vol. 69, Issue 5, pp. 733-741.
- Schwade, I.T., 1967, "Geologic quantification: description → numbers → success ratio", *AAPG Bulletin*, No. 51, pp. 1225–1239.
- Shackleton, J. R., Cooke, M. L. and Sussman, A. J., 2005, "Evidence for temporally changing mechanical stratigraphy and effects on joint-network architecture", *Geology*, Vol. 33, pp. 101–104.
- Selley R., 1998, "*Elements of petroleum Geology*", 2nd edition, USA, Academic Press.
- Sinclair, S.W., 1980, "Analysis of Macroscopic Fractures on Teton Anticline, NW Montana", M.S. Thesis, Dept. of Geology, Texas A&M University, College Station, Texas, 102 pp.
- Smart, K. J., Ferrill, D.A., Morris, A. P., 2009, "Impact of interlayer slip on fracture prediction from geomechanical models of fault-related folds". *AAPG Bulletin*, Vol. 93 (11), pp. 1447–1458.
- Stearns, D. W., 1968, "Certain aspects of fracture in naturally deformed rocks", in: NSF Advanced Science Seminar in Rock Mechanics, Special Report AD66993751, edited by R. E. Riecker, pp. 97–118, Air Force Cambridge Res. Lab., Bedford, Mass.
- Stearns, D.W., Friedman, M., 1972, "Reservoirs in fractured rocks", *AAPG Memory*, Vol. 16, pp. 82-100.
- Stern, R., Dickinson W. R., 2010, "The Gulf of Mexico is a Jurassic back-arc basin", *Geosphere*; Vol. 6; No. 6; pp. 739-754.

- Stewart, S.A., 1999, "Geometry of thin-skinned tectonic systems in relation to detachment layer thickness in sedimentary basins", *Tectonics*, Vol. 18, pp. 719-732.
- Suardana, M., Samodra, A., Wahidin, A., Sule, M.R., 2013, "Identification of Fractured Basement Reservoir Using Integrated Well Data and Seismic Attributes: Case Study at Ruby Field, Northwest Java Basin", *Search and Discovery Article*, No. 20195, Adapted from extended abstract prepared in conjunction with poster presentation at AAPG Annual Convention and Exhibition, Pittsburgh, Pennsylvania, May 19-22, 2013.
- Suppe, John, 1985, "*Principles of Structural Geology*", New Jersey, Prentice-Hall, Inc.
- Thomas, A. L., 1993, "Poly3D: a three-dimensional, polygonal-element, displacement discontinuity boundary element computer program with applications to fractures, faults, and cavities in the Earth's crust", MSc. thesis, Stanford University, California.
- Tuncay, K., Park, A., Payne, D., Ortoleva, P., 2003, "3D fracture network dynamics in reservoirs, faults and salt tectonic systems", *In* Ameen, M. (ed.) *Fracture and In-Situ Stress Characterization of Hydrocarbon Reservoirs*, Geological Society, London, Special Publications, Vol. 209, pp. 155-175.
- Twiss, R. J. and Moores, E. M., 1992, "*Structural Geology*", New York, W. H. Freeman & Co.
- Underwood, C.A., Cooke, M.L., Simo, J.A., Muldoon, M.A., 2003, "Stratigraphic controls on vertical fracture patterns in Silurian Dolomite, northeastern Wisconsin", *American Association of Petroleum Geologists Bulletin*, 87, pp.121– 142.
- Valdes, C., Villanueva Rodriguez, L. L., and Caballero Garcia, E., 2009, "Geochemical integration and interpretation of source rocks, oils, and natural gases in Southeastern Mexico", *in* Bartolini, C. and Roman Ramos, J.R., eds., *Petroleum systems in the Southern Gulf of Mexico: AAPG Memoir*, Vol. 90, pp. 337– 368.
- Van der Pluijm, B. and Marshak S., 2004, "*Earth Structure, Second Edition*", New York, W. W. Norton & Company, Inc.
- Watkins, H., Butler, R. W. H., Bond, C. E. and Healy, D., 2015, "Influence of structural position on fracture networks in the Torridon Group, Achnashellach fold and thrust belt, NW Scotland", *Journal of Structural Geology*, Vol. 74, pp. 64-80.
- Watkins, H., Butler, R. W. H., Bond, C. E. and Healy, D., 2018, "Implications of heterogeneous fracture distribution on reservoir quality; an analogue from the Torridon Group sandstone, Moine Thrust Belt, NW Scotland", *Journal of Structural Geology*, Vol. 108 (2018), pp. 180-197.

- Watson, P., 1998, "A process for estimating geological risk of petroleum exploration prospects", *APPEA J*, No. 34, pp. 577–583.
- Wennberg, O. P., Svana, T., Azzizadeh, M., Aqrabi, A. M. M., Brockbank, P., Lyslo, K. B. and Ogilvie, S., 2006, "Fracture intensity vs. mechanical stratigraphy in platform top carbonates: the Aquitanian of the Asmari Formation, Khaviz Anticline, Zagros, SW Iran", *Petroleum Geoscience*, 12, pp. 235-245.
- White, D.A., 1993, "Geological risking guide for prospects and plays", *AAPG Bulletin*, No. 77, pp. 2048–2061.
- Winker, C. D., and Buffler, R. T., 1988, "Paleogeographic evolution of early deep-water Gulf of Mexico and margins, Jurassic to Middle Cretaceous (Comanchean)", *AAPG Bulletin*, Vol. 72, pp. 318–346.
- Woodward, N.B., Boyer, S.E. and Suppe, J., 1985, "*An outline of balanced cross-sections*", University of Tennessee Dept of Geological Sciences, Studies in Geology, 11, (2nd edition.), 170 pp.
- Xiubin, L., Hanlin, Ch., Xiaogan, Ch., Zhongyan, S., Shufeng, Y., Ancheng, X., 2010, "Conceptual models for fracturing in fault related folds", *Mining Science and Technology*, Vol. 20, pp. 103-108.
- Zaldivar Ruiz, J., 1998, "*Filosofia de la Metodologia de la Orientacion del Fracturamiento en nucleos no orientados*", Instituto Mexicano del Petroleo.
- Zhou, H., Hu, H., Zou, Z., Wo, Y., Youn, O., 2018, "Reverse time migration: A prospect of seismic imaging methodology", *Earth-Science Reviews*, 179, pp. 207–227.
- Ziesch, J., Tanner, D.C., Krawczyk, Ch.M., 2019, "Subseismic pathway prediction by three-dimensional structural restoration and strain analysis based on seismic interpretation", *AAPG Bulletin*, Vol. 103, No. 10, pp. 2317–2342.